Biological and Medical Physics, Biomedical Engineering

Jiyuan Tu
Kiao Inthavong
Goodarz Ahmadi

# Computational Fluid and Particle Dynamics in the Human Respiratory System

Springer

# BIOLOGICAL AND MEDICAL PHYSICS, BIOMEDICAL ENGINEERING

For further volumes:
http://www.springer.com/series/3740

# BIOLOGICAL AND MEDICAL PHYSICS, BIOMEDICAL ENGINEERING

The fields of biological and medical physics and biomedical engineering are broad, multidisciplinary and dynamic. They lie at the crossroads of frontier research in physics, biology, chemistry, and medicine. The Biological and Medical Physics, Biomedical Engineering Series is intended to be comprehensive, covering a broad range of topics important to the study of the physical, chemical and biological sciences. Its goal is to provide scientists and engineers with textbooks, monographs, and reference works to address the growing need for information.

Books in the series emphasize established and emergent areas of science includingmolecular, membrane, and mathematical biophysics; photosynthetic energy harvesting and conversion; information processing; physical principles of genetics; sensory communications; automata networks, neural networks, and cellular automata. Equally important will be coverage of applied aspects of biological and medical physics and biomedical engineering such as molecular electronic components and devices, biosensors, medicine, imaging, physical principles of renewable energy production, advanced prostheses, and environmental control and engineering.




For other titles published in this series, go to
www.springer.com/series/3740

Jiyuan Tu • Kiao Inthavong • Goodarz Ahmadi

# Computational Fluid and Particle Dynamics in the Human Respiratory System

Springer

Jiyuan Tu
School of Aerospace
Mechanical and Manufacturing Engineering
RMIT University
Bundoora, Victoria
Australia

Goodarz Ahmadi
School of Engineering
Clarkson University
Potsdam, New York
USA

Kiao Inthavong
School of Aerospace
Mechanical and Manufacturing Engineering
RMIT University
Bundoora, Victoria
Australia

ISSN 1618-7210
ISBN 978-94-007-4487-5 ISBN 978-94-007-4488-2 (eBook)
DOI 10.1007/978-94-007-4488-2
Springer Dordrecht Heidelberg London New York

Library of Congress Control Number: 2012943581

*Prof Tu wants to dedicate this book to the memory of his father who died from lung cancer, and to his mother who has suffered from asthma for last 60 years. He would like to express his gratitude to his wife, Xue for her support and his son, Tian who has provided proofreading to this manuscript.*

*Dr. Inthavong would like to dedicate this book to his wife Laura for her encouragement, unconditional support, and fruitful discussions. He is grateful to his family, and friends who provided curious discussion and support and in particular his parents, Korm, and Bounma, and Jackie and Nino (for their proofreading). Also thanks to the Phal Des, and the students and staff from Royal University of Phnom Penh for their support during the time spent there writing.*

*Prof Ahmadi would like to dedicate this book to his mother and memory of his father for their unconditional love and sacrifices. He also would like to express his thanks to his daughter, Anahita Williamson and his son Amir G. Ahmadi for their support. Thanks are also given to Mrs. Barbara Bady for her proofreading of some of the chapters of the manuscript.*

# Preface

The study of the respiratory airway to understand its physiology has been limited to those in the medical fields. On the other hand computational fluid dynamics (CFD) was only used by academics, and engineers to model high speed flows in the aerospace industry. These two fields are important components in the study of inhalation toxicology, surgical and medical treatment, and respiratory drug delivery, and this has only been possible through the emergence of advanced technologies in medical imaging, and computers. CFD is a research and development tool that has infiltrated many non-engineering fields and has now advanced to a point where CFD can enhance health science research and facilitate biotechnology development. In particular when we deal with particles such as pollutants and medical aerosols or drug powders, and model it in conjunction with the flow we have what is referred to as Computational Fluid and Particle Dynamics (CFPD).

When a newcomer to this field first uses a CFD software package, the intuitive graphical user interface, along with automatic meshing and solution techniques can lead the user to have a false sense of capability. In fact, there is a steep learning curve to reach competency in CFD modeling alone, and for newcomers interested in CFPD in the respiratory airways, added dimensions of complexity are included. Under the glossy user interface, there are a large number of interconnected numerical algorithms that are processing during each simulation and with each click of a mouse button the user should understand its consequences.

The purpose of this book is to provide suitable information pitched at the right level of assumed knowledge of students and newcomers to CFD from a variety of backgrounds such as medicine, physiology, health science, pharmaceutical, engineers (chemical, mechanical) and scientists. It is not expected that an undergraduate student would have attained the entire breadth of knowledge from all disciplines involved with respiratory modeling, and therefore this book provides an important link between traditional engineering fields with the medical field. Therefore whatever background the reader has, this text will provide some new knowledge that is important for CFPD respiratory modeling.

Unlike many CFD books out on the market, the descriptions of the fundamental mathematical ideas are provided with the appropriate language, description and backed up with worked examples. This ensures that the reader is not overwhelmed

by advanced mathematical notation and theory. Having said this, the book assumes that the reader has fundamental grasp of calculus (i.e basic anti- and differentiation knowledge). A unique feature of this book is intuitive and systematic structure which aims at enhancing the learning process and allowing students to quickly use CFPD in practice. It is hoped that this approach will allow newcomers to quickly and effectively setup accurate and reliable CFPD simulations.

The book begins with an introduction in Chap. 1 to provide an overview of CFPD, its advantages and its numerous applications in the respiratory system. It aims to initiate curiosity and stimulate creativity for the reader to think of possible solutions to their own respiratory flow problems.

In Chap. 2 the human respiratory system is introduced in a concise and practical approach. This chapter is particularly important for those from non-medical backgrounds as it provides the basic description of the anatomy and physiology. This understanding serves as a basis for the computational fluid flow setup. There is also a focus on the geometry and its variations that may be encountered which provides the reader with some guidelines in geometry reconstruction based on scanned images of the respiratory organs.

Reconstruction of the conducting airways from scanned images is discussed in Chap. 3 which introduces the reader to different disciplines including biomedical imaging, manufacturing or reverse engineering, and CAD fields. The process is explained from what types of scanned images are available (MRI or CT scans) through to segmentation and finally model reconstruction. Important features such of each process and a clear informative description is given with practical advice in terms of what software are available.

After a geometric model has been created a computational mesh is applied to the model and this is presented in Chap. 4. This is by far the most challenging, very important and most visited stage in any CFPD problem as it is often the cause of many solution convergence problems. Generating a quality mesh requires as much creativity as it does technical knowledge. And therefore in this chapter we aim to provide practical information and guidelines to the reader so that they may begin experimenting and jumping into meshing models straight away, rather than get too bogged down in the difficult mathematical algorithms for meshing. Different types of mesh and its setup for common geometries as well as for the respiratory organs are shown.

Chapter 5 introduces the reader to the governing equations of fluid flow, namely the Navier-Stokes equations. Each term in the equations is described so that the reader can fully appreciate and understand its impact on the flow simulations. This includes the transport equation idea which describes the *local acceleration, convection*, and *diffusion*. Worked examples are given to help consolidate this understanding of links between mathematical terms and physical meanings. A gentle introduction to turbulence and its modelling is also given, which is not normally provided in this type of book. However we feel that it is important given that respiratory flows will no doubt exhibit some form of turbulent flow structures. A summary of different turbulence models is given with practical guidelines on setting up the near wall modelling, turbulence model selection, mesh creation, and boundary conditions.

The description of particles moving in a flow domain is described in Chap. 6. We introduce two modelling approaches, namely the Lagrangian and Eulerian approaches. An important focus of this chapter is to describe how the dynamics of particles are represented and how they are related to the fluid flow in the context of the numerical set of equations. It is expected that the reader is able to conceptualise the fluid-particle dynamics and its interactions. This will form a solid foundation for the interested student who wishes to explore further the exciting and interesting field of multiphase flows.

Chapter 7 describes how the equations that describe fluid and particle flows can be located (or applied) onto the mesh nodal points under a process called *discretisation.* The basic numerical breakdown of the equations and its solution methods are presented and to reinforce the student's learning we present worked examples for many classical flow cases such as diffusion equation, convection-diffusion equation, and Ordinary Differential Equations (ODEs). Finally some techniques on post processing are given which involves converting the raw data into graphical representations.

The final two chapters present the applications and examples of CFPD and how it is used for respiratory flows. The examples in Chap. 8 are case studies that demonstrate typical modelling strategies and how basic principles, theories and numerical techniques presented in previous chapters for various CFPD problems in the complex human respiratory system. Chapter 9 explores the future trends and more advanced modelling techniques. While the detailed treatment of these advanced techniques are beyond the scope of this book, it is hoped that the chapter will stimulate further excitement in the advancing capability and innovative use of CFPD for the human respiratory airways.

Jiyuan Tu
Kiao Inthavong
Goodarz Ahmadi

# Acknowledgments

The authors are grateful to the Springer, and Tobias Schwaibold in particular, for reviewing, endorsing, and supporting the idea of this book, and to Aldo Rampioni, who took over the project for a smooth completion. The authors like to thank their research students and fellows worked and working in the CFD Group at RMIT and in the Turbulence and Multiphase Flow Laboratory at Clarkson for contribution. Special thanks are given to Danny Q. J. Ge who has provided many worked examples in geometric modelling, CFD meshing and nano-particle simulations into this book. The collaboration between two geographically distant colleagues was made possible by a Fulbright Senior Scholarship to Prof Jiyuan Tu from The Australian-American Fulbright Commission and an International Visiting Fellowship to Prof Goodarz Ahmadi from RMIT-Foundation. It is also grateful to Australian Research Council (ARC) for providing an Australian Postgraduate Award to Mr Kiao Inthavong whose PhD thesis provides the basis results for case studies in this book, and thereafter for awarding an Australian Postdoctoral Fellowship to Dr Kiao Inthavong, allowing him to continue contributing to this book.

Finally, to those that the authors have failed to mention but have been involved in one way or another, the authors would like to take this opportunity of expressing their deepest appreciation.

# Contents

# Chapter 1
# Computational Fluid and Particle Dynamics (CFPD): An Introduction

## 1.1 What is CFPD

*Computational Fluid and Particle Dynamics* (CFPD) is an emerging research field that involves interdisciplinary research areas with a broad range of applications. Fluid-particle flows can be found all around us, from the airborne particles we breathe to industrial applications such as fuel spray in internal combustion engines, fluidised bed combustors, and mineral processing to name a few. In the health, pharmaceutical, and biomedical fields, interest is increasing in the use of computational modelling for inhalation toxicology analysis, effectiveness of drug delivery systems, respiratory and physiological flows. Computational modelling is being used in many industries as a valuable tool for cost and cycle time reductions during product development, and it can provide proof of concept for model designs. This technique has been encouraged by the rapid developments in computational models to reflect the physics, which is in line with the increase in computing power.

From an elementary viewpoint, CFPD can be seen as an extension of the well-known and established *Computational Fluid Dynamics* (CFD) knowledge, with additional modelling requirements to reflect the particle dynamics within the fluid flow (Fig. 1.1). The "*Computational*" of CFD refers to the study of the fluid flow represented by *mathematical* equations, which are solved using computer programs or software packages. The term "*Fluid Dynamics*" encompasses both the study of fluids either in motion (fluid in dynamic mode) or at rest (fluid in stationary mode). However, it is particularly dedicated to the former, fluids that are in motion—in their dynamic state.

The evolution of CFD can be traced back to its development within the high technology aerospace/aeronautical industries, which has forged the way to today's CFD. In its early beginnings, the models accounted for one and only one single fluid that is in motion. Today we see advances in CFD modelling for flows that often include at least a secondary phase which are commonly referred to as *multiphase flows*. For example, simulation of dust inhalation will involve a primary phase, air, and the secondary phase, the solid dust particle. Modelling for these types of flows can also involve chemical reactions (e.g., coal combustion, steam production from boiling water) or non-chemical reactions (e.g., granule flow). This book covers the

J. Tu et al., *Computational Fluid and Particle Dynamics in the Human Respiratory System,* Biological and Medical Physics, Biomedical Engineering,
DOI 10.1007/978-94-007-4488-2_1, © Springer Science+Business Media Dordrecht 2013

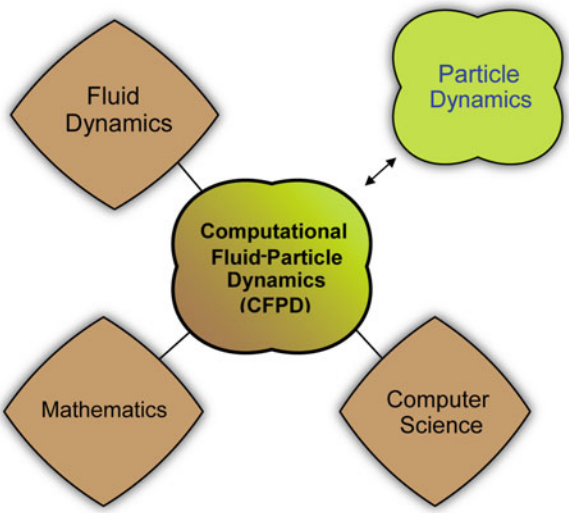


**Fig. 1.1** The addition of *particle dynamics* with other disciplines to make-up the multi-disciplinary CFPD

computational modelling of fluid-particle flows and the interactions between the two phases within the respiratory system.

## 1.2 Advantages of CFPD

The exponential growth in computing power, advancements in technology, and materialisation of interdisciplinary research has seen CFPD emerge within the last few decades as a practical tool in modern engineering practice. The costs of computing have decreased dramatically and new paths of theoretical development are being realised, which could not have been possible without the computational approach.

Computational modelling is also becoming a staple in research and development (R&D) in practical engineering and product design and in academic research. The computational results complement the experimental and analytical approaches by providing a cost-effective alternative to simulating real fluid flows. For example, the visualisation capabilities such as vectors and contours of computational models are extremely useful in describing the physics that occur in observed flow results in experiments. CFPD can be used to assist in precise prediction of fluid-particle flow behaviours, particularly for drug particle delivery and inhalation toxicology where experimental methods are naturally invasive and often difficult to perform. CFPD is an emerging tool that offers the ability to solve a range of complicated flow problems that the analytical approach cannot handle.

Finally, one major advantage of CFPD is the ability to simulate fluid-particle flows that are not reproducible in any experimental tests. This is especially significant in the medical and pharmaceutical fields where invasive experimental setups that deal with

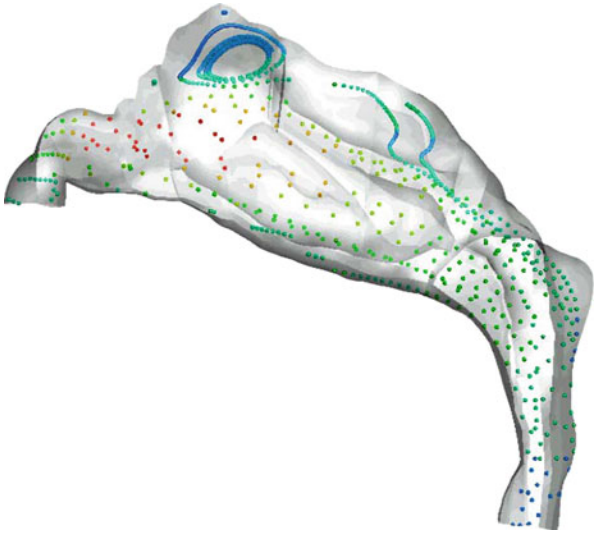

**Fig. 1.2** Spherical particle motion during inhalation in the left chamber of the nasal cavity

human subjects are difficult to undertake. For example, during normal respiration, inhaled air often contains foreign particles such as dust, fumes and general pollutants (Fig. 1.2). In addition, drug delivery via the nose and mouth involves drug particles suspended in the airflow. These flow behaviours of normal respiration and drug delivery can be simulated using the CFPD approach, which is indeed much safer and easier to perform than experimenting on a live human subject.

Nevertheless, the suggestion here is not that CFPD will replace experimental testing but rather will serve as a viable alternative that complements experimental methods. For example, the frontiers of CFPD research are still in a primitive state of development, and newly developed models rely on experimental data as validation for such topics as complex multiphase flows including drug powder aggregation or deaggregation, chemical reactions, and particle breakup. With the recent increased interest in this field, more capabilities and physics will be attainable. By using CFPD models through CFD software packages, visualization of numerical solutions using vectors, contours, or animated movies of unsteady flows can have a significant impact on delivering solutions to respiratory research problems. Some of the aims of this book are to introduce to the reader the current research trends and to enable the reader to understand and be able to make the right decisions when setting up the CFPD models. In particular, new users often encounter incorrect numerically produced flow characteristics that could have been wrongly interpreted as acceptable physical phenomena. Numerical results obtained must always be thoroughly examined before they are accepted. Therefore, the new user needs to learn how to properly analyse and judge the computed results.

## 1.3 CFPD and CFD Applications in the Respiratory System

### *1.3.1 CFPD as a Research Tool*

One of the many uses of CFPD is to reveal the physical nature of the interactions of particles in a fluid around and within designated objects. Fluid and particles are transported through a domain by many physical processes including dissipation, diffusion, convection, boundary layers and turbulence. The capabilities of CFPD are vast and while great advancements have been made there still remains a large undeveloped territory. CFPD, analogous to wind-tunnel and laser-photography particle analysis, can be employed as a *research tool* to perform numerical experiments in order to better understand the physical nature of the fluid-particle dynamics. By performing these numerical experiments, advanced models can then be developed to increase the capabilities of the computational modelling. One area of high level research activity is in the areas of atomization and sprays which are also applicable for the drug delivery devices. Models are being developed to account for the complex nature of atomization which involves a liquid phase breaking up into small droplets, which in turn experience further breakup and collisions or coagulation.

Figure 1.3 shows a snapshot in time of the unsteady atomization of a spray close to the nozzle region, which is referred to as the primary breakup. The flow structures reveal that the liquid exits the nozzle with a wave-like energy and atomizes into small droplets downstream. Following the primary breakup, the small droplets experience further atomization, which is referred to as the secondary breakup. This example illustrates how CFPD can provide detailed visualisation to better understand the observed flow structures and some important physical aspects of the fluid-particle flow, similar to a real laboratory experiment. More importantly, the simulations complement the experiments not only providing qualitative comparison but also a means to interpret some basic phenomenological aspects of the experimental condition.

In addition to the theoretical research into the fundamental physics, numerical experiments may be performed on problems that are difficult to perform experimentally. This may involve particle tracking and deposition, and particle size distributions that are involved with chemical species (heliox inhalation, see Sandeau et al. (2010), porous media (nasal hairs), non-Newtonian fluids (blood flow), and moving body problems (lung expansion/contraction). These problems highlight the capabilities of the CFPD as a non-invasive technique to study the human respiratory system.

### *1.3.2 CFPD and CFD as a Training Tool*

Traditional users of CFD had been limited to academic researchers at a graduate or post-graduate level who were developing their own computational code in pursuit of code development and applications. Nowadays, as CFD becomes a cornerstone of engineering practice, many engineers without any post-graduate education are

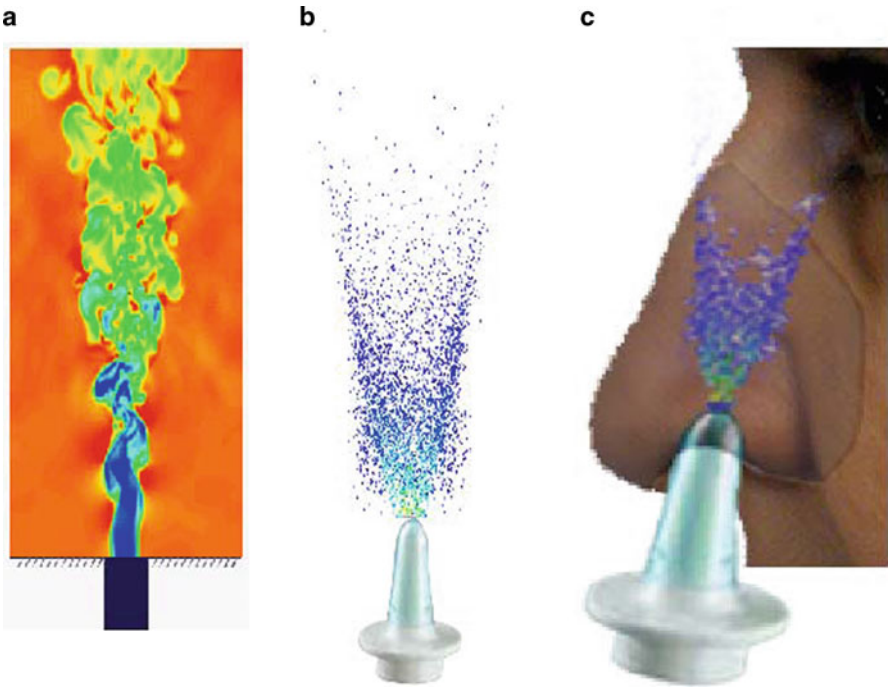


**Fig. 1.3** The atomization of a spray using. **a** the volume-of-fluid model for the near nozzle spray breakup. **b** The discrete phase model for tracking individual particles as primary atomization (secondary break-up). **c** Application of CFPD for nasal spray drug delivery

often expected to use it. This has led many engineering and science undergraduate courses to include CFD as part of their curriculum. Fortunately, the increase in the number of available CFD software in the market has been reflected by the same rapid development in interest and technology.

The authors believe that new users who take a hands-on approach to CFPD will progress rapidly in understanding fluid-particle dynamics, especially through the visualisation tools which work extremely well in conjunction with experimental labs. In addition, the use of CFPD modelling opens up new teaching methods (virtual surgery, 3D animation), and classes of problems such as human anatomy studies and the physiology of inhalation and respiration. Research has shown that the use of computational simulations increases learning efficiency and understanding (Kirkpatrick and Willson 1998; Wankat 2002) and provides an effective method for novel hands-on learning in combined physical and computational laboratories (Regan and Sheppard 1996).

Furthermore computational models can provide new training methods for medical students by virtual surgery, or virtual anatomy. Hands-on training for surgical procedures has obvious obstacles that can impede on learning. Virtual anatomy can contribute towards this learning by providing the three-dimensional models of the

anatomy that can be manipulated visually to convey the concepts. Surgical procedures can be made virtually, and then its effect on fluid flow patterns through the anatomy can be analysed. The surgeon therefore can make a more informed decision on the surgical procedure as well as devising a more effective post surgery recovery plans. One final advantage of the virtual anatomy and surgery (although not technically a training tool), is that communication between medical practitioners and the patient and their family will be improved through the visually demonstrating the anatomy and why surgery is or is not needed.

### *1.3.3 Respiratory Health Risk Assessment*

The inhalation of particles often causes adverse health problems. Increased levels of air pollution through urbanisation, by-products of industrial waste, and poor indoor air quality in the home and workplace are some contributors responsible for the increases in respiratory diseases. These may include allergies, sinusitis, bronchitis, pulmonary emphysema, asthma, alveolitis, lung cancer, and nasal cancer. Recently cases of mesothelioma and asbestosis have emerged in the public sphere where mining and building industries are being sued by affected workers. Because the symptoms of asbestos-related diseases are slow to develop and may only occur 20 years after the initial exposure, this example highlights the importance of respiratory health risk assessments.

Particle inhalation studies for respiratory health risk assessment using CFPD primarily deals with predictions of particle deposition. More importantly the local deposition sites (where the particles deposit) play a central role in health effect assessments (Schlesinger and Lippmann 1978) and the prediction of lung cancer development (Balashazy et al. 2003). Many respirable particles exist in the ultrafine size range ($d_p < 0.1$ μm) where they have been found to be more toxic than larger particles of the same material (Oberdörster et al. 2005). As such there has been a lot focus on ultrafine particle deposition in the lung airways (Hofmann et al. 2003; Longest and Xi 2007; Zhang et al. 2005a). CFPD studies in the lung airways may be traced back to the establishment of a single, representative lung model by Weibel (1963) and the models of Horsfield et al. (1971). These models lay the foundation for many early studies into particle deposition in the lung airways using computational and experimental approaches. The use of CFPD studies of the nasal cavity and extrathoracic airways began later than those of the lung airways and included the early work by Elad et al. (1993) who used a simplified model. A more realistic model was then studied by Keyhani (1995). Ultrafine particle deposition in the nasal cavity includes nanoparticle deposition (Wang et al. 2009; Zamankhan et al. 2006). It should be noted that the later developments of nasal cavity studies are largely due to the advancements in biomedical instrumentation and image processing techniques, where high resolution CT and MRI scans have allowed computational reconstruction of realistic models.

Furthermore, risk assessments are especially important during infectious disease outbreaks. Take, for example, the recent spate of acute epidemic outbreak of influenza

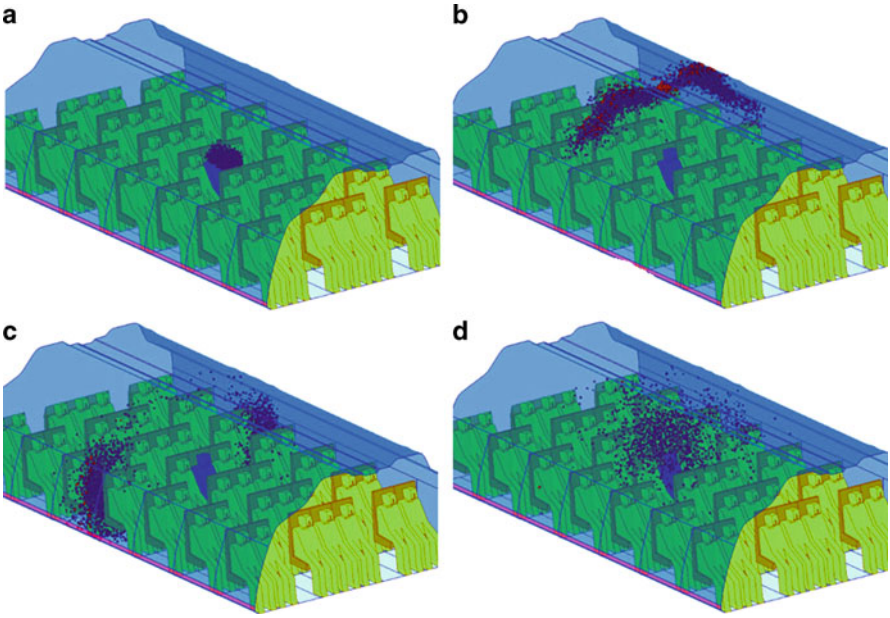


**Fig. 1.4** Cough droplet dispersion inside an aeroplane cabin. (Image courtesy of Prof Qingyan Chen, Purdue University)

such as the bird flu, SARS, and more specifically the H1N1 swine flu. With more people travelling by air than ever before, pathogens can move farther, faster and in greater numbers. During the H1N1 outbreak during March and April of 2009, international air travellers departing from Mexico unknowingly transported a novel influenza (H1N1) virus to cities around the world (Khan et al. 2009). CFPD methods were used to trace cough droplets and their spread within a cabin as a result of the cabin's air circulation and any cabin crew movement (Fig. 1.4), which allowed a prediction of which passengers were exposed to the cough droplets. As part of risk assessment and management, such tracking of the pathogens within the cabin during flight (Zhang et al. 2009) enabled authorities to identify those passengers at risk and to place them in quarantine.

### *1.3.4 Pulmonary Drug Delivery*

Pulmonary drug delivery has traditionally been used for the treatment of respiratory ailments such as asthma and cystic fibrosis. Research in this area has increased due to a number of factors including a rise in respiratory illnesses, the ability to deliver proteins and peptides, and the lung's large absorptive surface area that enables optimum bioavailability. Having said this, the physiology of the lung is not designed for systemic drug absorption but for gas exchange. The lung's defence mechanisms by either physical or mucosal clearance or breakdown by macrophages and enzymes

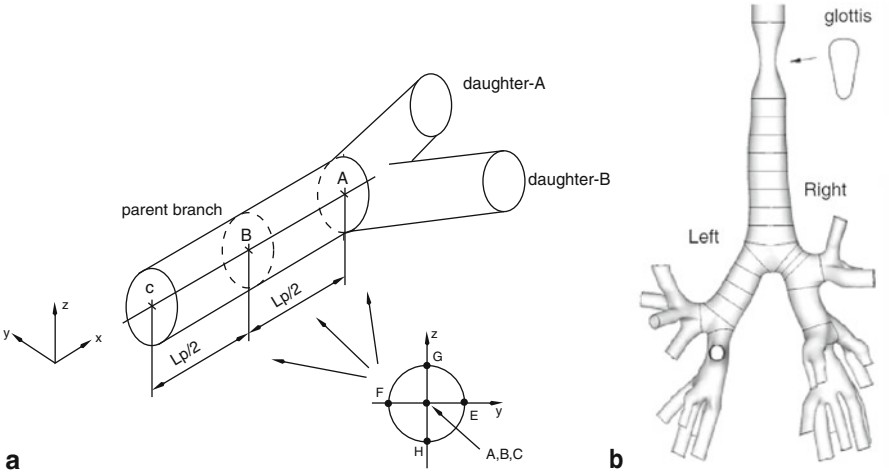


**Fig. 1.5** **a** Early computational model of the bronchial bifurcation model. (Image from Balashazy and Hofmann 1993) and **b** A more recent computational model of the tracheobronchial airway tree. (Image from Xi et al. 2008)

need to be overcome for effective drug delivery. The delivered drug is usually introduced through the mouth via an atomizing delivery device. For asthma treatment these devices can be a dry powder inhaler, metered dose inhaler, or nebuliser. The drug particle is released from the device and must pass through the oral cavity, pharynx, upper airways, and preferably reach the deep lung.

The main obstacle in pulmonary drug delivery is its efficacy. Inefficient drug delivery can arise, owing to excessive particle aggregation in an inhaler, early deposition in the mouth and throat, and overly rapid particle removal from the lungs by mucocilliary or phagocytic clearance mechanisms (Edwards et al. 1998), making it difficult to prolong a residence time to allow an effective drug release. The search for more effective delivery methods has been a long-time motivation for research in this pulmonary drug delivery. From a CFPD perspective, the drug delivered into the mouth involves a secondary phase material (e.g. drug particles, liquid drops, or a gaseous mixture) transported by the primary phase, air. The modelling involves many disciplines of science including the atomization of the drug formulation, fluid-particle dynamics during the particle trajectory, and finally a chemical related diffusion process at the alveolar epithelium during final absorption. CFPD studies of pulmonary drug delivery can be divided into three categories: (1) deposition in the airways, (2) drug morphology and (3) delivery device. Firstly, deposition studies in the airways (Fig. 1.5) have focussed on the local lung airway region, advancing from a single symmetrical lung airway bifurcation (Balashazy and Hofmann 1993) to a tracheobronchial airway tree up to 16 generations (Choi et al. 2007; Xi et al. 2008; Zhang et al. 2008a). Often airflow and particle data upstream of the trachea are studied separately from the tracheobronchial airway tree. This includes studies of fluid-particle flows in the mouth-throat (Jayarajua et al. 2008; Mitsakou et al. 2007).

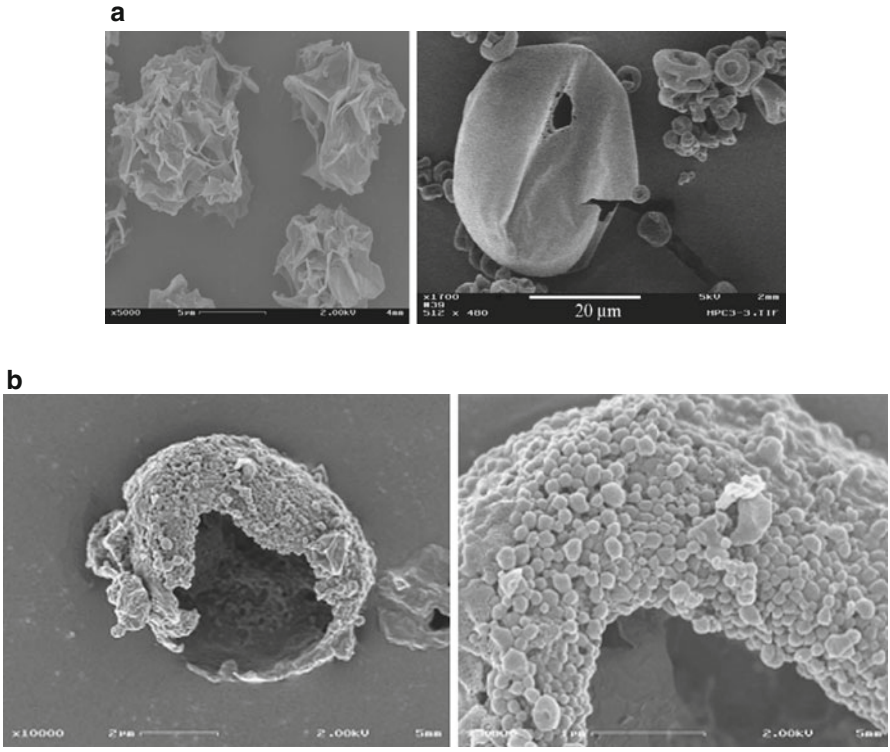


**Fig. 1.6** Scan electron microscope images of pulmonary drug particles using **a** large, porous particles. (Courtesy of Nicolas Tsapis at Laboratoire de Pharmacie Galénique) and **b** porous nanoparticle-aggregate particle PNAPs. (Image from Sung et al. 2009)

Secondly, drug particle morphology also plays an extremely important role in the aerodynamic behaviour. Edwards et al. (1998) discusses the potential for increasing particle size but lowering the particle mass density in order to achieve large porous particles, which have less tendency to agglomerate than convectional small nonporous particles. Nano and ultrafine particles, including nanofibres, have also been cited as a potential for site specific drug delivery because of their ability to enhance drug absorption, traffic through tissues and target cells (Gelperina et al. 2005). However, for pulmonary delivery, problems, such as stability of nanoparticles after preparation and high diffusion leading to early deposition in the mouth and throat, need to be overcome. Targeting capability is influenced by particle size, surface charge, surface modification, and hydrophobicity—characteristics which need to be considered in the particle physics. Porous nanoparticle-aggregate particles (PNAPs) (Fig. 1.6) are another approach which combines the aerodynamic flight ability of micron-scale porous particles with the composition of biodegradable nanoparticles that delivers the nanoparticles effectively to the lungs (Sung et al. 2009). As you will see later in Chap. 5, the particle size and, to a lesser extent, density plays a significant role in a particle's trajectory.

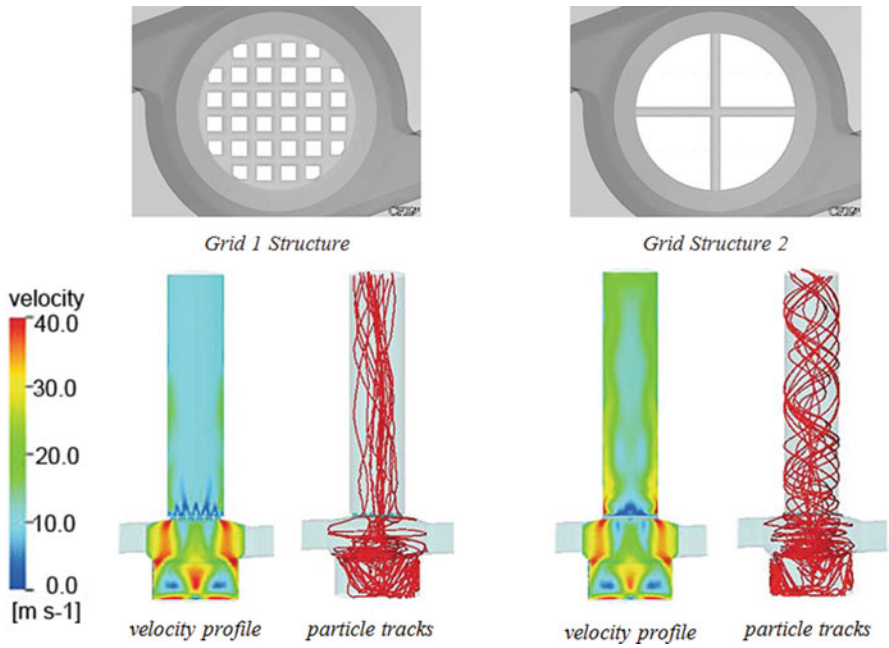


**Fig. 1.7** Effect of design on the performance of a dry powder inhaler using CFD. (Images from Coates et al. 2004)

Finally, as a further example of CFPD application for pulmonary drug delivery we present some recent research for an inhaler design. Coates et al. (2004) investigated the effects of modifying the design of the inhaler grid of a dry powder inhaler on the device performance. A variety of modelling methodologies may be used to evaluate the performance of the device and assist in characterising the dose concentration, dose variation and particle dispersion. Figure 1.7, adapted from the work by Coates et al. (2004), shows the velocity contours and particle tracks generated from two different inhaler grid configurations. The presence of the inhaler grid straightened the flow and reduced the level of swirl generated in the device. Particle tracking allows the frequency and location of particle impactions for the two different grid cases to be determined.

### *1.3.5 Nasal Drug Delivery*

Research activity in nasal drug delivery has historically lagged behind pulmonary drug delivery. Today, however, there is as much interest and development in the nasal route for delivery of systemic drug formulations such as peptide and protein drugs. Its attraction is due to the large surface area of the nasal cavity that allows drug absorption. The walls are highly vascularised and the venous blood (deoxygenated

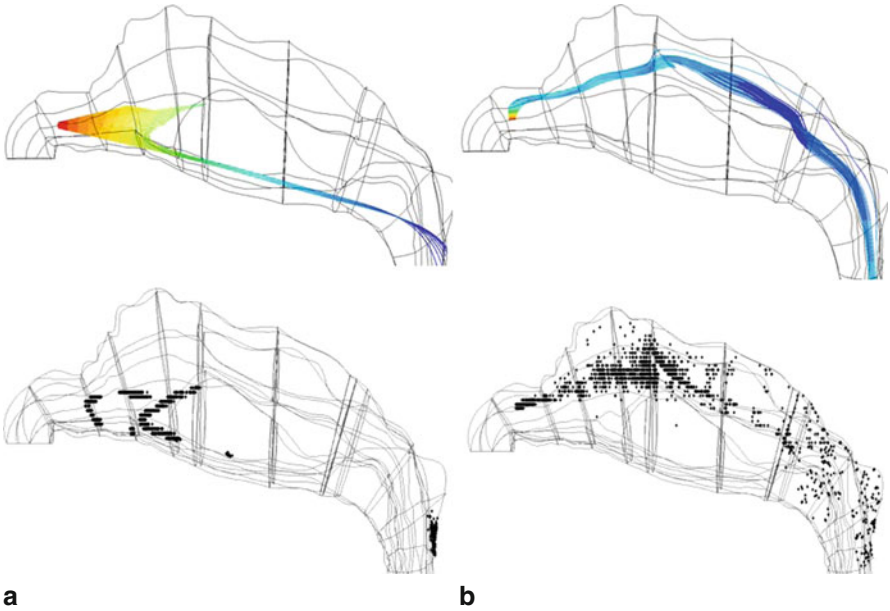


**Fig. 1.8** Particle trajectories shown by the *coloured lines* and deposition sites shown by *dots* for **a** 50 µm particles at a horizontal insertion and **b** 10 µm particles at vertical insertion. (From Inthavong et al. 2006b)

blood returning back to the heart) from the nose passes directly into the systemic circulation leading to a rapid onset of action from the initial drug absorption. This has further advantages, including avoiding loss of drug by first-pass metabolism in the liver, fewer side effects, painless compared to injections, and the drug may even be delivered directly to the brain along the olfactory nerves (Oberdörster et al. 2004).

Similar to lung airways, the physiological function of the nose is for respiration as well as olfaction. The nose's unique geometry has defence mechanisms to prevent foreign particles from entering into the main nasal passage. Experimental studies have found that particle deposition from nasal sprays primarily occurs in the anterior third (up to the nasal valve region) of the nasal cavity (Cheng et al. 2001; Newman et al. 1998). CFPD research can be used in conjunction with experiments to better understand the particle dynamics and final deposition in the nasal cavity. As an example, we present the particle trajectories and deposition sites for 50 and 10 µm particles released inside the nasal cavity at different directions that may be achieved by the nasal spray design. The visualisation in Fig. 1.8 shows that a horizontal insertion angle (90°) for 50 µm provides later deposition at the back of the nasopharyngeal region. Although 10 µm particles deposit more readily in the middle turbinate regions of the nasal cavity, their transport beyond the nasopharynx leads to undesirable deposition in the lungs.

The fate of each particle released from specific points was achieved by individually tracking the particle's trajectory through the nasal cavity. The deposition patterns

can be recorded and visualised through CFPD which helps to guide a pragmatic engineering design of the spray device or lead to better instructions for patients applying the spray (i.e. insertion at different angles, deeper insertion etc.). Published work in this area includes that of Kimbell et al. (2007) who investigated the deposition fractions of 20 and 50 μm particles from a nasal spray.

### *1.3.6 Therapies for Sleep Apnoea*

Sleep apnoea is a sleeping disorder characterised by repeated pauses in breathing of at least 10 s throughout sleep (an apnoea event) caused by an upper-airway obstruction in the pharyngeal region. This stops breathing, and the brain reacts by briefly waking the subject in order to re-open the airways and allow breathing to restart. In severe cases, a person may experience upto 600 apnoea events per night while for less severe cases the obstruction is only partial, and the airflow limitation is called hypo-apnea (Huupponen et al. 2009). In either case it has a significant impact on health, quality of life, and productivity. Symptoms during the night include loud snoring, choking or gasping during sleep (to get air into the lungs), and loss of sleep while long-term consequences contribute to excessive daytime sleepiness, weight gain, depression, irritability, high blood pressure, heart attack and stroke (Kiely and McNicholas 2000).

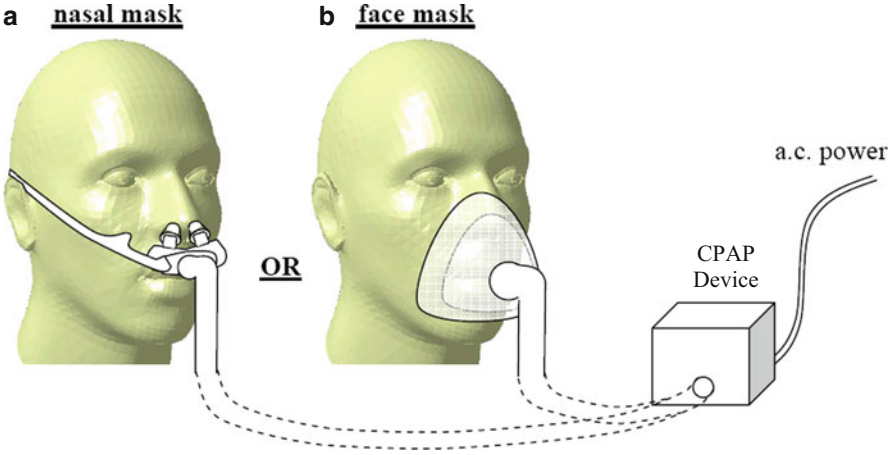


**Fig. 1.9** Nasal plug and nasal mask types of CPAP devices

The main treatment for obstructive sleep apnoea (OSA) is Continuous Positive Airway Pressure, or CPAP, (see Fig. 1.9) which can be used for the management of mild and severe OSA. The airway obstruction is relieved due to the positive intraluminal pressure, produced by the CPAP device, which overcomes the collapsing pressure of the upper airway.

A steady volumetric flow rate is delivered into the airway through a nasal mask. The pressure difference between the expansion of the lung and the ambient air induces

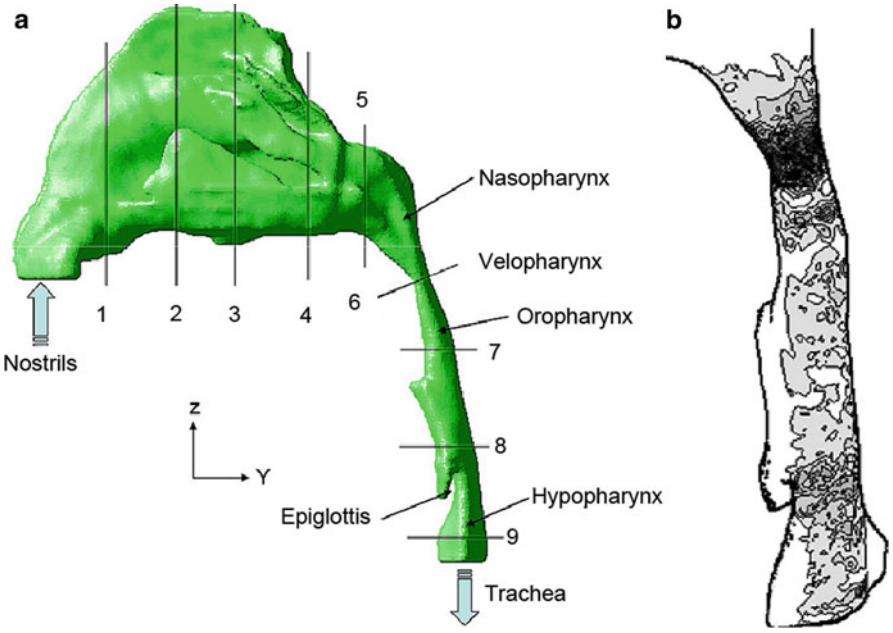


**Fig. 1.10** **a** Lateral view of the nasal cavity and pharynx with nine representative sections. **b** Shear force contour. (Image taken from Jeong et al. 2007)

the airflow into the respiratory system. When the mask is placed over the face the new pressure difference relieves the obstruction in the pharynx, reducing and/or preventing the apnoeas. Compliance with CPAP has been reported to range between 46 % and 90 % (Krieger 1992; Reeves-Hoche et al. 1994). Up to about 50 % of patients gave up the treatment because of some minor side effects, such as rhinitis, nasal bridge sores, discomfort, abdominal bloating, and claustrophobia. One common complaint made by patients is that the CPAP pressure is too high, leading to the discomfort (Polo et al. 1994) prior to sleep onset and increased expiratory effort as well.

Computational studies can provide detailed information about the flow characteristics in the pharynx area. For example, numerical measurements inside the nasal cavity can identify regions of discomfort which can help future designs of CPAP devices. These measurements allow an evaluation of the CPAP device to determine whether the effects on the airflow are beneficial for preventing OSA. This can lead to improved treatment therapy planning, cost-effectiveness of diagnosis and treatment, and patient use of CPAP devices. In addition, CFD studies in the pharyngeal region can also help in presurgical planning, for irreversible therapies such as tracheostomy or pharyngeal surgery. As an example a study into the flow characteristics that are produced by obstructive sleep apnea is shown (Jeong et al. 2007) which provides insight into the pathophysiology of the obstructive sleep apnea (OSA) disease (Fig. 1.10). The results found that the flow in the pharyngeal airway of patients with OSA comprises a turbulent jet formed by area restriction at the velopharynx—the region in between the nasopharynx and the oropharynx as shown in Fig. 1.10. This turbulent jet causes higher shear and pressure forces in the vicinity of the velopharynx,

and it can be deduced that the most collapsible area in the pharyngeal airway of OSA patients is the velopharynx where minimum intraluminal pressure and maximum aerodynamic force lie.

### *1.3.7 Studies in the Acinus and Olfactory Regions*

Gas exchange during respiration and the process of olfaction, the primary functions of the nose, are often difficult to assess experimentally. Respiration occurs in the distal regions of the lung called the acinar airways where the gas exchange takes place within the alveoli (Fig. 1.11). However, inhaled particles transported in the alveolar region of the lung are important for possible health risks or as a therapeutic inhaled drug therapy. Olfaction takes place in the upper regions of the main nasal passage within the nasal cavity, and this can lead to translocation of inhaled ultrafine particles to the brain. In this section we present some CFPD results in the literature firstly for the acinar airway, then for olfactory uptake.

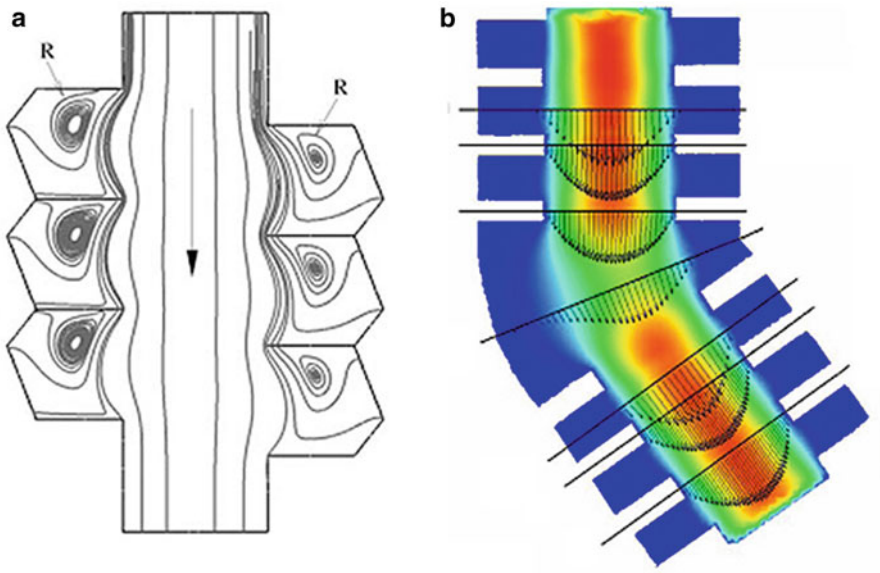


**Fig. 1.11** **a** 3D flow structure inside a geometry of a honeycomb-like alveolar duct (Re = 1.0). Image taken from Kumar et al. (2009). **b** Velocity field in the symmetry plane of an alveolar duct bend from the work of van Ertbruggen et al. (2008) for Re = 0.07

While the alveoli are normally depicted as little spheres or hemispheres attached to terminal ends of the lung airways, they have actually been modeled as densely-packed hollow polyhedron (Fung 1988; Mead et al. 1970). Some CFPD results are given in (Fig. 1.12) which include that of Kumar et al. (2009) which used a flexible-walled honeycomb-like polygonal geometry to examine the fluid flow under rhythmic breathing. The results show the flow structure dominated by the presence

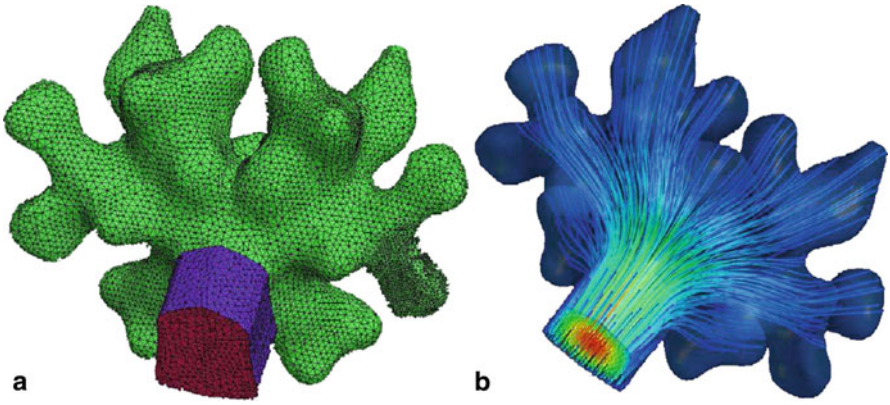


**Fig. 1.12** **a** Schematic representation of the pulmonary acinus with three-dimensional alveolar sacs. **b** Streamlines of velocity field magnitude, obtained at peak inspiration ($t = 0.1$ s) in the alveolar sac geometry. (Images taken from Sznitman 2008)

of a developing recirculation region within the cavity extending up to the third acinar generation. (van Ertbruggen et al. 2008) modelled the flow within a 3D alveolated bend which found that the presence of the alveolar cavities had a minimal effect on the main flow occurring in the central duct. Sznitman (2008) also developed a three-dimensional subregion of an entire pulmonary acinus, consisting of an acinar space-filling geometry, to study respiratory convective flows. The results also showed recirculation patterns, along with radial flows.

Although the primary function of the nose is to detect smells through olfaction, studies of olfaction uptake have shown that translocation of inhaled ultrafine particles to regions of the brain can take place through deposition on the olfactory mucosa (Elder et al. 2006; Oberdörster et al. 2004). The effects on the central nervous system by this neuronal translocation is uncertain; however it does open up the idea that drug delivery direct to the central nervous system is possible through airborne ultrafine particles depositing on the olfactory mucosa and translocating via the olfactory nerves. Some CFPD results found in the literature are presented here. Zhao et al. (2004) evaluated the degree to which variations in critical nasal areas, such as the olfactory slit and nasal valve, affected odorant transport (Fig. 1.13). The results showed that indeed the anatomical changes in the olfactory region (upper meatus below the cribriform plate) and the nasal valve region strongly affect airflow patterns and odorant transport through the olfactory region, with subsequent effects on olfactory function.

### *1.3.8 Assistance to Nasal Surgery*

Nasal surgery is a common procedure whether it is for cosmetic or remedial purposes. It may be performed to improve breathing, correct congenital or acquired deformities, repair nasal injuries, or to change the size or shape of the nose for cosmetic purposes.

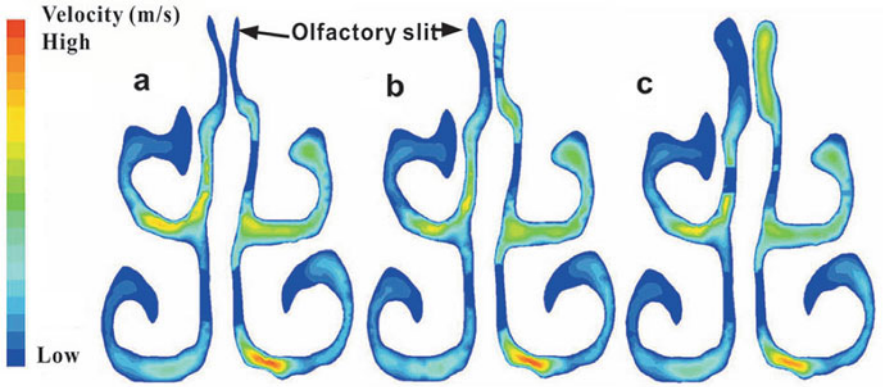


**Fig. 1.13** Contour plot of velocity magnitude on the coronal plane 6.2 cm from the tip of the external nares with varying olfactory slits. **a** Narrowed olfactory slit. **b** Original airway model generated from CT scans. **c** Widened olfactory slit. Total airway volume change in each of the modifications < 5 %. (Figure taken from Zhao et al. 2004)

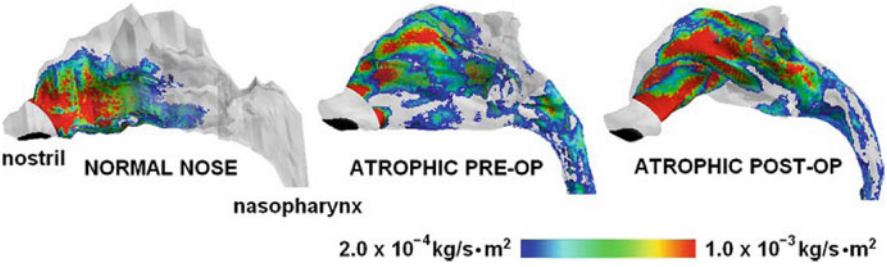


**Fig. 1.14** Results taken from Garcia et al. (2007b) showing regions of the nasal mucosa where the water flux per unit area exceeds $2 \times 10^{-4}$ kg/(s m$^2$) for pre- and post-surgery of an atrophic nose compared with a normal nose. Only the left cavity and the nasopharynx are shown

In any case, the use of computational models is beneficial to complement the standard rhinometric measurements because detailed changes in local airflow patterns, air conditioning and odorant uptake ability are not captured by rhinometry. The many advantages in using computational modeling as a tool for 'virtual surgery' include the ability to explain the surgical procedure and its predicted outcome to the patient and family members; better visualization which allows the doctors to be more confident in planning the surgery; and evaluation of the potential physiological performance of the nose based on the 'virtual surgery' which facilitates a more effective post-surgical treatment plan.

This section provides two examples of pre- and post-op studies of the nose. Garcia et al. (2007b) studied the air conditioning ability of a nose suffering from atrophic rhinitis pre- and post-surgery. The results of water flux at the inner nasal walls in a normal-, atropic pre-op, and atrophic post-op nose are shown in Fig. 1.14. The results

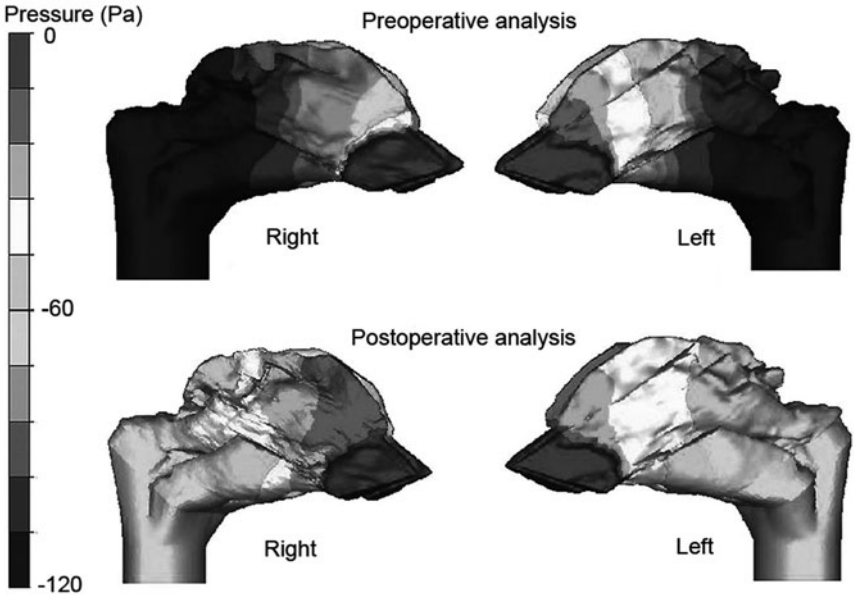


**Fig. 1.15** Pressure distributions of a nasal cavity in the preoperative. (affected by partial lateral turbinectomy) and postoperative models. (Image taken from Ozlugedik et al. 2008)

suggest that high water fluxes were more spread out in the atrophic nose, with high concentrations occurring at the superior nasal cavity and on the proximal aspect of the middle turbinate (bony intrusions in the nasal cavity—see Chap. 2 for anatomical descriptions). The results also provide a deeper insight into the pathology of atrophic noses.

Ozlugedik et al. (2008) presented a virtual surgery study to compare the aerodynamic characteristics of pre- and postoperative nasal cavity that had concha bullosa and septal deviation. Virtual septoplasty and partial lateral turbinectomy were performed on this model to generate the second postoperative model in Fig. 1.15. A general drop in the maximum airflow velocity and a significant reduction in the total nasal resistance were found. These two examples show the value of virtual surgery as a tool for preplanning in order to understand the consequences of surgical procedures on the airflow patterns, change in pressure drop and resistance, and heat and mass flux for the air conditioning ability of the nose.

## 1.4 Summary

The use of a computational approach to study human respiration and particle inhalation has been largely driven by the exponential growth in computing power, advancements in technology, and materialisation of interdisciplinary research to

provide CFPD as a practical tool in modern engineering applications. One major advantage of significance to the medical and pharmaceutical industries is the ability to simulate fluid-particle flows that are difficult to reproduce experimentally. For example clinical testing of human respiration of gases and particles is quite invasive and can be detrimental to a person's health and indeed a CFPD approach can provide a simpler alternative. A large number of examples have been presented which demonstrate the use of computational fluid and particle dynamics as an educational and research tool in many biomedical applications such as human respiration, drug delivery, and assistance to surgical procedures.

The use of CFPD in biomedical applications is indeed multi-disciplinary, incorporating the fundamentals of CFD (computational science, mathematics, fluid dynamics) with particle science and human anatomy and physiology. This leads to the question as to whether we actually require the expertise of five specific people—one from each discipline—to come together for the development of a biomedical simulation. The answer is obviously not. More likely, this field will require a person to obtain some knowledge subsets from each discipline. Therefore, this book is written to equip the reader with the necessary background material for an understanding of both the internal workings of a CFD code and its successful operation and its application to the human respiratory system. In the next chapter, we begin by presenting the anatomy and physiology of the human respiratory system which serves as a base for developing the CFPD simulation settings. The primary aim is to summarise the important features of respiration and how it will be incorporated into the final computational model.

## 1.5 Review Questions

1. How does CFPD differ from CFD?
2. What four disciplines does CFPD derive from?
3. What are some of the advantages of using CFPD?
4. What are the limitations and disadvantages of using CFPD?
5. How can CFPD be used as a training tool in medicine?
6. How can CFPD be used for evaluating the toxicology of inhaled particles?
7. What advantages does CFPD hold over experiments, in obtaining these results?
8. What are some applications of CFPD in the biomedical field?

# Chapter 2
# The Human Respiratory System

## 2.1 Introduction

Before delving into the computational methods of reconstructing the respiratory models, we first discuss the respiratory system from a functional point of view. In addition, descriptions, locations, geometry, and naming conventions for the anatomical parts are discussed in order to establish a basis for decision-making when reconstructing the model. This chapter provides the fundamentals of the anatomy and physiology of the respiratory system and may be skipped if the reader has an established background in this field.

The primary function of the respiratory system is gas exchange. Oxygen (which we need for our cells to function) from the external environment is transferred into our bloodstream while carbon dioxide (a waste product of cellular function) is expelled into the outside air. The billions of tissue cells in our body lie too far from the inhaled air to exchange gases directly, and instead blood circulates the oxygen to the cells. This occurs during each breath we take where oxygen first enters the nose or mouth during inhalation. The air passes through the larynx and the trachea which then splits into two bronchi. Each bronchus bifurcates into two smaller branches forming bronchial tubes. These tubes form a multitude of pathways within the lung and terminating at the end with a connection to tiny sacs called alveoli. The exchange of gases takes place at the alveoli, where oxygen ($O_2$) diffuses into the lung capillaries in exchange for carbon dioxide ($CO_2$). Exhalation begins after the gas exchange and the air containing $CO_2$ begins the return journey through the bronchial pathways and back out to the external environment through the nose or mouth. Secondary functions of the respiratory system include filtering, warming, and humidifying the inhaled air. This includes the vocal cords in the larynx for sound production, lungs for control (or homeostasis) of body pH levels, and the olfactory bulbs in the nose for smell.

The respiratory system can be separated into regions based on function or anatomy (Fig. 2.1). Functionally there is the conducting zone (nose to bronchioles), which consists of the respiratory organs that form a path to conduct the inhaled air into the deep lung region. The respiratory zone (alveolar duct to alveoli) consists of the alveoli and the tiny passageways that open into them where the gas exchange takes

J. Tu et al., *Computational Fluid and Particle Dynamics in the Human Respiratory System,* Biological and Medical Physics, Biomedical Engineering,
DOI 10.1007/978-94-007-4488-2_2, © Springer Science+Business Media Dordrecht 2013

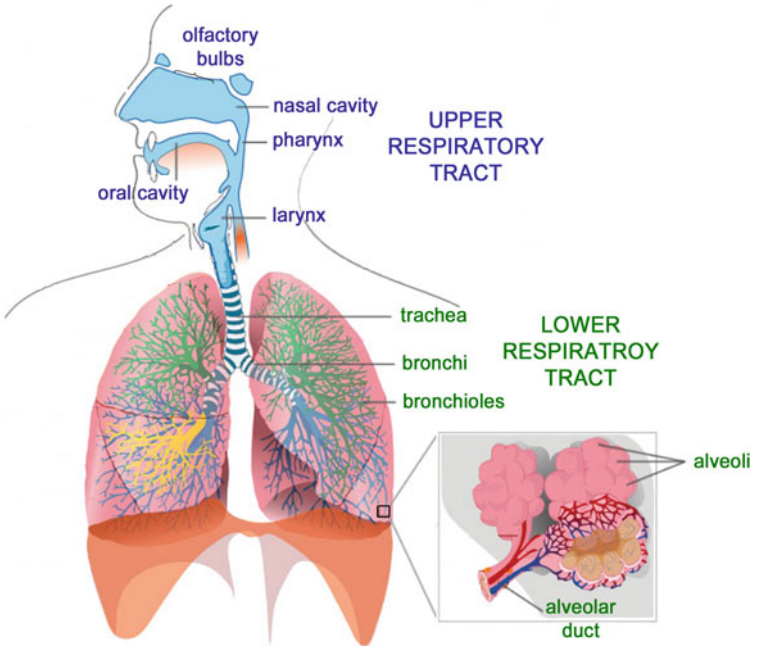


**Fig. 2.1** Schematic of the respiratory system displayed by the upper and lower respiratory tract region

place. Anatomically, the respiratory system can be divided into the upper and lower respiratory tract. The upper respiratory tract includes the organs located outside of the chest cavity (thorax) area (i.e. nose, pharynx, larynx), whereas the lower respiratory tract includes the organs located almost entirely within it (i.e. trachea, bronchi, bronchiole, alveolar duct, alveoli). In the next section, the individual respiratory organs are discussed.

## 2.2 Nose and Nasal Cavity

### *2.2.1 Anatomy of the Nose and Nasal Cavity*

The human nose differs in its anatomy and morphology between different racial and ethnic groups. Therefore, the following anatomical description is a generalisation and inter-racial variations exist. For completeness, structures that have synonyms are followed by their alternate names in parentheses and italicised. Structurally the nose can be divided into the external portion which is in fact termed as the nose and the internal portions being the nasal cavities (*nasal fossae; cavum nasi*). The nose is the only visible part of the respiratory system, protruding from the face, and lying

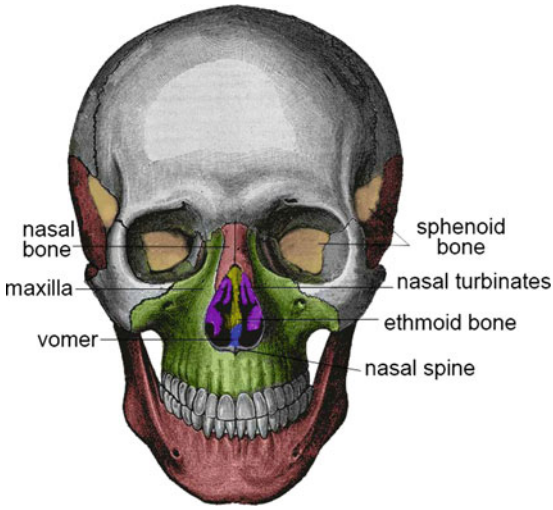


**Fig. 2.2** Skeletal structure of the human skull showing the nasal cavity and the supporting facial bones

in between the forehead and the upper lip. It is made up of a bony section and a cartilaginous section. The bony section is located in the superior half and contains a pair of nasal bones sitting together side by side, separated in the middle and fused posteriorly by the medial plates of the cheekbones (*maxilla bones*) (Fig. 2.2).

The cartilaginous section is located in the inferior half, consisting of flexible cartilages in the anterior, caudal portion of the nose (Fig. 2.3). The cartilages are connected to each other and to the bones by a tough fibrous membrane. At the base

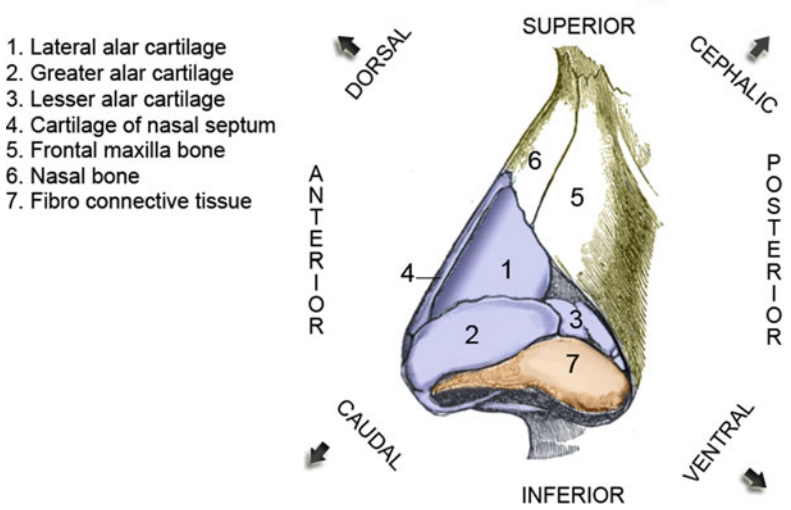


**Fig. 2.3** Lateral view of the external nose showing the cartilage and bone structure. Terminology for the anatomical directions is also given

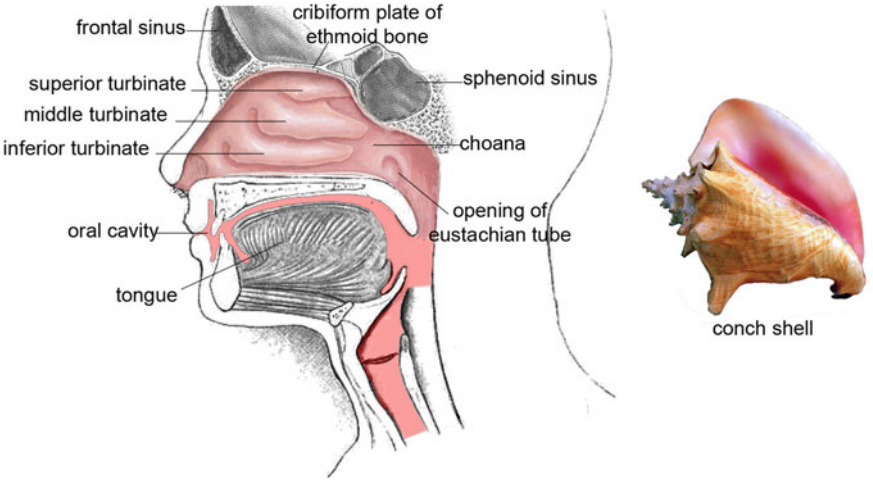


**Fig. 2.4** Structure of the internal nasal cavity. The turbinates are also referred to as concha because of its resemblance to a conch shell

of the nose are two openings called the nostrils (*anterior nares*, sing. *naris*) and are separated by nasal septum cartilage (*columna*). The nostrils are a portal for air and particulates to enter the nasal cavity. Its shape can be very elliptical to circular varying between people from different ethnicity and race.

Air enters the nasal cavity through the nostrils, which opens with a slight dilation into an enclosed area called the vestibule. It is enclosed by the greater alar cartilage and extends as a small recess toward the apex of the nose. The two nostril openings and consequently the two vestibules leading to two nasal chambers or cavities are separated by the septum. The anterior septum is primarily made of cartilage (*hyaline cartilage*) but posteriorly is composed of the vomer bone and the perpendicular plate of the ethmoid bone. It is a common occurrence for the septum to be deviated and in severe cases this can lead to nasal dysfunction requiring surgical procedures. The top of the nasal cavity is divided from the anterior cranial cavity by the cribiform plate of the ethmoid bone and the sphenoid bone. The cribriform plate is perforated with many small openings that allow the olfactory nerve branches that are responsible for the sense of smell to extend through to the brain. The lateral walls abut on either side with the maxillary bones, and the floor of the nasal cavity is separated from the top of the mouth by the palatal bones.

From the vestibule the air passes through a constricted cross-sectional area which has been termed the anterior nasal valve, before entering the main nasal passage. In each cavity there are three passageways (superior, middle, and inferior meati; singular, *meatus*) within the main nasal passage, formed by three corresponding curled bony plates that project medially into the main passage way from the septum wall, called the superior, middle and inferior nasal turbinates or conchae (so-called as they are shaped like a conch seashell, Fig. 2.4). At the posterior end of the main nasal

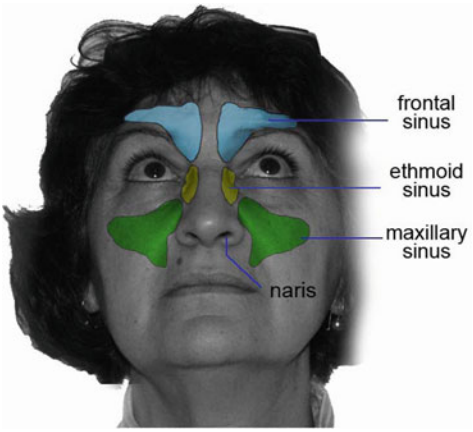


**Fig. 2.5** Frontal view of a human face showing the locations of the paranasal sinuses: frontal, ethmoid, and maxillary sinuses

passage are the oval-shaped orifices of the posterior nares, (*choanae*) approximately 1.5–3.0 cm in diameter. The choanae are openings that allow air to pass from the main nasal passage, into the nasopharynx. Once air has passed through the posterior nares, it has left the nasal cavity and enters the next major segment of the upper respiratory tract—the pharynx (Fig. 2.5).

The paranasal sinuses are four pairs of empty air spaces that open or drain into the nasal cavity. They are located in the frontal, sphenoid, ethmoid, and maxillary bones and as such their names are taken from where they are located. The frontal sinuses are located just above the orbit (eye sockets) and don't develop until around the age of seven. The maxillary, the largest of the sinuses extends laterally (into the maxilla) on either side of the nose and is present at birth and grows with the body's development. The sphenoid sinuses lie in the body of the sphenoid bone, deep in the face just behind the nose. This sinus does not develop until adolescence. The ethmoid sinuses are not single large cavities but rather a collection of small air pockets, located around the area of the bridge of the nose. This sinus is also present at birth, and grows with development.

### *2.2.2 Physiology of the Nose and Nasal Cavity*

The nose and its internal nasal cavity provides a passageway for the air to pass through to the lungs, warms and moistens (humidifies) the inhaled air, filters and cleans the inhaled air from any foreign particles, resonates sounds for speech, and houses the olfactory receptors for smell. At the entrance of the nasal cavity in the vestibule region, the surface wall is made up of stratified squamous epithelium (same as the external skin) which contains sebaceous glands, and nose hairs (*vibrissae*), serving to filter out inhaled particulates. In the main nasal passage the walls are lined with **respiratory mucosa**. This is made up of a pseudo stratified ciliated

columnar epithelium surface containing interspersed goblet cells that sits atop a lamina propia. The serous glands produce and deliver to the surface a watery fluid containing anti-bacterial enzymes while the mucous glands and goblet cells secrete a slimy, semi-sticky liquid called mucous. Approximately 125 mL of respiratory mucous (*sputum*) is produced daily which forms a continuous sheet called a 'mucous blanket'. The mucous traps any inhaled particulates such as dust, and bacteria, while the antibacterial enzymes destroy the particulates. The ciliated epithelium cells have cilia on their surface which are fine microscopic hair-like projections. These cilia move back and forth in a rhythmical movement (*mucociliary action*) which transport the secreted mucous blanket from the nasal cavity to the throat where it is swallowed into the digestive system. This movement occurs at a rate of about 1–2 cm/h. The respiratory mucosa in the turbinates has a thick, vascular and erectile glandular tissue layer which is subject to tremendous erectile capabilities of nasal congestion and decongestion, in response to the climatic conditions and changing needs of the body. This affects the flow resistance due to the airway passages narrowing or expanding. Near the roof of the nasal cavity in the region from the superior nasal concha and the opposed part of the septum at the olfactory region, the mucosa changes, having a yellowish colour and the epithelial cells are columnar and non-ciliated. This surface is referred to as the **olfactory mucosa** and it contains the sensory receptor cells for smell detection. The cells form the nerves that then pass through the cribiform plate to the olfactory centres within the brain.

**Heating and conditioning** of the inspired air occurs through a network of thin-walled veins that sits under the nasal epithelium. The superficial location and abundance of the blood vessels causes a natural heat transfer process to the colder inspired air. The turbinates that protrude into the main passage increases the mucosal surface area to enhance the heating and conditioning of the inspired air. The mucous walls are also supplied with sensory nerve endings, which trigger a sneeze reflex when it comes into contact with inhaled particles. The nose is also supplied by nerves capable of detecting pain, temperature and pressure. The surrounding sinuses lighten the skull, and also act as resonating chambers for speech. Each paranasal sinus is lined with the same respiratory mucosa found in the main nasal passage and therefore has the same heating and air conditioning capabilities. Particles can also be trapped by the mucous secretions produced in the sinuses which continually flow into the nose by the ciliated surface. In addition blowing of the nose helps to drain the sinuses.

**Smell** is another function of the nose. Sensory activity is transmitted via branches of the olfactory nerve, which cross the roof of the nasal cavity through the cribiform plate of the ethmoid bone. During the course of breathing the nasal cavity geometry can be affected by the **nasal cycle**. This physiologic phenomenon which has been reported in more than 80 % of normal individuals (Keay et al. 1987), is an important consideration when a patient undergoes a CT or MRI scan since the scan is an instant snapshot in time of the nasal cavity's physiological state. It also has a significant effect on the airflow through the nasal passage. The nasal cycle is defined

as a cyclic fluctuation in congestion and decongestion of the nasal venous sinusoids ranging over a period of 30 min to 6 h. Airflow through the nasal cavity is normally asymmetrical, where one nasal passage (left or right) is dominant. This asymmetry is referred to as the nasal cycle which is a result of congestion (swelling) of the erectile tissue (cavernous tissues of the mucosa) in one nasal cavity while at the same time decongestion (shrinking) occurs to the erectile tissue in the other cavity. The airflow through the each nasal cavity is then governed by the resistance caused by the cross-sectional area of each airway. The changes in nasal resistance associated with the nasal cycle are not always regular, and the term nasal cycle may be a misnomer, as there is little evidence to indicate a regular periodicity to the changes in nasal resistance (Eccles 1996). The functional role of the nasal cycle is not exactly known but some hypothesis include: a contribution towards respiratory defence during nasal infection (Eccles 1996); and increased contact of inspired air with the mucosa since there is increased airflow through a decongested airway which provides increased levels of turbulence (Lang et al. 2003).

### *2.2.3 Nasal Cavity Variations and Diseases*

Variations and diseases in the human anatomy are vast and this section introduces the reader to some of the possible variations to the nasal cavity that has an effect on the air and particle respiration. This theme is carried throughout the subsequent sections on variations and diseases of the other parts of the respiratory pathway (pharynx, larynx, and tracheobronchial and lung airway).

There have been a large number of studies indicating that morphological variation of the human nose is found among populations from different eco-geographical locations through adaptation to climate (Franciscus and Long 1991a). For example, in cold or dry environments the nose has a large external protrusion, small constricted nostrils, and is tall and narrow (*leptorrhine nose*). The nasal cross-sectional area is smaller to facilitate heat and moisture exchange (Carey and Steegmann 1981). For hot or moist environments, the nose has a small external protrusion, large flaring nostrils, and is short and broad (*platyrrhine nose*) in comparison to leptorrhine noses. The cross-sectional area is greater which reduces the heat transfer during exhalation (Seren and Seren 2009).The nasal index, which compares the width of the base of the nose with the height of the nose, (e.g. Index = (width $\times$ 100)/height) is used as a way to determine the nose type. A low index ($< 70$) indicates a narrow nose and is considered as leptorrhine, and a high index $> 85$ is considered platyrrhine. In between 70 and 85 the nose is considered messorhine. Other morphological differences include differences between males and females, and also one's age (child, adult, elderly) (Fig. 2.6).

Nasal obstruction is the term used for any increased resistance to the airflow that is experienced by a person. The sensation is subjective and can occur from the

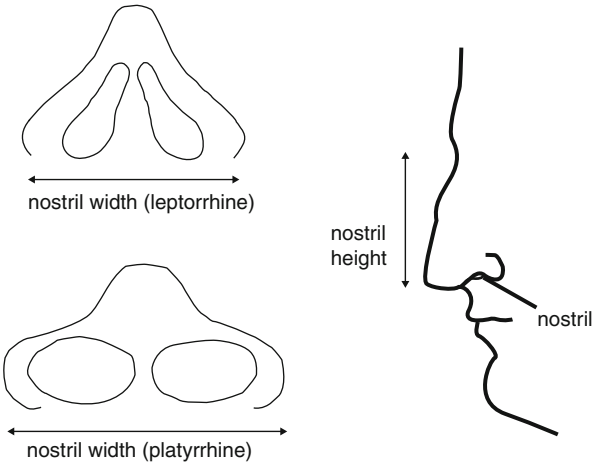


**Fig. 2.6** Nasal width and height definition used for the nasal index definition. Typical nostril shape for leptorrhine and platyrrhine shaped nostrils are also shown

natural nasal cycle or by sinonasal pathologies. Some common sino-nasal pathologies include:

- deviated septum—where the septum has severely deviated from the midline;
- nasal polyps—abnormal growth of tissues projecting from the mucous membrane in the nasal sinus;
- turbinate/mucosa hypertrophy—increase in the volume of the turbinate/mucosa due to inflammation or abnormal development.

On the other hand atrophic rhinitis is a disease that causes an increase in the nasal airway passageway due to the destruction of the nasal structures such as the nasal mucosa, turbinate bones, and any nerve endings attached to the nose, from a decreased blood supply. A similar occurrence, but caused by human intervention, is empty nose syndrome in which there is an increase in the nasal passageway caused by the over-zealous resection of the turbinates during surgery (Fig. 2.7).

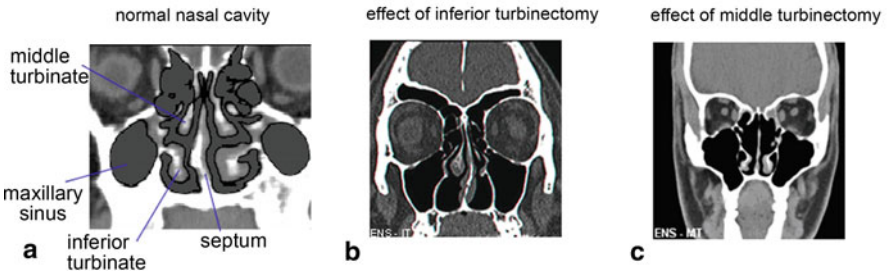


**Fig. 2.7** Coronal slice of a CT scan showing **a** nasal cavity without any abnormalities **b** a nasal cavity after having an inferior turbinectomy **c** nasal cavity with the effect of middle turbinectomy. Large empty spaces are evident which contribute towards complaints of *empty nose syndrome*

## 2.3 Pharynx

### 2.3.1 Anatomy of the Pharynx

The pharynx (*throat*) is a tubelike structure about 12.5 cm long that connects the posterior nasal and oral cavities to the larynx and oesophagus. It extends from the base of the skull to the level of the sixth cervical vertebrae. Structurally the pharynx can be divided into three anatomical parts according to its location as shown in Fig. 2.8, which are the nasopharynx (posterior to the nasal chambers), the oropharynx (posterior to the mouth), and the laryngopharynx (posterior to the pharynx).

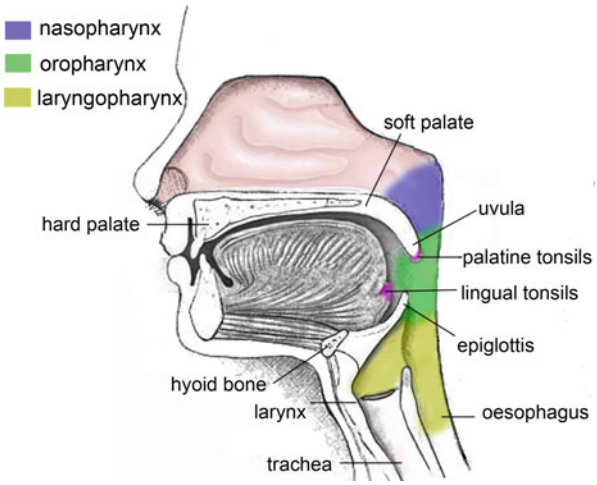


**Fig. 2.8** The pharynx and its subdivisions into the nasopharynx, oropharynx, and laryngopharynx

The **nasopharynx** is located between the internal nares and the soft palate and lies superior to the oral cavity. At the base of the nasopharynx are the soft palate and the uvula. At the wall of the nasopharynx are the auditory (Eustachian) tubes connected to the middle ear. The pharyngeal tonsils (adenoids) are located in the nasopharynx on its posterior wall opposite the posterior internal nares. The **oropharynx** is located posterior to the mouth, inferior from the soft palate, and superior to the level of the hyoid bone. At this location the mouth leads into the oropharynx and both food and inhaled air pass through it. The palatine (*faucial*) tonsils lie in the lateral walls of the fauces. The **laryngopharynx** (*hypopharynx*) extends from the hyoid bone to the oesophagus. It is inferior to the epiglottis and superior to the junction where the airway splits between the larynx and the esophagus. The lingual tonsils are found at the posterior base of the tongue which is near the opening of the oral cavity.

### 2.3.2 Physiology of the Pharynx

The pharynx serves to provide a passageway for both the digestive system and respiratory system since food and air pass through it. The food or air is directed down the

correct passageway, either the oesophagus or the trachea, by being controlled by the epiglottis. The epiglottis is a flap of elastic cartilage tissue that acts as a lid to cover the trachea when food is swallowed in order to prevent objects entering the larynx (see later Sect. 2.4 Larynx). During swallowing, the soft palate and its uvula point upwards closing the nasopharynx so that neither air nor food can pass through it, thus breathing is momentarily stopped. The connection opens and closes to equalise the air pressure in the middle ear to that of the atmosphere for the conduction of sound. The surface of the nasopharynx is covered by pseudo-stratified columnar epithelium. This is the same epithelium found in the nasal cavity and similarly the same mechanism of mucous secretion from goblet cells in the epithelium to filter, warm, and humidify the inhaled air occurs here. In the oropharynx and laryngopharynx, the surface is lined with non-keratinizing stratified squamous epithelium which is needed as it is exposed to food moving through the passageway.

### *2.3.3 Variations and Disease of the Pharynx*

Some disease of the pharynx that may have an effect on the airway geometry and airflow includes:

- Pharyngitis—Inflammation of the pharynx, which can be acute or chronic with many different causes such as bacteria or viruses. This can result in swelling and redness of the oropharynx and enlarged tonsils, restricting the passageway for breathing and swallowing.
- Tonsillitis—Inflammation of the tonsils, which is commonly caused by viral or bacterial infection. The tonsils become enlarged and this restricts the airway opening from the oral cavity to the oropharynx, causing breathing and swallowing problems.
- Pharyngeal Cancer—Cancer arising in the pharynx from the squamous epithelial cells can restrict the airway, altering the natural flow of air in the pharynx.

## 2.4 Larynx

### *2.4.1 Anatomy of the Larynx*

The larynx is commonly known as the **voice box** as it houses the vocal folds that are responsible for sound production (*phonation*). It serves as a sphincter in transmitting air from the oropharynx to the trachea and also in creating sounds for speech. It is found in the anterior neck, connecting the hypopharynx with the trachea, which extends vertically from the tip of the epiglottis to the inferior border of the cricoid cartilage (Fig. 2.9). At the top of the larynx is the epiglottis which acts as a flap that

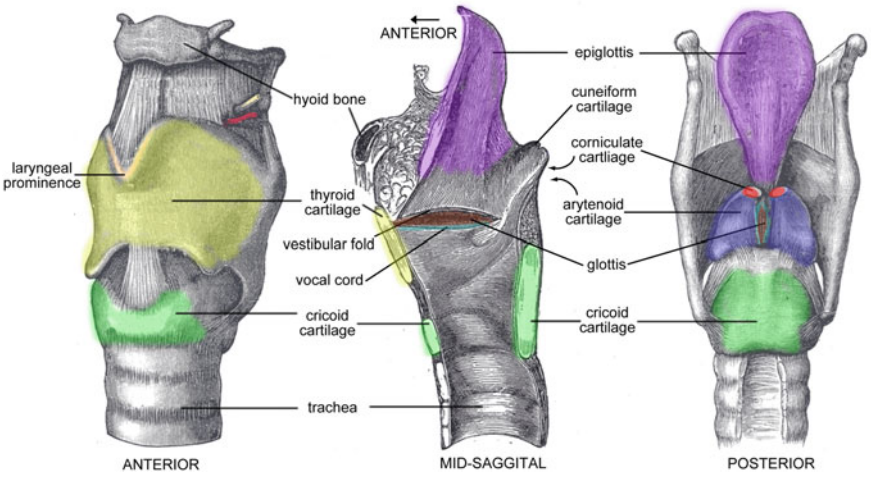


**Fig. 2.9** Anterior, mid-saggital (cut-away) and posterior views of the larynx

closes off the trachea during the act of swallowing to direct food into the oesophagus instead of the trachea. The laryngeal skeleton consists of nine cartilages, three single (thyroid, cricoid, and epiglottis) and three paired (arytenoid, corniculate, and cuneiform), connected by membranes and ligaments. The hyoid bone is connected to the larynx but is not considered part of the larynx. The single laryngeal cartilages are:

- The **epiglottis**—a leaf-shaped piece of elastic cartilage located at the top of the larynx. It is inferiorly anchored at one end between the back of the tongue and the anterior rim of the thyroid cartilage. The free superior end bends up and down like a flap to open and close the opening into the larynx.
- The **thyroid cartilage** (*Adam's apple*)—formed by the fusion of two cartilage plates and is the largest cartilage of the larynx. It is shaped like a triangular shield and is usually larger in males than in females due to male sex hormones stimulating its growth during puberty.
- The **cricoid cartilage**—a signet ring shaped cartilage so-called because the signet end forms part of the posterior wall of the larynx. It is attached to the top of trachea and is the most inferiorly placed of the nine cartilages.

The paired laryngeal cartilages form part of the lateral and posterior walls of the larynx, which are:

- The **arytenoid** cartilages—two upward protrusions located at the back of the larynx. The arytenoid cartilages are attached to the cricoarytenoid muscles, anchored by the cricoid cartilage and attached to the vocal cords. They are the most important because they influence the position and tension of the vocal folds.
- The **corniculate cartilages**—small and cone-shaped hyaline cartilages that sit on top of each of the arytenoid cartilages. During swallowing of food, the epiglottis

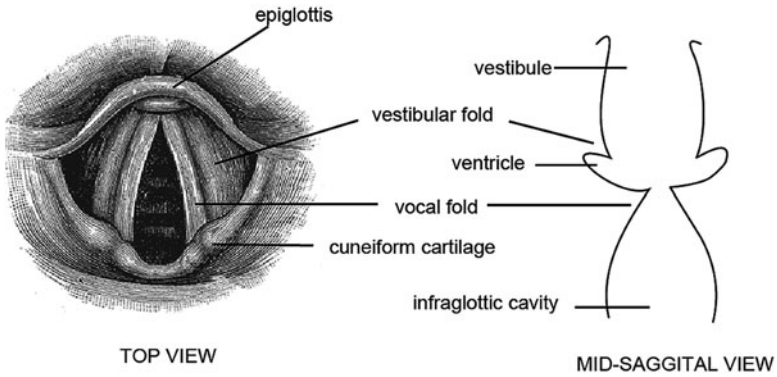


**Fig. 2.10** Larynx opening at the glottis, showing the vocal and vestibular folds that separate the region into sub-cavities

bends down and meets the corniculate cartilages to close off the pathway to the trachea.

- The **cuneiform cartilages**—small elongated rod-like elastic cartilages located at the apex of each arytenoid cartilage, and at the base of the epiglottis above and anterior to the corniculate cartilage.

The airway cavity of the larynx extends from a triangular shaped inlet at the epiglottis to a circular outlet inferior to the cricoid cartilage where it is continuous with the lumen of the trachea. Two pairs of mucous membrane foldings stretch inward and horizontally across the larynx. The upper pair of folds are the vestibular folds (*ventricular* or *false folds*) which only play a minimal role in phonation but protect the more delicate folds below. The lower pair of folds are the true vocal folds, which form a slit-like opening called the glottis. This is the narrowest part of the larynx. The vestibular and vocal folds divide the larynx into (1) the vestibule (upper chamber), located above the vestibular folds; (2) the ventricle, the small middle chamber located between the vestibular and vocal folds; and (3) the infraglottic cavity, which extends from the vocal folds to the lower border of the cricoid cartilage (Fig. 2.10). The vocal cords, are flat triangular bands and white in colour because of their their lack of blood supply (avascular) nature. They are attached posteriorly to the arytenoid cartilages, and anteriorly to the thyroid cartilage. The interior surface of the superior portion of the larynx is made up of stratified squamous epithelium which is an area that is subject to food contact. Below the vocal folds the epithelium is pseudo stratified ciliated columnar. Here mucociliary action directs mucous movement upward towards the pharynx, so that the mucous is continually being moved away from the lungs.

### *2.4.2 Physiology of the Larynx*

The ciliated mucous lining of the larynx further contributes towards the respiratory system's ability to remove foreign particles and to warm and humidify the inhaled air

(the same physiological feature as the nasal cavity). During intentional swallowing the back of the tongue that is joined to the top of the larynx, pushes upwards, forcing the epiglottis to close over the glottis, preventing food or foreign objects to enter the larynx. If the items do enter the larynx and contact the vocal folds, stimulation of the larynx muscles causes a cough reflex to try and expel the items in order to prevent choking. The other important function of the larynx is sound generation (*phonation*), where the pitch and volume of sounds are manipulated by the body. Sounds generated at the larynx are caused by the expired air released from the lungs that pass through the glottis and hence the vocal cords. By flexing and reflexing muscles in the larynx, the arytenoid cartilages are forced to pivot at its base (i.e. at the cricoid cartilage) to bring together or separate the vocal cords for speech or breathing respectively. The vocal and cricothyroid muscles then control their length and tension. This variable tension in the vocal cords allows a wide range of pitch and tones to be produced. Generally the tenser the vocal cords, the faster they vibrate and the higher the pitch. As young boy's experience puberty, the larynx enlarges which produces thicker and longer vocal cords. This leads to the cords, vibrating more slowly and his voice becomes deeper. Louder sounds can be achieved through greater exhalation force from the diaphragm, creating stronger vibrations of the vocal cords. Just like guitar strings the vocal cords produce a vibrating buzzing sound and the final sound produced is dependent on the surrounding resonating chambers of the pharynx, mouth, and nose and also the geometry of the tongue and lips.

### *2.4.3 Variations and Diseases of the Larynx*

One obvious variation of the larynx is the laryngeal prominence (*Adam's apple*) which is typically larger in men than in women. This protrusion is formed by the angle of the thyroid cartilage, which develops during puberty, protruding out the front of the neck more noticeably. Sound production in males is also usually lower pitched than in women as the male vocal cords are larger than female vocal cords. At birth the larynx is located more superiorly and is further forward (anteriorly) relative to its position in the adult body. As the child grows the larynx shifts downward. Some diseases of the larynx that may have an effect on the airway geometry and airflow includes:

- Laryngitis (acute and chronic)—inflammation and swelling of the larynx caused by the viruses, dust contaminated air, or by excessive shouting.
- Presbylarynx—a condition involving age-related atrophy of the vocal fold tissues of the larynx, resulting in a weak voice and restricted vocal range and stamina.
- Laryngomalacia—a common condition during infancy, where soft, immature cartilage of the upper larynx collapses inward during inhalation, causing airway obstruction.

## 2.5 Tracheobronchial Tree and Deep Lung Airways

### *2.5.1 Anatomy of the Tracheobronchial Tree and Lung Airways*

The **tracheobronchial tree** is the structure from the trachea, bronchi, and bronchioles that forms the upper part of the lung airways. It is referred to as a tree because the trachea splits into the right and left main bronchi, which further bifurcates or branches out into more progressively smaller airways. It is an asymmetric dichotomous (splitting of a whole into exactly two non-overlapping parts) branching pattern, with the daughter bronchi of a parent bronchus varying in diameter, length, and the number of divisions. The bronchial generation is normally referred to by a number, indicating the number of divisions from the trachea, which is assigned as generation number 0 or 1 as found in the literature.

The **trachea** (*windpipe*) is a hollow tube about 11–14 cm long connecting from the cricoid cartilage in the larynx to the primary bronchi of the lungs. Its cross-sectional diameter in normal human adult males is 1.3–2.5 cm in the coronal plane and 1.3–2.7 in the sagittal plane, while for females the diameters are slightly smaller (1.0–2.1 cm and 1.0–2.3 cm for coronal and sagittal diameters respectively) (Breatnach et al. 1984). The variation in the trachea cross-section between the coronal and sagittal plane is due to its shape being a horse-shoe where the anterior side is made up of C-shaped cartilaginous rings, and posteriorly by a flat band of muscle and connective tissue called the posterior tracheal membrane, closing the C-shaped rings. There are 16–20 tracheal rings, which hold and support the trachea preventing it from collapsing in on itself but also provides some flexibility for any neck movement. Further downstream, along subsequent bronchi, the cartilage support becomes progressively smaller and less complete. The tracheal mucosa consists of pseudo stratified, ciliated columnar epithelium, while its submucosa contains cartilage, smooth muscle, and seromucous glands.

The trachea divides into the **main bronchi** (*primary bronchi*) at the carina, with the right bronchus wider, shorter and more vertical than the left bronchus (Moore and Dalley 2006) (mean lengths of $\sim 2.2$ cm and $\sim 5$ cm respectively). This leads to increased chances of inhaled foreign particles depositing within the right bronchus. The right main bronchus bifurcates posterior and inferiorly into the right upper lobe bronchus and an intermediate bronchus. This bifurcation occurs earlier on the right than on the left lung in all models.

The left bronchus passes inferolaterally at a greater angle from the vertical axis than the right bronchus. It is located anterior to the oesophagus and thoracic aorta and inferior to the aortic arch. Each main bronchi leads into the lung on its respective side (Fig. 2.11). The right main bronchus subdivides into three lobar (*secondary*) bronchi (right upper lobe bronchus, right middle lobe bronchus, and right lower lobe bronchus) while the left main bronchus divides into two (left upper lobe bronchus and left lower lobe bronchus). Each lobar bronchus serves as the airway to a specific lobe of the lung.

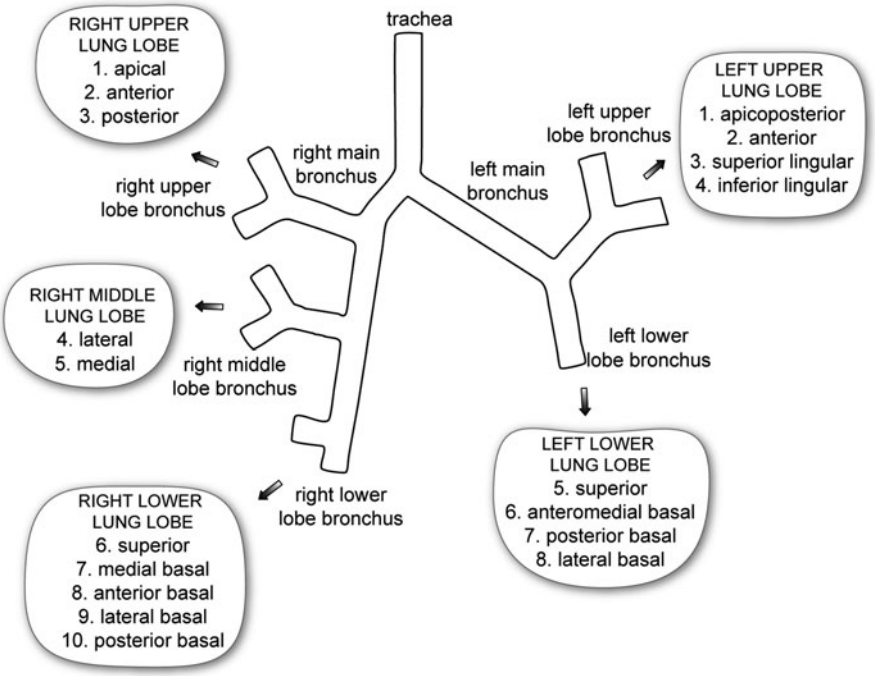


**Fig. 2.11** Schematic of the tracheobronchial airway showing the subdivisions in the first three generations and where the branches lead into the segments of the lung, subsequently called the bronchopulmonary segments. The right lung has three lobes and approximately ten segments. The left lung has two lobes and approximately eight segments

The lobar bronchi further divides into segmental bronchi (*tertiary bronchi*), which supply the bronchopulmonary segments of each lobe. Figure 2.12 and 2.13 show the first three generations of the tracheobronchial tree in the left and right lung respectively. A bronchopulmonary segment may be defined as an area of distribution of any bronchus (Jackson and Huber 1943). Technically there are ten bronchopulmonary segments in each lung, however in the left lung some of these segments fuse and there are as few as eight bronchopulmonary segments. The bronchi continually divide into smaller and smaller bronchi up to about 23–24 generations of divisions from the main bronchi. As the bronchi become smaller, their structure changes:

- the cartilaginous rings that support the branches turn into irregular plates of cartilage and eventually disappear by the time bronchioles are reached ($\sim 1$ mm in diameter). When the bronchi eventually lose all support (usually between generations 12–15) the airways are then referred to as bronchioles (Vanpeperstraete 1974);
- the epithelium changes from pseudo stratified columnar to columnar and then to cuboidal in the terminal bronchioles. There are no cilia or mucous producing cells

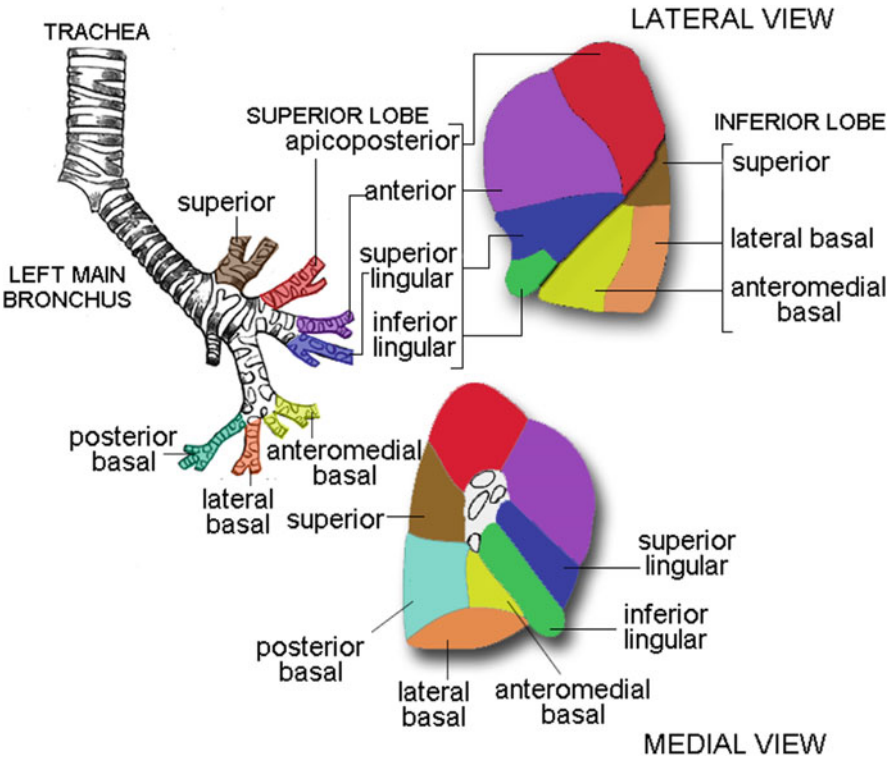


**Fig. 2.12** Left segmental bronchi and its attachment to the left lung segments

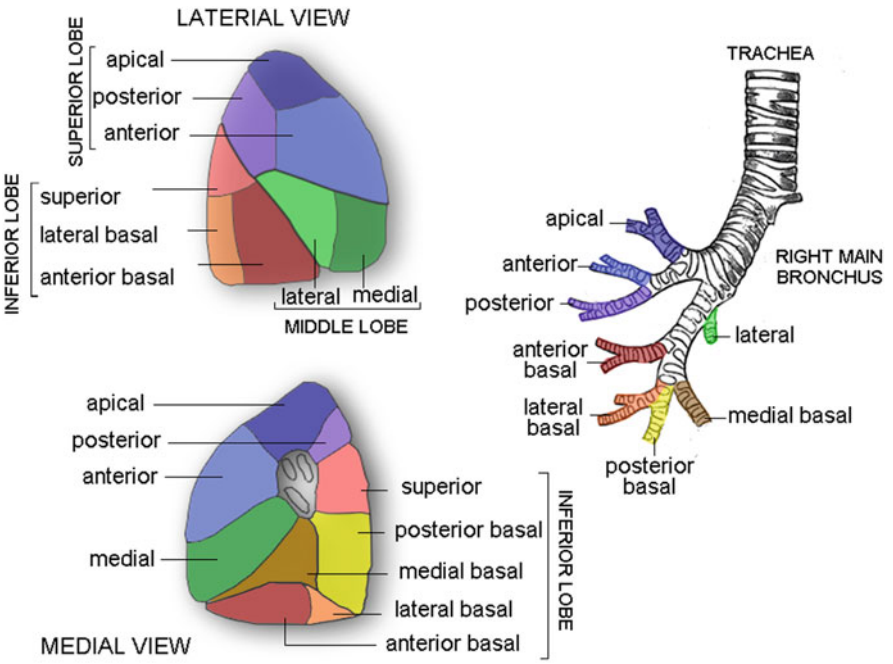


**Fig. 2.13** Right segmental bronchi and its attachment to the right lung segments

in the bronchioles and foreign particles are removed by macrophages located in the alveoli instead of mucociliary action;
- The amount of smooth muscle in the tube walls increases as the passageways become smaller.

The passageway from the trachea, bifurcating into the right and left main bronchi, which further divide into lobar, then segmental bronchi and continues this bifurcating process down to the terminal bronchioles (which are the smallest airways without alveoli) is called the *conducting airways* (Fig. 2.14). In this area, gas exchange does not take place because no alveoli are present, and it contributes to the *anatomic dead space* which takes up approximately 150 mL in volume.

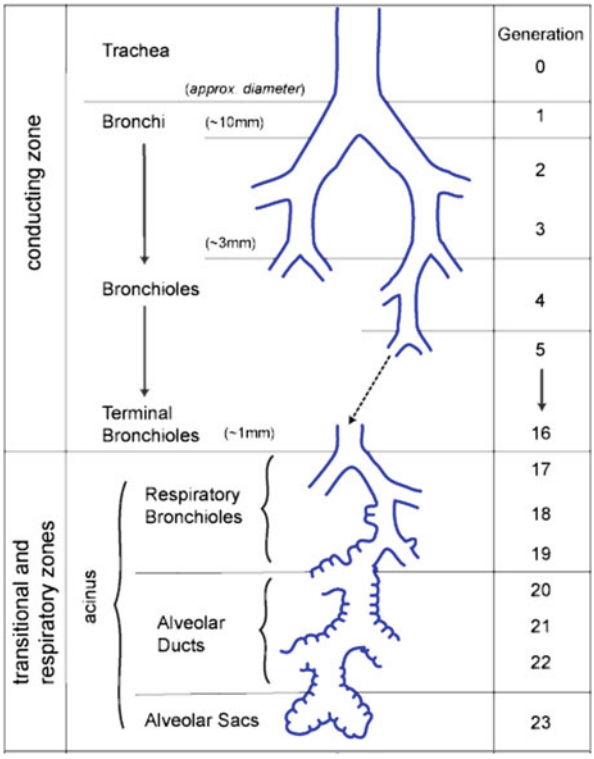


**Fig. 2.14** Schematic of the airway generations in the human adult lung. On average, a total of 21–25 generations are found between the trachea and the alveoli. (Redrawn from Weibel 1963)

The terminal bronchioles that divide into respiratory bronchioles are also called transitional bronchioles as they have occasional alveoli present at the walls. The respiratory bronchioles further divide into alveolar ducts which are completely lined with alveoli. This region is the *acinus* (meaning berry in Latin) region because of the cluster of cells that resemble a knobby berry, like a raspberry. It includes all parts distal to a single terminal bronchiole and on average is beyond the sixteenth generation (Haefeli-Bleuer and Weibel 1988). The acinus is therefore comprised of respiratory airways and forms the functional tissue of the lung, or, the lung parenchyma. It extends only a few millimetres for about eight generations with the first three

generations consisting of respiratory bronchioles (Sznitman 2008). In total the respiratory zone makes up most of the lung, with its volume being about 2.5–3 litres during rest (West 2008) in comparison to the conducting airways that make up 150 mL (anatomic dead space). The alveolar ducts are short tubes that are supported by a rich matrix of elastic and collagen fibres. The distal end of the alveolar duct opens into the alveolar sac, which is made up of an atrium and the alveoli (Fig. 2.15). The walls between adjacent alveoli have tiny holes known as *pores of Kohn* that serves as additional ventilation by allowing in air between the alveoli. This is the terminating end of all airway passages in the respiratory system. Because exchange takes place in the acinus, the area is surrounded by a rich network of blood capillaries. It has been estimated that each adult lung has about 300 million alveoli, with a total surface area for gas exchange of 70–80 $m^2$.

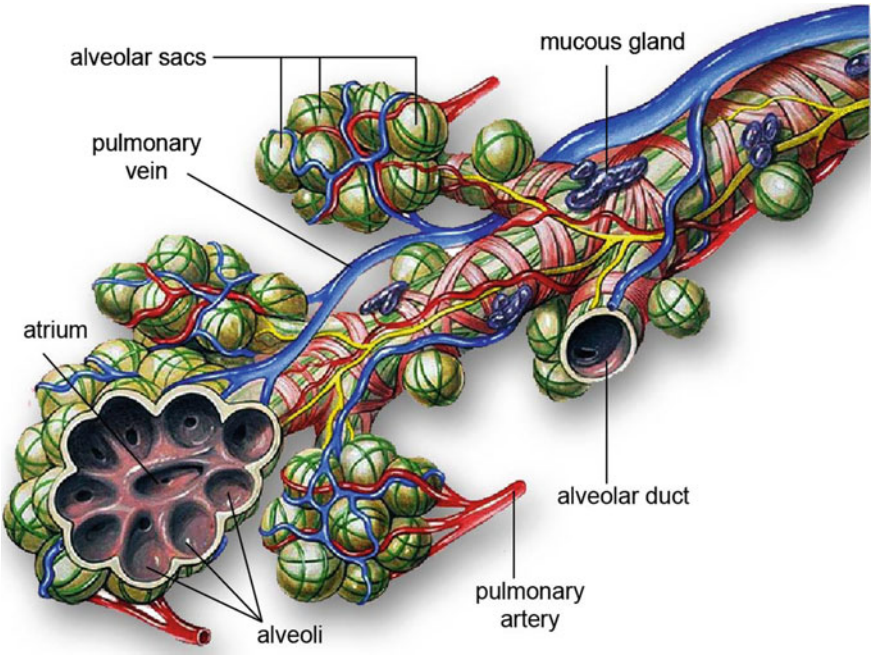


**Fig. 2.15** Acinus region showing the alveolar ducts, and a cutaway of the alveolar. (Original drawing courtesy of Patrick J. Lynch, medical illustrator)

### *2.5.2 Physiology of the Tracheobronchial Tree and Lung Airways*

The tracheobronchial tree conducts the inspired air to and from the alveoli. During inhalation the distal end and bifurcation of the trachea are displaced downwards, which is important for facilitating inspiration (Harris 1959). The epithelial changes in the bronchi reflect the physiological functions of the airway. For example the ciliated columnar epithelium in the early branch generations allow for both heating

and conditioning of the air as well as filtering through mucociliary action to remove mucous secretions in an upward motion towards the oesophagus. In the distal branches, the epithelium becomes cuboidal to allow for gas exchange. The cartilage support around the trachea and early branches also changes, progressively diminishing in order to maintain patency of the smaller airways. During gas exchange oxygen is brought into the body and is exchanged with carbon dioxide that is produced from cell metabolism. This occurs in the alveolar-capillary network which consists of a dense mesh-like network of the respiratory bronchioles, the alveolar ducts, the alveoli, and the pulmonary capillary bed. At the gas exchange surface of the alveoli is a lining that is 1–2 μm thick where $O_2$ and $CO_2$ passively diffuse across and into plasma and red blood cells. The diffusion occurs between the alveolar gas and blood in the pulmonary capillaries within less than one second.

### *2.5.3 Variation and Disease of the Tracheobronchial Tree and Lung Airways*

The cross-section of the trachea typically has a coronal-to-sagittal diameter ratio of 0.6:1.0, and narrowing of the coronal diameter producing a coronal/sagittal ratio of $< 0.6$ is then termed a sabre sheath trachea and is seen in patients with chronic obstructive pulmonary disease (Brant and Helms 2007). A slight tracheal deviation to the right after entering the thorax can be a normal radiographic finding and in some instances, the presence of the aortic arch can lead to the left lateral wall of the distal trachea being indented by the transverse portion of the aortic arch. In younger individuals the trachea is elastic and extensible, while in older people it is more rigid or even sometimes os sified, so that it is less distensible (Franciscus and Long 1991b). There are many reported diseases of the lung airways (*pulmonary disease*) ranging from the common cold to life-threatening examples such as bacterial pneumonia or cancer, and include:

- Chronic Obstructive Pulmonary Disease (COPD)—One of the most common pulmonary diseases (e.g. bronchitis, emphysema and asthma), resulting in the inflammation of the airways which in turn causes narrowing and obstruction of the airways, seriously affecting the capacity for normal respiratory function.
- Restrictive lung disease (*interstitial lung disease*)—is a disease of the lung parenchyma (covering layer of the lungs), and the connective tissue that hold the air sacs together. This results in a decreased ability to breathe in because of incomplete lung expansion and increased lung stiffness.
- Respiratory tract infection—any infection that can affect any part of the respiratory system such as viral or bacterial. This is normally categorised as an upper respiratory tract infection (nose, sinus, pharynx, larynx) or a lower respiratory tract infection. The most common lower respiratory tract infection is pneumonia.
- Lung cancer—is a disease of uncontrolled cell growth in tissues of the lung. The collection of these cells forms a tumour which is either malignant or benign. The

spread of the disease to other tissues in the lung and even other body organs has serious health effects and from a respiratory perspective results in a decline in all aspects of respiratory function.

## 2.6 Respiration Physiology

### *2.6.1 Lung Volumes and Capacity*

The lungs can be measured for different lung volumes and its value is important when deciding on what flow rates and conditions are needed for CFPD settings. Normally lung volumes are measured with a spirometer, and its lung capacity is then inferred from the measurements. Figure 2.16 shows a typical tracing measured from a spirometer. There are five volumes and four capacities used to define the lung space. They are:

- Tidal Volume (TV) is the amount of volume that is inspired and exhaled during normal quiet breathing. 7–9 mL/kg of ideal body weight ~ 8–10 % of TLC
- Inspiratory Reserve Volume (IRV) is the maximum volume that can be inhaled above the tidal volume.
- Expiratory Reserve Volume (ERV) is the maximum volume that can be expired after the expiration of a tidal volume.
- Residual Volume (RV) is the volume left in the lungs after maximum expiration.
- Functional Residual Capacity (FRC) is the volume of air left in the lungs that can be exhaled after normal expiration.
- Inspiratory Capacity (IC) is the volume of maximum inhalation.
- Vital Capacity (VC) is the volume of maximum inhalation and exhalation.
- Total Lung Capacity (TLC) is the maximum volume in the lungs.

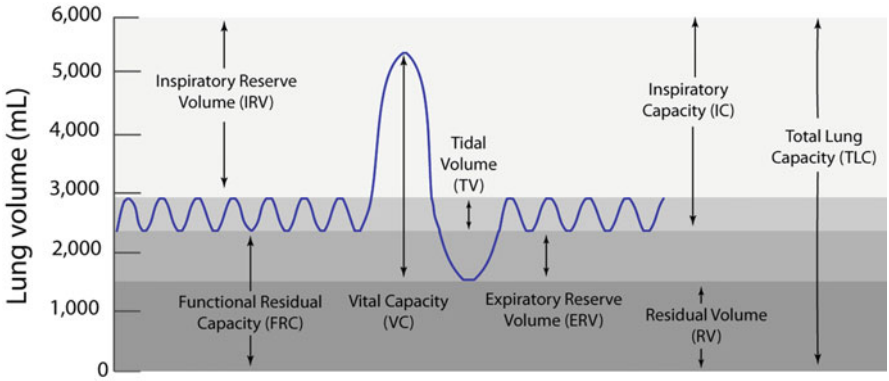


**Fig. 2.16** Static lung volumes and capacity tracing measured by a spirometer. The vertical axis is the volume and the horizontal axis is time

### 2.6.2 Mechanics of Breathing

Inhalation is initiated by the contraction of the diaphragm which contracts and descends about 1 cm during normal breathing and up to 10 cm on forced breathing. The diaphragm lines the lower part of the thorax, sealing it off air-tight from the abdominal cavity below. Its contraction causes muscles in the thorax to pull the anterior end of each rib up and outwards enlarging its volume. As a result, the pressure inside the thorax (intrathoracic pressure) and inside the lungs (intrapulmonary pressure) decreases relative to the outside atmospheric air pressure. The pressure difference induces the inhaled air from a higher pressure to a lower pressure in order to equalise the pressure. During exhalation the lung and chest wall return to its equilibrium position and shape. The thoracic cavity volume is reduced and the pressure builds up to release the air from the lungs. In quiet breathing only the elastic recoil of the lung and chest walls is needed to return the thorax to equilibrium (a passive process). However in forceful expiration additional muscles (intercostals) in the thorax and abdomen are also used to further increase the pressure.

A pressure-volume curve can be used to obtain information about how the lung deforms during breathing. It can describe the mechanical behaviour of the lungs and chest walls such as the elasticity of the lung, and its ability to expand and stretch (distensibilty) through the slope of the pressure-volume curve. This is referred to as lung compliance ($C_L$) and has units of mL/cm $H_2O$ to reflect the change in lung volume ($\Delta V$) as a result of a change in the pressure ($\Delta P$) of the lung (e.g. $C_L = \Delta V/\Delta P$). A pressure-volume curve from the literature (Harris 2005) is shown in Fig. 2.17. A high compliance value refers to a lung that is easily distended and is reflected with a steep pressure-volume curve. A low compliance means that

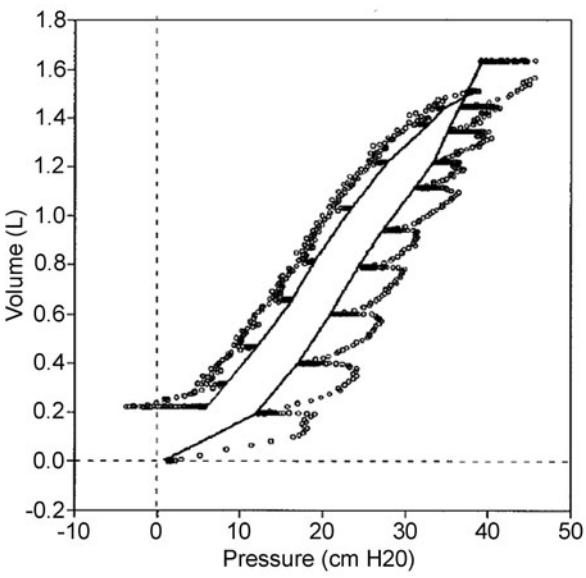


**Fig. 2.17** Pressure-volume curve taken from Harris (2005) acquired with the super-syringe method. The open circles are the data points plotted continuously during the maneuver. The solid lines show the quasi-static points connected to form a smooth P–V curve. The inflation and deflation points are not connected, because they were performed separately in this example

the lung is 'stiff', and is not easily distended with a flat pressure-volume curve. When reading the compliance slope the lung volume must be considered, since at low lung volumes the lung distends easily, but at high lung volumes large changes in pressure only produce small changes in lung volume. This is because at high lung volumes the all alveolar and airways have been maximally stretched. To account for the variations in volume, specific compliance (compliance divided by the lung volume usually FRC) is used.

### *2.6.3 Airflow Dynamics and Resistance*

Airflow through the respiratory system is driven by the pressure difference from one end to the other. During respiration, the glottis at the larynx opens allowing gas flow to enter from the upper respiratory tract into the lung airways. The flow in the airway can be defined as laminar or turbulent. Laminar flows are characterised by smooth streamlines while turbulent flows have eddies and fluctuations within the flow. In straight tubular or pipe flows this flow regime can be defined by the Reynolds number,

$$\mathrm{Re} = \frac{\rho D U}{\mu} \tag{2.1}$$

where $\rho$ is the density, $D$ is the hydraulic diameter, $U$ is the average velocity, and $\mu$ is the dynamic viscosity. For a given fluid with constant density and viscosity, increases in the flow velocity contributes to the flow becoming turbulent. While in the smaller airway bronchi and even bronchioles, the small diameters will essentially damp out the inertial effects and contribute towards a laminar flow. Fluid flow regimes are discussed in further detail in Sect. 5.3.

Airflow resistance in the respiratory airways is a concept that describes the opposition to air flow from its inhalation point to the alveoli, caused by frictional forces. It has the unit cm $H_2O$ s/L and is defined as the ratio of the driving pressure to the flow rate,

$$R = \frac{\Delta P}{\dot{V}} \tag{2.2}$$

where $\dot{V}$ is the flow rate given in L/s. For a laminar flow, the flow rate can be estimated through Poiseuille's law by:

$$\dot{V} = \frac{\Delta P \pi r^4}{8\,\mu L} \tag{2.3}$$

where $r$ is the radius, and $L$ is the airway length. It is therefore apparent that the resistance is inversely proportional to the fourth power of the radius and that a change in the airway geometry will have a greater effect in comparison to the other

variables. Therefore airway resistance decreases as lung volume increases because the airways distend as the lungs inflate, and wider airways have lower resistance. For turbulent flow, resistance is relatively large because a larger driving pressure is needed to produce the same flow rate in comparison with a laminar flow. There is no simple resistance relationship for turbulent flow since the pressure-flow relationship ceases to be linear.

High resistance that causes problems in respiration function may be a sign of obstructed pulmonary diseases such as asthma. While it is not applicable to control the airway geometry, other variables such as the inhaled gas mixture can be controlled for certain applications. It has been shown in clinical and theoretical studies (Jaber 2001; Sandeau et al. 2010) that there are benefits of helium–oxygen gas mixtures to improve respiratory assistance because the helium-oxygen gas mixture has a smaller density and higher viscosity in comparison to air. This can result in a lowering of respiratory effort, and assist in breathing for patients with obstructive lung diseases.

### *2.6.4 Gas Exchange*

Gas exchange during the respiration process takes place in the alveolus at its surface that separates the alveolus with the capillary. In addition each alveolus is smaller than a grain of salt, in which there are approximately 300 million of them in the lungs. Each alveolus is optimised for gas exchange by having a thin moist surface and a very large total surface area in total. The surfaces of the alveoli are covered with a network of capillaries which are narrow blood vessels. Oxygen is passed from the alveoli into the surrounding capillaries that contains oxygen deprived, carbon dioxide rich blood passed from the heart. Gas exchange takes place where the oxygen is dissolved in the water lining of the alveoli before it diffuses into the blood while carbon dioxide is removed from the blood and into the alveoli where it leaves the body during exhalation. After leaving the lungs, the refreshed blood is now oxygen-rich and returns back to the heart before it is redistributed to tissues in the human body (Fig. 2.18).

The exchange of $O_2$ and $CO_2$ occurs through diffusion which is the net movement of gas molecules from a region that has a higher partial pressure to another region that has a lower partial pressure. For example the partial pressure of oxygen in the inspired air within the alveolar spaces in the lung is greater than the partial pressure of oxygen in the blood which enables oxygen to diffuse into the red blood cells. The diffusion process is defined by Fick's law of diffusion which states that the diffusion of a gas across a boundary is directly related to its surface area ($A$), the diffusion constant of the specific gas ($D$), and the partial pressure difference of the gas on each side of the boundary ($P_1 - P_2$), and inversely related to the boundary thickness (T):

$$\text{Diff} \propto \frac{AD(P_1 - P_2)}{T} \tag{2.4}$$

Because the process is at a molecular level, the gas moves randomly in the direction of the partial pressure gradient, and is temperature dependent. This occurs until there

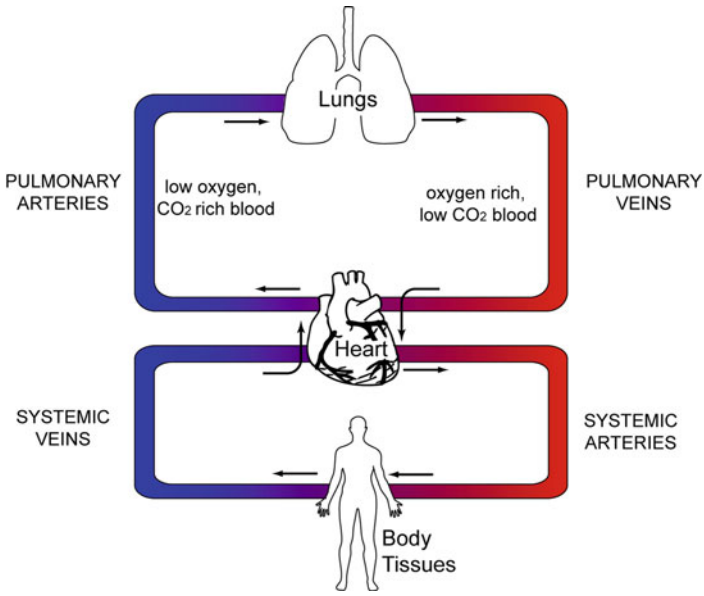


**Fig. 2.18** Schematic of blood flow from the body through the heart and lungs. Gas exchange takes place in the lungs which changes the state of the blood from being low in oxygen to highly rich in oxygen

is equilibrium and there is no longer a pressure gradient. As the gas enters the alveoli, it is slowed down due to an increased in cross-sectional area of the alveolar sacs. This lack of inertia assists in the gas moving across the 1 μm alveolus-capillary interface by diffusion (Fig. 2.19).

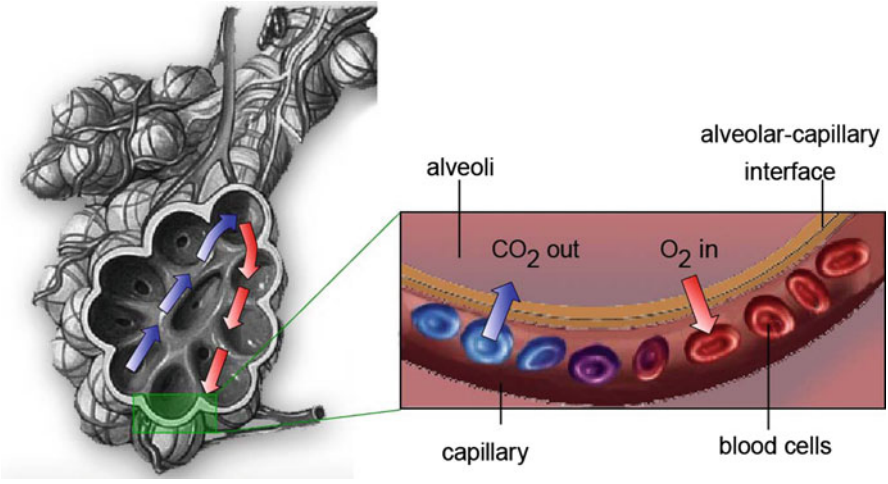


**Fig. 2.19** Oxygen and carbon dioxide gas exchange taking place at the alveolar-capillary interface in the deep lung airways

## 2.7 Summary

The primary function of the respiratory system is to supply the body with oxygen and remove carbon dioxide. During inspiration outside air is inspired into the body which travels from either the nose or mouth down to the lungs. The organs of the respiratory system can be divided functionally into the conducting zone and the respiratory zone. The conducting zone is the airway from the nose or mouth down to the bronchioles and is significant for CFPD as its anatomy and physiology is responsible for transporting air and any foreign particles. The respiratory zone includes the respiratory bronchioles down to the alveoli, where gas exchange takes place through a diffusion process.

The primary aim of this chapter is to summarise the important features of respiration by presenting the anatomy and physiology of the respiratory system. It by no means is a replacement for comprehensive anatomy and physiology study. However it is hoped that the reader has gained enough understanding of the anatomy and physiology of the respiratory system, and the mechanics of breathing, in order to reconstruct any section of the respiratory airway. Furthermore the physiology, variations and diseases of the respiratory organs should be taken into account as it influences many settings for computational modelling. Now that some theory of the respiratory system has been covered, the first step in CFPD, reconstruction of the airways, is presented in the next chapter. Techniques in extraction of data from CT or MRI scans and how to create the 3D model will be given.

## 2.8 Review Questions

1. What organs make up the upper and lower respiratory system?
2. What parts of the respiratory system does the *conducting airway* consist of?
3. The left and right chambers of the nasal cavity are separated by what bone? What material is it made of?
4. Based on the human nasal cavity geometry, describe in general the path inhaled air may take?
5. Which physiological functions of the nose may need to be considered when modelling the inhalation process in CFPD?
6. What factors can influence the nasal cavity geometry?
7. What are the anatomical parts that make up the pharynx? Of these three, which one connects to the nasal cavity, and which one connects to the oral cavity?
8. What physiological function does the pharynx serve, and how do you think this would be modelled in CFPD?
9. Draw a mid-sagittal plane view schematic of the larynx. Do you think the flow entering into the infraglottic cavity will be fast or slow? Why?
10. Describe the geometry of the trachea—what kind of shape surrounds it? If a smooth pipe was used instead, do you think more or less particles will deposit in the trachea?

11. Name the subregions or lung lobes that make up the lungs.
12. What is supporting structure that holds the early bronchi such as the primary bronchus, in place? When does this support disappear?
13. In most CFPD models, the respiratory walls are smooth and rigid. Describe the surface of a realistic tracheobronchial airway walls. What considerations would you need to make when reviewing the CFPD flow and particle results?
14. In the physiology of respiration, describe the difference between Tidal Volume and Total Lung Capacity.
15. Discuss in the terms of pressure difference, how respiration occurs within the lungs.
16. Referring to the Reynolds number, do you think the bronchiole airways will increase or decrease the inertial effects of the flow in comparison with the primary bronchi?
17. What is the transport process that allows the exchange of $O_2$ and $CO_2$ gas and in which anatomy does this occur?

# Chapter 3
# Reconstruction of the Human Airways

## 3.1 Introduction

Construction of a computational model of the human airways can be divided into three stages: image acquisition, segmentation and surface/volume reconstruction. Image acquisition involves medical images that can be obtained from various sources such as computed tomography (CT) and magnetic resonance imaging (MRI), which essentially provide similar information. A 3D matrix of a series of 2D cross-sections, separated by an interval distance, contains information about tissues and structures which are distinguished from one another by differences in brightness or greyscale. These images provide medical practitioners with 3D realistic computational models that can assist clinical diagnosis and medical treatment and planning. Visualisation and reconstruction of morphological structures from the medical image series involves segmentation of the desired region of interest of organs or structures. The general problem of segmentation can be summarised as the partitioning of an image into a number of homogeneous segments, such that any two neighbouring segments yields a heterogeneous segment. Some common algorithms based on thresholding, edge detection, and region characteristics are given in this chapter. The basics of these algorithms are given to introduce the reader to this active research field. While each segmentation technique is presented individually, in practice it is common to apply multiple segmentation techniques to a given problem. Finally the chapter concludes with examples to demonstrate different methods to develop respiratory airway models.

## 3.2 Medical Image Acquistion

### *3.2.1 Computed Tomography (CT)*

Computed Tomography (CT) or by its older name computed axial tomography, is a medical imaging procedure that using x-rays to create a series of planar cross-sectional images along an axis. It is a combination of mechanical and computer engineering which was first developed in 1972 by Sir Godfrey Hounsfield (Richmond

J. Tu et al., *Computational Fluid and Particle Dynamics in the Human Respiratory System,* Biological and Medical Physics, Biomedical Engineering,
DOI 10.1007/978-94-007-4488-2_3, © Springer Science+Business Media Dordrecht 2013

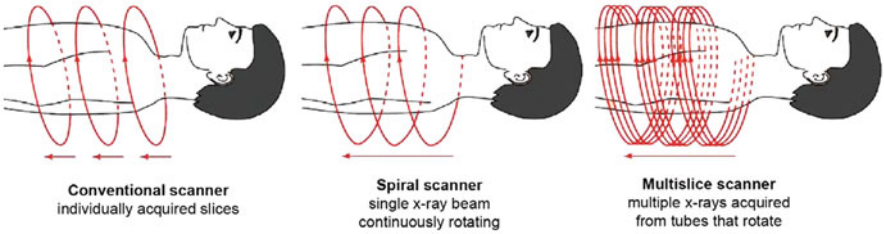


**Fig. 3.1** Three different types of computed tomography scanners and how they work

2004). During a typical CT procedure, the patient is placed on a table. The table then moves the patient in a supine position through a rotating gantry (a donut-shaped device), which houses the x-ray tube and electronic x-ray detectors. Multiple x-rays are taken in thin cross-sections in the region of interest along the person's body forming slices (like slicing a loaf of bread). The detectors collect the x-ray information from each cross-section and send them to a computer that combines them into a single image. In helical (spiral) CT continuous rotation can occur which averts the need to stop and start (Fig. 3.1).

These helical CT scanners provide quick scans which are significant for entire anatomic regions such as the lung which have to be scanned with the patient in one position and within one breath hold. The general procedure may include the following steps:

- A large drink or intravenous injection containing a type of dye may be given to the patient if a contrast agent is needed to enhance pictures.
- All metal objects need to be removed.
- The patient lies on the scanner in a supine position and is moved through the rotating gantry.
- The gantry moves in a circle around the patient as it takes the x-ray images, taking less than a second per revolution.
- Depending on the medical investigation, the CT scan typically take anywhere from 5–30 min.

The difference between a CT scan and a regular conventional x-ray, is that a CT study comprises of a set of 2D-cross-sectional slices instead of a single 2D image that represents a 3D body structure volume that have tissues and structures superimposed onto a 2D image plane. Therefore CT scans can be read into various planes of view (sagittal, coronal, or axial) or even as a 3D object (see Fig. 3.2 for all anatomical position definitions).

Each individual CT image is typically acquired with a matrix of $512 \times 512$ pixels and a resolution of 16-bit. During the scan the x-ray beam consisting of photons pass through, absorbed or redirected (i.e. scattered) by a structure which reduces the strength of the x-ray beam. The degree to which an x-ray beam is reduced is called attenuation. Each pixel is assigned a numerical value (gray scale), based onthe degree to which the structure corresponding to that pixel attenuates the x-ray beam. This is

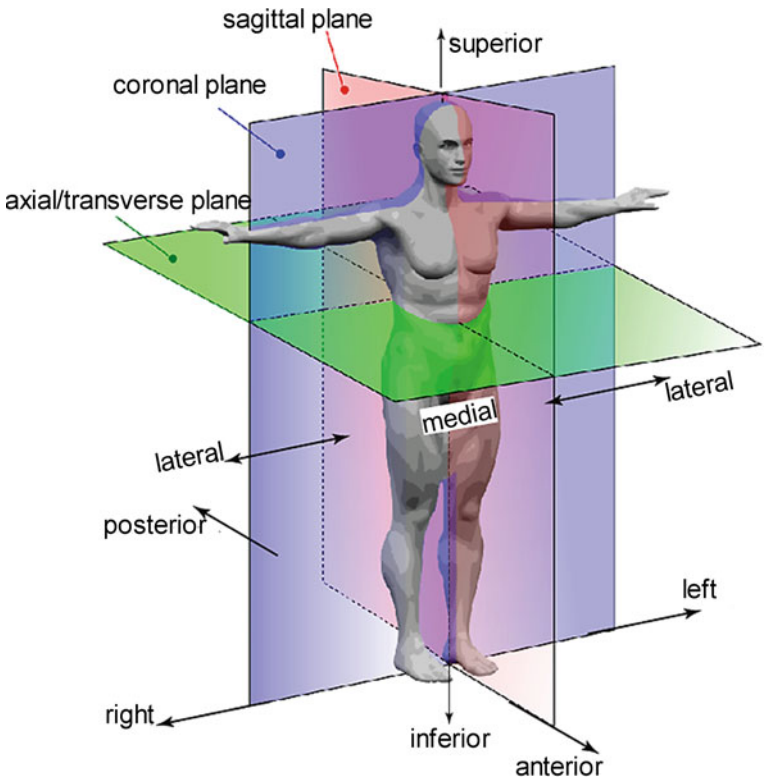


**Fig. 3.2** Anatomical planes and position definition. The axial plane also called transverse plane

expressed in terms of Hounsfield units (HU), defined as

$$\mathrm{HU} = 1000 \cdot \frac{\mu_P - \mu_W}{\mu_W}$$

where $\mu_P$ is the mean x-ray attenuation coefficient of the pixel, and $\mu_W$ is the mean x-ray attenuation coefficient of water. Bone structures attenuate the beam the greatest while air has minimal attenuation properties.

The scanned raw images are a series of cross-sectional images containing different greyscale information with respect to different organs or tissues. A typical CT image has a possible 4,096 grey levels (12-bit image) in a $512 \times 512$ pixel resolution. The greyscale represents a pixel map of the linear x-ray attenuation cogefficient or a measure of the radio-density. These greyscale pixel values can be represented in the Hounsfield scale (name after Sir Godfrey Hounsfield) and its typical values are shown in Fig. 3.3. Since each cross-sectional slice is separated by a known thickness the pixel data in the 2D-slice changes into a volume element known as a voxel.

The risk of any x-ray scan is the exposure to radiation which is relatively higher than other diagnostic x-ray procedures. Measurements of exposure are dependent

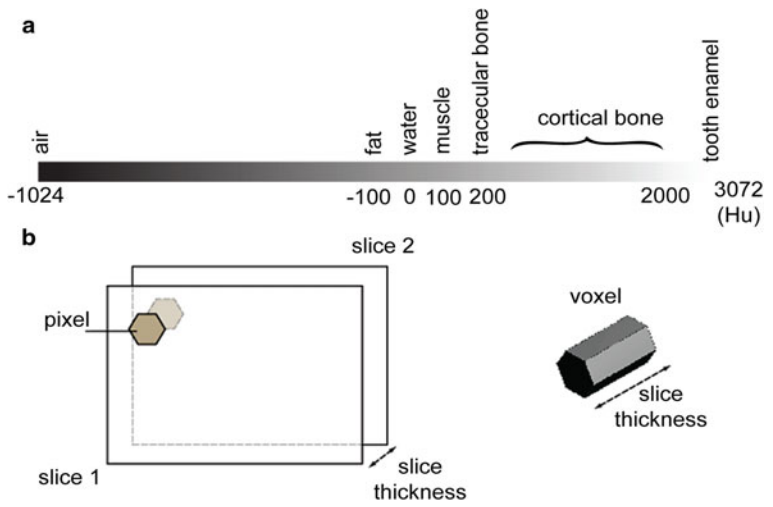


**Fig. 3.3** **a** Greyscale values interpreted as Hounsfield (Hu) units. **b** Representation of a pixel (2D space) and a voxel (3D space)

on the scan protocol which is the scan settings used to acquire the anatomical part. This includes the number of scans, the tube current and scanning time in milliampere seconds, the size of the patient, the axial scan range, the helical scan pitch (the degree of overlap between adjacent CT slices), the x-ray beam energy in the kilovolt peaks, and the specific design of the scanner being used (McNitt-Gray 2002). Depending on the scan protocol, the CT scanner, and the organ being studied, radiation doses range between 15 mSv (in an adult) to 30 mSv (in a neonate) for a single CT scan.

### *3.2.2 Magnetic Resonance Imaging (MRI)*

An MRI scanner uses magnetic fields, and radio waves to obtain cross-sectional images of a section of the body similar to CT. The main difference is that MRI does not have any radiation because it relies on the fact that the body is largely composed of water. Essentially the image is a distribution map of the hydrogen protons in the water molecules inside the body. An MRI scanner consists of a table that slides into a large cylinder. Inside the cylinder is a large superconducting magnet which is usually made up of many coils of wire (typically 1.5 T, which is approximately 50,000 times greater than the Earth's magnetic field). When the MRI is in operation an electric current passes through the coils, and a magnetic field is created. The hydrogen protons that normally spin in random directions then align with the magnetic field gyrating in its position. With the hydrogen protons aligned, a short burst of tuned radio waves is sent through which momentarily changes the quantum state of the protons (flips the spin of the proton). When the radio wave stops, the proton returns

to its original orientation and in doing so echo's its own radio signal that the scanner detects and deciphers into images. The time taken for the disturbed protons to return to their original orientation is called the relaxation time. There are two relaxation times of interest: longitudinal relaxation (T1) is the time for approximately 63 % of protons to realign with the magnetic field along the longitudinal axis; and transverse relaxation (T2), is the time for approximately 63 % of protons to process out of phase. Different tissues exhibit different T1 and T2 relaxation times, which results in high-contrast images. The contrast is provided by saturating the imaging plane with radio-frequency energy. Air that moves into the plane provides fresh spins and appears bright in the image, in contrast to the saturated tissues surrounding the airway. The general MRI procedure may include the following steps:

- A contrast agent called "gadolinium" may be injected in order to help obtain a clearer picture of the area being examined
- All metal objects need to be removed
- The patient should lie as still as possible although between sequences some minor movement may be allowed
- Depending on the medical investigation, the MRI scan may take around 15–45 min although some may take as long as 60-minutes or longer. This is obviously longer than the limit of a single breath hold, and imaging of the respiratory airway is susceptible to the natural cycle of the lung movement due to breathing. Optimal breathing techniques such as shallow, free breathing instead of maximum breath hold may be suggested to the patient in conjunction with of a higher magnetic field using dynamic contrast-enhanced MRI to minimize lung parenchyma movement (Kino et al. 2007).

### *3.2.3 CT vs MRI*

Both MRI and CT are non-invasive techniques that have ability to see inside the body by providing 3D volumetric data sets from a series of stacked 2D pixels which have an associated depth, or slice thickness. CT scans require the use of x-rays and therefore ionizing radiation exposure is a problem. On the other hand MRI scans poses almost no risk to the average patient, although the strong magnetic field will affect implanted medical devices that contain metals such as pacemakers, cochlear implants, or metallic pins. Therefore MRI has the advantage that a patient can undergo multiple scans successively in the short term, without the radiation exposure that would be encountered with CT. Depending on the anatomy for imaging, either MRI or CT will produce better quality images over the other. For example MRI has the ability to change the contrast of the images by small changes in the radio waves and magnetic field. The different contrast settings produce much higher detail in soft tissues and can highlight different types of tissue. MRI also has the ability to display the anatomy in multiple planes of projection while CT scans are limited to the plane of the gantry that is usually axial or coronal. CT images produce better detection of

**Table 3.1** Comparison of CT and MRI scanning

| Function | CT | MRI |
|---|---|---|
| Scan method | X-rays | Magnetic waves and radio waves |
| Radiation exposure | Moderate to high degree of exposure | No exposure to radiation |
| Bony structures | Provides good details, and is preferables | Provides comparatively lesser amount of details |
| Soft tissue details | Less details | More details |
| Time for scan (mins) | 5–30 | 15–60 |

bone structures which is an advantage over MRI. However dental metallic devices are one of the most problematic issues with CT scan quality. These devices cause considerable streak artefacts that obscure the nasal cavity and sinus anatomy. In terms of the nasal cavity, MRI distinguishes mucosal structures well, although the nasal turbinate cartilage location has to be inferred from its surrounding mucosa, since actual bone structures may not be visible. For the respiratory airways as a whole there is a predominance of air while the long scan time makes MRI susceptible to low signal to noise during inflation of the lung parenchyma. Respiratory triggered or breath hold sequences are needed for MRI imaging however a comparable image quality with CT can be difficult to achieve. Table 3.1 compares the differences of the two scans.

The scanned images can be stored in a variety of formats (e.g. Analyze, DICOM, GE Genesis, Interfile, Siemens Magnetom, Siemens Somatom and NEMA formats). However the most common and the standard is the DICOM (Digital Imaging and Communications in Medicine) format. DICOM files contain both image data and headers, which stores information about the patient and the medical image. It was created by the National Electrical Manufacturers Association (NEMA) to aid the distribution and viewing of medical images, such as CT scans, MRIs, and ultrasound. There are many DICOM viewers and software both freeware or as commercial licenses.

### *3.2.4 Other Medical Imaging Techniques*

There are many other medical imaging techniques which are used for different purposes such as scans for detecting cancer, bone fractures, and abnormalities in body organs. In this section we will only describe those techniques that provide useful data for respiratory airway reconstruction. As discussed earlier, CT provides excellent contrast between the airway wall and lumen measurement its ionizing raditiation limits its use, particularly for pediatric studies. Furthermore MRIs are limited in detecting obstructive lung diseases because of the lack of water content within the predominantly air-filled lungs. In addition standard CT and MRI are also limited by the scan resolution that can be achieved. More advanced imaging techniques are continually being developed and some of these include:

*Hyperpolarized Helium gas MRI (HPHe MRI):* Studies have shown promising results in detecting regional ventilation defects and that it is a reliable method for measuring the lung airways (Eric et al. 2011). It has greater resolution allowing imaging ventilation defects in the small airways and alveoli (Wang et al. 2008). The contrast between the gas in the airway and the lumen walls are quite different to MRI and CT and therefore a specific algorithm is needed for the HPHe MRI.

*Micro-CT, Micro-MRI:* Tiny structures associated with the alveolar region presents challenges for morphological and functional analysis using standard CT and MRI. Micro versions of these imaging techniques provide, less noise, and higher spatial resolution to allow greater detail for airway reconstruction. Some drawbacks of the micro systems include the higher costs of the system, the increased image acquisition time (spanning into hours), and images typically capture a snapshot of the body organs in time, thus it is unable to study the dynamic respiration cycle. However, 4D micro-CT has been used to study the cardiac structure and function of a mouse heart, with a temporal resolution of 10 ms (Badea et al. 2005).

## 3.3 Image Segmentation

### *3.3.1 Overview*

When an image is read digitally, it is defined as a 2D function, $f(x, y)$ over a rectangular grid, where $x$ and $y$ represent the spatial 2D coordinates, and the result $f$ is a value of the point at $x, y$. In 3D volumetric images obtained by CT or MRI, each slice has a thickness (in the $z$-direction) that represents the slab section at the location of the scan. For medical images, the pixel value is often referred to as the greyscale value or intensity Fig. 3.4. This value represents the attenuation of the x-ray beam caused by the internal structures of the respiratory system for CT-scanned images, while for MRI scans it represents the proton density.

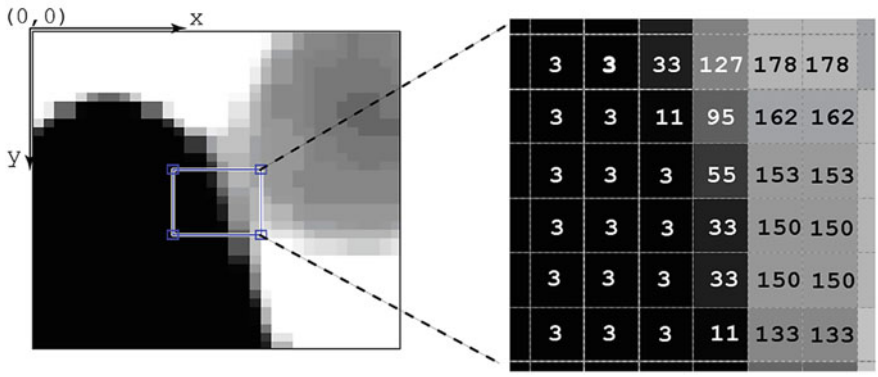


**Fig. 3.4** A *greyscale* image represented digitally by row ($x$) and column ($y$), and the *greyscale* function $f(x, y)$ applied over each pixel

The digital representation of an image can therefore be represented as matrices which are simply in the form of a 2D or 3D array. This forms the basis for segmentation which is performed by matrix calculation and manipulations. Segmentation is the process of extracting a region of interest from an image. More precisely, it is the process of assigning a label to every pixel in an image so that pixels with the same label can be extracted, identified or categorised. From a respiratory simulation perspective this involves extracting a 3D region from a series of 2D cross-sectional monochromatic DICOM images. This process can be manually performed by selecting individual pixels on the cross-sectional slices or automated through segmentation algorithms.

In manual segmentation the user selects the region of interest in every cross-sectional image in a set of scanned images which can have up to 1,000 images. Therefore this procedure is time-consuming and lends itself to inter-observer and intra-observer variability. Fully automated or semi-automated segmentation algorithms for monochrome images are generally based on discontinuities or similarities within the image based on greyscale values (referred to as intensity). For example, discontinuities at edges in an image can be identified based on abrupt changes in the intensity (greyscale level). Similarity in the intensity can be used to extract a region which exhibits similar properties according to a set of predefined criteria. This section provides the reader with an introduction to the field of image segmentation and provides a description of some of algorithms among the many that exist in the literature.

### *3.3.2 Edge Detection*

The basic idea behind edge detection is to locate an area in an image where the intensity changes rapidly. Edge detection of an image significantly reduces the amount of data and filters out useless information, while preserving the important structural properties in an image—an important step in the segmentation of the respiratory airways. There are a number of algorithms for this, but these may be classified as either:

- **derivative based**—where the first derivative of the intensity is greater in magnitude than a specified threshold case of first derivative at the edge of the image there is a rapid change of intensity or
- **gradient based**—to find regions where the second derivative of the intensity has a zero crossing (i.e. a point where the sign of a function changes from positive to negative or vice-versa and represented by a crossing of an axis with zero value). In gradient based edge detection a gradient of consecutive pixels is taken in $x$ and $y$ direction.

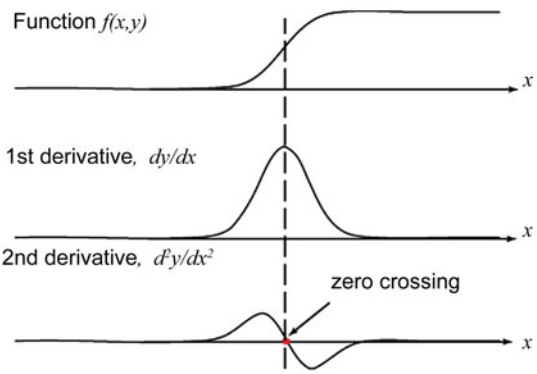


**Fig. 3.5** First-order and Second-order derivatives of a function applied to an edge shown by the jump in intensity

The first order derivative is the gradient of a 2D function $f(x, y)$ is defined as the vector

$$\nabla \mathbf{f} = \begin{bmatrix} G_x \\ G_y \end{bmatrix} = \begin{bmatrix} \frac{\partial f}{\partial x} \\ \frac{\partial f}{\partial y} \end{bmatrix}$$

Its magnitude is

$$\nabla f = \text{mag}(\nabla \mathbf{f}) = \sqrt{{G_x}^2 + {G_y}^2} = \sqrt{(\partial f/\partial x)^2 + (\partial f/\partial y)^2}$$

which is zero in areas of constant intensity. The angle at which the maximum rate of change occurs is:

$$\alpha(x, y) = \tan^{-1}\left(\frac{G_y}{G_x}\right)$$

The second order derivative is typically computed using the Laplacian function and when applied to a 2D function $f(x, y)$ gives:

$$\nabla^2 f(x, y) = \frac{\partial^2 f(x, y)}{\partial x^2} + \frac{\partial^2 f(x, y)}{\partial y^2}$$

From a graphical point of view, consider an edge which has a one-dimensional shape of a ramp and is depicted with a jump in intensity (Fig. 3.5). Taking the first derivative shows a maximum at the centre of the edge of the original function. This is the derivative based method which identifies a pixel as an edge location if the value of *dy/dx* exceeds some threshold. Since edges have higher pixel intensity values than its neighbours, you can set a threshold and compare the *dy/dx* value to find those values that exceed the threshold to detect edges. Taking the second derivative gives a zero at the maximum or turning point of the first derivative. As a result the gradient based

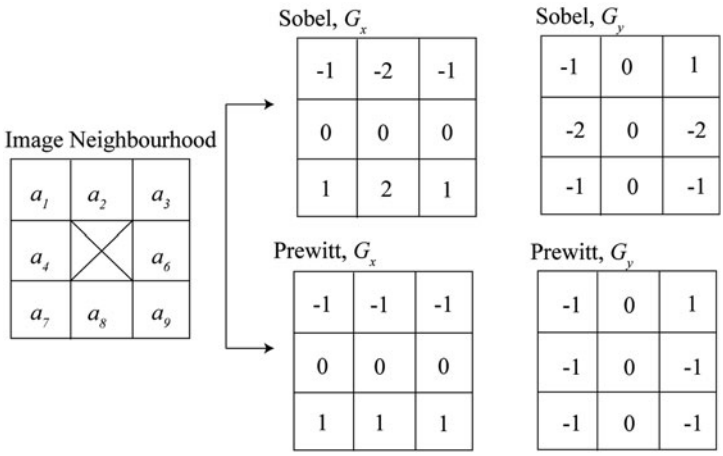


**Fig. 3.6** Sobel, Prewitt, and Roberts edge detector mask and the first order derivative implementation. The centre pixel in the image neighbourhood is marked with an X

method involves finding an edge based on the zero crossing in the second derivative curve. Taking the first and second order on each individual pixel of an image can be computationally intensive and hence can be impractical. A kernel (or mask), which is a small matrix itself, can be used to pass over an image to obtain an approximate derivative value. Some first-order derivative (derivative based) algorithms will be discussed followed by second order derivative (gradient based) algorithms.

The **Sobel** and **Prewitt** edge detectors are first order derivatives that perform a 2-D spatial gradient measurement on an image. It is used to find the approximate absolute gradient magnitude at each point in an input grayscale image. The Sobel edge detector uses a pair of $3 \times 3$ convolution (or filtering) masks, one estimating the gradient in the $x$-direction (columns), $G_x$ and the other estimating the gradient in the $y$-direction (rows), $G_y$. This is performed by applying the kernel onto the centre pixel in a neighbourhood as given in Fig. 3.6.

From matrix calculations this computes as:

**Sobel:**

$$\nabla f = \sqrt{G_x^2 + G_y^2} = \left\{ [(a_7 + 2a_8 + a_9) - (a_1 + 2a_2 + a_3)]^2 + [(a_3 + 2a_6 + a_9) - (a_1 + 2a_4 + a_7)]^2 \right\}^{1/2}$$

**Prewitt:**

$$\nabla f = \sqrt{{G_x}^2 + {G_y}^2} = \left\{ [(a_7 + a_8 + a_9) - (a_1 + a_2 + a_3)]^2 + [(a_3 + a_6 + a_9) - (a_1 + a_4 + a_7)]^2 \right\}^{1/2}$$

An edge is then identified at a pixel when that pixel has $\nabla f \geq T$, where $T$ is a specified threshold. The Prewitt detector produces somewhat noisier results as all its

$$\frac{1}{159}\begin{bmatrix} 2 & 4 & 5 & 4 & 2 \\ 4 & 9 & 12 & 9 & 4 \\ 5 & 12 & 15 & 12 & 5 \\ 4 & 9 & 12 & 9 & 4 \\ 2 & 4 & 5 & 4 & 2 \end{bmatrix}$$

**Fig. 3.7** An example of a $5 \times 5$ Gaussian filter that can be applied for as a mask for smoothing in the Canny detector method

coefficients are set to 1, while in the Sobel detector there is a coefficient with a value of 2, which provides smoothing.

For gradient based edge detection, the second order derivatives may be obtained by the Laplacian of a Gaussian (LoG) detector (Marr and Hildreth 1980), or the Canny edge detector (Canny 1986). These algorithms are more sensitive to noise because it differentiates the image signal twice.

Firstly, the **LoG** algorithm applies a smoothing filter to reduce noise by using a Gaussian function

$$h(r) = -\exp\left(-\frac{r^2}{2\sigma^2}\right)$$

where $r^2 = x^2 + y^2$ and $\sigma$ is the standard deviation, to the original image. It then computes the Laplacian of the smoothed image,

$$\nabla^2 h(r) = -\left[\frac{r^2 - \sigma^2}{\sigma^4}\right]\exp\left(-\frac{r^2}{2\sigma^2}\right)$$

and then searches for zero crossings by scanning along each row.

The **Canny detector** described in Canny (1986) begins with smoothing using a Gaussian filter with a specified standard deviation, $\sigma$ to reduce noise. Once a suitable mask has been calculated (Fig. 3.7), the Gaussian smoothing can be performed using standard convolution methods (filtering). The larger the width of the Gaussian mask, the lower the detector's sensitivity is to noise.

After smoothing, the strength of an edge can be found by taking the gradient of the image by applying the first derivative functions such as Sobel or Prewitt edge detectors. This establishes gradients in the image field and the edge direction angle is rounded to one of four angles representing vertical, horizontal and the two diagonals (e.g. 0°, 45°, 90°, and 135°). Note that any edge direction falling within the 0–22.5° and 157.5–180° is set to 0°. An edge point is defined at pixels whose strength is locally maximum in the direction of the gradient. The algorithm then tracks along the edge points and suppresses any pixel (sets it equal to 0) value that is not considered to be an edge so as to give a thin outline. This process is called non-maximum suppression. The pixels are thresholded using two thresholds T1 and T2, with $T1 < T2$. Pixels with

values greater than T2 are strong edge pixels and anything in between T1 and T2 are said to be weak edge pixels. Finally the algorithm creates the outline by selecting any pixel in the image that has a value greater than T1 and marks it as an edge pixel, and connects adjacent pixels that are greater than T1 and otherwise it ends.

### 3.3.3 Thresholding

The simplest segmentation algorithm is based on the greyscale levels of pixels which is referred to as thresholding. This segmentation method uses either global or local information to select only those pixels within a greyscale range (threshold) and a binary function is applied as,

$$g(x) = \begin{cases} 1 & \text{if} \quad \min_x(f(x)) \leq \theta \leq \max_x(f(x)) \\ 0 \end{cases} \tag{3.1}$$

where $\theta$ is the selected greyscale value and *f(x)* is the greyscale values of the images. The output is a binary image where each pixel is coloured as black or white, depending on a pixel's label of 1 or 0. It is most effective for images containing uniform regions with clear differentiation from a background or other objects in terms of pixel intensity values. The problem arising from this is the selection of an optimal threshold value. Some global threshold selection algorithms include Otsu (1979), which obtains the threshold values using an image histogram and the work by Ridler and Calvard (1978). Using a global threshold can be problematic since erroneous selections may occur in regions where signal noise is large compared to the image content (low signal to noise ratio) or when the object and background greyscales have large variations throughout the volume. In many software applications the pixel thresholds are can be adjusted interactively and displayed in real-time on screen. When a greyscale range is defined, boundaries are traced for all pixels within the range in the image. Greyscale thresholding works well when an image that has uniform regions and contrasting background.

### 3.3.4 Region Based Segmentation

In Sect. 3.3.2 the segmentation process involved finding boundaries between regions based on pixel differences (discontinuous intensity levels) while in Sect. 3.3.3 the regions were identified through threshold values based on the intensity values of the pixels. In this section, region based segmentation is presented which involves finding the region of interest directly. Unlike the previous methods, region-based segmentation works from the inside region out, instead of outside in, which produces coherent regions. However the difficulties lie in the criteria for region membership which are typically more difficult than applying edge detectors. In addition it generally can't find objects that span multiple disconnected regions.

***Region growing*** is the process where pixels are grouped into larger regions based on predefined criteria for the growth. To begin, *seed* pixels are defined which grow into regions by appending to each seed pixel its neighbouring pixels that satisfy a predefined criteria (i.e. specific range of grey level). The predefined criteria wield significant influence on the output. For example specifying pixels to be too similar gives good homogeneity and coherent regions, but it lends itself to *oversegmentation* whereby the region suffers from being smaller than the actual object and probably won't span over separate objects. More relaxed criteria can produce larger regions that fill the entire object but may lead to leaks across the boundaries of those objects and fill multiple objects unnecessarily. Selecting the criteria for DICOM images typically involves a threshold range on the pixel intensity, or to apply an average intensity over a neighbourhood around each pixel. For multiple regions, seed points should be selected within each of the desired regions since the seeded points grow through neighbouring pixels that are similar, and is expected to end at boundaries.

***Region splitting*** is an alternate method to region growing which begins by dividing up the whole image into disjointed sub-regions and then merges similar regions together. The splitting criteria continues as long as the properties of a newly split pair continue to differ from those of the original region by more than a threshold. Recursively splitting image into smaller regions becomes more efficient than region growing which involves recursively merging individual pixels to produce larger coherent regions. The main problem with this region splitting is the difficulty of deciding where to make the partition. One splitting technique is to subdivide the image into smaller quandrants building a quadtree structure. The process involves looking at an area of interest to determine if the region satisfies a set criteria. If so, then the area retains its region, if not, then the area is split into four equal sub-areas and each subarea is reconsidered with the set criteria. This process continues until no further splitting occurs. In the worst case the areas become so small that they are actually a single pixel. One can also allow merging of two adjacent regions if each has similar characteristics and satisfies the set criteria (Fig. 3.8).

The ***watershed algorithm*** concept comes from the field of topography, referring to the division of landscape into water catchment basins or areas. The grey scale image is seen as a topological surface, where each pixel is a point situated at some altitude as a function of its grey level. The white colour (grey level 255) is taken as the maximum altitude and the black colour (grey level 0) the minimum. Deep regions, known as catchment basins, will exist at local minima, and separated by ridges in the topology called watershed lines or simply watersheds. Two approaches may be used to extract the regions of interest. The first is to find basins, then their enclosing watersheds by taking a set complement. This is analogous to the topolgocial surface being filled with water. The catchment basins will fill up with water starting at these local minima. As the flood level rises, boundaries between adjacent segments (catchment regions) erode and those segments merge. The other approach is to compute a complete partition of the image into basins, and subsequently find the watersheds by boundary detection.

This section introduced the reader to some common algorithms that have been used as a basis for segmentation but is certainly not limited to these algorithms alone.

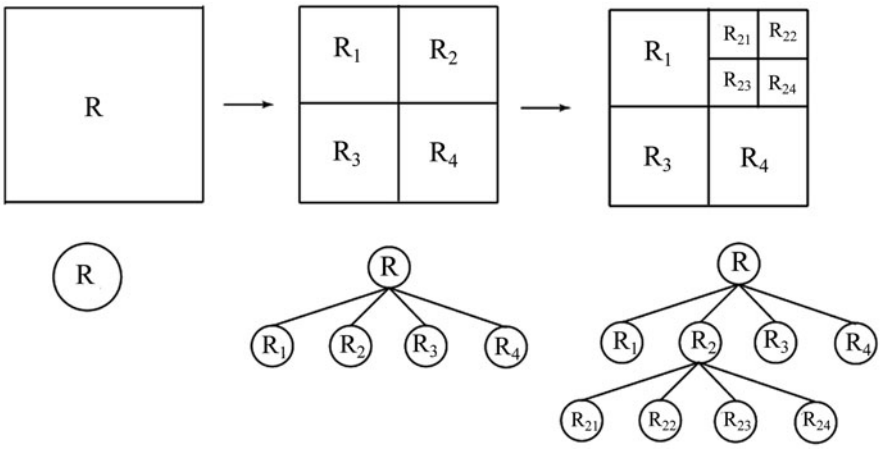


**Fig. 3.8** A single region in an image that is progressively split into quad-regions when adjacent regions do not satisfies a set criteria

For those interested in the field of computational science and image processing, the authors suggest the following textbooks and review articles that provide greater detail (Demirkaya 2009; González and Woods 2008; Suri 2005; Umbaugh 2005).

### *3.3.5 Using Specialised Medical Software*

Segmentation algorithms presented in the previous section is a sample of what exists in what is an active research field. Published algorithms in journals allow computer scientists, who are capable of advanced programming skills, to program and implement the algorithms using computer languages such as C, C++, and Java. For most engineers and medical practitioners this step is not feasible without programming skills. Fortunately there exists a number of commercial and free specialised medical software that converts the CT/MRI images and applies segmentation algorithms with an easy to use Graphical User Interface (GUI) or has a command line to execute actions. A brief description of free and commercial software is given in Appendix A which is a sample of what may be out in the public domain. Although each software may differ with its own interface, presentation, and algorithms available, there exists a generic work flow for extracting the required computational region from the scanned images.

### *3.3.6 Surface and Volume Reconstruction*

After segmentation the 3D output file can be saved under different CAD formats which need to have certain conditions to be mesh-able. For example the outputted

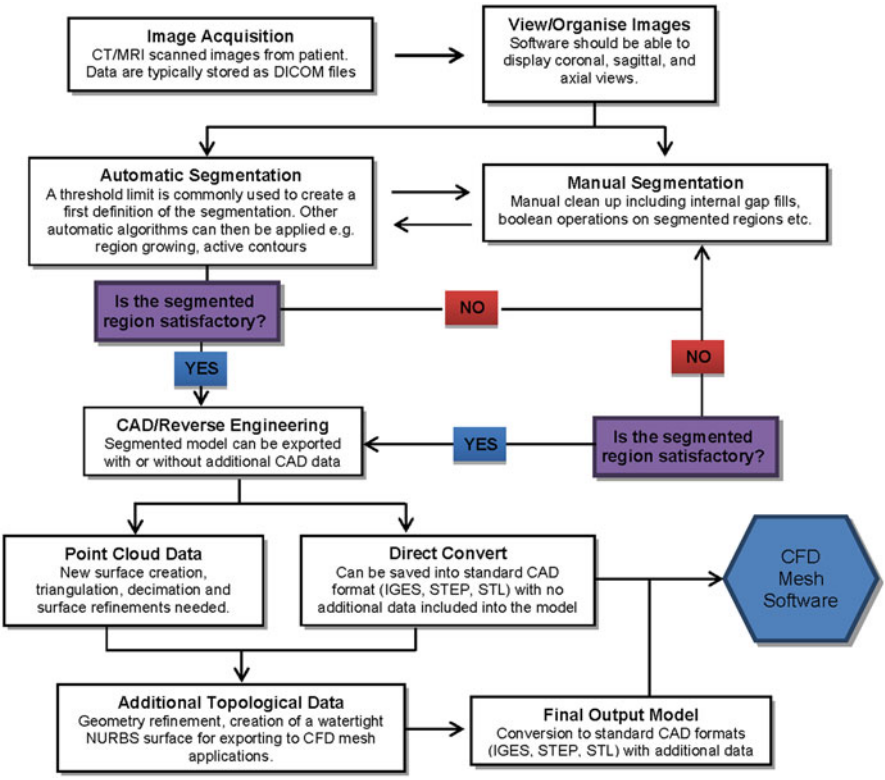


**Fig. 3.9** Flow chart showing the segmentation process to extract and export a region of interest into a 3D computer model commonly referred to as a Computer-Aided-Drawing (CAD) model

model may only contain a wireframe model which lacks geometric topological relationships such as vertex, lines, faces, and the topology of the face perimeters or volume shells. A generic work flow is shown as a flowchart in Fig. 3.9. After segmentation the output file can be directly read into a CFD meshing software or additional topological data can be included into the model. An advantage of including the topological data is that the file becomes more compatible with CFD software. During the addition of topological data, the geometry can be mathematically described with a Non-Uniform Rational B-Spline (NURBS) for simple integration into a CFD-mesh software. This involves patching or overlaying a water-tight surface (defined through NURBS) which holds point, line, and face data that are interconnected and relational. This is important since some CAD models will not be water-tight. The decision to directly output or apply a water-tight surface is dependent on the final CFD mesh software, since in some software, a lot of CAD processing is self contained and can be performed within the software.

It is important for the reader to appreciate the structure of 3D CAD models and its relationship to CFD meshing. The exported model should be in a format that can be read by the CFD meshing software. The format the model is saved as serves as an

intermediary between the exporting software and the receiving CFD/CAD software that reads in the intermediary format. Therefore there is a reliance on the file format adhering to standards to allow smooth data exchange. However this is not always the case and there are usually some variances of CAD formats among different software vendors. This causes loss of data and therefore loss of detail of the geometry, leading to what is known as a '*dirty*' CAD geometry. Such *dirty* geometries exhibit stray points, non-intersecting lines, cross-overs, and slivers in the geometry. When this occurs the user needs to clean up the geometry which can be performed within the CFD meshing program or external CAD-specific software. This is another reason for ensuring that the segmented model contains a water-tight surface.

The output file can be set as standard 3D CAD formats include STL, IGES (Initial Graphics Exchange Specification), or STEP. As an example, the data structure for the above mentioned CAD formats is given below:

- *STL* or stereolithography, files are commonly used for rapid proto-typing manufacturing. It contains only surface geometry of a three dimensional object only. The surface is made up of small triangulated faces, called facets. Each facet is represented by three vertices (corners of the triangle) and its perpendicular direction. user. If too many triangles are created, the STL file size can become unmanageable. If too few triangles are created, curved areas are not properly defined and a cylinder begins to look like a hexagon (see example below).
- *IGES* (Initial Graphics Exchange Specification) is a platform independent format used to allow digital translation between CAD software. It contains two main data entities: geometry (to describe shapes such as curves, surfaces, solids and relationships) and non-geometry (to describe graphical or computational data such as colour, mass, time etc). The format is standardised to allow file interchange between different vendors. Unfortunately, CAD vendors have their own interpretation of the IGES standard, which renders some the information useless to others. Additionally, the size of an IGES file can be typically larger than other formats because of the two data entities it stores.Further information on IGES format can be found in *www.steptools.com*.
- *STEP*, is the acronym for Standard for The Exchange of Product model data which is a proposed International Standards Organization (ISO) standard for electronic data exchange. It is also known as the product data exchange using STEP (PDES) in the United States.

## 3.4 Examples

The reconstruction of the different respiratory airway regions can be performed by using the generic flow process as was shown in Fig. 3.9. Segmentation algorithms form the core step in extracting the region of interest. However instead of presenting the same procedures in this section, alternative methods are shown. This is especially helpful if access to scanned images is not available. The nasal cavity model example highlights a typical reconstruction process for segmentation from CT or MRI scans.

The other examples provide alternative methods which help the reader to appreciate that reconstruction methods are not limited to segmentation algorithms alone.

### *3.4.1 Implementation of Different Segmentation Algorithms*

A DICOM image obtained from CT of the nasal cavity is shown in the axial plane through the middle of the maxillary sinuses. Segmentation algorithms presented in Sect. 3.3 are applied with an automatic threshold detection level (Fig. 3.10).

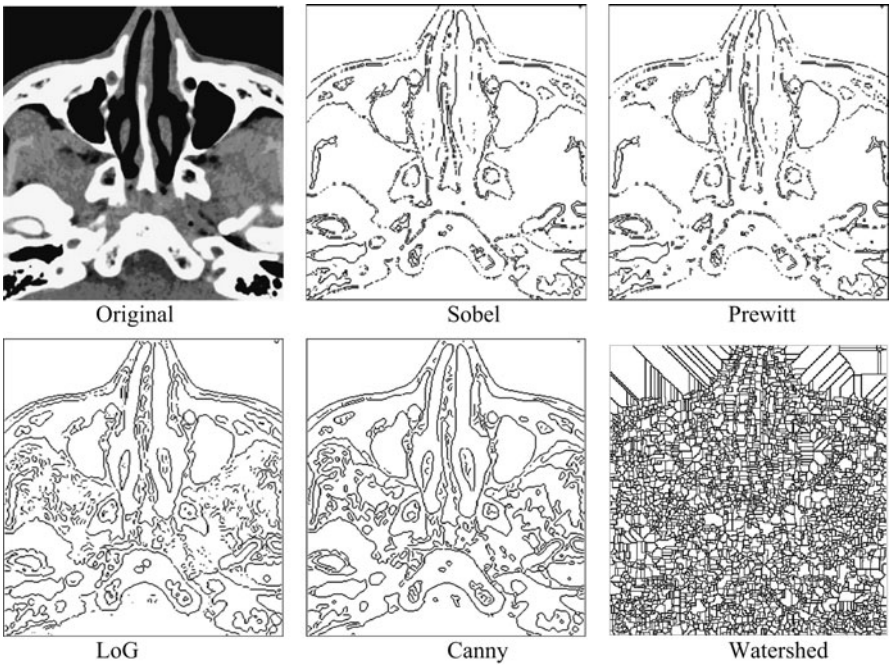


**Fig. 3.10** A DICOM slice image of a nasal cavity in the axial plane showing the middle region of the maxillary sinuses is shown with different segmentation algorithms applied

The Sobel and Prewitt edge detector algorithms produce discontinuous lines, and detect some tissue and bone region. It also misses an additional structure in the nasal passageways. For the region growing algorithms (LoG and Canny) the outline of the nasal cavity, sinuses and other structures such as teeth and bone are clearer. However there are too many false regions in the muscle and tissue region that does not belong. The watershed algorithm selects the entire image to decompose and too many ridges appear. It must be noted that in these examples the threshold levels were not controlled which would improve the output especially to filter out the unwanted greyscale levels.

### 3.4.2 *Nasal Cavity, Pharynx, and Larynx*

In this example the nasal cavity, pharynx and larynx are presented. Sets of CT-scans that included from the top of the nasal cavity down to the larynx were obtained. The images are in DICOM format and therefore need to be viewed with any DICOM reader. Figure 3.11 shows two slices taken from the directory set of images. In the corners of the images are specific details regarding the scan protocol. In the example shown in Fig. 3.11 a 37-year-old non-smoking, Asian male using a helical 64 slice multidetector row CT scanner was scanned. In DICOM images, data is embedded into the file directory and this is displayed in the slice images. The data reveals details of the scan, such as the image resolution—512 × 512 pixels, the field of view (FOV)—320 mm, the power rating—120 kV Peak and 200 mA, and the gantry tilt which is −8.00 mm.

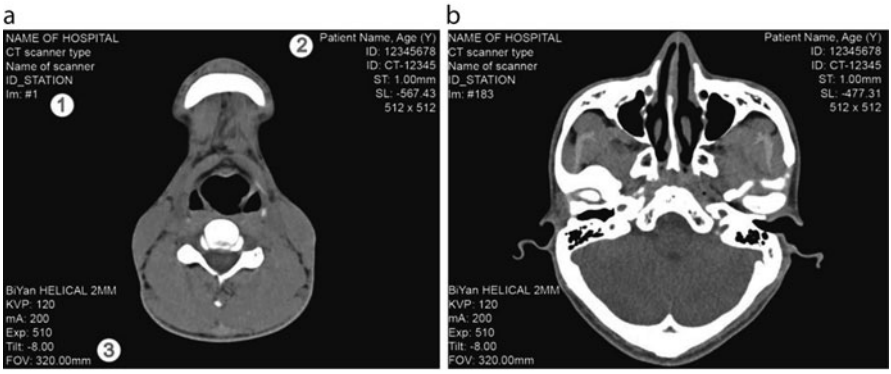


**Fig. 3.11** CT scans viewed in 2D using the free DICOM viewer '*MicroDicom*'. In the images specific details on the scan protocol are displayed and labelled as *1*, *2*, and *3* in the figure. Data in these section are: *1* gives the hospital, scanner details, and scan image number; *2* provides patient details, and image resolution in pixels (512 × 512); *3* type of CT scan (helical in the example) and scan protocol

A gantry tilt is the angle that the CT slices are taken from the perpendicular and is used for a number of reasons. This includes reduction of radiation dose to sensitive regions of the body such as the lens of the eye or the thyroid gland, avoiding artefacts from fillings, or to achieve a better perspective of the region of interest. When a gantry tilt is used, an interpolation or correcting function within the segmentation algorithm is needed to realign the images (Fig. 3.12).

Segmentation of the scanned images is performed through the freeware ITK-SNAP. The images are first loaded into the software and the steps given in Fig. 3.9 are followed through. The CT images are coloured by tissue density represented as grey scale values. In this example the airway filled with air is identified by selecting an appropriate intensity range. This ensures that a boundary surrounding the air region can be identified. Screenshots showing the segmentation of a nasal cavity is

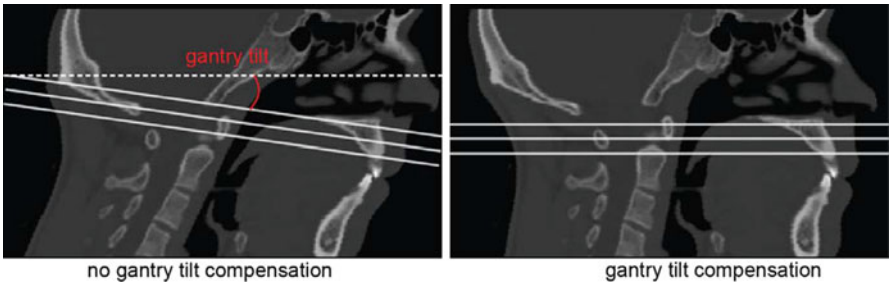


**Fig. 3.12** Image scanned with a gantry tilt, showing the influence of no gantry tilt compensation and with compensation

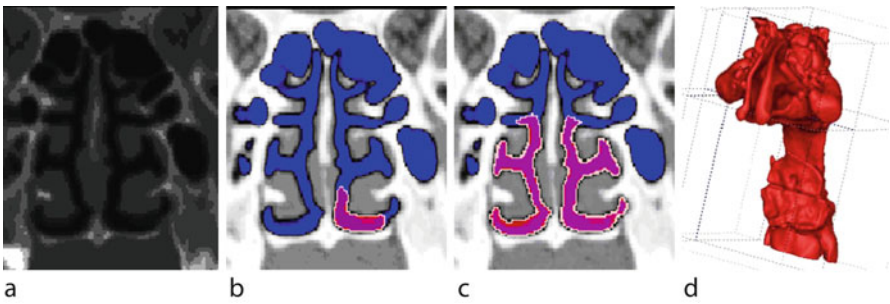


**Fig. 3.13** 3D active contour (snake) segmentation of a human nasal cavity using the open source application '*ITK-SNAP*' (Yushkevich 2006). **a** Unprocessed DICOM image. **b** Intensity thresholding creates the outlined blue region, and the active contour segmentation (maroon colour) after 100 iterations shows the selection '*snaking*' through the region. **c** Active contour segmentation after 400 iterations. **d** Final output model as an .stl file

given in Fig. 3.13 which uses the active contour segmentation algorithm. To initiate the active contour segmentation, the region needs to be seeded by manual selection. Successive iterations are performed which grows or '*snakes*' through the geometry, automatically filling up the airway.

The segmentation process took under 10-minutes on a desktop computer with 4 GB-RAM, 3 GHz-processor, and 256 MB-Video-RAM. Because the external air surrounding the face is contiguous with the nasal cavity via the nostrils, it will also be selected during the automated region growing segmentation. This region can be included if the simulation is to explore the effects of the external nose and the outside airflow on the inhalation/exhalation flow profiles. On the other hand, it would be deleted out of the geometry if the nasal cavity is the only region required. Recent studies have begun incorporating the external nose and the external airflow to investigate their influence (Lee 2010; Taylor 2010). The final exported model was in STL format which is readable in most CAD software and CFD-mesh programs.

### 3.4.3 Oral Cavity

It is rare to find existing scans that have the oral cavity opened. Typically a patient undergoing a scan for other medical purposes has their mouth closed and therefore this region is not shown in the scans. In addition the shape of the oral cavity during breathing can differ during inhalation, exhalation, high exertion activities such as running, or smoking. An alternative is to obtain an imprint such as those made from the dentists that provide a physical model. This model can then undergo reverse-engineering techniques by scanning the model and importing the data into a CAD software for clean up and to create a volume by closing the model. As an alternative method, the following example will make use of existing data found in the literature. 2D cross-sections of the oral cavity at 0.3 cm intervals are shown in Fig. 3.14.

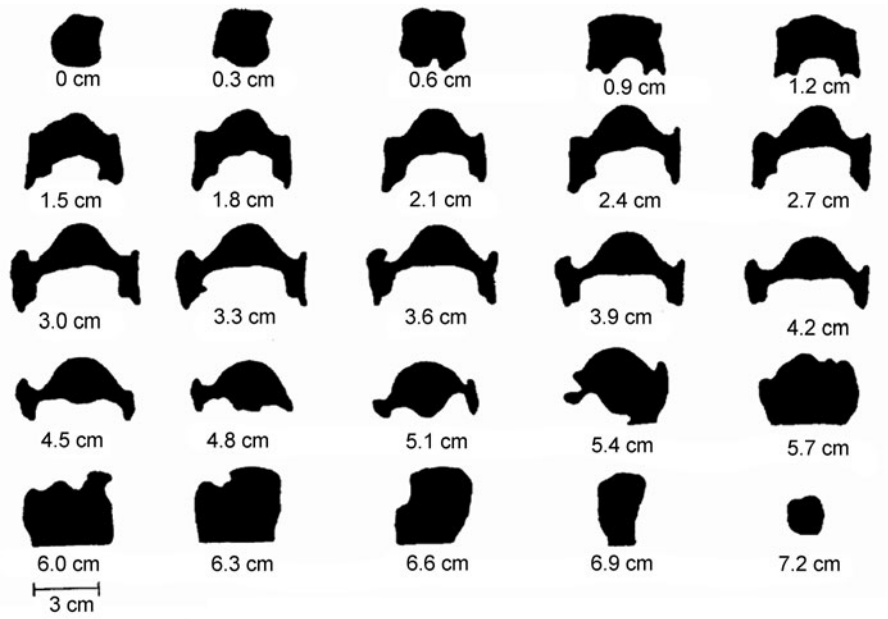


**Fig. 3.14** Coronal sections of the oral cavity at 0.3 cm intervals extending from the lips to the oropharynx. The distance from the oral entrance (denoted as the origin) is given under each cross-section. This data is taken from Cheng et al. (1997)

The figure is taken from the work of Cheng et al. (1997) which also provide perimeters and cross-sectional areas of each coronal cross-section. Using CAD or any specialised 3D-graphic design software, the outline from each cross-section is laid out in 3D space separated by 0.3 cm intervals. The outline of each slice then needs to be stitched together to form a surface shell, or to apply 3D volume-rendering methods. The accuracy of this technique is heavily reliant on the interpolating function that is used to stitch the outlines together. Furthermore a smaller interval distance between each cross-section would improve the accuracy of the model greatly.

Figure 3.15 shows some the process used in this reconstruction technique.

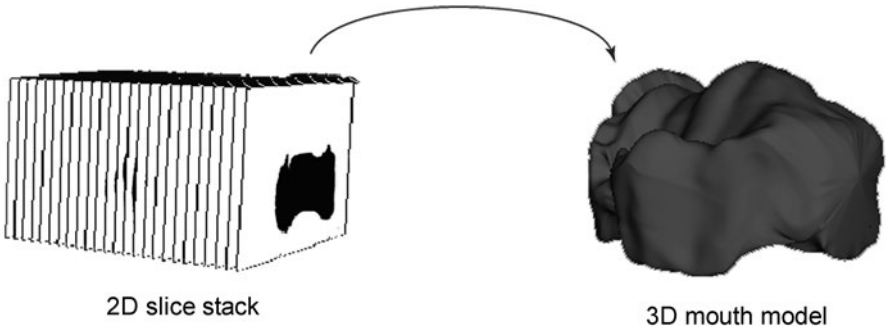


**Fig. 3.15** 2D Images from Fig. 3.14 are spaced out by 0.3 cm intervals in a 3D modelling program. Using mathematical interpolation algorithms, splines and curves can be integrated into the model to create a surface

### *3.4.4 Tracheobronchial Airway Tree*

The airways in the human lungs are a complex asymmetric branching structure. However, most of the airways models in both experimental and numerical investigations have used highly simplified models in order to reduce the computational/experimental cost and the complexity in producing the highly complex airways structure. In this section two methods for reconstructing the tracheobronchial airway tree is given. The first example involves the reconstruction via segmentation methods, while the second example is to use published geometric data as a base for sketching and modelling the airway in CAD software.

*Segmentation Method*: Scanned data was acquired with 1 mm collimation, a 40 cm field of view (FOV), 120 kV peak and 200 mA. At baseline, 2 cm axial length of lung caudal to the inferior pulmonary ligament was scanned during a single full inhalation total lung capacity breath-hold, which yielded 254 contiguous images (slices) of 1 mm thickness with voxel size of 0.625 mm $\times$ 0.625 mm $\times$ 1 mm. Identification (segmentation) of the airway tree in the scans can be performed manually by an image analyst expert such as a radiologist of physician. Each 2D slice is segmented independently before they are stacked together in 3D. This is a time consuming and tedious process because of the complexity of the tree and the large number of slices in the data set. Instead, the use of semi-automated algorithms built into an image processing software is the best option. A segmentation algorithm partitions pixels from the 2D image and into connected regions that possess a meaningful correspondence to object surfaces in a 3D scene. In this segmentation a smaller adaptive region of interest (ROI) that followsthe airway tree branches as they are segmented is used to reduce computational complexity and minimise segmentation leakage (where unwanted regions are automatically selected). The ROI hasa cylindrical shape and adapts its geometric dimensions, its orientation,and position to the predicted size, orientation, and positionof the airway branch to be segmented. This concept can be illustrated by Fig. 3.16.

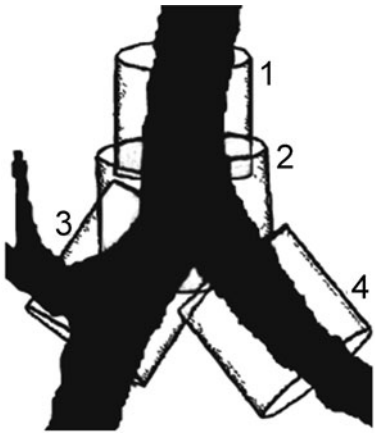


**Fig. 3.16** Adaptive cylindrical regions of interest (numbered grey cylinders) that follows the airway tree branches as the fuzzy connectivity segmentation progresses. This leads to faster segmentation time as the segmentation process is kept close to the airway and fewer background voxels need be analysed. In addition any segmentation leaks can be detected and dealt with early segmentation leakage

After segmentation the model can be smoothed to reduce any artificial regions created due to the effects from noise found in the scanned images. In addition, if the model is too rough it will create problems during the surface fitting and meshing process. On the other hand if it is too smooth some important topological features will be omitted. The outputted STL model from the particular segmentation software used lacked geometric topological relations for CFD meshing. The model needs to go through CAD-based modelling process which is a reverse-engineering process. The STL model is full of triangulated faces which have a NURBS surface definition applied to it. 1,084 NURBS patches were generated on the airway tree and the surface model is saved as IGES file (Fig. 3.17).

*CAD-based Method:* An alternative method for airway reconstruction is to use existing data available in the literature. A widely used model is Weibel's symmetric model from Weibel (1963) with an updated set of data given in Weibel (Weibel 1997).

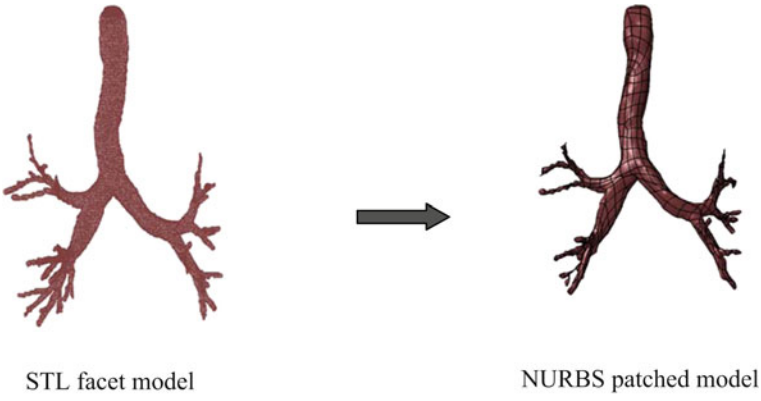


**Fig. 3.17** Tracheobronchial airway tree with NURBS surface model applied from a triangulated STL file

**Table 3.2** Representative data for the first six generations of a symmetrical tracheobronchial airway tree with lung volume of 4800 $cm^3$ at about 75 % total lung capacity, based on Weibel (1997)

| Generation number | Number of airways | Airway diameter (cm) | Airway length (cm) | Distance from the carina* to end of airway | Total cross sectional area per generation | Total airway volume per generation |
|---|---|---|---|---|---|---|
| 0 (trachea) | 1 | 1.80 | 12.00 | – | 2.54 | 30.5 |
| 1 | 2 | 1.22 | 4.76 | 4.76 | 2.33 | 11.1 |
| 2 | 4 | 0.83 | 1.90 | 6.66 | 2.13 | 4.11 |
| 3 | 8 | 0.56 | 0.76 | 7.42 | 2.00 | 1.50 |
| 4 | 16 | 0.45 | 1.27 | 8.69 | 2.48 | 3.23 |
| 5 | 32 | 0.35 | 1.07 | 9.76 | 3.11 | 3.29 |
| 6 | 64 | 0.28 | 0.90 | 10.66 | 3.96 | 3.55 |

*the **carina** is the ridge at the lower end of the trachea that runs between the two primary bronchi, where the trachea bifurcates

**Table 3.3** Representative data for the first six generations of a symmetrical tracheobronchial airway tree with lung volume of 3300 $cm^3$, based on Horsfield (1994)

| Generation number | Number of airways | Airway diameter (cm) | Airway length (cm) | Branching angle | Inclination angle (0° = vertical axis, 90° horizontal axis) |
|---|---|---|---|---|---|
| 0 (trachea) | 1 | 1.65 | 9.10 | – | 0 |
| 1 | 2 | 1.20 | 3.80 | 36 | 20 |
| 2 | 4 | 0.85 | 1.50 | 35 | 31 |
| 3 | 8 | 0.61 | 0.83 | 28 | 43 |
| 4 | 16 | 0.44 | 0.90 | 35 | 39 |
| 5 | 32 | 0.36 | 0.81 | 39 | 39 |
| 6 | 64 | 0.29 | 0.66 | 34 | 40 |

It is based on measurements of the major conducting airway branches from a plastic cast of a pair of human lungs. Horsefield et al. (1971) and Yeh and Schum (1980) also provide similar data but included some asymmetry into the models. Several models have been developed by the International Commission on Radiological Protection (ICRP) with each successive model an improved iteration from the previous model. Their first model is described in ICRP-2 (ICRP 1960) with a successive model published in ICRP-66 (ICRP 1994). The published data for the first six generations of the tracheobronchial airway from the models of Weibel and ICRP are given in Table 3.1, 3.2 and 3.3. In the reconstruction of tracheobronchial airway tree, it is possible to sketch the model because of the available data. In this example, the geometry details of Weibel's model are used in a CAD software to sketch and create a 3D-model and the final CAD model is shown in Fig. 3.18.

### *3.4.5 Pulmonary Acinar Region*

The acinus region is the terminating region of the respiratory airway. They are also the smallest in size which makes the image processing difficult. Until recently all models studied have been simplified models due to limitations in the spatial resolution of

**Fig. 3.18** Weibel's model reconstructed using CAD software

imaging techniques (Tsuda 2008). In this section three models are discussed and are presented from simplest to most complex method.

*Simple Alveolar Duct Model:* A single spherical alveolus placed on a cylindrical duct can be used to demonstrate alveolar flows. Early studies have used semi-circular alveolar tori on a cylindrical duct (Henry 2002; Tsuda 1995) or even hemispherical alveolus on horizontal planes (Haber 2000). In this example the duct is modelled as a cylindrical shell with length of $L_d = 0.5$ mm and diameter $D_d = 0.25$ mm. The alveolus is modelled by a spherical cap with diameter of $D_s = 0.3$ mm and is connected to the centre of the duct at a depth of $H_d = 0.1$ mm (Fig. 3.19).

*Alveolar Ductal Tree*: Like the tracheobronchial airway tree, idealised models can be created based on published data. In the description of the acinus region by Fung (1988), the alveoli are assumed to be initially equal and space filling, ventilated as uniformly as possible and obey the laws of elasticity. The basis of these assumptions are made on photographs of the microstructure of the lung that show the alveolar walls

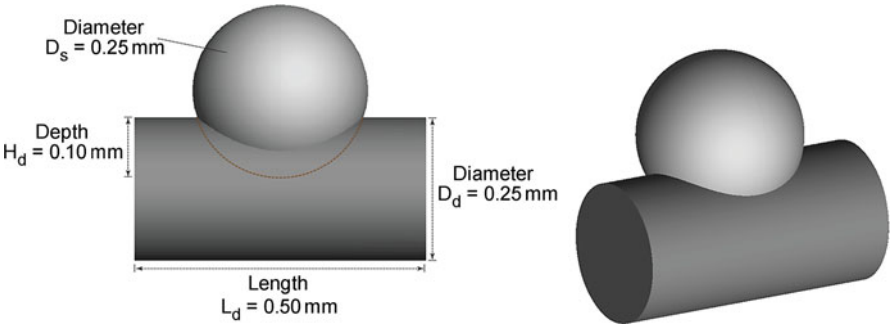


**Fig. 3.19** Simple alveolar duct with single alveolus

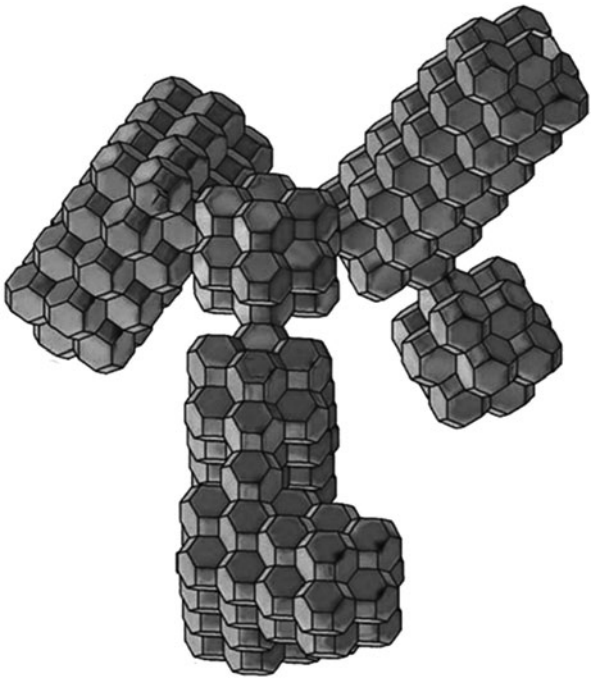

**Fig. 3.20** Assembly of 14-sided polyhedra into an alveolar ductal tree created by Sznitman (2008) and reproduced here

are predominantly hexagons and rectangles, with occasional pentagons. The alveoli is then depicted as a cluster of 14-sided polyhedrons connected to each other by matching faces forming a solid unit without any gaps (space-filling). In the centre is a 14-sided polyhedron that has its faces removed and the edges become mouths of the surrounding alveoli. Based on this model Snznitman (2008) produced an acinar tree generation with characteristic alveolar dimension of 0.14 mm. The entire geometry consists of 190 polyhedra for a total sub-acinar volume of $\sim$0.2 mm$^3$ which is $\sim$0.2 % of the average volume of an entire acinus (Haefeli-Bleuer and Weibel 1988) and is shown in Fig. 3.20.

*X-ray Tomographic Microscopy:* Scanned images of the acinar region need to be obtained through high resolution scanners such as a synchrotron radiation-based X-ray tomographic microscopy (SRXTM). This is because the surface area of the lung parenchyma is extremely large (order of metres, i.e. $10^0$) in comparison with the alveolar (order of microns, i.e. $10^{-6}$). In the study by Tsuda et al. (2008) it is shown that SRXTM can render volumes up to $10^9$ µm$^3$ of lung tissue with resolution to a voxel size of 1.4 µm$^3$. Their model was segmented using a threshold as a basis and then region growing through an '*object connectivity analysis*'. Some smoothing was performed and the final model is reproduced and shown here in Fig. 3.21.

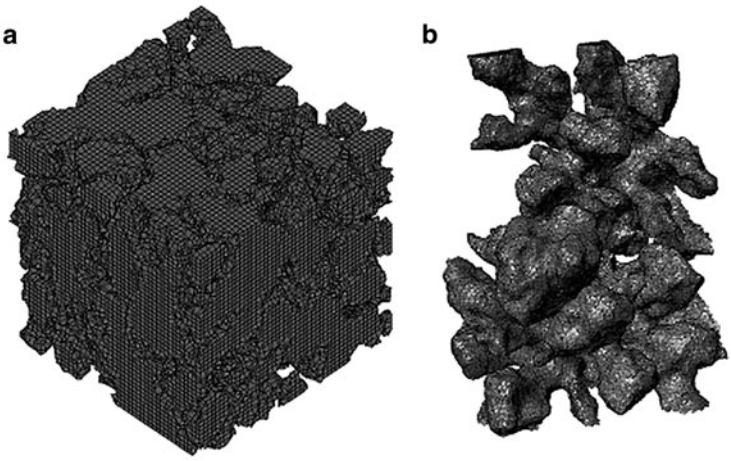


**Fig. 3.21** **a** Reconstruction of 3D air spaces separated by tissues from region of interest. **b** Enlargement of a small alveolated air section isolated from the centre of region of interest. (Image from Tsuda et al. 2008)

## 3.5 Summary

The reconstruction of the respiratory airways begins with obtaining the relevant data for the application. For realistic airway models, medical imaging techniques using the latest technology are needed especially for regions where there are micro structures like the acinus region. However the use of SRXTM scanners and its data are not as widely available as those from CT and MRI. Regardless the scanned images are 2D contiguous slices that are separated by a known interval distance. The reconstruction of this data from 2D to 3D requires extraction of the region of interest in what is known as the segmentation process. A number of algorithms have been developed by researchers and biomedical scientists which can be accessed through either open-source/free software or commercial software. Access to the algorithms is available either through a graphical user interface or command line text. After segmentation, the extracted region typically needs to be 'cleaned' for any noise or artificial regions that are not needed. Sometimes the model may need further processing in CAD software. An important step before moving to a CFD mesh model is to ensure that the segmented model has a water-tight surface. Although the reconstruction process is dependent on segmentation techniques, there are alternatives and these alternatives are also provided for the different regions of the respiratory airway.

This chapter aimed to bring the reader up to speed with techniques of reconstruction that cross over into different disciplines including biomedical imaging, manufacturing/reverse engineering, and CAD/drafting fields. The content presented is an overview of some theory and its application and is certainly not an exhaustive description of what exists for the disciplines mentioned. However it is hoped that the

reader has gained an appreciation for the cross-discipline nature of CFPD research. In the following chapter meshing of the 3D models for fluid and particle analysis is introduced. This is the first step in any CFPD problem.

## 3.6 Review Questions

1. Why are the scanned images from CT referred to as *'slices'*?
2. What is the significance of water content in the body for MRI scans?
3. For the following anatomy, which scan (MRI or CT) would you use:
   - soft tissue,
   - bone structure,
   - mucous walls.
4. For the respiratory airway, what are the main issues to consider when using MRI and CT scans?
5. What is the Hounsfield scale?
6. What is the difference between a pixel and a voxel?
7. What does manual segmentation involve?
8. What is the problem with using a fully automated segmentation?
9. What is the threshold greyscale range? What are you looking to segment if you had a range of 2000–3072 HU?
10. What is the main property of pixels in an image where an edge occurs?
11. Why do images that use the LoG and Canny edge detection schemes need to be smoothed?
12. What does the term '*zero crossing*' mean?
13. The Roberts edge detection algorithm uses the following mask:

| Prewitt, $G_x$ | |
|---|---|
| -1 | 0 |
| 0 | 1 |

| Prewitt, $G_y$ | |
|---|---|
| 0 | -1 |
| 1 | 0 |

    What would the approximate first derivative of a pixels intensity be?
14. Give a brief description of a region-based segmentation algorithm. How does it differ from edge detection algorithms?
15. What is a '*dirty*' CAD geometry?
16. What problems arise when accessing CAD models between different software?

# Chapter 4
# Generation of Computational Mesh for CFPD Simulations

## 4.1 Introduction

Generation of a quality mesh is of extreme importance for obtaining reliable computational solutions. A good quality mesh improves numerical stability, and increases the likelihood of attaining a reliable solution. A mesh can be viewed as a number of smaller meshes or grid cells that overlays the entire domain geometry. In general the set of fundamental *mathematical* equations that represent the flow physics are applied to each cell. These equations, which calculate the changes in each cell within the domain, are subsequently solved to yield the corresponding *discrete* values of the flow-field variables such as the velocity, pressure, and temperature.

In the computational fluid dynamics community, mesh generation is also referred to as grid generation, which has become a separate discipline in itself and remains a very active area of research and development. This chapter does not intend to elaborate on various methods of grid generation. There are many books dedicated to this subject alone, such as Thompson et al. (1985), Arcilla et al. (1991), and Lisekin et al. (1999). We also note that many existing commercial codes in the market have their own powerful, built-in mesh generators; a number of independent grid generation packages are given in Appendix A. Although, many of the mesh-generation packages are designed with very user-friendly interfaces, and are easy to utilize, proficient management of these software packages still relies on the reader's aptitude to operate them.

Generating a mesh is as much an art form as it is science. One has to decide on the arrangement of discrete points (nodes) throughout the computational domain, and the type of connections of each point, which leads to either the great success or utter failure of the numerical solution. In this chapter, guidelines and best practices are given for developing quality meshes. Furthermore the material presented will give the reader an introduction into mesh construction.

J. Tu et al., *Computational Fluid and Particle Dynamics in the Human Respiratory System,* Biological and Medical Physics, Biomedical Engineering
DOI 10.1007/978-94-007-4488-2_4, © Springer Science+Business Media Dordrecht 2013

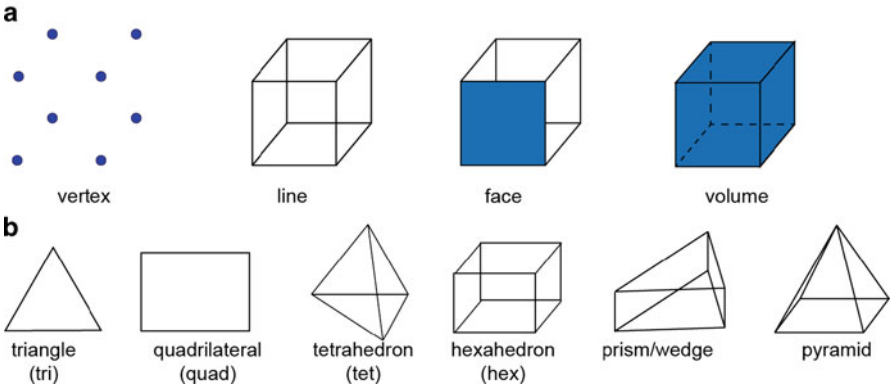


**Fig. 4.1** Mesh topology hierarchy from lowest (*left*) to the highest (*right*). **a** Topology heirachy. **b** 2D and 3D mesh element types

### *4.1.1 Mesh Topology*

A computational mesh topology has a hierarchical system whereby higher topology assumes the existence of the topologies beneath it (Fig. 4.1). For example, the creation of a volume cell automatically inherits the lower topologies (i.e. a volume cell contains face, line and vertex structures). For a 2D mesh, all nodes (discrete points) lie in a given plane with its resulting 2D mesh elements being quadrilaterals or triangles. For a 3D mesh, nodes are not constrained to a single plane with its resulting 3D mesh elements being hexahedra, tetrahedra (tets), square pyramids (pyramids, extruded triangles, wedges or triangular prisms) or polyhedra. Since all 3D elements are bounded by 2D faces, it is obvious that 3D meshes are constructed with 2D elements at boundaries. Typically many meshing algorithms start by meshing the enclosed surface before filling the interior with 3D elements. In this case, care should be taken to generate a good quality surface.

## 4.2 Structured Mesh Systems

### *4.2.1 Structured Mesh Properties*

By definition, a structured mesh is a mesh containing cells having either a regular-shape element with four-nodal corner points in two dimensions or a hexahedral-shape element with eight-nodal corner points in three dimensions. It is characterised by regular connectivity that is a straightforward prescription of an orthogonal (90°) mesh in a Cartesian system. The use of a structured mesh brings certain benefits in CFPD computations. Being relatively easy to construct, it allows novel ideas or

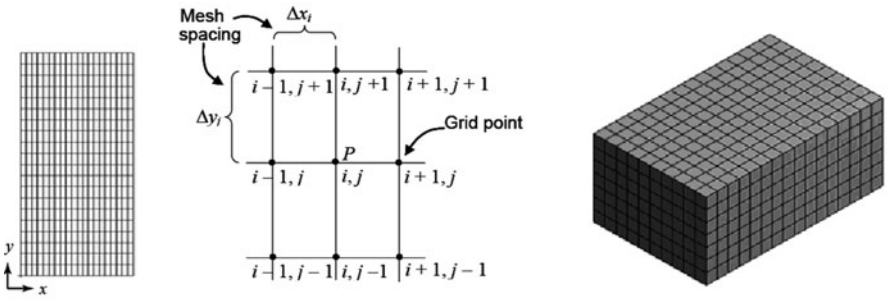


**a** uniform rectangular mesh in 2D (with its coordinate grid points), and 3D.

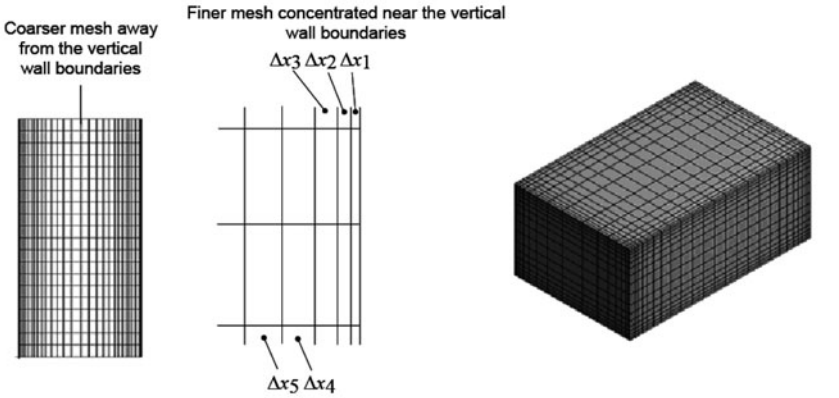


**b** non-uniform rectangular mesh in 2D (with its coordinate grid points near the wall) and 3D

**Fig. 4.2** (**a**) A uniform and (**b**) Non-uniform structured mesh in 2D and 3D for a simple rectangular geometry. Note the evenly distributed grid points in the uniform mesh in contrast to the biased concentration of cells near the wall for a non-uniform structured mesh

concepts to resolve the complex features of fluid-particle flows to be tested in a more efficient way. A more rigorous and thorough assessment of any proposals of new models or enhancements to the numerical algorithms can be performed instead of specifically dealing with the many complicated aspects of grid generation prior to implementation in a wider general application. Figure 4.2 shows the application of a uniform and non-uniform structured mesh on a simple vertical rectangular domain in 2D and 3D. For the uniform mesh, the spacing of each cell is essentially a single representative value in all directions (i.e. $\Delta x_i = \Delta y_j = \Delta z_k$). Note the regular-shaped four-nodal grids points of a rectangular element in 2D (or regular blocks in 3D). For non-uniformly distributed grid points, the spacing of either $\Delta x$, $\Delta y$ or $\Delta z$ can effectively take any values. The particular arrangement shown in Fig. 4.2 is usually regarded as a "stretched" mesh where the grid points are considered biased towards the wall boundaries.

### 4.2.2 *Body-fitted Mesh*

For non-orthogonal geometries, such as a 90° pipe bend, applying an orthogonal mesh to the geometry produces simplifications to the computational domain particularly on the curved boundaries where staircase-like steps are found (Fig. 4.3). This further causes difficulties in developing an approximate boundary description, and the steps at the boundary introduce errors in computations of the wall stresses, heat fluxes, boundary layer effects, etc. The treatment of the boundary conditions at stepwise walls generally requires a fine Cartesian mesh to resolve the curved geometry, but this requires additional computational storage and resources due to unnecessary refinement in interior regions which are of minimal interest. This example shows that grid generation methods that are based on Cartesian coordinate systems have limitations in irregular geometries. It is therefore more advantageous to work with meshes that can handle curvature and geometric complexity more naturally.

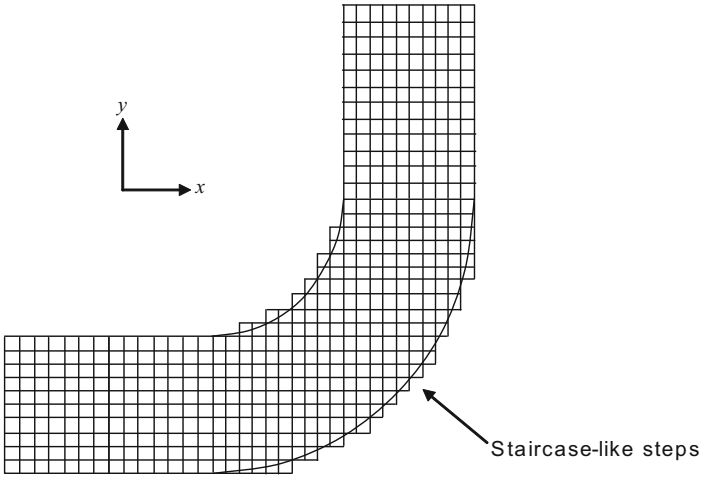


**Fig. 4.3** An example of a mesh using *staircase-like steps* for the 90° bend geometry

A similar type of structured mesh called a *body-fitted* mesh can be applied. Essentially, the basic concept of this approach centres on the mapping of a distorted region in physical space onto a rectangular region in the curvilinear coordinate space through the use of some transform coordinate function. In applying the body-fitted mesh to the 90° bend geometry, it would be appropriate to make the walls coincide with lines of constant $\eta$ (see Fig. 4.4). The location along the geometry, say from $A$ to $B$ or $D$ to $C$, subsequently corresponds to specific values of $\xi$ in the computational domain. Corresponding points on $AB$ and $CD$ connected by a particular $\eta$ line will have the same value of $\xi_i$ but different $\eta$ values. At a particular point $(i, j)$ along this $\eta$ line, $\xi = \xi_i$ and $\eta = \eta_j$. A corresponding point $x = x\ (\xi_i, \eta_j)$ and $y = y\ (\xi_i, \eta_j)$ in the computational domain exists in the physical domain.

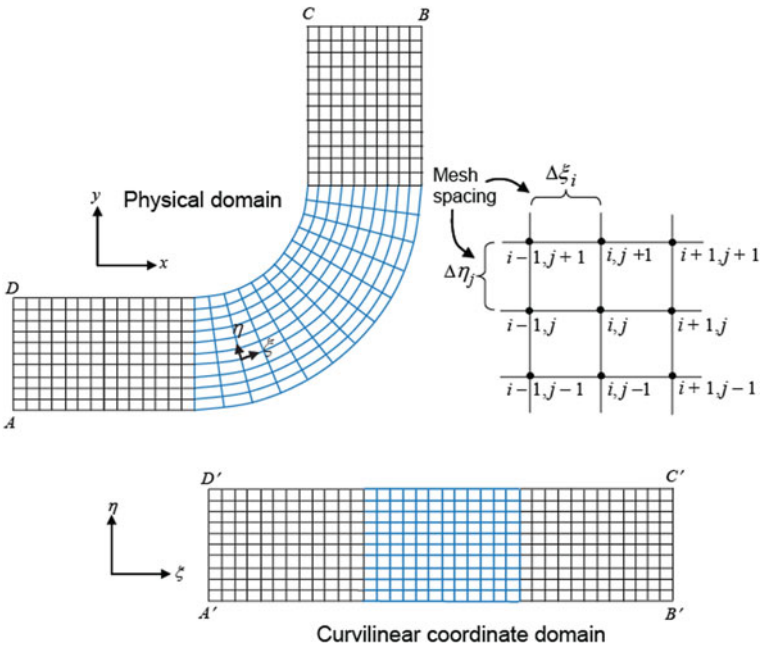


**Fig. 4.4** An example of a body-fitted mesh for the 90° bend geometry and corresponding computational geometry

In Fig. 4.4, the transformation must be defined such that there is a one-to-one correspondence between the rectangular mesh in the computational domain and the curvilinear mesh in the physical domain. The algebraic forms of the governing equations for the multiphase problems are carried out in the computational domain which has uniform spacing of $\Delta\xi$ and uniform spacing of $\Delta\eta$. Computed information is then directly fed back to the physical domain via the one-to-one correspondence of grid points. Because of the need to solve the equations in the computational domain, they have to be expressed in terms of the curvilinear coordinates rather than the Cartesian coordinates, which means that they must be transformed from $(x, y)$ to $(\xi, \eta)$ as the new independent variables.

### *4.2.3 Multi-block Mesh*

Block-structured or *multiblock mesh* is another special case of a structured mesh. This is particularly effective for complicated shapes where it is difficult to apply a single block. A multiblock mesh allows the computational domain to be subdivided into topological blocks. In Fig. 4.5, the mesh is assembled from a number of structured blocks attached to each other. Here, the attachments of each face of adjacent

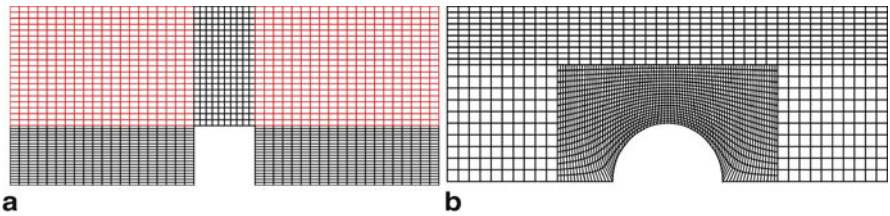


**Fig. 4.5** Multiblock-structured mesh with matching and non-matching cell faces. **a** Matching cell faces. **b** Non-matching cell faces

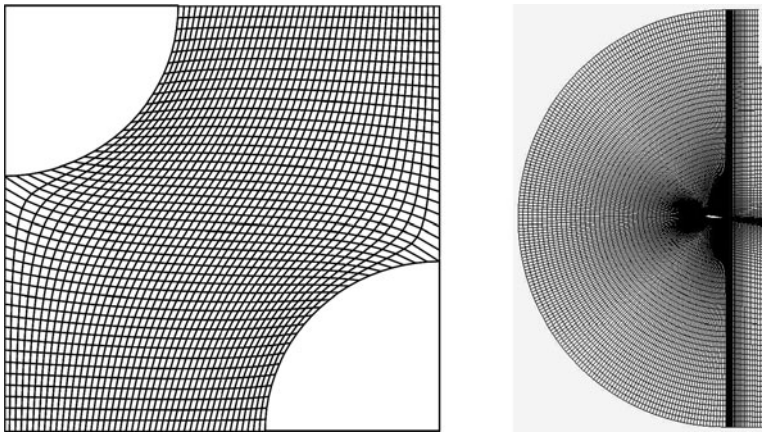

**Fig. 4.6** Example of a structured H-grid for the flow calculation in a symmetry segment of a staggered tube bank, and a C-grid for slow simulation around an aerofoil

blocks may be regular (i.e. having matching cell faces) or arbitrary (i.e. having non-matching cell interfaces). Generation of grids, especially those with non-matching cell interfaces, is certainly much simpler than the creation of a single-block mesh fitted to the whole domain. This approach provides the flexibility to choose the best grid topology for each of the subdivided blocks. Whatever the reason for using multiple blocks in a computational domain, the blocks will have to communicate with each other via an interface algorithm.

Within each block of the multiblock, the user may select an appropriate grid topology based on structured O-, C-, or H-grids or even an unstructured mesh of tetrahedral or hexahedral elements to fill each block. An O-grid will have lines of points where the last point wraps around and meets the first point, hence creating a circular '*O*' shape. Similarly a C-grid will have lines that bend in a semicircle shaped like the letter '*C*'. An H-grid is pretty much any structured grid that isn't an O-grid or a C-grid. (Fig. 4.6).

Consider a circular region that may be found within a multiblock. Using a body-fitted structured mesh will lead to highly skewed and deformed cells at the perimeter of the geometry (as highlighted by the red circles in Fig. 4.7), since the interior

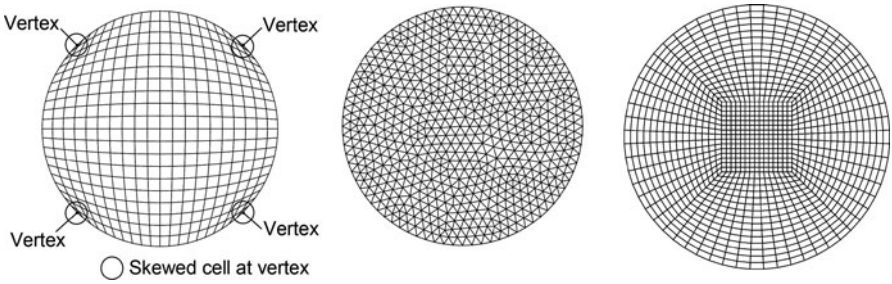


**Fig. 4.7** Generation of body-fitted mesh, unstructured mesh and O-grid for the circular cross-sectional conduit

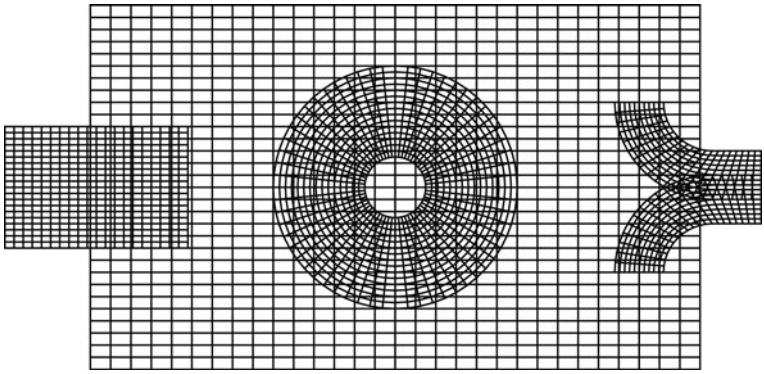

**Fig. 4.8** A structured overlapping grid for a cylinder in a channel with inlet–outlet mappings

of the domain must be built to satisfy the geometrical constraints imposed by the circular domain boundary. This particular type of mesh generally leads to numerical instabilities and deterioration of the computational results. Hence, it would have been more preferable to re-mesh the geometry with an O-grid. In this operation, the O-grid fills the external circular cross-sectional conduit, while a square block fills the centre.

Finally, grids may be overlapped on top of one another to cover an irregular flow domain which further presents another grid generation approach in handling complex geometries and is referred to as Chimera grids. This type of grid differs from a single, flat, block-structured mesh where different blocks are connected by neighbouring blocks. Chimera grids allow rectangular, cylindrical, spherical, and nonorthogonal grids to be combined with the parent Cartesian grid in the solution domain. An example of an overlapping grid for a cylinder in a channel with inlet–outlet mappings is shown in Fig. 4.8.

This approach is attractive because the structured mesh blocks can be placed freely in the domain to fit any geometrical boundary while satisfying the essential resolution requirements. Information between the different grids is achieved through

the interpolation process. The advantages of employing such grids are that complex domains are treated with ease and they can especially be employed to follow moving bodies in stagnant surroundings. Some examples can be found in Tu and Fuchs (1992) and Hubbard and Chen (1994). The disadvantages of these grids are that conservation is usually not maintained or enforced at block boundaries, and the interpolation process may introduce errors or convergence problems if the solution exhibits strong variation near the interface.

## 4.3 Unstructured Mesh Systems

### *4.3.1 Unstructured Mesh Properties*

Geometries encountered in the respiratory system are more likely to involve complex geometries that do not fit exactly in Cartesian coordinates where a structure mesh could immediately be applied. As an alternative to a body-fitted mesh, an unstructured mesh could be constructed to fill the interior of curvilinear geometries. The unstructured mesh is most commonly comprised of triangles or tetrahedra, laid out in an irregular pattern (Fig. 4.9). There are no coordinate lines that correspond to the curvilinear directions $\xi$ and $\eta$ such as those in a body-fitted mesh, and the cells are totally unstructured which makes the mesh highly suitable for complex geometries such as the nasal cavity and lung airways. This means that additional computations are needed to establish a scheme to connect neighbouring grid points. In the computational programming, new data structures (e.g. edge based, face based or cell based) are needed to store the connectivity scheme which is complicated by the fact that a node of one cell can be connected to any number of nodes from any number of other cells. The descriptions of some of these connectivity algorithms (Delauney, Quadtree/Octree, and Advancing front) are briefly described in this section.

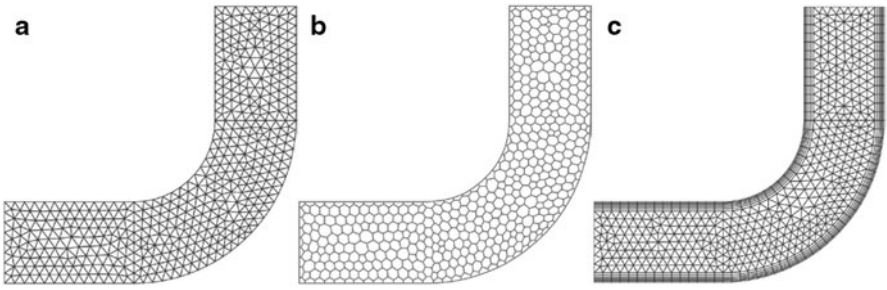


**Fig. 4.9** Unstructured mesh filled with **a** triangular cells, **b** polyhedral cells, and **c** a hybrid mesh combining quadrilateral cells at the wall boundaries and triangular cells in the centre

The current state of unstructured mesh CFD technology has matured, and its use has become more prevalent with commercial CFD vendors adopting the method. In

addition, a large number of grid generation software and open source codes exist and the full listing is given in Appendix A. Typically a good meshing program will be able to automatically fill the CAD geometry with triangles on surfaces (2D) and tetrahedrals in a volume (3D). This process typically involves meshing the edges first, followed by filling the enclosed face with elements connecting the edges (advancing front method). Finally for a 3D geometry the interior volume is filled, and all the elements are reconnected (Delauney method). In more recent times there has been considerable development towards mesh containing *polyhedral* cells to fill the interior domain. A clear potential benefit of applying polyhedral mesh is that it allows the flexibility of an unstructured mesh to be applied to a complex geometry without the overhead associated with a large tetrahedral mesh. The application of such cells is still in its infancy. Nevertheless, polyhedral meshing has been shown, thus far, to have tremendous advantages over tetrahedral meshing with regard to the attained accuracy and efficiency of the numerical computations.

Unstructured meshes may also involve the use of hexahedral, pyramid, and wedge cells in combination with tetrahedral cells, whereas a structured mesh is reliant on hexahedral cells or the use of block-structured mesh only. A mesh with a combination of different cell types is called a *hybrid mesh* and typically involves matching mesh cells with the boundary surfaces and allocating cells of various element types in other parts of the complex flow regions. Hexahedral elements are excellent near solid boundaries (where flow field gradients are high) and afford the user a high degree of control, but these elements are time consuming to generate. Prismatic elements (usually triangles extruded into wedges) are useful for resolving near-wall gradients, but suffer from the fact that they are difficult to cluster in the lateral direction due to the underlying triangular structure. In almost all cases, tetrahedral elements are used to fill the remaining volume. Pyramid elements are used to transition from hexahedral elements to tetrahedral elements. Many codes try to automate the generation of prismatic meshes by allowing the user to define the surface mesh and then marching off the surface to create the 3D elements. While very useful and effective for smooth shapes, the extrusion process can break down near regions of high curvature or sharp discontinuities.

Hybrid grid methods are designed to take advantage of the positive aspects of both structured and unstructured grids. Hybrid grids utilize some form of structured grid in local regions while using unstructured grid in the bulk of the domain. This generally leads to both accurate solutions and better convergence for the numerical solution methods. However one disadvantage of hybrid methods is that they can be difficult to use and require user expertise in laying out the various structured grid locations and properties to get the best results. Hybrid methods are typically less robust than unstructured methods. While the flow solver will use more resources than a structured block code, it should be very similar to an unstructured code. Post processing the flow field solution on a hybrid grid suffers from the same disadvantages as does an unstructured grid. The time required for grid generation is usually measured in hours or days.

### 4.3.2 Delaunay Triangulation

Triangle and tetrahedral meshing are by far the most common forms of unstructured mesh generation because they allow maximum flexibility in matching cells with highly curved boundaries and inserting the required cells to resolve the flow regions where they matter most. A common method for triangle and tetrahedral meshing is to apply the Delaunay triangulation criterion. Here, the most important property of a Delaunay triangulation is that it has the *empty circumcircle* (*circumscribing circle of a tetrahedra*) *property* (Jonathan Richard 2002): there must not be any node within a circumcircle. In 2D, a circumcircle of a triangle can be defined as the unique circle that passes through all three vertices of its triangle whereby nodes from other triangles do not exist within the circle. Figure 4.10 shows that the circumcircle of every Delaunay triangular cell within the mesh generated is free from other nodes.

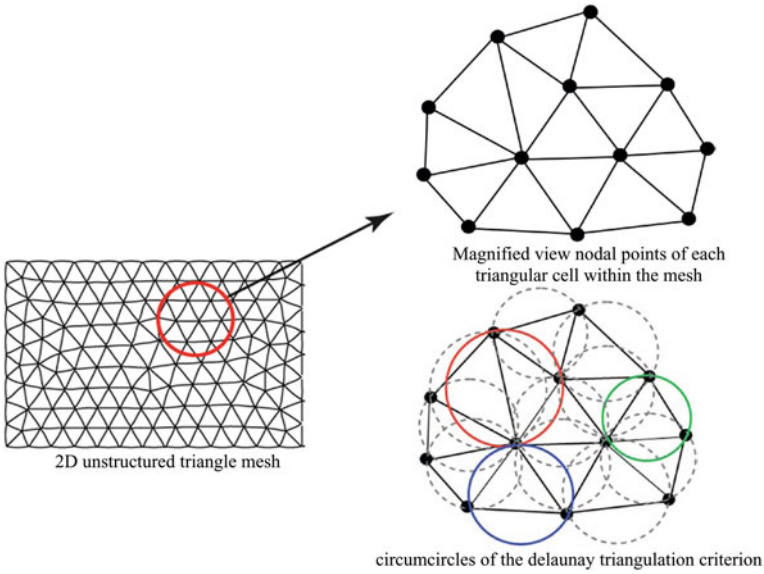


**Fig. 4.10** A triangular mesh based on Delaunay triangulation. *Coloured circumcirlces* highlight the relationship between the triangle points and the absence of any external nodal points inside the circumcircle

Algorithms for computing Delaunay triangulations are needed in order to generate nodal points in space that comply with the Delaunay criterion. These algorithms need to be fast operations for detecting when a grid point is within a triangle's circumcircle and an efficient data structure for storing triangles and edges. A typical approach is to first mesh the boundary (lines, then faces, in the mesh topology), then begin to repeatedly add one node at a time and, lastly, re-triangulate (or redefine) the affected triangles locally in order to maintain the Delaunay criterion. In 3D the Delaunay triangulation technique for 2D is extended naturally to three dimensions by

considering the *circumsphere* (*circumscribing sphere*) associated with a tetrahedron. For in-depth descriptions of this method, the reader is strongly encouraged to refer to a review paper by Mavriplis (1997) and a book by de Berg et al (2008) for a more thorough understanding on the basic concepts of Delaunay triangulation and meshing.

### *4.3.3 Quadtree/Octree Subdivision*

Mesh generation by the quadtree (2D geometries) or octree (3D geometries) method is based on the divide-and-conquer principle. In quadtree, a 2D geometric shape is recursively subdivided into four smaller regions or quadrants. These regions may be square, rectangular, or an arbitrary shape. Each region is subsequently subdivided until it meets some criterion such as a homogeneous attribute, or the size of the cell is smaller or the number of cells is greater than a certain value. An example for a quadtree subdivision is given for the 90° bend in Fig. 4.11. The vertices of the resulting quadtree structure are used as nodal points, and the tree quadrants are divided up into triangular or tetrahedral elements. It should however be noted that the quadtree cells intersecting the boundary surfaces must somehow be required to be displaced or wrapped in order to coincide with the boundary.

Octrees are based on the same principle of divide-and-conquer as in quadtrees but instead applied to 3D geometries. The geometry is normally subdivided with three mutually perpendicular planes. For each subsequent subdivision a criterion is used to determine whether further subdivisions are needed. Overall, the quadtree/octree method is relatively simple, inexpensive and produces good quality meshes in interior regions of the domain. One drawback of the method is that it has a tendency of generating an irregular cell distribution near boundaries. For detailed descriptions of quadtrees/octrees the reader is strongly encouraged to refer to the work by Yerry and Shephard (1984) and Shephard and Georges (1991) (Fig. 4.12).

### *4.3.4 Advancing Front Connectivity*

An unstructured mesh is created using the advancing front method by adding individual elements inwards, one at a time, from an existing front of generated elements (i.e. a boundary or edge). In a 2D geometry, the initial front is created by an initially prescribed boundary edge setting set by the user. New triangular cells are created by extending this front. Thus an active front is maintained where the new triangular cells are formed which, in turn, create more line segments on the front. The front thus constitutes a stack, and the edges of the stack are continuously added to or removed. The process continues until the stack is empty, which is when all fronts have merged upon each other and the domain is entirely covered. For three-dimensional grid generation, a surface grid is first constructed by generating a two-dimensional

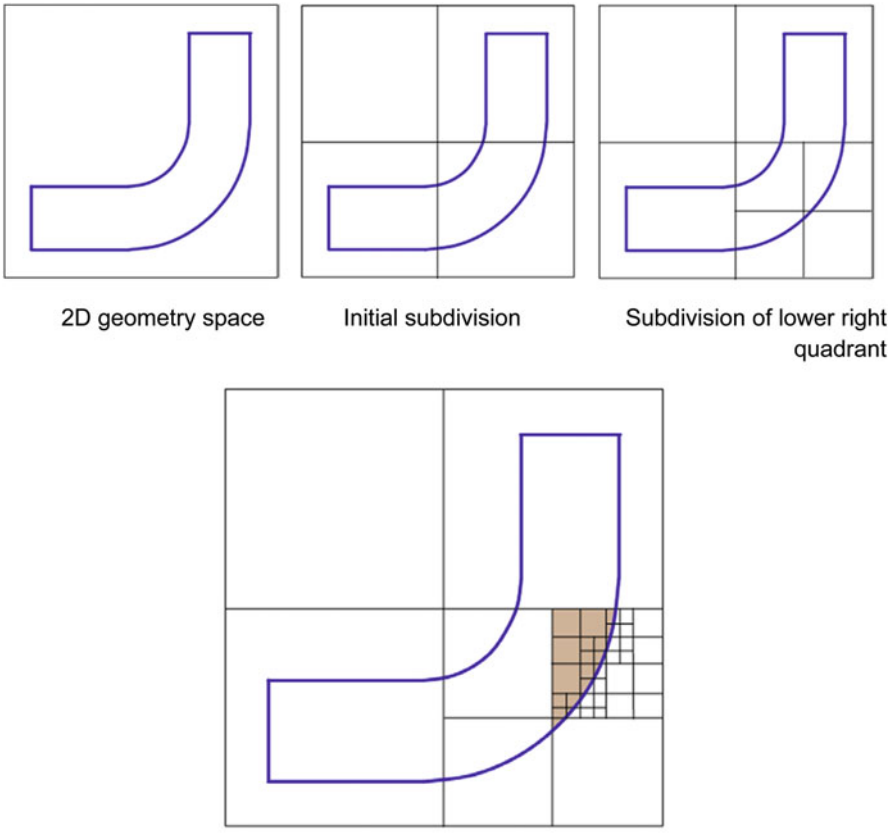


**Fig. 4.11** A quadtree subdivision concentrating only on the bottom right corner region. A criterion of whether a region is filled by the interior of the 90° bend is used. Any region that does not contain any interior region is neglected. The interior region is *shaded* to highlight the selected region

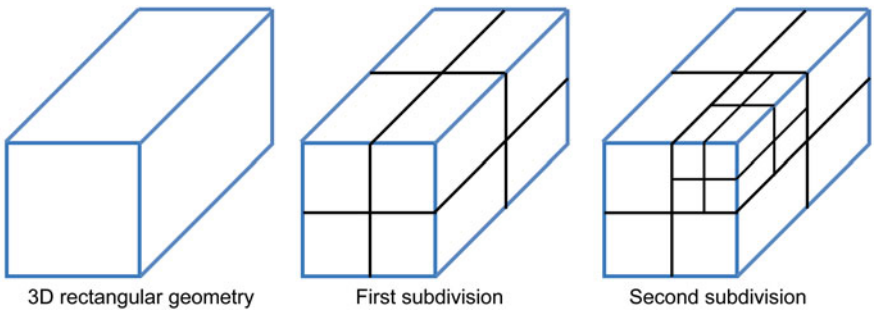


**Fig. 4.12** Octree of a simple rectangular geometry

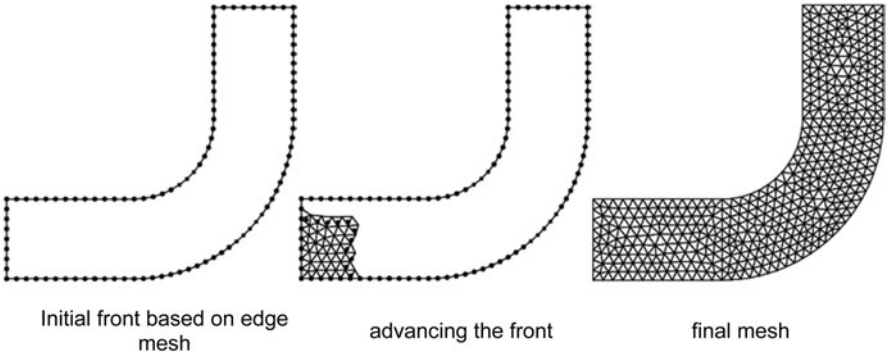


**Fig. 4.13** Mesh construction based on advancing front method on a 90° bend pipe. **a** Initial front is established on the edge mesh setting. **b** New triangular mesh element is added by inserting one new point to form a triangle and this continues to create a front. **c** Final completed mesh

triangular mesh on the surface boundaries of the domain. This mesh forms the initial front, which is then advanced into the physical space by placing new points ahead of the front and forming tetrahedral elements. The required intersection checking now involves triangular front faces rather than edges as in the two-dimensional case. For detailed descriptions of the advance front method the reader is strongly encouraged to refer to the work by Lo (1985), and Marcum and Weatherill (1995) (Fig. 4.13).

### *4.3.5 Comparisons Between Structured and Unstructured Mesh*

The main advantage of using an unstructured mesh is its ability to conform onto complex geometries where it may be impossible to apply a structured mesh. With advances in mesh generation algorithms, combined with a user friendly graphical interface within the software, an unstructured mesh can usually be created automatically or with minimal user interaction. In comparison, a structured mesh requires laying out a single mesh block that is then split, merged, or has O-, and C- grids applied, even within commercial mesh packages. This process is much more difficult to perform and requires experience in the blocking strategy.

Some drawbacks of unstructured mesh include the treatment of the nodal points of any cell which cannot be simply treated or addressed by a double of indices $(i, j)$ in two dimensions or a triple of indices $(i, j, k)$ in three dimensions. Instead additional data calculations are needed to connect an arbitrary number of neighbouring nodes, which requires additional computational memory and further complicates the solution algorithms that are used to solve the flow-field variables. This typically results in increased computational times to obtain a solution and erodes the gains in computational efficiency compared with a structured mesh. Furthermore an unstructured mesh is ineffective in resolving wall boundary layers since triangles and tetrahedrals do not deform (stretch or bend) during local refinement to make the cells very small.

Tetrahedral cells are also prone to high aspect ratios that affect the skewness of the cell. Additionally tetrahedral cells can be difficult to align with the flow direction. These two problems can impede convergence and lead to artificial errors in the solution, known as *numerical diffusion*. This common source of error is also called *false diffusion* because it is a product of numerical error and does not represent a physically occurring phenomenon. A few techniques may be applied to minimise the likelihood of false diffusion such as choosing higher order discretisation schemes (discussed later in Chap. 7) and increasing the resolution of the mesh.

## 4.4 Mesh Generation

### *4.4.1 Mesh Design Strategy and Quality*

Generating a quality mesh is by no means a trivial exercise. In fact, it can be seen as much of an art form as it is technical, and often a user's experience in mesh designs dictates the final mesh quality. To begin, the user should create an initial coarse mesh for evaluating and testing the setup of a particular CFD problem (i.e. to use a small number of mesh elements in relation to the final model which will have a significantly higher number of elements). This strategy allows the computational model to evaluate the specific computer code's storage and running time. More importantly, a suitable coarse mesh allows a number of "test-runs" to be carried out in quick turnaround time to assess the convergence or divergence behaviour of the numerical calculations, and the application of physical models (e.g. different drag coefficient). When the numerical model is setup correctly and is suitable, and the solution is found to be converging, mesh refinement within the flow domain can then be undertaken to achieve a more accurate CFD solution. If the solution is diverging, the user needs to investigate the problems arising during the numerical calculations. Some possible sources of errors can be attributed to *physical modelling* and *human* errors. During the testing phase, it is not recommended that a fine mesh be used because this could take hours or days, only to find the solution is diverging or that the physical model was applied incorrectly.

The quality of a generated mesh depends on the consideration of the cell shape based on its *aspect ratio*, *skewness*, and *warp angle*. A quadrilateral cell having a mesh spacing of $\Delta x$ and $\Delta y$ and an angle of $\theta$ between the grid lines of a cell is shown in Fig. 4.14. The grid*aspect ratio* of the cell is defined as $AR = \Delta y/\Delta x$. Large aspect ratios should always be avoided in important flow regions inside the computational domain (e.g. jets, flow separation, attachment and recirculation) as they can degrade the solution accuracy and may result in poor iterative convergence (or divergence) depending on the computational flow solver during the numerical computations.

It is recommended that the $AR$ be maintained within the range of $0.2 < AR < 5$ within the interior region, if possible. For near-wall boundaries the condition for $AR$ can, however, be relaxed. If the fluid flow is in the $y$ direction, then the first mesh requirement is to resolve the velocity gradient in the $y$-direction. This means that

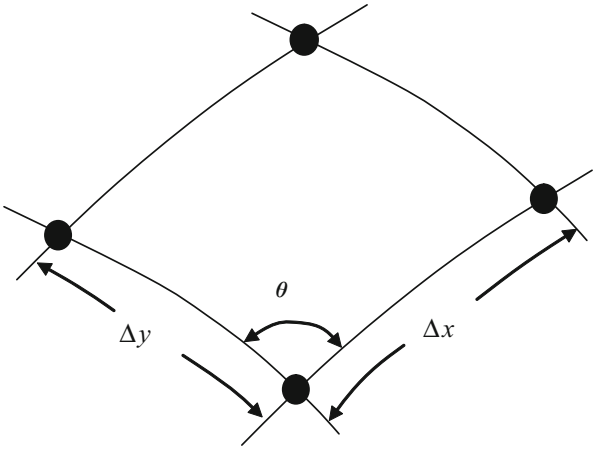


**Fig. 4.14** A quadrilateral cell having mesh spacing of $\Delta x$ and $\Delta y$ and an angle of $\theta$ between the grid lines of the cell

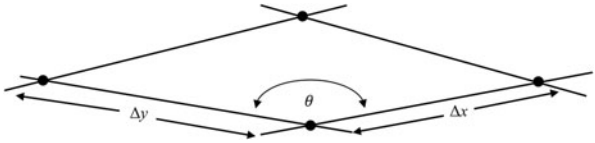


**Fig. 4.15** An example of a highly skewed quadrilateral cell having $\theta > 135°$

to avoid poor AR, the $\Delta x$ mesh spacing should also be small enough to produce an AR within the suitable range. Such consideration can assist in possibly alleviating convergence difficulties and enhancing the solution accuracy especially where appropriately resolving the wall boundary layers is necessary.

Mesh *distortion* or *skewness* is measured by determining the angle $\theta$ between the mesh lines (Fig. 4.15). For minimal distortion, it is most desirable for the mesh lines to be at an angle $\theta$ of approximately 90° (orthogonal). If the angle is $\theta < 45°$ or $\theta > 135°$, the mesh becomes skewed and often exhibits deterioration in the computational results or leads to numerical instabilities.

A typical example of highly skewed cells is that of a non-orthogonal shape filled by a body-fitted structured grid such as the interior circular cylinder shown earlier in Fig. 4.7. For complicated geometries, there is a high probability that the generated mesh may contain cells that are just bordering the *skewness* angle limits. The convergence behaviour deteriorates with such a mesh. It is also necessary to avoid non-orthogonal cells near the geometry walls. The angle between the mesh lines and the boundary of the computational domain (especially the wall, inlet or outlet boundaries) should be kept as close as possible to 90°. The reader should pay special attention to this requirement, as it is stronger than the requirement given for the mesh lines in the flow field far away from the domain boundaries.

If an unstructured mesh is adopted, special care needs to be taken to ensure that the *warp angles* measuring between the surfaces' normal to the triangular parts of the faces are not greater than 75° as indicated by the angle $\beta$ in Fig. 4.16. Cells with large deviations from the co-planar faces can lead to serious convergence problems.

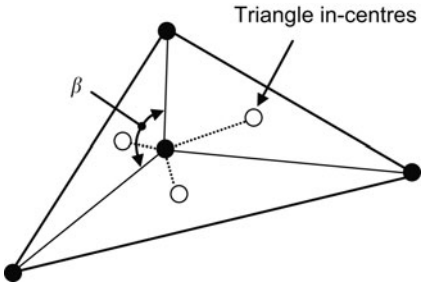


**Fig. 4.16** A triangular cell having an angle of $\beta$ between the surfaces normal to the triangular parts of the faces connected to two adjacent triangles

In many grid generation packages, the problem can be overcome by a grid smoothing algorithm to improve the element *warp angles*. Whenever possible, the use of tetrahedral elements should be avoided in wall boundary layers. Prismatic or hexahedral cells are preferred because of their regular shape.

Since there is no restriction on the use of the type of cells in an unstructured grid, a *hybrid* mesh can be used which combines different element types, such as triangular and quadrilateral in two dimensions or tetrahedral, hexahedra, prisms and pyramids in three dimensions. This allows maximum flexibility in matching appropriate cells with boundary surfaces and allocating cells of various element types in other parts of the complex flow regions. For the example of a 90° bend geometry, grid quality can be enhanced through the placement of quadrilateral or hexahedral elements in resolving the viscous boundary layers near the walls whilst triangular or tetrahedral elements are generated for the rest of the flow domain as was shown in Fig. 4.9. This normally leads to both accurate solutions and better convergence for the numerical solution methods.

Finally, special grid design features such as the H-grid, O-grid or C-grid introduced earlier need careful consideration to locate block interfaces because this significantly improves the overall quality of a block-structured mesh. The presence of arbitrary mesh coupling, non-matching cell faces, or extended changes of element types at block interfaces should always be avoided in critical regions of high flow gradients or high shear. Wherever possible, finer and more regular mesh in these critical regions should be employed. This also applies to regions that exhibit significant changes in the geometry or where suggested by error estimates. In all cases, it is recommended that the CFD user check the assumptions made when setting up the grid with regards to the critical regions of high flow gradients; and if necessary, proceeds to rearrange the grid nodal points.

### *4.4.2 Local Refinement and Solution Adaptation*

In order to capture critical flow regions an adequate mesh resolution is needed. Such regions may include flows around obstacles that cause flow separation, attachment and recirculation, near-wall boundaries, interface shear regions, and converging and diverging regions. These regions typically exhibit sharp flow property gradients (e.g.

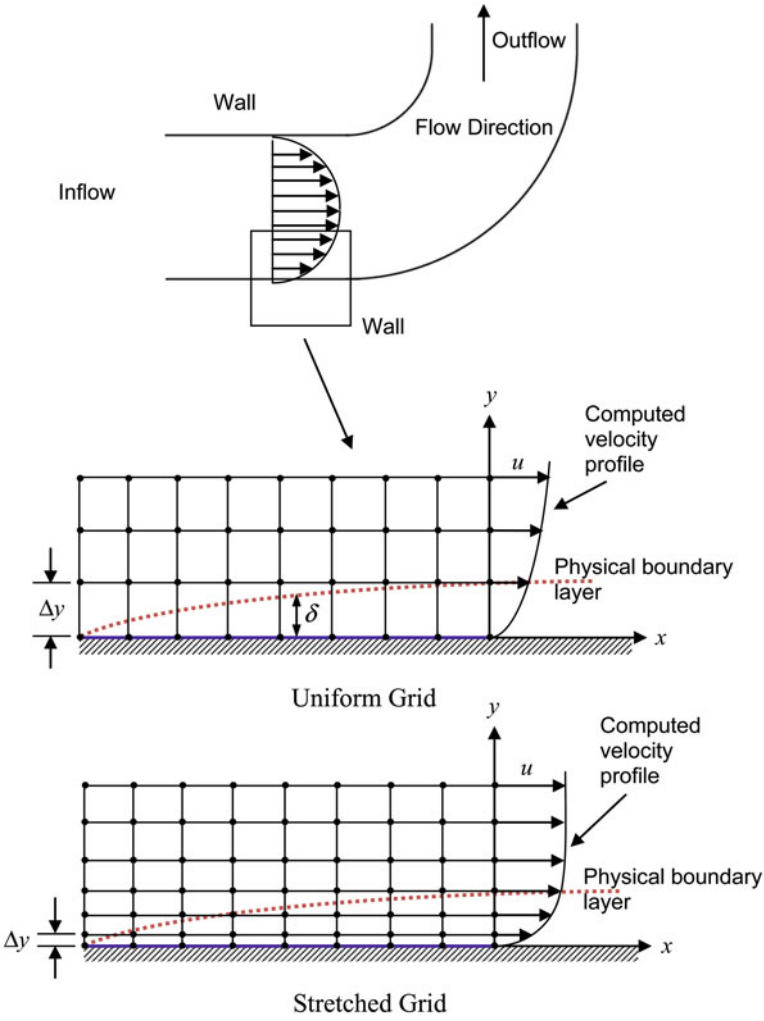


**Fig. 4.17** Two schematic illustrations demonstrating the need for local refinement in the near vicinity of the bottom wall to resolve the physical boundary layer

velocity, pressure, temperature) which require a fine mesh to resolve the flow region. Furthermore, a well resolved mesh has an enormous impact in ensuring the stability and convergence of the numerical procedure.

A local refinement technique that is commonly used in CFD applications is the concept of a refined mesh close to obstacle boundaries and walls. For a viscous flow bounded with solid wall boundaries, clustering a large number of small cells within the physical boundary layer is important. As an illustration, the entrance section of a 90° bend is shown in Fig. 4.17 to highlight the near-wall mesh refinements. In a

real physical flow, a boundary layer develops at the wall, growing in thickness as the fluid enters the left boundary and migrates downstream along the bottom wall of the domain. The local thickness of the boundary layer is given as $\delta$, which increases with $x$ and therefore $\delta = \delta(x)$. It is evident that a coarse uniform mesh, in essence, misses the physical boundary layer as it develops. In contrast, the stretched mesh with clustered nodes near the wall at the very least catches some of the boundary layer development. It is therefore not surprising that the accuracy of the computational solution is greatly influenced by the mesh distribution inside the boundary layer region.

When applying a stretched mesh as described above, care must be taken to avoid sudden changes in the mesh size. The mesh spacing should be continuous and mesh size discontinuities should be removed as much as possible in regions of large flow changes, particularly when dealing with multi-block meshing of arbitrary mesh coupling, non-matching cell faces or extended changes of element types. Discontinuity in the mesh size destabilizes the numerical procedure due to the accumulation of truncation errors in the critical flow regions. Making sure that the grid changes slowly and smoothly away from the domain boundary, as well as within the domain interior, will assist in overcoming the divergence tendency of the numerical solution. It is also worthwhile noting that most built-in mesh generators in commercial codes and independent grid generation packages have the means of prescribing suitable mesh stretching or expansion ratios (rates of change of cell size for adjacent cells).

Local mesh refinement allows the allocation of additional nodal points to resolve important fluid flow regions' action or reduction or to remove the nodal points from other regions where there is little or no action. However, it should be noted that local mesh refinements are prescribed *prior* to the solution of the flow field being calculated. This raises the question of whether the generated stretched grid is sufficient for capturing the major fluid flow action or whether the real flow action is far away from the intended significant flow activity to be resolved by the generated stretched grid region, which is not known *a priori*. One method to overcome this uncertainty is to refine the mesh by *solution adaption*. This method allows a mesh to be refined and coarsened based not only on geometric but also numerical solution data in regions where they are needed, thus enabling the features of the flow field to be better resolved. This typically involves clustering nodal points in regions where large gradients exist in the flow field. It therefore employs the solution of the flow properties to locate the mesh nodal points in the physical flow domain. During the course of the solution, the mesh nodal points in the physical flow domain *migrate* in such a manner as to *adapt* to the evolution of the large flow gradients. Hence, the actual mesh nodal points are constantly in motion during the solution of the flow field and become stationary when the flow solution approaches some quasi-steady state condition. An adaptive mesh is therefore intimately linked to the flow field solution and alters as the flow field develops unlike the stretched mesh described above where the mesh generation is completely separate from the flow field solution. For this purpose, unstructured meshes are well suited especially in automating the generation of elements such as triangular or tetrahedral meshes of various sizes to solve the critical flow regions. Figure 4.18 shows the evolution of the adaptive mesh for fluid flowing

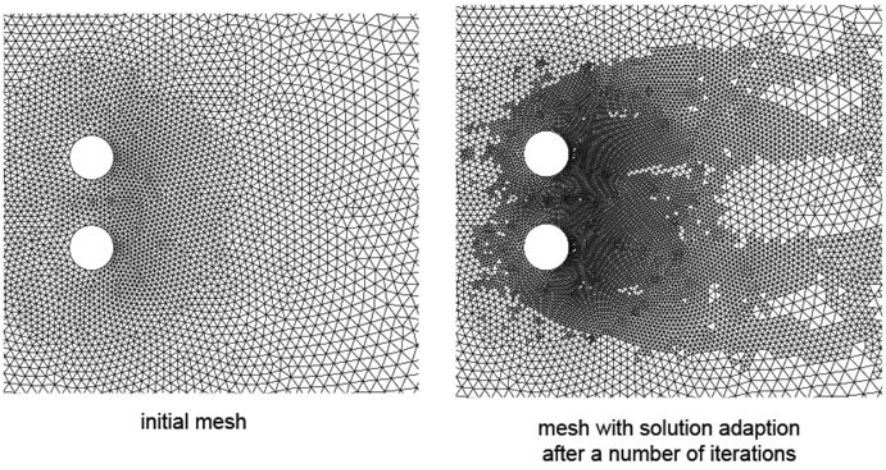


**Fig. 4.18** A demonstration of solution adaptation through the use of *triangular meshes* for the fluid flowing over two cylinders

over two cylinders using a triangular mesh. For this flow problem, the wake region has been further resolved to capture the essential formation and shedding of vortices behind the two cylinders.

### *4.4.3 Mesh Independence*

It is desirable that a mesh independence study is performed to analyse the suitability of the mesh and to yield an estimate of the numerical errors in the solution. In addition, such a study is used to determine the minimum mesh resolution required to generate a solution that is independent of the mesh size used. This typically involves monitoring a fluid flow parameter that is of interest to the study (e.g. velocity or pressure) and how it changes under successive grid refinements. Ideally, at least three significant, different grid resolutions should be employed, where each subsequent mesh is refined or coarsened. This implies that the grid cells become smaller and the number of cells in the flow domain increases. The authors recommend working from a coarse mesh and building up the mesh through refinement as this will provide faster solutions when working with smaller meshes. A scaling or refinement factor should be determined which would typically be between 1.3 and 2.0 times. If a global mesh refinement is not feasible, selective local refinement of the grid in critical flow regions of the domain can be applied. After each refinement the model is simulated and the results and settings (such as boundary conditions, number of iterations needed to reach convergence) should be recorded. The mesh is considered independent when the selected flow field variable does not change with an increase in the mesh size. This leads to a mesh that is optimised and hence is grid independent for the flow field where a compromise between computational resources and accuracy has been made.

### 4.4.4 Mesh Generation Software

Mesh generation is a research field in itself, whereby new algorithms are constantly being developed in order to provide significant benefites in mesh generation. This includes producing algortihms that provide higher quality connectivity between the nodal points, improved data structures, and more efficient storage and data handling. Typically commercially available software will have general capability to generate both structured and unstructured meshes. A graphical user interface is used to start the automated mesh generation, and therefore these software requires the user to become familiar with the tools and functions of the software. Open source software are typically more specialised in their functionality. They tend to produce either one type of mesh such as triangular/tetrahedral quadrilateral or hexahedral. These software are normally available as source codes which need to be run and compiled under the programming language it is available in.

## 4.5 Examples

### 4.5.1 Meshing the Nasal Cavity

After extracting the nasal cavity airway by segmentation, the computational file should be saved as an IGES, STL, or STEP in order to be cross-compatible with a range of 3D modelling and meshing programs. Typically the meshing procedure can begin by applying a simple unstructured tetrahedral mesh all over which produces a single contiguous mesh. However for easier post processing of local flow variables and particle deposition fractions, the computational model may be split into smaller sub-regions during the CAD surface and volume generation stage, prior to meshing. While the process of subdividing the computational model into smaller regions can be performed within some CFD packages, it is not always an easy task; therefore it is recommended that the division be performed in CAD packages that have NURBS functionality. Figure 4.19 shows a nasal cavity subdivided into ten sections.

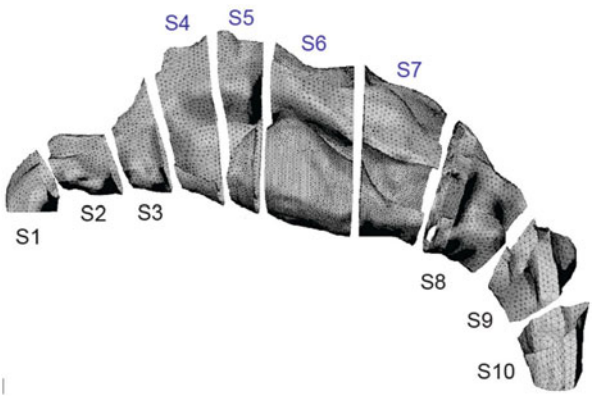


**Fig. 4.19** Nasal geometry subdivided into ten sections and labelled with *S* and a number representing the section. *S1–S3* represents the *anterior*, *S4–S7* the *middle*, and *S8–S10* the *posterior* nasal cavity. An artificial extension is added after *S10* to assist in the simulation

Surfaces were then created and stitched up to create a computational mesh. An initial model with 82,000 cells was created and used to solve the air flow field at a flow rate of 10 L/min. The original model was refined by cell adaptation techniques that included refining large volume cells, cells that displayed high velocity/pressure gradients and near-wall refinements. This process was repeated twice, with each repeat producing a model with a higher cell count than the previous model. Two models, one containing 82,000 and the other containing 2.5 million cells, are shown in Fig. 4.20.

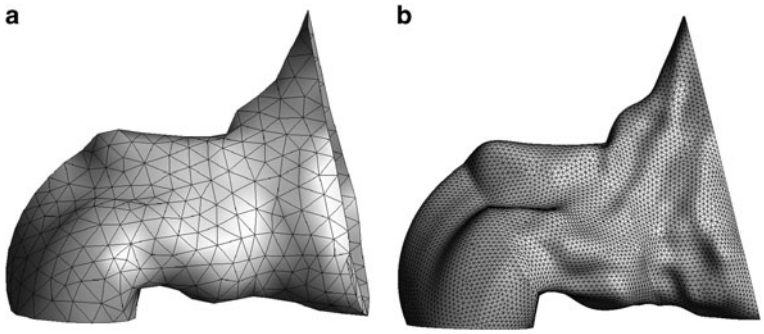


**Fig. 4.20** Surface mesh of the first two sections *S1* and *S2* (anterior nose entrance region) from Fig. 4.19 of the nasal cavity. **a** An initial coarse mesh. **b** After mesh refinement, the mesh count is increased

Prism meshes are often used to resolve the thin boundary layers that are present in wall bounded flows. The first mesh element adjacent to the wall is a very thin layer, and subsequent mesh elements above the first mesh element become progressively thicker until it the layers cover the distance of the boundary layer. As discussed earlier, the mesh should change slowly and smoothly away from the domain boundary. Figure 4.21 shows the application of a hybrid mesh that contains tetrahedral elements inside the domain and prism layers along the surface or domain boundaries.

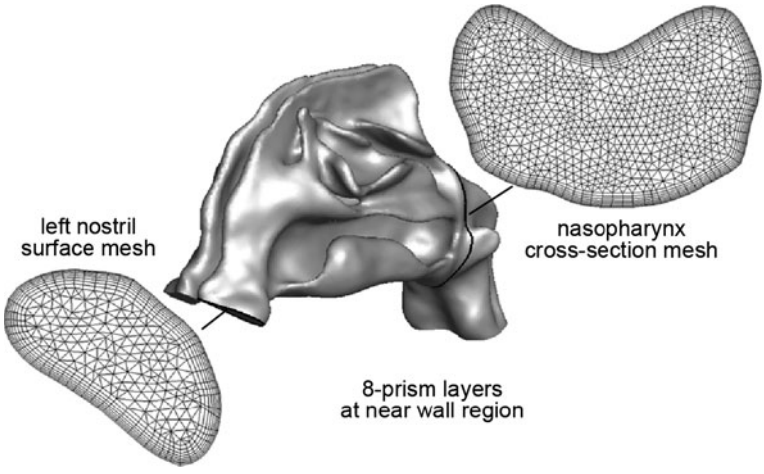


**Fig. 4.21** Near-wall mesh that has an 8-prism layer for a nasal cavity model

### 4.5.2 *Meshing the Trachea and Primary Bronchi*

The trachea and primary bronchi conducting airway are extracted via the segmentation stage as shown in Fig. 4.22. Here we present a different method to reconstruct the airway, by exporting the bounding airway surface location data as discrete coordinate points (point clouds). This is a common procedure referred to as reverse engineering. The point clouds form the basis for developing the surface using B-Spline or NURBS algorithms where the actual surface wraps around the object by effectively joining up the cloud points. After the CAD reconstruction, the domain is subdivided into smaller regions for local analysis. Meshing of the airway is achievable because the primary bronchi are large enough that the mesh does not need to become too small and prohibitive. However as the bronchial airway bifurcates, the next generation airway's diameter decreases. For example, in the trachea the diameter is approximately 18 mm while the third generation branch diameters are approximately 5–7 mm (Inthavong et al. 2010). Further downstream these diameters become even smaller and often this leads to a loss of resolution. In this case the small airways which do not resemble a coherent tubular shape are cut, and an artificial extension is applied to the outlets. This allows the meshing to be more manageable. Using a meshing program, an automatic unstructured mesh is initially applied to create both the surface and volume mesh. Mesh refinements were applied in a similar manner to that of the nasal cavity discussed earlier.

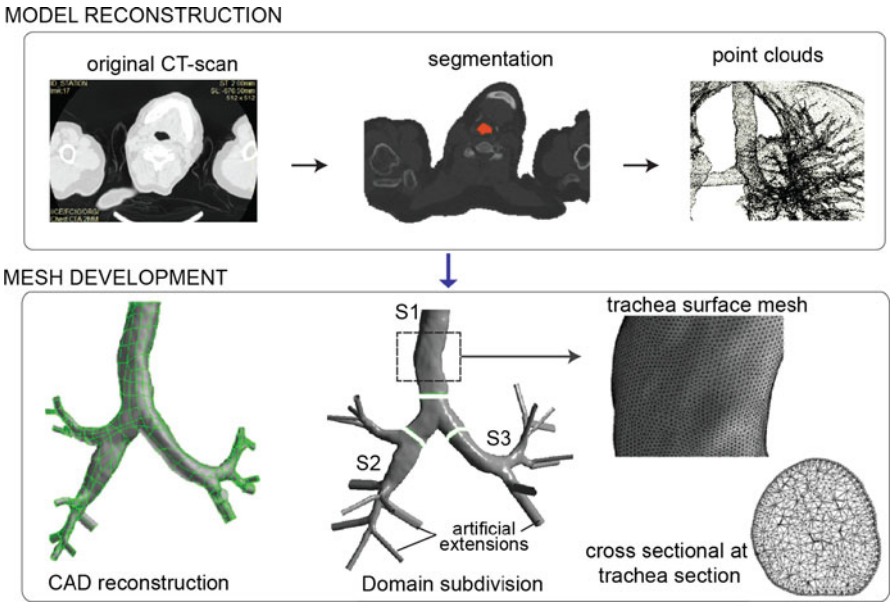


**Fig. 4.22** Mesh generation from the trachea and primary bronchi

### 4.5.3 *Meshing the Upper Respiratory Airway Inside a Human Body*

The procedure of meshing any geometry model follows a similar methodology. The creation of a mesh is typically dependent on the user and his or her experience. Furthermore, the selection of different types of cell elements and mesh configurations will indeed produce different CFD meshes. In this section we present the mesh for some parts of the conducting airways in the respiratory system and provide a short description of each mesh design. Mesh design, at times, requires some creativity to use the different mesh elements in different combinations in order to satisfy the flow problem.

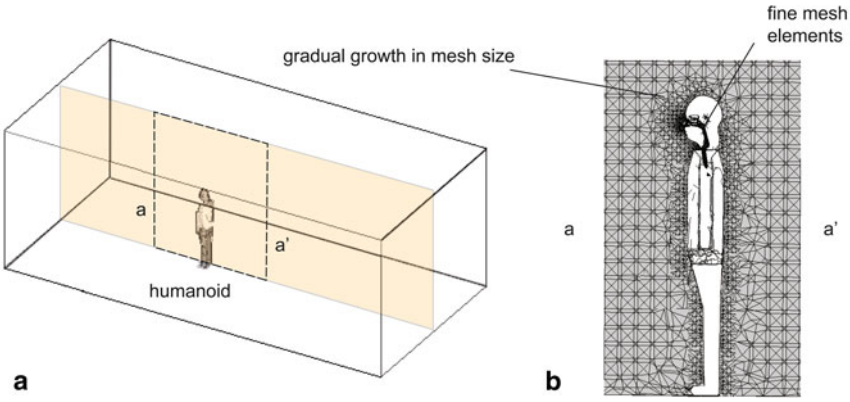


**Fig. 4.23** **a** Model of a human body placed inside a room. Slice a–a' is at the *mid-plane* of the room that cuts through the human body. **b** *Mesh elements* that are present in slice a–a'

**Humanoid in a Room** In this section a human body (which will be referred to as a humanoid) is placed inside an enclosed room. Air from the room is to be simulated through the nostrils and into the respiratory system. The mesh that is generated for this flow problem is shown in Fig. 4.23. The geometric scales that need to be resolved have a large variation: mesh dimensions inside the nose are in millimetres, while outside of the respiratory airway and inside the room, we are dealing with dimensions in metres. For such cases a *growth factor* or *inflation* technique is used to allow a fine mesh to be built in the small respiratory airway and to gradually grow in size from the nostrils outwards in the room. Figure 4.23b is a slice taken across the middle of the humanoid. The dark regions inside the airway in the figure indicate clustering of mesh elements. Note that the fluid flow field is a contiguous passage through both nostrils and this field is bounded by the walls of the room and the trachea surface. Therefore the humanoid is simply a shell with the hollow

section being the respiratory airway. Furthermore, the body part of the humanoid is simplified to a single block geometry to allow easier meshing. Because we are not concerned with the outside flow, a detailed section of the legs and feet is not necessary. However, if we were to study the effects of the humanoid torso on the upwards flow towards the nostrils, then a more accurate model of the torso and legs might need to be considered.

**Head of the Humanoid in a Room** The head of the humanoid is shown in Fig. 4.24. The geometry can be viewed as a shell casing with mesh elements filling the conducting respiratory airway passage. In designing such a mesh, the user needs to delineate the wall boundaries which act as a determinant of the enclosed space to be meshed.

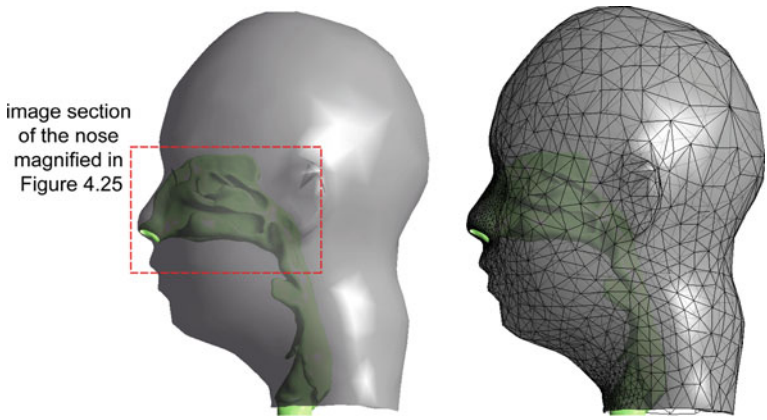


**Fig. 4.24** Model of the humanoid head, showing that tetrahedral mesh elements are present on the surface of the head. The dotted box is the nasal region that is re-shown in magnified form later in Fig. 4.25

**Nasal Cavity, Nasopharynx** Figure 4.25 shows the position of the nasal cavity geometry in relation to the head and face. The fine mesh near the walls and its gradual growth factor outwards from the surfaces are evident. Note that the nostrils are open casings to allow the contiguous passageway for the internal mesh elements.

**Larynx, Trachea** The larynx and trachea in Fig. 4.25 has similar meshing features to the nasal cavity as expected because it is simply a connection to upstream geometries. This region is closed at the oropharynx. This is typical of most reconstructed realistic oropharynx-larynx-trachea airways since it relies on CT scanned images where the patient usually has the mouth closed and the back of the tongue closes the oral passageway (Fig. 4.26).

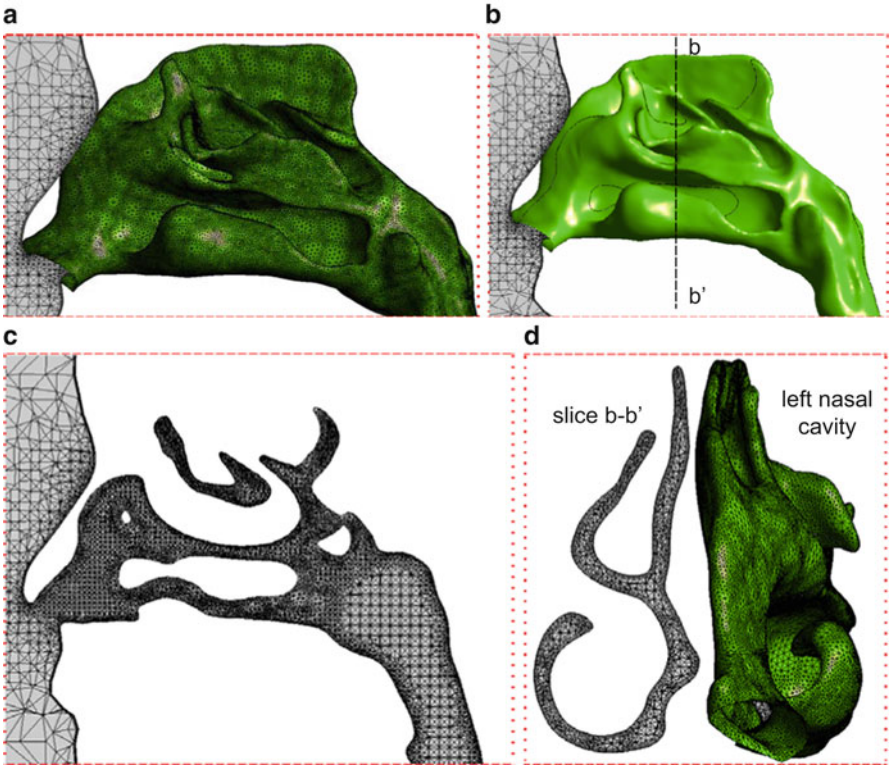


**Fig. 4.25** **a** Magnified view of the image section defined in Fig. 4.24 showing the nasal cavity geometry with the face outline, and external surrounding mesh. **b** Nasal cavity model with mesh. The darker image is due to the increased number of mesh lines. **c** Mesh elements present in slice a–a' defined earlier in Fig. 4.23. The outline of the face can be seen. **d** Frontal view of the nasal cavity, with the mesh and the coronal cross-section cut of slice b–b'

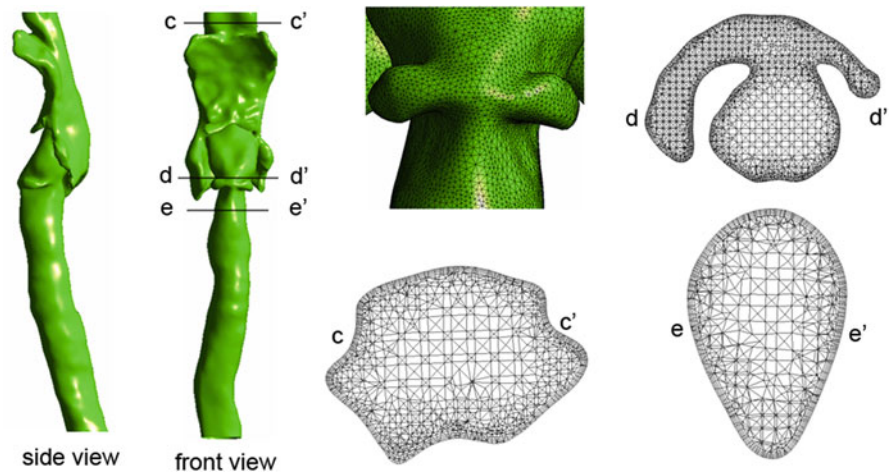


**Fig. 4.26** Side and frontal view of the trachea. *Three cross-sectional slices* are created to highlight the geometry and its internal mesh

## 4.6 Summary

The importance of generating a quality mesh in order to obtain reliable computational solutions has been discussed. Also discussed was the hierarchy for a mesh element: placing points, lines, faces, and then volumes, respectively, from the lowest to highest topology. The type of mesh element used (or combination of elements) determines whether the mesh can be set up as a structured or unstructured mesh. Structured mesh has the advantage of smaller computational memory and better solution convergence; however, it can be difficult to apply to complex geometries such as the respiratory organs. An unstructured mesh, on the other hand, has the ability to conform to complex geometries but requires more computational memory because of the need to connect up an arbitrary number of neighbouring nodes.

Generating a quality mesh requires as much creativity as it does technical knowledge. Therefore different techniques and strategies are presented for both structured and unstructured mesh to provide the reader with some ideas that can be applied to generating a quality mesh for different flow problems. This includes the importance of developing a coarse mesh to begin with for initial flow field testing and implementing a mesh independence test to ensure an optimum mesh has been used.

The mesh represents nodal points that are used to apply the set of fundamental *mathematical* equations that represent the flow physics. These equations are referred to as the governing equations of fluid flow or the Navier-Stokes equations. In the next chapter, we present the governing equations and how they are derived to represent the conservation principles related to fluid flow.

## 4.7 Review Questions

1. What are some of the benefits of a well-designed grid?
2. What are some of the advantages of a structured mesh?
3. Why is it difficult to write CFD programs that involve a structured mesh for complex geometries?
4. Discuss some of the advantages of an unstructured grid.
5. What are some of the difficulties that arise regarding programming of CFD problems for an unstructured mesh?
6. What conditions and constraints apply if you had to use a structured mesh for the outer wall geometry below? What about for an unstructured mesh? Discuss the advantages and disadvantages for these cases.

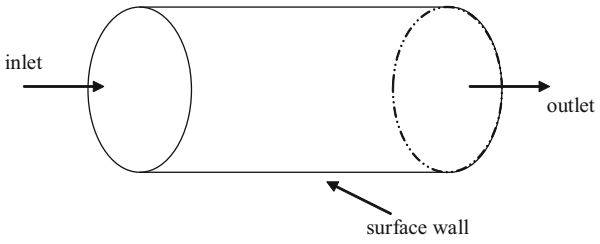

7. For the geometry below discuss how using a block-structured mesh has advantages over a single-structured or unstructured mesh.

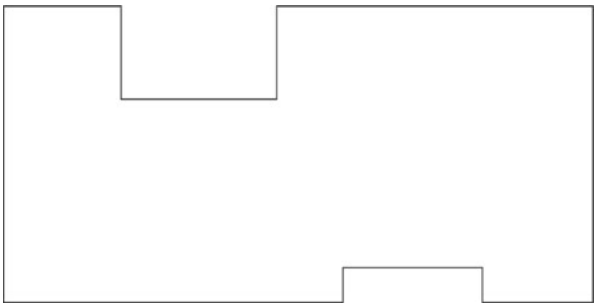

8. Why is it better to start off with a coarse mesh when you first begin to solve a CFD problem?
9. The stretched grid technique is an example of a local refinement technique that is applied before a solution is obtained. What is one problem associated with this technique?
10. Describe how solution adaptation uses an adaptive grid to refine its mesh.
11. What are some problems/difficulties in setting up correct boundary conditions?
12. Discuss why tetrahedral elements are a poor choice for meshing near walls and boundaries.
13. A computational domain with boundary types for the flow around a human body is shown below. Show where a fine mesh should be located.

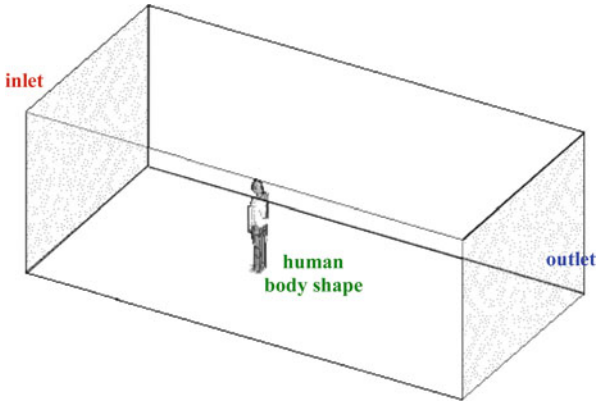

# Chapter 5
# Fundamentals of Fluid Dynamics

## 5.1 Introduction

Ultimately, the goal of Computational Fluid Dynamics (CFD) is to provide a numerical description of fluid flow behaviour. This is achieved through solving the governing equations that are mathematical statements of the physical *conservation laws*:

- conservation of mass;
- balance of momentum (Newton's second law, the rate of change of momentum equals the sum of forces acting on the fluid) and;
- conservation of energy (first law of thermodynamics, the rate of change of energy equals the sum of rate of heat addition to, and the rate of work done on, the fluid).

The governing equations represent not only the transport of mass, momentum, and energy but also the interaction of phenomena such as diffusion, convection, boundary layers, and turbulence. This chapter presents the derivation of the governing equations for a single fluid phase, and provides an understanding of the basic processes of fluid flow and the significance of different *terms* in the governing equations. Furthermore, a CFD user must understand the physical behaviour of fluid motion, as it is these phenomena that CFD analyses and predicts.

## 5.2 Fluid Dynamics and Governing Equations

### *5.2.1 Mass Conservation*

The conservation of mass is the basic principle which states that *matter may neither be created nor destroyed.* This means that a fluid in motion moves through a region of space in a way that the mass is conserved. In steady flow, *the rate of mass entering the control volume equals the net rate at which mass exits the control volume*

J. Tu et al., *Computational Fluid and Particle Dynamics in the Human Respiratory System,* Biological and Medical Physics, Biomedical Engineering
DOI 10.1007/978-94-007-4488-2_5, © Springer Science+Business Media Dordrecht 2013

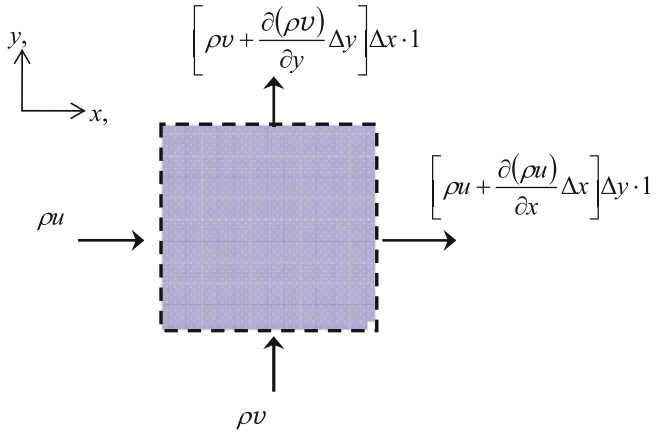


**Fig. 5.1** Mass flow into and out of a 2D control volume element

(inflow = outflow). In other words,

$$0 = \sum_{in} \dot{m} - \sum_{out} \dot{m} \tag{5.1}$$

Recalling that the mass flow rate is given by $\dot{m} = \rho \mathrm{U} A$, which is the product of density, average velocity, and cross-sectional area normal to the flow, then the rate at which mass enters the control volume is $\rho u A$, where $A = \Delta y \cdot 1$ for a unit depth, i.e. $\Delta z = 1$ (Fig. 5.1). Thus,

$$\dot{m}_{in} = \rho u A_x = \rho u(\Delta y \cdot 1) \tag{5.2}$$

and the rate at which the mass leaves the surface at $x + \Delta x$ may be expressed as

$$\dot{m}_{out} = \left[(\rho u) + \frac{\partial(\rho u)}{\partial x}\Delta x\right]\Delta y \cdot 1 \tag{5.3}$$

Similarly in the $y$-direction,

$$\dot{m}_{in} = \rho v(dx \cdot 1) \qquad \dot{m}_{out} = \left[(\rho v) + \frac{\partial(\rho v)}{\partial y}\Delta y\right](\Delta x \cdot 1)$$

Substituting the mass in and mass out terms into Eq. (5.1) for a two-dimensional control volume we get

$$0 = \left[(\rho u) + \frac{\partial(\rho u)}{\partial x}\Delta x\right](\Delta y \cdot 1) - \rho u(d\Delta \cdot 1) + \left[(\rho v) + \frac{\partial(\rho v)}{\partial y}\Delta y\right](\Delta x \cdot 1) - \rho v(\Delta x \cdot 1)$$

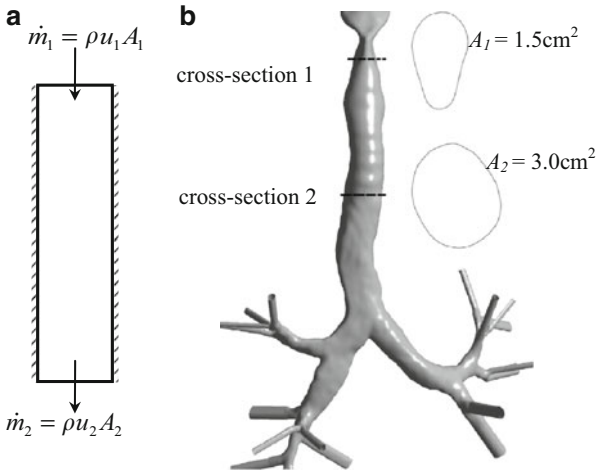


**Fig. 5.2** **a** Pipe. **b** trachea with two cross-sectional slices are shown. *Cross section* 1 is taken just after the larynx and has a cross-sectional area of 1.5 $\text{cm}^2$. *Cross section* 2 is taken in the main trachea region and has a cross-sectional area of 3.0 $\text{cm}^2$

For an incompressible flow such as inhaled air, density can be treated as a constant; therefore, we can simplify the above equation by dividing out $\rho$ and $\Delta x \cdot \Delta y \cdot 1$ which gives

$$0 = \frac{\partial u}{\partial x} + \frac{\partial v}{\partial y} \tag{5.4}$$

Equation (5.4) is the statement of conservation of mass, which is also known as the continuity equation for a steady two-dimensional flow of a fluid with constant density. If we repeat the derivation in the $z$-direction, we then get the relation under three-dimensions

$$0 = \frac{\partial u}{\partial x} + \frac{\partial v}{\partial y} + \frac{\partial w}{\partial z} \tag{5.5}$$

While the derivation shown is for steady flow, Eqs. (5.4) and (5.5) are valid for steady as well as unsteady flows for incompressible fluids.

**Physical Interpretation** Before the availability of imaging diagnostic tools (e.g. MRI, CT scans), early studies of the trachea airway were based on a uniform pipe model. Additionally, in most Fluid Mechanics textbooks, the principal of mass conservation is often explained by a fluid flowing in a uniform pipe. Therefore, let us consider flow in the trachea using both a uniform pipe geometry and a realistic CT-scan based model shown below in Fig. 5.2. The mass entering both geometries can be denoted by the mass flow rate $\dot{m}_1$, which is equivalent to the product of the density, inlet velocity and cross-sectional area, i.e. $\rho\ u_1\ A_1$. This mass must be equal to the mass flow rate leaving the pipe, which is denoted by $\dot{m}_2$ given as $\rho\ u_2\ A_2$. If we consider the uniform pipe, then both the inlet and outlet cross-sections of the pipe are equal, i.e. $A_1 = A_2$. Based on the mass conservation, the outlet velocity $u_2$ must

be equal to the inlet velocity $u_1$. However if we consider the realistic model, the two cross-sections shown have different cross-sectional areas, where $A_1 = 1.5\,\text{cm}^2$ and $A_2 = 3.0\,\text{cm}^2$. This means that $A_1 = ½ A_2$ and $u_1 = 2\,u_2$ (from mass conservation) which means that the flow *decelerates* from the larynx down through the trachea during steady inhalation. Conversely during steady exhalation, the flow moves from a larger to a smaller cross-section, from $A_2$ to $A_1$, which means that the flow accelerates as it approaches the larynx.

### 5.2.2 Momentum Balance

The balance of momentum is a fundamental law of physics based on *Newton's second law of motion,* which states that the sum of forces that act on a control volume equals the product of its mass, *m,* and acceleration, *a*, of the control volume, which is precisely the time rate of change of its momentum:

$$\sum F = ma$$

$\sum F$ is the sum of all forces, namely *body forces* and *surface forces,* acting on a control volume. We can also rewrite the mass $m$ as the product of the density $\rho$ and volume $\Delta x\,\Delta y\,\Delta z$, and rewrite the acceleration as $\frac{D\mathrm{U}}{Dt}$, which then gives us the following:

$$\sum F_{\text{body}} + \sum F_{\text{surface}} = (\rho \Delta x \Delta y \Delta z)\frac{D\mathrm{U}}{Dt} \tag{5.6}$$

Body forces act over the entire volume and as such are sometimes called volume forces. Typically these forces include gravity, centrifugal, Coriolis and electromagnetic forces, which act at a distance to the control volume. These effects are usually incorporated by introducing them into the momentum equations as additional source terms that add to the contribution of the surface forces. If we denote the body force per unit mass acting on the fluid element in the $x$-direction as $\mathbf{F}_{B,}$ then the total body force acting over the entire fluid element is

$$\text{body force} = \mathbf{F}_B \rho(\Delta x \Delta y \Delta z)$$

Surface forces are those forces that act on the surface of the fluid element causing it to deform (Fig. 5.3).

These surface forces include the normal stress $\sigma_{xx,}$ a combination of pressure $p$ exerted by the surrounding fluid and normal viscous stress components $\tau_{xx}$ that act perpendicular to fluid element surface, and also the tangential stresses $\tau_{yx}$ and $\tau_{zx}$ that act along the surfaces of the fluid element. The surface forces only for the velocity component $u$ (i.e. one-dimensional) are shown in Fig. 5.4.

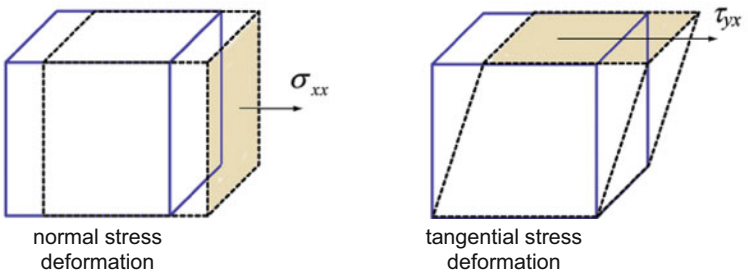


**Fig. 5.3** Deformed fluid element due to the action of the surface forces, in the form of normal and tangential stresses

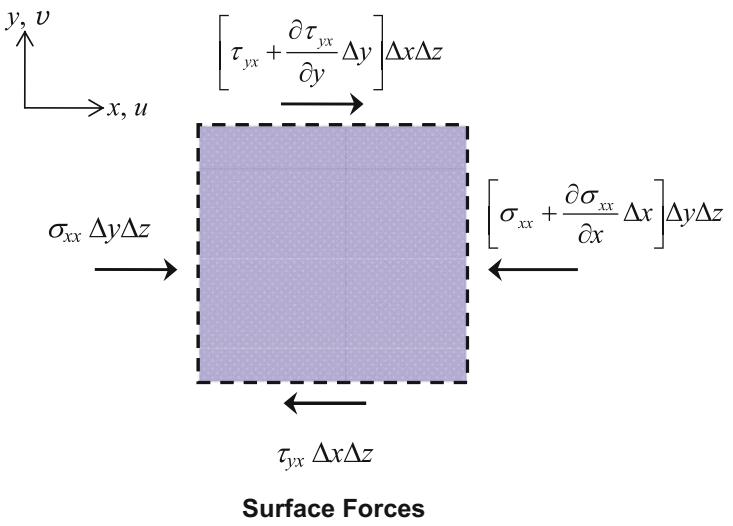


**Fig. 5.4** Surface forces acting on 2D control volume for the velocity component $u$

Combining the sum of these surface forces on the control volume together in the $x$-direction we get

$$\begin{aligned} F_{\text{surface},\,x} &= \left[\sigma_{xx}\Delta y\Delta z - \left(\sigma_{xx} + \frac{\partial \sigma_{xx}}{\partial x}\Delta x\right)\Delta y\Delta z\right] \\ &\quad + \left[\left(\tau_{yx} + \frac{\partial \tau_{yx}}{\partial y}\Delta y\right)\Delta x\Delta z - \tau_{yx}\Delta x\Delta z\right] \\ &= -\frac{\partial \sigma_{xx}}{\partial x}\Delta x\Delta y\Delta z + \frac{\partial \tau_{yx}}{\partial y}\Delta x\Delta y\Delta z \end{aligned} \tag{5.7}$$

If we assume the fluid is Newtonian and isotropic—since all gases and majority of liquids are isotropic—the normal stress $\sigma_{xx}$ can be formulated in terms of pressure $p$

and normal viscous stress components $\tau_{xx}$ as

$$\sigma_{xx} = -p + \tau_{xx}$$

The formulation of the appropriate stress-strain relationships for a Newtonian fluid is based on Newton's law of viscosity and given as:

$$\tau_{xx} = 2\mu \frac{\partial u}{\partial x} \qquad \tau_{yx} = \mu \left( \frac{\partial u}{\partial y} \right) \tag{5.8}$$

where $\mu$ is the molecular dynamic viscosity that relates stresses to linear deformation rate. For the $x$-velocity component we combine Eqs. (5.6), (5.7), and (5.8), and cancel out the volume term $\Delta x \Delta y \Delta z$, which gives:

$$\rho \frac{Du}{Dt} = -\frac{\partial p}{\partial x} + \mu \left( \frac{\partial^2 u}{\partial x^2} + \frac{\partial^2 u}{\partial y^2} \right) + \rho \sum \mathbf{F}_B \tag{5.9}$$

The acceleration term is the total derivative of $u$ (the rate of change of velocity of a moving fluid particle) which can be expressed in 2D as

$$\frac{Du}{Dt} = \frac{\partial u}{\partial t} + u \frac{\partial u}{\partial x} + v \frac{\partial u}{\partial y} \tag{5.10}$$

Putting Eq. (5.10) into (5.9), and rearranging by dividing through by $\rho$, the balance of momentum equation in the $x$-direction becomes:

$$\frac{\partial u}{\partial t} + u \frac{\partial u}{\partial x} + v \frac{\partial u}{\partial y} = -\frac{1}{\rho} \frac{\partial p}{\partial x} + \nu \left( \frac{\partial^2 u}{\partial x^2} + \frac{\partial^2 u}{\partial y^2} \right) + \sum \mathbf{F}_B \tag{5.11}$$

and its corresponding $y$-direction component is:

$$\frac{\partial v}{\partial t} + u \frac{\partial v}{\partial x} + v \frac{\partial v}{\partial y} = -\frac{1}{\rho} \frac{\partial p}{\partial y} + \nu \left( \frac{\partial^2 v}{\partial x^2} + \frac{\partial^2 v}{\partial y^2} \right) + \sum \mathbf{F}_B \tag{5.12}$$

Note that $\nu$ is the kinematic viscosity which is related to the dynamic viscosity, $\mu$ as $\nu = \frac{\mu}{\rho}$.

**Physical Interpretation** The negative product of mass and acceleration may be interpreted as the so-called inertia force. The balance of momentum equation is then rewritten in a form that represents the balance of four forces (inertial, pressure, viscous, and body force) acting on a body. Let us consider the $y$-momentum equation and its application in the vertical respiratory flows in the tracheal region. Each force is reflected by different terms in the equation where the inertial force appears through the local acceleration and convection term; the pressure force via the pressure gradient; and the viscous force via the diffusion term. These terms are clearly identified in Eq. (5.13).

$$\underbrace{\frac{\partial v}{\partial t}}_{\textit{local acceleration}} + \underbrace{u \frac{\partial v}{\partial x} + v \frac{\partial v}{\partial y}}_{\textit{convection}} = - \underbrace{\frac{1}{\rho} \frac{\partial p}{\partial y}}_{\textit{pressure gradient}} + \underbrace{\nu \frac{\partial^2 v}{\partial x^2} + \nu \frac{\partial^2 v}{\partial y^2}}_{\textit{diffusion}} + \underbrace{\sum \mathbf{F}_B}_{\textit{body force}} \tag{5.13}$$

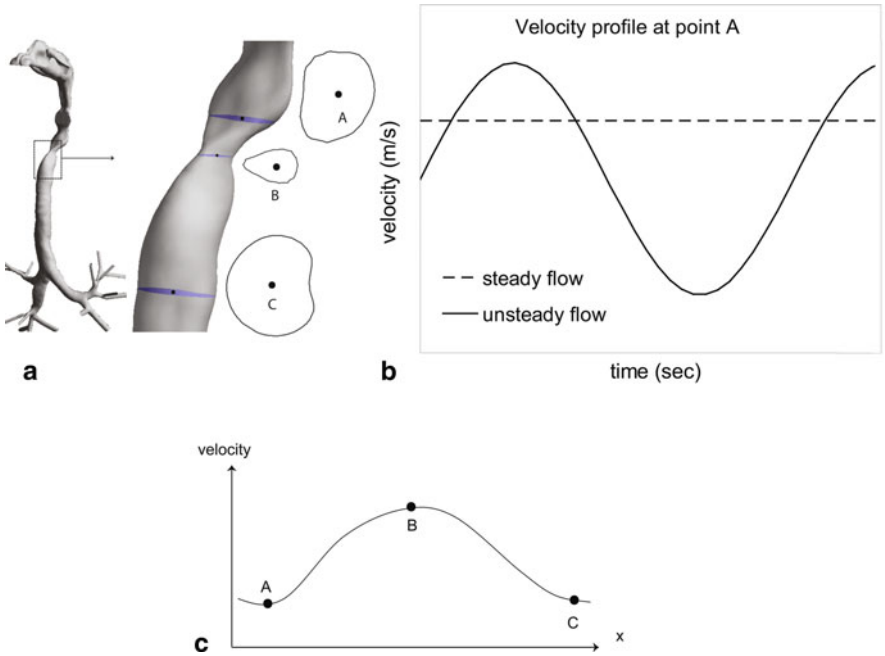


**Fig. 5.5** **a** The motion of fluid in the laryngeal region taken at three locations. **b** Velocity profile monitored at a fixed location at point *A* for a steady and unsteady flow. **c** The motion of a fluid particle passing through points *A*, *B*, *C*

Consider the steady flow of air passing Point A near the larynx of the respiratory system (Fig. 5.5). Under a steady flow, the velocity profile is a horizontal line which means that the acceleration is zero. A breathing cycle may be represented idealistically by a sinusoidal pattern which generates an unsteady airflow. The velocity profile at Point A for an unsteady flow then simply follows the sinusoidal breathing pattern. If we consider the vertical velocity component $v$ as the flow direction, then in the $y$-momentum equation the velocity profile at Point A is represented by the *local acceleration* term $\partial v/\partial t$ for the velocity component $v$. This term describes the motion of the fluid changing locally at a fixed point and varying with time.

The second term of the inertial force is the convection term, which describes the fluid acceleration spatially. If we now follow a fluid particle that happens to pass through points A, B, and C in the laryngeal region under a steady flow condition so that the velocity in itself is not fluctuating with time, the velocity component $v$ now has a local *acceleration* in space where the velocity is accelerating between the locations of A and B, i.e. the velocity gradient in the term $v\partial v/\partial y$ of Eq. (5.12) is increasing. Similarly, after the larynx, from point B to C, the velocity is decreasing and the local *acceleration* gradient in space is negative, i.e. a deceleration. We describe the fluid motion sweeping past points in space by the convection term in the momentum equations.

The pressure term describes the existence of a pressure gradient caused by a pressure difference in the flow domain. If we consider the steady flow through the 2D

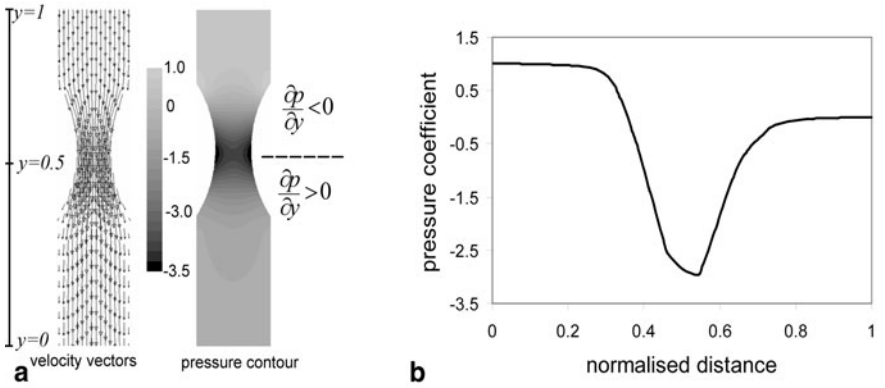


**Fig. 5.6** **a** Velocity vectors and pressure contour field in a 2D idealised larynx. **b** Pressure profile in the vertical distance highlighting the change in pressure

idealised larynx in Fig. 5.6, we see that there is a so-called laryngeal jet characterised by the converging-diverging geometrical shape (Lin et al. 2007; Martonen et al. 1993; Xi et al. 2008). As the fluid accelerates into the narrowest section of the larynx, the pressure gradient is negative, $\partial P/\partial y < 0$, which corresponds to an increase in fluid velocity. After the flow exits the larynx, there is a positive pressure gradient, $\partial P/\partial y > 0$, which corresponds to a decrease in the fluid velocity. This can be seen in the pressure coefficient profile (Fig. 5.6b). Lets us neglect the influence of viscosity in the momentum equation; therefore, assume that the flow is inviscid where all the shear stresses are zero. That is, $\tau = 0$ and the diffusion terms are zero. The $y$-momentum equation then becomes:

$$\frac{\partial v}{\partial t} + u\frac{\partial v}{\partial x} + v\frac{\partial v}{\partial y} = -\frac{1}{\rho}\frac{\partial p}{\partial y} + \nu\frac{\partial^2 v}{\partial x^2} + \nu\frac{\partial^2 v}{\partial y^2}$$

$$= 0 \qquad = 0 \qquad = 0$$

The above equation reduces to

$$\frac{\partial v}{\partial t} + v\frac{\partial v}{\partial y} = -\frac{1}{\rho}\frac{\partial p}{\partial y} \tag{5.14}$$

and we see that the pressure gradient is related to the total acceleration of the fluid (i.e. sum of the local *acceleration* and *convection*). The negative sign denotes that a positive pressure produces a decrease in acceleration, and vice-versa.

Finally let us consider the influence of the diffusion term on the flow development in the respiratory airway. In the modelling of the tracheobronchial region only, the upstream geometry that includes the oral/nasal cavity, pharynx and larynx is neglected as this would require great demands of computational processing power. For

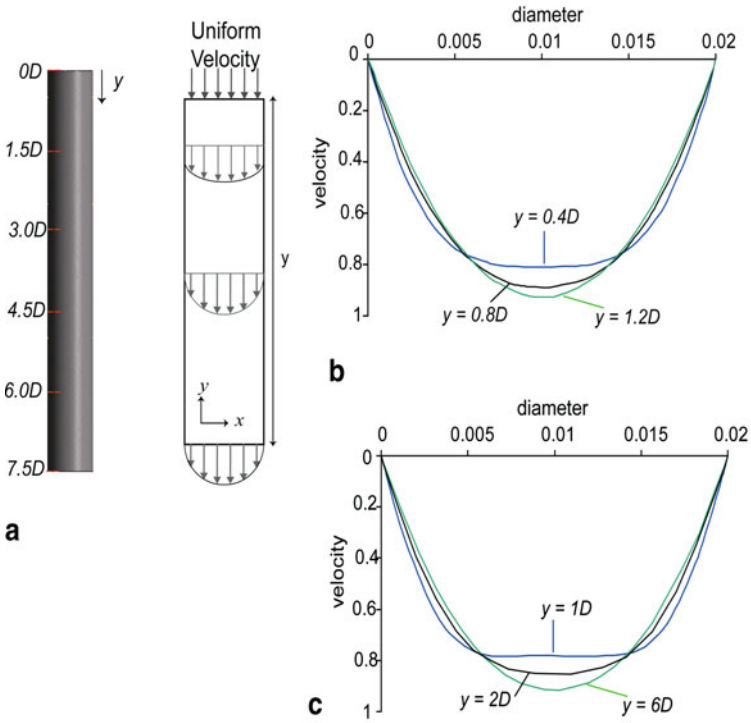


**Fig. 5.7** Velocity profiles at different locations of diameter distances from the inlet for $u_{in} = 0.01$ m/s and dynamic viscosity of **a** $\mu_1 = 4 \times 10^{-5}$ kg/m · s, and **b** $\mu_2 = 10^{-5}$ kg/m · s

these cases, the inlet profile can be prescribed with a uniform velocity inlet, but this neglects the upstream flow conditions developed by the upper respiratory airway. To account for some flow development, studies in the literature have used a parabolic profile at the tracheobronchial inlet for a laminar steady flow (Liu et al. 2003) while more recent studies also include the influence of the laryngeal jet effect (Luo and Liu 2009; Zhang et al. 2005a). The development of the velocity flow profile through internal flows is primarily due to the diffusion term in the momentum equation. To illustrate this, let us consider an internal pipe flow, which again may represent a highly simplified trachea that has a uniform velocity profile applied to the inlet. Here, the dimensions of the pipe are given as height $L = 15$ cm and diameter $D = 2$ cm. Using CFD, the development of the velocity profiles between the inlet and the outlet can be visualized with air (density $\rho = 1.2\,\text{kg/m}^3$) as the working fluid, for a fixed inlet velocity $u_{in} = 0.05$ m/s, and with dynamic viscosities $\mu_1 = 4 \times 10^{-5}$ kg/m · s (Case 1) or $\mu_2 = 10^{-5}$ kg/m · s (Case 2).

Although the dynamic viscosity $\mu$ is used in the cases above, it is related to the kinematic viscosity which is presented in Eq. (5.13) by $\nu = \mu/\rho$. Therefore the influence of the diffusion term is represented by the variation in the dynamic viscosities in Case 1 and Case 2. Based on a CFD simulation, Fig. 5.7 shows the velocity profiles at different downstream locations measured by the diameter distances from the inlet

surface. The results show that for a given *inertial* force, the higher dynamic viscosity in Case 1 produces a higher *friction* force or diffusion of the inertial flow property. This increased diffusion inhibits the fluid momentum and leads to a quicker transition of the flow to a fully developed parabolic profile at a shorter distance. The developed profile is reached at a downstream distance of $y = 1.2$D. Case B has a smaller viscosity, so its diffusion term is smaller and there is less frictional resistance. This leads to a slower development of the parabolic profile where the fully developed flow occurs at a distance of $y = 6$D.

In fluid dynamics, the concept of *dynamic similarity* is frequently encountered. This involves normalizing the mathematical equations to yield the non-dimensional governing equations. In the example presented in Fig. 5.7, viscosity plays a role in holding the fluid together by resisting any motion. The inertia or flow velocity, in contrast to viscosity, moves the fluid with through the pipe. When the viscosity was decreased by a factor of four from $4 \times 10^{-5}$ to $1 \times 10^{-5}$ kg/m · s, the fluid velocity travelled farther before it was developed. If we were to decrease the velocity by the same factor for Case 2, then this would equalise the change in viscosity and, consequently, the developing length would be the same.

Likewise for any combination of different inlet velocities and dynamic viscosities, the same fluid flow effect is obtained in reference to the development of the flow. Extending this idea we can also increase the air density by a factor of four, from $\rho_1 = 1.2$ kg/m$^3$ to $\rho_2 = 4.8$ kg/m$^3$, while fixing the inlet velocity and dynamic viscosity at 0.01 m/s and $\mu = 4 \times 10^{-5}$ kg/m · s, respectively; and the same results are obtained.

The same results occur because the increase of density contributes to the increase of the inertia force, which has the same effect as increasing the inlet velocity. An important non-dimensional parameter that encapsulates these variables and describes the flow characteristics is the Reynolds number (*Re*) defined as:

$$\mathrm{Re} = \frac{\textit{Inertia Force}}{\textit{Friction Force}} = \frac{\rho u_{in} D}{\mu} \tag{5.15}$$

where $\rho$ is density, $D_h$ is the hydraulic diameter such as in pipes or ducts, $U$ is the fluid velocity, and $\mu$ is the viscosity.

For a given Re number, different combinations of the density, dynamic viscosity, and velocity values will yield the same flow entrance behaviour. Another important use of the Reynolds number is to indicate whether the flow is laminar or turbulent. For internal circular pipe flows that are smooth and free of sharp curvatures, the flow will remain laminar for $\mathrm{Re} < 2{,}300$, turbulent for $\mathrm{Re} > 4{,}000$, and transitional in- between those numbers.

In fluid dynamics, the dimensionless number groups play an important role in describing fluid flow under different scales. It reduces the need to test and evaluate the different parameters which are correlated within the dimensionless parameter. In the Reynolds number example described above, the parameters, $\rho$, $u_{in}$, $D$, $\mu$ need not be evaluate separately as they are neatly described by the Reynolds number. Furthermore non-dimensionalization of the governing equations of fluid flow can be performed which provides further physical insight into the importance of various terms in the

system of governing equations. A list of the more important dimensionless numbers relevant to CFPD and fluid dynamics is given in Appendix C.

### 5.2.3 Energy Conservation

The equation for the conservation of energy is derived from the consideration of the *first law of thermodynamics,* which states that during a steady flow the total energy content of a control volume does not change. Therefore the amount of energy entering the control volume must equal the amount of energy leaving it. Similar to the mass conservation, we have

$$\frac{DE}{Dt} = \begin{matrix}\text{Net rate of}\\ \text{heat added}\end{matrix} \left(\sum \dot{Q}\right) + \begin{matrix}\text{Net rate of}\\ \text{work done}\end{matrix} \left(\sum \dot{W}\right) \tag{5.16}$$

The energy term $E$ is the energy of the fluid per unit mass and is expressed in terms of the specific heat capacity $C_p$ and temperature $T$:

$$E = C_p T$$

Similar to Eq. (5.10), the total derivative of $E$, $\frac{DE}{Dt}$, represents the rate of change of energy of a moving fluid particle, which can be expressed in 2D as

$$\frac{DE}{Dt} = \frac{\partial E}{\partial t} + u\frac{\partial E}{\partial x} + v\frac{\partial E}{\partial y} = C_p\left(\frac{\partial T}{\partial t} + u\frac{\partial T}{\partial x} + v\frac{\partial T}{\partial y}\right) \tag{5.17}$$

The total amount of energy in a 2D fluid element by mass is given by

$$\rho\frac{DE}{Dt}\Delta x\Delta y\cdot 1 = \rho C_p\left(\frac{\partial T}{\partial t} + u\frac{\partial T}{\partial x} + v\frac{\partial T}{\partial y}\right)\Delta x\Delta y\cdot 1 \tag{5.18}$$

where $\Delta z = 1$. The terms $\Sigma\dot{Q}$ and $\Sigma\dot{W}$ describe the net rate of heat added to the fluid element and the net rate of work done by body and surface forces on the fluid element. $\Sigma\dot{Q}$ due to the heat flow in the $x$ direction is given by the difference between the heat at surface at $x$ and heat loss at surface $x + \Delta x$, as depicted in Fig. 5.8. In heat transfer, the amount of heat flow per unit area is given by the heat flux, defined as $\dot{q} = \dot{Q}/A$.

From Fourier's heat conduction equation we have

$$\dot{Q}_x = kA_x\frac{\partial T}{\partial x} = \dot{q}_x A_x = \dot{q}_x\Delta y\cdot 1$$

Thus the net heat transferred in the $x$ direction into the fluid element is

$$\left[q_x + \frac{\partial q_x}{\partial x}\Delta x\right]\Delta y\cdot 1 - q_x\Delta y\cdot 1 = \frac{\partial q_x}{\partial x} = k\frac{\partial^2 T}{\partial x^2}\Delta x\Delta y\cdot 1 \tag{5.19}$$

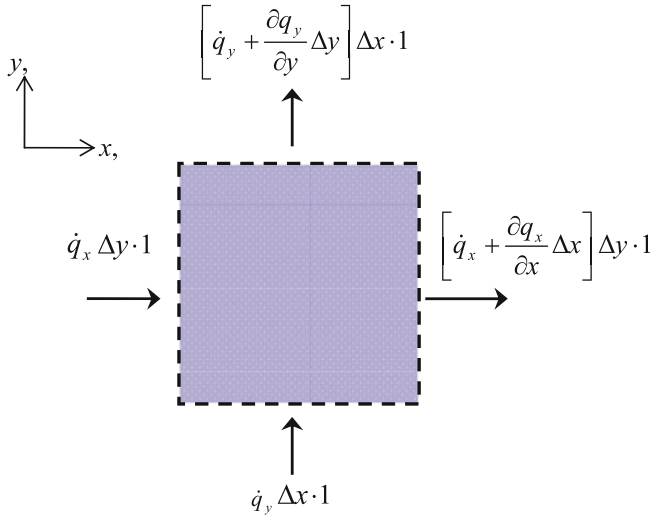


**Fig. 5.8** Heat energy flowing through the*x* and *y* directions of a 2D control volume

Similarly, in the *y-direction* we have

$$\left[q_y + \frac{\partial q_y}{\partial y}\Delta \mathrm{y}\right]\Delta x \cdot 1 - q_y \Delta x \cdot 1 = \frac{\partial q_y}{\partial y} = k\frac{\partial^2 T}{\partial y^2}\Delta x \Delta y \cdot 1 \tag{5.20}$$

The rate of work done by the body force is determined by the product of the force and the component of velocity in the direction of the force. Usually these values are only considered when the body forces, such as gravity, electric or magnetic effects, are significant. For the surface forces that include both the normal viscous stress $\sigma_{xx}$ and tangential viscous stresses $\tau_{yx}$ and $\tau_{zx}$, each stress acting on the surface of the fluid element (Fig. 5.4) is multiplied by the component of velocity in the direction of the force. Shear stresses that arise from viscous effects are typically very small and can be neglected in many cases. Therefore we can write $\sum \dot{W} \approx 0$.

Rewriting Eq. (5.16) by substituting Eq. (5.19) and (5.20) and cancelling out the volume term $\Delta x \Delta y \Delta z$, we get the energy equation in 2D:

$$\underbrace{\frac{\partial T}{\partial t}}_{\textit{local acceleration}} + \underbrace{u\frac{\partial T}{\partial x} + v\frac{\partial T}{\partial y}}_{\textit{convection}} = \underbrace{\frac{k}{\rho C_p}\frac{\partial^2 T}{\partial x^2} + \frac{k}{\rho C_p}\frac{\partial^2 T}{\partial y^2}}_{\textit{diffusion}} \tag{5.21}$$

**Physical Interpretation** Physically, Eq. (5.21) defines the temperature of a differential fluid control volume as it travels past a point, taking into consideration the local acceleration derivative (where the temperature in itself may be fluctuating with time at a given point) and also the convection derivative (where the temperature changes spatially from one point to another). To reinforce the physical meaning of

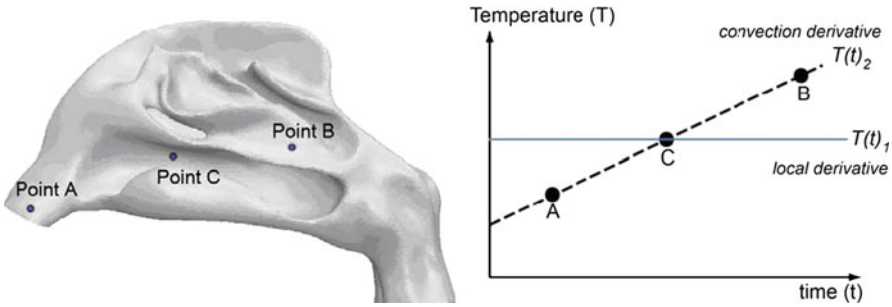


**Fig. 5.9** Temperature variation with time for a steady flow rate in the nasal cavity

these derivatives, consider a *steady flow* of air, initially at 20 °C, through the nasal cavity. The mucous walls of the nasal cavity are maintained at a surface temperature of 37 °C throughout the geometry (Fig. 5.9).

If we took temperature measurements at Point C over time, then the temperature profile would be represented by $T(t)_1$ which is constant because the flow that passes Point C will have the same temperature. This means that the local acceleration derivative in the energy equation is zero:

$$\frac{\partial T}{\partial t} = 0$$

Now if we follow a fluid particle along its trajectory as it travels from A through C and then B, then there is some variation in the temperature profile which is represented by $T(t)_2$. The temperature from point A through to B shows the air temperature heating up because of the surrounding walls. This spatial variation is represented by the convective derivative, which describes the temperature variation from one point to another:

$$u\frac{\partial T}{\partial x} + v\frac{\partial T}{\partial y} \neq 0$$

If we consider the local acceleration derivative during an unsteady inhalation cycle, then $\frac{\partial T}{\partial t} \neq 0$ and will vary with time—specifically the air temperature will rise more rapidly when the inhalation is slowest. If we follow a fluid particle for the convective derivative, the air temperature will fluctuate not only with the inhalation cycle but also with the temperature variation in the spatial coordinates $x$, $y$, and $z$. The total derivative of energy is, therefore, the instantaneous time rate of change at a given point following a moving fluid element. This is made up of the local derivative, which is the time rate of change at the given point, and the convective derivative, which is the time rate of change due to the spatially changing fluid property as the fluid element moves to that given point within the flow field.

The remaining term in Eq. (5.21) represents the heat flow due to conduction (the *diffusion*), where the thermophysical property $k$ is the thermal conductivity of the fluid. To examine the physical interaction of the diffusion terms with the convective

terms, imagine the problem concerning the fluid flowing in a pipe (Fig. 5.7) whose walls are now heated. If the surrounding fluid velocity is very low, the surrounding fluid temperature within the pipe increases due to the heat flowing from the pipe surface into the bulk fluid—this corresponds to the case that the heat conduction dominates the local *convection* of the fluid. However, if the surrounding fluid velocity is high, the heat of the fluid is carried away by the relatively cooler fluid. The high temperatures are only found near the hot surface of the pipe walls—this corresponds to the case that the local *convection* dominating the heat *diffusion*.

## 5.3 Turbulent Flow

### *5.3.1 What is Turbulence?*

Fluid flow can be classified into one of two main regimes, namely laminar flow and turbulent flow. *Laminar flows* are characterised by smooth fluid layers passing over each other without mixing. The viscosity of the fluid plays a significant role in holding the fluid together in its layered formation; thus, if a fluid particle was tracked throughout the flow, its path could be predicted. *Turbulent flows* on the other hand are characterised by the random fluctuations, irregular and chaotic motion, and high level of vortices. The fluctuation velocities of the fluid play a significant role in transporting and dispersing the fluid across different regions, thus, breaking down the layered motion that is present in laminar flows. If a fluid particle was tracked throughout the flow, it would have an irregular path with no discernable pattern. The presence of turbulence significantly increases dispersion, mixing, energy dissipation, and heat, mass and momentum transfer. Many flows found in nature and in industrial applications are in a turbulent regime, such as rivers, wind flows, and smoke rising from a cigarette (Fig. 5.10).

If you have looked over the ocean from above you may have noticed the water flow is chaotic and random, with little pockets of vortices. The smoke rising from a cigarette begins with a smooth plume (laminar flow) before it becomes disturbed and breaks out into random fluctuating smoke streaks (turbulent flow). Disturbances originate from the free stream of the cigarette smoke, amplify and lead to formation of turbulent flow. However, these disturbances can be induced by surface roughness in internal flows as well, where they may be amplified in the direction of the flow, in which case turbulence will occur. The onset of turbulence depends on the ratio of the inertia force to viscous force, which is indicated by the Reynolds number, as described earlier in Eq. (5.15). For internal pipe flows,

- the flow is laminar for $\mathrm{Re} < 2{,}000$,
- the flow is transitional between $2{,}000 < \mathrm{Re} < 4{,}000$ and
- the flow is turbulent for $\mathrm{Re} > 4{,}000$.

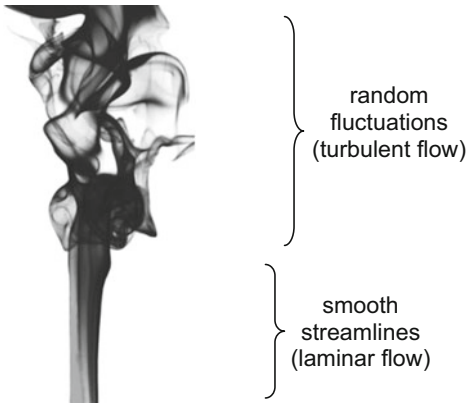


**Fig. 5.10** Turbulent flow found in smoke plume. (*Courtesy of RGBstock.com*)

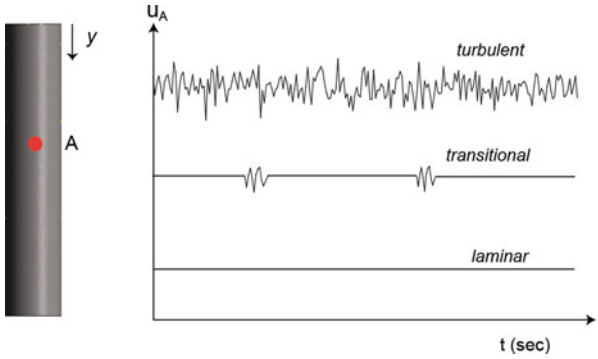


**Fig. 5.11** Velocity measurements taken at a fixed point for laminar, transitional, and turbulent flows

At low Reynolds number, inertia forces are smaller than the viscous forces. The naturally occurring disturbances are dissipated by the fluid viscosity, and the flow remains laminar. At high Reynolds number, the inertia forces are sufficiently large to amplify the disturbances, and a transition to turbulence occurs. Here, the steady motion becomes intrinsically unstable, and the velocity and all other flow properties are varying in a random and chaotic way.

Flows in the respiratory airways are internal flows which may experience both laminar and turbulent regimes. This is evident for airflows that are at very low respiratory rates. However, as the flow rate increases, the presence of highly irregular geometric features of the nasal cavity, extra-thoracic area, and lung airways promotes inertial disturbances that disrupt the fluid streamlines of a laminar flow. This eventually leads to a chaotic and random state of motion—which is a characteristic of turbulent flows. These flow regimes can be illustrated by considering flow inside a pipe. During a steady flow, the fluid velocity is measured at Point A in the pipe and is plotted (Fig. 5.11). For a laminar flow, the velocity is constant without any perturbations or fluctuations. If the flow rate is increased to the point where the *Re* number reaches to the transitional regime, small and random disturbances occur in the flow. When the flow is increased even further so that the flow becomes turbulent, the measured velocity at Point A exhibits a random state with large fluctuating

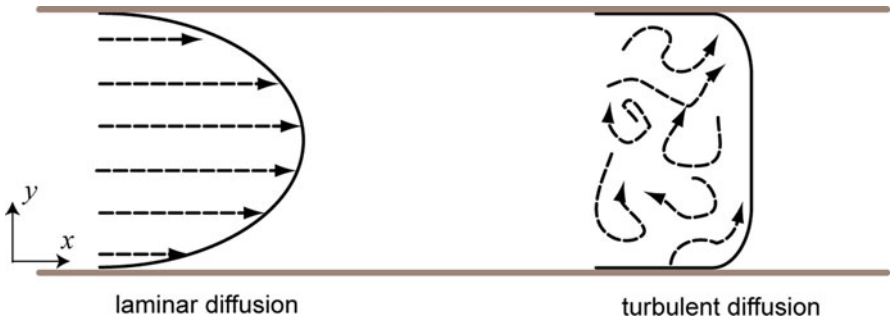


**Fig. 5.12** Velocity profiles in a 2D pipe flow showing the difference between a laminar and a turbulent velocity profile. (In fluid mechanics the flow of fluid through a pipe of uniform cross-section is known as Hagen–Poiseuille flow

components. Random, irregular fluctuations in the flow are characteristic features of turbulent flows.

**Velocity Profiles** One important flow feature of laminar and turbulent flows is the influence of the viscosity and its mixing effect. Under a laminar flow the velocity profile is parabolic in shape. Let us imagine fluid passing over a pipe surface as layers of molecules. The molecules are transported mainly by the flow in the streamwise direction ($y$-direction in Fig. 5.12), but they also exhibit random motion due to the molecular state which causes them to momentarily move vertically into adjacent layers of molecules. This process is called *molecular diffusion*. At the wall surface, the air molecules stick to the surface and the velocity is zero. The adjacent layer of air molecules immediately above are slowed down as they collide with the molecules that have stuck to the surface. In turn, these molecules slow down the flow in the layer just above it, and this continues until far from the surface where the slowing effects (or viscosity effects) from the stationary wall are weak. This creates a thin layer of fluid, called the boundary layer, near the surface in which the velocity changes from zero at the surface to the free stream value far away from the surface. Under a laminar flow, the slowing down process due to molecular diffusion of the molecules from one 'layer' to its adjacent layer above occurs gradually, since the molecules mainly travel in an orderly path through the pipe.

For turbulent flows the velocity is no longer orderly, and there are no discernable layering motions of the fluid but rather the fluid elements swirling and fluctuating randomly within the boundary layer. It has been suggested that turbulence is a collection of *eddies,* which are parcels of rotating fluids. These eddies have a spectrum of vorticities and provide a high level of mixing in the fluid. Turbulence eddies carry and rapidly disperse momentum, mass and heat in the transverse direction. This leads to greater momentum and heat transfer in turbulent flows, and, thus, significantly higher values of friction and heat transfer coefficients, in comparison to laminar flows.

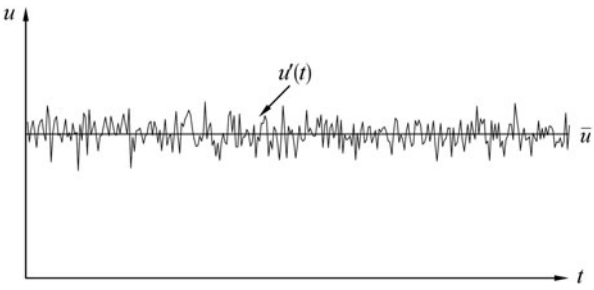


**Fig. 5.13** Instantaneous velocity fluctuating with time at a specific point in a turbulent flow

**Turbulence Intensity** Turbulence is associated with the intense *random velocity fluctuations* in the fluid. This behaviour can be exemplified by a typical velocity measurement as a function of time at a point in the turbulent flow as shown in Fig. 5.13. The random nature of flow produces strong velocity fluctuations which are transient and their instantaneous values vary stochastically with time. Typically, the velocity is decomposed into a steady mean value $\bar{u}$ and a fluctuating component $u'(t)$ that varies with time. That is $u(t) = \bar{u} + u'(t)$. In application, a turbulent flow is characterized by the mean values of the flow properties ($\bar{u}$, $\bar{v}$, $\bar{w}$, $\bar{p}$, etc.) and the corresponding statistics of fluctuating property ($u'$, $v'$, $w'$, $p'$, etc.). This gives rise to the root mean square (RMS) fluctuation velocities and turbulence intensity which is a parameter that describes the turbulence level of the flow. The RMS and turbulence intensity are defined as the following:

$$\sqrt{\overline{u'^2_x}},\ \sqrt{\overline{u'^2_y}},\ \sqrt{\overline{u'^2_z}}\ \text{(RMS velocities)}$$

$$I = \frac{u'}{\bar{u}} \quad \text{where } u' = \sqrt{\frac{1}{3}\left(\overline{u'^2_x} + \overline{u'^2_y} + \overline{u'^2_z}\right)} \text{ and } \bar{u} = \sqrt{\bar{u}_x^2 + \bar{u}_y^2 + \bar{u}_z^2} \tag{5.22}$$

Here, a bar on the top denotes an ensemble averaging.

**Turbulence Shear Stress** At wall boundaries, the fluid velocity slows to zero, leading to a shear stress (i.e. resistance to fluid flow due to the fluid viscosity). Momentum exchange occurs through fluid particles that are travelling at different velocities within the boundary layer and moving from one region to another region. A faster moving particle moving into a slower moving region will increase the momentum at the new location. If this motion of the fluid particle is caused by molecular diffusion, then the momentum exchange is due to the fluid viscosity. If we now consider turbulent flow there is additional mixing of fluid particles, which is caused by turbulence dispersion due to the instantaneous velocity fluctuations. The instantaneous rate of momentum exchange due to the velocity fluctuations in the $x$- and $y$-direction is given by $\rho\, u'_x\, u'_y$ per unit volume of fluid. The turbulence shear stress ($\tau_T$) is then given as

$$\tau_T = -\rho \overline{u'_x u'_y} \tag{5.23}$$

The turbulence stress is also referred to as the *Reynolds stress* and is an unknown that needs to be modelled. While the turbulence stress is a physical stress, its constitutive modelling is different from the viscous stress that has a constant coefficient of viscosity. This is because the Reynolds stress is the consequence of the flow velocity fluctuations unlike the viscous stress which is due to molecular fluctuations. The time and length scales of the Reynolds stresses are comparable with those of the flow itself; therefore, there is strong statistical coupling of the turbulence stresses with the mean fluid motion. Reynolds was the first to provide the decomposition of the flow variables into the statistical mean and fluctuating components and to perform averaging of the governing equations. The statistical averaging forms the basis of many semi-empirical equations which have been developed to model the Reynolds stress and to provide the so-called mathematical *closure* to the averaged governing equations of turbulence motion. These semi-empirical equations are called **turbulence models**.

### *5.3.2 Introduction to Turbulence Modelling*

When the governing equations for classical conservation laws are averaged, they lead to the generation of new unknown stresses and fluxes that are a consequence of turbulence fluctuations and the nonlinearity of the convective transport terms. Turbulence modelling is referred to the inclusion of additional algebraic or transport equations to augment the governing averaged equations (continuity, momentum, and energy) to account for the Reynolds stresses as given by Eq. (5.28) and turbulence fluxes. Turbulence modelling has a long history and many models have been derived and improved over time by many researchers, based on experimental measurements and physical and mathematical reasoning. There are a number of turbulence models that range in complexity, which are summarised in this section.

The Reynolds Averaged Navier Stokes (RANS) based turbulence models are most commonly used. They get their name from the Reynolds decomposition of the flow variables into average and fluctuating components and from averaging the governing equations. The RANS equations for flow and heat transfer in a two-dimensional domain are given as

$$\frac{\partial \bar{u}}{\partial x} + \frac{\partial \bar{v}}{\partial y} = 0 \tag{5.24}$$

$$\frac{\partial \bar{u}}{\partial t} + \frac{\partial (\bar{u}\bar{u})}{\partial x} + \frac{\partial (\bar{v}\bar{u})}{\partial y} = -\frac{1}{\rho}\frac{\partial \bar{p}}{\partial x} + \frac{\partial}{\partial x}\left(\nu \frac{\partial \bar{u}}{\partial x}\right) + \frac{\partial}{\partial y}\left(\nu \frac{\partial \bar{u}}{\partial y}\right) + \frac{\partial}{\partial x}\left[\nu \frac{\partial \bar{u}}{\partial x}\right] + \frac{\partial}{\partial y}\left[\nu \frac{\partial \bar{v}}{\partial x}\right] - \left[\frac{\partial (\overline{u'u'})}{\partial x} + \frac{\partial (\overline{u'v'})}{\partial y}\right] \tag{5.25}$$

$$\frac{\partial \bar{v}}{\partial t}+\frac{\partial(\bar{u}\bar{v})}{\partial x}+\frac{\partial(\bar{v}\bar{v})}{\partial y}=-\frac{1}{\rho}\frac{\partial \bar{p}}{\partial y}+\frac{\partial}{\partial x}\left(\nu\frac{\partial \bar{v}}{\partial x}\right)+\frac{\partial}{\partial y}\left(\nu\frac{\partial \bar{v}}{\partial y}\right)+\frac{\partial}{\partial x}\left[\nu\frac{\partial \bar{u}}{\partial y}\right]+\frac{\partial}{\partial y}\left[\nu\frac{\partial \bar{v}}{\partial y}\right]-\left[\frac{\partial(\overline{u'v'})}{\partial x}+\frac{\partial(\overline{v'v'})}{\partial y}\right] \tag{5.26}$$

$$\frac{\partial \overline{T}}{\partial t}+\frac{\partial(\bar{u}\overline{T})}{\partial x}+\frac{\partial(\bar{v}\overline{T})}{\partial y}=\frac{\partial}{\partial x}\left(\frac{k}{\rho C_p}\frac{\partial \overline{T}}{\partial x}\right)+\frac{\partial}{\partial y}\left(\frac{k}{\rho C_p}\frac{\partial \overline{T}}{\partial y}\right)-\left[\frac{\partial \overline{u'T'}}{\partial x}+\frac{\partial \overline{v'T'}}{\partial y}\right] \tag{5.27}$$

where $\bar{u}$, $\bar{v}$, $\bar{p}$, $\overline{T}$ are mean values and $u'$, $v'$, $p'$, $T'$ are turbulence fluctuations. The term $k/\rho\ C_p$ is the thermal diffusivity of the fluid. The equations listed above are similar to those for laminar flows, except for the presence of additional unknown terms of the form $\overline{u'u'}$, $\overline{u'v'}$, and $\overline{v'v'}$. That is, we have three additional unknowns (or six additional unknowns in three dimensions), known as the Reynolds stresses, in the time-averaged momentum equations. Similarly, the time-averaged temperature equation shows the extra terms $\overline{u'T'}$ and $\overline{v'T'}$ (in three dimensions, we also have $\overline{w'T'}$). The earliest and simplest turbulence model was introduced by Boussinesq (known as the *Boussinesq assumption*) who suggested that the Reynolds stresses can be related to the mean rates of deformation similar to the way viscous shear stress is related to the deformation rate. That is,

| Laminar shear stress: | Turbulent shear stress: |
|---|---|
| $\tau=\mu\frac{du}{dy}$. | $\tau_{turb}=-\rho\overline{u'v'}\approx\mu_t\left(\frac{d\bar{u}}{dy}\right)$ |

(5.28)

Equation (5.28) assumes that the turbulent momentum transport is proportional to the mean gradients of velocity. Here $\mu_t$ is the turbulence or eddy viscosity because the turbulence mixing is hypothesised to be the consequence of the motion of turbulence eddies that transport momentum.

Similarly the turbulent transport of temperature is taken to be proportional to the gradient of the mean temperature (the transported quantity). In another words,

$$-\rho\overline{v'T'}=\Gamma_T\frac{\partial \overline{T}}{\partial y} \tag{5.29}$$

where $\Gamma_T$ is the turbulence diffusivity. Since the turbulent transport of momentum and heat is due to the same mechanisms of "eddy mixing", the value of the turbulence heat diffusivity can be taken to be close to that of turbulence (eddy) viscosity $\mu_T$. The corresponding turbulence Prandtl number, $Pr_T$, is defined as

$$Pr_T=\frac{\mu_T}{\Gamma_T} \tag{5.30}$$

Experimental data suggested that this ratio is often nearly constant and around unity. Most CFD models assume this to be the case and use values of $Pr_T$ around unity.

The total shear stress is then is given as

$$\tau = (\mu + \mu_t)\frac{d\bar{u}}{dy} \tag{5.31}$$

It should be emphasized that the eddy viscosity is not a fluid property but rather is a conceptual term that relates the Reynolds stresses to the mean deformation rates (velocity gradients). The eddy viscosity is strongly flow-dependant, and determining its value as a function of flow parameters is the central objective of RANS turbulence models.

### 5.3.3 Additional Equations for the k-ω Turbulence Model

In this section we present a summary of the $k$-$\omega$ turbulence model because it has shown promising results for internal flows in transitional and/or low Reynolds number turbulent flow regimes. In particular, the *k-ω-SST* model has attracted considerable attention for flows with a low level of turbulence (Menter et al. 2006), and has been widely adopted as the turbulence model for respiratory flows (Kleinstreuer and Zhang 2010; Liu et al. 2010a; Shi et al. 2008). This is because of the presence of laminar, transitional, and turbulent flow regimes in the respiratory airways. The family of $k$-$\omega$ models requires solving two additional transport equations for the kinetic energy of turbulence, $k$, and the specific dissipation rate, $\omega$ (Wilcox 1993), and in general is classed as a two-equation model. The model provides accurate predictions for flow separation from smooth surfaces (Bardina et al. 1997). Its variant models, the *k-ω-SST* (Shear Stress Transport $k$-$\omega$ model) as described by Menter (1994) and the LRN-$k$-$\omega$ (Low Reynolds Number $k$-$\omega$ model) and more recently the *k-ω-SST-transistional* model (4 equations) have shown to provide good results for respiratory airway modelling.These model are inherently an LRN model and expands the solution region all the way to the wall, which means that the mesh near the wall needs to be fine to provide accurate results.

To describe the model, some preliminary definitions are required first. The turbulence kinetic energy $k$ and the specific dissipation of turbulence energy $\omega$ (i.e. the dissipation rate per unit of turbulence kinetic energy) can be defined and expressed in Cartesian tensor notation as

$$k = \frac{1}{2}u'_i u'_i \quad \text{and} \quad \omega = \frac{\varepsilon}{k},$$

$$\text{where } \varepsilon = \nu_T \overline{\left(\frac{\partial u'_i}{\partial x_j}\right)\left(\frac{\partial u'_i}{\partial x_j}\right)} \quad \text{and } i,j = 1,2,3$$

The turbulent (eddy) viscosity $\mu_T$ can be evaluated in terms of the local values of $k$ and $\omega$ as

$$\mu_T = \alpha^* \frac{\rho k}{\omega}$$

and the kinematic turbulent or eddy viscosity is denoted by $\nu_T = \mu_T/\rho$. For the standard $k$-$\omega$ model $\alpha^* = 1$; but for its variants, such as the LRN and SST versions, $\alpha^*$ is a variable coefficient that accounts for damping of the eddy viscosity.

By substituting the expressions for Reynolds stress given by Eq. (5.28) and the turbulent heat flux terms in Eq. (5.29) into the governing Eqs (5.24)–(5.27), and for simplicity removing the over bar for the average quantities, we obtain

$$\frac{\partial u}{\partial x} + \frac{\partial v}{\partial y} = 0 \tag{5.32}$$

$$\frac{\partial u}{\partial t} + u\frac{\partial u}{\partial x} + v\frac{\partial u}{\partial y} = -\frac{1}{\rho}\frac{\partial p}{\partial x} + \frac{\partial}{\partial x}\left[(\nu + \nu_T)\frac{\partial u}{\partial x}\right] + \frac{\partial}{\partial y}\left[(\nu + \nu_T)\frac{\partial u}{\partial y}\right] + \frac{\partial}{\partial x}\left[(\nu + \nu_T)\frac{\partial u}{\partial x}\right] + \frac{\partial}{\partial y}\left[(\nu + \nu_T)\frac{\partial v}{\partial x}\right] \tag{5.33}$$

$$\frac{\partial v}{\partial t} + u\frac{\partial v}{\partial x} + v\frac{\partial v}{\partial y} = -\frac{1}{\rho}\frac{\partial p}{\partial y} + \frac{\partial}{\partial x}\left[(\nu + \nu_T)\frac{\partial v}{\partial x}\right] + \frac{\partial}{\partial y}\left[(\nu + \nu_T)\frac{\partial v}{\partial y}\right] + \frac{\partial}{\partial x}\left[(\nu + \nu_T)\frac{\partial u}{\partial y}\right] + \frac{\partial}{\partial y}\left[(\nu + \nu_T)\frac{\partial v}{\partial y}\right] \tag{5.34}$$

$$\frac{\partial T}{\partial t} + u\frac{\partial T}{\partial x} + v\frac{\partial T}{\partial y} = \frac{\partial}{\partial x}\left[\left(\frac{\nu}{\mathrm{Pr}} + \frac{\nu_T}{\mathrm{Pr}_T}\right)\frac{\partial T}{\partial x}\right] + \frac{\partial}{\partial y}\left[\left(\frac{\nu}{\mathrm{Pr}} + \frac{\nu_T}{\mathrm{Pr}_T}\right)\frac{\partial T}{\partial y}\right] \tag{5.35}$$

The term $\nu/Pr$ appearing in the temperature Eq. (5.35) is obtained from the definition of the laminar Prandtl number, $Pr = \nu/\alpha$, where $\alpha = k/\rho\ C_p$. Interestingly, the time-averaged equations above have the same form as those developed for the laminar equations except for the additional turbulent (eddy) viscosity found in the diffusion terms for the momentum and the energy equations. Hence, the solution to turbulent flow in engineering problems entails greater diffusion that is imposed by the turbulent nature of the fluid flow. The additional differential transport equations that are required for the standard $k$-$\omega$ model, for the case of a constant fluid property, are the following:

$$\frac{\partial k}{\partial t} + u\frac{\partial k}{\partial x} + v\frac{\partial k}{\partial y} = \frac{\partial}{\partial x}\left[(\nu + \sigma_k \nu_T)\frac{\partial k}{\partial x}\right] + \frac{\partial}{\partial y}\left[(\nu + \sigma_k \nu_T)\frac{\partial k}{\partial y}\right] + P_k - D_k \tag{5.36}$$

$$\frac{\partial \omega}{\partial t} + u\frac{\partial \omega}{\partial x} + v\frac{\partial \omega}{\partial y} = \frac{\partial}{\partial x}\left[\nu + \sigma_\omega \nu_T)\frac{\partial \omega}{\partial x}\right] + \frac{\partial}{\partial y}\left[(\nu + \sigma_\omega \nu_T)\frac{\partial \omega}{\partial y}\right] + P_\omega - D_\omega \tag{5.37}$$

The terms $P_k$ and $D_k$ represent the production and destruction/dissipation of $k$ and similarly $P\omega$ and $D\omega$ are the production and destruction/dissipation of $\omega$. The terms $\sigma_k$ and $\sigma_\omega$ are, respectively, the turbulent Prandtl numbers for $k$ and $\omega$. Eqs (5.35) and

(5.36) form the statement: *The rate of change and the convective transport of k or ω equal the diffusion transport combined with the rate of production and destruction of k or ω*. Improvements to the standard *k-ω* model have been made by Menter (1994) who created the *k-ω-SST* model. The improved model uses the original *k-ω* by Wilcox (1993) in the inner region of the boundary layer but then switches to the standard *k-ε* model in the outer region. This modification improves the prediction of the flow with adverse pressure gradients ($\partial p/\partial x > 0$) where flow separation tends to occur. This is common in the laryngeal region (Fig. 5.6). It is important to note that the use of the *k-ω* model in the inner region of the boundary layer means that the model directly resolves the flow behaviour all the way down to the wall. This means that a very fine mesh is needed in the vicinity of the wall (see later Sect. 5.3.5). Some disadvantages of the model include its overprediction of *k* in regions of accelerating and stagnating flows.

### 5.3.4 Other Turbulence Models

*k-ε Models* One of the most widely used turbulence models in a wide range of engineering applications is the *k-ε model*. The model is also classed as a two-equation model as it has two additional transport equations, solving for the turbulence kinetic energy *k* and the turbulence dissipation rate *ε*. The eddy viscosity is then given by

$$\mu_t = C_\mu \rho \frac{k^2}{\varepsilon} \tag{5.38}$$

where $C_\mu$ is a model constant. The standard *k-ε* model was derived empirically mainly for fully turbulent flows. It can be used with the so-called wall function boundary conditions that connect the core turbulent flows to the wall and therefore obviate the need for a fine mesh close to the wall. The model's performance has been assessed against a number of practical flows. It has achieved notable successes in predicting thin shear layers, boundary layers and duct flows without the need for case-by-case adjustment of the model constants. It has also been shown to perform quite well when the Reynolds shear stresses are dominant in confined flows. This accommodates a wide range of flows with industrial applications, which explains the model's popularity among CFD users. Sometimes the *k-ε* model is used as an initial run to establish a turbulent flow field before embarking on more complex models. Some variations of the *k-ε* model that are commonly found in commercial CFD codes include the Low-Reynolds-Number (LRN), Realizable, and the ReNormalisation Group (RNG) *k-ε* models. The LRN[1] model allows full resolution of the near-wall boundary layer but requires a fine mesh. Both the Realizable and RNG models improve to an extent the performance of the standard model by better predicting flows involving moderate swirl, vortices, and locally transitional flows.

[1] It should be noted that the term LRN does not refer to the bulk flow Reynolds number, but rather the turbulent Reynolds number, which is low in the viscous sublayer (see Sect. 5.3.5 for *viscous sublayer* description). In fact the LRN models can be applied for a fluid flow that has a high flow Reynolds number.

*Weaknesses of k-ε, k-ω and Other Two-Equation Models* Some common issues encountered with most two-equation models include its inability to predict weak shear layers—far-wake and mixing-layer unconfined separated flows. Also, for the case of the axisymmetric jets in stagnant surroundings, the spreading rate is overpredicted where, in major parts of these flows, the rate of production of the turbulent kinetic energy is much less than the rate of dissipation. The difficulties can, however, be overcome by making *ad hoc* adjustments to the model constants thereby reducing the model's generality and robustness. Numerous problems are also experienced with the model in predicting swirling flows and flows with large, rapid, extra strains (for example, highly curved boundary layers and diverging passages) since the model is unable to fully describe the effects of the streamline curvature on turbulence.

*RSM Models (Reynolds Stress Model)* The $k$-$\omega$ and the $k$-$\varepsilon$ models described above are in the class of so-called two-equation models that use two additional transport equations. These models all assume that the eddy viscosity is isotropic and leads to mean square velocity fluctuations which are the same in different directions (i.e. $\overline{u'^2} = \overline{v'^2} = \overline{w'^2}$). This implies that the two-equation model fails to capture accurate details of anisotropic features of turbulent flows. This is particularly an issue for predicting the flows, such as swirling flows and flows with strong curvatures that are highly anisotropic. The RSM models use an additional five transport equations in 2D flows and seven transport equations in 3D flows to solve explicitly for each component of the Reynolds stresses to account for the anisotropy. This model is superior to the other RANS models in that it avoids the isotropic eddy viscosity assumption; however, it requires more computational time and memory and can be difficult to converge due to the close coupling of the additional equations.

**LES and DNS Modelling** Large Eddy Simulation (LES) has attracted considerable attention in recent years. With the Reynolds (statistical) averaging, all fluctuations are averaged and the physics of the transient large-scale structure of turbulent fluctuation is lost. In the LES, a filtering function is applied to the governing equations whereby large turbulence structures, in the form of eddies/vortices, are resolved and computed directly (i.e. with no modelling), while smaller eddies are modelled. From the classical Kolmogrorov theory of turbulence, it is known that the large scales depend strongly on the nature of the turbulent flow and boundary conditions; while the small scale turbulence is nearly homogenous and isotropic and also independent of the large scale flow. Thus it is easier to model the small scale but simulate the large scale turbulent fluctuating motions. LES is time-dependent and has to be performed in 3D. Typically, LES uses the mesh size as the filtering scale. This places a high demand on computational resources, since the mesh and time step sizes need to be sufficiently fine to resolve down to the small scales of turbulence. The computational resource requirement becomes increasingly severe for near wall regions where the scales are smaller than those in the bulk flow region. LES is clearly more advanced approach compared to RANS-based models and can handle transitional flows. The LES has the ability to capture the turbulence coherent structures, and large scale turbulent fluctuation, while modelling the small subgrid scale fluctuations.

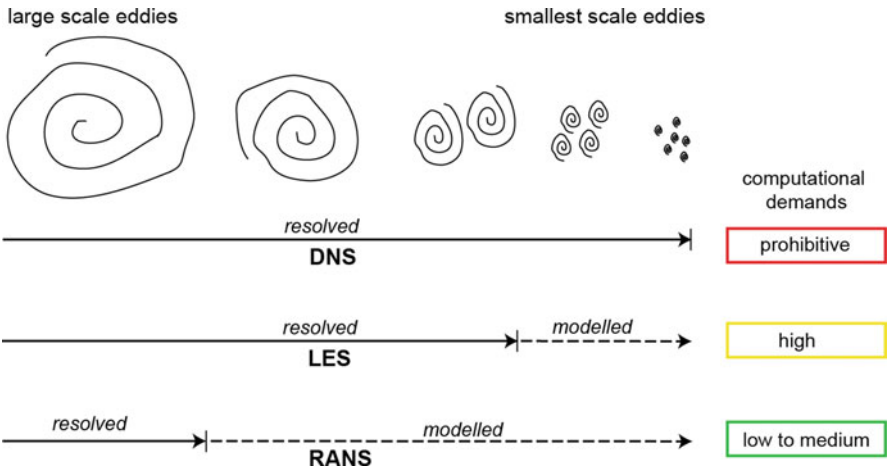


**Fig. 5.14** Comparison of turbulence models and the amount of flow physics that is resolved or modelled

Direct Numerical Solution (DNS) is the most accurate computational approach for simulating turbulent flows. In fact, DNS does not require modelling; rather it directly solves the governing Navier-Stokes equations using sufficiently refined mesh and time steps to capture all relevant scales of turbulence. DNS, however, requires enormous computational resources, particularly for flows in complex domains. For example, a typical turbulent flow in a duct having a cross-sectional area of 0.1 m by 0.1 m at a Reynolds number of about $10^5$ will contain eddies as small as 10 or 100 µm in size. This means that to resolve the flow at all length scales, a computational mesh of $10^9 - 10^{12}$ grid points are needed. Furthermore, the fastest events that can take place have a frequency of the order of 10 kHz, which would require a time step of about 100 µs. With the available computational resources, at the present time and in the near future, the DNS of turbulent flows for practical applications at high Reynolds numbers is not feasible. Only low to moderate Reynolds numbers in simple geometries can be handled with the fastest computers today. This means that for practical engineering applications, DNS is an unrealistic approach. Furthermore, in many engineering applications the detailed knowledge of the smallest eddies of turbulence is not needed, and the LES or RANS is more than adequate. Figure 5.14 shows a comparison of the different modelling approaches in terms of how much of the flow is modelled or resolved, and the required computational demand for each approach.

**Turbulence Modelling in Respiratory Applications** Airflow in the respiratory airways may exhibit laminar, transitional, or turbulent flow characteristics due to the variations in the airway geometry and dimensions. In the nasal cavity, the precise estimate of the local Reynolds number is difficult because of the complex nature of the geometry. Even with a Reynolds number that indicates the flow is dominated by the viscous forces, and hence should be in laminar flow regime, some nasal cavity

models exhibit turbulence characteristics such as formation of eddies, cross-currents, and mixing (Churchill et al. 2004). Further downstream, the flow becomes turbulent in the laryngeal region before becoming laminar deep in the bronchial airway tree.

In order to capture as much of the flow physics in the different flow regimes but still use accessible computing resources, a suitable LRN turbulence model may be used. This may be achieved through RANS-based models such as the LRN-$k$-$\varepsilon$ and LRN-$k$-$\omega$ models. However, it has been suggested that the LRN k-$\varepsilon$ model fails to simulate the transition to turbulent flow while the $k$-$\omega$ showed better ability in reproducing the behaviour of all flow regimes in the airways (Zhang and Kleinstreuer 2003). The LES model is also capable in capturing all flow regimes; however, the mesh requirements and temporal resolution must be sufficiently refined to capture the relevant turbulent flow features, and therefore this model is computationally restrictive. It is anticipated that future trends in the choice of turbulence models will slowly shift from RANS to LES or a hybrid RANS-LES model (such as the Detached Eddy Simulation model), as computational power increases and access to such resources become more widely available. The main drawback of RANS models is in the requirement to decompose the flow into a mean and fluctuating component that contains large and small scale turbulence. Thus, a RANS model cannot capture the large scale transient structure of turbulence that may be needed for many research applications. The DNS approach for respiratory flows remains out of reach at the present time due the rather complex shape of the airway passages.

### *5.3.5 Near-Wall Modelling*

Airflow through the respiratory passages is confined by the surrounding walls and can be broadly classified as internal flows or wall bounded flows. In terms of fluid dynamics, the near-wall regions are primary sources of vorticity and turbulence as they are the regions with a sharp velocity gradient where the moving fluid rapidly decreases to a velocity of zero at the wall surface. In describing the near-wall velocity profile, dimensionless variables with respect to the local conditions at the wall are typically used. If we let $y$ be the normal distance from the wall and $u$ be the time-averaged velocity parallel to the wall, then the dimensionless velocity $u^+$ and wall distance $y^+$ can be appropriately described in the form as $u^+ = u/u_\tau$ and $y^+ = yu_\tau/\upsilon$, respectively. Within these dimensionless parameters, the wall friction (shear) velocity $u_\tau$ is related to the wall shear stress $\tau_w$ as $u_\tau = \sqrt{\tau_w/\rho}$.

The velocity profiles in Fig. 5.12 show a thinner profile for turbulent flows, which consist of three regions based on the distance from the wall. The layer closest to the wall is the *viscous sublayer* which is very thin and is dominated by molecular viscosity (i.e. viscous laminar-like profile and negligible turbulence effects). In this region viscous damping reduces the tangential velocity fluctuations, leading to turbulent dissipation. Its profile is nearly linear and can be described by the equation known as the *law of the wall*:

$$u^+ = y^+ \qquad \text{for } y^+ < 5.$$

Rearranging the equation for $y^+ = 5$, the thickness of the viscous sublayer $y$ is

$$5 = yu_\tau/\nu, \quad 5 = u^+ = \frac{u_\delta}{u_\tau} \rightarrow y = \frac{5\nu}{u_\tau} = \frac{25\nu}{u_\delta} \tag{5.39}$$

where $u_\delta$ is the flow velocity at the edge of the viscous sublayer. This shows an inverse relationship between the thickness of the viscous sublayer and the mean flow velocity while the thickness is directly proportional to the kinematic viscosity. This means at higher velocities (and therefore a higher Reynolds number) a thinner viscous sublayer will be produced. This is an important consideration when dealing with the near-wall mesh requirement to resolve this flow feature. Furthermore, the presence of a mucous layer creates a non-smooth surface, and since CFD modelling of the respiratory airways normally treats the walls as a smooth surface, this should be kept in mind.

The outer flow is the turbulent core where turbulence effects dominate over molecular viscous effects. Closer to the wall where the viscous effects are still negligible, but wall effects becomes important, we reach to the *transition sublayer* ($5 < y^+ < 30$). In this region both turbulence and viscous effects are equally important. Furthermore the production of turbulence kinetic energy reaches its peak value due to large gradients in the mean velocity field and the presence of finite turbulence shear stress. Thereafter there is the *logarithmic sublayer* ($30 < y^+ < 300 \sim 400$). In this region, the flow is characterized by one velocity scale (shear velocity) and one length scale (distance from the wall), and the mean flow velocity has a logarithm profile that can be expressed as

$$u^+ = 2.5 \ln (y^+) + 5.45 \qquad for\ 30 < y^+ < 400 \tag{5.40}$$

Figure 5.15 shows the different regions of the mean turbulent velocity profile near a wall. The logarithmic profile approximates the velocity distribution well and provides a method to compute the wall shear stress.

Resolving the near-wall region in turbulent flows is important for many applications such as particle deposition in airway passages and for estimating the pressure drop that depends on the local wall shear stress. In addition, most turbulence models such as the $k$-$\varepsilon$ are only valid in the turbulent core region and the log layer, which means that they cannot be applied down to the wall. Two approaches are generally used to model the flow in the near wall region.

The first is to use a low Reynolds number (LRN) turbulence model which resolves the wall region with very small mesh elements in the direction normal to the wall. These elements are typically stretched hexahedron mesh elements in 3D or quad elements in 2D and referred to as prism layers or inflation layers (Fig. 5.16). The LRN turbulence model equations based on the dimensionless wall distance $y^+$ resolve the velocity profile through the viscous sublayer and all the way down to the wall. The computational demands are greater for the LRN models because of the increased number of mesh elements needed to provide the resolution in the near wall region to capture the sharp variations in the velocity profile.

The second approach is to use *wall functions* which are specialized empirical correlations that serve as boundary conditions to connect the flow properties at the wall

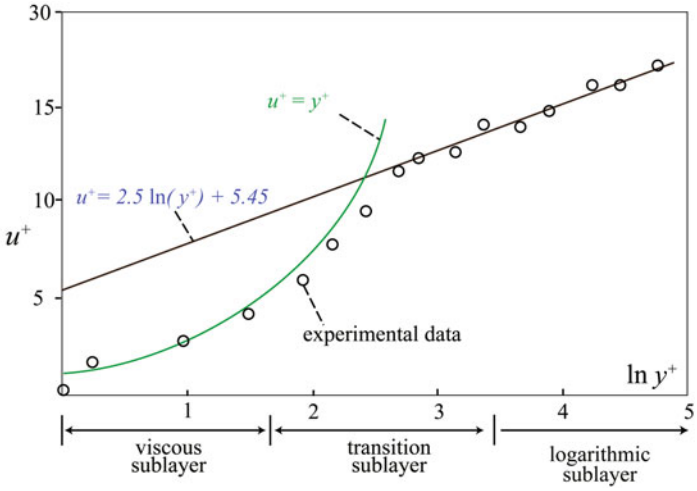


**Fig. 5.15** Sublayers within a turbulent velocity boundary layer. *Viscous sublayer* occurs at $y^+ < 5$. *Transition layer* occurs between $5 < y^+ < 30$ where turbulence production is maximum. *Log layer* is between $30 < y^+ < 400$. There is a law of the wake (not shown on graph) which occurs for $y^+ > 400$

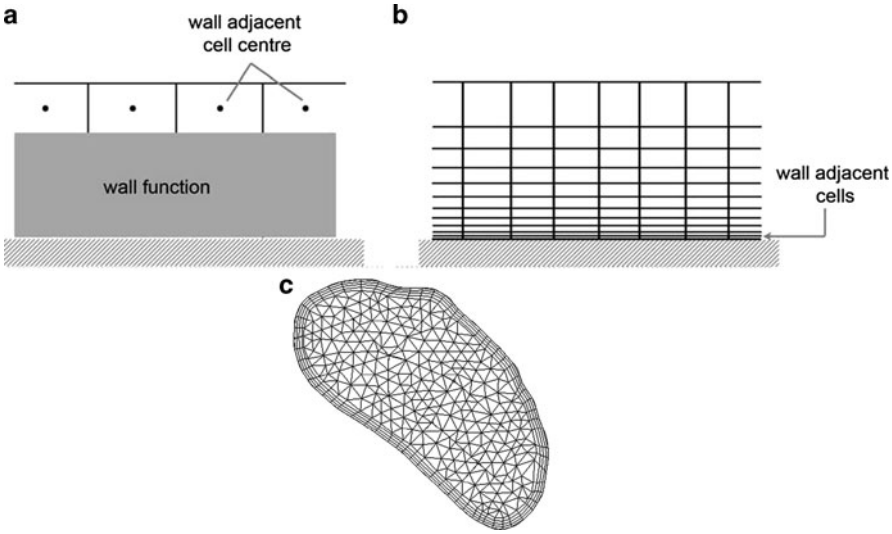


**Fig. 5.16** **a** Wall function approach where the near-wall region is modelled by a wall function. **b** LRN approach using a fine near-wall mesh to capture the sharp changes in the flow parameters. **c** An example of a hybrid mesh of the nostril inlet using inflation/prism layers for the LRN approach

adjacent cells to corresponding quantities at the wall. This relaxes the requirement of a very fine mesh in the near-wall region, and leads to significant reduction in computational resources, especially for high Reynolds number flows where the turbulent boundary layer becomes very thin. There are a wide range of wall functions and its implementation needs to concur with the near-wall mesh. For example some wall

functions will model up to the viscous sublayer ($y^+ < 5$) while others will model up to the log layer ($y^+ > 30$), which means that the wall-adjacent cells must exist in the correct sublayer by determining its $y^+$ value. The wall function loses its accuracy for certain cases such as flows with severe adverse pressure gradients, strong body forces and rapidly changing fluid properties near the wall. For these cases the LRN approach with a fine near-wall mesh needs to be used.

### 5.3.6 *Turbulence Modelling Approach*

**Defining the Problem** The task of resolving a turbulent flow through the selection of a turbulence model, a compliant mesh, and additional boundary conditions has many options and can appear daunting to a new CFD user. This section aims to provide an overview of some techniques and approaches to complete this task. The first step is to determine the required level of complexity of the CFD model in relation to the available resources. Figure 5.17 summarises the questions that need to be addressed to help define the problem. Initially the physical problem can be estimated by the amount of flow physics that need to be captured (e.g. is the flow indeed turbulent?), and the level of accuracy required. Then one must decide on the modelling requirements which involve selecting the appropriate turbulence model and should be based on the established results and best practices for the same class of problems. This leads to the appropriate mesh generation where there is a direct correlation between the mesh size, the amount of flow physics needed, and the complexity of the selected turbulence model. Finally, the computational resources and time required by these choices must be available for the given problem.

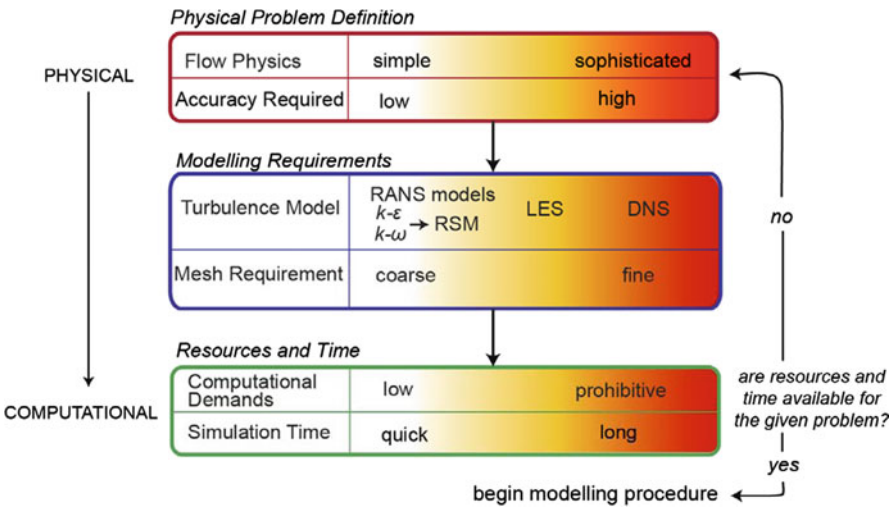


**Fig. 5.17** Turbulent modelling considerations

**Selecting a Turbulence Model** The selection of an appropriate turbulence model will be determined by the level of accuracy required and the available time and

computational resources. In CFD, different types of turbulent flows require use of different turbulence models. For first time users and in the event that insufficient knowledge precludes the selection of more advanced models, we strongly encourage the use of the two-equation model such as the *standard k-ε model* as a starting point for turbulent flow analysis. This model offers the simplest level of closure since it has no dependence on the geometry or flow regime input. As a first step to turbulence model selection, the *standard k-ε model* is robust, stable, and as good as other more sophisticated turbulence models in some applications. In fact, it is often used as a base model to establish a turbulent flow field before applying other turbulence models that may experience convergence problems. Nevertheless, the *standard k-ε model* is not without any weaknesses, as mentioned earlier, and alternative models are needed.

Respiratory flows are of internal wall bounded type flows that produce wall attached boundary layers. Turbulent fluctuations are suppressed adjacent to the wall due to the viscous effects becoming prominent in this region particularly in the *viscous sublayer*. This turbulent flow structure generally precludes the application of the two-equation models, such as *standard k-ε model*, *RNG k-εmodel* and *realizable k-ε model* or even the *Reynolds Stress Model,* in the near-wall region, which thereby requires special near-wall modelling procedures. Selecting an appropriate near-wall model represents another important strategy in the context of turbulence modelling. Here, the user has to decide whether to adopt the so-called wall-function method, in which the near-wall region is bridged with wall functions, or a low Reynolds number model, in which the flow structure in the *viscous sublayer* is fully resolved. This decision will certainly depend on the availability of computational resources and the accuracy requirements for resolution of the boundary layer. In addition respiratory flows exhibit a spectrum of flow regimes from laminar, to transitional, to fully turbulent flow, and the choice of turbulence model to account for as much physics as possible against the available computational resources must be decided upon by the user.

With increased computational resources, it is becoming possible to handle the very small time steps, and a fine mesh particularly in the near-wall region for the use of the more sophisticated LES model. Although the LES provides more detail of the flow physics, it requires a high level of expertise. For example, the smallest mesh size element must be calculated based on the smallest eddy to be resolved directly, while eddies smaller than the grid are modelled. Furthermore since the model is an unsteady simulation, analysis of the instantaneous flow is required; and the user needs to have a comprehensive knowledge of turbulence, instability theory and turbulent structures. The choice of mesh elements (either tetrahedral, or hexahedral) will have a significant influence on the flow behaviour and needs to be carefully designed to avoid *false diffusion*. Finally, the inlet boundary conditions are not known a priori, and they require a careful setup since the properties of the upstream flow will have a significant effect on the development downstream. Typically a stochastic method to initiate some perturbations at the inlet is used to prescribe the mean velocity profile with a fluctuating component in order to define the correct level of turbulence at the inflow boundaries.

Whichever model is chosen, the user needs to take on the necessary task of carrying out careful *validation* and *verification* to ensure confidence in the solution in order to fully justify the application of the turbulence model chosen to solve the particular problem. For more strategies on turbulence modelling and simulations, the reader is encouraged to refer to the work of Nallasamy (1987), Spalart (2000), and Wilcox (1993).

**Creating the Mesh** After determining the feasibility of converting a physical model into a CFD model, the modelling procedure can begin. This involves the construction of a suitable mesh that will increase the likelihood of attaining a converged and stable solution. Mesh construction involves the subdivision of the computational domain into a number of smaller mesh or grid cells overlaying the entire domain geometry. For internal turbulent flows and any non-moving surfaces, proper resolution of the boundary layer is imperative. Wall functions can be used to relieve the high computational demands, where the particular physics related to the boundary layer is not as important as the flow field far away from the boundary walls. There are many wall functions each of which can model up to different sublayers of the boundary layer.

The use of wall functions is to relate flow variables within the sublayers up to the first computational mesh point, thereby removing the requirement to resolve the actual structures in between the boundary wall and the $y^+$ of the first nodal point. This point must be carefully placed so that it does not fall into the region actually being modelled. As an example, let us consider a wall function that models up to the transtional sublayer (i.e. this includes the viscous sublayer). The mesh should then be arranged so that the values of $y^+$ at all the wall-adjacent integration points are considered around the sublayer limit of $y^+ = 30$. It should be noted that, for non-uniform geometries, there will be inevitable variations of $y^+$ across the wall surface due to the different flow conditions. This means that besides checking the lower limit of $y^+$, it is also important to ensure that the upper limit of $y^+$ is not too far from the sublayer limit (e.g. $y^+ >> 30$).

Let us also assume that the boundary layer extends up to $y^+$ between 300 and 500. If the first integration point is placed at a value of $y^+ = 100$, then this will certainly yield an inadequate solution due to insufficient resolution for the region. Adequate boundary layer resolution generally requires at least ten nodal points in the layer, and it is recommended that a post-analysis of the CFD solution be undertaken by measuring the $y^+$ plus values across the surface walls to determine whether the degree of resolution is achieved.

Wall functions may not be applicable in all cases, as discussed earlier; in this case, the LRN turbulence model approach is used. This involves resolving the flow through to the wall, requiring a higher demand on computational resources to produce the near-wall mesh. Typically the mesh is of an order of magnitude greater than when wall functions are used. In order to resolve the viscous sublayer inside the turbulent boundary layer, $y^+$ at the first node adjacent to the wall should be set to as close to 1 as possible. Nevertheless, a higher $y^+$ is acceptable so long as it is still well within the viscous sublayer ($y^+ < 5$). Depending on the Reynolds number and in order to properly resolve the mean velocity and turbulent quantities, the user should ensure

that there are between five and ten grid nodal points between the wall and the location where $y^+$ equals to 20, which is within the viscosity-affected near-wall region. This most likely will result in about 30 grid nodal points inside the viscous and transition layer to achieve adequate resolution.

**Boundary Conditions and Settings** Specifying appropriate boundary conditions is particularly important in turbulence modelling. Depending on the type of boundary imposed, different information is needed to specify the boundary conditions. For turbulent flows, specification of the turbulence quantities (e.g. turbulent kinetic energy $k$ and dissipation rate $\varepsilon$) at the inlet can be difficult mainly because they are usually evaluated from the flow field. Experimentally verified quantities should always be applied as inlet boundary conditions for $k$ and $\varepsilon$ when available. In many cases turbulent data at the inlet and outlets are unavailable, and their values have to be prescribed using reasonable engineering assumptions. The selection of values then must be examined against sensitivity tests with different simulations to determine the influence of the settings. For the specification of the turbulent kinetic energy $k$, appropriate values can be specified through a turbulence intensity $I$ that is defined by the ratio of the fluctuating component of the velocity to the mean velocity. In general, the inlet turbulence condition is a function of the upstream flow conditions. Approximate values for $k$ can be determined according to

$$k_{inlet} = \frac{3}{2}(u_{inlet} I)^2 \tag{5.41}$$

where $I$ is the turbulence intensity defined in Eq (5.22). For internal flows, a turbulence level between 3 and 10 % is deemed to be appropriate, although lower Reynolds number flows will have a smaller intensity value. The inlet dissipation rate $\varepsilon$ can be approximated by

$$\varepsilon_{inlet} = C_\mu^{3/4} \frac{{k_{inlet}}^{3/2}}{C_\mu^{1/4} D} \tag{4.52}$$

where $D$ is the characteristic length scale, typically the hydraulic diameter for internal flows. If the $k$-$\omega$ model is employed, $\omega$ at the inlet can be approximated as

$$\omega_{inlet} = \frac{{k_{inlet}}^{1/2}}{C_\mu^{1/4} D} \tag{5.42}$$

If the Reynolds stress model is being used, each stress component is required to be properly specified. If these are unavailable, as often is the case, the diagonal components $\overline{u'^2}$, $\overline{v'^2}$ and $\overline{w'^2}$ are taken to be equal to $2/3k$, and the extra-diagonal components $\overline{u'v'}$, $\overline{u'w'}$, and $\overline{v'w'}$ are set to zero (which assumes isotropic turbulence). In cases where problems arise in specifying appropriate turbulence quantities, the inflow boundary should be moved sufficiently far away from the region of interest so that the turbulence is allowed to be developed naturally.

At the walls, boundary conditions for $k$ and $\varepsilon$ or $\omega$ are also applied, and these are typically built into the turbulence model itself or within the wall functions. At the outlet or symmetry boundaries, the symmetry conditions are used. That is

$$\frac{\partial k}{\partial n} = 0 \quad \text{and} \quad \frac{\partial \varepsilon}{\partial n} = 0$$

which states that the derivative of $k$ and $\varepsilon$ normal to the flow is zero.

### *5.3.7 Laminar and Turbulent Flow Examples*

Consider the flow in a straight pipe to demonstrate the laminar and turbulent nature of a fluid flow. Using CFD with the dimensions of diameter $D = 0.02$ m and length $L = 0.15$ m of the pipe, we will evaluate the mean velocity and eddy viscosity profiles in the fully developed region with the working fluid taken as air (density $\rho = 10\,\text{kg/m}^3$ and dynamic viscosity $\mu = 2 \times 10^{-5}$ kg/m · s) for inlet velocities of $u_{in1} = 0.02$ m/s and $u_{in2} = 1$ m/s. The problem schematics are shown in Fig. 5.18.

For an inlet velocity of $u_{in1} = 0.02$ m/s, the Reynolds number for the flow is 200, and the flow is laminar. However, for an inlet velocity of $u_{in2} = 1$ m/s, the Reynolds number is 10,000, which is well above the critical Reynolds number of 2,200; and hence the flow is in turbulent regime. The simulation results are shown in Fig. 5.19. It is seen that there is a significant difference in the velocity profiles in the laminar and turbulent flow regimes. In the fully developed region, the velocity profile for laminar flow is parabolic but the velocity profile for turbulent flow has a flat profile in the centre and core region of the channel with a steep velocity gradient near the walls. That is the high level of turbulent viscosity diffuses the momentum across the flow (as discussed earlier, Fig. 5.12).

The molecular viscosity and the computed eddy viscosity corresponding to the same location of the velocity profiles are compared in Fig. 5.20. It is seen that the eddy viscosity varies significantly across the duct and reaches its peak value at the centre. Furthermore, the turbulent (eddy) viscosity is significantly higher by order of magnitudes compared to the molecular viscosity at the centre of the channel. The molecular viscosity which is a constant becomes larger than the eddy viscosity only in the very thin region near the wall.

To further illustrate the physical characteristics of the turbulence and eddy viscosity, the profiles of the turbulence kinetic energy $k$ and the specific dissipation $\omega$ across the pipe at the same location of the velocity profiles are plotted in Figs. 5.20 and 5.21. The results show that both $k$ and $\omega$ have peaks near the walls but with different profiles. Right at the wall, $k$ is zero while $\omega$ is at its maximum. This suggests that turbulence generated in the near-wall region, and in fact the peak production, is in the transition region and is also dissipated primarily due to the viscous effects within the viscous sublayer as well as in the transition layer region. Away from the wall, $\omega$

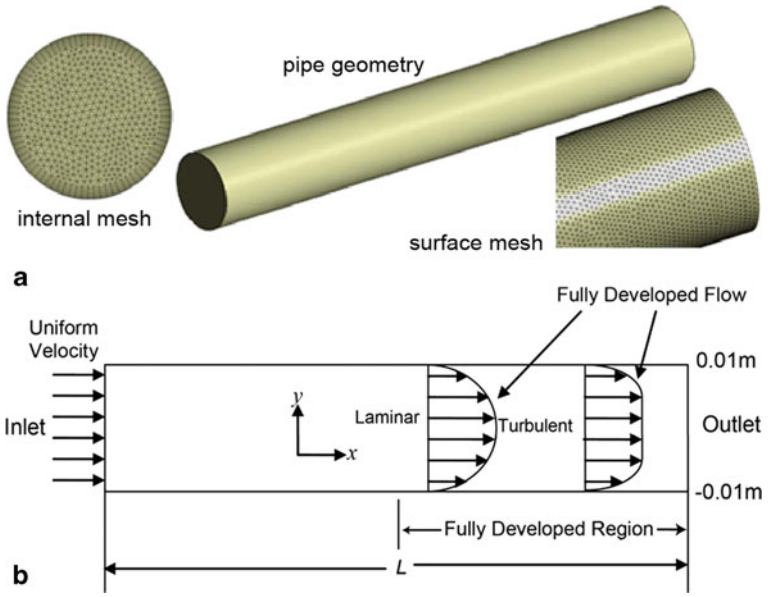


**Fig. 5.18** **a** Pipe geometry showing the surface and internal mesh. **b** Schematic of a laminar and turbulent flow in a pipe flow

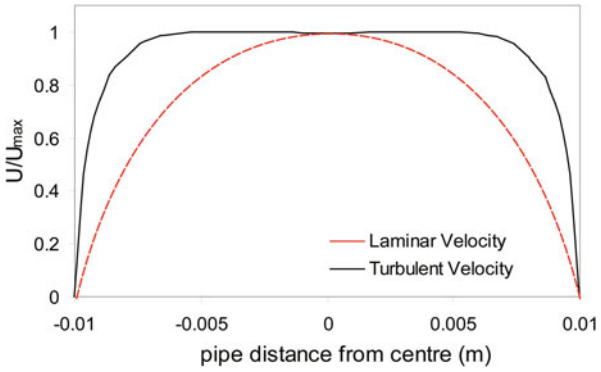


**Fig. 5.19** Laminar and turbulent velocity profiles in the fully developed region

becomes very small, while although $k$ is also reduced it is not as small leading to a larger value of turbulence viscosity (Fig. 5.22).

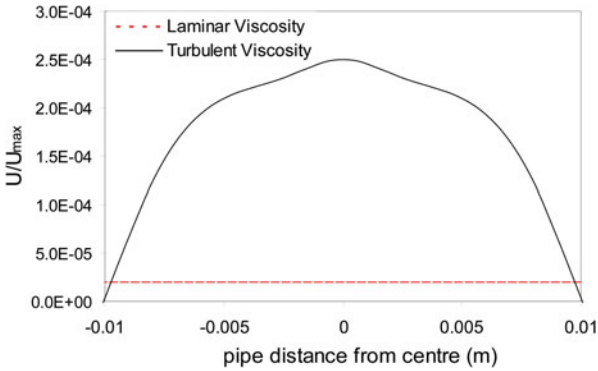


**Fig. 5.20** Laminar and turbulent viscosities in the fully developed region

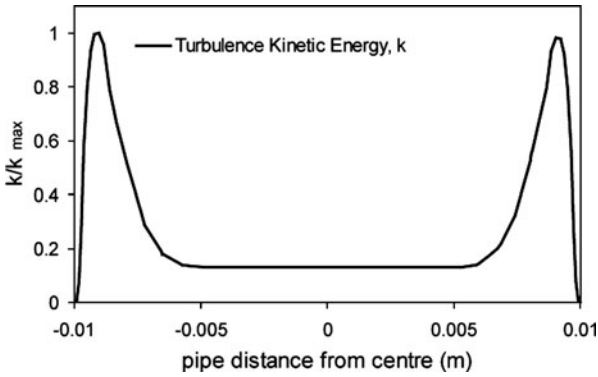


**Fig. 5.21** Kinetic energy $k$ profile for the turbulent flow in the fully developed region

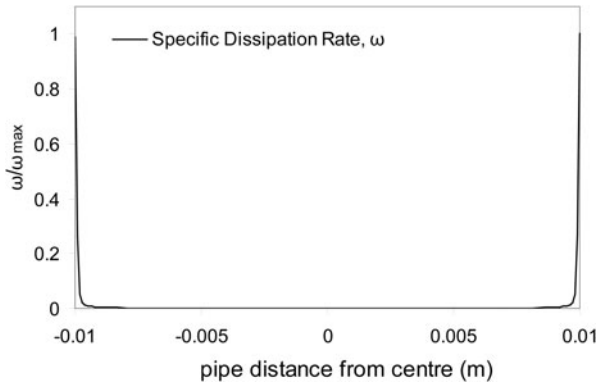


**Fig. 5.22** Dissipation rate $\varepsilon$ profile for the turbulent flow in the fully developed region

Some further issues commonly arise when dealing with turbulence modelling:

- *What happens if a turbulence model is used for a laminar or transitional flow?*
- *What flow regime should be chosen for a Re number in the transitional regime?*

The use of a turbulence model to represent a flow field that is not fully turbulent must be applied with caution. In the case where the flow field is laminar, the application of a turbulence model will include an additional turbulent viscosity $\mu_t$ term. This leads to the flow field experiencing a greater effective viscosity that comprises the fluid viscosity plus the turbulent viscosity, $\mu_{eff} = \mu_{lam} + \mu_t$ instead of $\mu_{lam}$ for a laminar flow. The increased level of viscosity that also is increasing with distance from the wall will enhance the diffusion of the fluid properties and tend to make the velocity profile in a pipe more flat in comparison with a laminar flow which exhibits a parabolic profile.

Reynolds Averaged Navier-Stokes (RANS) turbulence models such as $k$-$e$, $k$-$\omega$ and RSM were developed based on fully developed turbulent flows (Re > 2,200, for pipe flows), although modifications have been made to formulate low-Reynolds number models that reproduce the transitional behaviour. However, in these models the physics of transitional flow behaviour is not actually resolved but rather a modelled approach is applied. Therefore, caution should be exercised when analysing the results since in local regions of low flow rates, where laminar effects are dominant, the turbulence models provide greater diffusion due to their inherent eddy viscosity. The low-Reynolds number turbulence models such as low-Reynolds $k$-$\varepsilon$ and $k$-$\omega$ have shown to provide improvements over the standard RANS models. Sophisticated models such as LES and Direct Numerical Simulations, however, do resolve the transitional behaviour but are computationally expensive.

## 5.4 Generic Form of Governing Equations

The governing equations derived earlier in Sect. 5.2 is summarised in 3D in Table 5.1.

These governing equations show that they have the same generic form. If we introduce a general variable $\vartheta$ and express all the fluid flow equations, the equation can usually be written in the conservative *incompressible* form:

$$\frac{\partial \phi}{\partial t} + \frac{\partial (u\phi)}{\partial x} + \frac{\partial (v\phi)}{\partial y} + \frac{\partial (w\phi)}{\partial z} = \frac{\partial}{\partial x}\left[\Gamma \frac{\partial \phi}{\partial x}\right] + \frac{\partial}{\partial y}\left[\Gamma \frac{\partial \phi}{\partial y}\right] + \frac{\partial}{\partial z}\left[\Gamma \frac{\partial \phi}{\partial z}\right] + S_\phi \tag{5.43}$$

Equation (5.44) is the so-called **transport equation** for the property $\phi$ which, as its name suggests, represents the various physical transport processes occurring in the fluid for a given flow variable. It is otherwise referred to as the scalar transport of $\phi$, where $\phi = (u, v, w, T, k, \omega$ etc.). The transport equation includes the *local acceleration* and *convection* terms on the left-hand side which is respectively equivalent to the *diffusion* term ($\Gamma$ = diffusion coefficient) and the *source* term ($S_\phi$) on the right-hand side. In order to bring forth the common features, we have, of course, combined the

**Table 5.1** Governing equations for incompressible flow in Cartesian coordinates

*Mass conservation*

$$\frac{\partial u}{\partial x}+\frac{\partial v}{\partial y}+\frac{\partial w}{\partial z}=0$$

*u-momentum*

$$\frac{\partial u}{\partial t}+\frac{\partial (uu)}{\partial x}+\frac{\partial (vu)}{\partial y}+\frac{\partial (wu)}{\partial z}=-\frac{1}{\rho}\frac{\partial p}{\partial x}+\frac{\partial}{\partial x}\left[(\nu+\nu_T)\frac{\partial u}{\partial x}\right]+\frac{\partial}{\partial y}\left[(\nu+\nu_T)\frac{\partial u}{\partial y}\right]+\frac{\partial}{\partial z}\left[(\nu+\nu_T)\frac{\partial u}{\partial z}\right]+S_u$$

*v-momentum*

$$\frac{\partial v}{\partial t}+\frac{\partial (uv)}{\partial x}+\frac{\partial (vv)}{\partial y}+\frac{\partial (wv)}{\partial z}=-\frac{1}{\rho}\frac{\partial p}{\partial y}+\frac{\partial}{\partial x}\left[(\nu+\nu_T)\frac{\partial v}{\partial x}\right]+\frac{\partial}{\partial y}\left[(\nu+\nu_T)\frac{\partial v}{\partial y}\right]+\frac{\partial}{\partial z}\left[(\nu+\nu_T)\frac{\partial v}{\partial z}\right]+S_v$$

*w-momentum*

$$\frac{\partial w}{\partial t}+\frac{\partial (uw)}{\partial x}+\frac{\partial (vw)}{\partial y}+\frac{\partial (ww)}{\partial z}=-\frac{1}{\rho}\frac{\partial p}{\partial z}+\frac{\partial}{\partial x}\left[(\nu+\nu_T)\frac{\partial w}{\partial x}\right]+\frac{\partial}{\partial y}\left[(\nu+\nu_T)\frac{\partial w}{\partial y}\right]+\frac{\partial}{\partial z}\left[(\nu+\nu_T)\frac{\partial w}{\partial z}\right]+S_w$$

*Energy equation*

$$\frac{\partial T}{\partial t}+\frac{\partial (uT)}{\partial x}+\frac{\partial (vT)}{\partial y}+\frac{\partial (wT)}{\partial z}=\frac{\partial}{\partial x}\left[\left(\frac{\nu}{\mathrm{Pr}}+\frac{\nu_T}{\mathrm{Pr}_T}\right)\frac{\partial T}{\partial x}\right]+\frac{\partial}{\partial y}\left[\left(\frac{\nu}{\mathrm{Pr}}+\frac{\nu_T}{\mathrm{Pr}_T}\right)\frac{\partial T}{\partial y}\right]+\frac{\partial}{\partial z}\left[\left(\frac{\nu}{\mathrm{Pr}}+\frac{\nu_T}{\mathrm{Pr}_T}\right)\frac{\partial T}{\partial z}\right]+S_T$$

*k equation*

$$\frac{\partial k}{\partial t}+u\frac{\partial k}{\partial x}+v\frac{\partial k}{\partial y}=\frac{\partial}{\partial x}\left[(\nu+\sigma_k\nu_T)\frac{\partial k}{\partial x}\right]+\frac{\partial}{\partial y}\left[(\nu+\sigma_k\nu_T)\frac{\partial k}{\partial y}\right]+P_k-D_k$$

*ω equation*

$$\frac{\partial \omega}{\partial t}+u\frac{\partial \omega}{\partial x}+v\frac{\partial \omega}{\partial y}=\frac{\partial}{\partial x}\left[(\nu+\sigma_\omega\nu_T)\frac{\partial \omega}{\partial x}\right]+\frac{\partial}{\partial y}\left[(\nu+\sigma_\omega\nu_T)\frac{\partial \omega}{\partial y}\right]+P_\omega-D_\omega$$

terms not shared between the equations inside the source terms. It is noted that the additional source terms for the momentum equations $S_{\phi,u}$, $S_{\phi,v}$ and $S_{\phi,w}$ comprise the pressure and non-pressure gradient terms and other possible sources such as gravity that influence the fluid motion, while the additional source term $S_T$ in the energy equation may contain heat sources or sinks within the flow domain. By setting the transport property $\phi$ equal to 1, $u$, $v$, $w$, $T$, $k$, $\omega$ and selecting appropriate values for the diffusion coefficient $\Gamma$ and source terms $S_\phi$, we obtain the special forms presented in Table 5.2 for each equation for the conservation of mass, momentum, energy, or turbulent properties.

## 5.5 Summary

Derivation of the governing equations of fluid flow was presented in detail: from basic conservation principles based on an infinitesimal control volume to conserve mass and energy to the statement that the net force acting on the control volume is equal

**Table 5.2** General form of governing equations for incompressible flow in Cartesian coordinates

| $\Phi$ | $\Gamma^{\Phi}$ | $S_{\Phi}$ |
|---|---|---|
| 1 | 0 | 0 |
| $u$ | $\nu + \nu_T$ | $-\frac{1}{\rho}\frac{\partial p}{\partial x} + S'_u$ |
| v | $\nu + \nu_T$ | $-\frac{1}{\rho}\frac{\partial p}{\partial y} + S'_v$ |
| w | $\nu + \nu_T$ | $-\frac{1}{\rho}\frac{\partial p}{\partial z} + S'_w$ |
| $T$ | $\frac{\nu}{\mathrm{Pr}} + \frac{\nu_T}{\mathrm{Pr}_T}$ | $S_T$ |
| $k$ | $\nu + \sigma_k \nu_T$ | $P_k - D_k$ |
| $\omega$ | $\nu + \sigma_\omega \nu_T$ | $P_k - D_k$ |

to the time rate of change of momentum. It was shown that these equations conform to a generic transport equation. Fundamentally the transport equation describes that the *transient* and *convective transport* of a fluid variable is balanced by the *diffusive transport* and the s*ources terms*.

The nature of turbulent flow and its characteristics were introduced to provide insight into the inherent differences in comparison to laminar flows. The complex geometry and the nature of the respiratory airways produce flows that are not only laminar, and turbulent, but also in transitional regimes. The influence of flow characteristics on quantities such as wall shear stress, pressure drop, and velocity profiles were discussed. A summary of different turbulence models available in CFPD was provided to introduce the reader to the difficulties associated with the task of simulating turbulent flows. Practical guidelines on turbulence model selection, mesh creation, near-wall consideration, and boundary conditions are given to help the users take the first steps in setting up the computational model for flow analysis problems correctly.

## 5.6 Review Questions

1. Simplify the general continuity equation $\frac{\partial \rho}{\partial t} + \frac{\partial(\rho u)}{\partial x} + \frac{\partial(\rho v)}{\partial y} + \frac{\partial(\rho w)}{\partial z} = 0$, for a two-dimensional constant density case.
2. In a converging nozzle, the flow accelerates due to the narrowing geometry. Discuss the changes in the velocity gradients $\frac{\partial u}{\partial x}$ and $\frac{\partial v}{\partial y}$ during the flow (assume a constant density). What is its corresponding pressure gradient?
3. Write a force balance equation for all the forces acting on a 2D differential control volume. What is its equivalent 3D form?
4. For the momentum of a fluid property in the $x$ direction discuss how the local acceleration $\frac{\partial u}{\partial t}$ and the convection terms $u\frac{\partial u}{\partial x} + v\frac{\partial u}{\partial y}$ contribute to the overall transport of the fluid.

5. A simplified one-dimensional inviscid, incompressible, laminar flow is defined by the following momentum equation in the $x$ direction: $\frac{\partial u}{\partial t} + u\frac{\partial u}{\partial x} = -\frac{1}{\rho}\frac{\partial p}{\partial x}$. Name each term and discuss its contribution to the flow.
6. The momentum of a fluid in the $y$ direction is given by the following equation: $\frac{\partial v}{\partial t} + u\frac{\partial v}{\partial x} + v\frac{\partial v}{\partial y} = -\frac{1}{\rho}\frac{\partial p}{\partial y} + \nu\frac{\partial^2 v}{\partial x^2} + \nu\frac{\partial^2 v}{\partial y^2} - g$. Discuss the forces that act to transport the fluid.
7. What are the differences between the momentum equation in Question 5.7 and the following momentum equation: $\rho u\frac{\partial u}{\partial x} + \rho v\frac{\partial u}{\partial y} = -\frac{\partial p}{\partial x} + \mu\left(\frac{\partial^2 u}{\partial x^2} + \frac{\partial^2 u}{\partial y^2}\right)$.
8. The hydrodynamic length for a channel flow shown below is equal to $L_e$ when air is used ($u_{in} = 0.03$ m/s, $\mu_1 = 1.65 \times 10^{-5}$ kg/m · s, and $\rho = 1.2$ kg/m$^3$). To obtain the same hydrodynamic length for water, what inlet velocity is required ($\mu_1 = 1.003 \times 10^{-3}$ kg/m · s, $\rho = 1{,}000$ kg/m$^3$).

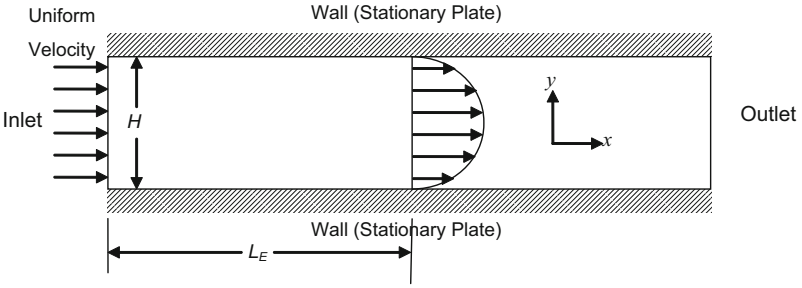


9. The Reynolds number is a ratio of two fluid properties. What are they?
10. If the Reynolds is very high ($Re \gg 10{,}000$), what does this suggest? If it is very low ($Re \ll 100$), what does this imply?
11. Apply *Fourier's law of heat conduction* to obtain the heat flux in the $x$-direction.
12. Write the equation that defines the substantial derivative for the transport of temperature in terms of the local acceleration derivative and the convection (also known as advection) derivative of temperature and why?
13. If a car travels across a warmer environment, the car body will experience a rise in temperature. Is this an example of the local *acceleration* derivative or *convection* derivative at work?
14. In what type of situation can you simplify the general 2D energy equation $\frac{\partial T}{\partial t} + u\frac{\partial T}{\partial x} + v\frac{\partial T}{\partial y} = \frac{k}{\rho C_p}\frac{\partial^2 T}{\partial x^2} + \frac{k}{\rho C_p}\frac{\partial^2 T}{\partial y^2}$ to reach the well-known Laplace's equation: $\frac{\partial^2 T}{\partial x^2} + \frac{\partial^2 T}{\partial y^2} = 0$.
15. Why do large eddies tend to be anisotropic in nature? Why are small-scaled eddies isotropic in nature?
16. The use of Direct Numerical Simulation (DNS) remains a problem for engineering applications. Why?

# Chapter 6
# Fundamentals of Particle Dynamics

## 6.1 Introduction

The previous chapters have described the dynamics of fluid motion through the solution of the Navier-Stokes and continuity equations, as well as different turbulence models for turbulent flows. This chapter describes the fundamentals of particle dynamics in order to understand how particles move through the respiratory airway. Particulate pollutant penetration into the respiratory passages and deposition are serious health concerns, particularly for children and elderly people. It has been well established that particulate pollutants are linked to a variety of symptoms including decrease in lung function, aggravated asthma, chronic bronchitis, heart attacks and premature death for people with heart disease history. Thus, understanding the transport and deposition of inhalable particles in the respiratory airways has attracted considerable attention in recent years.

Before discussing the particle dynamics, the terminology for particles needs to be defined in the context of this book and to distinguish it from other fields that study particles (i.e. quantum, nuclear physics). A *particle* can be defined as a discrete object or quantity of matter that is separated from the surrounding environment by an interface. Suspension of solid or liquid particles in a gas is referred to it as an *aerosol particle* or simply *aerosol*. Dust, smoke, mists, fog, haze, and smog are various forms of common aerosols/particles. If the particle is made up of solid material, then we can refer to it as a *solid particle* or *particulate matter* (*PM*) whereby the solid particle does not deform. If the particle is made up of a liquid material then we refer to it as a *droplet* where deformation, breakup and coalescence of the droplets may occur. Dust, smoke, mist, fog, haze, and smog are various forms of common aerosols in the atmosphere. As a generalisation, we shall refer to all the forms described above simply as particles.

In this chapter the fundamentals of aerosol particle dynamics, its motion, transport and deposition are described, which include expressions for hydrodynamic forces including drag and lift, particle relaxation time, gravitational sedimentation velocity, and stopping distance. Special considerations need to be made to model nanoparticle transport including the Brownian motion and the Cunningham slip correction to the drag. The particle transport and deposition can be analysed by the Eulerian or

J. Tu et al., *Computational Fluid and Particle Dynamics in the Human Respiratory System,* Biological and Medical Physics, Biomedical Engineering,
DOI 10.1007/978-94-007-4488-2_6, 

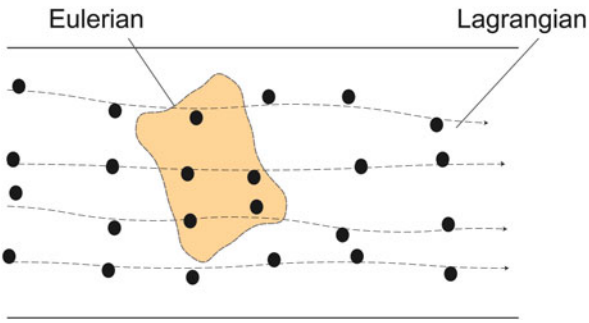


**Fig. 6.1** Lagrangian and Eulerian descriptions of particle motion in a flow domain

the Lagrangian approaches. In the Eulerian approach, the particles are treated as a transferable scalar with their concentration satisfying a diffusion equation with a Fickian diffusivity. In the Lagrangian approach, the motion of an individual particle is tracked as it moves through fluid. The Eulerian or the Lagrangian set of governing equations are linked with the equations of fluid flow described in Chap. 5.

## 6.2 Describing Particle Motion

A description of particles moving in a flow domain can be viewed from a Lagrangian or Eulerian perspective. For each method there are different coupling schemes to link the equations that describe the particle motion with the fluid flow. The Lagrangian approach involves following the trajectories of each individual discrete particle as it moves through the flow domain. The Eulerian approach, on the other hand, focuses on fixed locations in the space, and the particle concentration as they pass through is observed. Figure 6.1 illustrates the Lagrangian and Eulerian perspectives. In the Lagrangian, we observe and follow individual particle trajectories. For the Eulerian method, we observe all particles that pass through a fixed location.

From a computational fluid dynamics perspective, the application of the Lagrangian and Eulerian approaches is considerably different. Consider the example of inhalation of solid particles transported by the airflow through the airways. We refer to the particles as the *disperse phase* and the carrier medium (i.e. air), as the *continuous phase*. In the Lagrangian approach the motion of the particles is determined by tracking the motion of either the actual particles or an ensemble of a large number of representative particles. The details of the airflow around each of the particles significantly affect the drag, lift and other forces that could alter the trajectory of these particles. In the Eulerian approach, however, the particles (disperse phase) are treated as another continuous phase intermingling and interacting with the air (or carrier medium). This approach neglects the discrete nature of the disperse phase but provides the statistical averaged information of the disperse phase, such as particle velocity and concentration as a function of space and time.

### 6.2.1 Lagrangian Method

Particles in the Lagrangian method are treated in the form of points in space that are tracked individually using *Newton's second law of motion*. The Lagrangian approach is widely used because the associated equation of motion is in the form of an ordinary differential equation, which can be integrated to calculate the path of a discrete particle as it traverses through a flow domain. The force balance equation of the particle is given as

$$\rho^p V_p \frac{du_p}{dt} = \sum F_n \tag{6.1}$$

where $u_p$ is the instantaneous particle velocity and the mass of the particle is given by the product of the particle density $\rho_p$ and the particle volume $V_p$. On the right-hand side is the sum of the forces that act on the particle, which include the *drag, lift, buoyancy, pressure gradient, thermophoretic,* and *diffusion forces* (which are discussed in Sect. 6.4). In most practical flows of engineering interest, the drag force is the most important force exerted on the particle by the surrounding fluid.

Each particle is tracked from its release point until it exits the flow domain, is terminated after it has impacted onto a surface, or the number of integration time steps has been reached. The particles can exchange mass, momentum, and energy with the continuous phase through source terms in the governing equations of fluid flow. Typically, the shape of the particle is assumed to be spherical; however, non-spherical particles can be considered through the drag correlation. Particle interactions with the boundaries occur when the distance between the boundary and the particle centre is equal or less than the particle radius. By tracking individual particles, we are able to determine precisely the particle deposition sites in the respiratory airways. Furthermore, we can introduce additional forces and relevant physics, including thermal history and mass exchange due to phase change. This method is also called the Eulerian-Lagrangian method because the fluid phase is modelled by the Eulerian method, and the dispersed phase is modelled by the Lagrangian method.

The forces that are applied to each particle depend on its interaction with the surrounding air (particle-fluid interaction) and with other particles (particle-particle interaction). Let us first consider fluid-particle interaction, which is called coupling, between phases. For *one-way coupling,* the fluid influences the particles trajectory but the particles do not affect the fluid. This occurs when the disperse phase is *dilute* and has a very low volume fraction in comparison to the continuous phase. The volume fraction $\alpha$ is defined as the fraction of volume occupied by a phase within a given volume. The sum of the volume fraction of all the phases in a volume is equal to 1. Typically, one-way coupling can be used where the discrete phase volume fraction is $10^{-3}$ or less. This means that the volume taken up by the particles is small enough that its influences, including the forces exerted on the continuous phase, can be neglected. At increased loading for higher volume fractions, the particles occupy more volume and the influence of the forces they exert on the fluid phase increases (Fig. 6.2).

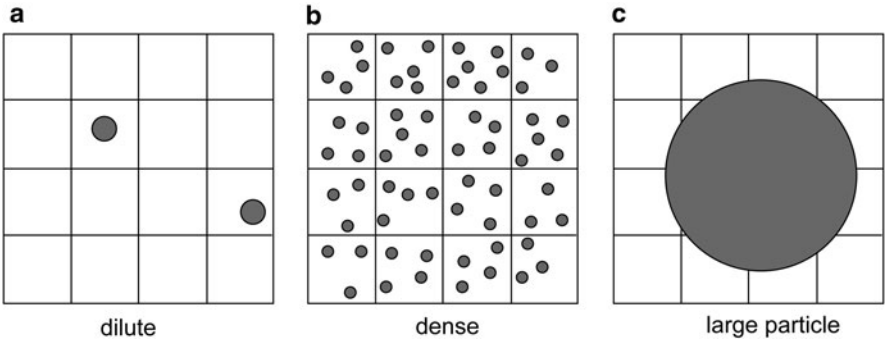


**Fig. 6.2** Dilute and dense flows as described by Kuipers (2000). **a** Dilute flows where, on average, less than one particle is present in a computational cell; **b** dense flows where a relatively high number of particles are present in a computational cell; **c** dilute or dense flows where a large number of computational cells are contained in a single particle

When this occurs, the volume fraction of the discrete phase can no longer be neglected ($10^{-3} < \alpha < 10^{-1}$); and, more importantly, the forces that they impart on the fluid become significant. Then a *two-way coupling* approach where the fluid influences the particle and, in return, the particle influences the fluid is used. Two-way coupling requires that the particle force source terms be included in the momentum equations of the fluid phase. The momentum sources are due to drag, list and other forces. The particle originated source terms are generated for each particle as it is tracked through the flow. These sources are applied in the control volume that the particle is travelling in during the time step. For very high volume discrete phase fractions, the flow is considered *dense* and *four-way coupling* can occur. That is, in addition to the two-way couple between the continuous and the discrete phases, the particle-particle collisional effects become quite important and need to be accounted for. In practice, for dense flows, the Lagrangian method may not be suitable as there are too many particles to track and the model must analyse the particle-particle collisions, as well as the possible frictional contacts. In these cases, the Eulerian-Eulerian approach is often used. For fluid-particle flows in the respiratory airways, the disperse phase is typically dilute and one-way coupling is sufficient. In rare occasions, a two-way coupling analysis may be required.

Particle-particle interactions in dense flows include collisions, leading to particle rebound for solid particles, and breakup or coalescence for droplets Furthermore, solid particle-wall collisions can result in particle rebounding and/or deposition. Droplets impacting a wall lead to breakup and/or deposition. In addition to accounting for these interactions, governing equations of particle motions are coupled to each other by collisions, as well as coalescence, and break for the case of droplets; thus for a large number of particles, this can be computationally prohibitive. In practice, a separate computational method, the Discrete Element Method (DEM), is used. This method is closely related to molecular dynamics and relies on efficient nearest neighbour sorting. DEM is widely used for modelling granular flows. For in-depth

descriptions of this method, the reader is referred to Kawaguchi et al. (1998), Zhu et al. (2007), and Radjai and Dubois (2011).

When the number of particles becomes more than several millions so that individual particle tracking is not feasible, the use of the concept of parcels was suggested. In this approach, each parcel is a statistical representation of a fixed number of physical particles. Thus, the number of parcels in a simulation needs to be sufficient to satisfy a representative sample. In its simplest form, there is no mass transfer, breakup or coalescence, and the parcel is monodispersed–having constant physical attributes (e.g. velocity, diameter, density etc.). This means that the number of particles per parcel per flow rate is determined by the total mass flow rate divided of the mass of a single particle. For a polydispersed parcel, a probability density function is applied to the particle diameter attribute, where the distribution is measured by a series of bins representing discrete ranges of particle diameter. Resolving the polydisperse parcel will then involve integration over each of the particle bin ranges.

### *6.2.2 Eulerian Method*

For a two-phase, gas-particle flow system, the continuous phase occupies a connected region of space, while the disperse phase consisting of particles occupies disconnected regions of space (Fig. 6.3). In the Eulerian (or Eulerian-Eulerian) approach, both the dispersed and continuous phases are treated as interpenetrating continua. This approach is also referred to as the two-fluid model where the discrete phase is replaced by an effective fluid phase occupying the same space. Thus, the two phases co-exist simultaneously in the flow domain and often exhibit relative motion between each other, which results in momentum exchange between phases. The two-fluid model also allows for heat transfer between the phases.

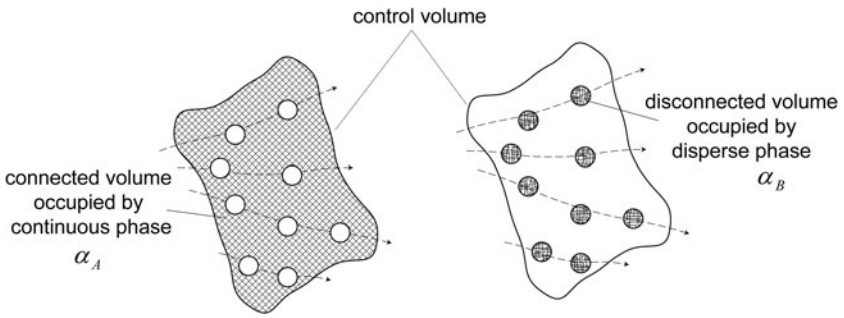


**Fig. 6.3** Eulerian representations of volume fractions and the occupied volumes of a two-phase flow with a continuous and disperse phase

A major difference of the Eulerian method in comparison with the Lagrangian is that microscopic motions of the individual particles are not analysed. Instead the

gross features of the phasic fluid flows and heat transfers are solved, which provide sufficient information for the behaviour of the mixture.

A detailed derivation of the Eulerian method is beyond the scope of this book; instead the final form of the governing equations is presented. Furthermore, there are different approaches to link the Eulerian particle phase with the fluid phase, such as the *mixture*, and *Volume of Fluid* (VOF) models, but we will limit our discussion to the *two-fluid* Eulerian-Eulerian model. For a full derivation and discussion on these issues, the reader may refer to the books of Crowe et al. (1998), Brennan (2005), and Yeoh and Tu (2009). The derivation of the multiphase equations may begin by considering an arbitrary volume subject to two conditions: (i) is much smaller than the distance over which the flow properties will vary significantly, and (ii) is large enough so that it contains representative samples of each of the phases. In practice, however, these two conditions are not always satisfied, and an averaging process, which restricts the solutions to macroscopic flows, is applied. Generally averaging may be performed in time, space, over an ensemble, or in some combination of these. For each phase to be modelled there is a set of $n$ conservation equations to represent the $n$ number of phases that is solved with the volume fractions being tracked within every computational cell. The volume fraction of a component or phase can be denoted by $\alpha_N$. The sum of all phase volume fractions is equal to 1; thus for a two-phase flow having components or phases $A$ and $B$, we have $\alpha_A + \alpha_B = 1$.

There are a few different approaches to link the Eulerian particle phase with the fluid phase. For a 2D steady flow, the **continuity equation** for each phase is given as

$$\frac{\partial(\alpha_N u)}{\partial x} + \frac{\partial(\alpha_N v)}{\partial y} = \chi_N \tag{6.2}$$

where $\chi_N$ is the net rate of mass transfer to/from the nth phase.

The $u$ and $v$ **momentum equations** are

$$\begin{aligned}\frac{\partial(\alpha_N uu)}{\partial x} + \frac{\partial(\alpha_N vu)}{\partial y} = &-\alpha_N \frac{1}{\rho}\frac{\partial p}{\partial x} + \frac{\partial}{\partial x}\left[(\nu + \nu_T)\frac{\partial(\alpha_N u)}{\partial x}\right] \\ &+ \frac{\partial}{\partial y}\left[(\nu + \nu_T)\frac{\partial(\alpha_N u)}{\partial y}\right] + \chi_{N,u} + \sum F_{N,u}\end{aligned} \tag{6.3}$$

$$\begin{aligned}\frac{\partial(\alpha_N uv)}{\partial x} + \frac{\partial(\alpha_N vv)}{\partial y} = &-\alpha_N \frac{1}{\rho}\frac{\partial p}{\partial y} + \frac{\partial}{\partial x}\left[(\nu + \nu_T)\frac{\partial(\alpha_N v)}{\partial x}\right] \\ &+ \frac{\partial}{\partial y}\left[(\nu + \nu_T)\frac{\partial(\alpha_N v)}{\partial y}\right] + \chi_{N,v} + \sum F_{N,v}\end{aligned} \tag{6.4}$$

$\chi_{N,u}$ and $\chi_{N,v}$ account for both the net rate of momentum exchange between phase N and other phases. $F_{N,u}$ and $F_{N,v}$ are the additional body forces that act on the $N$th phase. These additional momentum exchanges include *drag, lift, buoyancy, pressure gradient, thermophoretic,* and *diffusion forces*.

To summarise, Table 6.1 provides a comparison between the two modelling approaches, their characteristics, and advantages/disadvantages.

**Table 6.1** Advantages and disadvantages of the Lagrangian and Eulerian particle representation

| | Advantages | Disadvantages |
|---|---|---|
| Lagrangian | Considers microscopic transport processes. Detailed information such as individual particle location, residence time, deposition sites are available | Turbulence dispersion is idealised and its coupling with the fluid flow is restrictive. Full turbulence coupling is difficult and computationally expensive |
| | Can handle different particle sizes and characteristics such as mass and heat transfer more effectively | Is not practical for large discrete phase volume fractions. The occupied space is not typically accounted for in the fluid flow equations |
| Eulerian | Computationally more economical and can handle industrial multiphase flow applications | Different size particles are treated as different phases |
| | Can handle both dilute and dense flows | Requires constitutive modelling of the interaction forces, which are difficult to prescribe, and may have to be adjusted for different flow regimes |

### *6.2.3 Linking the Fluid and Particle Equations*

In Chap. 5 we derived the governing equations for fluid flow, and in this section we have presented the equations that describe particle motion. Before moving on, it is desirable to summarise these equations of motion and how they are linked to each other computationally in order to give the reader a visual framework to better understand CFPD modelling. Figure 6.4 illustrates the link between the fluid and particle phase equations. The Eulerian-Eulerian method provides full coupling where the phases are intermingling and interacting with each other. In each computational cell, the volume fraction $\alpha_N$ defines the amount of occupied space by each phase that is present.

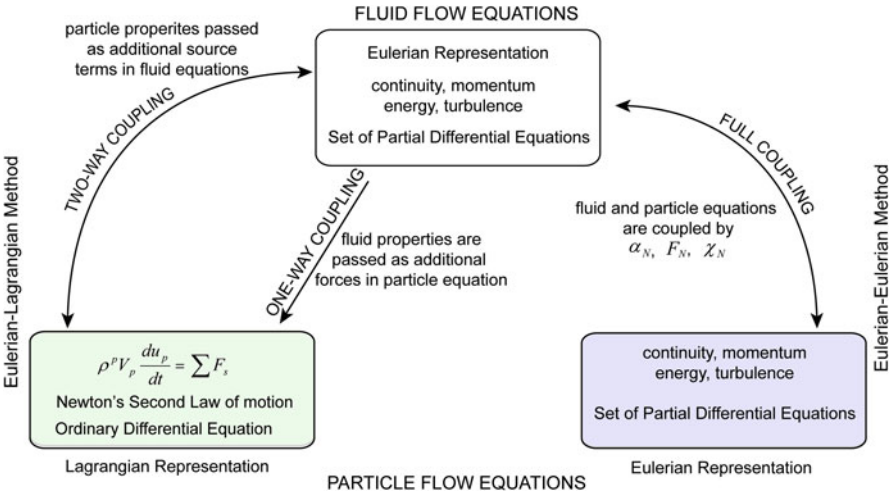


**Fig. 6.4** Fluid and particle equations and their relationships

In the Eulerian-Eulerian approach, the influence of flow properties (mass, momentum, energy, etc.) from one phase on the other is represented by the terms $\chi_N$ and $F_N$ in the governing equations. In the Eulerian-Lagrangian method, the flow properties of the fluid phase are stored in the computational cell. The disperse particle phase is mesh independent as the particle trajectory is tracked by solving an ordinary differential equation (ODE). After each integration time step, the particle is moved and its position and velocity are evaluated. At this new location, the forces acting on the particle by the surrounding fluid are computed from the values stored in the computational cell. For one-way coupling, the fluid phase properties do not change and therefore no iteration is needed. For two-way coupling, the fluid phase properties at the cell in which the particle is present will change due to the particle's motion; and, thus, an iterative process is needed to compute the new flow condition and particle position and velocity. In the next section we describe the particle dynamics and the different forces that act on the particle.

## 6.3 Particle Diameters

Except for clean rooms, the air typically contains some form of solid particles or droplets. Particle size influences its physical behaviour, affecting its motion and dispersion in an airflow field. Therefore, it is important to characterise the particle properties such as mean diameters, and size distributions.

A particle's characteristics vary due to its originating source, such as the dispersion of pollen in the air from flowers and bees, diesel/exhaust fumes from cars, and the atomization of liquid in a nasal spray device or of a powder in metered dose inhalers. The range of diameters of common aerosol particles is between 0.01 μm to about 10–40 μm (Fig. 6.5). The lower limit of 10 nm roughly corresponds to the transition from molecules to particles. Particles larger than 40 μm normally do not remain

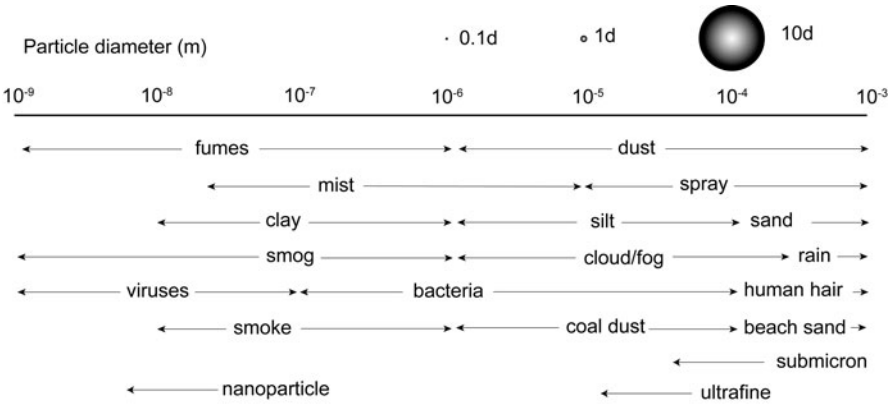


**Fig. 6.5** Typical range of particle diameters. The particles shown are scaled in size relative to each other

suspended in air for a sufficient amount of time. In the study of inhalation toxicology and particulate matter, we can categorise particles by their size. Thus we have coarse particulate matter, PM (2.5–10 μm), fine PM (<2.5 μm) ultrafine particles (<0.1 μm), and nanoparticles (<100 nm). Particles greater than 5–10 μm are usually removed by the upper respiratory system. Particles smaller than 5 μm, however, can penetrate deep into the lung and become a health hazard.

### *6.3.1 Particle Shape and Equivalent Diameters*

Particles that are spherical in shape are simply defined by their diameter. For non-spherical particles, a range of equivalent diameters or descriptive diameters are used. For excipients and drug products, we can consider an image of a drug particle for analysis under optical microscopy which produces the particle in its two-dimensional projection. From this image, the *Feret diameter* is defined as the maximum distance from edge to edge of a particle in a pre-defined direction. The *Martin diameter* is the length of the line in a pre-defined direction which separates a particle into two equal portions. The *projected area diameter* is the diameter of a circle having the same projected area as the particle in question (Fig. 6.6).

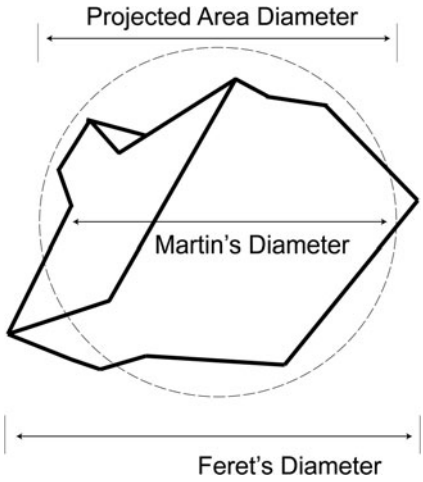


**Fig. 6.6** Diameter descriptors using optical microscopy for a non-spherical particle

Particulate matter and aerosols consist of a large number of particles/droplets. Different mean diameter descriptors are used to represent an equivalent diameter for the group of particles that is being analysed. Let us consider three particles having a diameter of 3, 4, and 5 μm, respectively. The arithmetic mean is

$$D_{10} = \sum \frac{d_i}{n} \tag{6.5}$$

which gives $D_{10} = 4\,\mu m$. However for drug absorption or the uptake of deposited toxic particles onto the mucosal walls of the respiratory tract, the surface area of a particle is of importance, and therefore we should consider the surface mean diameter. Each diameter is converted into its surface area and summed together to give the total surface area produced from all particles. This value is then divided by the number of particles to produce a mean value that represents the effect surface area of the particles. The diameter of this value gives the surface mean diameter, $D_{20}$. Since the surface area of a sphere is $\pi d^2$, we get

$$D_{20} = \sqrt{\sum \frac{{d_i}^2}{n}} \tag{6.6}$$

which gives $D_{10} = 4.08$.

When the volume of a sphere, which in turn is also its mass (scaled with the material density), becomes important, the volume mean diameter $D_{30}$ is used. Similar to the method for finding $D_{20,}$ the diameters are cubed before dividing by the number of particles, and cube rooting is taken to give

$$D_{30} = \sqrt[3]{\frac{\sum {d_i}^3}{\sum n_i}} \tag{6.7}$$

which gives $D_{10} = 4.16$.

The Sauter Mean Diameter (SMD) is the equivalent diameter of a sphere that has the same volume/surface area ratio as the particle of interest and is given as

$$D_{32} = \frac{\sum {d_i}^3}{\sum {d_i}^2} \tag{6.8}$$

which gives $D_{32} = 4.32\,\mu m$. The SMD is particularly relevant to hydrodynamics and mass transfer, since both drag and reaction rates are proportional to particle/droplet area.

Two other important diameters are the *Stokes* and *aerodynamic diameters* which describe the particles as they are transported through the respiratory airways. The Stokes (sedimentation) diameter of a particle is the diameter of a sphere having the same density, which is settling with the terminal velocity of the particle in a quiescent fluid. The aerodynamic diameter of a particle $d_{ae}$ is the diameter of a sphere with the density of water or unit density ($\rho = 1000\ kg/m^3$), which is settling with the terminal velocity of the particle. This is given as

$$d_{ae} = d\sqrt{\frac{\rho}{1000}} \tag{6.9}$$

For spherical particles, the aerodynamic diameter is different from their diameters except for water droplets.

## 6.4 Forces Acting on a Particle

### *6.4.1 Drag Force and Drag Coefficient*

Small particles suspended in a gas are transported by the action of hydrodynamic forces. The main hydrodynamics force is the drag force that moves the particles along the flow stream line. The other hydrodynamic force is the lift force that tends to move the particle perpendicular to the flow direction. For low Reynolds numbers in the creeping flow regime (Re < 1.0), the Stokes drag force acting on a spherical particle is given by

$$F_D = 3\pi\nu(u^f - u^p)d \tag{6.10}$$

where $d$ is the particle diameter, $\nu$ is the kinematic viscosity and $u$ is the velocity of either the fluid or the particle. The superscripts $f$ and $p$ represent the fluid/gas (e.g. air) and particle, respectively, and the Reynolds number is defined as

$$\mathrm{Re}_p = \frac{\rho_f(u^f - u^p)d}{\mu} \tag{6.11}$$

Equation (6.10) was first obtained by Stokes under the so-called creeping flow assumption, where the effect of fluid inertia is neglected. Because most particles suspended in the air have diameters in the micron and submicron range, they are typically in the Stokes flow regime, while larger particles may be outside the Stokes flow region. The corresponding expression for the drag coefficient in the Stokes regime is given as

$$C_D = \frac{F_D}{\frac{1}{2}\rho_f(u^f - u^p)^2 A} = \frac{24}{\mathrm{Re}_p} \tag{6.12}$$

where $\rho$ is the fluid density and $A = \pi d^2/4$ is the projected area of the sphere on a plane perpendicular to the flow direction. At higher Reynolds numbers, the drag coefficient deviates from Eq. (6.12). Oseen (1910) included the effect of fluid inertia by an approximate linearization and developed a correction to the Stokes drag, which given as

$$C_D = \frac{24}{\mathrm{Re}_p}\left(1 + \frac{3}{16}\mathrm{Re}_p\right) \tag{6.13}$$

The Oseen (1910) equation has a limited range of validity, and at higher Re it overestimates the drag force. For practical applications with $1 < \mathrm{Re}_p < 1000$ (sometimes referred to as the transition regime), the following expressions may be used (Clift et al. 1978b):

$$C_D = \frac{24}{\mathrm{Re}_p}\left(1 + 0.15\mathrm{Re}_p{}^{0.687}\right) \tag{6.14}$$

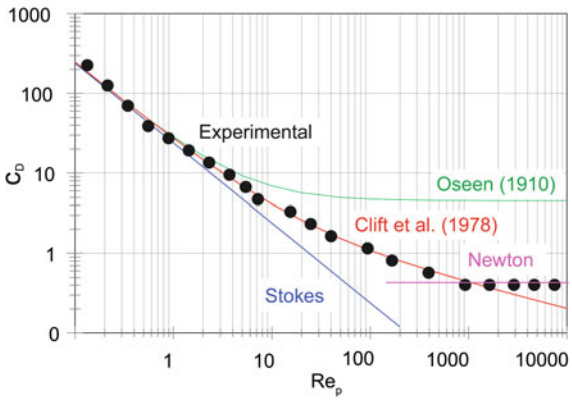


**Fig. 6.7** Predictions of various models for drag coefficient for a spherical particle

Equation (6.14) is an empirical fit to the data and is quite useful for analysis of aerosol motion.

For higher $\mathrm{Re}_p$ in the range of $10^3 < \mathrm{Re}_p < 2.5 \times 10^5$, the drag coefficient is roughly constant ($\mathrm{C_D} = 0.4$). This regime is referred to as the Newton regime. However this regime is typically not applicable for airborne particulates, where the particle diameters are in the order of nanometer and micrometer, leading to low $\mathrm{Re}_p$ numbers. Predictions of various models for drag coefficient with the trend of the experimental data are shown in Fig. 6.7.

For a particle moving near a wall, the drag force varies with the distance of the particle from the surface. Brenner (1961) analysed the drag acting on a particle moving toward a wall under the creeping flow condition. To the first order, the drag coefficient is given as

$$C_D = \frac{24}{\mathrm{Re}_p}\left(1 + \frac{d}{2h}\right) \tag{6.15}$$

where $h$ is the distance of the particle centre from the wall.

For a particle moving parallel to the wall, the Stokes drag force needs to be modified. For large distances from the wall, the following equation was suggested by Faxen (1923):

$$C_D = \frac{24}{\mathrm{Re}_p}\left(1 - \frac{9}{16}\left(\frac{d}{2h}\right) + \frac{1}{8}\left(\frac{d}{2h}\right)^3 - \frac{45}{256}\left(\frac{d}{2h}\right)^4 - \frac{1}{16}\left(\frac{d}{2h}\right)^5\right)^{-1} \tag{6.16}$$

### *6.4.2 Cunningham Correction Factor*

When a particle becomes so small that its size becomes comparable to the mean free path of the molecules of the surrounding gas, the flow field can no longer be

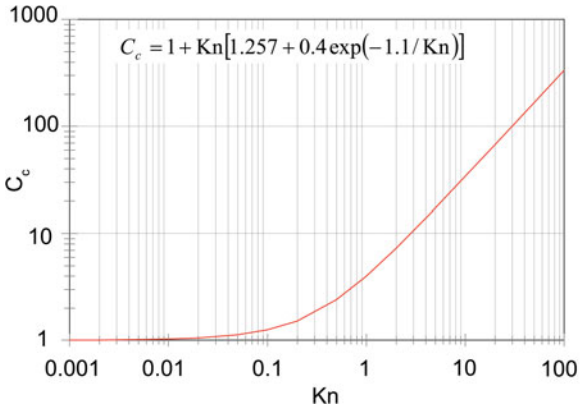


**Fig. 6.8** Variation of the Cunningham correction with Knudsen number

considered a continuum. Gas flow slip occurs and the expression for drag must be modified accordingly. The Stokes drag force with the correction becomes

$$F_D = \frac{3\pi\nu(u^g - u^p)d}{C_c} \tag{6.17}$$

where the Cunningham correction factor $C_c$ is given by

$$C_c = 1 + \frac{2\lambda}{d}[1.257 + 0.4\exp(-1.1d/2\lambda)] \tag{6.18}$$

Here $\lambda$ denotes the molecular mean free path in the gas. The mean free path of a gas is given as

$$\lambda = \frac{1}{n\sqrt{2}\pi d_m^2} = \frac{kT}{\sqrt{2}\pi d_m^2 P} \tag{6.19}$$

In Eq. (6.19) $n$ is the gas molecule number density, $d_m$ is the gas molecule (collisional) diameter, $k = 1.38\times10^{-23}$ J/K is the Boltzmann constant, $P$ is pressure, and $T$ is temperature in Kelvin. For air, $d_m = 0.361$ nm and $\lambda = \frac{(23.1\times10^{-6})T}{P}$. Note that $C_c \geq 1$ for all values of $d$ and $\lambda$.

The term $2\lambda/d$ in the $C_c$ equation is the dimensionless Knudsen (Kn) number, which is the ratio of the molecular mean free path length to the particle radius. Figure 6.8 shows the variation of $C_c$ with Kn. It is seen that $C_c$ is about 1 for $\mathrm{Kn} < 0.1$ and increases sharply as Kn increases beyond 0.5.

Table 6.2 illustrates the variation of the Cunningham correction factor with particle diameter in air under normal pressure and temperature conditions with $\lambda = 0.07$ μm.

Equation (6.18) is applicable to a wide range of $\mathrm{Kn} = \frac{\lambda}{d} \leq 1000$ that covers slip, transition and part of free molecular flows. The Stokes-Cunningham drag given by Eq. (6.17) is valid as long as the particle Reynolds number and Mach number (based on relative velocity) are small. More recent studies on slip correction factor have been reported by Moshfegh et al. (2009).

**Table 6.2** Variations of $C_c$ with $d$ for $\lambda = 0.07$ μm

| Diameter (μm) | $C_c$ |
|---|---|
| 10 | 1.018 |
| 1 | 1.176 |
| 0.1 | 3.015 |
| 0.01 | 23.775 |
| 0.001 | 232.54 |

### 6.4.3 *Particle Relaxation Time, Stokes Number*

Consider an aerosol particle in fluid flow as shown in Fig. 6.9. Combining Eq. (6.1) with drag force (6.10), the equation of motion of a spherical particle of mass $m$ and diameter $d$ is given as

$$m\frac{du^p}{dt} = \frac{3\pi\mu d}{C_c}(u^f - u^p) + mg \tag{6.20}$$

where $g$ is the acceleration of gravity. Here it is assumed that the particle is far away from walls and the Stokes drag is also assumed. Buoyancy effect in the air is also neglected.

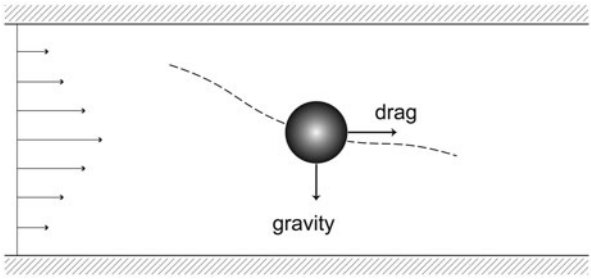


**Fig. 6.9** Schematic of particle motion in airflow

Dividing Eq. (6.20) by $3\pi\mu d/C_c$ and rearranging, we find

$$\tau\frac{du^p}{dt} = (u^f - u^p) + \tau g \tag{6.21}$$

where the *particle relaxation time* is defined as

$$\tau = \frac{mC_c}{3\pi\mu d} = \frac{d^2\rho^p C_c}{18\mu} = \frac{Sd^2 C_c}{18\nu} \tag{6.22}$$

where $m = \frac{\pi d^3\rho^p}{6}$, $\nu$ is the kinematic viscosity of the fluid, and $S = \rho^p/\rho^f$ is the density ratio. In practice, for particles which are not too small, $C_c \approx 1$ and the relaxation time becomes

$$\tau \approx \frac{d^2\rho^p}{18\mu} \tag{6.23}$$

**Table 6.3** Terminal velocity, relaxation time, and stopping distance for a unit density particle in air ($p = 1$ atm, $T = 20\,^{\circ}$C)

| Diameter (μm) | $u^t = \tau g$ | $\tau$ (sec) | Stop Distance $u_o = 1$ m/s | Stop Distance $u_o = 10$ m/s |
|---|---|---|---|---|
| 0.05 | 0.39 μm/s | $4 \times 10^{-8}$ | 0.04 μm | $4 \times 10^{-4}$ mm |
| 0.1 | 0.93 μm/s | $9.15 \times 10^{-8}$ | 0.092 μm | $9.15 \times 10^{-4}$ mm |
| 0.5 | 10.1 μm/s | $1.03 \times 10^{-6}$ | 1.03 μm | 0.0103 mm |
| 1 | 35 μm/s | $3.57 \times 10^{-6}$ | 3.6 μm | 0.0357 mm |
| 5 | 0.77 mm/s | $7.86 \times 10^{-5}$ | 78.6 μm | 0.786 mm |
| 10 | 3.03 mm/s | $3.09 \times 10^{-4}$ | 309 μm | 3.09 mm |
| 50 | 7.47 cm/s | $7.62 \times 10^{-3}$ | 7.62 mm | 76.2 mm |

The particle relaxation time is a key parameter for the dynamics of a particle suspended in a fluid. To illustrate this, we consider a particle's *terminal velocity* and its *stopping distance*. Terminal velocity occurs when the drag force on the particle becomes equal to its weight, and therefore its sedimentation velocity remains constant. For a falling particle, solving Eq. (6.21) gives

$$u^p = (u^f + \tau g)(1 - e^{-t/\tau}) \tag{6.24}$$

where $u^f$ is assumed to be a constant vector. For $u^f = 0$ and large $t$, the terminal velocity of particle $u^t$ is given by

$$u^t = \tau g = \frac{\rho^p d^2 g C_c}{18\mu} \tag{6.25}$$

The stopping distance is the maximum distance a particle with an initial velocity $u_o^p$ travels before coming to rest. Here the particle is only affected by the drag force. The solution of Eq. (6.20) in the absence of gravity and fluid flow is given as

$$x^p = \tau u_o^p (1 - e^{-t/\tau}) \tag{6.26}$$

where $x^p$ is the particle position. As t becomes large, the stopping distance is given as $x^p = \tau u_o^p$.

The terminal velocity, relaxation time, and stopping distance is tabulated in Table 6.3 for different particle sizes with unit density in air. It is seen that for particles in the submicron range the relaxation times and terminal velocities are extremely small. These values, however, increase rapidly as particle size increases. Similarly, the stopping distance increases rapidly with particle size. The particle relaxation time is the time it takes for a particle to adapt from one velocity state to another. Thus, it is a measure of the particle's inertia.

The expression for particle velocity given by Eq. (6.24) and its position given by Eq. (6.26) are exponential functions. This means that at time $t = \tau$ the particle velocity reaches 63 % of its terminal velocity, and reaches to 95 % $u^t$ at $t = 3\tau$. This means that small particles <2 μm can be assumed to reach their terminal velocity almost immediately and behave as gas tracers without noticeable errors. Similarly,

at time $t = 3\tau$ a particle will reach 95 % of its stopping distance. This measure is important when considering particle flows in 90° turns, such as those found in the nostril-to-nasal passage and the nasopharynx region. In these regions, particles with short stopping distances will be able to follow the fluid streamlines, while those with longer stopping distances will not adapt to the change in the flow direction, but will continue their paths until their stopping distances are reached. Thus, if these particles are at distances from the wall that are shorter than their stopping distances, then they will deposit on the airway bends.

As was noted before, the particle relaxation time characterises the particle response time, but the particle behaviour is also affected by the airflow conditions. For example, consider a particle with a high relaxation time, $\tau$, moving through a narrow 90° pipe bend with velocity $u$. We are interested to know if the particle is likely to impact the pipe walls. The likelihood of particle impaction depends, in addition to the relaxation time, on the velocity $u$ and pipe diameter. If the pipe has a wider diameter, the likelihood for impaction decreases. To account for the flow environment surrounding the particle, the ratio of the particle relaxation time to a characteristic fluid flow time scale is defined as the particle Stokes number. That is,

$$St^p = \frac{\tau u_f}{d_c} \tag{6.27}$$

where $u_f$ is the fluid low velocity and $d_c$ is the characteristic dimension of the geometry. For small Stokes numbers ($St \ll 1$), the particle relaxation time is sufficiently small compared with the time scale of the flow, and therefore the particles act as gas tracers in the flow field. For larger Stokes numbers ($St \gg 1$), particles will separate from any curved streamlines and continue in their original direction.

### 6.4.4 Non-spherical Particles

For non-spherical particles such as fibres, typically a shape factor correction is used to modify the Stokes drag law as a first approximation. Thus,

$$F_D = 3\pi\mu(u^f - u^p)d_{ve}k \tag{6.28}$$

where $d_{ve}$ is the diameter of a sphere having the same volume as the non-spherical particle. That is,

$$d_{ve} = \left(\frac{6}{\pi}Volume\right)^{1/3} \tag{6.29}$$

and $k$ is a correction factor (Fig. 6.10).

For a cluster of $n$ spheres, $d_e = n^{1/3}d$. For tightly packed clusters, $k \leq 1.25$. For a chain of equal size spheres moving perpendicularly to the line of the chain, $k$ depends on the number of spheres in the chain. For example chains of two, four and

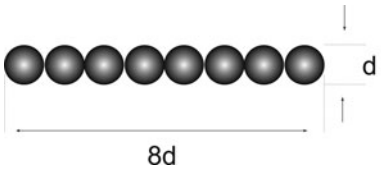


**Fig. 6.10** Representation of a non-spherical particle such as a fibre, using a cluster of spheres

six spheres, respectively, $k$ is 1.12, 1.32, and 1.57. For other combinations of spheres, the values of shape factors can be found in the literature (Hidy 1984; Lerman 1979; Tran-Cong et al. 2004).

The aerodynamic flight of a fibre can be described by the spherical drag coefficient as described in Eq. (6.14); however the fibre has to be converted into an equivalent aerodynamic diameter. This can be performed by applying the following correlations. An equivalent aerodynamic diameter for a fibre is given as

$$d_{ae} = d_{ve}\sqrt{\frac{\rho}{(1000 \cdot k)}} \tag{6.30}$$

where $d_{ve}$ is the volume equivalent diameter, $\rho$ is the density of the fibre, and $k$ is the dynamic shape factor. The dynamic shape factor taking the length oriented perpendicularly to the flow is given as

$$k_{\perp} = \frac{(8/3)(\beta^2 - 1)}{[(2\beta^2 - 3)/\sqrt{\beta^2 - 1}\,]\ln(\beta + \sqrt{\beta^2 - 1}) + \beta} \tag{6.31}$$

and for the length oriented parallel to the flow,

$$k_{||} = \frac{(4/3)(\beta^2 - 1)\beta^{1/3}}{[(2\beta^2 - 1)/\sqrt{\beta^2 - 1}\,]\ln(\beta + \sqrt{\beta^2 - 1}) - \beta} \tag{6.32}$$

where $\beta$ is the aspect ratio and is defined as the ratio of the fibre length to the diameter. For random orientation of the fibre, the shape factor is a combination of the two orientations and is given as

$$\frac{1}{k_R} = \frac{2}{3k_{\perp}} + \frac{1}{3k_{||}} \tag{6.33}$$

If we consider carbon fibre (density of 1830 kg/m$^3$) and asbestos fibre (density of 300 kg/m$^3$), the range for its equivalent aerodynamic diameter for random orientation of the fibre is given in Table 6.4

Therefore the asbestos fibre has a shorter relaxation time than does the carbon fibre, and we expect that the asbestos is likely to penetrate the upper respiratory airways and into the lungs while the carbon fibre will deposit onto the respiratory walls earlier, especially where the passageways have sharp turns.

**Table 6.4** A comparison of aerodynamic diameters for asbestos and carbon fibre with varying lengths

| | Density (kg/m$^3$) | Diameter (μm) | Length (μm) | $d_{ae}$ (μm) |
|---|---|---|---|---|
| Asbestos | 300 | 1 | 10 | 1.09 |
| | | | 100 | 1.44 |
| | | | 300 | 1.59 |
| Carbon fibre | 1830 | 3.66 | 10 | 7.60 |
| | | | 100 | 11.30 |
| | | | 300 | 12.80 |

### 6.4.5 Additional Forces

*Lift Force* As shown in Fig. 6.11, small particles, typically smaller than a few microns, experience a lift force perpendicular to the direction of flow due to velocity shear. The lift force was first sensed from the observations that blood corpuscles in the capillaries tend to keep away from the walls. The shear lift originates from the inertia effects in the viscous flow around the particle and is fundamentally different from aerodynamic lift force. The expression for the shear lift first obtained by Saffman (1965), and Saffman (1968) is given as

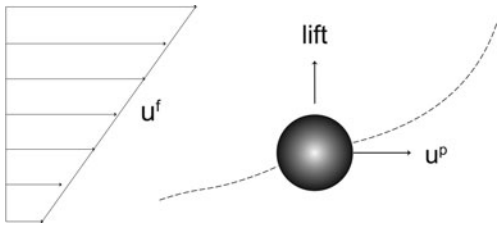


**Fig. 6.11** Schematic of the lift force acting on a particle in a shear flow

$$F_{L(Saff)} = 1.615\rho\nu^{1/2}d^2(u^f - u^p)\left|\frac{du^f}{dy}\right|^{1/2}\text{sgn}\left(\frac{du^f}{dy}\right) \tag{6.34}$$

Here $u^f$ is the fluid velocity at the location of the mass centre of the particle, $u^p$ is the particle velocity, $d$ is the particle diameter, and $\rho$ and $\nu$ are the fluid density and viscosity. The word 'sgn' is the signum of the term inside the brackets (i.e. when *the term* is less than, equal to or greater than zero, *sgn* returns $-1$, zero and one, respectively). Note that $F_L$ is in the positive $y$-direction if $u^f > u^p$. Further refinement of the Saffman lift expression includes the work by McLaughlin (1991, 1993), Cherukat and McLaughlin (1990), Cherukat et al. (1994), and Mei (1992).

*Virtual Mass, Basset History* A particle accelerating in a fluid will experience unsteady forces that can be divided into two parts: the virtual mass effect and the Basset history force. When a particle is moving and is accelerating in a fluid, then the fluid that surrounds the particle is displaced and is accelerated from its initially stagnant motion. As a result the fluid will gain kinetic energy as its velocity changes, and

the particle experience an increase in its effective mass by the addition of the fluid mass that is moving with the particle. The virtual mass force for a spherical particle is half of the volume of the sphere times the density of the fluid. The corresponding effective inertial force is given as

$$F_{VM} = \frac{1}{2}\frac{\rho_f}{\rho_p} m \left( \frac{du^f}{dt} - \frac{du^p}{dt} \right) \tag{6.35}$$

That is, the expression given by (6.35) needs to be added to the right-hand side of Eq. (6.20). The virtual mass effects are particularly important when the fluid density is greater than the particle density ($\rho \gg \rho_p$) such as for bubbles in a liquid.

The Basset history force describes the unsteady drag force that acts on an accelerating particle and is given as

$$F_{Bass} = \frac{3\pi\mu d^2}{2\sqrt{\pi\nu}} \int_{t_0}^{t} \frac{(du^f/dt - du^p/dt)|_{t_1}}{\sqrt{t - t_1}} dt_1 \tag{6.36}$$

The Basset history force becomes important for high frequency unsteady motions.

*Magnus Effect* A rotating spherical particle moving in fluid will experience a force perpendicular to the direction of its velocity, which is known as the Magnus effect. In Fig. 6.12, a particle spins counter-clockwise, with an oncoming free stream fluid velocity of $u_0^f$. The contribution by the rotating boundary layer will oppose the velocity near the top of the particle, and assists the velocity flow in the front of the particle (near the lower part). This means that $u_2^f > u_0^f > u_1^f$, and thus the pressure near the upper surface of the particle becomes larger than that near the lower surface. This pressure difference generates the aerodynamic lift that is referred to as the Magnus force, and can be written as

$$F_M = \frac{1}{2}\rho_f u_f^2 A C_L \tag{6.37}$$

where $A$ is the cross-sectional area of the particle and $C_L$ is the coefficient of lift.

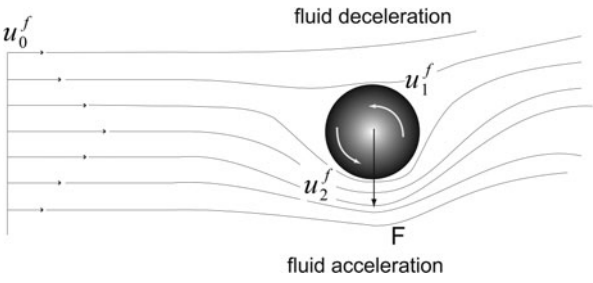


**Fig. 6.12** Schematic of a spinning particle creating the Magnus effect. The velocities $u_0^f$, $u_1^f$, and $u_2^f$ are the upstream, particle front, and particle rear velocities, respectively. $F$ represents the resulting force perpendicular to the fluid flow direction

## 6.5 Nanoparticle Transport

With rapid advances in nanotechnology, the potential for exposure to nanoparticles has increased significantly. Therefore, better understanding of nanoparticle transport and deposition is critical for assessing their potential health hazards and/or the effectiveness of nanomedicine. Since nanoparticles are in the size range of the mean free path of air molecules under normal pressure, their behaviour differs markedly from that of micron size particles. Most notably, nanoparticles are significantly affected by the influence of Brownian motion, and their fluid drags are significantly reduced due to the molecular slip. When a small particle is suspended in a fluid, it is subjected to the impact of the gas or liquid molecules. For ultrafine (nano) particles, the instantaneous momentum imparted to the particle varies randomly, which causes the particle to move on an erratic path now known as Brownian motion (Fig. 6.13).

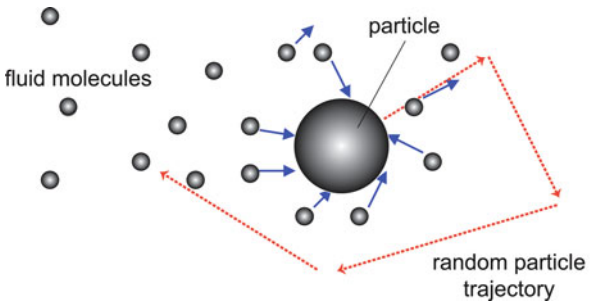


**Fig. 6.13** Brownian motion of a particle subjected to impact by fluid molecules causing the particle to travel in a random trajectory

Nanoparticle dispersion and deposition can be evaluated by either the Lagrangian particle tracking or Eulerian diffusion model approach. These two approaches are described in the following sections.

### *6.5.1 Lagrangian Particle Tracking*

For sub-micron particles, the effects of the Brownian random force generated by the impact of gas molecules on the particle can be included as an additional force term in the particle equation of motion given by Eq. (6.1). The intensity of the Brownian force per unit mass of a particle can be modelled as a white noise stochastic process. White noise is a zero mean Gaussian random process with a constant power spectrum with equal power for any frequency. The Brownian excitation is modelled as a Gaussian white noise random process with a spectral density $S_o$ (Li and Ahmadi 1992) given as,

$$S_0 = \frac{216\nu k_b T}{\pi^2 \rho_f d^5 \left(\frac{\rho_p}{\rho_f}\right)^2 C_c} \tag{6.38}$$

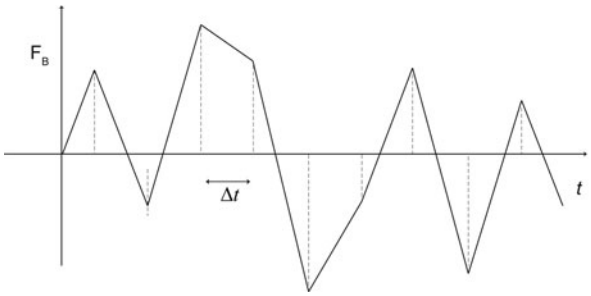


**Fig. 6.14** Schematic of a numerically generated Brownian excitation force

where $k_b = 1.38 \times 10^{-23}$ J/K is the Boltzmann constant, and $T$ is the temperature. The Cunningham correction factor, $C_c$ (described earlier in Sect. 6.4.2) becomes very important for nanoparticles. The Brownian force per unit mass of a particle is then

$$F_B = \zeta \sqrt{\frac{\pi S_o}{\Delta t}} \tag{6.39}$$

where $\zeta$ is a zero-mean, unit-variance-independent Gaussian random number and $\Delta t$ is the time step size in which the amplitudes of the Brownian force components are evaluated (Fig. 6.14). The time step size should be much smaller than the particle relaxation time in order to resolve the particle motion correctly.

In practice, the fluid drag, lift as well as Brownian forces act simultaneously on nanoparticles, so that the coupling effects need to be studied. Therefore, there is a need to simulate the random force exerted on the particle. Figure 6.14 shows the schematics of a numerically generated Brownian excitation.

*Simulation Results* Lagrangian simulation studies for dispersion and deposition of particles emitted from a point source in the viscous sublayer of a turbulent channel flow were first reported by Ounis et al. (1991b). For different particle diameters, Fig. 6.15 displays the time variations of their simulated root mean square particle position and comparison with the exact solution. Here, for each particle size, 500 sample trajectories were evaluated, compiled and statistically analysed. It is seen that small nanoparticles are spread much faster by the action of the Browning motion when compared with the larger micrometer-sized particles. The simulated root mean square responses are in good agreement with the exact solution.

The increased spreading of submicron particles due to Brownian diffusion is strongly affected by their size. This is because the power spectral intensity of the Brownian force is inversely proportional to the fifth power of their diameter. For respiratory inhalation and deposition studies, this means that as the particle diameter decreases, the number of deposited particles is expected to increase sharply because of the increased dispersion. Additionally, the deposition rate will decrease as the distance from the source to the wall increases. Figure 6.15 further shows that the Brownian motion process is a significant mechanism for nanoparticle diffusion and wall deposition.

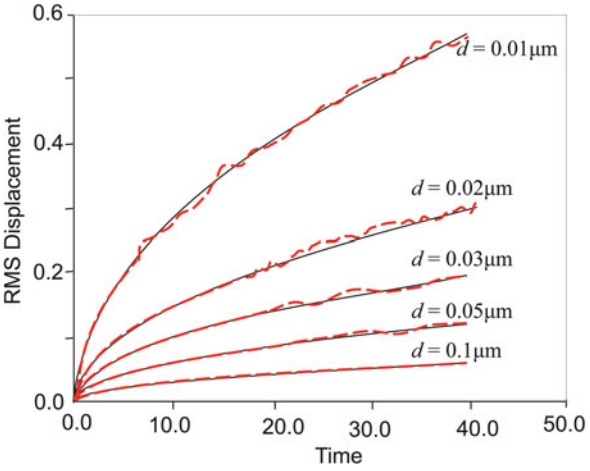


**Fig. 6.15** Variations of RMS particle vertical displacement with time for a density ratio of $\rho_p/\rho_f = 2000$ and different diameters

### 6.5.2 *Eulerian Diffusion Models*

The Eulerian diffusion model assumes a dilute suspension of nanoparticles that is treated as a chemical component or species with the use of a diffusion-convection equation. The diffusion of nanoparticles is governed by Fick's law:

$$J = -D\frac{dC}{dx} \tag{6.40}$$

where $C$ is the concentration, $J$ is the flux, and $D$ is the diffusion coefficient given by

$$D = \frac{\tau k_b T}{m} = \frac{k_b T C_c}{3\pi\mu d} \tag{6.41}$$

where $m$ is the mass of the spherical particle. Equation (6.41) was first obtained by Einstein (1905) from a thermodynamics analysis. It is seen that the particle diffusivity decreases as particle diameter increases. Furthermore, the diffusivity is independent of particle density. Typical values of diffusivity for particles in the size range of 10 nm to 10 μm under normal temperature conditions in air are listed in Table 6.5. It is seen that the diffusivity decreases sharply as particle diameter increases.

**Table 6.5** Particle mass diffusivity for different particle diameters

| $d$ (μm) | $D$ (cm$^2$/s) |
|---|---|
| $10^{-2}$ | $5.24 \times 10^{-4}$ |
| $10^{-1}$ | $6.82 \times 10^{-6}$ |
| 1 | $2.74 \times 10^{-7}$ |
| 10 | $2.38 \times 10^{-8}$ |

When the effect of particle inertia is negligible, we have a convection-diffusion transport equation for the chemical component/species in two-dimensions:

$$\frac{\partial C}{\partial t} + \frac{\partial (uC)}{\partial x} + \frac{\partial (vC)}{\partial y} = \frac{\partial}{\partial x}\left(D\frac{\partial C}{\partial x}\right) + \frac{\partial}{\partial y}\left(D\frac{\partial C}{\partial y}\right) \tag{6.42}$$

The solution of Eq. (6.42) results in the particle concentration field.

In the absence of flow and when the particle source is far from walls, the mean-square displacement of Brownian particles in one direction is given as

$$\overline{x^2}(t) = 2Dt \tag{6.43}$$

One terminology used commonly in the aerosol community is the *diffusion velocity*, which is defined as flux to the wall per unit concentration. That is,

$$u_D = \frac{J}{C_0} \tag{6.44}$$

Similarly, a diffusion force may be defined as

$$F_{diff} = 3\pi \mu u_d / C_c \tag{6.45}$$

*Analysis* For a one-dimensional case, the diffusion equation given by Eq. (6.42) in the absence of a flow field becomes

$$\frac{\partial C}{\partial t} = D\,\frac{\partial^2 C}{\partial y^2} \tag{6.46}$$

For an initially uniform concentration of aerosols in the neighbourhood of an absorbing wall, the initial and boundary conditions are $C(y,0) = C_o$, $C(0,t) = 0$ and $C(\infty,t) = C_o$, where $C_o$ is the particles number concentration at the initial time and far from the wall. The solution to Eq. (6.46) then becomes

$$C(y,t) = C_0 erf\left(\frac{y}{\sqrt{4Dt}}\right) \tag{6.47}$$

Where

$$erf(\xi) = \frac{2}{\sqrt{\pi}} \int_0^{\xi} e^{-\xi^2} d\xi; \quad erf(0) = 0; \quad erf(\infty) = 1$$

The flux to the wall then is given by

$$J = -D\,\frac{\partial c}{\partial x}\bigg|_{y=0} = C_o\sqrt{\frac{D}{\pi t}} \tag{6.48}$$

The corresponding deposition velocity, which is defined as flux per unit concentration, is then given by

$$u_D = \frac{J}{C_0} = \sqrt{\frac{D}{\pi t}} = \frac{D}{\delta_c} \tag{6.49}$$

Here $\delta_c$ is the diffusion boundary layer thickness given as

$$\delta_c = \sqrt{\pi Dt} \tag{6.50}$$

The corresponding diffusion force is defined as

$$F_d = \frac{3\pi\mu d u_D}{C_c} \tag{6.51}$$

The total number of particles that are deposited in an interval $dt$ is given as

$$dN = Jdt = C_0\sqrt{\frac{D}{\pi t}}dt \tag{6.52}$$

The total number of particles that are deposited per unit area in the time interval 0 to $t$ may be obtained by integrating Eq. (6.52). Thus,

$$N = C_0\sqrt{\frac{4Dt}{\pi}} \tag{6.53}$$

The analysis presented here may be used to estimate the particle deposition in a tube. For a constant velocity gas flow in a tube of length $L$ and radius $R$, the residence time is $t = L/u$, where $u$ is the gas velocity. Assuming that the wall deposition process is similar to that of a uniform concentration near a wall, and using (6.53) it follows that

$$\frac{C_{out}}{C_{in}} = 1 - \frac{4}{\sqrt{\pi}}\sqrt{\frac{DL}{uR^2}} \tag{6.54}$$

Equation (6.54) provides an approximate estimate of the change in the concentration of particles along a tube. A detailed analysis of duct flow leads to

$$\frac{C_{out}}{C_{in}} = 1 - 2.56\phi^{2/3} + 1.2\phi + 0.177\phi^{4/3}, \quad \phi = \frac{DL}{uR^2} \tag{6.55}$$

## 6.6 Turbulent Particle Dispersion

Particles that are transported under a turbulent flow are subjected to the characteristics of turbulence from the fluid. The additional coupling and linking of the fluid turbulence to the particle equations increases the complexity of the CFPD modelling. In this chapter we will pay particular attention to the Lagrangian particle trajectory analysis because it allows a more intuitive understanding of turbulent transport and dispersion of particles to be introduced. However we begin by describing the general Eulerian two-fluid model approach.

The turbulent equations of motion for a single phase were derived in Chap. 5. It was shown that representing turbulence for a single fluid itself was difficult and

that assumptions are needed in order to establish turbulence models. Therefore the addition of particles to such a flow will only increase the complexity of the problem. In the Eulerian two-fluid model, each phase has its own set of governing equations and in the case of turbulence will contain a set of transport equations for the turbulence quantities (i.e. $k$, $\omega/\varepsilon$). Additional terms in each set of equations are included to accommodate the production and dissipation of turbulence due to the interaction between the continuous fluid phase and the disperse particle phase. For example, large particles are known to enhance turbulence due to the production or a turbulent wake behind the particle in most situations while small particles are known to suppress the turbulence in the flow field. The turbulent interactions between gas and particle require further terms to be included in the transport of momentum and turbulence equations, to account for the interphase transfers. This makes the modelling more difficult and computationally intensive. The reader is referred to the work of Crowe et al. (1998), Zaichik et al. (2008), and Yeoh and Tu (2009) for in-depth coverage of turbulent multiphase flows.

### *6.6.1 Turbulent Fluctuations*

In the Lagrangian method, the effect of turbulence on the transport and dispersion of particles is introduced through the instantaneous fluid velocity, which is composed of the mean velocity plus a fluctuating velocity component. The fluid velocity in Eq (6.21) becomes $u^f = \bar{u} + u'$. In the turbulent flow field, turbulent diffusion by instantaneous flow fluctuations is the dominant mechanism for particle dispersion and depositions. Therefore, it is critical to incorporate an appropriate model for simulating turbulence fluctuations for accurate analysis of particle transport and deposition processes.

The most accurate procedure for simulation of fluctuation velocity is the Direct Numerical Simulation (DNS). The DNS, however, is currently only practical for low Reynolds number duct flows. The use of large eddy simulation (LES) has also attracted considerable attention. In this approach the large eddies are simulated, and the effect of scales smaller than grid size are modelled. While LES can be used for higher Reynolds number flows, the need for computational effort is quite extensive. Also, a completely satisfactory approach for including the subgrid scale fluctuations on particle dispersion is yet to be developed. For most practical applications, however, turbulence fluctuation can be estimated by using a variety of stochastic approaches. Two commonly used stochastic simulation methods that generate appropriate random fields with correct fluctuating velocities and integral time scales are described in this section.

Continuous Filtered White-Noise (CFWN) Model: The Continuous Filtered White-Noise (CFWN) Model was suggested by Thomson (1987) for numerical simulation of turbulent fluctuations and used extensively in the literature and commercial codes (He and Ahmadi 1999; Tian and Ahmadi 2007). In this model, the instantaneous fluid velocity is simulated using the turbulence local mean velocity and mean

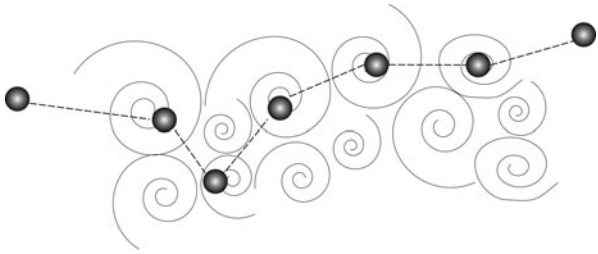

**Fig. 6.16** Random discrete eddies assumption in a turbulent flow field for the Eddy Lifetime model

square fluctuations via the following Langevin equation:

$$\frac{du'_i}{dt} = -\frac{u'_i - U_i}{T_L} + \frac{\sqrt{2\overline{u_i'^2}}}{T_L}\xi_i(t) \tag{6.56}$$

Here $T_L$ is the Lagrangian integral time scale, and $\xi_i(t)$ is a vector Gaussian white-noise random process with spectral density $1/\pi$. The Lagrangian integral time scale $T_L$ is estimated using

$$T_L = C_1 \frac{k}{\varepsilon} \tag{6.57}$$

where $C_1$ is a constant. The solution of Eq. (6.56) provides the fluctuation velocity vector at every time step.

Eddy Interaction Model (EIM): The EIM assumes that the flow field is comprised of turbulent eddies that interacts with the particles (Fig. 6.16). As a particle moves through the flow domain it interacts with the discrete eddy that surrounds it. The fluctuation eddy velocity is given as,

$$u_i' = G\sqrt{\overline{u_i'^2}} \tag{6.58}$$

where $G$ is a zero mean, unit variance normally distributed random number, $\sqrt{\overline{u_i'^2}}$ is the root mean-square (RMS) local fluctuation velocity in the $i$th direction. The time scale $\tau_e$ associated with each eddy (eddy lifetime) is given as

$$\tau_e = 2T_L \tag{6.59}$$

where $T_L$ is given by Eq. (6.57). In addition to the eddy lifetime, a particle eddy crossing time $t_{cross}$ is defined as

$$t_{cross} = -\tau \ln\left[1 - \left(\frac{L_e}{\tau\left|u^f - u^p\right|}\right)\right] \tag{6.60}$$

Here $\tau$ is the particle relaxation time, $L_e$ is the eddy length scale, and $|u^f - u^p|$ is the magnitude of the relative slip velocity. The frequency of the particle encountering turbulence eddies is the reciprocal of the lesser of $\tau_e$ and $t_{cross}$. Therefore, Eq. (6.56) is used to generate a new random fluctuation velocity when the minimum of the eddy lifetime or eddy crossing is reached.

## 6.7 Summary

Governing equations for describing particle dynamics, transport and deposition were described. The Lagrangian or Eulerian approaches for analysing particle motion in a flow domain were introduced, and their advantages and disadvantages were discussed. For example, in the Lagrangian method, individual particle movement and deposition can be visualised, while in the Eulerian approach, particle volume fraction or the concentration representing the amount of particle phase in each cell is evaluated and the mass flux to the wall is computed for the particle phase deposition. These different approaches may be selected for optimal handling different classes of problems.

The most influential force acting on a particle is the dag force, and for most inhaled particles (that are in the micron or submicron size range), the flow around the particle can be typically considered to be in the Stokes flow regime. Additional forces such as the lift, virtual mass, Basset history, and Magnus lift were also described.

For non-spherical particles, equivalent diameters are typically used to provide the description of their transport process based on the more readily available analysis methods for spherical particles. For example, the equivalent aerodynamic diameter is used to describe the flight path of a particle.

Finally the special topics of nanoparticles and turbulent dispersion, which have wide- reaching applications in respiratory flows, were discussed. Having set the foundations for describing fluid and particle flows through their governing equations, the numerical solution procedures for solving the equations will be discussed in the next chapter.

## 6.8 Review Questions

1. Describe the differences in the Lagrangian and Eulerian perspectives in particle flow.
2. Describe the equation (e.g. its type, format and structure) that is used to describe a particle in the Lagrangian frame of reference.
3. How is a dilute particle phase defined? What is the opposite of a dilute phase, and how is this defined?
4. What does one-way and two-way coupling mean?
5. How are particles represented in each computational cell in the Eulerian phase?
6. What is Feret's diameter?
7. What is the Sauter Mean Diameter (SMD), and in what process is it important?
8. For four particles having a geometric diameter of 8, 11, 13, 14 μm, respectively, determine the SMD.
9. Copper particles have a density of 8960 kg/m$^3$, while carbon particles have a density of 2260 kg/m$^3$. If both particles have a geometric diameter of 10 μm, what are their aerodynamic equivalent diameters?
10. If a particle has a short relaxation time, what does this describe about the particle?

11. The density of a wheat grain is approximately 700 kg/m$^3$. At a temperature of 20 °C, what is its relaxation time and stopping distance for a 5 μm particle?
12. In Particle Image Velocimetry, particles are used as gas-tracers to track and visualise the fluid flow. Would a copper particle or carbon particle be more useful for this?
13. Describe the particle Stokes number. How does it differ from the particle relaxation time?
14. Under what particle Reynolds number is Stokes drag applicable?
15. Why does the Cunningham correction ($C_c$) factor need to be considered for submicron particles? What is its value for a 50 μm diameter particle?
16. What causes the so-called Saffman lift force in small particles?
17. Explain how the Magnus effect influences a spinning particle.
18. What is the typical motion or path of a nanoparticle?
19. Would a 1 nm particle disperse radially from its origin more or less than a 100 nm particle would? Explain why?
20. In the Lagrangian model, how are particles affected by the flow field turbulence?

# Chapter 7
# Numerical Methods and Its Solution

## 7.1 Introduction

The conservation equations for fluid flow (i.e. mass, momentum and energy) derived in Chap. 5 are partial differential equations (PDEs) that are non-linear and cannot be solved analytically. The equations for particle flows derived in Chap. 6 can be in Eulerian form which are in the same form as the fluid flow equations, or in Lagrangian form which is an ordinary differential equation (ODE). The single ODE for the particle equation in Lagrangian form, is simpler to solve compared to the coupled non-linear PDEs. In this chapter we first present the discretisation and numerical solution for the set of PDEs, followed by numerical integration techniques for the ODE.

The general transport equation for the flow variables that govern fluid flow must be converted into a set of algebraic equations and solved numerically. There are two processes involved in obtaining the computational solution. Figure 7.1 presents these processes where the first process is the conversion of governing equations (which are partial differential equations) derived in Chap. 5 into algebraic equations and applied to the flow domain that has been divided into smaller cells, i.e. the mesh generation. This process is called *discretisation*. As its name suggests, applying a discretisation on the governing equations means that the solutions obtained are at discrete points in the domain, namely the mesh points. This differs from analytical solutions which provide a continuous solution throughout the domain.

For the discretisation we present two approaches. The first is the finite difference method which is a natural introduction to the discretisation features, and the second approach is the finite volume method which has been readily adopted by many CFD codes. The application of these methods is shown for simplified CFD problems such as a one-dimensional steady state diffusion and a steady state convection-diffusion problem.

The discretisation forms the numerical framework that is ready to be solved, and this process is known as its numerical solution. Direction solution methods and iterative solutions are presented which are basically in the form of matrix solvers. A key ingredient in the numerical solution of convective flow problems is to solve the

J. Tu et al., *Computational Fluid and Particle Dynamics in the Human Respiratory System,* Biological and Medical Physics, Biomedical Engineering,
DOI 10.1007/978-94-007-4488-2_7, © Springer Science+Business Media Dordrecht 2013

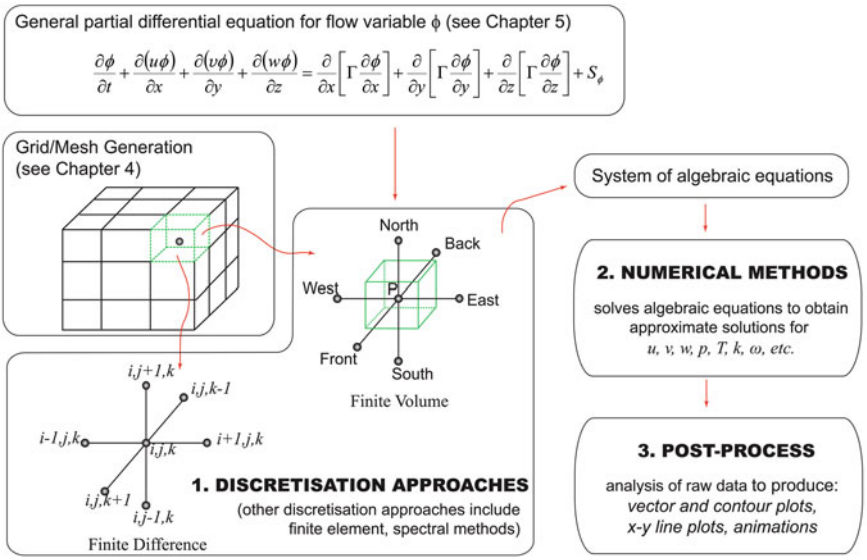


**Fig. 7.1** Overview process of the computational solution procedure

velocity field based on a coupling between the pressure and velocity fields. The well known SIMPLE algorithm is described.

Finally the approximate solutions of the flow variables need to be analysed using advanced visualisation techniques, i.e. through post-processing. The data provided from a numerical simulation in raw form is simply representative numbers stored at locations within the computational domain. The ability to analyse and create meaningful results from this vast array of data is a significant and important part of any CFD solution.

## 7.2 Discretisation of Governing Equations

In this book, amongst the available discretisation methods, we concentrate only on the basic derivations of the finite difference (FD) and finite volume (FV) methods. The finite difference method is illustrated because of its simplicity in formulating the algebraic equations and it also forms the foundation of comprehending the essential basic features of *discretisation*. The finite volume method is employed in the majority of all commercial CFD codes today. We believe the reader should familiarize themselves with this approach because of its ability to be applied to not only structured mesh but also unstructured mesh that is gaining in popularity and usage in handling arbitrary geometrical shapes. Other methods include the finite element method and spectral methods which are not discussed here.

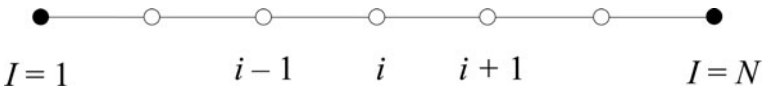


**Fig. 7.2** A representation of a one-dimensional and two-dimensional uniformly distributed cartesian grid for the finite difference method (full symbols denote boundary nodes and open symbols denote computational nodes)

### *7.2.1 Finite Difference Method*

In the finite difference (FD) method, the partial derivatives are approximated by FD equations at each grid nodal point through the Taylor series expansions. These derivatives, replaced by FD approximations, yield an algebraic equation for the flow solution at each grid point. In principle, FD can be applied to any type of grid system. However, the method is more commonly applied to structured grids since it requires a mesh having a high degree of regularity. The grid spacing between the nodal points need not be uniform, but there are limits on the amount of grid stretching or distortion that can be imposed, to maintain accuracy. Additionally the grid is usually taken to be locally structured, which means that each grid node may be considered the origin of a local coordinate system, whose axes coincide with the grid lines. These two grid lines also imply that they do not intersect elsewhere and that any pair of grid lines belonging to the different families intersects only once at the grid point. In three dimensions, three grid lines intersect at each node; none of these lines intersect each other at any other grid nodal point.

Figure 7.2 illustrates a one-dimensional uniformly distributed Cartesian grid commonly used in the FD method. Within this grid system, each node is uniquely identified by an index, which represents nodal points on the grid lines ($i$). In two-dimensions the indices are ($i$, $j$) and in three-dimensions ($i$, $j$, $k$). The neighbouring nodes are defined by increasing or reducing one of the indices by unity. The spacing of the grid points in the $x$ direction are assumed to be uniform and given by $\Delta x$ respectively. The spacing of $\Delta x$ need not necessarily be uniform and it could have easily been dealt with using totally unequal spacing in both directions. As is frequently handled in CFD, the numerical calculations can be performed in a transformed computational space that has uniform spacing in the transformed independent variables but still corresponds to a non-uniform spacing in the physical space.

Before we introduce the discretisation through the Taylor series expansion for the FD equations, let us consider a derivative and its definition from first principles as

$$f'(a) = \lim_{h \to 0} \frac{f(a+h) - f(a)}{h} \tag{7.1}$$

then its approximation is simply

$$f'(a) \approx \frac{f(a+h) - f(a)}{h} \tag{7.2}$$

where $h$ must be small enough to provide a reasonable approximation to represent the actual continuous function. This is the basic idea behind the FD method which will be demonstrated.

The Taylor series is defined as:

$$f(x) \approx f(a) + \frac{f'(a)}{1!}(x-a) + \frac{f''(a)}{2!}(x-a)^2 + \frac{f^{(3)}(a)}{3!}(x-a)^3 + \cdots \quad (7.3)$$

which can be rewritten in sigma notation as

$$f(x) \approx \sum_{n=0}^{\infty} \frac{f^{(n)}(a)}{n!}(x-a)^n$$

Referring to Fig. 7.2, at the point $(i)$, we let there be a generic flow field variable $\phi$. Following the Taylor series, we substitute $f(a)$ as $\phi_i$ and $f(x)$ as $\phi_{i+1}$. This gives the variable at point $(i+1)$ expanded about the point $(i)$ as

$$\phi_{i+1} = \phi_i + \left(\frac{d\phi}{dx}\right)_i \Delta x + \left(\frac{d^2\phi}{dx^2}\right)_i \frac{\Delta x^2}{2} + \left(\frac{d^3\phi}{dx^3}\right)_i \frac{\Delta x^2}{6} + \cdots \quad (7.4)$$

Rearranging to obtain the derivative we get

$$\left(\frac{d\phi}{dx}\right)_i = \frac{\phi_{i+1} - \phi_i}{\Delta x} + \left(\frac{d^2\phi}{dx^2}\right)_i \frac{\Delta x}{2} + \left(\frac{d^3\phi}{dx^3}\right)_i \frac{\Delta x^2}{6} + \cdots \quad (7.5)$$

If we only take the first term on the right hand side as the approximation for the partial derivative of the left hand side, we have

$$\left(\frac{\partial\phi}{\partial x}\right)_i \approx \frac{\phi_{i+1} - \phi_i}{\Delta x} \quad (7.6)$$

which is in the same form as that presented in Eq. (7.2). The terms that are omitted constitute the truncation error, which we can write as

$$\left(\frac{\partial\phi}{\partial x}\right)_i = \frac{\phi_{i+1} - \phi_i}{\Delta x} + \underbrace{\mathrm{O}(\Delta x)}_{\textit{Truncation error}}$$

$$\text{where} \quad \mathrm{O}(\Delta x) = \left(\frac{\partial^2\phi}{\partial x^2}\right)_i \frac{\Delta x}{2} + \left(\frac{\partial^3\phi}{\partial x^3}\right)_i \frac{\Delta x^2}{6} + \cdots \quad (7.7)$$

The term $\mathrm{O}(\Delta x)$ signifies the truncation error of the FD approximation, which measures the accuracy of the approximation and determines the rate at which the error decreases based on the lowest-order term in the truncated terms. In Eq. (7.7), this value is $\Delta x$ which is of first order and hence the FD is *first-order-accurate*. Additionally since the Eq. (7.7) describes the function from a point $(i)$ to a position in front of it at $(i+1)$, the FD formulation is called a *forward difference* as it is formulated and therefore biased from information to the right or in front of the origin.

Similarly the Taylor series expansion for the variable at point $(i-1)$ with respect to point $(i)$ is

$$\phi_{i-1} = \phi_i - \left(\frac{d\phi}{dx}\right)_i \Delta x + \left(\frac{d^2\phi}{dx^2}\right)_i \frac{\Delta x^2}{2} - \left(\frac{d^3\phi}{dx^3}\right)_i \frac{\Delta x^3}{6} + \cdots \tag{7.8}$$

and rearranging to obtain the derivative we get

$$\left(\frac{d\phi}{dx}\right)_i = \frac{\phi_i - \phi_{i-1}}{\Delta x} + \underbrace{\mathrm{O}(\Delta x)}_{\textit{Truncation error}}$$

$$\text{Where} \quad \mathrm{O}(\Delta x) = \left(\frac{d^2\phi}{dx^2}\right)_i \frac{\Delta x}{2} - \left(\frac{d^3\phi}{dx^3}\right)_i \frac{\Delta x^2}{6} + \cdots \tag{7.9}$$

Equation (7.9) is the *backward difference* approximation that uses information to the left or behind of the origin and is first-order-accurate.

If we now combine the forward and backward difference equations by subtracting Eq. (7.8) from Eq. (7.4), so that we obtain information from points in front of and behind the origin $(i)$, we get

$$\phi_{i+1} - \phi_{i-1} = 2\left(\frac{d\phi}{dx}\right)_i \Delta x + 0 + 2\left(\frac{d^3\phi}{dx^3}\right)_i \frac{\Delta x^2}{6} + \ldots \tag{7.10}$$

and rearranging to obtain the derivative we get

$$\left(\frac{d\phi}{dx}\right)_i = \frac{\phi_{i+1} - \phi_{i-1}}{2\Delta x} + \underbrace{\mathrm{O}(\Delta x^2)}_{\textit{Truncation error}}$$

$$\text{Where} \quad \mathrm{O}(\Delta x^2) = \left(\frac{d^3\phi}{dx^3}\right)_i \frac{\Delta x^2}{3} + \cdots \tag{7.11}$$

This equation is called *central difference,* is dependent equally on values to both sides of the node at $x$ and is *second-order-accurate* because the truncation error is of order 2. The accuracy term is a major simplification and its validity depends on the size of $\Delta x$, where smaller $\Delta x$ generally provides increased accuracy.

For the grid points in the $y$-direction, where the nodal points vary with $j$ the difference equations are obtained in the same manner as those for the $y$-direction, which are given as

$$\left(\frac{d\phi}{dy}\right)_j = \frac{\phi_{j+1} - \phi_j}{\Delta y} + \underbrace{\mathrm{O}(\Delta y)}_{\textit{Truncation error}} \quad \textit{Forward difference} \tag{7.12}$$

$$\left(\frac{d\phi}{dy}\right)_j = \frac{\phi_j - \phi_{j-1}}{\Delta y} + \underbrace{\mathrm{O}(\Delta y)}_{\textit{Truncation error}} \quad \textit{Backward difference} \tag{7.13}$$

$$\left(\frac{d\phi}{dy}\right)_j = \frac{\phi_{j+1} - \phi_{j-1}}{2\Delta y} + \underbrace{\mathrm{O}(\Delta y^2)}_{\textit{Truncation error}} \quad \textit{Central difference} \tag{7.14}$$

The examples so far have dealt with first order derivatives. For second order derivatives, such as the diffusion term in the momentum equation, $\nu\left(\frac{\partial^2 u}{\partial x^2}+\frac{\partial^2 u}{\partial y^2}\right)$ (Eq. 5.11 from Chap. 5) we sum the Taylor series expansions from Eq. (7.4) and Eq. (7.8), which gives

$$\left(\frac{d^2\phi}{dx^2}\right)_i = \frac{\phi_{i+1}-2\phi_i+\phi_{i-1}}{(\Delta x)^2} + \underbrace{\mathrm{O}(\Delta x^2)}_{\textit{Truncation error}} \qquad \textit{Central difference} \tag{7.15}$$

This equation represents the central finite difference for the second order derivative with respect to $x$ evaluated at the point $(i)$. The approximation is second order accurate. An analogous expression can easily be obtained for the second order derivative with respect to $y$, which results in

$$\left(\frac{d^2\phi}{dy^2}\right)_j = \frac{\phi_{j+1}-2\phi_j+\phi_{j-1}}{(\Delta y)^2} + \underbrace{\mathrm{O}(\Delta y^2)}_{\textit{Truncation error}} \quad \textit{Central difference} \tag{7.16}$$

The Taylor series expansion for time derivatives can also be obtained similar to those of the Taylor series expansion for space, Eq. (7.1). Since the numerical solution is more likely to be marched continuously in discrete time interval of $\Delta t$, the finite approximation derived for the first order spatial derivatives applies equally for the first order time derivative. For a forward difference approximation in time,

$$\left(\frac{d\phi}{dt}\right) = \frac{\phi_i^{n+1}-\phi_i^n}{\Delta t} + \underbrace{\mathrm{O}(\Delta t)}_{\textit{Truncation error}} \qquad \textit{Forward difference} \tag{7.17}$$

The above equation introduces a truncation error of $\mathrm{O}(\Delta t)$. More accurate approximations to the time derivative can be obtained through the consideration of additional discrete values of $\phi_I$ in time.

*Visual Representation* We have presented a number of different finite-difference expressions each in 1D form. In this section we present them in 2D form and in its geometric representation to give the reader a better understanding of each approximation. The ordinary differential operator $d$ is now replaced with the partial differential operator $\partial$ and so $d\phi/dx$ becomes $\partial\phi/\partial x$. Figure 7.3 shows the grid points that are involved and their contribution in terms of being added or subtracted towards the FD approximation for the first order derivative $\partial\phi/\partial x$.
First order derivative $\partial\phi/\partial x$.

Similarly the geometric representation is shown for the second order derivative in Fig. 7.4. It should be noted that there are two circles at the origin point $(i, j)$ to emphasise that the nodal point is used twice to obtain the FD difference between the forward and the backward point. We also notice that the mesh size given by the grid distance $\Delta x$, or $\Delta y$ has more significance in the approximation as it is now to the power of 2 in comparison to the first order derivatives which were to the power of 1.

Second order derivative $\partial^2\phi/\partial x^2$.

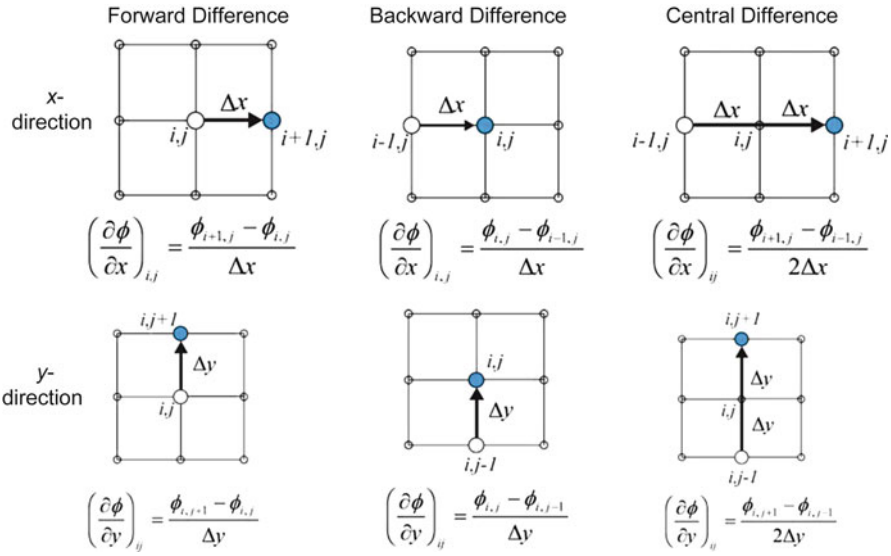


**Fig. 7.3** FD approximations for the first order derivatives $\partial\phi/\partial x$ and $\partial\phi/\partial y$. *White circles* represent a negative value, While *shaded circles* represent a positive value, at a specified point each of which contribute towards the FD approximation

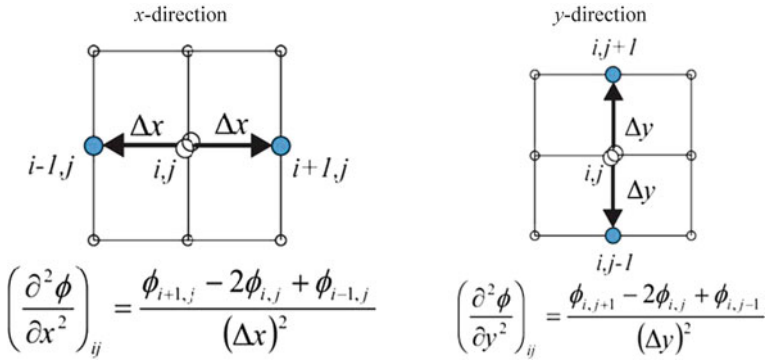


**Fig. 7.4** FD approximations for the second order derivatives $\partial^2\phi/\partial x^2$ and $\partial^2\phi/\partial y^2$. *White circles* represent a negative value, While *shaded circles* represent a positive value, at a specified point each of which contribute towards the FD approximation

We further explore the idea behind finite difference approximations that is borrowed directly from the definition of derivatives. A geometric interpretation of the forward, backward and central difference approximations is shown in Fig. 7.5. The first order derivative $\partial\phi/\partial x$ at the point $i$ in the direction of $x$ is the slope of tangent to the curve $\phi(x)$ at that point and is the line marked 'exact' in the figure. Its slope can be approximated by the slope of a line passing through the neighbouring points $(i + 1)$ and $(i - 1)$ on the curve. The forward difference is evaluated by the slope

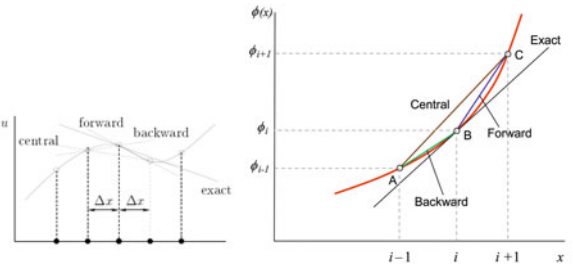


**Fig. 7.5** Finite difference representation of the first order derivative for $\partial\,\phi/\partial x$

BC between the points $i$ and $i+1$ while the backward difference is achieved by the slope AB between the points $i-1$ and $i$. The line labelled 'central' represents the approximation by a central difference that evaluates the slope AC. From the figure, it can be seen that some approximations are better than others. The line for the central difference, indicated by the slope AC, appears to be closer to the slope of the exact line; if the function $\phi(x)$ were a second-order polynomial and the points equally spaced in the $x$-direction, the slopes would match exactly. It also appears that the quality of approximation improves when additional points are made closer to point, i.e. as the grid is refined, the approximation improves.

### *7.2.2 Finite Volume Method*

Since fluid flow moves through a domain, it is intuitive to represent the fluid dynamics and its properties across the domain through smaller subdomains – precisely mesh cells acting as control volumes. If we consider a single control volume (Fig. 7.6) and apply the fundamental physical principle that mass is conserved, then

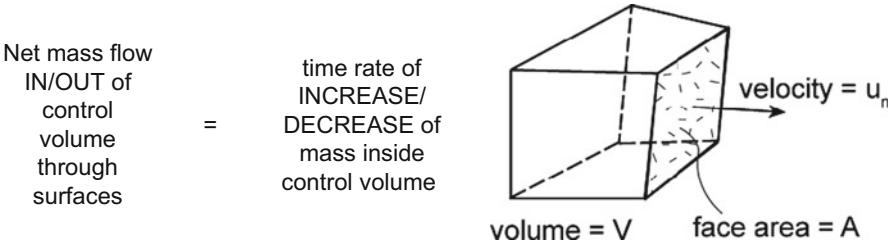


**Fig. 7.6** Conservation principle applied to a single control volume

That is, '*the flux of a variable (i.e. net rate of a mass of a variable that crosses the control surface) is equal to the net change in quantity of the variable inside the control volume'*. This conservation principle is the cornerstone of the finite volume (FV) method. Since the control volumes can take arbitrary shapes, it allows for more flexibility of representing the grid by either structured or unstructured mesh, as it is not limited by the cell shape. A disadvantage of FV is that it is susceptible to

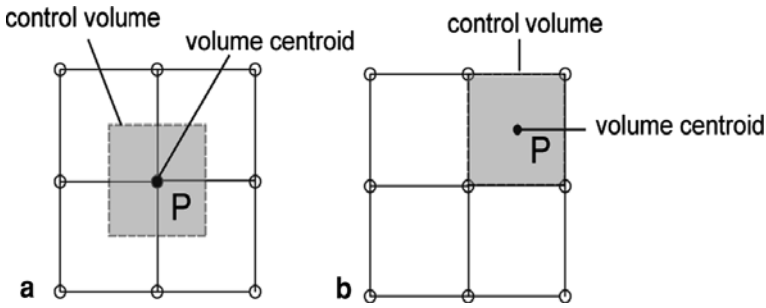


**Fig. 7.7** Finite volume method showing **a** vertex centred and **b** cell-centred

false/numerical diffusion when simple numerics and poor choice of mesh design is applied.

The first step of the FV method is to divide the computational domain into a finite number of discrete contiguous control volumes. Within each control volume, there is a centroid where the variable values are calculated and stored. These values can be coincident with a grid node, and hence is a *vertex-centred* FV mesh or the control volume can coincide with the grid boundaries and nodes, and hence the centroid is *cell-centred* (Fig. 7.7). In either case, interpolation is used to express variable values at the control volume surfaces in terms of the values at the control volume centre and suitable quadrature formulae are applied to approximate the surface and volume integrals.

In a control volume, the bounding surface areas of the element are the faces in which the flux of a dependent variable moves across. Here, the surface areas in the normal direction to the volume surfaces as indicated in Fig. 7.8 shows the projected surface areas where each face is projected in the normal direction ($\vec{n}$). The projected areas are positive if their outward normal vectors from the volume surfaces are directed in the same directions of the Cartesian coordinate system; otherwise they are negative.

To begin the discretisation let us consider the first order differential term, $\partial\phi/\partial x$ integrated over a control volume so that the rate of change of the variable $\phi$ with respect to $x$ is defined by the total change that is occurring inside the control volume,

$$\frac{\partial \phi}{\partial x} = \frac{1}{\Delta V} \int_V \frac{\partial \phi}{\partial x} dV$$

By applying Gauss' divergence theorem to the volume integral, we relate the volume integral to the net flux of $\phi$ that crosses the bounding surface of the control volume.

$$\underbrace{\frac{1}{\Delta V} \int_V \frac{\partial \phi}{\partial x} dV}_{\text{total change inside control volume}} = \underbrace{\frac{1}{\Delta V} \int_A \phi dA^x \approx \frac{1}{\Delta V} \sum_{i=1}^{N} \phi_i A_i^x}_{\text{net flux crossing control surface}} \rightarrow \frac{\partial \phi}{\partial x} \approx \frac{1}{\Delta V} \sum_{i=1}^{N} \phi_i A_i^x \tag{7.18}$$

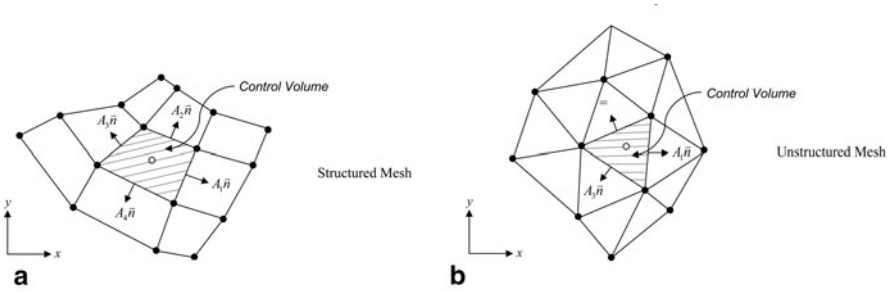


**Fig. 7.8** A representation of **a** Structured and **b** Unstructured mesh for the finite volume method (full symbols denote element vertices and open symbols at the centre of the control volumes denote computational nodes)

where $\phi_i$ are the variable values at the elemental surfaces and $N$ denotes the number of bounding surfaces on the elemental volume. Equation (7.18) applies for any type of finite volume element that can be represented within the numerical grid. For a quadrilateral element in two dimensions for the structured mesh as seen in Fig. 7.8, $N$ has the value of four since there are four bounding surfaces of the element. In three dimensions, for a hexagonal element, $N$ becomes six. Similarly, the first order derivative for $\phi$ in the $y$ direction is obtained in exactly the same fashion, which can be written as

$$\underbrace{\frac{1}{\Delta V}\int_V \frac{\partial \phi}{\partial y} dV}_{\text{total change inside control volume}} = \underbrace{\frac{1}{\Delta V}\int_A \phi dA^y \approx \frac{1}{\Delta V}\sum_{i=1}^{N} \phi_i A_i^y}_{\text{net flux crossing control surface}} \rightarrow \frac{\partial \phi}{\partial y} \approx \frac{1}{\Delta V}\sum_{i=1}^{N} \phi_i A_i^y \tag{7.19}$$

As a demonstration of the FV approach, let us discretise the two-dimensional continuity equation: $\frac{\partial u}{\partial x} + \frac{\partial v}{\partial y} = 0$ on a structured uniform grid arrangement with data points stored at cell-centres as shown in Fig. 7.9. The centroid of the control volume is indicated by the point $P$, which is surrounded by the adjacent control volumes having their respective centroids indicated by the points: east, $E$; west, $W$; north, $N$; and south, $S$. This notation is referred to as the *compass point notation*, where the upper case letters (*P, E, W, N, S*) refer to the location of the nodes, and the lower case letters (*e, w, n, s*) refer to the cell faces. The control volume face between points $P$ and $E$ is denoted by the area $A_e^x$. Subsequently, the rest of the control volume faces are respectively: $A_w^x$, $A_n^y$ and $A_s^y$. Since it is a 2D representation the area values are given with a unit depth so that $A^x = \Delta y \cdot 1$, and $A^y = \Delta x \cdot 1$.

The control volume integration, forms the key step of the finite volume method. Applying Eq. (7.18) and (7.19) yields the following expressions

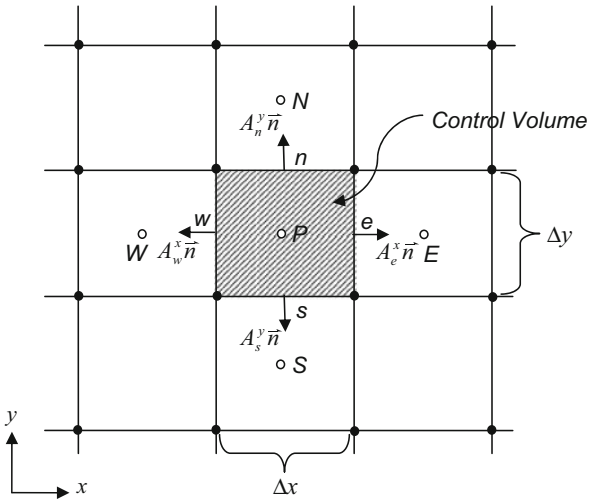


**Fig. 7.9** Control volume for the two-dimensional continuity equation problem

$$\frac{1}{\Delta V}\int_V \frac{\partial u}{\partial x} dV = \frac{1}{\Delta V}\int_A u dA^x \approx \frac{1}{\Delta V}\sum_{i=1}^{4} u_i A_i^x = \frac{1}{\Delta V}\left(u_e A_e^x - u_w A_w^x + u_n \overbrace{A_n^x}^{=0} - u_s \overbrace{A_s^x}^{=0}\right)$$

and

$$\frac{1}{\Delta V}\int_V \frac{\partial v}{\partial x} dV = \frac{1}{\Delta V}\int_A v dA^x \approx \frac{1}{\Delta V}\sum_{i=1}^{4} v_i A_i^y = \frac{1}{\Delta V}\left(v_e A_e^y - v_w A_w^y + v_n \overbrace{A_n^y}^{=0} - v_s \overbrace{A_s^y}^{=0}\right)$$

For the structured uniform grid arrangement, the projection areas $A_n^x$ and $A_s^x$ in the $x$ direction, and the projection areas, $A_e^y$ and $A_w^y$ in the $y$ direction, are zero. One important aspect demonstrated here by the finite volume method is that it allows direct discretisation in the physical domain (or in a body-fitted conformal grid) without the need of transforming the continuity equation from the physical domain to a computational domain. So far we have only applied the conservation principle to a control volume. We need to determine how the velocities $u$ and $v$ varies between the cell centroids and its bounding surface, and this is performed typically by interpolation methods. If we use a linear variation and since the grid has been taken to be uniform, with cell-centred nodes, then the face velocities $u_e$, $u_w$, $v_n$ and $v_s$ of each control volume is defined as,

$$u_e = \frac{u_P + u_E}{2}; \quad u_w = \frac{u_P + u_W}{2}; \quad v_n = \frac{v_P + v_N}{2}; \quad v_s = \frac{v_P + v_S}{2}$$

By substituting the above expressions to the discretised form of the velocity first order derivatives, Eqs. (7.18) and (7.19), the final form of the discretised continuity equation becomes

$$\left(\frac{u_P + u_E}{2}\right) A_e^x - \left(\frac{u_P + u_W}{2}\right) A_w^x + \left(\frac{v_P + v_N}{2}\right) A_n^y - \left(\frac{v_P + v_S}{2}\right) A_s^y = 0$$

From Fig. 7.9, $A_e^x = A_w^x = \Delta y$ and $A_n^y = A_s^y = \Delta x$, the above equation can then be expressed by

$$\left(\frac{u_P + u_E}{2}\right)\Delta y - \left(\frac{u_P + u_W}{2}\right)\Delta y + \left(\frac{v_P + v_N}{2}\right)\Delta x - \left(\frac{v_P + v_S}{2}\right)\Delta x = 0$$

and reduced to

$$\frac{u_E - u_W}{2\Delta x} + \frac{v_N - v_S}{2\Delta y} = 0$$

For a uniform grid arrangement, the distances between $P$ and $E$ and $W$ and $P$ are all equal to $\Delta x$. Similarly, the distances between $P$ and $N$ and $S$ and $P$ are all equal and given by $\Delta y$. If the finite difference method is applied to discretise the continuity equation through the central difference scheme, we obtain the same discretised form of the equation at point $P$ as compared to the form derived through the finite volume method. The accuracy obtained is of second order, as inferred from the finite difference central difference scheme.

The purpose of this example is to demonstrate the use of the finite volume method to discretise the two-dimensional continuity equation and compare its form to the finite difference approximation. We observed that the exact representation of the discretised form for the continuity equation can be obtained by applying either the finite volume or finite difference method for a uniform grid arrangement. Nevertheless, there are two major advantages that the finite volume method holds over the finite difference method. Firstly, it has good conservation properties from the physical view point and secondly, it allows the accommodation of complicated physical domains to be discretised in a simpler way rather than the need to transform the equation to generalized coordinates in the computational domain.

From the above example, the first order derivatives that appear in the continuity equation have been discretised through the finite volume method. Similarly, discretisation of the second order derivative in the $x$ direction can be evaluated by

$$\left(\frac{\partial^2\phi}{\partial x^2}\right) = \frac{1}{\Delta V}\int_{\Delta V}\frac{\partial^2\phi}{\partial x^2}dV = \frac{1}{\Delta V}\int_{A}\frac{\partial\phi}{\partial x}dA^x \approx \frac{1}{\Delta V}\sum_{i=1}^{N}\left(\frac{\partial\phi}{\partial x}\right)_i A_i^x \tag{7.20}$$

An analogous expression can be also easily obtained for the second order derivative with respect to $y$, which is given by

$$\left(\frac{\partial^2\phi}{\partial y^2}\right) = \frac{1}{\Delta V}\int_{\Delta V}\frac{\partial^2\phi}{\partial y^2}dV = \frac{1}{\Delta V}\int_{A}\frac{\partial\phi}{\partial y}dA^y \approx \frac{1}{\Delta V}\sum_{i=1}^{N}\left(\frac{\partial\phi}{\partial y}\right)_i A_i^y \tag{7.21}$$

From Eqs (7.20) and (7.21), it can be seen that in order to approximate the second order derivatives, the respective first order derivatives of $(\partial\phi/\partial x)_i$ and $(\partial\phi/\partial y)_i$ appearing in the equations are required to be evaluated at the elemental surfaces of the control volume.

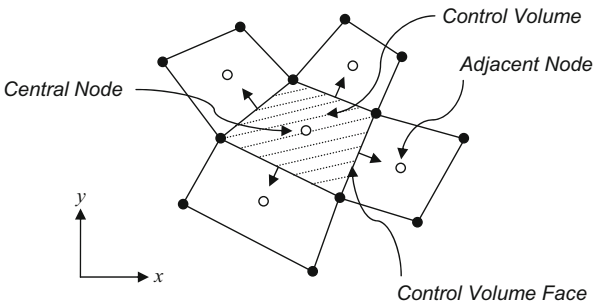


**Fig. 7.10** A representation of a structured mesh arrangement (open symbols at the centre of the control volumes denote computational nodes) for the evaluation of the face first order derivatives

The approximation of the first order derivatives at the control volume faces is usually determined from the discrete $\phi$ values of the surrounding elements. For example, in a structured mesh arrangement as shown in Fig. 7.10 where the central control volume (shaded) is surrounded by only one adjacent control volume at each face, the first order derivatives could be approximated by a piecewise linear gradient profile between the central and adjacent nodes. This will be shown in the examples in Sect. 7.2.4.

### *7.2.3 One-dimensional Steady State Diffusion*

The general transport equation for fluid flow is given in Chap. 5 by:

$$\underbrace{\frac{\partial \phi}{\partial t}}_{\substack{\text{local}\\ \text{accleration}}} + \underbrace{\frac{\partial (u\phi)}{\partial x} + \frac{\partial (v\phi)}{\partial y} + \frac{\partial (w\phi)}{\partial z}}_{\text{convection}} = \underbrace{\frac{\partial}{\partial x}\left[\Gamma \frac{\partial \phi}{\partial x}\right] + \frac{\partial}{\partial y}\left[\Gamma \frac{\partial \phi}{\partial y}\right] + \frac{\partial}{\partial z}\left[\Gamma \frac{\partial \phi}{\partial z}\right]}_{\text{diffusion}} + \underbrace{S_\phi}_{\text{source}} \tag{7.22}$$

For a steady state, one dimensional flow without any convection term, we are left with the diffusion equation. It is the simplest transport process and is commonly used to describe heat conduction by diffusion.

$$0 = \frac{\partial}{\partial x}\left(\Gamma \frac{\partial \phi}{\partial x}\right) + S_\phi \tag{7.23}$$

where $\Gamma$ is the diffusion coefficient and $S\phi$ is the source term. In this example we will demonstrate the techniques to attain the algebraic form of the governing equation. It will be shown that this discretised equation can be extended to accommodate for two- and three-dimensional diffusion problems. As an example, a numerical method is developed by initially considering the simplest transport process: pure

diffusion in steady state. We further simplify the problem by working through a one-dimensional steady state diffusion equation to demonstrate the application of discretisation techniques to attain the algebraic form of the governing equation. It will be seen that this discretised equation can be extended to accommodate for two- and three-dimensional diffusion problems.

#### 7.2.3.1 Finite Difference Discretisation

*Mesh creation* The first step is to create a geometric domain with discrete nodal points. Let us consider a general nodal point $P$ and its surrounding neighbouring nodal points to the west and east, $W$ and $E$, for the one-dimensional geometry as shown in Fig. 7.11. The uniform grid has spacing of $\Delta x$.

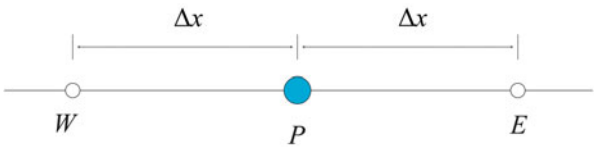


**Fig. 7.11** Representation of the *uniform grid* spacing along the $x$ direction for the one-dimensional geometry

*Discretisation* The next step is to discretise the governing equation around the nodal point $P$. We focus only on one point at a time to establish a general set of equations which then can be applied to other nodal points. To derive a suitable expression for the FD method, Eq. (7.23) needs to be expanded into its non-conservative form, which is given by

$$0 = \frac{d\Gamma}{dx}\frac{d\phi}{dx} + \Gamma\frac{d^2\phi}{dx^2} + S_\phi \tag{7.24}$$

By applying the central differencing of the first order derivative and second order derivative equations (see Fig. 7.3) the discretised terms of Eq. (7.24) are

$$\frac{d\Gamma}{dx} = \frac{(\Gamma_E - \Gamma_W)}{2\Delta x}; \quad \frac{d\phi}{dx} = \frac{(\phi_E - \phi_W)}{2\Delta x}; \quad \Gamma\frac{d^2\phi}{dx^2} = \Gamma_P\frac{(\phi_E - 2\phi_P + \phi_W)}{\Delta x^2}$$

Putting it together we get:

$$\frac{(\Gamma_E - \Gamma_W)}{2\Delta x}\frac{(\phi_E - \phi_W)}{2\Delta x} + \Gamma_P\frac{(\phi_E - 2\phi_P + \phi_W)}{\Delta x^2} + S_\phi = 0 \tag{7.25}$$

It is convenient to re-arrange and group the terms together, which gives

$$\frac{2\Gamma_P}{\Delta x^2}\phi_P = \left[\frac{(\Gamma_E - \Gamma_W)}{4\Delta x^2} + \frac{\Gamma_P}{\Delta x^2}\right]\phi_E + \left[-\frac{(\Gamma_E - \Gamma_W)}{4\Delta x^2} + \frac{\Gamma_P}{\Delta x^2}\right]\phi_W + S_\phi \tag{7.26}$$

The coefficients of $\phi_E$ and $\phi_W$ and $\phi_P$ can be defined as

$$a_P\phi_P = a_E\phi_E + a_W\phi_W + b \tag{7.27}$$

Where

$$a_E = \frac{(\Gamma_E - \Gamma_W)}{4\Delta x^2} + \frac{\Gamma_P}{\Delta x^2}; \quad a_W = -\frac{(\Gamma_E - \Gamma_W)}{4\Delta x^2} + \frac{\Gamma_P}{\Delta x^2}; \quad a_P = \frac{2\Gamma_P}{\Delta x^2}; \quad b = S_\phi \tag{7.28}$$

#### 7.2.3.2 Finite Volume Discretisation

*Mesh creation* For the FV method the geometric domain is divided into finite control volumes surrounding the nodal points $W$, $P$ and $E$ as shown in Fig. 7.12. The distances between the nodes $W$ and $P$, and between nodes $P$ and $E$, are identified by the respective notations $\Delta x_W$ and $\Delta x_E$. For this one-dimensional case, the control volume width surrounding the nodal point $P$ is $\Delta x$ since $\Delta y$ and $\Delta z$ have dimensions of unit length.

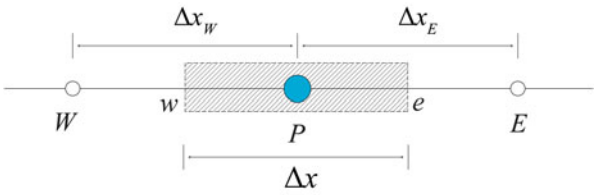


**Fig. 7.12** Representation of a control volume around node $P$ in a one-dimensional domain using the finite volume method. $W$: west node, $w$: west face, $E$: east node, $e$: east face

*Discretisation* The FV discretisation involves the integration of the governing equation over a control volume in order to achieve the conservation principle. Therefore if integrate and then apply Gauss' divergence theorem as before in Eq. (7.18) we get

$$\frac{d}{dx}\left(\Gamma\frac{d\phi}{dx}\right) = \frac{1}{\Delta V}\int_{\Delta V}\frac{d}{dx}\left(\Gamma\frac{d\phi}{dx}\right)dV = \frac{1}{\Delta V}\int_{A}\left(\Gamma\frac{d\phi}{dx}\right)dA^x \approx \frac{1}{\Delta V}\sum_{i=1}^{2}\left(\Gamma\frac{d\phi}{dx}\right)_i A_i^x$$

integration divergence theorem

(7.29)

The projected areas $A_i^x$ is the cross-sectional area of the control volume face, and for a one-dimensional case are given by $A_1^x = -A_w$ and $A_2^x = A_e$. Its value is of unity length squared, since $\Delta y$ and $\Delta z$ have dimensions of unit length. The finite control volume $\Delta V$ is therefore the width $\Delta x$. The diffusive flux at the control volume faces, (east, $e$ and west, $w$) are

$$\left(\Gamma\frac{d\phi}{dx}\right)_e A_E - \left(\Gamma\frac{d\phi}{dx}\right)_w A_w \tag{7.30}$$

The diffusion gradient $d\phi/dx$ at the control volume faces, (east, $e$ and west, $w$) needs to be defined algebraically, and a linear gradient approximation is used spanning

the nodal points between $W$ and $P$ and between $P$ and $E$. The diffusive fluxes are evaluated as

$$\left(\Gamma\frac{d\phi}{dx}\right)_e A_E = \Gamma_e A_E\left(\frac{\phi_E-\phi_P}{\Delta x_E}\right);$$

$$\left(\Gamma\frac{d\phi}{dx}\right)_w A_W = \Gamma_w A_W\left(\frac{\phi_P-\phi_W}{\Delta x_W}\right) \tag{7.31}$$

and the source term is

$$\frac{1}{\Delta V}\int_{\Delta V} S_\phi dV = S_\phi \tag{7.32}$$

where $S_\phi$ is assumed to be constant within $\Delta V$ which is the finite control volume. The final form of the discretised equation becomes

$$\frac{\Gamma_e A_E}{\Delta V}\left(\frac{\phi_E-\phi_P}{\Delta x_E}\right)-\frac{\Gamma_w A_W}{\Delta V}\left(\frac{\phi_P-\phi_W}{\Delta x_W}\right)+S_\phi=0 \tag{7.33}$$

It can be seen that the discretised equation represents the difference between the diffusive fluxes of $\phi$ at the east and west faces of the control volume equal to the generation of $\phi$ and constitutes a balance equation for $\phi$ over the control volume. Equation (7.33) can be re-arranged as

$$\frac{1}{\Delta V}\left(\frac{\Gamma_e A_E}{\Delta x_E}+\frac{\Gamma_w A_W}{\Delta x_W}\right)\phi_P=\frac{1}{\Delta V}\left(\frac{\Gamma_e A_E}{\Delta x_E}\right)\phi_E+\frac{1}{\Delta V}\left(\frac{\Gamma_w A_W}{\Delta x_W}\right)\phi_W+S_\phi \tag{7.34}$$

which gives the rate of change per unit volume. Multiplying out the volume term and grouping together the coefficients of $\phi_E$, $\phi_W$, and $\phi_P$ as $a_E$, $a_W$ and $a_P$, gives

$$a_P\phi_P = a_E\phi_E + a_W\phi_W + b \tag{7.35}$$

Where

$$a_P = a_E + a_W;\quad a_E=\frac{\Gamma_e A_E}{\Delta x_E};\quad a_W=\frac{\Gamma_w A_W}{\Delta x_W};\quad b=S_\phi\Delta V \tag{7.36}$$

If the values for the diffusion coefficient, $\Gamma$ at the control volume faces, $e$ and $w$ need to be known then for a uniform grid, a linear interpolation can be performed and we get:

$$\Gamma_e=\frac{\Gamma_P+\Gamma_E}{2};\quad \text{and}\quad \Gamma_w=\frac{\Gamma_P+\Gamma_W}{2}$$

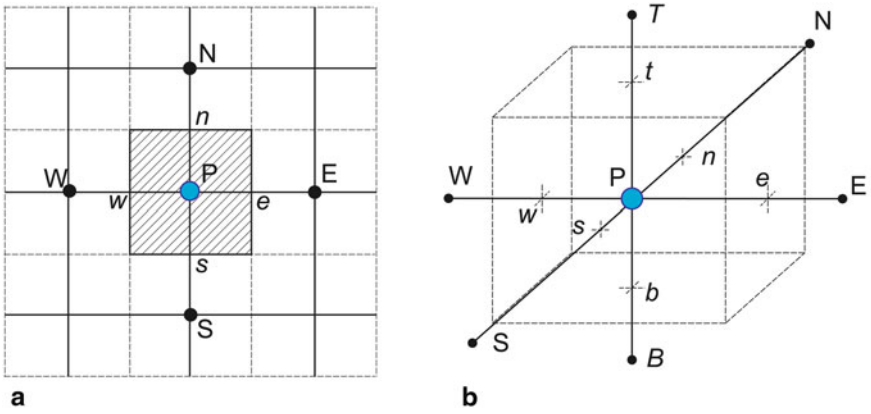


**Fig. 7.13** Nodal point *P*, and its surrounding neighbour nodes in a structured **a** 2D grid and **b** 3D grid

**Table 7.1** The coefficients at each node of a control volume in 1D, 2D, and 3D

| | $a_E$ | $a_W$ | $a_S$ | $a_N$ | $a_B$ | $a_T$ |
|---|---|---|---|---|---|---|
| 1D | $\frac{\Gamma_e A_e}{\Delta x_{PE}}$ | $\frac{\Gamma_w A_w}{\Delta x_{WP}}$ | – | – | – | – |
| 2D | $\frac{\Gamma_e A_e}{\Delta x_{PE}}$ | $\frac{\Gamma_w A_w}{\Delta x_{WP}}$ | $\frac{\Gamma_s A_s}{\Delta y_{SP}}$ | $\frac{\Gamma_n A_n}{\Delta y_{PN}}$ | – | – |
| 3D | $\frac{\Gamma_e A_e}{\Delta x_{PE}}$ | $\frac{\Gamma_w A_w}{\Delta x_{WP}}$ | $\frac{\Gamma_s A_s}{\Delta y_{SP}}$ | $\frac{\Gamma_n A_n}{\Delta y_{PN}}$ | $\frac{\Gamma_b A_b}{\Delta z_{BP}}$ | $\frac{\Gamma_t A_t}{\Delta z_{PT}}$ |

**Extension to 2D and 3D** The discretisation method for 2D and 3D domains follows the same steps to determine a nodal point, P with its neighbouring nodes being E, W, (east, west) and S, N (south and north for 2D) and E, W, S, N and T, B (top and bottom for 3D). The corresponding cell volume faces have the notation of *e, w, s, t*, and *b* and is illustrated in Fig. 7.13.

The diffusion equation in 2D and 3D are:

$$0 = \frac{\partial}{\partial x}\left[\Gamma \frac{\partial \phi}{\partial x}\right] + \frac{\partial}{\partial y}\left[\Gamma \frac{\partial \phi}{\partial y}\right]$$

$$\text{and} \quad 0 = \frac{\partial}{\partial x}\left[\Gamma \frac{\partial \phi}{\partial x}\right] + \frac{\partial}{\partial y}\left[\Gamma \frac{\partial \phi}{\partial y}\right] + \frac{\partial}{\partial z}\left[\Gamma \frac{\partial \phi}{\partial z}\right]$$

The discretised equations can be summarised in the general form as:

$$a_P \phi_P = \sum a_{nb} \phi_{nb} + b$$

where the subscript *nb* represents the neighbouring nodes. The coefficients for each neighbouring node is summarised in Table 7.1 for 1D, 2D, and 3D.

**Comparison of the FD and FV discretisations** Although the same algebraic form of equation for the steady-state one-dimensional diffusion process is obtained, different expressions for the coefficients of $a_E$, $a_W$ and $a_P$ are derived as seen in Eq. (7.28) for the FD method and Eq. (7.35) for the FV method. Nevertheless, let us consider for a special case where the diffusion coefficient, $\Gamma$ is spatially invariant and the mesh is uniformly distributed. The coefficients in the algebraic equation for the FD and FV methods, both reduce to

$$a_E = \frac{\Gamma}{\Delta x^2}; \quad a_W = \frac{\Gamma}{\Delta x^2}; \quad a_P = a_E + a_W; \quad b = S_\phi$$

where the control volume is $\Delta x$ (uniform grid and $\Delta y$, $\Delta z$ is unity). From the example of the continuity equation discretisation, the resultant algebraic equations are exactly the same whether adopting either the FD or FV discretisation. It should be noted that the FD method generally requires a uniformly distributed mesh in order to apply the first and second order derivative approximations to the governing equation. For an arbitrary grid shape, some mathematical manipulation (e.g. transformation functions) is required to transform Eq. (7.24), into a computational domain in generalized coordinates before applying the FD approximations. This requirement is however not a prerequisite for the FV method. Because of the availability of having different control volume sizes, any non-arbitrary grid could therefore be easily accommodated.

The FD method is mathematically derived from the Taylor series, whereas the FV method applies the conservation principle by integration of the variable over the control volume, and thus it retains this physical significance throughout the discretisation process. Almost all commercial CFD codes adopt the finite volume discretisation of the Navier-Stokes equation to obtain numerical solutions for complex fluid flow problems as the mesh is not restricted to structured-type elements but can include a variety of unstructured-type elements of different shapes and sizes.

**Worked Example** Consider a steady heat conduction problem in a large plate with a uniform heat generation, $q = 500\ \text{kW/m}^3$. The left and right walls have temperatures $T_L = 100\ ^\circ\text{C}$ and $T_R = 400\ ^\circ\text{C}$, and the thickness of the plate is $L = 2.40\ \text{cm}$. The diffusion coefficient $\Gamma$ governing the heat conduction problem becomes the thermal conductivity $k$ of the material which is constant at $k = 6\ W/m^2.\text{K}$. Assuming that the dimensions in the $y$ direction and $z$ direction are so large that the temperature gradients are only significant in the $x$ direction, we can reduce the problem to a one-dimensional analysis. We apply the FV method to obtain the solution of this simple heat conduction problem (Fig. 7.14).

Firstly, let us divide the domain into four control volumes giving $\Delta x = 0.006\ \text{m}$. After, we will investigate the influence of a larger number of control volumes. There are four nodal points, each representing the central location for the four control volumes. For illustration purposes a unit area is considered in the $y - z$ plane, and thus $\Delta V = \Delta x$. The general discretised form of the one-dimensional diffusion equation for point P (node 3) is

$$a_P T_P = a_E T_E + a_W T_W + b$$

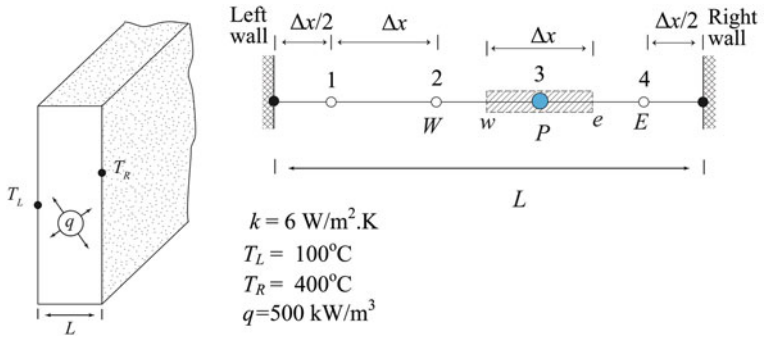


**Fig. 7.14** Representation of a large plate with heat generation

Since the thermal conductivity is constant, we can define $k = k_e = k_w$ and the volumetric source term $S_\phi$ equal to q. The coefficients from Eq. (7.36) are:

| $a_P$ | $a_E$ | $a_W$ | b |
|---|---|---|---|
| $a_E + a_W$ | $\frac{kA}{\Delta x}$ | $\frac{kA}{\Delta x}$ | $q\Delta x$ |

For the control volumes containing nodes 1 and 4 we apply a linear approximation for the temperatures between the boundary points and its adjacent nodal point of the control volume. At the west face of the control volume at the left wall, the temperature is known by $T_L$ (Fig. 7.15).

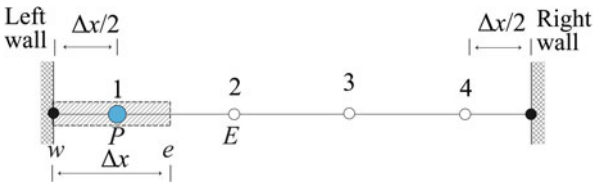


**Fig. 7.15** Finite volume discretisation of the large brick plate domain, showing the first control volume

For a constant thermal conductivity and uniform heat generation, the FV discretisation equation for node 1 is

$$\frac{k}{\Delta V}\left(\frac{dT}{dx}\right)_e A - \frac{k}{\Delta V}\left(\frac{dT}{dx}\right)_w A + q = 0 \tag{7.37}$$

Introducing linear approximations to the gradients at the east and west faces of the control volume 1, gives

$$\frac{kA}{\Delta V}\left(\frac{T_E - T_P}{\Delta x}\right) - \frac{kA}{\Delta V}\left(\frac{T_P - T_L}{\Delta x/2}\right) + q = 0$$

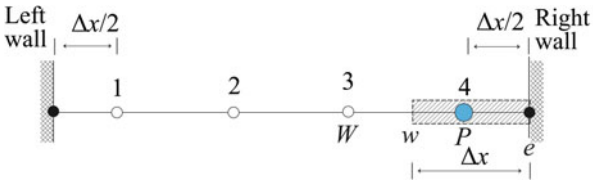


**Fig. 7.16** Finite volume discretisation of the large brick plate domain, showing the fourth control volume

The above equation can be re-arranged to yield the discretised equation for node 1 by

$$\left(\frac{2kA}{\Delta x}+\frac{kA}{\Delta x}\right)T_P=\left(\frac{kA}{\Delta x}\right)T_E+(0)T_W+\left(\frac{2kA}{\Delta x}\right)T_L+q\Delta V$$

Also the volume $\Delta V$ has unit depth and height $\Delta z=\Delta y=1$, then $\Delta V=\Delta x\Delta y\Delta z=\Delta x$

$$a_P T_P=a_E T_E+a_W T_W+b$$

where the coefficients are

| $a_P$ | $a_E$ | $a_W$ | b |
|---|---|---|---|
| $a_E+a_W+\frac{2kA}{\Delta x}$ | $\frac{kA}{\Delta x}$ | 0 | $q\Delta x+\frac{2kA}{\Delta x}T_L$ |

At node 4, the temperature of the east face of the control volume is known (Fig. 7.16).

The node is similarly treated and we obtain

$$kA\left(\frac{T_R-T_P}{\Delta x/2}\right)-kA\left(\frac{T_P-T_W}{\Delta x}\right)+q\Delta V=0$$

with the discretised equation for node 4 given as:

$$a_P T_P=a_E T_E+a_W T_W+b$$

where the coefficients are

| $a_P$ | $a_E$ | $a_W$ | b |
|---|---|---|---|
| $a_E+a_W+\frac{2kA}{\Delta x}$ | 0 | $\frac{kA}{\Delta x}$ | $q\Delta x+\frac{2kA}{\Delta x}T_R$ |

Substitution of numerical values for the thermal conductivity $k=5\ \mathrm{W/m^2.K}$, heat generation $q=500\,\mathrm{kW/m^3}$, $\Delta x=0.008\,\mathrm{m}$ and unit area $A=1\,\mathrm{m^2}$ throughout provides the coefficients of the discretised equation summarized in Table 7.2.

The resulting set of algebraic equations rearranged in matrix form as

$$\begin{bmatrix} 3000 & -1000 & 0 & 0 \\ -1000 & 2000 & -1000 & 0 \\ 0 & -1000 & 2000 & -1000 \\ 0 & 0 & -1000 & 3000 \end{bmatrix}\begin{bmatrix} T_1 \\ T_2 \\ T_3 \\ T_4 \end{bmatrix}=\begin{bmatrix} 203000 \\ 3000 \\ 3000 \\ 803000 \end{bmatrix}$$

**Table 7.2** The Coefficients at each node of the control volumes

| Node | $a_P$ | $a_E$ | $a_W$ | $b$ |
|---|---|---|---|---|
| 1 | 3,000 | 1,000 | 0 | 3,000+2,000 $T_L$ |
| 2 | 2,000 | 1,000 | 1,000 | 3,000 |
| 3 | 2,000 | 1,000 | 1,000 | 3,000 |
| 4 | 3,000 | 0 | 1,000 | 3,000+2,000 $T_R$ |

The above set of equations yields the steady state temperature distribution for the given situation. For a one-dimensional steady heat conduction process we obtained the algebraic equations in matrix form. Because the problem only involves a small number of nodes, the matrix can be solved easily. Analytically the matrix can be solved by methods such as Gaussian elimination which is discussed later in Sect. 7.3. This matrix algorithm will be discussed in the next section.

### *7.2.4 One-dimensional Steady State Convection-diffusion*

Respiratory flows involve moving air (considered as an incompressible fluid) and as such the effects of convection are important. The convection terms moves the scalar variable, $\phi$ through the flow domain in the flow direction determined by the velocity components while the diffusion process distributes the variable in all directions by its diffusion coefficient, $\Gamma$ and its gradient. If we ignore the source terms and focus on the steady convection and diffusion of the variable $\phi$ in one dimension, its equation is

$$\frac{d(u\phi)}{dx} = \frac{d}{dx}\left[\Gamma \frac{d\phi}{dx}\right] \tag{7.38}$$

Note that the convection diffusion equation, Eq. (7.38), is representative of the momentum equation if $\phi = u$ and $\Gamma = \nu$, and the energy equation if $\phi = T$ and $\Gamma = \frac{\nu}{\mathrm{Pr}}$. In this section we demonstrate the FV approach. The 1D mesh for nodal point $P$, and its neighbouring nodes is given in Fig. 7.17.

Integration of Eq. (7.38) over the control volume gives

$$\underbrace{(u\phi)_e - (u\phi)_w}_{\text{convective flux}} = \underbrace{\left(\Gamma_e \frac{d\phi}{dx}\right)_e - \left(\Gamma_w \frac{d\phi}{dx}\right)_w}_{\text{diffusive flux}}$$

where the two diffusive fluxes are approximated with a linear interpolation as

$$\left(\Gamma_e \frac{d\phi}{dx}\right)_e = \Gamma_e \frac{\phi_E - \phi_P}{\Delta x_{PE}} = D_e(\phi_E - \phi_P);$$

$$\left(\Gamma_w \frac{d\phi}{dx}\right)_w = \Gamma_w \frac{\phi_P - \phi_W}{\Delta x_{WP}} = D_w(\phi_P - \phi_W)$$

where $D_e = \Gamma_e/\Delta x_{PE}$ and $D_w = \Gamma_w/\Delta x_{WP}$

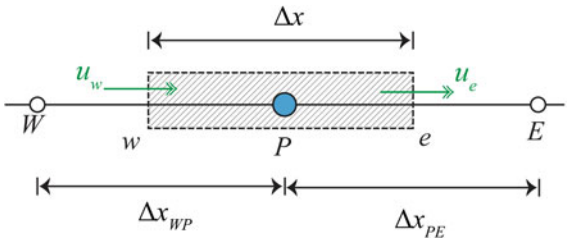


**Fig. 7.17** A one-dimensional mesh used to solve Eq. (7.38). The mesh is uniform, but the finite volume method is not restricted to uniform meshes

**Central Differencing (CD)** The values of $\phi_e$ and $\phi_w$ in the convective flux needs to be evaluated, since the values of the scalar are stored at the nodes *P, E*, and *W*. Using central differencing and for a uniform grid, we obtain

$$\phi_e = (\phi_P + \phi_E)/2 \quad \phi_w = (\phi_W + \phi_P)/2$$

Putting the terms together, and rearranging, the discretised equation becomes

$$\frac{u_e}{2}(\phi_P + \phi_E) - \frac{u_w}{2}(\phi_W + \phi_P) = D_e(\phi_E - \phi_P) - D_w(\phi_P - \phi_W)$$

$$\left[\left(D_e - \frac{u_e}{2}\right) + \left(D_w + \frac{u_w}{2}\right) + (u_e - u_w)\right]\phi_P = \left(D_e - \frac{u_e}{2}\right)\phi_E + \left(D_w + \frac{u_w}{2}\right)\phi_W$$

We can rearrange the terms to identify the coefficients of $\phi_E$ and $\phi_W$ and $\phi_P$ as

$$a_P\phi_P = a_E\phi_E + a_W\phi_W \tag{7.39}$$

Where

$$a_P = a_E + a_W + (u_e - u_w); \quad a_E = D_e - \frac{u_e}{2}; \quad a_W = D_w + \frac{u_w}{2}; \tag{7.40}$$

The central differencing discretisation is second order accurate, however it is unable to exhibit any bias in the flow direction. It has been well documented (Patankar 1980; Versteeg and Malalasekera 2007) that the scheme fails in strongly convective flows as it is unable to identify the flow direction. To overcome the problem due to central differencing, variations to the interpolation scheme are made. Two commonly used schemes are the upwind differencing and QUICK which are introduced here. The reader should be aware that other schemes exist, such as Total Varaible Diminishing (TVD), which is not shown here. Through the central differencing approximation, the face value at *e* is always assumed to be weighted by the influence of the available variables at the neighbouring points; the downstream value at *E* is always required during the evaluation of *e* which is usually not known *a priori* in the majority of flow cases. However, by exerting an unequal weighting influence, a numerical solution can be designed to recognize the direction of the flow in order to appropriately determine the interface values. This is essentially the hallmark of the *upwind* or *donor-cell* concept.

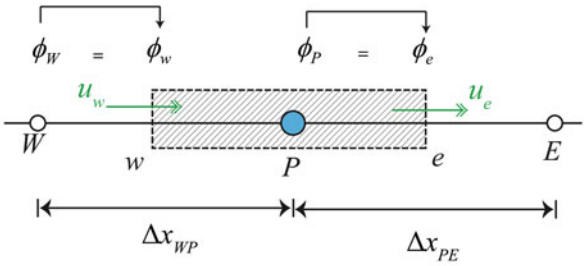


**Fig. 7.18** Control volume representation for UD discretisation of nodal point $P$

**Upwind Differencing (UD)** In the upwind differencing, the value of a cell face is taken to be equal to the value at the upstream node. If we limit our example to a flow direction from left to right, then $\phi_e = \phi_P$ and $\phi_w = \phi_W$ (Fig. 7.18).

The resulting discretised equation becomes

$$u_e\phi_P - u_w\phi_W = D_e(\phi_E - \phi_P) - D_w(\phi_P - \phi_W)$$

and rearranging the terms to identify the coefficients of $\phi_E$ and $\phi_W$ and $\phi_P$ as before

$$a_P\phi_P = a_E\phi_E + a_W\phi_W \tag{7.41}$$

Where

$$a_P = a_E + a_W + (u_e - u_w); \quad a_E = D_e; \quad a_W = D_w + u_w; \tag{7.42}$$

Effectively, the convection term is discretised by applying a backward difference scheme which is first order accurate. If a flow direction is from right to left then a forward difference scheme is used (Fig. 7.19).

**QUICK** The Quadratic Upstream Interpolation for Convective Kinetics, (QUICK) scheme uses a quadratic approximation across two variable points at the upstream and one at the downstream. The unequal weighting influence of this particular scheme still hinges on the knowledge biased towards the upstream flow conditions. Again

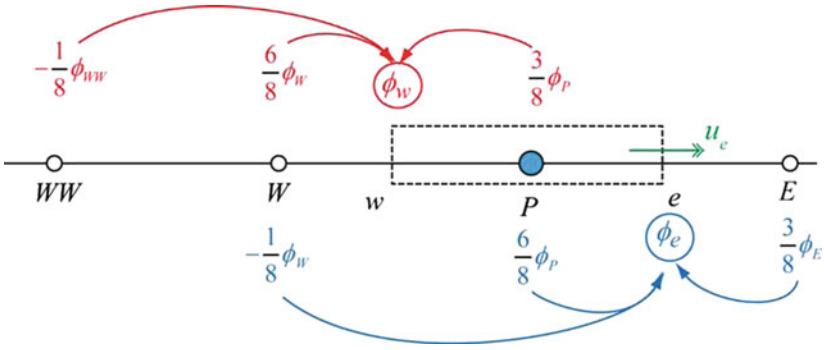


**Fig. 7.19** Control volume representation for the QUICK discretisation of nodal point $P$

if we limit our example to a flow direction from left to right the nodal points are evaluated as:

$$\phi_w = -\frac{1}{8}\phi_{WW} + \frac{3}{8}\phi_P + \frac{6}{8}\phi_W \quad \text{and} \quad \phi_e = -\frac{1}{8}\phi_W + \frac{6}{8}\phi_P + \frac{3}{8}\phi_E$$

The resulting discretised equation becomes

$$u_e\left(-\frac{1}{8}\phi_w + \frac{6}{8}\phi_P + \frac{3}{8}\phi_E\right) - u_w\left(-\frac{1}{8}\phi_{WW} + \frac{3}{8}\phi_P + \frac{6}{8}\phi_W\right)$$
$$= D_e(\phi_E - \phi_P) - D_w(\phi_P - \phi_W)$$

and rearranging the terms to identify the coefficients of $\phi_E$ and $\phi_W$ and $\phi_P$ as before

$$a_P\phi_P = a_E\phi_E + a_W\phi_W \tag{7.43}$$

Where

$$a_P = a_E + a_W + a_{WW} + (u_e - u_w); \quad a_E = D_e - \frac{3}{8}u_e;$$
$$a_W = D_w + \frac{6}{8}u_w + \frac{1}{8}u_e \tag{7.44}$$

**Comparisons of schemes** During discretisation we have the coefficient $a_p$ equal to the sum of all its neighbouring nodes,

$$a_p\phi_p = \sum a_{nb}\phi_{nb} + b$$

In CD it was shown that for a uniform mesh, $a_E = D_e - \frac{u_e}{2}$ which means that the coefficient becomes negative if $2D_e < u_e$ and this leads to problems with the solution where large undershoots and overshoots occur in the solution, eventually causing the numerical calculations to diverge. The dimensionless Peclet number, Pe

$$Pe = \frac{uL_c}{\Gamma} \tag{7.45}$$

which is a measure of the ratio of convective to diffusive transport of $\phi$. If we consider the characteristic length scale $L_c$ as the mesh cell length $\Delta x$, then the quantity is referred to as the cell Peclet number,

e.g. across face *e,* $$Pe_c = \frac{u_e\Delta x}{D_e}.$$

From the above description, we see that problems can arise if the convective fluxes are too large in comparison to the diffusive fluxes and that as long as $Pe_c \leq 2$ then we are guaranteed with positive coefficients and the solution can converge. Similarly in the QUICK scheme we obtain $a_E = D_e - \frac{3}{8}u_e$ which means that $Pe_c \leq 8/3$. Equation (7.45) shows that the Pe number is a function of the grid size, and this

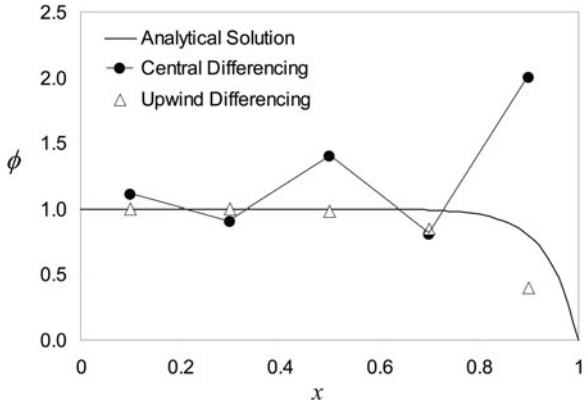


**Fig. 7.20** Flow variable solution using CD and UD schemes. Un-physical oscillations are produced with the CD scheme whereas the UD shows a more realistic solution

implies a minimum spatial grid size to ensure that Pe is small enough for the discretisation scheme. We notice that the problem of negative coefficients arises due to the arithmetic averaging. In UD, the value of $\phi$ on a cell face is determined by the flow direction and the neighbouring coefficients are guaranteed to have positive values (Eq. (7.42)).

To demonstrate the dependence of Pe and the discretisation scheme, on the solution, we can compare the numerical solution with the exact analytical solution. The analytical solution for a 1D steady convection-diffusion problem is

$$\frac{d(u\phi)}{dx} - \frac{d}{dx}\left[\Gamma\frac{d\phi}{dx}\right] = 0 \quad \rightarrow \quad \frac{\phi - \phi_0}{\phi_L - \phi_0} = \frac{\exp(ux/\Gamma) - 1}{\exp(uL/\Gamma) - 1}$$

In this example, the length of the domain is 1 m which is divided into five control volumes. The boundary conditions include $\phi_0 = 0$ and $\phi_L = 1$. The velocity, $u$ is 1.6 m/s and diffusion coefficient, $\Gamma$ has a value of 0.1. The resulting Pe number is Pe = 3.2 and as such leads to an unstable solution when the CD scheme is applied. Figure. 7.20 shows the 'undershoots' and 'overshoots' occurring in the solution for CD. A similar oscillating pattern is found for the QUICK scheme as well (although not shown in the figure) since it has a restriction of Pe < 8/3. The UD has no restrictions on the Pe number and produces the trendline of the analytical solution. However it can be seen that the accuracy of the UD solution drops off as $x$ approaches 1. For both discretisation schemes, improved results can be obtained if the grid spacing/mesh resolution is refined (i.e. increase the number of control volumes).

**False diffusion** Despite the UD scheme being unconditionally stable, it is essentially a backward differencing formula of first order accuracy and it produces artificial/false diffusion. False diffusion is the non-physical diffusion of a transported variable $\phi$ that results in the variable to be wrongly distributed through the flow domain. This occurs when the flow direction is not aligned with the grid lines and hence a nonzero gradient exists in the direction normal to flow. To demonstrate this, the scalar variable $\phi$, and its transport equation is simplified to a 2D pure convection only $\left(\text{no diffusion term, and hence} \frac{d(u\phi)}{dx} + \frac{d(v\phi)}{dy} = 0\right)$. When the flow moves through the domain horizontally in line with the rectangular grid as shown in Fig. 7.21a, the UD

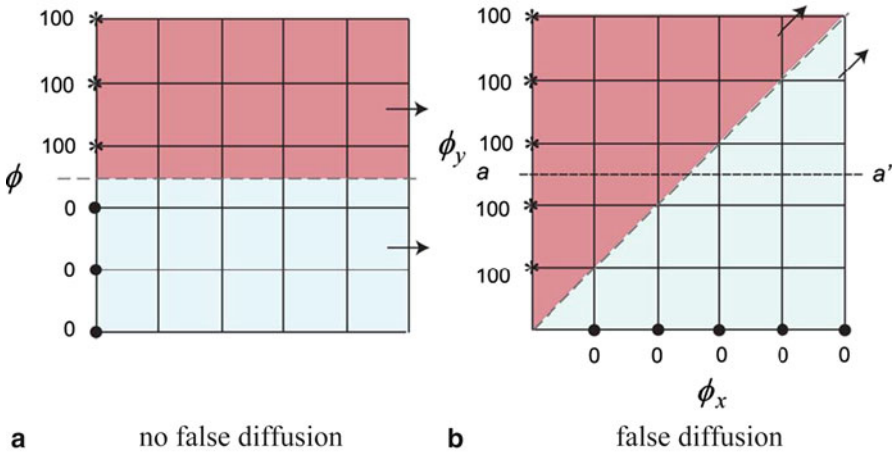


**Fig. 7.21** Transport of the scalar variable $\phi$ by pure convection. Line *a*-*a*' is a horizontal line half way up the domain. **a** The variable is convected through the domain aligned with the computational grid lines. **b** The variable is convected through the domain at an angle of 45° to the computational grid lines

solution provides a good representation and no false diffusion occurs. However, if the flow is now oriented at 45° to the grid lines (Fig. 7.21b), then false diffusion will occur.

In the absence of physical diffusion, the transported variable should exhibit a uniform temperature of 0 below the dashed line, and 100 above the dashed line for all nodal points in the domain. If we take the temperature values along the horizontal line half way up the domain labelled as *a*-*a*'in Fig. 7.21, the results however, show that the UD scheme (using a $5 \times 5$ control volume discretised domain), cannot capture the step profile of the exact solution. Instead the variable, $\phi$ exhibits false diffusion behaviour whereby it is spread across the domain and distributed more evenly rather than producing a step profile. Improvements to the result can be obtained if the mesh is refined. The UD scheme using a $10 \times 10$ control volume mesh shows that the profile is closer to the exact solution.

To illustrate why this occurs let us look at the UD scheme in more detail. The discretised 1D convection-diffusion Eq. (7.38) is rewritten with the diffusion term set to zero:

$$\frac{d(u\phi)}{dx} = 0 \quad \Rightarrow \quad u\left(\frac{\phi_P - \phi_W}{\Delta x}\right) = 0 \tag{7.46}$$

assuming $u_e = u_w$. The convective fluxes are defined at the control volume faces as $\phi_e = \phi_P$ and $\phi_w = \phi_W$. Let us expand $\phi_W$ through a Taylor series expansion and hence

$$\phi_W = \phi_P - \Delta x \frac{d\phi}{dx} + \frac{\Delta x^2}{2!}\frac{d^2\phi}{dx^2} - \ldots$$

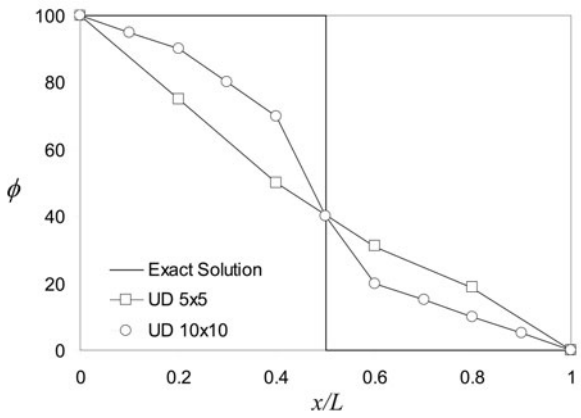


**Fig. 7.22** Solutions for the convection transport of $\phi$

and rearranging

$$\frac{\phi_P - \phi_W}{\Delta x} = \frac{d\phi}{dx} - \frac{\Delta x}{2}\frac{d^2\phi}{dx^2} + \mathrm{O}(\Delta x^2) \tag{7.47}$$

If we substitute Eq. (7.47) into Eq. (7.46) we get

$$u\frac{d\phi}{dx} - \frac{u\Delta x}{2}\frac{d}{dx}\left[\frac{d\phi}{dx}\right] + \mathrm{O}(\Delta x^2) = 0 \tag{7.48}$$

Equation (7.48) represents the continuous equation of the UD scheme that we have applied using finite volume approach. The first term, $u\frac{d\phi}{dx}$ is the convective transport of $\phi$ and the remaining terms are in the form are the additional terms form the Taylor series expansion which consists of the order error term. It can be seen that this term resembles the diffusion term in the convection-diffusion Eq. (7.38). Therefore we see that although we apply a discretisation on pure convection, the UD results in a solution that has some diffusion occurring. This false diffusion occurs through the numerical scheme as shown and is not a physical mechanism such as the diffusion that occurs through viscosity. The false diffusion coefficient is proportional to the control volume size and therefore refining the mesh will reduce the influence of the false diffusion as was seen earlier (Fig. 7.22). While the UD scheme can provide converging results under situations where $\mathrm{Pe} > 2$, it is not entirely accurate given that it is first order accurate and it is prone to false diffusion.

## 7.3 Numerical Solution

A system of linear or non-linear algebraic equations is produced from the discretisation step, and this can be solved by some numerical methods. The complexity and size of the set of equations depends on the dimensionality and geometry of the physical problem. In this section we present essentially two types of numerical methods: *direct methods* and *iterative methods*.

Direct methods compute the solution to a problem in a finite number of steps. One example is the Gaussian elimination, and the TDMA (TriDiagonal Matrix Algorithm) described in Sect. 7.3.1 which applies matrix algebra such as row operations to transform the matrix into a form that is easier to solve. Typically direct methods are the preferred solution method for low to medium sized systems (e.g. < 1000 equations) as it is computationally inexpensive and requires a minimum amount of storage in the core memory.

In contrast to direct methods, iterative methods are based on repeated applications of an algorithm leading to its eventual convergence after a number of repetitions. A convergence criterion is specified to determine when a suitable solution has been reached. Typically iterative methods are used for very large systems. For non-linear problems, they are used out of necessity but are just as valuable for sparse linear systems. Well-known point-by-point methods such as Jacobi and Gauss-Siedel are described in Sect. 7.3.2 in order to provide the reader some basic understanding of iterative methods. Other variants from these two iterative methods will also be described particularly those algorithms that are used in solving CFD problems.

### *7.3.1 Direct Solution Methods*

One of the most basic methods for solving linear systems of algebraic equations is the *Gaussian elimination*. The algorithm derives from the basis of systematic reduction of large systems of equations to smaller ones. Let us suppose that the systems of equations can be written in the form:

$$A\phi = B$$

where $\phi$ is the unknown nodal variables. Matrix $A$ contains non-zero coefficients of the algebraic equations as illustrated below:

$$A = \begin{bmatrix} A_{11} & A_{12} & A_{13} & \cdots & A_{1n} \\ A_{21} & A_{22} & A_{23} & \cdots & A_{2n} \\ A_{31} & A_{32} & A_{33} & \cdots & A_{3n} \\ \vdots & \vdots & \vdots & \ddots & \vdots \\ A_{n1} & A_{n2} & A_{n3} & \cdots & A_{nn} \end{bmatrix}$$

while $B$ comprises of known values of $\phi$, for example, that are given by the boundary conditions or source/sink terms. It can be observed that the diagonal coefficients of the matrix $A$ are represented by the entries of $A_{11}$, $A_{22}$,..., $A_{nn}$. The first step is to apply *Forward Elimination* which involves eliminating the entries below the diagonal to yield a lower triangle of zero's. This means eliminating the elements of $A_{21}$, $A_{31}$, $A_{32}$,..., $A_{nn\text{-}1}$ by replacing them with zeros. We begin the elimination process by considering the first column elements of $A_{21}$, $A_{31}$, ..., $A_{n1}$ in the matrix $A$. By multiplying the first row of the matrix by $A_{21}/A_{11}$ and subtracting these values from the second row; all the elements in the second row are subsequently modified, which

includes the terms in $B$ on the right hand side of the equations. The other elements $A_{31}, A_{41}, \ldots, A_{n1}$ in the first column of matrix $A$ are treated similarly by repeating this process down the first column (e.g. Row3 − Row1 × $A_{31}/A_{11}$), all the elements below $A_{11}$ are reduced to zero. The same procedure is then applied for the second column, (for all elements below $A_{22}$) and so forth until the process reaches the $n-1$ column. Note that at each stage we need to divide by $A_{\mathrm{nn}}$ and therefore it is imperative that the value is non-zero. If it is, then row exchange with another row below that has a non-zero needs to be performed.

After this process is complete, the original matrix $A$ becomes an *upper triangular matrix* that is given by:

$$U = \begin{bmatrix} A_{11} & A_{12} & A_{13} & \cdots & A_{1n} \\ 0 & A_{22} & A_{23} & \cdots & A_{2n} \\ 0 & 0 & A_{33} & \cdots & A_{3n} \\ \vdots & \vdots & \vdots & \ddots & \vdots \\ 0 & 0 & 0 & \cdots & A_{nn} \end{bmatrix}$$

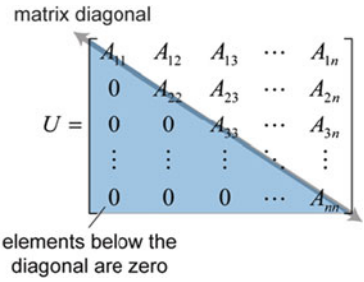


All the elements in the matrix $U$ except the first row differ from those in the original matrix $A$ and our systems of equations can be rewritten in the form:

$$U\phi = B$$

The upper triangular system of equations can now be solved by the *Back Substitution* process. It is observed that the last row of the matrix $U$ contains only one non-zero coefficient, $A_{nn}$, and its corresponding variable $\phi_n$ is solved by

$$\phi_n = \frac{B_n}{U_{nn}}$$

The second last row in matrix $U$ contains only the coefficients $A_{n\text{-}1,n}$ and $A_{nn}$ and, once $\phi_n$ is known, the variable $\phi_{n\text{-}1}$ can be solved. By proceeding up the rows of the matrix we continue substituting the known variables and $\phi_i$ is solved in turn. The general form of equation for $\phi_i$ can be expressed as:

$$\phi_i = \frac{B_i - \sum_{j=i+1}^{n} A_{ij}\phi_j}{A_{ii}} \tag{7.49}$$

It is not difficult to see that the bulk of the computational effort is in the *forward elimination* process; the back substitution process requires less arithmetic operations and is thus much less costly. Gaussian elimination can be expensive especially for a full matrix containing a large number of unknown variables to be solved but it is as good as any other methods that are currently available.

In the worked example in Sect. 7.2.3 the matrix obtained is in the form of a tri-diagonal matrix which is a special case of matrices that occurs frequently. A tri-diagonal matrix has nonzero elements only on the diagonal plus or minus one column such as:

$$A = \begin{bmatrix} A_{11} & A_{12} & 0 & \cdots & 0 \\ A_{21} & A_{22} & A_{23} & \cdots & 0 \\ 0 & A_{32} & A_{33} & \cdots & 0 \\ \vdots & \vdots & \vdots & \ddots & \vdots \\ 0 & 0 & 0 & \cdots & A_{nn} \end{bmatrix}$$

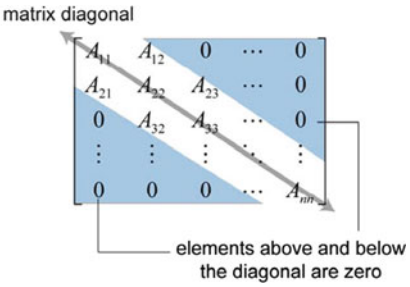


In this form it is advantageous to consider variants of Gaussian elimination such as the *TriDiagonal Matrix Algorithm* (**TDMA**), also known as the Thomas algorithm. Let us consider a general tri-diagonal form of a system of algebraic equations as:

$$\begin{bmatrix} A_{11} & A_{12} & 0 & 0 & 0 & 0 & 0 \\ A_{21} & A_{22} & A_{23} & 0 & 0 & 0 & 0 \\ 0 & \cdots & \cdots & \cdots & 0 & 0 & 0 \\ 0 & 0 & A_{ii-1} & A_{ii} & A_{ii+1} & 0 & 0 \\ 0 & 0 & 0 & \cdots & \cdots & \cdots & 0 \\ 0 & 0 & 0 & 0 & A_{nn-2} & A_{n-1n-1} & A_{n-1n} \\ 0 & 0 & 0 & 0 & 0 & A_{nn-1} & A_{nn} \end{bmatrix} \begin{bmatrix} \phi_1 \\ \phi_1 \\ \cdots \\ \phi_i \\ \cdots \\ \phi_{n-1} \\ \phi_n \end{bmatrix} = \begin{bmatrix} B_1 \\ B_2 \\ \cdots \\ B_i \\ \cdots \\ B_{n-1} \\ B_n \end{bmatrix}$$

The TDMA like the Gaussian elimination solves the system of equations above in two parts: *forward elimination* and *back substitution*. For the *forward elimination* process, the neighbouring entries are eliminated below the diagonal to yield zero entries. This means replacing the elements of $A_{21}$, $A_{32}$, $A_{43}$,..., $A_{nn\text{-}1}$ with zeros. For the first row, the diagonal entry $A_{11}$ is normalized to unity and the neighbouring entry $A_{12}$ and the matrix $B$ term $B_1$ are modified according to

$$A'_{12} = \frac{A_{12}}{A_{11}}, \quad B'_1 = \frac{B_1}{A_{11}} \tag{7.50}$$

Like the Gaussian elimination, by multiplying the first row of the matrix by $A_{21}$ and subtracting it from the second row; all the elements in the second row are subsequently modified (where $A_{21}$ becomes zero), which also include the terms in $B$ on the right hand side of the equations. Applying the same procedure to the rest of the rows of the matrix, the neighbouring element entries and the matrix $B$ terms in general form are:

$$A'_{ii+1} = \frac{A_{ii+1}}{A_{ii} - A_{ii-1}A'_{i-1i}}, \quad B'_i = \frac{B_i - A_{ii-1}B'_{i-1}}{A_{ii} - A_{ii-1}A'_{i-1i}} \tag{7.51}$$

The matrix containing the non-zero coefficients is therefore manipulated into:

$$\begin{bmatrix} 1 & A'_{12} & 0 & 0 & 0 & 0 & 0 \\ 0 & 1 & A'_{23} & 0 & 0 & 0 & 0 \\ 0 & \cdots & \cdots & \cdots & 0 & 0 & 0 \\ 0 & 0 & 0 & 1 & A_{ii+1} & 0 & 0 \\ 0 & 0 & 0 & \cdots & \cdots & \cdots & 0 \\ 0 & 0 & 0 & 0 & 0 & 1 & A_{n-1n} \\ 0 & 0 & 0 & 0 & 0 & 0 & 1 \end{bmatrix} \begin{bmatrix} \phi_1 \\ \phi_1 \\ \cdots \\ \phi_i \\ \cdots \\ \phi_{n-1} \\ \phi_n \end{bmatrix} = \begin{bmatrix} B'_1 \\ B'_2 \\ \cdots \\ B'_i \\ \cdots \\ B'_{n-1} \\ B'_n \end{bmatrix}$$

The second stage involves *back substitution*, to evaluate $\phi_{nm}$ and $\phi_i$ as

$$\phi_n = B'_n \quad \text{and} \quad \phi_i = B'_i - \phi_{i+1} A'_{ii+1} \tag{7.52}$$

The TDMA is more economical than the Gaussian elimination because of the absence of arithmetic operations (multiplication and divisions) in obtaining $\phi_i$ during back substitution.

As mentioned earlier during the forward elimination stage the term $A_{nn}$ may consist of a zero value. The reader should be aware that in order to prevent ill-conditioning of a matrix for both of the direct methods presented, it is necessary to ensure that

$$|A_{ii}| > |A_{ii-1}| + |A_{ii+1}| \tag{7.53}$$

This means that the diagonal coefficients are required to be much larger than the sum of the neighbouring coefficients. If this is not the case, matrix row swapping (otherwise known as *pivoting*) can be performed.

### 7.3.2 Iterative Methods

Direct method such as Gaussian elimination can be employed to solve any system of equations. Unfortunately, in most CFD problems that usually result in a large system of non-linear equations, the cost of using this method is generally quite high as it requires a lot pre-conditioning of the matrix to prepare it for the direct method process. This leaves the option of employing iterative methods. In an iterative method, one guesses the solution, and uses the equation to systematically improve the solution until it reaches a specified level of convergence. If the number of iterations is small in achieving convergence, an iterative solver may cost less to use than a direct method. This is usually the case for CFD problems.

The simplest method from the various classes of iterative methods is the *Jacobi* method which solves the left hand side of the matrix expression, using previous values for $\phi$ on the right hand side. Let us revisit the system of equations, $A\,\phi = B$,

as described in the previous section; the general form of the algebraic equation for each unknown nodal variables of $\phi$ can be written as:

$$\sum_{j=1}^{i-1} A_{ij}\phi_j + A_{ii}\phi_i + \sum_{j=i+1}^{n} A_{ij}\phi_j = B_i \tag{7.54}$$

In Eq. (7.54), the Jacobi method requires that the nodal variables $\phi_j$ (non-diagonal matrix elements) are assumed to be known at iteration step $k$ and the nodal variables $\phi_i$ are treated as unknown at iteration step $k+1$. Solving for $\phi_i$, we have

$$\phi_i^{(k+1)} = \frac{1}{A_{ii}} \left( B_i - \sum_{j=1}^{i-1} A_{ij}\phi_j^{(k)} - \sum_{j=i+1}^{n} A_{ij}\phi_j^{(k)} \right) \tag{7.55}$$

The iteration process begins by an initial guess of the nodal variables $\phi_j$ ($k=0$). After repeated application of Eq. (7.55) to all the $n$ unknowns, the first iteration, $k=1$, is completed. We proceed to the next iteration step, $k=2$, by substituting the iterated values at $k=1$ into Eq. (7.54) to estimate the new values at the next iteration step. This process is continuously repeated for as many iterations as required to converge to the desired solution.

A more immediate improvement to the Jacobi method is provided by the *Gauss-Siedel* method in which the updated nodal variables $\phi_j^{(k+1)}$ are immediately used on the right-hand side of Eq. (7.54) as soon as they are available. In such a case, the previous values of $\phi_j^{(k)}$ that appear in the second term of the right-hand side of Eq. (7.55) are replaced by the current values of $\phi_j^{(k)}$, which the equivalent of Eq. (7.55) becomes

$$\phi_i^{(k+1)} = \frac{B_i}{A_{ii}} - \sum_{j=1}^{i-1} \frac{A_{ij}}{A_{ii}}\phi_j^{(k+1)} - \sum_{j=i+1}^{n} \frac{A_{ij}}{A_{ii}}\phi_j^{(k)} \tag{7.56}$$

Comparing the above two iterative procedures, the Gauss-Siedel iteration is typically twice as fast as the Jacobi iteration. After repeated applications of Eqs. (7.55) and (7.56), convergence can be gauged in a number of ways. One convenient condition to terminate the iteration process is to ensure that the maximum difference between each iteration, $\phi_j^{(k+1)} - \phi_j^{(k)}$ falls below some predetermined value. If the relative change is continually increasing with each iteration, then the solution is diverging.

### *7.3.3 Solution for a One-dimensional Steady Diffusion Equation*

**TDMA method** The solution for the steady heat conduction problem in a large brick plate with a uniform heat generation in Sect. 7.2.3 is presented here. The system of

equations for the 4-cell discretisation in matrix form is

$$\begin{bmatrix} 3000 & -1000 & 0 & 0 \\ -1000 & 2000 & -1000 & 0 \\ 0 & -1000 & 2000 & -1000 \\ 0 & 0 & -1000 & 3000 \end{bmatrix} \begin{bmatrix} T_1 \\ T_2 \\ T_3 \\ T_4 \end{bmatrix} = \begin{bmatrix} 203000 \\ 3000 \\ 3000 \\ 803000 \end{bmatrix}$$

where the boundary temperatures of $T_L$ and $T_R$ is 100 °C and 400 °C. In this worked example, we will illustrate the arithmetic operations of the TDMA, given that the matrix is in the form of a tri-diagonal. Substituting the temperatures of $T_L = 100$ °C and $T_R = 400$ °C into the right-hand side of the forcing terms, we have

$$\begin{bmatrix} 3000 & -1000 & 0 & 0 \\ -1000 & 2000 & -1000 & 0 \\ 0 & -1000 & 2000 & -1000 \\ 0 & 0 & -1000 & 3000 \end{bmatrix} \begin{bmatrix} T_1 \\ T_2 \\ T_3 \\ T_4 \end{bmatrix} = \begin{bmatrix} 203000 \\ 3000 \\ 3000 \\ 803000 \end{bmatrix}$$

We first normalise the top row by making $A_{11}$ to unity (divide by Row1 by 3000). We then multiply first row of the matrix by $A_{21}$ and subtract it from the second row.

$$\begin{bmatrix} 1 & -1/3 & 0 & 0 \\ 0 & 1666\frac{2}{3} & 1000 & 0 \\ 0 & -1000 & 2000 & -1000 \\ 0 & 0 & -1000 & 3000 \end{bmatrix} \begin{bmatrix} T_1 \\ T_2 \\ T_3 \\ T_4 \end{bmatrix} = \begin{bmatrix} 67^{2}/_{3} \\ 70666^{2}/_{3} \\ 3000 \\ 803000 \end{bmatrix}$$

Repeating the first step, but for the second row, $A_{22}$ is set to unity (divide Row2 by $1666\frac{2}{3}$). We then multiply second row of the matrix by $A_{32}$ and subtract it from the third row.

$$\begin{bmatrix} 1 & -1/3 & 0 & 0 \\ 0 & 1 & -3/5 & 0 \\ 0 & 0 & 1400 & -1000 \\ 0 & 0 & -1000 & 3000 \end{bmatrix} \begin{bmatrix} T_1 \\ T_2 \\ T_3 \\ T_4 \end{bmatrix} = \begin{bmatrix} 67^{2}/_{3} \\ 42^{2}/_{5} \\ 45400 \\ 803000 \end{bmatrix}$$

Repeating for the rest of the matrix, we get:

$$\begin{bmatrix} 1 & -1/3 & 0 & 0 \\ 0 & 1 & -3/5 & 0 \\ 0 & 0 & 1 & -5/7 \\ 0 & 0 & 0 & 2285^{5}/_{7} \end{bmatrix} \begin{bmatrix} T_1 \\ T_2 \\ T_3 \\ T_4 \end{bmatrix} = \begin{bmatrix} 67^{2}/_{3} \\ 42^{2}/_{5} \\ 32^{3}/_{7} \\ 835428^{4}/_{7} \end{bmatrix}$$

The second stage of the TDMA simply involves the *back substitution* process. Using Eq. (7.52), the solution to the above system is

$$T_1 = 140.5; \quad T_2 = 218.5; \quad T_3 = 293.5; \quad T_4 = 365.5$$

For this simple problem, we could have obtained the solution using the Gaussian elimination instead of the Thomas algorithm. For such a small matrix, the additional

arithmetic operations required for the Gaussian elimination to perform on the zero entries may not be as significant comparing to the Thomas algorithm. Nevertheless, this is not true when a number of grid points is used to better predict the temperature distribution across the plate. This is because of the additional and more cumbersome numerical computations (multiplication and divisions) that have to be performed on the matrix entries. The algorithm degenerates and becomes inefficient once the order of the matrix becomes higher ($>10$).

**The Jacobi method** To illustrate the *Jacobi method*, the resulting set of algebraic equations as previously derived is rewritten

$$\begin{aligned}
3000T_1 - 1000T_2 + 0 \times T_3 + 0 \times T_4 &= 203000 \\
-1000T_1 + 2000T_2 - 1000T_3 + 0 \times T_4 &= 3000 \\
0 \times T_1 - 1000T_2 + 2000T_3 - 1000T_4 &= 3000 \\
0 \times T_1 + 0 \times T_2 - 1000T_3 + 3000T_4 &= 803000
\end{aligned}$$

The above set of equations can be reorganized so that the required variable is on the left hand side of the equation.

$$\begin{aligned}
T_1 &= (T_2/3) + (203/3) \\
T_2 &= (T_1/2) + (T_3/2) + 3/2 \\
T_3 &= (T_2/2) + (T_4/2) + 3/2 \\
T_4 &= (T_3/3) + (803/30)
\end{aligned}$$

By employing initial guesses: $T_1^{(0)} = T_2^{(0)} = T_3^{(0)} = T_4^{(0)} = 100$, the nodal temperatures for the first iteration are determined as:

$$\begin{aligned}
{T_1}^{(1)} &= (100/3) + (203/3) &&= 101.000 \\
{T_2}^{(1)} &= (100/2) + (100/2) + 3/2 &&= 101.500 \\
{T_3}^{(1)} &= (100/2) + (100/2) + 3/2 &&= 101.500 \\
{T_4}^{(1)} &= (100/3) + (803/3) &&= 301.000
\end{aligned}$$

The above first iteration values of $T_1^{(1)} = 101$, $T_2^{(1)} = 101.5$, $T_3^{(1)} = 101.5$ and $T_4^{(1)} = 317\frac{2}{3}$ are substituted back into the system of equations; the second iteration yields

$$\begin{aligned}
{T_1}^{(2)} &= (101.5/3) + (203/3) &&= 101.500 \\
{T_2}^{(2)} &= (101/2) + (101.5/2) + 3/2 &&= 102.750 \\
{T_3}^{(2)} &= (101.5/2) + (301/2) + 3/2 &&= 202.750 \\
{T_4}^{(2)} &= (101.5/3) + (803/3) &&= 301.500
\end{aligned}$$

After repeated applications of the iterative process up to 10 and 20 iterations, the nodal temperatures have advanced to

$$\begin{bmatrix} T_1^{(10)} \\ T_2^{(10)} \\ T_3^{(10)} \\ T_4^{(10)} \end{bmatrix} = \begin{bmatrix} 137.247 \\ 208.837 \\ 286.388 \\ 361.080 \end{bmatrix} \text{ and } \begin{bmatrix} T_1^{(20)} \\ T_2^{(20)} \\ T_3^{(20)} \\ T_4^{(20)} \end{bmatrix} = \begin{bmatrix} 140.3632 \\ 218.092 \\ 293.200 \\ 365.313 \end{bmatrix} \text{ and } \begin{bmatrix} T_1^{(40)} \\ T_2^{(40)} \\ T_3^{(40)} \\ T_4^{(40)} \end{bmatrix} = \begin{bmatrix} 140.500 \\ 218.500 \\ 293.500 \\ 365.500 \end{bmatrix}$$

From the previous example 4.3, we obtained the exact direct solution by the TDMA algorithm. It is observed that the nodal temperatures after 20 iterations are edging closer towards the exact nodal temperature values.

**The Gauss-Siedel method** We begin as in the Jacobi method with the set of equations

$$T_1 = (\mathrm{T}_2/3) + (203/3)$$
$$T_2 = (T_1/2) + (T_3/2) + 3/2$$
$$T_3 = (T_2/2) + (T_4/2) + 3/2$$
$$T_4 = (T_3/3) + (803/30)$$

Employing the same initial guesses, the first iteration yields

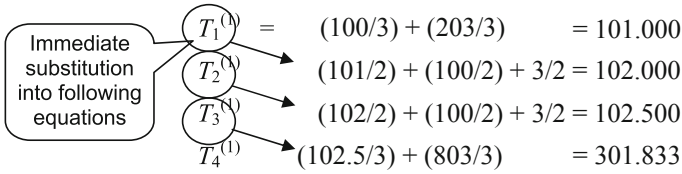


After performing 10 iterations, the nodal temperatures have advanced to

$$\begin{bmatrix} T_1^{(10)} \\ T_2^{(10)} \\ T_3^{(10)} \\ T_4^{(10)} \end{bmatrix} = \begin{bmatrix} 140.021 \\ 217.737 \\ 292.944 \\ 365.315 \end{bmatrix} \text{ and } \begin{bmatrix} T_1^{(20)} \\ T_2^{(20)} \\ T_3^{(20)} \\ T_4^{(20)} \end{bmatrix} = \begin{bmatrix} 140.499 \\ 218.499 \\ 293.499 \\ 365.500 \end{bmatrix}$$

The temperature values obtained through the Gauss-Siedel method at this present stage are comparable to the values obtained by the Jacobi method at 20 iterations. We can infer from this example that the Gauss-Siedel iteration is twice as fast as the Jacobi iteration. Convergence is achieved quicker by the Gauss-Siedel method because of the *immediate substitution* of the temperatures to the right-hand side of the equations whenever they are made available. Thus far, we have not discussed the issue of terminating the iteration process for this particular problem. The degree to which you wish convergence to be achieved is entirely up to you. If the absolute

maximum difference $\left|\phi_j^{(k+1)} - \phi_j^{(k)}\right|$ is chosen as the condition for the termination process, the accuracy of the solution depends on the targeted number of significant figures you wish to obtain for the temperatures. The smaller the acceptable error, the higher the number of iterations but this will achieve greater accuracy.

### 7.3.4 Pressure-velocity Coupling

The discretisation methods that have been presented are for a single equation. If we consider the governing equations for a 2D incompressible steady laminar flow we have

$$0 = \frac{\partial u}{\partial x} + \frac{\partial v}{\partial y} \qquad \textit{continuity}$$

$$\underbrace{\frac{\partial u}{\partial t}}_{\textit{local acceleration}} + \underbrace{u\frac{\partial u}{\partial x} + v\frac{\partial u}{\partial y}}_{\textit{convection}} = - \underbrace{\frac{1}{\rho}\frac{\partial p}{\partial x}}_{\textit{pressure gradient}} + \underbrace{\nu\frac{\partial^2 u}{\partial x^2} + \nu\frac{\partial^2 u}{\partial y^2}}_{\textit{diffusion}} + \underbrace{\sum F_B}_{\textit{body force}} \qquad x\textit{-momentum}$$

$$\underbrace{\frac{\partial v}{\partial t}}_{\textit{local acceleration}} + \underbrace{u\frac{\partial v}{\partial x} + v\frac{\partial v}{\partial y}}_{\textit{convection}} = - \underbrace{\frac{1}{\rho}\frac{\partial p}{\partial y}}_{\textit{pressure gradient}} + \underbrace{\nu\frac{\partial^2 v}{\partial x^2} + \nu\frac{\partial^2 v}{\partial y^2}}_{\textit{diffusion}} + \underbrace{\sum F_B}_{\textit{body force}} \qquad y\textit{-momentum}$$

where there are three unknowns, $u$, $v$ and $p$ with the other variables, $\nu$, $\rho$ determined from the material property of the fluid. The velocity field $u$ and $v$ can be obtained after discretisation of its transport equation (i.e. the $x$- and $y$- momentum equations above) if we know the pressure field, (because of the pressure gradient term in the momentum equation). However for an incompressible flow assumption, the governing equations lack an independent equation for pressure. With the additional continuity equation, this system of equations is self-contained; there are three equations for three dependents $u$, $v$ and $p$, however we cannot use the continuity equation directly to obtain $p$. In order to link the pressure with the velocity for an incompressible flow, a correction to the pressure field is made to ensure that the continuity and momentum equations are satisfied.

Within this section, we describe the basic philosophy behind one of the most popular schemes of pressure-velocity coupling for an incompressible flow. It belongs

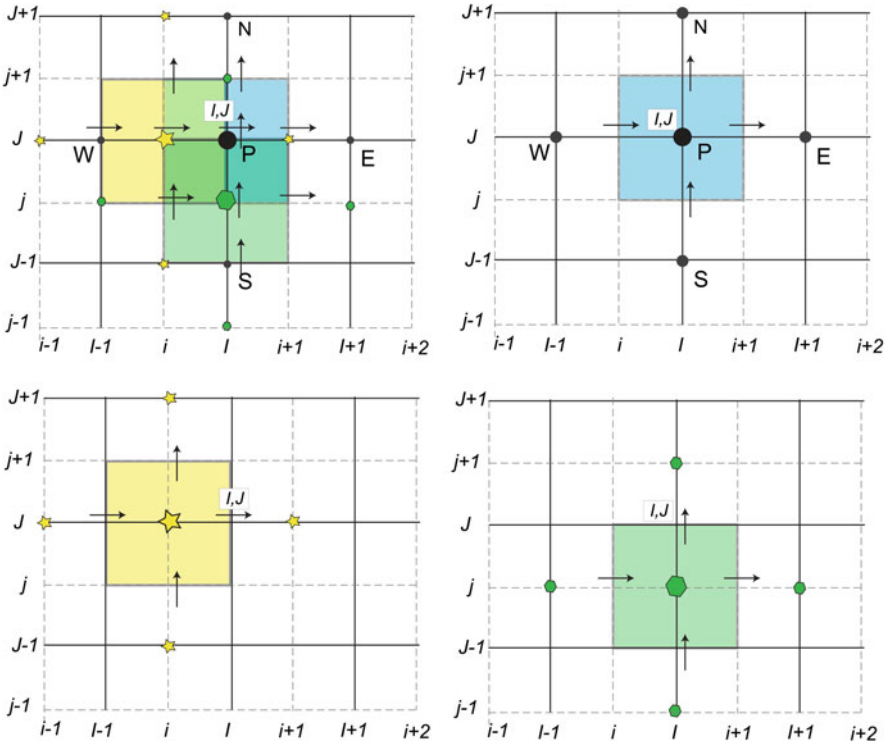


**Fig. 7.23** A backward staggered mesh system for the pressure velocity coupling

to the class of iterative methods, which is embodied in a scheme called SIMPLE where the acronym stands for Semi-Implicit Method for Pressure-Linkage Equations. This scheme was developed for practical engineering solutions by Patankar and Spalding (1972) and has found widespread application in the majority of CFD codes. In this scheme, a guessed pressure field is used to solve the momentum equations, thus the *u, v* velocities are obtained. A pressure correction equation, deduced from the continuity equation, is then solved to obtain a pressure correction field, which in turn is used to update the velocity and pressure fields. The equations are solved sequentially which means that an unknown variable is solved one at a time using the known values of the other variables, and hence only one variable changes at a time. The guessed fields are iterated where the momentum and continuity equations are continuously changing to ensure mass conservation.

**Variable arrangement on the grid** Before describing the SIMPLE scheme, we present the *staggered* grid arrangement. The aim of having a *staggered* grid arrangement for CFD computations is to evaluate the velocity components at the control volume faces while the rest of the variables governing the flow-field, such as the pressure, temperature and turbulent quantities, are stored at the central node of the control volumes. A typical arrangement is depicted in Fig. 7.23 on a structured finite

volume grid and it can be demonstrated that the discrete values of the velocity component, $u$, from the $x$-momentum equation are evaluated and stored at the east, $e$, and west, $w$, faces of the control volume.

By evaluating the other velocity components using the $y$-momentum and $z$-momentum equations on the rest of the control volume faces, these velocities allow a straightforward evaluation of the mass fluxes that are used in the pressure correction equation. This arrangement therefore provides a strong coupling between the velocities and pressure, which helps to avoid some types of convergence problems and oscillations in the pressure and velocity fields. The staggered grid is typically the simplest strategy for incompressible flow calculations and it is used in this chapter to demonstrate the pressure-velocity coupling.

Let us establish the staggered grid where scalar variables (e.g. pressure) are stored at nodal points while the velocity components are stored at the control volume faces. In the staggered arrangement the central node for pressure and other scalar variables $\phi$ are stored at nodal point $P(I, J)$. This control volume is used for the pressure term and is sometimes called the scalar control volume since other scalar variables are also stored here. The velocity vector $u$, however is stored at nodal point $u(i, J)$ and $v$ is stored at point $v(I, j)$. This means that the vectors and scalars are stored in staggered locations and there are three partially overlapping control volumes. The example shown in Fig. 7.23 is a backward staggered grid, although a forward staggered grid may also be used.

**SIMPLE algorithm** The SIMPLE scheme is essentially a guess-and-correct procedure for the calculation of pressure through the solution of a pressure correction equation. The method is illustrated by considering a two-dimensional steady laminar flow problem in a structured grid with staggered arrangement as shown in Fig. 7.23. Firstly we discretise the momentum equations for a two-dimensional incompressible flow using FV on a staggered mesh. The pressure gradient term for the $u$- and $v$- control volumes are

$$\frac{\partial p}{\partial x} = \frac{p_P - p_W}{\Delta x} = \frac{p_{I,J} - p_{I-1,J}}{\Delta x}; \quad \frac{\partial p}{\partial y} = \frac{p_P - p_S}{\Delta y} = \frac{p_{I-1,J} - p_{I,J}}{\Delta y}$$

where $\Delta x$ and $\Delta y$ are the length and height of the control volume respectively. Discretising the momentum equations we get

$$\begin{aligned} a^u_{i,J} u_{i,J} &= a^u_{i,j} u_{i,j} + a^u_{i,j+1} u_{i,j+1} + a^u_{I-1,J} u_{I-1,J} + a^u_{I,J} u_{I,J} \\ &\quad - \frac{p_{I,J} - p_{I-1,J}}{\Delta x} \Delta V + b^u \Delta V \\ a^v_{I,j} v_{I,j} &= a^v_{I,J-1} v_{I,J-1} + a^v_{I,J} v_{I,J} + a^v_{i,j} v_{i,j} + a^v_{i+1,j} v_{i+1,j} \\ &\quad - \frac{p_{I-1,J} - p_{I,J}}{\Delta y} \Delta V + b^v \Delta V \end{aligned}$$

where $b^u$ and $b^v$ are source terms that may include gravity, and other effects. We retain the subscript notation for the pressure term using the compass point notation

to highlight that the pressure term and any other scalar value is stored in the scalar control volume. The above equations can be rewritten as:

$$a^u_{i,J}u_{i,J} = \sum a^u_{nb}u_{nb} - \frac{p_P - p_W}{\Delta x}\Delta V + b^u\Delta V$$
$$a^v_{I,j}v_{I,j} = \sum a^v_{nb}v_{nb} - \frac{p_P - p_S}{\Delta y}\Delta V + b^v\Delta V \tag{7.57}$$

The coefficients $a_{nb}$ are defined by the discretisation scheme that is chosed (Central Differencing, Upwind Differencing, QUICK). The SIMPLE scheme provides a robust method of calculating the pressure and velocities for an incompressible flow. When coupled with other governing variables such as temperature and turbulent quantities, the calculation needs to be performed sequentially since it is an iterative process. The details of the sequence of operations in a typical CFD iterative process that embodies the SIMPLE scheme is discussed below.

*Step 1* The iterative SIMPLE calculation process begins by first initialising the pressure field, by giving a guessed value $p^*$ to solve the momentum equations. The discretised Eq. (7.57) are solved based on $p^*$ to give

$$a^u_{i,J}u^*_{i,J} = \sum a^u_{nb}u^*_{nb} - \frac{p^*_P - p^*_W}{\Delta x}\Delta V$$
$$a^v_{I,j}v^*_{I,j} = \sum a^v_{nb}v^*_{nb} - \frac{p^*_P - p^*_S}{\Delta y}\Delta V \tag{7.58}$$

where the neighbouring coefficients and $u^*_{nb}$ and $v^*_{nb}$ denotes the calculated neighbouring nodal velocity components based on $p^*$. The asterisk notation represents the value is the guessed value.

*Step 2* The velocities $u^*$, and $v^*$ obtained from the momentum equations, typically will not satisfy the continuity equation. We need to apply corrections $u'$ and $v'$ at each node so that the velocity terms satisfy the continuity equation. Thus we relate the desired velocities $u$ and $v$ to the guessed velocities $u^*$ and $v^*$ and similarly the correct pressure $p$ with the guessed pressure $p^*$ by

$$p = p^* + p'$$
$$u = u^* + u'$$
$$v = v^* + v' \tag{7.59}$$

Note that at this stage $u^*$ and $v^*$ are the velocities determined from the guessed $p^*$, that initially satisfied the momentum equation but don't satisfy the continuity equation. The correction terms $u'$ and $v'$ are not known and these need to be determined. We begin by subtracting Eqs. (7.58) from (7.57) we obtain

$$a^u_{i,J}(u_{i,J} - u^*_{i,J}) = \sum a^u_{nb}(u_{nb} - u^*_{nb}) + \frac{(p_W - p^*_W) - (p_P - p^*_P)}{\Delta x}\Delta V$$

$$a^v_{I,j}(v_{I,j} - v^*_{I,j}) = \sum a^v_{nb}(v_{nb} - v^*_{nb}) - \frac{(p_S - p^*_S) - (p_P - p^*_P)}{\Delta y}\Delta V \tag{7.60}$$

Substituting the correction formulae (Eq. 7.59) into the above equations we obtain our correction terms,

$$\begin{aligned} a^u_{i,J}u'_{i,J} &= \sum a^u_{nb}u'_{nb} + \frac{p'_W - p'_P}{\Delta x}\Delta V \\ a^v_{I,j}v'_{I,j} &= \sum a^v_{nb}v'_{nb} - \frac{p'_S - p'_P}{\Delta y}\Delta V \end{aligned} \tag{7.61}$$

Now we apply an approximation to the equation by omitting the terms $\sum a^u_{nb}u'_{nb}$ and $\sum a^v_{nb}v'_{nb}$. This is essence of the SIMPLE algorithm. The resulting equations give

$$\begin{aligned} u'_{i,J} &= d^u\left(p'_W - p'_P\right) \\ v'_{I,j} &= d^v\left(p'_S - p'_P\right) \end{aligned} \tag{7.62}$$

where $d^u = \dfrac{\Delta V}{a^u_{i,J}\Delta x}$ and $d^v = \dfrac{\Delta V}{a^v_{I,j}\Delta y}$.

It is noted that this scheme is an iterative approach, and there is no reason why the formula designed needs to be physically correct. Hence, we are allowed to construct a formula that is simply a numerical artifice with the aim to expedite the convergence of the velocity field to a solution that satisfies the continuity equation. The omission of the $\sum a^u_{nb}u'_{nb}$terms will not affect the final solution since a converged solution implies that the pressure and velocity corrections will converge to zero. The equations in (7.62) are the velocity corrections which are substituted back into Eq. (7.59) to adjust the guessed velocities $u^*$ and $v^*$. This gives

$$\begin{aligned} u_{i,J} &= u^*_{i,J} + d^u\left(p'_W - p'_P\right) \\ v_{I,j} &= v^*_{I,j} + d^v\left(p'_S - p'_P\right) \end{aligned} \tag{7.63}$$

Although the Eq. (7.63) that have been developed to correct the velocities from the guessed velocities at the central node of the control volume, these correction formulae can also be generally applied to any location where the velocity components reside within the computational grid (as shown in Fig. 7.23, the velocities may be located at central node $P$ or at the control volume faces or at the vertices of the control volume).

Up to now we have a definition for the velocity field, however we are still lacking a formula for the pressure correction term that will adjust the initial guessed pressure term. It is noted that the pressure correction term is needed to obtain the desired velocities $u$ and $v$ as shown in (7.63). The derivation of a pressure correction equation begins by differentiating Eq. (7.63) with respect to its coordinate axis (i.e. $u$-velocity by $\partial x$ and $v$ -velocity by $\partial y$) and summing them together yields

$$-\frac{\partial}{\partial x}\left(d^u\left(p'_W - p'_P\right)\right) - \frac{\partial}{\partial y}\left(d^v\left(p'_S - p'_P\right)\right) + \underbrace{\frac{\partial u^*}{\partial x} + \frac{\partial v^*}{\partial y}}_{\text{guessed velocity gradients}} = \underbrace{\frac{\partial u}{\partial x} + \frac{\partial v}{\partial y}}_{\text{correct velocity gradients}} = 0$$

The term on the right hand side is the continuity equation, which equals zero for mass conservation and the equation becomes

$$\frac{\partial}{\partial x}\left(d^u\left(p'_W - p'_P\right)\right) + \frac{\partial}{\partial y}\left(d^v\left(p'_S - p'_P\right)\right) = \underbrace{\frac{\partial u^*}{\partial x} + \frac{\partial v^*}{\partial y}}_{\text{mass residual}} \tag{7.64}$$

Similarly, Eq. (7.64) can be discretised into the general form of

$$a_{I,J}\, p'_{I,J} = a_P\, p'_P = \sum a_{nb}\, p'_{nb} + b'_P \tag{7.65}$$

where $b'_P$ constains the $u^*$ and $v^*$ terms.

*Step 3* To recap, we started with an initial guess of $p^*$ which produces $u^*$ and $v^*$. These guessed values need to be corrected and therefore their correction formulae were derived to obtain $p'$, $u'$ and $v'$. The pressure and velocity components are subsequently updated through the correction formulae of Eq. (7.59). If the solution only concerns a laminar CFD flow problem, the iteration process proceeds directly to check the convergence of the solution. If the solution is not converged, the process is repeated by returning to Step 1. The source term appearing in the pressure correction Eq. (7.64), commonly known as the *mass residual*, is normally used in CFD computations as a criteria to terminate the iteration procedure. As the mass residual continues to diminish, the pressure correction $p'$ will be zero thereby yielding a converged solution of $p^* = p, u^* = u$ and $v^* = v$.

Under some cases where the mesh contains highly skewed cells or the physical problem is complex, the correction equations encounter difficulties in converging, and in fact can diverge, and the solution is not achieved. In these cases, an under-relaxation factor, $\alpha$ is applied during the iterative steps, whereby the correction formulae is rewritten as

$$\begin{aligned} p &= p^* + \alpha_p p' \\ u &= u^* + \alpha_u u' \\ v &= v^* + \alpha_v v' \end{aligned} \tag{7.66}$$

The under-relaxation factor is a value between 0 and 1 which aims to reduce large changes in the variable which can cause divergence in the solution. However the value should not be set too small as this will slow down the solution. Therefore there this is an optimal value that is low enough to prevent divergence in the solution but still high enough to provide rapid convergence. The selection of a suitbale under-relaxation factor is flow dependent and different for each case, and so a single value cannot be used.

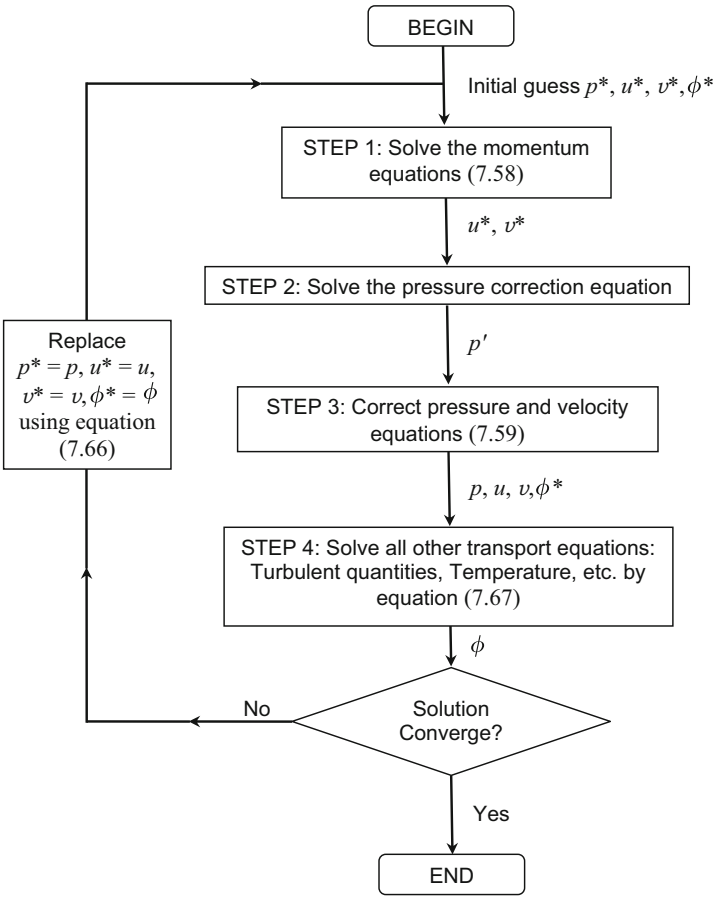


**Fig. 7.24** The SIMPLE scheme

*Step 4* If the flow problem includes additional scalar variables ($\phi$) that are being solved such as temperature ($\phi = T$) or turbulent quantities ($\phi = k, \omega, \varepsilon$) then the additional transport equations governing such a flow system need to be solved by

$$a_P^u \phi_P = a_W u_W + a_E u_E + a_S u_S + a_N u_N + b^\phi \tag{7.67}$$

before convergence is checked. We note that the scalar is discretised within the scalar control volume (i.e. the pressure control volume as shown in Fig. 7.23). If the solution is not converged, the iterative process returns to Step 1 and repetitive calculations are carried out until convergence is reached. The four steps that have been discussed describe the application of the SIMPLE scheme and is summarised in Fig. 7.24.

The reader should be aware that there are other types of pressure-velocity coupling algorithms that employ a similar philosophy to the SIMPLE algorithm. These variants have been formulated with the aims of better improving the robustness and

convergence rate of the iterative process. We do not intend to provide the reader with all the details of the available algorithms but to briefly indicate and describe the modifications made to the original SIMPLE algorithm.

The SIMPLEC (SIMPLE-Consistent) algorithm follows the same iterative steps as in the SIMPLE algorithm with the main difference being that the discretised momentum equations are manipulated so that the SIMPLEC velocity correction formulae omit terms that are less significant than those omitted in SIMPLE. Another pressure correction procedure that is also commonly employed is the PISO (Pressure Implicit with Splitting of Operators) algorithm. This pressure-velocity calculation procedure was originally developed for non-iterative computation of unsteady compressible flows. Nevertheless, it has been adapted successfully for the iterative solution of steady state problems. PISO is simply recognized as an extension of SIMPLE with an additional corrector step that involves an additional pressure correction equation to enhance the convergence. The SIMPLER (SIMPLE-Revised) also falls within the framework of two corrector steps like in PISO. Here, a discretised equation for the pressure provides the intermediate pressure field before the discretised momentum equations are solved. A pressure correction is later solved where the velocities are corrected through the correction formulae as similarly derived in the SIMPLE algorithm. There are other SIMPLE-like algorithms such as SIMPLEST (SIMPLE-ShorTened), SIMPLEX, or SIMPLEM (SIMPLE-Modified) that share the same essence in their derivations.

## 7.4 Numerical Solution OF ODES

The Lagrangian particle tracking equation (from Eq. 6.10 in Chap. 6) is in the form of an Ordinary Differential Equation (ODE) and can be rewritten as

$$\frac{du}{dt} = f(u,t) \tag{7.68}$$

The ODE in Eq. (7.68) defines the gradient or rate of change at any point by the terms on the right hand side. There are many numerical methods which can be used but in this section we present an introduction to some common methods which aims to illustrate the main ideas of numerical solutions to ODEs.

### *7.4.1 Forward Euler Ethod*

Euler's method is the simplest one-step numerical scheme for integration an ODE. It solves the ODE by applying the change in the velocity term from time $t$ to time $t+h$ where $h$ is a time step size $h = \Delta t$. This means that each successive approximation $u_{t+1}$ can be represented through a Taylor series expansion which gives

$$u_{t+\Delta t} = u_t + \frac{du}{dt}\Delta t + \underbrace{\frac{d^2u}{dt^2}\frac{\Delta t^2}{2} + \ldots}_{\text{truncation error}} \tag{7.69}$$

where the derivative *du/dt* is replaced by the terms on the right hand side of Eq. (7.68). The forward Euler's method can be read as

$$new\ value = current\ value + gradient \times time\ step$$

The highest order term that is used is of first order and therefore the Euler method is of first order accuracy. The basic approach to the solution is a stepwise process whereby we start with a known initial value ($u_0$, $t_0$) and increment forward in time to determine the next values ($u_1$, $t_1$), ($u_2$, $t_2$), ($u_3$, $t_3$) etc.

To illustrate the forward Euler method, let us consider a 1D gas-particle flow where a 1 μm particle($\tau = 35 \times 10^{-6}$m/s) initially at rest, is introduced into a flow field that has uniform velocity $u^f = 1$m/s throughout. Considering only the drag force the particle equation of motion is given as

$$\frac{du^p}{dt} = \frac{1}{\tau}\left(u^f - u^p\right) \tag{7.70}$$

and its exact solution is

$$u^p = u^f - u^f \exp\left(-t/\tau\right) \tag{7.71}$$

based on initial values of $t = 0$ $u = 0$. Using the forward Euler method we select a time step size of $h = 0.00001$ s and stepping forward in time for we can obtain the solution numerically as:

| $t$ | $du^p/dt$ | $(du^p/dt)h$ | $u^p + (du^p/dt)h$ | Analytical | Error |
|---|---|---|---|---|---|
| 0.00000 | | | 0.00000 | 0.00000 | 0.00000 |
| 0.00001 | 28571.4 | 0.285714 | 0.28571 | 0.24852 | 0.037192 (15 %) |
| 0.00002 | 20408.2 | 0.204082 | 0.48980 | 0.43528 | 0.054514 (13 %) |
| 0.00003 | 14577.3 | 0.145773 | 0.63557 | 0.57563 | 0.059941 (10 %) |

A comparison with the analytical results shows that error in the first time step is 15 % and decreases as the solution steps forward in time. The solution converges after $t \approx 0.0002$ sec. as shown in Fig. 7.25.

Errors in the Euler method are primarily due to truncation errors since the gradient of the curve over an interval is based on information at the beginning of an interval and is assumed to be constant. Typically this error is far larger than other methods for a given step size. A reduction in the time step will significantly reduce this type of error. Another problem with the Euler method is that it is prone to numerical instabilities. In the example given the time step size used was $h = 0.00001$ s. If this time step was set as $h = 0.00006$ s we see that the solution oscillates about the exact analytical solution Fig. 7.26.

There are many ways to determine the gradient (i.e. derivative) and a more advanced method is the Runge-Kutta method which creates a more symmetrical gradient to account for changes over the step size interval.

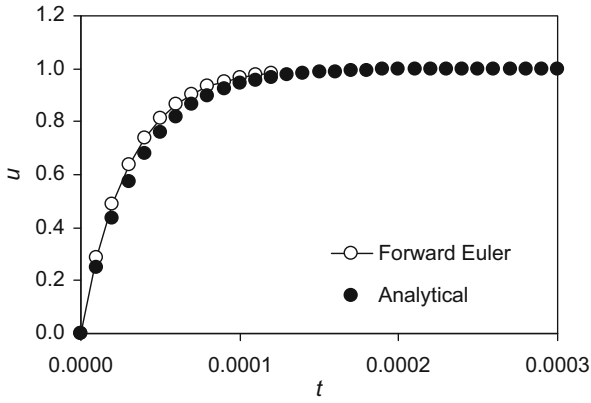


**Fig. 7.25** A comparison of the solution based on the explicit forward Euler method and the exact analytical method. Time step $h = 0.00001$ s

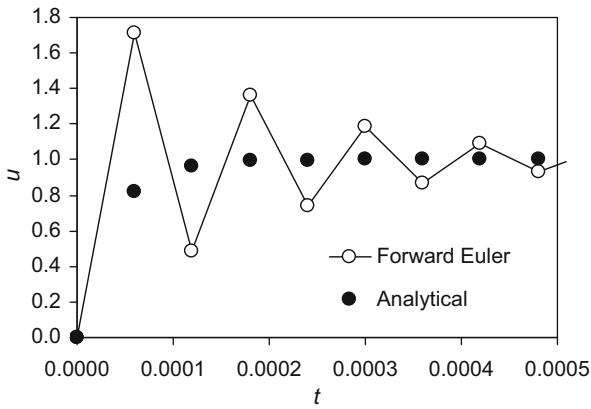


**Fig. 7.26** A comparison of the solution based on the explicit forward Euler method and the exact analytical method. Time step $h = 0.00006$ s

### *7.4.2 Runge-Kutta Method*

The Runge-Kutta Method is a higher order approximation to the Euler method and comes in different orders based on the number of terms used to calculate the gradient. In this section we present the fourth order Runge-Kutta (RK4) method as it is one of the most widely used algorithms for solving ODEs. The gradient of an interval is determined by taking gradient approximations at four different points within the interval (Fig. 7.27).

Referring back to Eq. (7.68) the right side of the equation is evaluated by four terms with weighted coefficients.

$$u_{t+1} = u_t + \frac{1}{6}(k_1 + 2k_2 + 2k_3 + k_4)h$$

$$k_1 = f(t, u)$$

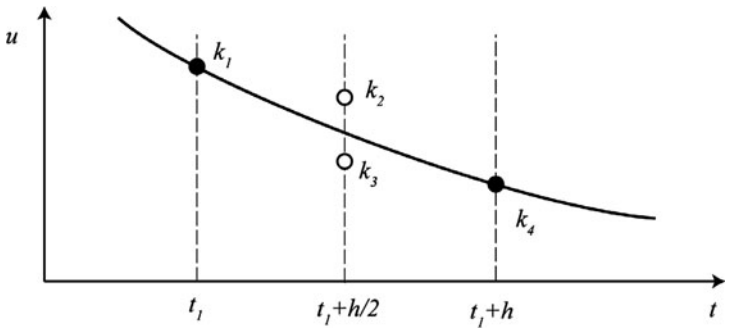


**Fig. 7.27** Geometric representation of the fourth order Runge-Kutta method

$$k_2 = f\left(t + \frac{h}{2}, u + \frac{k_1 h}{2}\right)$$
$$k_3 = f\left(t + \frac{h}{2}, u + \frac{k_2 h}{2}\right)$$
$$k_4 = f(t + h, u + k_3 h) \tag{7.72}$$

To start the method, the initial values for a starting point $u(0) = u_t$ is used. The $k$ terms are solved sequentially and summed before adding to $u_t$ to obtain $u_{t+1}$. To illustrate the RK4 we take the same example as earlier, and solve Eq. (7.70) as follows.

The initial values are $t(0) = 0$ $u(0) = 0$, and therefore for the first time step,

$$k_1 = f(0{,}0) = \frac{1}{\tau}(1 - 0) = 28571.4$$

$$k_2 = f\left(0 + \frac{0.00001}{2}, 0 + \frac{28571.4 \times 0.00001}{2}\right)$$
$$= \frac{1}{\tau}\left(1 - \frac{28571.4 \times 0.00001}{2}\right) = 24489.8$$

$$k_3 = f\left(0 + \frac{0.00001}{2}, + 0 + \frac{24489.8 \times 0.00001}{2}\right)$$
$$= \frac{1}{\tau}\left(1 - \frac{28571.4 \times 0.00001}{2}\right) = 25072.9$$

$$k_4 = f(0 + 0.00001, 0 + 25072.9 \times 0.00001)$$
$$= \frac{1}{\tau}(1 - 25072.9 \times 0.00001) = 21407.7$$

Putting the terms together we get

$$u_{t+1} = 0 + \left(\frac{28571.4}{6} + \frac{24489.8}{3} + \frac{25072.9}{3} + \frac{21407.7}{6}\right) 0.00001 = 0.248508$$

Repeating for successive time steps we get the following values

| $t$ | $u$ | $k_1$ | $k_2$ | $k_3$ | $k_4$ | $u_{t+1}$ | Analytical | Error |
|---|---|---|---|---|---|---|---|---|
| 0.00000 | 0.00000 | 28571.4 | 24489.8 | 25072.9 | 21407.7 | 0.24851 | 0.24852 | 0.006 % |
| 0.00001 | 0.24851 | 21471.2 | 18403.9 | 18842.1 | 16087.8 | 0.43526 | 0.43528 | 0.005 % |
| 0.00002 | 0.43526 | 16135.5 | 13830.4 | 14159.7 | 12089.8 | 0.57560 | 0.57563 | 0.004 % |
| 0.00003 | 0.57560 | 12125.7 | 10393.4 | 10640.9 | 9085.4 | 0.68107 | 0.68109 | 0.004 % |

It can be seen that the RK4 method provides much better accuracy over the Euler method for the same time step size used. In the example presented a small $h$ is used because the solution changes with time rapidly. The time step that was applied is a fixed time step and an alternate approach is to apply an automatic step size that adapts to the solution and therefore is variable. This is known as a time step adaptive method.

**Other Approaches** The Euler and RK4 method are examples of explicit one-step methods. An explicit method is one that derives its solution $u_{t+1}$ from the function of $u_t$ explicitly. The alternate to this is an implicit method which is discussed in Sect. 7.4.3. Other methods include the predictor-corrector approach which involves applying an initial prediction to give a crude approximation. This value is then corrected by some function to refine the solution, thus this method is a two-step approach. Such approaches include the *Trapezoidal*, *Adams-Bashforth*, and *Heun's* methods.

### *7.4.3 Implicit Methods for Stiff ODEs*

A *stiff* ODE is one that has a rapidly changing term with respect to other terms in the equation and its solution will become numerically unstable (oscillations in the solution) if its step size is not small enough. Micron particles in a moving fluid, as in the example described earlier, exhibit rapid changes in its aerodynamic flight because of relaxation time that is in the order of $10^{-6}$ m/s. Therefore very small time steps are needed to account for the rapid changes. This implies that an ODE is stiff, if the explicit Euler method has constraints on its step size in order for a stable solution to be obtained. It was shown in Fig. 7.26 that an increase in the time step created an

unstable solution using the Euler method. Typically for explicit methods, numerical stability can be improved by decreasing the step size. An alternative is to use an implicit method which allows more flexibility in the step size selection. The implicit method makes use of information at a future step, $u_{t+1}$, as well as at $u_{t.}$ To illustrate the structure of an implicit approach we present the one-step backward Euler method which is given as

$$u_{t+1} = u_t + h \times f(t_{t+1}, u_{t+1}) \tag{7.73}$$

We notice that the implicit backward Euler method has the $u_{t+1}$ term on both the left and right hand side of Eq. (7.73) and we don't have an explicit formula for $u_{t+1}$. Instead, we have to solve an equation to find the roots for $u_{t+1}$. This step makes the implicit scheme much more time consuming than the explicit Euler method and if the differential equation is complicated, an implicit method can be very difficult to use. Taking the same example we have been using we rewrite Eq. (7.73) as

$$u_{t+1} = u_t + h \times \frac{1}{\tau}(u^f - u_{t+1}) \tag{7.74}$$

and after rearranging and substituting in the values with $h = 0.00006$, the first increment is

$$u_{t+1} = \frac{u_t + \frac{h}{\tau}u^f}{1 + \frac{h}{\tau}} = \frac{0 + \frac{0.00001}{0.000035}}{1 + \frac{0.00001}{0.000035}} = 0.63158$$

If we repeating for successive time steps and plot it against the explicit forward Euler method, we can see that the implicit method is stable (Fig. 7.28).

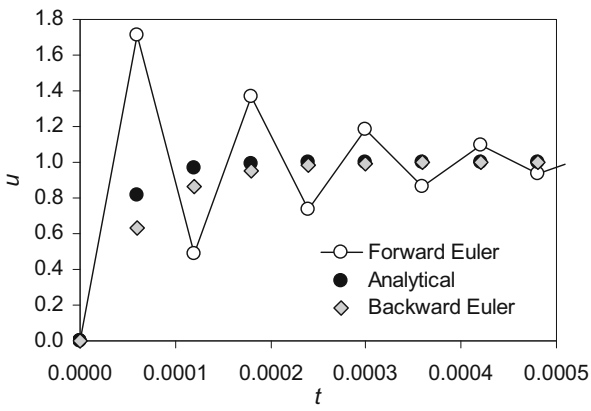


**Fig. 7.28** A comparison of the solution based on the implicit backward Euler method with the explicit forward Euler and the exact analytical method. Time step $h = 0.00006$ s

We have introduced some numerical methods for solving ODEs and it is hoped that this will allow the reader to tackle some commonly used Lagrangian particle tracking models used in many CFD packages. For the interested reader, any academic textbook on numerical analysis will provide deeper insight into this field.

## 7.5 Solution Analysis

### *7.5.1 Consistency, Stability, Convergence, Accuracy*

The respresentation of the governing partial differential equations into a system of algebraic eqquations is then solved through numerical methods. This produces approximate or otherwise referred to as *computational solutions* to the governing equations. The quality of a CFPD simulation required is dependent on the use of results. In engineering and industry practice, general trends and gross flow features may be sufficient, while for academic research purposes, detailed micro scales (and even down to the Kolmogorov scales) may be necessary to establish new findings. Whatever the requirement, we can perform a number of analyses to demonstrate the relevance and credibility of computational solutions by addressing the concepts of *consistency*, *stability*, *convergence* and *accuracy* that concern a CFD solution. In this section we present a brief introduction to these four concepts and for the interested reader additional references are given for further reading.

The idea of *consistency* deals with the discretisation of the partial differential equations where the approximation performed should diminish or become exact if the finite quantities, such as the time step $\Delta t$ and mesh spacing $\Delta x$, $\Delta y$ and $\Delta z$, tend to zero. In sect. 7.2.1 of the finite difference method, the concept of *truncation error* measures the discrete approximation obtained through a Taylor series expansion about a single nodal point. Essentially, the truncation error represents the difference between the discretised equation and the exact one. As a result, the original partial differential equation is recovered by the addition of a remainder, the truncation error. This error basically measures the accuracy of the approximation and determines the rate at which the error decreases as the time step and/or mesh spacing are reduced.

In addition to consistency, another property that also strongly governs the numerical solution is *stability*. This property concerns the growth or decay of errors introduced at any stage during the computation. It is noted that the errors being referred here are those that occur because of rounding-off at every step of computation due to the finite number of significant figures the computer hardware can accommodate. A numerical solution method is therefore considered to be stable if it does not magnify the errors that appear in the course of the numerical solution process. Stability in the context of iterative methods ensures that the solution does not diverge.

If a numerical method can satisfy the two important properties of consistency and stability, we generally find that the numerical procedure is convergent. *Convergence* of a numerical process can therefore be stated as the solution of the system of algebraic equations approaching the true solution of the partial differential equations having the same initial and boundary conditions as the refined grid system (grid convergence). In the majority of commercial CFD codes, the system of algebraic equations is usually solved iteratively. When dealing with these codes, there are three important rules to abide by for iterative convergence. Firstly, all the discretised equations (momentum, energy, etc.) are deemed to be converged when they reach

a specified tolerance at every nodal location. Secondly, the numerical solution no longer changes with additional iterations. Thirdly, overall mass, momentum, energy and scalar balances are obtained. During the numerical procedure, the imbalances (errors) of the discretised equations are monitored and these defects are commonly referred to as the residuals of the system of algebraic equations, i.e. they measure the extent of imbalances arising from these equations and terminate the numerical process when a specified tolerance is reached. For satisfactory convergence, the *residuals* should diminish as the numerical process progresses. In the likelihood that the imbalances grow, as reflected by increasing residual values, the numerical solution is thus classified as being divergent. It is noted that iterative convergence is not the same as grid convergence. Grid convergence seeks a grid independent solution.

The previous discussion of *convergence*, *consistency* and *stability* has been primarily concerned with the solution behavior where the finite quantities, such as the time step $\Delta t$ and mesh spacing $\Delta x$, $\Delta y$ and $\Delta z$, diminish. Since the discretised forms of the transport equations governing the flow and energy transfer are always solved numerically on a finite grid layout, the solution obtained is always approximate. The corresponding issue of *accuracy* therefore becomes another important consideration.

One method where accuracy can be assessed on a finite grid is to apply it to a related but simplified problem that possesses an exact solution. However, accuracy is usually problem dependent; an algorithm that is accurate for one model problem may not necessarily be as accurate as for another more complicated problem. Another probable way for assessing accuracy is to obtain solutions on successively refined grids (mesh indpendence) and to check that, with successive refinements, the solution is not changing satisfying some predetermined accuracy. This technique assumes that the approximate solutions will converge to the exact solution as the finite quantities diminish and then the approximate solution on the finest grid can be used in place of the exact solution. Assuming that the accuracy of this approximate solution can be assessed it is important to consider the related question of how accuracy may be improved. It is important the reader be aware that *a converged solution does not necessarily mean an accurate solution*. Some possible sources of solution error can occur through numerical calculations of the algebraic equations. If these errors are to be minimized, some systematic steps to perform numerical analysis can be performed.

In summary, the conceptual framework linking the various aspects of *consistency*, *stability*, *convergence* and *accuracy* beginning from the governing partial differential equations as considered and arriving at the approximate solution of the algebraic equations can be seen in Fig. 7.29.

For more indepth material on these concepts, the interested reader is referred to the following textbooks and journal publications for the following: consistency (Ferziger and Perić 1999; Fletcher 1991); stability (Tu et al. 2008; Yeoh and Tu 2009); convergence (Roy 2003; Tannehill et al. 1997); accuracy (AIAA 1998; Wendt and Anderson 2009).

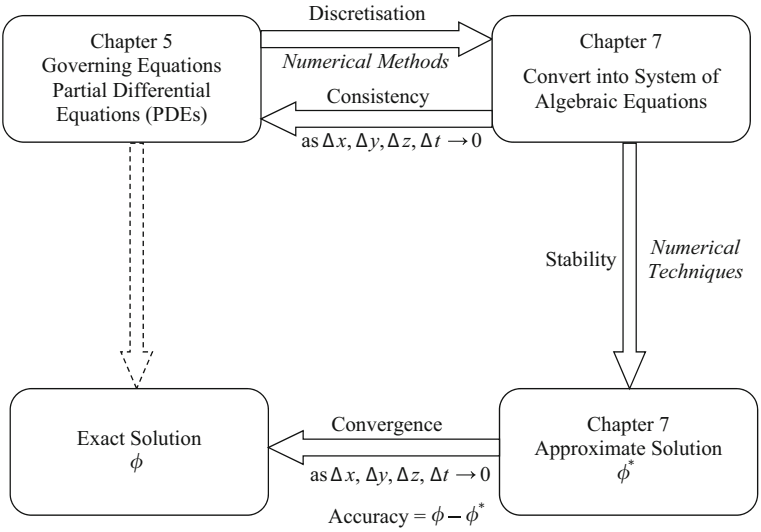


**Fig. 7.29** A conceptual framework linking the various aspects of consistency, stability, convergence and accuracy in arriving at a solution for the transport equations

### *7.5.2 Solution Errors*

Errors are introduced because the numerical solutions of the fluid flow and heat transfer problems are only *approximate solutions*. Some prevalent source of errors dealing with numerical solutions includes the following classification:

- *Discretisation error*
- *Round-off error*
- *Iteration or convergence error*
- *Physical modeling error*
- *Human error*

It should be noted that based on the publication of AIAA Guide for the Verification and Validation of Computational Fluid Dynamics Simulations (AIAA 1998) that there is some difference between error and uncertainty. The AIAA guide defines error as *a recognizable deficiency that is not due to lack of knowledge* while uncertainty can be defined as *a potential deficiency that is due to lack of knowledge*.

*Discretisation error* These errors are due to the difference between the exact solution of the modeled equations and a numerical solution with a limited time and space resolution. They arise because an exact solution to the equation being solved is not obtained but numerically approximated. For a consistent discretisation of the algebraic equations, the computed results are expected to become closer to the exact solution of the modeled equations as the number of grid cells is increased. However,

the results are strongly affected by the density of the mesh and distribution of the grid nodal points.

*Round-off error* These errors exist due to the difference between the machine accuracy of a computer and the true value of a variable. Every computer represents numbers that have a finite number of significant figures. The default value of the number of significant digits for many computers is 7 and this is commonly referred to as *single precision*. However, calculations can also be performed using 15 significant figures, which is referred as *double precision*. The error due to the retaining of a limited number of computer digits available for storage of a given physical value is therefore called the round-off error. This error is naturally random and there is no easy way of predicting it. It depends on the number of calculations, rounding off method, rounding-off type, and even sequence of calculations.

*Iteration or Convergence error* These errors occur due to the difference between a fully converged solution of a finite number of grid points and a solution that has not fully achieved convergence. The majority of commercial CFD codes solve the discretised equations iteratively for steady state solution methodologies. For procedures requiring an accurate intermediate solution at a given time step, this is solved iteratively in transient methods. It is expected that progressively better estimates of the solution are generated as the iteration step proceeds and ideally satisfies the imposed boundary conditions and equations in each local grid cell and globally over the whole domain. However, if the iterative process is terminated prematurely then errors arise. Convergence errors therefore can occur because of either being impatient to allow the solution algorithm to complete its progress to the final converged solution or applying too large convergence tolerances to halt the iteration process when the CFD solution may still be considerably far from its converged state.

*Physical modeling error* These errors are those due to uncertainty in the formulation of the mathematical models and deliberate simplifications of the models. Here, we reinforce the definition of uncertainty from above where the Navier-Stokes equations can be considered to be exact and solving them is impossible for most flows of engineering interest because of lack of sufficient knowledge to model them. The sources of uncertainty in physical models are:

- the phenomenon is not thoroughly understood,
- parameters employed in the model are known to possess some degree of uncertainty,
- appropriate models are simplified thus uncertainty is introduced, and
- experimental confirmation of the models is not possible or is incomplete.

*Human error* There are essentially two categories of errors associated with human error. Firstly, computer programming errors involve human mistakes made in programming, which are the direct responsibility of the programmers. These errors can be removed by systematically performing verification studies of subprograms of the computer code and the entire code, reviewing the details inserted into the code, and performing validation studies of the code. Secondly, usage errors are also due to application of the code in a less-than-accurate or improper manner. Inexperience in

handling CFD codes may result from either incorrect computational domains (such as improper geometry construction or grid generation) or inappropriate setting of boundary conditions. Selection of bad numerical schemes or computational models to simulate certain flow problems compounds the undesirable usage errors. The reader should note that the potential for usage errors increases with the increased level of options available in CFD. Nevertheless, usage errors can be minimized and controlled through proper training and analysis and the accumulation of experience.

### *7.5.3 Validation and Verification*

In addition to errors, uncertainties can arise whilst performing a numerical simulation. These can be due to the improper modeling of physics such as a misunderstanding of the phenomena leading to falsifying assumptions or the incorrect computational design such as making wrong approximations and simplifications about the parameters that govern the fluid dynamics. For a CFD solution to be credible, it requires a detailed analysis to be performed, to quantify the modeling and numerical uncertainties in the simulation. Verification and validation procedures are the means by which a CFD solution can be properly assessed through quantitatively estimating the inherent errors and uncertainties.

Verification and validation have very distinct definitions. Although there is an absence of a universal agreement on the details of these definitions, there is a fairly standard and consistent agreement on their usage. In this book, we will adopt definitions that are focused on numerical errors and uncertainties where they cannot be considered negligible or overlooked.

An important aspect to remember about verification and validation is that it is applied in two very distinct ways. We can differentiate verification and validation in the following. Verification can be defined *as a process for assessing the numerical simulation uncertainty and when conditions permit, estimating the sign and magnitude of the numerical simulation error and the uncertainty in that estimated error*. This procedure concerns primarily to the input parameters used for geometry, initial conditions and boundary conditions. They are required to be carefully checked and systematically documented. It is also important that mesh and time step sensitivity studies are extensively performed to bound the errors, whether they may be insufficient spatial discretisations, too large temporal advancement, lack of iterative convergence or computer programming errors, that are associated with the discrete approximations employed for the partial differential equations. On the other hand, validation can be defined *as a process for assessing simulation model uncertainty by using benchmark experimental data and when conditions permit, estimating the sign and magnitude of the simulation modeling error itself*. This procedure simply means validating the calculations by establishing a range of physical conditions obtained from the calculations, and performing comparisons of the results from the CFD code with experiments that span the range of conditions.

## 7.6 Solution Procedure

Up to this point we have covered a large proportion of developing and solving a CFPD flow in the respiratory system. To summarise the flow process, Fig. 7.30 illustrates the interconnections of the three main elements of a CFPD analysis.

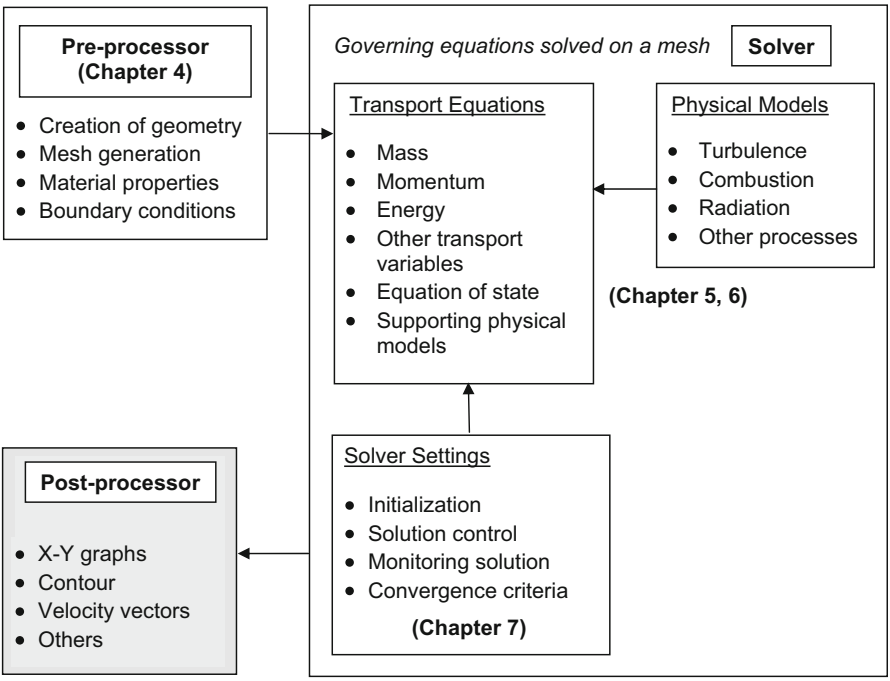


**Fig. 7.30** Flow process of the three main elements within a CFPD analysis framework

### *7.6.1 Pre-processing Stage*

The first step in any CFD analysis is the definition and **creation of a geometry** for the region of interest, i.e. the computational domain for the CFD calculations. Let us consider two flow cases: a fluid flowing between two stationary parallel plates and a fluid passing through two cylinders in an open surrounding. It is important that the reader always bear in mind the real physical flow representation of the problem that is to be solved as demonstrated by the respective physical domains. For a typical respiratory flow, the geometry will be an internal flow bounded by walls with single or multiple inlets and outlets.

The second step involves mesh generation which constitutes one of the most important steps during the pre-processing stage. The sub-division of the computational

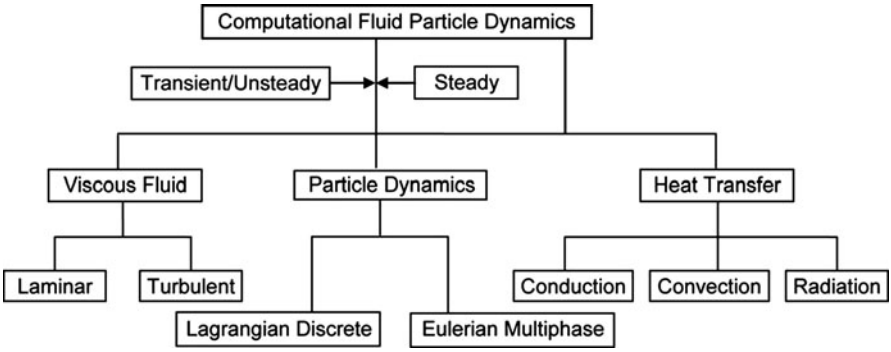


**Fig. 7.31** A flowchart encapsulating the various flow physics in CFPD

domain into a number of smaller, non-overlapping sub-domains allows flow physics within the domain geometry to be applied. This results in the **generation of a mesh** (or grid) of *cells* (elements or control volumes) overlaying the entire domain geometry. The essential fluid flow that is described in each of these cells is usually solved numerically so that the discrete values of the flow properties such as the velocity, pressure, temperature and other scalars of interest are determined. This yields the CFD solution to the flow problem that is being solved. The accuracy of a CFD solution is governed by the number of cells in the mesh within the computational domain. In general, the provision of a large number of cells leads to the attainment of an accurate solution. However, the accuracy of a solution is strongly dependant on the imposed limitations dominated by the computational costs and calculation turnover times.

The **selection of the fluid properties and physics** determines the required equations that govern the fluid and particle flows. For example inhalation and exhalation may be simplified as a steady flow rate if generalised results are required and localised transient changes can be neglected. The inhaled air is typically taken as a *viscous* fluid which can exist in a *laminar* or *turbulent* state. Also, the transport of heat may contribute significantly to the fluid flow process, which comprises of three heat transfer modes: *conduction*, *convection* and *radiation,* (although radiation heat transfer is unlikely to occur in the respiratory system). In terms of modelling the particle phase a decision has to be made as to whether either a Lagrangian discrete phase or a fully coupled Eulerian multiphase. It is therefore imperative that a CFD user carefully identifies the underlying flow physics that is unique to the particular fluid flow system (Fig. 7.31).

The complex nature of the fluid flow behaviour has important implications in which boundary conditions are prescribed for the flow problem. The appropriate boundary conditions selected need to mimic real physical representation of the fluid flow.

In this section we present briefly some basics regarding settings and specification of boundary conditions. At boundaries where the fluid is entering or leaving the flow

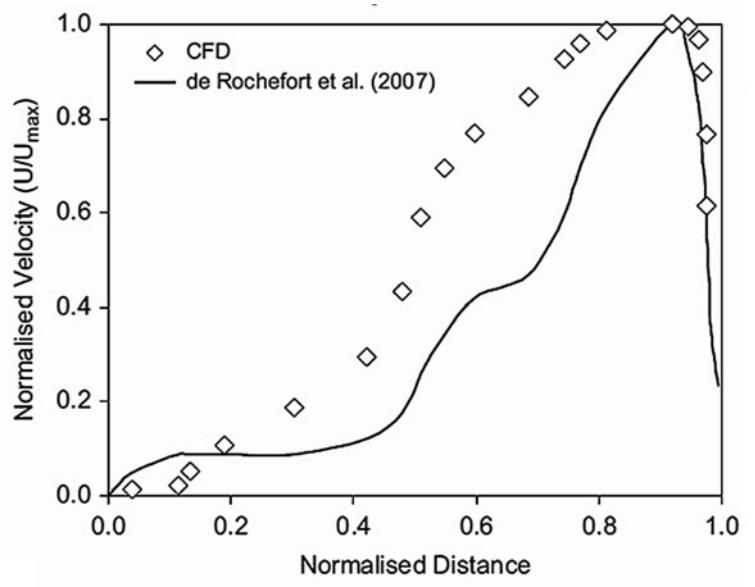


**Fig. 7.32** Example of some possible boundary condition settings

domain, *inflow* and *outflow* boundary conditions are suitable. The flow domain may also be bounded by *open* boundaries. Appropriate boundary conditions are also required to be assigned for external stationary *solid wall* boundaries that bound the flow geometry and the surrounding walls of possible internal obstacles within the flow domain. The flow domain may also be bounded by *open* boundaries. Although the intricacies of *open* boundary conditions are still subject to much theoretical debate, this boundary condition remains the simplest and cheapest form to prescribe. Appropriate boundary conditions are also required to be assigned for external stationary solid wall boundaries that bound the flow geometry and the surrounding walls of possible internal obstacles within the flow domain.

General purpose CFD codes also allow the prescription of inflow and outflow *pressure* or *mass flow rate* as boundary conditions. By setting fixed pressures values, sources and sinks of mass at the boundaries are calculated to ensure the correct mass flow into and out of the solution zone. It is also feasible to directly allocate sources and sinks of mass at the boundaries by the mass flow rate instead of pressures to retain the overall mass balance for the flow domain. To take advantage of special geometrical features that the solution region may possess, *symmetric* and *cyclic* boundary conditions can be employed to reduce the computational domain size Fig. 7.32). This in turn allows the user to place additional cells to the reduced, simplified geometry, thus enhancing the computational accuracy.

### 7.6.2 Numerical Solver

The numerical methods and solution presented in this chapter is the basis of the second main element of a CFPD simulation. A core understanding of the underlying numerical aspects inside the solver is imperative to obtain reliable results. The steps in a solver can be described in Fig. 7.33.

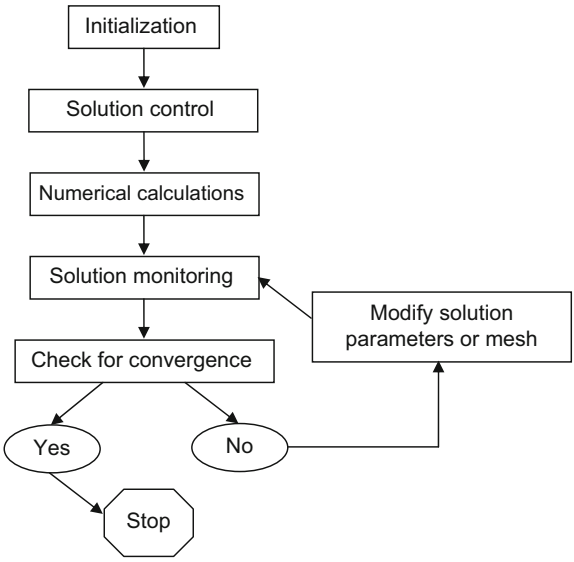


**Fig. 7.33** An overview of a numerical solver within a CFD software package

To begin the iterative solution process the flow domain needs to be initialised with initial boundary values. Discrete values of flow properties such as the velocity, pressure, temperature and other transport parameters of interest are defined at every computational cell (**initialisation**) before calculations can begin. In theory, initial conditions can be purely arbitrary. However, in practice, a good set of initial values will achieve quicker solution convergence. Additionally if the initial conditions are very unrealistic the solution may actually diverge and a solution cannot be reached.

The **solution control** stage involves selection of the appropriate *discretisation* (*interpolation*) *schemes* and *iterative solvers*. In many CFD software packages, the finite volume method is used, although some packages may use the finite difference, finite element, or mesh-free methods such as Lattice Boltzmann or smooth particle hydrodynamics. The different discretisation schemes and the pressure-velocity coupling for finite volume and finite difference have been described in this chapter. Similarly the numerics for the particle phase are selected. For the Eulerian model there are interphase coupling schemes while for the Lagrangian method, there are a number of numerical integration methods for the particle equation of motion.

The iterative solvers within the software are the so-called number crunching engines for the numerical calculations which are used to resolve the algebraic equations. Robust solvers such as Algebraic Multi Grid (AMG) algorithm and conjugate gra-

dient methods are standard features in many commercial codes. Solver controlling parameters that exist inside these solvers in commercial codes tend to be optimally configured for efficient matrix calculations. The desired performance can usually be achieved through the default settings prescribed within the codes.

During the actual numerical calculations the user should undertake solution monitoring which involves *checking for convergence* of the iterative process and performing a **grid independence**. Convergence can usually be assessed by progressively tracking the imbalances that originate from the initialized boundary conditions and are a measure of the overall conservation of the flow properties. Ideally an exact solution will produce an imbalance equal to zero but in practice a value close to zero should suffice. These imbalances are also commonly known as residuals. The user should monitor the residuals to ensure that it has a moving downwards which implies removal of imbalances leading to a converging solution, as opposed to possible accumulation of any unwanted imbalances which is a diverging solution. A converged solution is achieved when the residuals fall below some convergence criteria that are preset inside the solver controlling parameters of the iterative solvers. Besides examining the residuals, the user may use other monitoring variables such as the lift, drag or moment force to ascertain the convergence of the numerical computations.

Progress towards a converged solution can be greatly assisted by the careful selection of various *under-relaxation factors*. Most commercial codes adopt some form of under-relaxation factors to enhance the stability of the numerical procedure and ensure the convergence of the iterative process. The incorporation of under-relaxation factors into the system of algebraic equations that govern the fluid flow is intended to significantly moderate the iteration process by limiting the change in each of the transport variable from one iterative step to the next. There are no straightforward guidelines for pertinent choices of these factors. More often than not, in-depth experience on the selection of appropriate values of these factors can only be gained by the extensive investigation on a variety of flow problems.

### *7.6.3 Post Processing*

The post processing stage involves analysis of the numerical data that is produced. In its raw form, this data is simply a collection of numbers stored at coordinates based on the mesh design. The conversion of raw data into meaningful results is called the post-processing stage. CFPD has the capability to produce colourful graphics, and precise detailed data. In this section, we first present some post processing techniques frequently encountered in the presentation of CFPD data. This is followed up by presenting an integral part of the results analysis, namely the validation of results section.

*X-Y Plots* These plots two-dimensional graphs usually represent the variation of one dependent transport variable against another independent variable. They are usually meant to be very easily identifiable; i.e. the reader can simply read the results without resorting to any mental or arithmetic interpolation. They are a popular

way of directly comparing numerical data with experimentally measured values (e.g. Fig. 7.34a). Also, logarithmic scales allow the identification of important flow effects occurring especially in the vicinity of solid boundaries. Furthermore they are common in representing line profiles of velocity and for plots of surface quantities such as pressure and skin-friction coefficient.

*Vector Plots* A vector plot displays a vector quantity at discrete points (usually velocity) with an arrow whose orientation indicates direction and whose size indicates magnitude. It generally presents a perspective view of the flow field in two dimensions. In a three-dimensional flow field, different slices of two-dimensional planes containing the vector quantities can be generated in different orientations to better scrutinize the global flow phenomena (see Fig. 7.34b). If the mesh density is considerably high, the CFD user can either interpolate or reduce the numbers of output locations to prevent the clustering of these arrows "obliterating" the graphical plot.

*Contour Plots* In contrast to X-Y plots, contour plots provide a global description of the fluid flow encapsulated in one view, a feature found in vector plots (e.g. Fig. 7.34a). Generally, contours are plotted such that the difference between the numerical value of the dependent transport variable from one contour line to an adjacent contour line is held constant. The use of contour plots is not usually targeted for precise evaluation of numerical values between contour lines but rather to give a qualitative perspective. A contour line (also known as *isoline*) can be described as a line indicative of some property that is constant in space. Its equivalent representation in three-dimensions is an *isosurface.* In practice, the contours are usually linearly scaled. However, to better capture the hidden details in some small regions within the flow field, the reader may be required to employ a finer scaling choice to reveal these isolated flow behaviors. For the contour plots where the *isoline* interval values are the same, then clustering of these lines indicates rapid changes in the flow quantities.

*Particle Trajectory and Deposition Plots* When a Lagrangian method is used, particle trajectories can be plotted. In more complex flow problems such as multiphase flows that involve the transport of solid particles, *particle tracks* associated with the discrete particles of a certain diameter and mass being injected inside the bulk fluid fall in this same category. Here, important information on the particle residence time, particle velocity magnitude and other properties can be duly extracted. When a particle hits a surface wall, the particle tracking can be terminated and the particle's impaction onto the wall can be recorded. By plotting these coordinates onto the computational geometry, a deposition plot can be achieved. Figure 7.35 shows the deposition sites of particles after it has travelled through the nasal cavity and finally deposited onto the nasal walls. Some things to note for this case include the assumption that there is no mass or momentum transfer from the particle to the surface wall and the particle does not bounce/rebound or splatter upon impact. Furthermore when producing a particle deposition plot, there are limitations on the number of particles that can be displayed on the computer screen based on the graphical processing ability of the computer being used. Typically 10,000 particles on today's standard desktop computers will be the limit (based on 1 Gb graphics card).

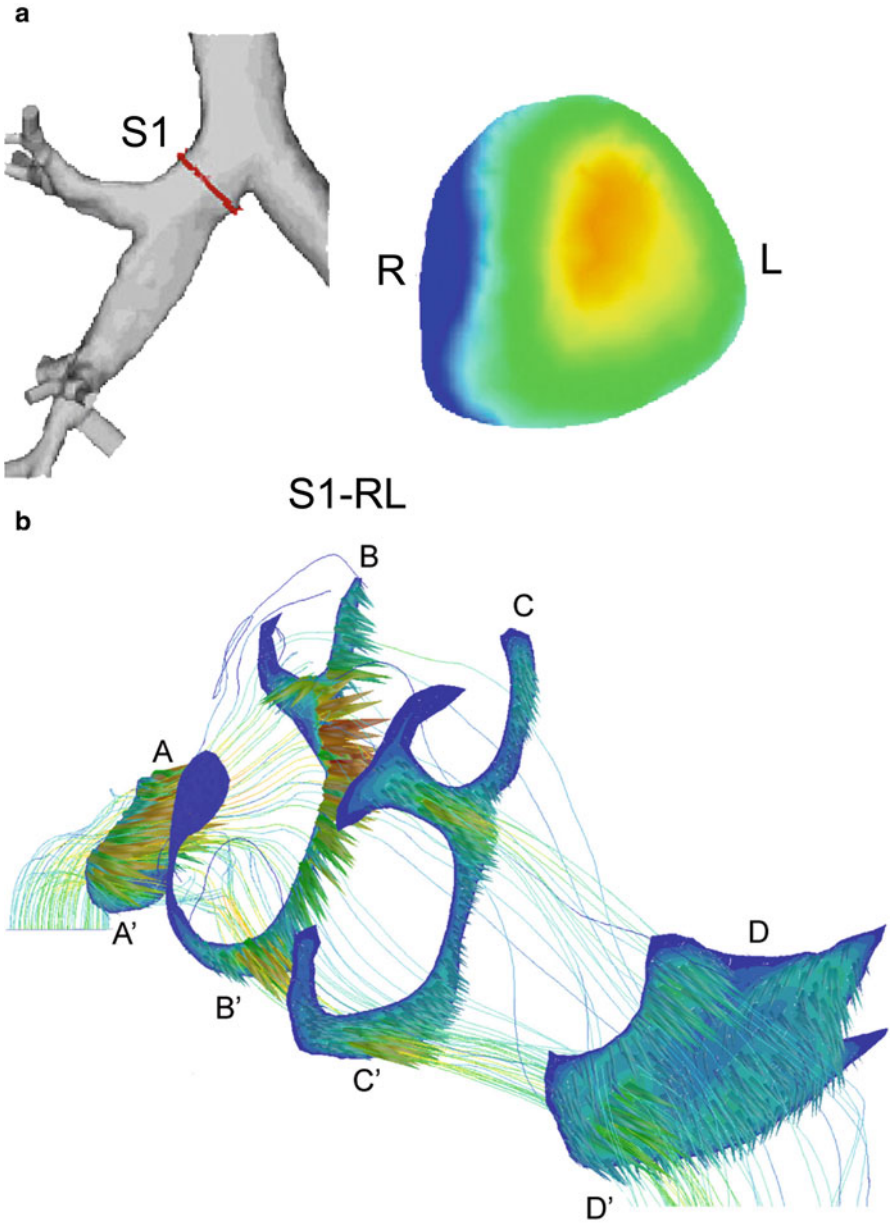


**Fig. 7.34** Various examples of post processing analysis. **a** CFD simulation in showing the velocity contour plot and its corresponding normalised velocity profile comparisons with the work of de Rochefort et al. (2007). **b** Airflow streamlines passing through velocity contours taken at different coronal sections in the right nasal cavity. Velocity vectors on each coronal section shaped by cones are also presented. (Inthavong et al. 2008a)

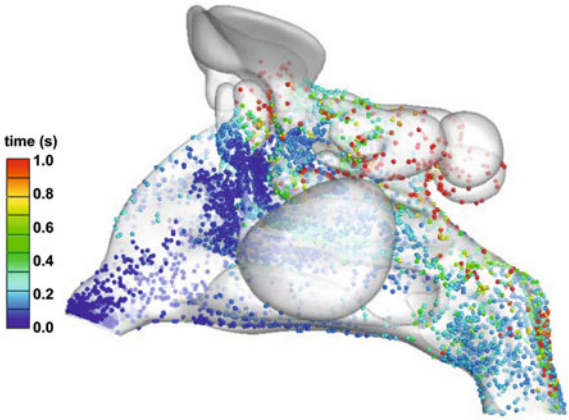


**Fig. 7.35** Nanoparticle deposition pattern in the nasal-sinus cavity for 10 nm – resulting in 29.8 % deposition. Particles are coloured by trajectory time within the nasal cavity before impacting onto the surfaces at 10 L/min

*Other Plots* *Streamlines* are used for examining the nature of a flow either in two or three dimensions (e.g. (Fig. 7.34b). By definition, *streamlines* are parallel to the mean velocity vector where they trace the flow pattern using *massless* particles. They can generally be obtained by integrating the spatial three velocity components expressed in a three-dimensional Cartesian frame: $dx/dt = u, dy/dt = v$ and $dz/dt = w$. Streamlines are also called *streamtraces*, *streaklines* or *path lines*.

*Animations* CFD data lends itself very neatly to the animation category – *moving pictures* of the data produced through the CFD simulation. Animation, as with other graphical display tool, represents not only a technical record of quantitative results; it is an artistic work of art. Nowadays, a collection of short-length animated videos or movies with multiple frames of brightly colourful representations of CFD simulations can be found in many internet websites. It is undoubtedly an effective visualization tool for education and marketing purposes.

## 7.7 Summary

In this chapter we have introduced the basic computational techniques to solve the governing equations of fluid dynamics. The first stage of obtaining the computational solution involves the conversion of the governing equations into a system of algebraic equations. This is usually known as the *discretisation stage*. We have discussed some of the *discretisation tools* such as the finite difference and finite volume methods, which form the foundation of understanding the basic features of *discretisation*. Both of these methods are abound in many CFD applications.

The second stage involves numerically solving the system of algebraic equations, which can be achieved by either the *direct methods* or *iterative methods*. Basic direct methods such as the Gaussian elimination and the Thomas algorithm have been described of which the latter is highly economical for a tri-diagonal matrix system and is a standard algorithm for the solution of fluid flow equations in a structured

mesh. Simple iterative methods such as the point-by-point Jacobi and Gauss-Siedel methods are also described.

In solving the continuity and momentum equation, the transport of a fluid property i.e. convection and diffusion transport, has been described. It was found that there was an absence of an explicit pressure equation which meant that a pressure-velocity coupling scheme had to be used. An iterative algorithm for the calculation of pressure and velocity fields based on the SIMPLE scheme is presented for an incompressible flow. The basic philosophy behind this popular scheme is to initially guess a pressure field in the discretised momentum equations to yield the intermediate velocities. The continuity equation in the form a pressure correction is subsequently solved, which are then used to correct the velocity and pressure fields. These guessed fields are continuously improved until convergence is reached. The Lagrangian particle tracking equation is in the form of an ordinary differential equation which differs from the governing equations of fluid flow which is in the form of a set of partial differential equation. Some common techniques, (among many available) to solve an ODE were presented.

This chapter culminates by presenting the information from Chaps. 4–6 in the context of the general flow process in performing a CFPD problem. The preprocessing stage, mainly covered in Chap. 4 is the first main element of the flow process. This stage sets up the preliminaries for the flow problem at hand. The next main element is the numerical solver which includes the selection of the necessary equations and the solution algortihms (Chaps. 5–7). During the numerical calculations, the user needs to monitor the results and make adjustments where needed to ensure a converging solution. Finally the post processing stage involves converting the raw data into graphical representations. This chapter wraps up the stages in developing and solving CFPD flow problems. In the next Chap. 8, some respiratory gas-particle flow examples are presented. The physical and computational issues that arise from the selected examples are discussed.

## 7.8 Review Questions

1. What are the differences between solving a fluid flow problem analytically compared with solving numerically? What are the advantages and disadvantages of each method?
2. What are the main advantages and disadvantages of discretisation of the governing equations through the finite difference method?
3. Is finite difference more suited for structured or unstructured mesh geometries? Why?
4. Consider the following finite difference formulation for a simplified flow: $\frac{\phi_{n-1}-2\phi_n+\phi_{n+1}}{\Delta x^2} = 0$.
   Is the flow steady or transient?
   Is it one- two- or three dimensional?
   Is the nodal spacing constant or variable?

5. Using finite difference, show that the one-dimensional heat conduction equation, $q = k\frac{\Delta T}{\Delta x}$ can be expressed as $\frac{T_{n-1}-2T_n+T_{n+1}}{\Delta x^2} = 0$?
6. What is the second term in the central difference approximation for a first order derivative (given below) called and what does it measure? $\left(\frac{\partial \phi}{\partial x}\right) = \frac{\phi_{i+1,j}-\phi_{i-1,j}}{2\Delta x} + O(\Delta x^2)$ Which of the following, *forward difference*, *backward difference* and *central difference*, is most accurate and why?
7. What are the main advantages and disadvantages of discretisation of the governing equations through the finite volume method?
8. Is finite volume method more suited for structured or unstructured mesh geometries? Why?
9. What is the significance of the integration of the governing equations over a control volume during the finite volume discretisation?
10. For the control volume below, show how the one-dimensional steady state diffusion term $\frac{\partial}{\partial x}\left(\Gamma \frac{\partial \phi}{\partial x}\right)$ is discretised to obtain its discretised equation $\left(\Gamma \frac{\partial \phi}{\partial x}\right)_e A_E - \left(\Gamma \frac{\partial \phi}{\partial x}\right)_w A_w$ for central grid nodal point $P$?

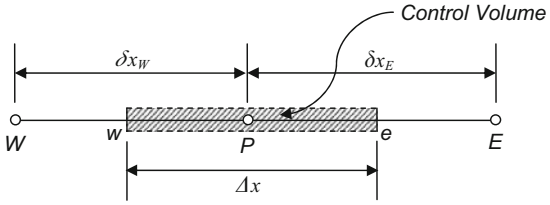


11. In a finite difference scheme, data is resolved at nodal points, how is this different to the finite volume scheme?
12. How is a steady convective-diffusion process different from a pure diffusion process?
13. Why are upwind schemes important for strongly convective flow?
14. Why are higher order upwind schemes more favourable than the first order upwind scheme?
15. For the unsteady convection-diffusion process, what is the difference between *explicit* and *implicit* time-marching approaches?
16. What is the difference between using a direct method and an iterative method to solve the discretized equations?
17. Is the direct method or iterative method more suitable in solving for a large system of non-linear equations?
18. Why does the Gauss-Siedel iterative method converge to a solution quicker than the Jacobi method?
19. What is the technique of the *successive overrelaxation* and why is it used?
20. Where are the flow field variables located in collocated grids? How is this different to the locations in a staggered grid?

21. Write down the formulation of central difference scheme for 'U' velocity in the $x$-direction. What is its truncation error in terms of $\Delta$x? And state the order of this discretisation scheme?
22. What is the purpose of the SIMPLE scheme? Does it give us a direct solution or depend on the iterative concept?
23. What is the Gaussian elimination method based on? Can this method be used to solve a system of nonlinear algebraic equations?
24. Solve the following set of equations by Gaussian elimination:

$$\begin{bmatrix} 100 & 100 & 0 \\ 200 & 100 & - \\ 300 & - & - \\ - & 200 & 300 \end{bmatrix} \begin{bmatrix} T_1 \\ T_2 \\ T_3 \\ T_4 \end{bmatrix} = \begin{bmatrix} 400 \\ 100 \\ -300 \\ 400 \end{bmatrix}$$

25. Solve the following set of equations by the Thomas Algorithm:

$$\begin{bmatrix} 100 & - & 200 & - \\ 200 & - & 300 & - \\ 100 & 100 & 100 & 0 \\ 100 & - & 400 & 300 \end{bmatrix} \begin{bmatrix} T_1 \\ T_2 \\ T_3 \\ T_4 \end{bmatrix} = \begin{bmatrix} 800 \\ -2000 \\ -200 \\ 400 \end{bmatrix}$$

26. Solve the following set of equations using the Gauss-Seidel method:

$$\begin{bmatrix} -1000 & -100 & 200 \\ -100 & -1100 & -100 \\ 200 & -100 & 1000 \\ 0 & 300 & -100 \end{bmatrix} \begin{bmatrix} T_1 \\ T_2 \\ T_3 \\ T_4 \end{bmatrix} = \begin{bmatrix} 600 \\ -2500 \\ 1100 \\ 1500 \end{bmatrix}$$

27. For the same matrix given in question 4.26, use the Jacobi method to solve the set of equations. Compare the number of iterations for convergence between the Jacobi method and the Gauss-Seidel method.
28. Solve the following set of equations using the Gauss-Seidel method.

(a)

$$\begin{aligned} 3x_1 - x_2 + 3x_3 &= 0 \\ -x_1 + 2x_2 + x_3 &= 3 \\ 2x_1 - x_2 - x_3 &= 2 \end{aligned}$$

(b)

$$\begin{aligned} 10x_1 - x_2 + 2x_3 &= 6 \\ -x_1 + 11x_2 - x_3 + 3x_4 &= 25 \\ 2x_1 - x_2 - 10x_3 - x_4 &= -11 \\ 3x_2 - x_3 + 8x_4 &= 15 \end{aligned}$$

29. Following the grid arrangement below, derive the following expression:

$$\left(\frac{\partial^2 u}{\partial x \partial y}\right)_{i,j} = \frac{u_{i+1,j+1} - u_{i+1,j-1} - u_{i-1,j+1} + u_{i-1,j-1}}{4\Delta x \Delta y}$$

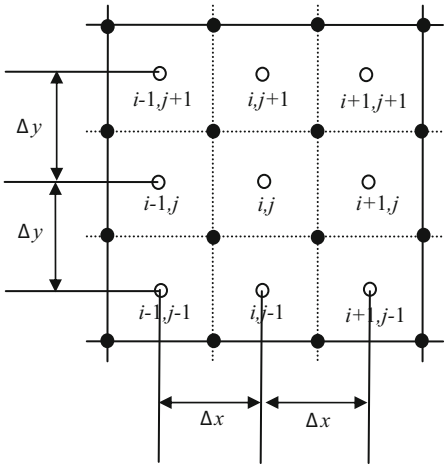


30. Explain the difference between implicit and explicit methods in solving Ordinary Differential Equations (ODEs).
31. Explain the difference in obtaining the gradient of a curve using the forward Euler, Runge-Kutta, and the backward Euler methods.
32. Solve the following ODE $\left(\frac{\partial u}{\partial t}\right) = -u$, using the explicit forward Euler method where $u(0) = 1$ using $h = 0.2$ s.
    Compare the errors between the numerical method with the analytical solution which is given as, $u = \frac{1}{\exp(t)}$.
    Repeating the solution but using $h = 0.4$ s, and 0.1 s, determine the new errors.
33. Solve the following ODE $\left(\frac{\partial u}{\partial t}\right) = \sin(u)$, using the explicit forward Euler, Runge-Kutta, and implicit backward Euler methods. $u(0) = 1$ using $h = 0.2$ s.
    Compare the errors between the numerical methods with the analytical solution which is given as, $u = 2\tan^{-1}(\exp(t + \ln(\tan(1))))$

# Chapter 8
# Case Studies in the Human Respiratory System

## 8.1 Introduction

The use of CFD in biomedical applications has emerged as a legitimate alternative to traditional cast models and human experimental methods. With recent developments in computational hardware, biomedical imaging instruments and CFD techniques, new and exciting research possibilities for the human respiratory system have emerged—some of which were discussed in Chap. 1. In the preceding chapters important fundamental steps were described in relation to the development of computational models of the respiratory system. The morphology and physiological nature of the respiratory system outlined in Chap. 2 highlights the increased level of complexity that is involved in biomedical CFD applications. For example, small scales, surface irregularities, and high curvatures are all characteristic of the nasal cavity, larynx and upper lung airway. These issues bring to fore the need for convergence of multi-disciplines, involving biomedical imaging, reverse engineering in Computer-Aided-Design (CAD), and finally CFD. In Chap. 3 the needed steps for reconstructing the respiratory passage were discussed. In fact, these preparatory steps can be viewed as a prerequisite for construction of any complex geometry. From the reconstructed CAD model, CFD simulations can then be undertaken by first developing a computational mesh (Chap. 4), and then applying the appropriate physics to suit the problem at hand. For example, fluid flow problems, such as inhalation and humidification of the inhaled air, need to consider the fundamentals of fluid dynamics as described in Chap. 5, whereas the inclusion of inhaled particles for drug delivery or for harmful particles suspended in the atmosphere require additional particle equations and models which were discussed in Chap. 6. The correctly defined problem is then ready to be solved computationally. The numerical schemes and algorithms found in Chap. 7 are the cornerstone of any CFD analysis. Fundamental understanding of the conservation equations and numerical approximations is prerequisite for generating efficient solutions.

Having laid the groundwork to establish a strong theoretical base, this chapter culminates in the foundational knowledge attained by applying the theories and putting them into practice through selected demonstrative applications. From a practical viewpoint, the selected detailed case studies in this chapter will provide the reader

J. Tu et al., *Computational Fluid and Particle Dynamics in the Human Respiratory System,* 233
Biological and Medical Physics, Biomedical Engineering,
DOI 10.1007/978-94-007-4488-2_8, © Springer Science+Business Media Dordrecht 2013

with confidence in applying the techniques to a wide range of biomedical engineering applications. The computational model of a human nasal cavity and the upper lung airways developed and described in Chaps. 3 and 4 is used for the case studies herein. Analyses of the results are shown to inform the reader how to translate the myriad of contours, vectors, and line plots and what to look out for in case of any spurious results. Just like a medical practitioner reading CT or MRI scans needs the ability to look for abnormalities, the colourful CFD results need expertise for interpreting and distinguishing their significant features. Therefore this chapter has the following important aims:

- apply the theoretical knowledge attained from previous chapters through worked case studies,
- demonstrate different setup procedures that reflect the needs of individual cases,
- demonstrate how to convert raw data into presentable contour and vector maps, and line plots, and
- demonstrate how to analyse the results and what type of results should be expected under different cases.

## 8.2 Modelling Inhalation and Heat Transfer in the Nasal Cavity

The human nasal cavity, which performs a variety of physiological functions, is an important component of the respiratory system. Individual aspects of the nasal cavity, such as the geometry and flow rate, collectively affect nasal function by bringing inspired air into contact with mucous-coated walls, thereby humidifying and warming the air before it enters the lungs. The inspired air is heated and humidified within the short distance from the nostrils to the nasopharynx (Inthavong et al. 2009b; Keck et al. 2000a). To better understand the physiology of the nose, detailed airflow patterns between the left and right nasal cavities can provide data that are pertinent to the prediction of gas–particle flows and regional tissue exposure to inhaled air. Because of the inter-subject variations inherent between nasal cavity geometries, the numerical results herein are compared with experimental data available in the literature to complement and reinforce the current knowledge base.

The fundamental physics and the CFD setup details that are needed in order to study the effects of morphological differences in the left and right nasal cavities on the airflow and heat transfer of inhaled air are discussed. The differences in the left and right cavities will be explored and the effects they have on the flow field, especially in the nasal valve and middle turbinate regions, are discussed. Geometrical differences are also compared with available data in the literature. Additionally, variations in the flow patterns and flow features such as pressure drop, wall shear stress, velocity, and flow distribution between the left and right cavity as well as different geometries are also presented. The flow in the nasal valve and turbinate region is studied in particular detail to provide better insight into flows in this region.

### 8.2.1 Inhalation Through the Anatomy and Its Physiology

The anatomy and physiology of the nasal cavity during inhalation have been discussed in detail in Chap. 2, and only a summary of the important features in relation to the CFD modelling needs are discussed here. In the succeeding descriptions, the $+x$ coordinate is from the anterior tip of the nostril inlet running posterior to the back of the nose at the nasopharynx, which is referred to as the axial direction (Fig. 8.1).

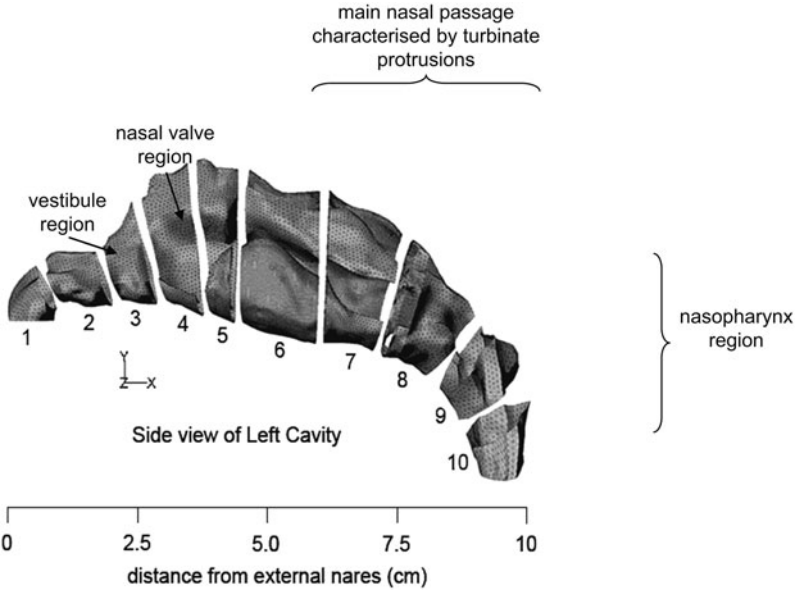


**Fig. 8.1** Side view of the *left* nasal cavity which is sectioned into ten regions used for local deposition analysis

The nose can be divided axially into four regions: the vestibule, the nasal valve, the turbinate and the nasopharynx regions. The first three-quarters of the nasal cavity are divided into the left and right cavity separated by the nasal septum wall. Air enters each cavity through the oval-shaped external nostrils into the vestibule. The flow changes direction, 90° towards the horizontal, before entering the nasal valve region. The flow increases in this region where the cross-sectional area is smallest causing an acceleration of the air. At the end of the nasal valve region, the cross-sectional area of the nasal cavity increases suddenly. This expansion is the beginning of the turbinate region where the profile is complicated and asymmetrical. Finally, at the nasopharyngeal region, the left and right cavities merge together causing the flow in this region to mix intensely.

The main factors that contribute to the airflow patterns are the nasal cavity geometry and the flow rate. For a realistic human nasal cavity, geometric variations between the left and right-sided nasal cavities exist at any one time as a result of a combination of its natural geometry, due to the nasal cycle, and any other physiological reactions at the time. Inhalation is caused by the negative pressure induced

by the diaphragm flattening out to increase the volume of the pleural cavity (see Sect. 2.3.2). Flow rates for adults can range between 5–12 L/min for light breathing and 12–40 L/min for non-normal conditions, such as during exertion and physical exercise. Usually breathing switches from pure nasal flow to oral-nasal flow at this higher range. Additionally, flow rates for extreme forced inhalation conditions have been found to reach 150 L/min (Robert 2001). Issues pertaining to the geometry and physiologic features discussed in Chap. 2 also need to be kept in mind when setting up the numerical model and interpreting the results.

### *8.2.2 Boundary Conditions*

The reconstructed computational model of the human nasal cavity from Chaps. 3 and 4 is used in this case study. Modelling the inhalation process raises some important conditions that need to be determined:

- is the flow *laminar or turbulent*,
- *steady or unsteady*,
- the type of *inlet/outlet conditions* for the nasopharynx and nostril inlets
- additional equations that are needed to account for *heat transfer*.

*Laminar or Turbulent* Laminar flows are normally characterised by a smooth motion where the fluid's viscosity dominates allowing high molecular diffusion and dampening out any fluctuations in the flow. This leads to adjacent layers of fluid sliding past each other in an orderly fashion (like layers of lamina). However for a nasal cavity which has a complex geometry that is highly convoluted, flow separation and recirculation can exist especially in the region from the nasal valve to the main nasal passage where a rapid increase in the cross-sectional area is observed (Proctor 1982), enhancing flow instabilities. It must be mentioned that although flow separation and recirculation are typical characteristics of turbulent flow, the presence of these characteristics does not necessarily indicate that the flow is turbulent, since they may be found in laminar flows as well.

The dimensionless parameter, the Reynolds number (*Re*), is often used to determine the flow regime. For higher velocities the effects of turbulent disturbances become significant with the presence of velocity fluctuations in the flow field while for lower velocities the viscosity dominates to dampen out any fluctuations. The critical flow rate and therefore the *Re* number at which the flow changes from a laminar to a turbulent flow regime are difficult to succinctly define due to the complexity of the airway, which has led to some debate concerning the type of airflow regime to implement for numerical simulations. Experimental studies by Kelly et al. (2000) have suggested that a laminar flow regime dominates for low flow rates around 10 L/min. While the results of Hahn et al. (1993) also agree, the authors mention that the flow is a disturbed laminar regime. Churchill et al. (2004) studied ten nasal cast replicates and found that at the lowest flow rate of 1.5 L/min, small local turbulent characteristics were present. However they pointed out that some of the turbulence

**Table 8.1** Summary of viscous model and flow setup for selected human nasal cavity simulations

| Researcher | L/min (peak) | Viscous model | Steady/ Unsteady | Heat transfer | Mesh size |
|---|---|---|---|---|---|
| Pless et al. (2004) | 30 | Turbulent | Steady | Yes | 360,000 |
| Weinhold and Mlynski (2004) | 12–84 | Turbulent | Steady | No | Not reported |
| Zhao et al. (2006) | 14–55 | Both | Steady | No | Not reported |
| Lindemann et al. (2005) | 18 | Turbulent | Steady | Yes | 360,000 |
| Naftali et al. (2005) | 15 | Laminar | Unsteady | Yes | 300,000 |
| Schroeter et al. (2006) | 15 | Laminar | Steady | No | 156,000 |
| Croce et al. (2006) | 21 | Laminar | Steady | No | 1.3 million |
| Garcia et al. (2007b) | 15 | Laminar | Steady | Yes | 1.3 million |
| Xiong et al. (2008) | 21 | Laminar | Steady | No | 1.8 million |
| Doorly et al. (2008) | 6 | Not reported | Steady | No | 3.6 million |
| Lee et al. (2010) | 35 (peak) | Turbulent | Unsteady | No | 2.9 million |
| Liu et al. (2010a) | 30–90 | Turbulent | Steady | No | 4.0 million |
| Horschler et al. (2010) | 9–47 | Not reported | Both | No | 4.5 million |
| Zhu et al. (2011) | 10 | Laminar | Steady | No | 3.9 million |
| Xi et al. (2011) | 20 | Turbulent (transitional) | Steady | No | 1.75 million |
| Inthavong et al. (2011) | 20 | Turbulent (transitional) | Steady | No | 3.5 million |

observed reflected local flow regimes that have little effect on the bulk flow through the nose. The average flow rate at which flow switched from transitional to turbulent for the ten cast replicates was 11 L/min. To give the reader a feel for which flow regime setup to use, Table 8.1 summarises work from the literature in regard to the choices the researchers made. The survey of work in Table 8.1 shows a consensus among researchers in choosing a laminar flow for flow rates less than 20 L/min. In this study, flow rates of 7.5 and 15 L/min were used with a prescribed laminar flow regime. These flow rates represent the combined total volume inhaled from both nostrils per minute; thus each nostril will experience half the total flow rates (3.75 and 7.5 L/min respectively).

*Steady or Unsteady* The inhalation process is clearly unsteady with an oscillatory motion. In order to assess the importance of the unsteadiness on the mean or average flow characteristics obtained through a steady solution, we make use of the Womersley number $\alpha$ and the Strouhal number $S$. The Womersley number is a ratio of unsteady forces to viscous forces named after John R. Womersley (1907–1958) and is defined as

$$\alpha = \frac{D}{2}\left(\frac{\omega}{\nu_g}\right)^{0.5} \tag{8.1}$$

where $D$ is the characteristic length which is taken as the inlet hydraulic diameter of the nostrils equals 0.01 m: $\nu_g$ is the kinematic viscosity of air, and $\omega$ is the breathing frequency equal to $\omega = 2\pi f = 1.57\ \mathrm{s}^{-1}$; and $u_{ave}$ is the average velocity through the nasal passage under the flow rate of 15 L/min which is equal to 0.9 m/s. When $\alpha$ is small (1 or less), the oscillatory effects are sufficiently low that the inlet conditions,

such as a parabolic velocity profile, have time to develop during each cycle, and the flow will be very nearly in phase with the pressure gradient. When $\alpha$ is large (10 or more), the oscillation effects are sufficiently large that the velocity profile does not develop in time and the mean flow characteristics lag the pressure gradient by about 90°, Womersley (1955). The Strouhal number is a ratio of the unsteady forces to the inertial forces named after Vincenc Strouhal (1850–1922) and is defined as

$$S = \frac{\omega D}{u_{ave}} \tag{8.2}$$

where $u_{ave}$ is the mean airflow velocity. For large $S(>1)$, the oscillations become important. For low $S(\ll 1)$, the contribution of the velocity dominates the oscillations. The calculated $\alpha$ and $S$ numbers for the nasal cavity in this case study are 1.68 and 0.01, respectively. Although $\alpha$ is greater than 1, it is not much greater, while the low value for $S$ suggests that the flow may be assumed to be quasi-steady. It has, however, been shown experimentally that the oscillatory effects are not present until $\alpha > 4$ (Isabey and Chang 1981). Other studies have also concluded that under most conditions, especially low flow rates, the nasal airflow can be considered quasi-steady (Chang 1989; Hahn et al. 1993; Sullivan and Chang 1991).

*Inlet/Outlet Conditions* Boundary conditions for the computational surfaces need to be defined. While the surface walls are easily understood in terms of their definition as a rigid wall boundary (see Sect. 9.2 for dealing with elastic walls), the nostril inlets and the nasopharynx outlet provide the user with more options for definition. In this case study, a uniform flow perpendicular to the nostril inlet was specified. This assumption is based on the data of Keyhani et al. (1997) which showed that a velocity profile at the nostrils for a given flow rate did not show significant differences on the downstream flow field when compared with experimental data. In addition, the flow rates of the left and right nostrils are assumed to be the same. This does not simulate real breathing perfectly since the flow is induced from the lungs drawing the air from the nostrils which are affected by geometrical differences leading to varied flow rates between the cavities.

However, for this case study, the focus is to present the ability of CFD to capture the micro-fluid structures that exist in flow patterns within the left and right cavities under a steady-state solution while being able to compare these results against available experimental data that are based on a fixed flow rate through a single nasal cavity side (Keyhani et al. 1995; Subramaniam et al. 1998). Therefore, it is important to maintain similar settings and to keep the flow rates between the two cavities the same.

To give the reader a more complete understanding of applying boundary conditions, the pressure boundary condition for modelling the breathing cycle is discussed here. The breathing cycle is caused by the pressure difference induced by the diaphragm flattening/contracting to increase/decrease the volume of the pleural cavity. Therefore it is natural to assign the nostril inlets and the nasopharynx outlet as pressure conditions. The inlet pressure condition is used to define the total pressure and other scalar quantities at flow inlets. It is an ideal condition to use when the

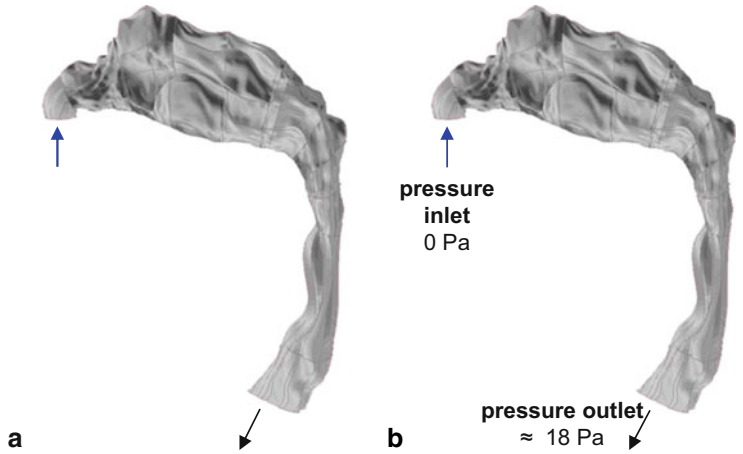


**Fig. 8.2** Applying pressure boundary conditions when the pressure outlet is unknown. **a** initial simulation to establish pressure difference, **b** applying the known pressure difference from initial simulation

pressure at the inlet is known (atmospheric at the nostrils) but the flow rate and/or velocity is unknown. A pressure outlet is used to define the static pressure at the flow outlets (and also other scalar variables, in case of backflow). However, the problem with the pressure outlet is that it is unknown in relation to the nostril inlet to induce the required flow rate. A modelling strategy to overcome this is to first simulate the flow field with the known mass flow rate in mind using a mass flow rate condition (Fig. 8.2). Upon completion of the simulation, the pressure difference between the nostril inlet and nasopharynx will be known, and thus the pressure at the outlet can be defined.

*Heat Transfer Setup* Two climatic conditions are used for the inspired ambient air, the first is air at 25 °C, 35 % relative humidity, which is similar to the ambient temperatures that have been used in *in-vivo* studies (Garcia et al. 2007a; Holden et al. 1999; Keck et al. 2000a). This condition is referred to as Normal Air Condition. The second condition is air at 12 °C, 13 % relative humidity which is referred to as 'Cold Dry Air Condition'. These air properties are applied at the inlet boundary condition. The inner mucosal walls which are covered by a wet mucus layer are assumed to be fully saturated with water vapour and to have an unlimited supply of heat and water. Lienar et al. (2003) were able to measure local nasal mucosal wall temperatures after exposure to air at different climatic conditions which ranged from 32.3–34.7 °C for normal air conditions and 30.6–33.7 °C for cold dry air. Therefore a value of 33.5 °C and a value of 32.1 °C were applied at the wall boundary condition for the normal air and the cold dry air cases, respectively.

In addition to the continuity, momentum, and energy equations, the following definitions are applied:

$$E = h - \frac{p}{\rho} + \frac{u^2}{2} \tag{8.3}$$

*where E* is the energy term from Eq. 5.16 and is related to the sensible enthalpy ($h$), pressure, and kinetic energy. The mass transfer equation for water vapour can be written as

$$\frac{\partial(\rho Y u_i)}{\partial x_i} = -\frac{\partial J_i}{\partial x_i} \tag{8.4}$$

where $Y$ is the vapour mass fraction and $J$ is the vapour diffusion flux which arises due to concentration gradients. For a laminar flow,

$$J_i = -\rho D \frac{\partial Y}{\partial x_i} \tag{8.5}$$

where $D$ is the diffusivity which varies with temperature and is expressed by the semi-empirical correlation from Vargaftik (1975):

$$D = 2.16\, e^{-5} \left( \frac{T}{273.15} \right)^{1.8} \tag{8.6}$$

Equations (8.3) to (8.5) are usually defined automatically within the CFD software package. Eq. (8.6) is a fluid property and is usually defined with a constant value. In this case, the diffusivity varies with temperature, and therefore a customised function is needed.

### *8.2.3 Geometry Comparisons*

Fourteen cross-sections evenly spaced apart in the $x$-direction were created to be used for geometry and flow analysis. The cross-sectional areas versus distance from the anterior tip of the nose of the left and right cavities are compared in Fig. 8.3. In the anterior region of the nasal cavity ($x < 26$ mm) and the posterior turbinate region ($x > 44$ mm), the cross-sectional area of the right cavity is larger than that of the left, while in the middle region the right side is smaller than the left.

The developed computational model was also compared with other nasal cavities of which existing data were available. Although inter-subject variations in the nasal cavity geometries exist, a general trend can be observed on a macro level. For example, a local minimum is found for all profiles just after the inlet where the nasal valve region exists. The nasal valve is the narrowest region where the cross-sectional area was found to be 1.4 $cm^2$ which compares with 1.6, 1.9 and 2.0 $cm^2$ in the models by Subramanian et al. (1998); Cheng et al. (1996) and Keyhani et al. (1995), respectively. At the anterior turbinate region, the airway expands to accommodate the olfactory sensors and the turbinate bone projections. This is reflected by an increase in the cross-sectional profiles which is observed immediately after the nasal valve region. For the current geometry, the nasal valve region is located about 2.0 cm from the anterior tip of the nose, which compares with the other models that are all located around 3.0 cm away from the anterior tip of nose (Fig. 8.3).

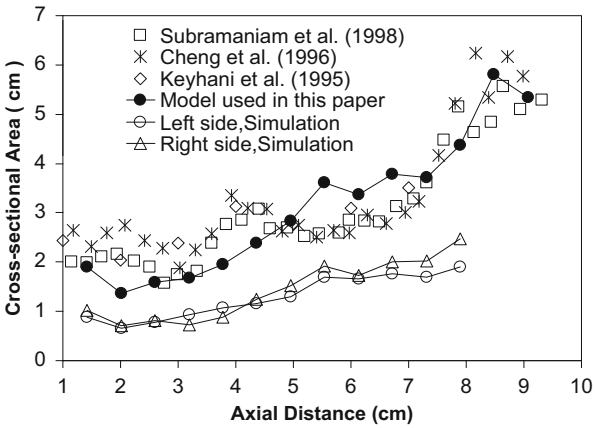


**Fig. 8.3** The comparison of cross-sectional areas versus distance from anterior tip of nose for different geometries

### *8.2.4 Wall Shear Stress*

Analysis of wall shear stress is important in terms of identifying physiological reactions to levels of stresses that are exerted on the epithelia lining of the respiratory tract. For example, studies have shown that mucous secretion can occur in response to stimuli such as wall shear stresses (Kim et al. 1997; Rogers 1994) while nasal sensation detected by the mechano- and thermoreceptors and nerve endings can also be impacted by the wall shear stress. Two other important clinical observations have been discussed in the work by Elad et al. (2006) and are summarised here:

- When the mucosal surfaces of the septum and the turbinates are in close proximity, they are assumed to cause chronic tension headache (Apodaca 2002; Behin et al. 2005) as a result of high shear stress at specific points.
- Following rhinoplasty, stuffy noses are commonly reported which may be attributed to a lessening of the cross-sectional nasal valve area with the secondary elevation of nasal wall shear stress. This may impose physical strain on the nasal mucosa, including that of the inferior and middle turbinates, and lead to abnormal response, i.e., hypertrophy (Caughey et al. 2005).

The average wall shear stress for each subdivided region (see Fig. 8.1) was calculated by summing the local shear stress at each surface and dividing by the total number of surfaces within each region. For a Newtonian fluid, the average wall shear stress induced by the flowing air on the gas-wall interface is given by

$$\tau_{ave} = \frac{\sum_{i=1}^{x} \left( \mu \frac{\partial U}{\partial n} \right)_i}{x} \tag{8.7}$$

where $\mu$ is the gas viscosity, $x$ is the number of cells along a wall and $n$ is the unit vector normal to the cavity surface. The general trend for the wall shear stress at different flow rates is similar (Fig. 8.4). Maximum shear stresses have been found in

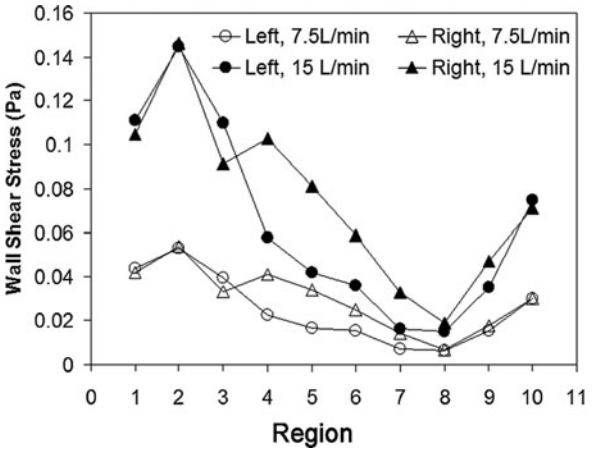


**Fig. 8.4** Area averaged wall shear stress on different regions surface, at flow rates of 7.5 and 15 L/min. The region definitions are found in Fig. 8.1

the range of 0.2 Pa (Elad et al. 1993) on the septal wall across the inferior turbinate at a peak inspiration of 20 L/min. Comparatively, the stresses in uniform regions of large arteries are in the range of 1.5–2 Pa (Nucci et al. 2003).

The highest wall shear stresses are found in Region 2 where the nasal valve exists. Additionally, the flow in this region has changed direction from being vertically aligned to a horizontal direction which causes the high stresses. The average wall shear stress in this region is 0.056 and 0.144 Pa for a flow rate of 7.5 and 15 L/min, respectively. Locally the maximum value shown in Fig. 8.5 is much higher, reaching up to 0.18 Pa for a flow rate of 7.5 L/min. The concentration of the maximum values is found near the nasal valve region and at the beginning of the main nasal passage. The wall shear stress decreases gradually corresponding to the airway expansion in the middle region where the velocity decreases. Minimum values are found in Region 8 before increasing again. The increase is caused by the two cavities merging and a change in the flow direction at the nasopharynx where the air travels downwards towards the lungs. Wall shear stresses, especially high local maximums, are likely

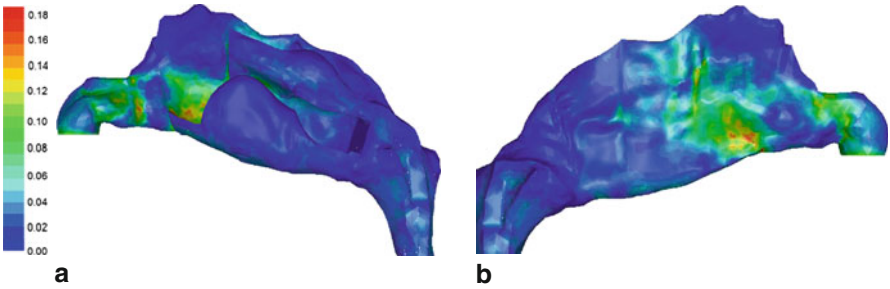


**Fig. 8.5** Local wall shear stress in the left nasal cavity at a flow rate of 7.5 L/min. **a** Lateral view of the left nasal cavity. **b** Reverse lateral view of the left nasal cavity (septum)

to stimulate epithelium cellular mechanisms, thus contributing to the induction of goblet cell secretion (Rogers 1994).

As shear stresses are linearly related to the local velocity, these values significantly increase as breathing efforts increase. High shear stresses that are concentrated locally may cause irritation of the blood vessels within that area. The maximum shear stresses that occur in the nasal valve region and to a lesser extent in the main nasal passageway may lead to dysfunctional effects on nasal sensation of airflow and therefore play a role in the well-being of nasal breathing. By mapping out the distribution of external stresses on the nasal cavity walls, predictions of the mechanoreceptor response can be estimated.

### *8.2.5 Flow Visualisation*

*Path streamlines* Path streamlines, which act as massless particle tracers to track the flow path of the inhaled air, were released from the nostril inlet to provide qualitative visualisation of the flow field. The streamlines in the left nasal cavity at a flow rate of 7.5 L/min show flow separation and reversed flow just posterior to the narrowest valve (Fig. 8.6a). A prominent vortex in the upper anterior part of the cavity was formed. This vortex is a result of the adverse pressure gradient caused by the abrupt

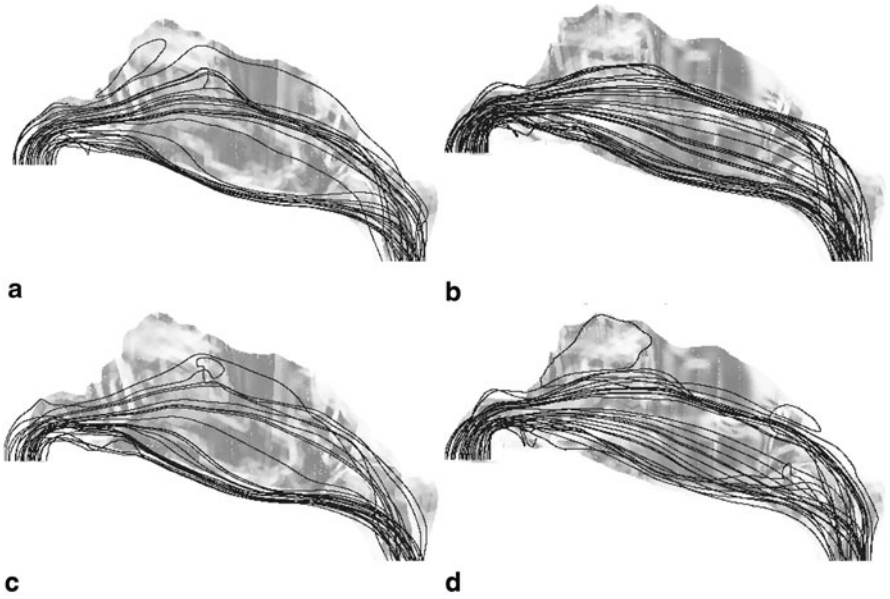


**Fig. 8.6** Representation of flow streamlines in current nasal cavity. A comparison of streamlines produced in the literature shows similar trends (see Fig. 8.7). **a** *Left cavity*, 7.5 L/min. **b** *Right cavity*, 7.5 L/min. **c** *Left cavity*, 15L/min. **d** *Right cavity*, 15L/min

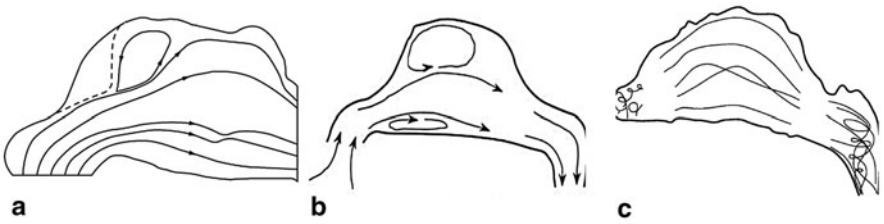


**Fig. 8.7** Representation of flow streamlines in other nasal cavities. **a** Keyhani et al. (1997). **b** Schreck et al. (1993). **c** Subramaniam et al. (1998)

increase in the cross-sectional area from the nasal valve to the main nasal passage. A similar trend was found in the experimental work of Weinhold and Mlynski (2004) and Kelly et al. (2000). As the flow rate increased to 15 L/min (Fig. 8.6c), the vortex moved to the middle region of turbinate and was smaller. The streamlines in the right cavity at a flow rate of 7.5 L/min (Fig. 8.6b) showed no recirculation, and most of the streamlines are concentrated in the middle and lower regions of the nasal cavity. At a flow rate of 15 L/min (Fig. 8.6d), two vortices are found. The bigger vortex is just posterior to the nasal valve while the smaller vortex is found in the posterior turbinate region. Both vortices are found in the upper region of the nasal cavity.

The simulated results were then compared with data available from the literature (Fig. 8.7) in which Keyhani et al. (1997) found a recirculating zone downstream of the airway. The vortex extends up to the anterior end of the middle turbinate but does not reach the olfactory slit. The larger vortex is found in the upper region while a smaller vortex is found near the floor of the airway. This smaller vortex occurs directly after the nasal valve region where a favourable pressure gradient promotes flow separation. These disturbances are also found in the current simulation where the streamlines are erratic but do not reach the same magnitudes as the vortex found by Schreck et al. (1993). The simulations by Subramaniam et al. (1998) are most different where prominent recirculating streams are found in the vestibule and complex spiralling flow patterns are found in the nasopharynx. There is no obvious recirculation zone inside this nasal cavity.

*Airflow Analysis* The effect of asymmetry of the left and right side of the cavity on the airflow dynamics is shown in Fig. 8.8 which combines the contours of the axial velocity ($x$-component of velocity) with streamlines of secondary flow ($y$-$z$ component of velocity). The red contours suggest the main flow field since the direction of flow is in the $x$-axis and, therefore, the blue contours show low flow in the $x$-axis. At the beginning of the flow at A, air flows upwards as shown by the streamlines pointing in the positive y direction. No cross flow in the vertical $z$-direction is found. The flow accelerates at B as the airway decreases in area where the nasal valve region begins to form. At this cross-section, the flow has changed directions, 90° from the inlet; and coupled with the narrower region, cross flows in the y and z directions are more prevalent especially in the left side. Additionally the flow begins to split into two directions with the majority flowing upwards and a smaller proportion flowing downwards.

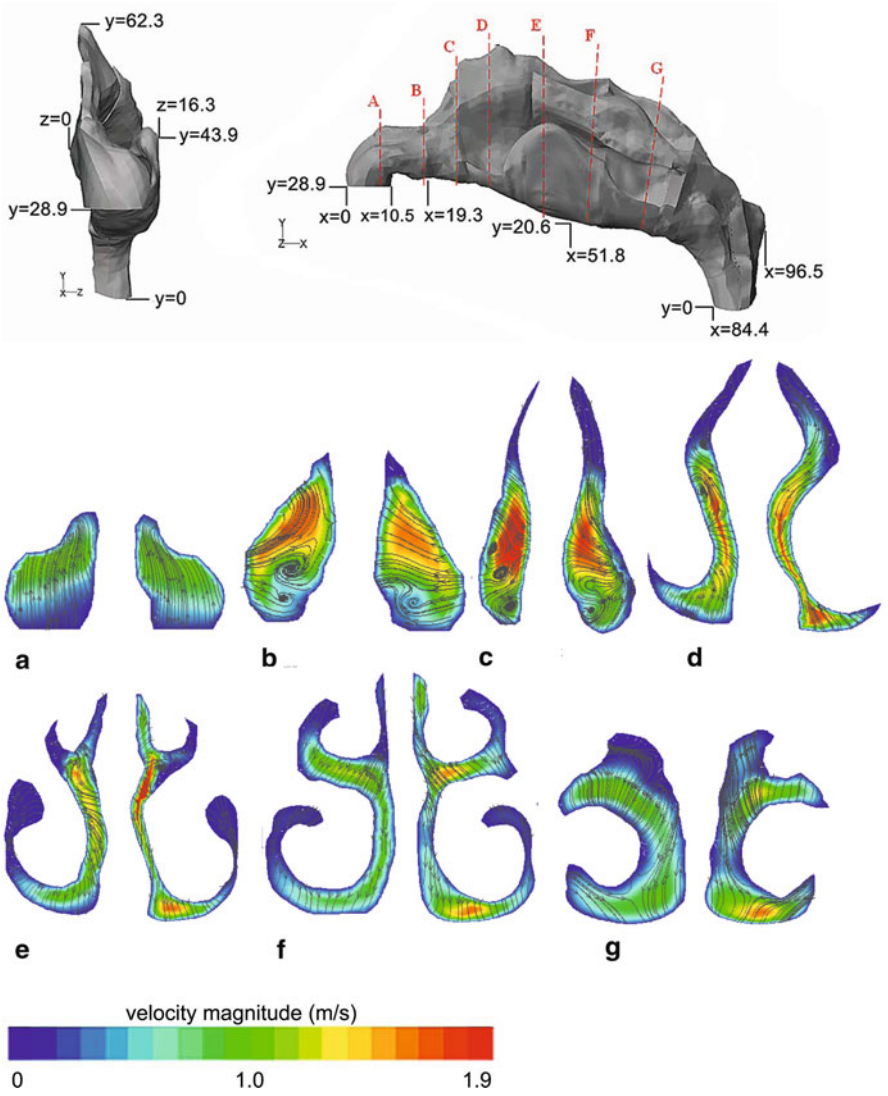


**Fig. 8.8** Contours of axial velocity (*x-direction*) and streamlines of cross-flow (*y-z direction*). *Red* contours represent maximum values while *blue* represent minimums

The geometry continues to become narrow, and this accelerates the bulk flow through the middle of *C*. The flow away from the centre is found to be moving away from the septum walls and pushing upwards and downwards, coinciding with the geometry which is expanding vertically. This flow feature continues through *D* as the meatus forms. At the turbinate region *E, F, G*, the main axial flow remains close to the septum walls and little flow reaches the outer meatus region. As the geometry begins

to curve downwards, the flow streamlines reflect this by pointing in the negative $y$-direction.

### 8.2.6 *Flow Features in the Nasal Valve*

Two cross-sectional areas located just proximal to the anterior nasal valve at $x = 2.6$ cm and $x = 3.2$ cm were chosen to highlight the rapid changes in the flow field since the anterior nasal valve was located at $x = 2$ cm posterior to the anterior nares. The naming convention used in this paper for the left and right cavity takes on the side that the cavity sits anatomically. The cross-section shown in Fig. 8.9 is from a frontal perspective (positive flow into the paper) and therefore the right cavity is depicted on the left side. Similar to Fig. 8.8. contour plots of the axial velocity ($x$-component of velocity) combined with streamlines of secondary flow ($y$-$z$ component of velocity) is shown here.

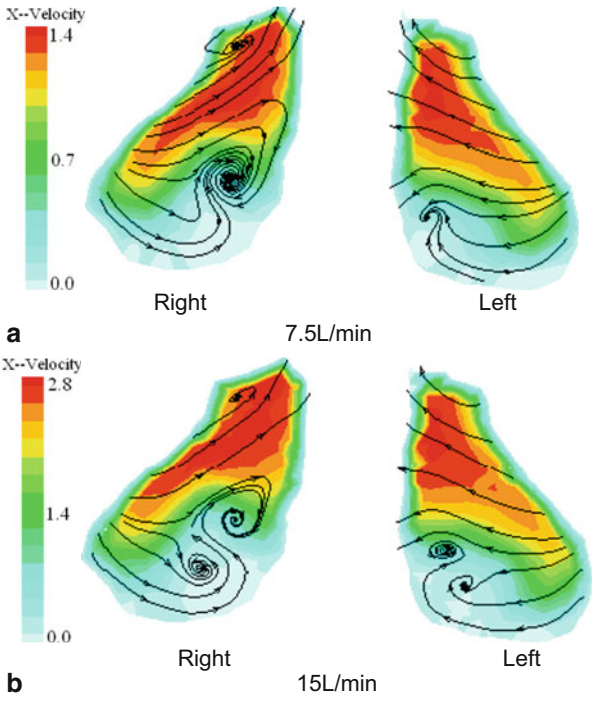


**Fig. 8.9** Velocity field in the coronal cross-section located at 2.60 cm from the anterior tip of the nose. **a** At flow rate of 7.5 L/min and **b** At flow rate of 15 L/min

By applying the directional streamlines, secondary flow features such as vortices can be visualised. The air enters the vestibule region with a vertical direction. And as the distance increases from the anterior tip of the nostrils, the nasal geometry becomes narrow as the airstream turns posterior, approximately 90° towards the nasopharynx. This transition coupled with the narrowing geometry forces the flow to emerge from the outer walls from the septum and be directed inwards. The presence

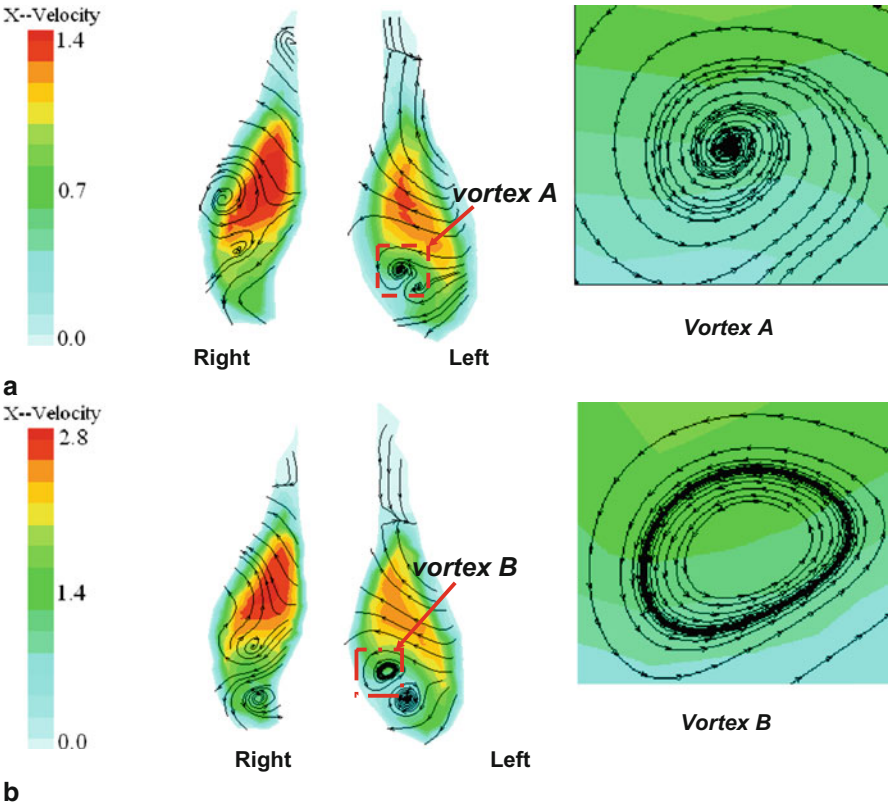


**Fig. 8.10** Velocity field in the coronal cross-section located at 3.20 cm from the anterior tip of the nose. **a** At flow rate of 7.5 L/min and **b** At flow rate of 15 L/min

of the wall along with the bulk flow that exists in the upper regions restricts the flow in the lower regions (light blue colour) and forces the flow to recirculate thus formulating vortices. For the cross-section located at 2.6 cm from the anterior tip of the nose, two vortices in the right cavity and one in the left are found for a flow rate of 7.5 L/min (Fig. 8.9a). When the flow rate increases to 15 L/min, the number of vortices in both of the cavities increases in the low flow regions and the streamlines are more dispersed (Fig. 8.9b).

At the cross-section located at $x = 3.2$ cm from the anterior tip of the nose, the bulk flow is concentrated more centrally as the air stream is developing (Fig. 8.10). At a flow rate of 7.5 L/min, there are two vortices in the left cavity while in the right cavity some recirculation occurs, forming weaker vortices (Fig. 8.10a). The direction of the streamlines in *vortex A* all point to the centre of the vortex, which demonstrates that the axial velocity gradient is positive and the pressure gradient is negative along the axial direction (Escudier 1988; Stabl 1992). As the flow rate increases to 15 L/min, the magnitude of the recirculation and hence the vortices increase (Fig. 8.10b). The direction of all the vortices except for the upper vortex in

the left cavity (*vortex B*) all point inwards. *Vortex B* shows the outer streamlines of the vortex directed inwards while the inner streamlines are directed outwards from the centre.

The nasal valve is considered as a region rather than an oblique cross-sectional area of the nasal passageway and resembles a constriction-expansion region which causes the majority of the total airflow resistance. The streamlines in the anterior nasal valve are all directed from the outer wall towards the inner septum wall (Fig. 8.9) whereas in the right cavity, the opposite occurs (Fig. 8.10)—the flow is directed from the inner side, outwards. As the air enters the nasal valve region after the 90° turn, the transition coupled with the narrowing geometry forces a majority of the flow direction to come from the opposite side of the septum walls. This is consistent with the larger contour areas (red-colour) of high velocity found for the right cavity. After the flow is aligned and the airway begins to expand, the resistance at the walls causes the flow to rebound and flow in the opposite direction. We will see in later case studies that this flow feature is important for prediction of particle deposition. The direction of the streamlines that initially accelerate from the outer wall will enhance the deposition of inhaled particles onto the inner nasal septum wall side rather than on the outer surfaces.

### 8.2.7 *Flow Features in the Middle Turbinates*

The same contour-streamline plot was applied to the middle turbinate area located at 6.10 cm from the anterior nares. The streamlines show that flow is directed downwards with the bulk of flow concentrated in the upper and lower region close to the septum walls. There are no visible vortices but some weak recirculation occurs, possibly due to the narrow geometry (Fig. 8.11). Velocities in this region are lower

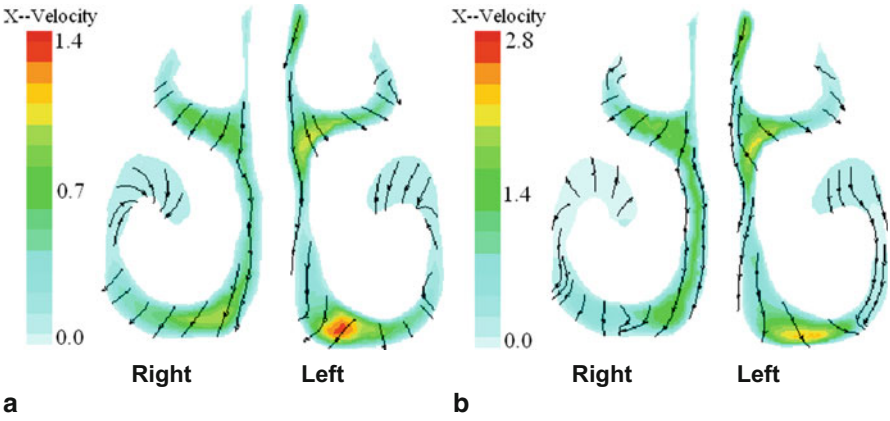


**Fig. 8.11** Velocity field in the cross-section located at 6.10 cm from the anterior tip of the nose. **a** Flow rate of 7.5 L/min. **b** At flow rate of 15 L/min

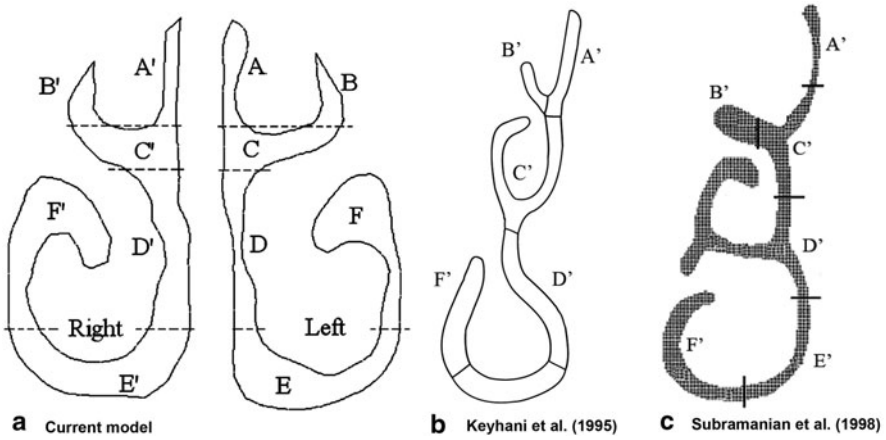


**Fig. 8.12** The coronal sections are divided into sub-sections which are indicated by letters *A′*-*E′* for the *right* cavity side and *A*-*E* for the *left* cavity side. **a** Cross-section located at 6.1 cm from the anterior tip of the nose used in this paper. **b** Cross-section located at 6.2 cm from the anterior tip of the nose used by Keyhani et al. (1995). **c** Cross-section located at 6.0 cm from the anterior end of the nose used by Subramaniam et al. (1998)

**Table 8.2** Flow distribution on the plane in the middle of turbinate for flow rate of 15 L/min

| *Left* | | | | | | *Right* | | | | |
|---|---|---|---|---|---|---|---|---|---|---|
| Region | A ($mm^2$) | Q (ml/s) | % $Q_{tot}$ | $U$ (m/s) | $U_x$ (%) | A ($mm^2$) | Q (ml/s) | % $Q_{tot}$ | $U$ (m/s) | $U_x$ (%) |
| A′ | 13.7 | 13.9 | 11.6 | 1.3 | 78.1 | 10.4 | 3.1 | 2.5 | 0.42 | 70.5 |
| B′ | 9.7 | 1.4 | 1.2 | 0.2 | 62.6 | 8.6 | 1.6 | 1.3 | 0.24 | 75.6 |
| C′ | 23.2 | 25.6 | 21.4 | 1.4 | 79.2 | 29.1 | 28.5 | 23.7 | 1.12 | 87.1 |
| D′ | 21.6 | 24.4 | 20.3 | 1.2 | 90.8 | 36.9 | 34.7 | 28.8 | 1.00 | 94.2 |
| E′ | 50.3 | 52.4 | 43.7 | 1.1 | 95.8 | 50.5 | 50.2 | 41.7 | 1.06 | 93.8 |
| F′ | 42.8 | 2.2 | 1.8 | 0.1 | 80.0 | 53.5 | 2.5 | 2.1 | 0.11 | 41.8 |
| *Total* | *161.3* | *119.9* | | | | *189.0* | *120.5* | | | |

than in the nasal valve region as the geometry has expanded. The downward direction is due to the airway which is now heading toward the nasopharynx. Therefore, the overall flow path undertakes a U-turn shape where the flow enters upwards and travels horizontally, ending downwards towards the lungs.

To further study and compare the distribution of airflow in the turbinate region with other work in the literature, the cross-section in the middle turbinate region was subdivided into separate regions and labelled from *A* through to *E*. This enabled measurement of the local distribution (Fig. 8.12). Local volumetric flow was determined by integrating the velocity component normal to the plane over the cross-sectional area of each region. The results of the airflow distribution at a flow rate of 15 L/min for left and right sides are given in Table 8.2.

There are obvious differences between the nasal geometries of Keyhani et al. (1995); Subramaniam et al. (1998) and the current model in this study (Fig. 8.12).

**Table 8.3** Flow distribution on the right plane in the middle of turbinate for flow rate of 15 L/min

| Keyhani et al. (1995) | | | | | | Subramaniam et al. (1998) | | | | |
|---|---|---|---|---|---|---|---|---|---|---|
| Region | A ($mm^2$) | Q (ml/s) | % $Q_{tot}$ | $U$ (m/s)[a] | $U_x$ (m/s) | A ($mm^2$) | Q (ml/s) | % $Q_{tot}$ | $U$ (m/s) | $U_x$ (%) |
| A′ | 15.6 | 14.1 | 11.4 | – | 0.91 | 7.9 | 2.1 | 1.9 | 0.51 | 52.9 |
| B′ | 6.0 | 3.8 | 3.0 | – | 0.63 | 15.4 | 2.1 | 1.9 | 0.24 | 58.3 |
| C′ | 35.5 | 34.2 | 27.3 | – | 0.96 | 20.8 | 12.9 | 11.3 | 0.78 | 79.5 |
| D′ | 27.9 | 22.8 | 18.3 | – | 0.82 | 54.8 | 53.2 | 46.7 | 1.20 | 87.5 |
| E′ | 27.9 | 35.9 | 28.7 | – | 1.29 | 20.5 | 27.8 | 24.4 | 1.39 | 97.8 |
| F′ | 26.5 | 14.1 | 11.3 | – | 0.53 | 28.9 | 15.8 | 13.9 | 0.79 | 69.6 |
| *Total* | *139.4* | *124.9* | | | | *148.3* | *113.9* | | | |

[a]Data not available

The most striking difference is that the current model only has two meatus extensions ($B'$ and $F'$) in comparison with the other models that have three extensions: $B'$, $C'$, $F'$ for Keyhani et al. (1995) and $B'$, $D'$, $F'$ for Subramanian et al. (1998). The cross-sections are all located at a similar region in the nasal airway–in the middle of nasal turbinate. The location of our model is located at 6.1 cm away from the anterior tip of nose while for Keyhani et al. (1995) and Subramaniam et al. (1998) the locations are 6.2 cm and 6.0 cm, respectively. The $\%Q_{total}$ describes the proportion of flow as a percentage of the total flow rate.

The main flow direction is not easily specified for complex geometries such as that of the nose. Therefore the average velocity magnitudes $U = (u_x^2 + u_y^2 + u_z^2)^{1/2}$ and $U_x$ in the $x$-direction (axial) are used for analysis. The flow analysis through the left cavity (Table 8.2) shows that 85 % of the air passes through the superior medial airway (region $C$), the middle medial airway (region $D$) and the ventral medial airway (region $E$). These regions cover 59 % of the entire cross-section. The right cavity is slightly wider and the regions $C'$, $D'$ *and* $E'$ take up 61.6 % of the right section while the $\%Q_{total}$ is 94 %. Despite the small difference in area coverage, region $D$ in the left cavity exhibits a small constricting section which causes a higher resistance in the flow and, hence, the smaller proportion of air flow through $C$, $D$ and $E$. For the Keyhani et al. (1995) model, the majority of the flow occurs in $C'$ and $E'$ (56 % in total) which are the central and lower passages. The flow also dominates in similar regions $D'$ and $E'$ for Subramanian et al. (1998) totalling 71 % (Table 8.3).

The flow in the left cavity stays close to the wall while its distribution is mainly in the middle sections and more dominant in the lower sections while a small percentage (11.6 %) is found in the upper section. In the right cavity, the flow is concentrated within the middle sections. The flow in the left olfactory slit (section $A$) is found to be larger than that of the right side (zone $A'$). The axial flow values represented by the $x$-component of velocity $U_x(\%)$ because a percentage of the total velocity magnitude $U$ were high, which implies that the flow is dominant in the $x$-direction. Low velocity regions found in $B'$ and $F'$ for all the models show a much lower axial velocity. These regions become susceptible to recirculating flows as they are far away from the bulk flow regions.

The high flow rates found in regions $A$ and $A'$ may be considered as undesirable since it can lead to damage to the olfactory regions. Normally, low flow characteristics are required in the olfactory region as it is a defence mechanism that prevents particles whose trajectories are heavily dependent on flow patterns from being deposited onto the sensitive olfactory nerve fibres, while vapours are allowed to diffuse for olfaction.

The turbinate region consists of a narrow, curled bone that protrudes into the main airway. The middle and inferior turbinate are an important structure for filtration, heating and humidification where the mucosal wall surface area is increased. However, only a small percentage of air reaches this outer surface area within the meatus region ($F$). The surface area of the turbinates that is in contact with the airflow affects less than 2 % of the flow field in terms of heating and humidification. This suggests that the role of the turbinates to condition the air may not be solely reliant on the surface area contact but may in fact be influenced by the nature of the flow that the turbinates cause. The airflow distribution results obtained confirm this idea; however further studies involving a larger sample of geometries are needed to confirm this hypothesis.

### *8.2.8 Temperature Profiles*

Temperature profiles were obtained from the averaged temperature at each cross-section throughout the airway for a breathing rate of 10 L/min, so that comparisons could be made with other data found in the literature. The results for the normal air condition were compared with experimental work (Keck et al. 2000a, b) whose results from a population of 50 and 23 volunteers, respectively, were averaged. The profile showed good agreement in the frontal regions of the nasal airway, while a small discrepancy is observed in the back regions towards the nasopharynx. The profile converged to a steady value at a distance of 40 mm from the inlet, suggesting that the air is conditioned early in the front region.

The profiles for the inhalation of cold dry air were recorded for the left and right sides of the nasal cavity and also shown in (Fig. 8.13). The temperature profiles converge to a peak value of 30.7 °C for the last ten measurements away from the inlet. This compares with the inhalation of normal air which has a value of 33.3 °C for the last ten measurements. The distance at which the profile converged to a steady value is 71 mm from the inlet, which is the location where the left and right cavities begin to merge together.

For normal air conditions, heating of the air is dominant in the frontal region of the airway. The temperature difference is stable after the anterior turbinate region and the heat transfer is minimal. One role of the highly vascularised turbinate region that has been widely discussed is to condition the inhaled air. However, in the case of normal air conditions, the turbinate region does not actually apply much heat transfer but rather acts as a heat source through its constant temperature maintained by the underlying capillary bed on the mucosal surface that provides the walls with this energy. The majority of the temperature increases occur in the frontal regions where the temperature difference is greatest. For the cold dry air case, the temperature

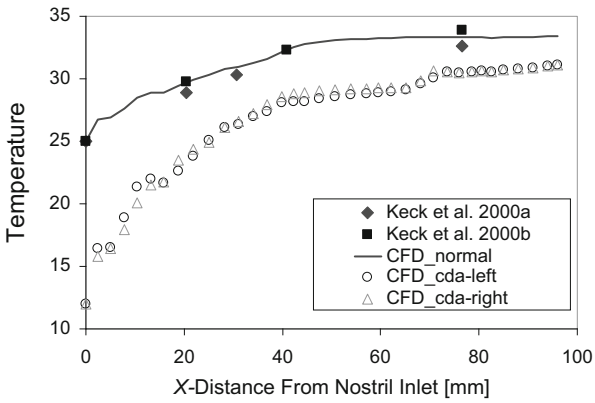


**Fig. 8.13** Temperature profiles across the nasal cavity from the inlet. The solid *black line* represents a normal inhalation condition compared with experimental work. The *colourless symbols* represent the simulated results for cold dry air

profile follows a similar curve, but shifts downward to accommodate the temperature decrease.

Given that other dependent variables, such as wall temperature and a steady air flow, were kept constant in this study, the effects of the differences in nasal morphology and hence the differences in the flow field could be isolated for analysis. The averaged temperatures at different cross-sections shown in Fig. 8.14 were recorded and compared. The left cavity produces higher temperatures in the front regions before the airway expands just after cross-section B ($x \approx 19$ mm); however after the airway expansion the right cavity produces higher values.

The contour plots reveal that the cooler air is found at the central locations of each cross section furthest from the wall. The temperatures at the olfactory regions (top of sections D and E) remain high because little airflow reaches this upper region and the region is heated by the close surrounding walls. This is an important feature of the human body as the olfactory epithelium is lined with delicate olfactory receptor neurons which need to be void of any cold dry air exposure to prevent any damage. At section C, the left-side is thinner; however the bulk of the flow remains in the middle region which accelerates through. The bulk flow regions are the last to be heated up to a peak value of 30.7 °C. A comparison of the temperature contour plots in Fig. 8.14 with the axial velocity contours in Fig. 8.8 shows that at high axial velocity regions, the temperature is at its lowest. This is due to the finite heat source provided by the constant wall temperature where the heating of the cold air is dependent on the mass flow rate as depicted by the thermodynamic balance equation:

$$\dot{Q} = \dot{m} C_p (T_{wall} - T_{air}) \tag{8.8}$$

This implies that the flow residence time $\dot{m}$ is critical for the inhaled air to be heated, given that the heat source is driven by the difference in the constant wall temperature and the inhaled air.

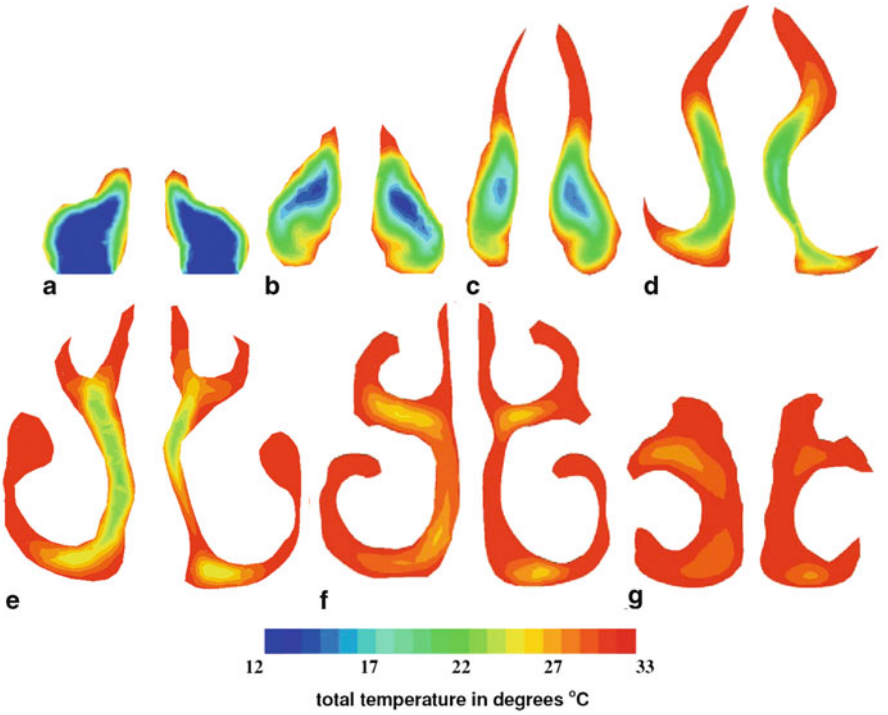


**Fig. 8.14** Contours of total temperature at cross-sections throughout the nasal cavity

### *8.2.9 Closure*

The modelling requirements for steady inhalation and the heat transfer process to heat the inhaled air were shown. Particular attention was given to these critical issues:

- the flow being *laminar or turbulent*,
- *steady or unsteady*,
- the type of *inlet/outlet conditions* for the nasopharynx and nostril inlets, and the
- additional equations that are needed to account for *heat transfer*.

In summary, the flow could be assumed as laminar for flow rates below 15 L/min and turbulent for flow rates above 25 L/min. Transitional flows are much more difficult to resolve, and care must be taken when analysing the results in terms of the laminar or turbulence model used. The quasi-steady assumption was found to be applicable when the Womersley number $\alpha$ and Strouhal number $S$ in the human nasal cavity are less than 4 and 1, respectively. The type of inlet/outlet condition for breathing requires a pressure boundary condition at the inlet and outlet which allows for the flow to be induced from the nasopharynx. Finally, to account for the heat transfer, additional equations that are needed, such as the mass transfer equation for water vapour, are shown.

The computational model developed in Chap. 2 was simulated. Statistical analysis and geometric comparisons were performed against existing data found in the literature which provided important macro and micro flow features of the nasal cavity. The main distinctions of the reconstructed nasal cavity used in this paper in comparison with others are (i) a narrower nasal valve region, (ii) wider turbinates and (iii) a shorter length. The model exhibited the smallest cross-sectional area for the nasal valve region and had the largest cross-sectional area in the turbinate region in comparison with other models.

Visualisation of the flow field was performed through different post processing techniques such as contour and streamline plots. Path streamlines showed that recirculation was prevalent in the olfactory region and in the nasal valve region where the flow experiences sharp changes in the flow conditions. Differences in the size and location of the vortices between the models were attributed to geometrical differences such as an increase in airway height.

Two regions of interest within the nasal cavity, the internal nasal valve and the middle turbinate region, were investigated further because of their physiological importance. Streamlines revealed that complex flow patterns such as vortices and acceleration were present in the nasal valve region, which may be a method for filtering out micron sized particles–this is important for toxic inhalation but a problem for drug delivery. For the middle turbinate region, an airflow distribution analysis through the meatus regions found that only a large proportion of air remained close to the septum walls. Thus the efficiency of the turbinates to heat and humidify the air through an increase in surface area of the meatus regions was found to be very low.

In terms of the heat transfer, the results of the contour and streamline plots of the airflow revealed that the nasal valve region forces the airflow closer to the walls, exposing them to the warmer surface, although this is offset by an acceleration of the air in this region. The temperature profiles showed that the air was heated to its near maximum value by the time it reached the turbinate region. This suggests that the heat transfer process is more dominant in the anterior regions of the nasal cavity rather than in the turbinate regions. The temperature difference is stable after the anterior turbinate region, and the heat transfer is minimal.

Since the flow field will be the main contributor in transporting the particles through the airway, this case study served to establish the main flow features which set a good foundation for the inclusion of particles in the nasal cavity. In the next case study, different particles found in toxicology studies are introduced into the system.

## 8.3 Toxic Particles and the Effects of Particle Morphology

Airborne particles are present in virtually every aspect of life from small and mid-range scale industrial processes, such as those producing glass particles, to large scale processes, such as environmental pollution, dust storms and hurricanes. During normal respiration, harmful particles, such as dust, fumes and general pollutants, and their inhalation become undesirable. In contrast, drug delivery via the nasal cavity has motivated the study of drug deposition within the airway in order to improve

efficiency in the drug delivery. In terms of modelling, the introduction of particles involves a secondary phase (usually solid or liquid) to be present in conjunction with the primary phase (usually gas or liquid), leading to the field of multiphase flows. This case study presents different modelling strategies required to account for a variety of particles that include spherical, non-spherical, and fibrous particles. A brief description of each particle type is first given.

## *8.3.1 Characterisation of Toxic Particles*

### 8.3.1.1 Wood Dust Particles

Wood dust is one of the most common organic dusts to which humans are exposed due to the extensive use of wood for construction material and furniture (Enarson and Chan-Yeung 1990). The International Agency for Research on Cancer estimated that at least 2 million people in the world are exposed to wood dust occupationally (IARC and WHO 1995). Exposure is common in many types of work, especially in the primary wood industries such as logging, lumber mills, and pulp mills and even more so in secondary wood industries such as cabinet making, furniture manufacture, wood pattern and work shops, and other manufacturing industries (Enarson and Chan-Yeung 1990). The processing of the raw timber from the use of high-powered reciprocating tools, such as sanders and saws, generates large quantities of fine, inhalable wood dust (Fig. 8.15). Direct contact with the wood dust leads to inhalation

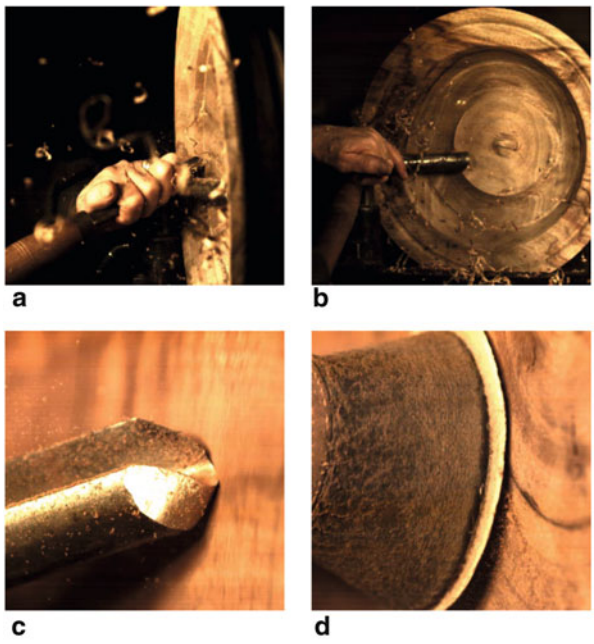


**Fig. 8.15** Wood dust generated from different wood turning stations. **a** side-view of a hard cut of camphor wood. **b** front-view of a hard cut of camphor wood. **c** finish cut of red gum wood. **d** sanding of red gum wood

of the particles via the nasal cavity. It is not surprising, then, that significant health effects have resulted from direct contact of the inhaled wood dust with tissues of the respiratory tract. While ingestion is also common, no health effects have been reported.

In this case study, the application of spherical particles is applied to wood dust inhalation, which has important implications for occupational injury to woodturners who frequently encounter nose bleeds. Spherical particle modelling is quite common because the assumption of a spherical particle allows a simplified drag correlation. This advantage often outweighs the need to consider all the physics involved with non-spherical particles, since approximate values can provide sufficient accuracy for common engineering problems. Numerical simulations (Zhang et al. 2002, 2004, 2005b) have made use of spherical particles to represent the characteristics of general particles.

Wood dust from pine (softwood) and from light and heavy oak (hardwood) was simulated (Tian et al. 2007). The respective densities are 560, 590 and 930 kg/m$^3$. A study carried out by Chung et al. (2000) examined the particle size distribution of dust during sawing and sanding of pine and oak. Oak dust generated by sawing exhibited smaller particle sizes than the pine dust, while similar size distributions were found for both pine and oak dust when generated by sanding. Therefore, only nasal deposition of wood dust with size distributions from sawing will be investigated herein. Figure 8.16 illustrates the measured and simulated particle size distribution of both pine and oak. It is noted that the particle size distributions were based on the particle number fraction and not volume fraction or mass fraction. Both heavy oak dust and light oak dust were assumed to have the same size distribution. All particles in this study were assumed to be spherical, which is not strictly true. However for demonstration purposes, the spherical assumption is sufficient. Non-spherical particles are treated in the next section.

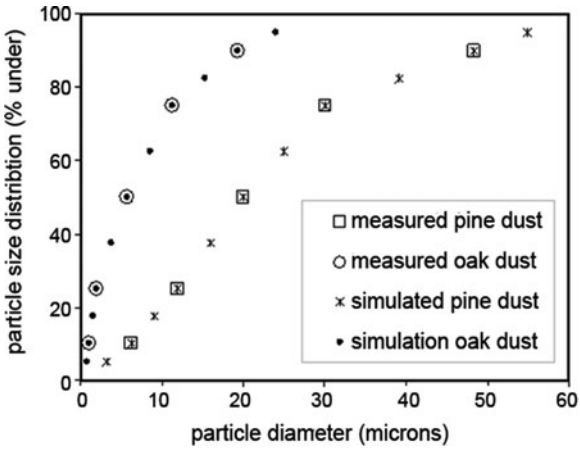


**Fig. 8.16** Simulated particle size distribution and measured particle size distribution of dusts generated by sawing. (From Chung et al. 2000)

### 8.3.1.2 Pollen and Rough Surface Particles

The symptoms of hay fever (allergic rhinitis) caused by airborne pollen have been well established while more recently its relationship to asthma has been proposed (Bousquet et al. 2001). The morphology of pollen comes in various shapes, diameters and densities, as shown in Fig. 8.17, which is subjected to different aerodynamic properties. One particular pollen grain that is highly allergenic is ragweed pollen which is a primary cause of hay fever. Its geometric diameter generally ranges from 16–27 μm (Crowder et al. 2002), has low densities and exhibits spiny protrusions that sit on a spherical surface base. The nasal airway acts as an air filter for the respiratory system where high inertial particles readily deposit onto the nasal walls by impaction leading to inflammation of the mucosa and other effects of hay fever. The lower density ragweed will lower the aerodynamic diameter, but this may be countered with the protrusions that will alter its drag coefficient.

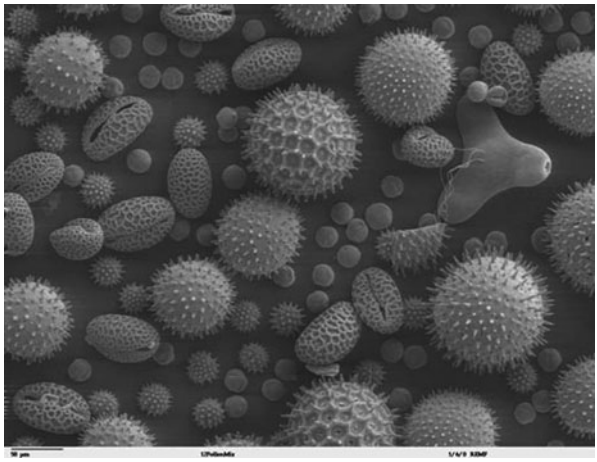

**Fig. 8.17** Scan electron microscope image of pollen grains from a variety of common plants. Zeiss DSM 962 SEM (Dartmouth College—*Rippel Electron Microscope Facility*)

### 8.3.1.3 Fibrous Particles

Inhalation of fibrous materials such as asbestos is one case that has been identified in the workplace. Asbestos (Fig. 8.18) was once popular among manufacturers and builders in the late 19th century due to its resistance to heat, sound absorption and tensile strength.

However, since the finding that inhalation of asbestos fibres causes serious illnesses such as asbestosis and mesothelioma, the use of asbestos has been banned in many countries. Nevertheless, the risk of exposure still exists mainly through the demolition of older buildings and materials where the fibres become airborne. The alternative for asbestos fibres is man-made vitreous fibres (MMVFs) of inorganic materials such as glass, natural rock and amorphous silicates. MMVFs themselves

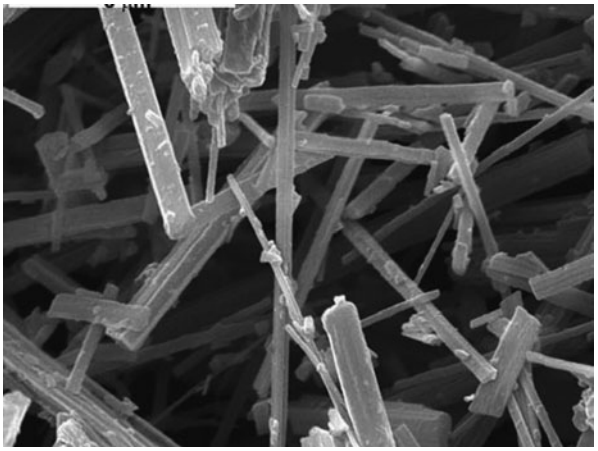

**Fig. 8.18** Electron microscope image Amosite asbestos. (U.S. Geological Survey—www.usgs.gov)

are not free from toxic properties. The levels of toxicity vary, depending on the fibre length and its biopersistence in the lungs (Lippman 1990; Timbrell 1982).

#### 8.3.1.4 Diesel Fumes, Vapours, Smoke and Nano Particles

The physiological effects of air pollution consisting of very fine particles, such as the exhaust fumes from diesel engines, vapours and smoke, have a detrimental impact on the health of the respiratory system. Chronic inhalation of diesel fumes leads to the development of cough and sputum, known as chronic bronchitis (Morgan et al. 1997), and interferes with brain functioning and information processing (Crüts et al. 2008) which is a serious problem in highly urbanised, busy cities.

Recent advances in nanotechnology have seen the manufacture of engineered nanoparticles for many commercial and medical applications such as targeted drug delivery and gene therapy. Engineered nanoparticles can exhibit a large surface area to size ratio leading to greater biologic activity. This increased biologic activity can be desirable. For example, magnetic nanoparticles can be used for magnetic resonance imaging (MRI), targeted drug and gene delivery, tissue engineering, cell tracking and bioseparation (Gupta and Gupta 2005; McCarthy et al. 2007). However the increased biologic activity can also have adverse repercussions due to toxicity, induction of oxidative stress or cellular dysfunction (Oberdörster et al. 2005). Transport of nanoparticles is mainly attributed to Brownian motion which is the random movement of the gas or liquid molecules impacting on small nanoparticles. The instantaneous momentum imparted to the particle varies in a random fashion which causes the particle to move on an erratic path known as Brownian motion.

Fumes, vapours, and smoke are characteristically small, existing in the submicron range. Technically speaking, nanoparticles are considered as having a diameter $<10$ nm; ultrafine particles have diameters $<10$–100 nm; and submicron particles are any particle less than 1 μm. The deposition mechanism of nanoparticles will be

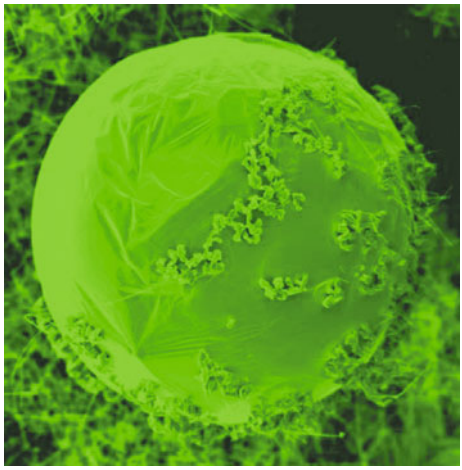

**Fig. 8.19** Electron microscope image of a nanoparticle

diffusion-based in comparison with micron particles which deposit by inertial impaction and sedimentation. The results can be interpreted for toxicological studies where the adverse health effects of toxic nanoparticle absorption may be problematic (Fig. 8.19).

### *8.3.2 Numerical Considerations for Particle Tracking*

Simulations of the discrete secondary phase in a Lagrangian frame of reference allows for individual tracking of the particles. This secondary phase consists of spherical particles (which may be taken to represent droplets or bubbles) dispersed in the continuous phase. Where the particle morphology strays from a spherical shape, such as different shape, surface, and size as presented in the previous section, additional numerical considerations are needed. Therefore the purpose of this section is to provide some empirical approaches that allow the user to account for irregular particles (fibres, rough surfaces) and also very extreme particles (nanoparticles) when modelling the particle trajectory.

The trajectories of any individual particle can be calculated by integrating the force balance equations on the particle as

$$\frac{du_p}{dt} = F_D(u_g - u_p) + \frac{g(\rho_p - \rho_g)}{\rho_p} + F_s \tag{8.9}$$

$F_D$ is the drag force per unit particle mass which is one important variable that differs for the different particle morphology. A considerable amount of research has been performed in order to establish correct drag coefficients (Flemmer and Banks 1986; Ganser 1993; Haider and Levenspiel 1989; Leith 1987; Littman et al. 1995; Tran-Cong et al. 2004) for spherical and non-spherical particles. In this section

numerical considerations for different particle morphology are discussed. The middle term, $\frac{g(\rho_p - \rho_g)}{\rho_p}$ represents the force due to gravity and can sometimes be neglected (i.e. when $g$ is weak in comparison to other terms and when $\rho_p \approx \rho_g$). It is noted that the gravity term $g$ is $-9.81$ m/s$^2$ taken in relation to the ground and hence is applicable for an upright position. The term $u_p$ presents the particle velocity, and $\rho_p$ is the particle density. The final term $F_s$ acts as an additional source term which is inclusive of additional forces (force/unit particle mass) that affect the particle motion and are added as needed for the particle type in question.

For **spherical particles**, $F_D$ is given by

$$F_D = \frac{18\mu_g}{\rho_p d_p^2} \frac{C_D \mathrm{Re}_p}{24} \tag{8.10}$$

where $d_p$ is the particle volume equivalent diameter. The drag coefficient $C_D$ is given by Morsi and Alexander (1972) as

$$C_D = a_1 + \frac{a_2}{\mathrm{Re}_p} + \frac{a_3}{\mathrm{Re}_p^2} \tag{8.11}$$

where the $a's$ are empirical constants for smooth spherical particles over several ranges of the particle Reynolds number. $\mathrm{Re}_p$ is the particle Reynolds number, which is defined as:

$$\mathrm{Re}_p \equiv \frac{\rho_p d_p \left| u_g - u_p \right|}{\mu_g} \tag{8.12}$$

There are variations to the drag correlations for spherical particles, such as the models from Clift et al. (1978a) as discussed in Sect. 6.2.1, but each drag correlation for spherical particles should represent the drag coefficient curve given in Fig. 6.7. No other forces are added and therefore $F_s = 0$ in Eq. (8.9). In nearly all commercial CFD codes, Eq. (8.9) can be found as a default option for tracking the individual particles. Variations between CFD codes are usually due to the handling of the drag force $F_d$, and the additional forces within $F_s$. To implement different or custom models to represent any of the force terms, commercial CFD software will usually allow add-on functions that a user can write in computer programming languages such as FORTRAN or C to modify certain parts of the CFD simulation.

As mentioned earlier, spherical particle modelling is quite common as the assumption of a spherical particle allows a simplified drag correlation. The application of the spherical particles will be applied to three wood dusts: pine dust and light and heavy oak dust.

For **non-spherical particles** the drag coefficient will differ considerably from the standard drag coefficient curve for a spherical particle as shown earlier in Fig. 6.4. From Eq. (8.9) the drag force takes on the same form as the spherical particle in Eq. (8.10); however the definition of the $C_D$ needs to be corrected to account for the non-sphericity of the particle. The obvious problem with non-spherical particles is that the actual shape of the particle can take any shape or form. This has led

to considerable development in formulating a single correlation for any shape and orientation. One correlation is given by Haider and Levenspiel (1989) which provides accurate representation for certain irregular shapes. The correlation defines the $C_D$ as a function of the particle Reynolds number and a shape factor which is given as

$$C_D = \frac{24}{\mathrm{Re}_p}\left(1 + a\mathrm{Re}_p{}^b\right) + \frac{c\mathrm{Re}_p}{d + \mathrm{Re}_p} \tag{8.13}$$

where the coefficients are

$$\begin{aligned} a &= \exp\left(2.3288 + 6.4581\phi + 2.4486\phi^2\right) \\ b &= 0.0964 + 0.5565\phi \\ c &= \exp\left(4.905 - 13.8944\phi + 18.4222\phi^2 - 10.2599\phi^3\right) \\ d &= \exp\left(1.4681 + 12.2584\phi - 20.7322\phi^2 + 15.8855\phi^3\right) \end{aligned}$$

The shape factor $\phi$ is defined as

$$\phi = \frac{A_s}{A_p} \tag{8.14}$$

where $A_s$ is the equivalent surface area of a sphere having the same volume as the non-spherical shaped particle, and $A_p$ is the actual surface area of the particle. An advantage of the method by Haider and Levenspiel (1989) is that it provides a simple correlation to fit all types of shapes; however, its generality makes it inaccurate and unsuitable for shapes that are very non-spherical.

A later development for non-spherical particles is the technique presented by Tran-Cong et al. (2004) which uses agglomerates of spheres to represent different particle shapes. Two equivalent diameters, surface-equivalent-sphere $d_A$ and the nominal diameter $d_n$, and a shape factor called the particle circularity (Wadell 1933) are used for the drag correlation. The surface equivalent sphere diameter is defined as

$$d_A = \sqrt{\frac{4A_p}{\pi}} \tag{8.15}$$

where $A_p$ is the projected area of the sphere. The volume equivalent sphere diameter, also known as the nominal diameter, is defined as

$$d_n = \sqrt[3]{\frac{6V}{\pi}} \tag{8.16}$$

where $V$ is the particle volume. The shape factor used is based on the surface sphericity and is defined as

$$c = \pi\left(\frac{d_A}{P_P}\right) \tag{8.17}$$

**Table 8.4** Shape of agglomerate of spheres to model pollen particles

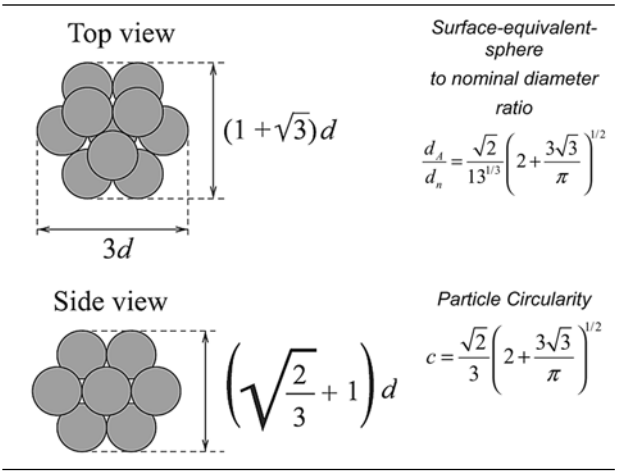


where $P_p$ is the projected perimeter of the particle in its direction of motion. The empirically defined correlation for the drag coefficient is given as

$$C_D = \frac{24}{\mathrm{Re}_p}\frac{d_A}{d_n}\left[1+\frac{0.15}{\sqrt{c}}\left(\frac{d_A}{d_n}\mathrm{Re}_p\right)^{0.687}\right]+\frac{0.42\left(\frac{d_A}{d_n}\right)^2}{\sqrt{c}\left[1+42500\left(\frac{d_A}{d_n}\mathrm{Re}_p\right)^{-1.16}\right]} \tag{8.18}$$

The application of this model for pollen particles assumes the non-spherical shape to be an agglomerate of spheres that form a shape referred to as close-to-sphere particles. The resulting terms, $d_A/d_n$ and $c$, for the representative pollen particle are given in Table 8.4.

During the pollen season, pollen in the air can either be wet or dry according to the stage of pollen development. The dry pollen lacking water content was found to have a density of 550 kg/m$^3$ (Crawford 1949) while wet pollen has a density of 1,320 kg/m$^3$ (Harrington and Metzger 1963). In the current simulation only the dry pollen was considered because this is more justifiable in terms of the developed pollen drifting in the air. The effects of a higher density will lead to an increase in the aerodynamic diameter which will enhance the impactability of the particle.

For **fibres**, the approach by Tran-Cong et al. (2004) is again used here, since it has been reported that the accuracy of the Haider-Levenspiel method, Eq. (8.13) decreases as the shape factor decreases (Gabitto and Tsouris 2007). The fibre is represented by spherical aggregate particles clustered into a cylindrical bar configuration. The resulting terms, $d_A/d_n$ and $c$, which satisfy the drag coefficient in Eq. (8.18) for a representative fibre having a length of $7d$ and a diameter of $1d$, are given in Table 8.5.

**Table 8.5** Shape of agglomerate of spheres to model a sample fibre particle with diameter $d$ and length $7d$

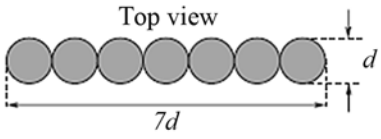


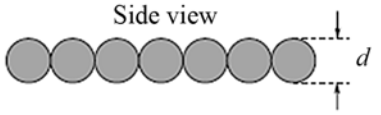


*Surface-equivalent-sphere to nominal diameter ratio*

$$\frac{d_A}{d_n} = 7^{1/6}$$

*Particle Circularity*

$$c = \frac{1}{\sqrt{7}}$$

Normalisation of the fibres can be performed through correlations from Stöber (1972) for an equivalent aerodynamic diameter ($d_{ae}$) given as

$$d_{ae} = d_{ve}\sqrt{\frac{\rho}{(1000 \cdot \kappa)}} \tag{8.19}$$

where $d_{ve}$ is the volume equivalent diameter, $\rho$ is the density of the fibre and $\kappa$ is the dynamic shape factor for a prolate spheroid. The dynamic shape factor taking the length oriented perpendicular to the flow is given as

$$\kappa_{\perp} = \frac{\frac{8}{3}\left(\beta^2 - 1\right)\beta^{1/3}}{2\beta^2 - 3/\sqrt{\beta^2 - 1}\,\ln\left(\beta + \sqrt{\beta^2 - 1}\right) + \beta} \tag{8.20}$$

and also for the length oriented parallel to the flow is given as

$$\kappa_{||} = \frac{\frac{4}{3}\left(\beta^2 - 1\right)\beta^{1/3}}{2\beta^2 - 1/\sqrt{\beta^2 - 1}\,\ln\left(\beta + \sqrt{\beta^2 - 1}\right) - \beta} \tag{8.21}$$

where $\beta$ is the aspect ratio and is defined as the ratio of the fibre length to the diameter. For random orientation of the fibre, the shape factor is a combination of the two orientations and is given as

$$\frac{1}{\kappa_R} = \frac{1}{3\kappa_{||}} + \frac{2}{3\kappa_{\perp}} \tag{8.22}$$

Taking the random orientation for the dynamic shape factor, the equivalent aerodynamic diameter range for carbon fibre is 7.6–12.8 μm for, respectively, lengths of 10–300 μm.

**Submicron and nanoparticles**, which may be considered here as spherical, are extremely small in size and therefore require additional forces to be included to

account for their different motion as discussed earlier in Sect. 6.4. The following description summarises the terms used in Eq. (8.9) for submicron modelling. The drag force takes the form of Stokes' drag law (Ounis et al. 1991a) defined as

$$F_D = \frac{18\mu}{d_p^2 \rho_p C_c} \left(u_i^g - u_i^p\right) \tag{8.23}$$

A comparison with Eq. (8.10) shows that there is an additional term $C_c$, the Cunningham slip correction (Cunningham 1910) which is used when particles are in the nanometre range; the particle is of the same magnitude as the mean free path of the surrounding fluid (primary phase). Therefore the fluid can no longer be considered continuous. This leads to molecular slip where the particle no longer moves as a continuum in the primary phase but rather as a discrete molecule amongst the primary phase molecules.

The additional force terms include the Brownian force $F_B$, $F_B = \zeta\sqrt{\frac{\pi S_0}{\Delta t}}$, the lift force $F_L$, $F_L = \frac{2K\nu^{1/2}\rho d_{ij}}{\rho_p d_p (d_{lk} d_{kl})^{1/4}}(\vec{v} - \vec{v}_p)$, and the thermophoretic force $F_T$, $F_T = -D_T \frac{1}{m_p T}\frac{\partial T}{\partial i}$. Since the motion of nanoparticles is diffusion driven, the Eulerian modelling approach can be applied which involves a single mixture fluid with the nanoparticles treated as a chemical species within the mixture. A scalar $c$, representing the concentration of the chemical species (nanoparticles), is applied to the transport equation as

$$\frac{\partial(u_j c)}{\partial x_j} = \frac{\partial}{\partial x_j}\left[\left(\tilde{D} + \frac{\upsilon_T}{S}\right)\frac{\partial c}{\partial x_j}\right] \tag{8.24}$$

The morphological characteristics, typical mean values and numerical models to account for the different particle types are summarised below in Table 8.6.

### *8.3.3 Deposition Patterns of Inhaled Particles*

#### 8.3.3.1 Deposition Patterns of Wood Dust Particles

Figure 8.20 compares the local deposition efficiency of wood dust in the nasal cavity regions (defined in Fig. 8.1), while Fig. 8.21 below displays the deposition patterns in the nasal cavity of different wood dust generated by sawing. High deposition was found in the anterior nasal segment (regions 1–5) for all dusts. This is consistent with experimental observations of Keck et al. (2000a), and Fry and Black (1973).

In the previous case study, the nasal valve was found to have the smallest cross-sectional area which led to complex flow features that included flow acceleration which enhances the particle deposition by inertial impaction. The nasal valve accounts for approximately half of the total airway resistance and has been considered a major obstruction to the delivery of inhaled pharmaceuticals by nasal spray (Schroeter et al. 2006). Posterior to the nasal valve, particles deposit in Region 3 on the septum

**Table 8.6** Summary of toxic particles and their morphological characteristics, typical mean values and numerical models

**Wood Dust Particles**

| Shape | Typical size range | Density | Drag Model |
|---|---|---|---|
| Sphere | Particle Size Distribution defined by Chung et al. (2000)<br>Pine: 3μm-55μm<br>Heavy Oak: 1μm-24μm<br>Light Oak: 1μm-24μm | Pine - 560 kg/m$^3$<br>Heavy Oak - 930 kg/m$^3$ |  <br>*Morsi and Alexander(1972)* |

**Ragweed Pollen**

| Shape | Typical size range | Density | Real Image | Modelled Image |
|---|---|---|---|---|
| Sphere with rough surface | 16-30 μm<br>*Crowder et al. (2002)* | 550 kg/m$^3$<br>*Crawford (1949)*<br>840–1320 kg/m$^3$<br>*Harrington and Metzger (1963)* | 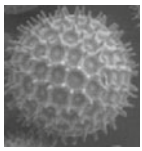 <br>*Photo Courtesy of Dartmouth College Rippel Electron Microscope Facility* |  <br>*Agglomerates of spheres method by Tran-Cong et al. (2004)* |

**Fibres**

| Shape | Typical size range | Density | Real Image | Modelled Image |
|---|---|---|---|---|
| Elongated cylinders | Asbestos Diameter < 3 μm | Asbestos 260-400 kg/m$^3$ | 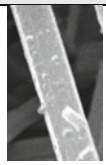 <br>*Photograph Courtesy of the U.S. Geological Survey* |  <br>*Elongated cylinder method by Haider and Levenspiel (1989)* |
| | MMVF Diameter ≈ 2-15 μm | MMVF 1830kg/m$^3$<br>*Su and Cheng (2005)* | | |
| | Fibre Length > 5 μm<br>Aspect Ratio > 3 | | | |

**Diesel Fumes, Vapours, Smoke, and Nanoparticles**

| Shape | Typical size range | Density | Drag Model |
|---|---|---|---|
| Sphere | 1-100 nm | 1000 kg/m$^3$ |  <br>*Ounis et al. (1991)* |

walls of both sides of the cavity. The second highest concentration of particle deposition of all wood dust is found on the anterior parts of the middle turbinates in Region 6 while a small portion of particles deposited at the back of the nasal cavity where the flow changes directions from horizontal to vertically downwards. The change in the flow direction at the nasopharyngeal region again acts like an inertial impactor device, filtering out high inertial particles.

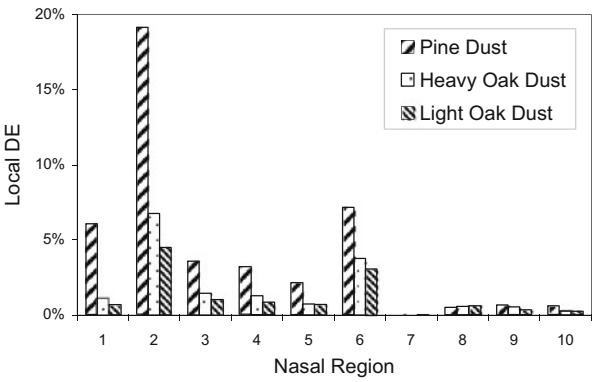


**Fig. 8.20** Local DE of all wood dust within regions of the nasal cavity. The nasal regions are defined in Fig. 8.1

There are two major clearance mechanisms of inhaled wood particles in the nasal cavity: the mucociliary mechanism and by physical means. Particles deposited on the ciliated epithelium of the nose are cleared by the mucociliary action, i.e. cilia beating that moves the mucus secretion to remove particles towards the pharynx. The anterior one-third of the nose is not covered by ciliated epithelium but by cutaneous epithelium like the skin. The clearance mechanism of deposited wood particles in these regions is assumed to be by physical means, such as sneezing, wiping and blowing (Swift and Kesavanathan 1996), which lead to a slower clearance than in the ciliated epithelium region. In a study of wood dust deposition in the nose of furniture workers (Hadfield 1972), wood particles were found to accumulate in two major regions: (i) in a small oval-shaped area on the anterior part of the nasal septum near the floor of the nose, and (ii) on the anterior part of the middle turbinate. In the current CFD study, it is noticeable that these regions also exhibit high particle deposition efficiency. Inhaled wood dust depositing on these regions is retained, and any toxic substance which it may contain remains in contact with this part of the epithelium for a longer time than on other regions that are covered by the ciliated epithelium (Fry and Black 1973) and therefore damages the exposed layer of soft tissues.

Under the assumption of spherical particles, and with the different wood types exhibiting different densities, a comparison in terms of their aerodynamic properties (inertia and settling properties) can be made through the equivalent aerodynamic diameter $d_{ae}$ defined as

$$d_{ae} = d_p \sqrt{\frac{\rho_p}{1000}} \tag{8.25}$$

This means that, very dense particle with a small diameter can have the same aerodynamics as one with a large diameter, less dense particle if their $d_{ae}$ are the same.

A parameter used for normalising impaction-dominant deposition studies is the inertial parameter, IP, given by

$$IP = Q d_{ae}^2 \tag{8.26}$$

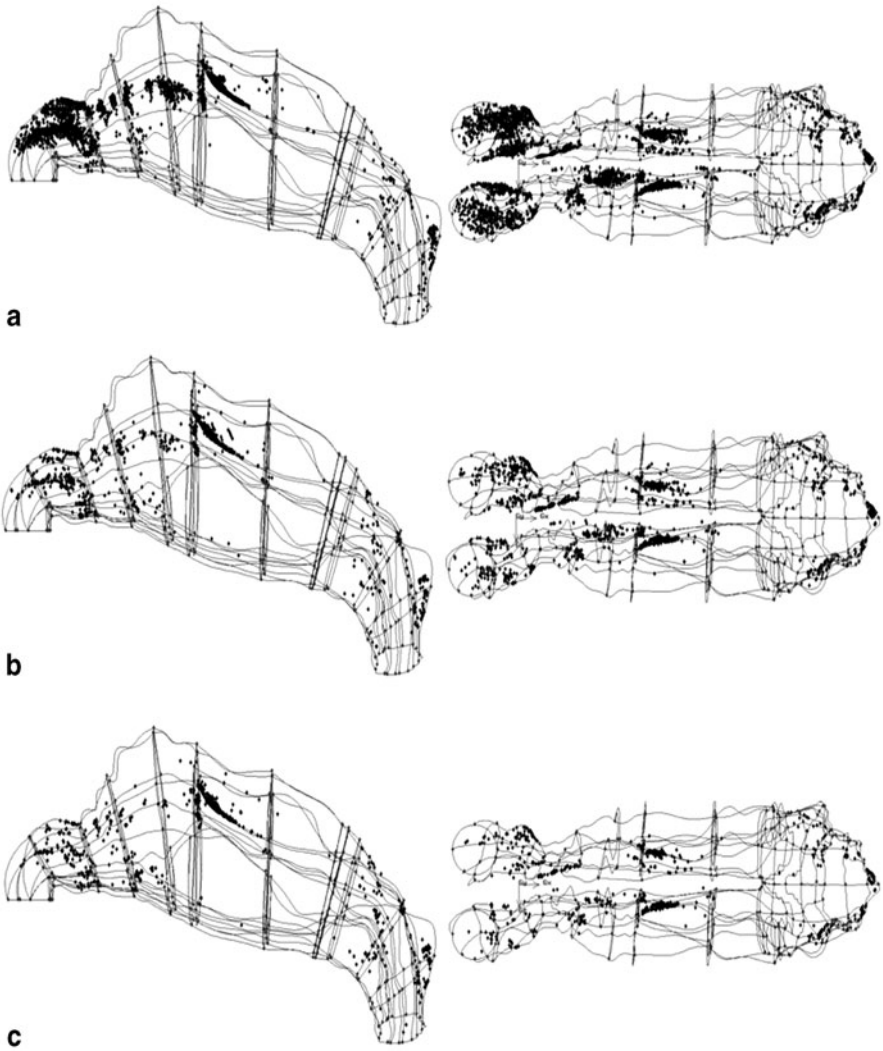


**Fig. 8.21** Deposition patterns of wood dust with different particle size distributions. **a** Pine Dust (Density = 560 kg/m$^3$). **b** Heavy Oak Dust (Density = 930 kg/m$^3$). **c** Light Oak Dust (Density = 590 kg/m$^3$)

where $Q$ is the air flow rate given in cm$^3$/s and $d_{ae}$ is the aerodynamic diameter given in µm. Additional particles in the range of 1–30 µm were released passively (with the airflow) into the nasal cavity under additional flow rates of 5, 7.5, 10 and 15 L/min. The deposition of the spherical particles over a range of the inertial parameter is shown in Fig. 8.22 and is compared with other normalised experimental results.

The deposition efficiency curves in Fig. 8.22 act as a convenient tool to predict the deposition efficiency when the aerodynamic diameter and flow rate is known. The

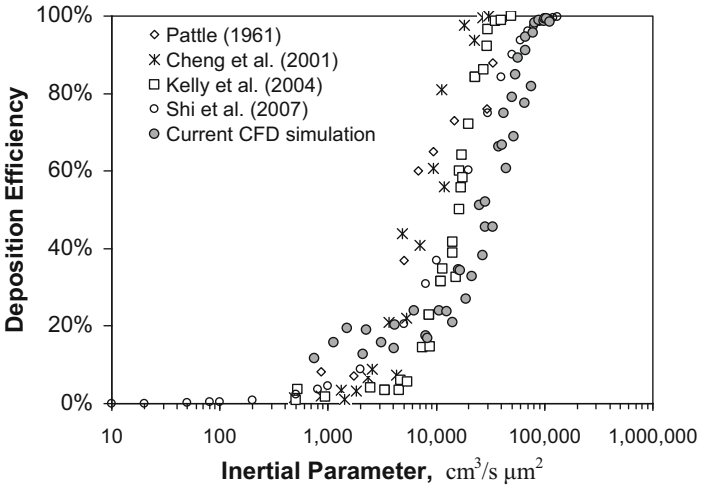


**Fig. 8.22** Deposition efficiency vs Inertial parameter comparisons (Pattle 1961; Shi et al. 2007) for the simulation micron spherical particles

variations in the curves have been attributed to the differences in the methods (experimental measurements and numerical simulations) and the nasal cavity geometries. However, with additional studies, a general trend may be observed and a better generalisation of the deposition efficiency may be achieved. Shanley et al. (2008) found an empirical expression for the deposition efficiency to fit their simulated data that incorporates the effects of particle diameter and density, breathing rate, and anatomy of the subject through the appropriate length. This expression is given as:

$$E_d = 1 - \exp\left(-\beta(\mathrm{Stk})^2\right) \tag{8.27}$$

where Stk is the particle Stokes number, and the constant $\beta$ is found to be 250.

An extension to the study of the dangers of wood dust inhalation is to investigate the surrounding environment where the wood dust is generated. In typical working areas, a ventilation system is used in an effort to remove the wood dust away from the breathing region. CFD modelling can be extended to incorporate the flow field in the breathing vicinity and the effectiveness of the ventilation systems (Inthavong et al. 2009a). Screen shots of a typical simulation is shown in Fig. 8.23 which demonstrates the ability of CFD modelling to provide further information to help prevent inhalation of toxic particles.

#### 8.3.3.2 Deposition Patterns of Pollen

Two pollen sizes, 16 and 30 μm, were investigated and the fate of each pollen was individually tracked. It was found that the highest deposition occurs in the frontal regions within the nasal vestibule (Fig. 8.24). As discussed earlier, the space in

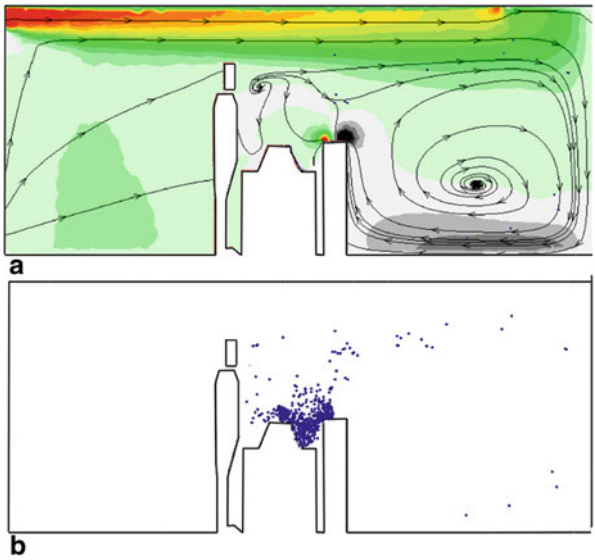


**Fig. 8.23** Typical CFD results demonstrating. **a** flow field through streamlines and velocity contours and **b** wood dust particles passing through a breathing plane, for a wood turning work station

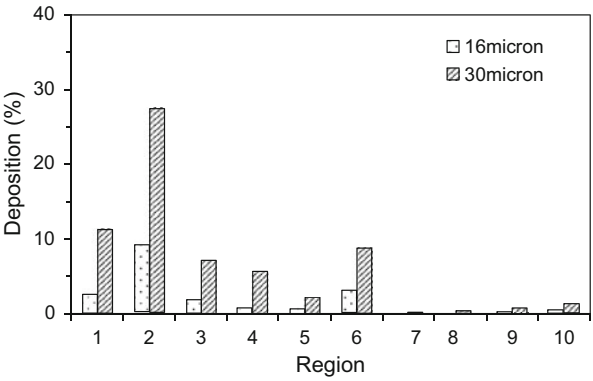


**Fig. 8.24** Cumulative deposition efficiency and regional deposition for 16 and 30 μm pollen particles

between Region 2–3 is the nasal valve region—the smallest cross-sectional area that causes acceleration of the fluid flow. Posterior to the nasal valve, the particles deposit in the upper region of the nasal cavity due to the momentum of the particles exiting the nasal valve. The deposition of particles in Region 6 may also be a cause for irritation and inflammation to the mucosal walls. Further along the nasal cavity, the deposition pattern (Fig. 8.25) shows particles depositing at the nasopharynx where the flow changes direction at 90° (i.e. inertial impaction).

A comparison with a normal spherical particle having the same aerodynamic diameter can be made through the inertial parameter. Table 8.7 shows that higher deposition occurs for spherical particles in comparison with near-spherical particles.

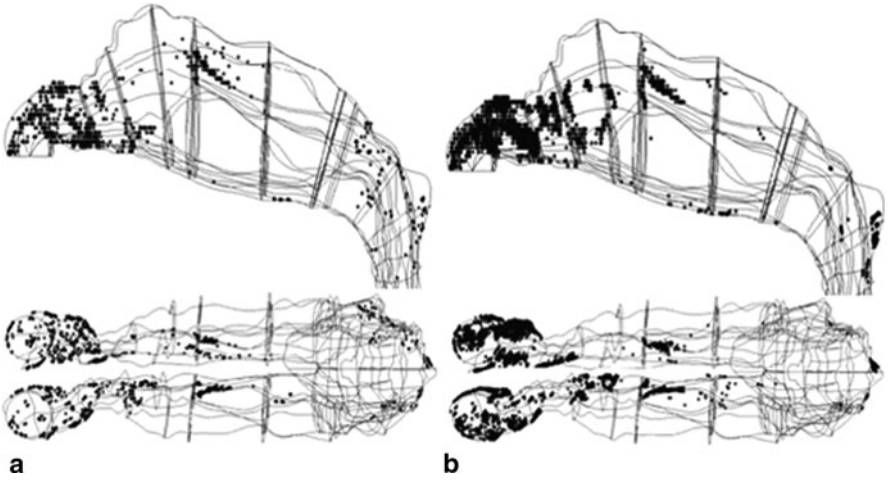


**Fig. 8.25** Deposition patterns for 16 and 30 µm pollen particles. **a** 16 µm, 550 kg/m$^3$. **b** 30 µm, 550 kg/m$^3$

**Table 8.7** A comparison of particle deposition efficiency for 16 and 30 µm pollen particles against an aerodynamic equivalent sphere

| Density | $d_p$ | $d_{ae}$ | Inertial Parameter (IP) | Deposition sphere (%) | Deposition pollen (%) |
|---|---|---|---|---|---|
| 550 | 16 | 11.86 | 23,443 | 30.3 | 19.9 |
| 550 | 30 | 22.25 | 82,500 | 86.0 | 66.2 |

This can be explained by the difference in the drag coefficient used for the non-spherical shape of the pollen. Further analysis can be performed in the CFD software by tracking the drag coefficient of the particle.

The drag coefficient comparison (Fig. 8.26) shows low drag coefficients for both particles near the entrance of the airway, which steadily increases and reaches large values near the nasopharynx. The increased drag coefficient assists in slowing down the particle's momentum and thus reduces the required particle relaxation time (i.e. Stokes number) the particle needs to complete the sudden changes of direction in the flow field. From the drag coefficient Eqs. (8.11) and (8.18), it is apparent that a relationship exists between the drag coefficient and the particle Reynolds number, $Re_p$, and this is visible in the opposing trendlines in Fig. 8.26 (i.e. where a peak in the $Re_p$ is found, a corresponding low exists for the $C_d$).

#### 8.3.3.3 Deposition of Fibres

MMVFs with a diameter of 3.66 mm, density at 1.83 g/cm$^3$ and varying lengths were simulated through the left and right nasal cavities at a flow rate of 7.5 L/min

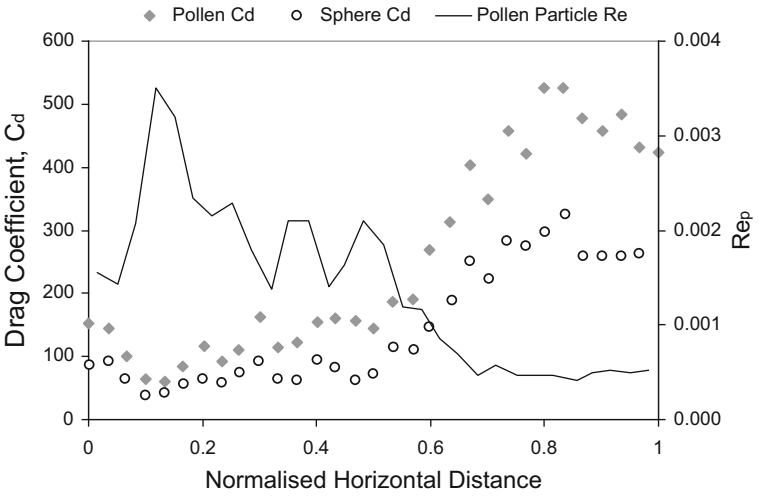


**Fig. 8.26** A comparison of the variation of the local average drag coefficient variation along the horizontal axial distance for a 30 μm pollen particle and an aerodynamic equivalent sphere

(Inthavong et al. 2008b). The two approaches, HL-model and TC-model (see Sect. 6.2.4), in modelling the aerodynamic flight of the fibres were used. The simulation found close agreement between the experimental data and the deposition values in the nasal cavity using the TC-model (Fig. 8.27). At short fibre lengths the deposition difference between the two models is similar while for long fibre lengths a difference of 37 % is observed.

The differences between the HL- and the TC-models are consistent, and it is the handling of the drag coefficient through the model correlations that provides the variances in the particle trajectory. The HL-model uses a shape factor to define the fibre elongation where, according to its definition (Eq. 8.13), the shape factor of a sphere is equal to one. The greater the aspect ratio and hence the greater length to diameter ratio, the lower the shape factor becomes. For isometrically shaped particles, the shape factor is considered the best single parameter for describing the shape of falling particles; however at low shape factors, the accuracy becomes compromised (Haider and Levenspiel 1989). On the other hand the TC-model uses a circularity parameter that has the advantage of allowing the correlation of flow dependence on particle orientation Eq. (8.17). The other major cause of deposition differences is in the nasal geometry variations between subjects as well as the differences in the left and right cavities. This factor is discussed in the next section.

The drag coefficient is inherently linked to the particle Reynolds number ($Re_p$). Given that the particle shape is controlled, it is the slip velocity attained through the aerodynamic flight of the particles in relation to the fluid path that is the deterministic cause of $Re_p$. For the scales of magnitudes of velocity ($10^1$), particle size ($10^{-6}$) and viscosity ($1/10^{-6}$), the calculated $Re_p$ are in the range of 0.02–1. A longer fibre length causes greater elongation, and therefore the drag coefficient increases due

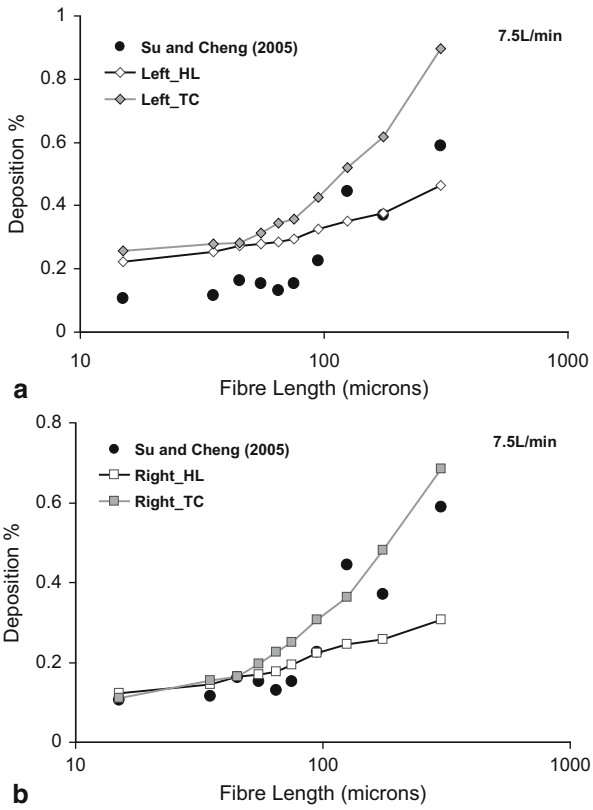


**Fig. 8.27** Fibre deposition comparison in the cavity using the two different drag correlations, HL-model and the TC-model against the experimental data

to the non-spherical shape. For long fibre lengths, the shape factor and circularity values decrease. This leads to the greatest differences between the two models at the longest fibre lengths where the empirical correlations become less accurate. At shorter lengths, the models have closer agreement to each other and provide more accurate data fits (Haider and Levenspiel 1989).

Deposition of fibres in the lungs can be carcinogenic where the toxicity has been linked to its length. The effects of fibre length on the average deposition in the left and right nasal cavities are shown in Fig. 8.28. Deposition of asbestos fibres in the nasal airway is low and exhibits little variation despite the significant variation in length. The low deposition rates (14 %) suggest that inhalation of the asbestos fibres will lead to deep respiratory deposition such as in the lungs. In contrast, deposition of the MMVFs increases from 18 to 80 % as the fibre length increases from 10 to 300 μm. The cross-sectional diameter for the MMVF is approximately three times that of asbestos while the density is six times as great. The length for MMVFs therefore becomes more significant due to a greater mass per unit length. This finding is important for providing alternatives to fibrous materials used in the manufacturing

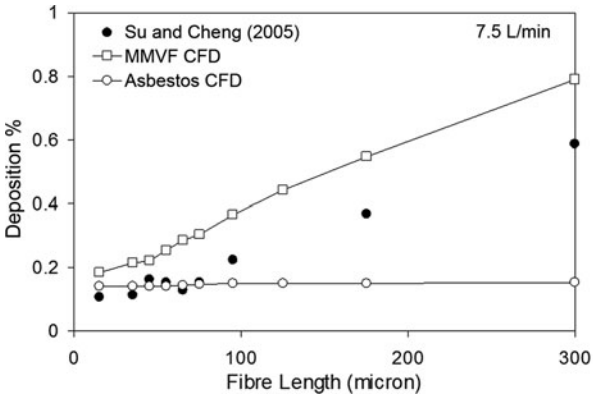


**Fig. 8.28** Average deposition efficiency for asbestos and the MMVF at different fibre lengths

industry, especially since asbestos has been found as the culprit for asbestosis and mesothelioma.

The deposition of the fibres was performed through the Lagrangian tracking method. In this tracking scheme, the fibre was considered as a point location in space with an equivalent aerodynamic diameter. The fibre is considered deposited onto a wall when the distance between the wall and the point in space is less than half the equivalent aerodynamic diameter. Thus its elongated shape is not considered, and deposition by interception is not achieved. Deposition by interception can occur if the particle travels close enough to a surface of the airway passages where an edge of the particle touches the surface. Usually the fibre length determines whether the particle will be intercepted. Typical fibres with a diameter of 1 μm and a length of 200 μm have been found to deposit in the bronchial tree (Sussman et al. 1991). Although the nasal airway is more treacherous in comparison to the tracheobronchial airway, the nose is much larger in size and the effects of deposition of long fibre lengths may be marginal. The work by Su and Cheng (2005) also discusses this issue, where deposition in the nasal airway was mainly due to impaction and that short fibres could have the same deposition fraction as long fibres in a specific nasal airway region or subregion, as long as the inertial parameters for both fibres are in the same range. However for asbestos ($d_{ae} \approx 1$ μm) at low flow rates such as 7.5 L/min, the inertial parameter is low and deposition by interception may be more significant for very long fibre lengths.

The deposition of the MMVFs and asbestos fibres over a range of the inertial parameter is used to compare against previous studies of total deposition efficiencies of spherical particles in the nasal cavity (Fig. 8.29). The deposition efficiency increases as the inertial parameter increases. The range in which the deposition efficiency reaches 90 % or more is from 20,000 (Cheng et al. 2001) to 50,000 (Su and Cheng 2005). The simulation results used the TC-model show the combined deposition efficiency for the left and right cavity. For $IP < 10{,}000$ the deposition efficiency is higher for the simulation than for Su and Cheng (2005). The higher

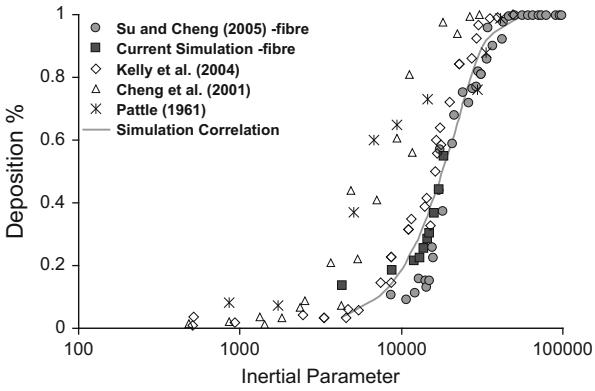


**Fig. 8.29** Comparison of deposition efficiencies between fibres and spherical particles using the Inertial Parameter

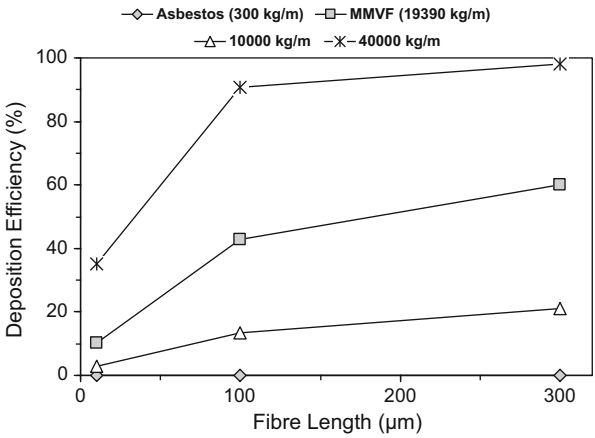


**Fig. 8.30** Fibre deposition efficiency for asbestos, the MMVF and other arbitrary fibres with varying $\rho A_{cross}$ values

values for the smaller inertial particles may be improved by the addition of a wall roughness model (Shi et al., 2007).

As mentioned earlier, the deposition efficiency curves help to predict the deposition for a given aerodynamic diameter and flow rate. With the production of man-made fibres, there is an opportunity to control properties of the fibre, such as length, that may lead to adverse health effects. In the case of MMVFs, the longer fibre lengths helped increase deposition within the nasal cavity thereby reducing deep lung inhalation. Conversely, deposition of asbestos fibres was found to be independent of their lengths given the lighter density and smaller diameters. By taking the product of the density with the cross-sectional area, the parameter of mass per unit length, $\rho A_{cross}[kg/m]$, can be used to define the resulting $d_{ae}$ and the deposition efficiency. Figure 8.30 and Table 8.8 show the significance of the fibre lengths on the effects for different $\rho A_{cross}$ values.

The deposition of the fibres can then be predicted by combining the mass per unit length with the equations of Stöber (1972) given in Sect. 8.3.2 to obtain the resultant deposition efficiency. As $\rho A_{cross}$ increases, $d_{ae}$ increases as expected but is

**Table 8.8** A comparison of particle deposition efficiency for Asbestos, the MMVF and other arbitrary fibres with varying $\rho A_{cross}$ values

| | Density (kg/m$^3$) | Diameter (μm) | $\rho A_{cross}$ (kg/m) | Length (μm) | $d_{ae}$ (μm) | Equivalent $d_{ae}$ total deposition (%) |
|---|---|---|---|---|---|---|
| *Asbestos* | 300 | 1 | 300 | 10 | 1.09 | *0.00* |
| | | | | 100 | 1.44 | *0.01* |
| | | | | 300 | 1.59 | *0.02* |
| | | | | 10 | 7.60 | *10.1* |
| *MMVF* | 1,830 | 3.66 | 19,390 | 100 | 11.38 | *42.8* |
| | | | | 300 | 12.84 | *60.1* |
| | | | | 10 | 5.49 | *2.8* |
| *Fibre 1* | 1,000 | 3.56 | 10,000 | 100 | 8.20 | *13.5* |
| | | | | 300 | 9.25 | *21.2* |
| | | | | 10 | 10.69 | *35.1* |
| *Fibre* 2 | 3,190 | 4 | 40,000 | 100 | 16.18 | *90.7* |
| | | | | *300* | *18.31* | *98.1* |

most significant in the smaller length range. The $\rho A_{cross}$ value for asbestos and the MMVF fibre is 300 and 19,390, respectively.

For asbestos fibres at the same length range, the $d_{ae}$ range is 1.0–1.6 μm. This is due to the properties of asbestos that exhibit a light density and small cross-sectional diameter and cause the $d_{ae}$ to be independent of its length.

#### 8.3.3.4 Deposition Patterns of Submicron and Nanoparticles

The diffusion deposition of submicron particles (1–150 nm) was simulated under flow rates of 4, 10 and 15 L/min (Wang et al. 2009). Comparisons of the simulated results were made with the available experimental data reported by Cheng et al. (1996) which investigated a variety of nasal cavities with different anatomical features. Here the solid lines correspond to the model prediction. High deposition reaching 80 % was found for 1 nm particles (Fig. 8.31). High diffusion deposition is found for particles up to approximately 50 nm where particles that are larger provide little change in the total deposition. The deposition for 50 nm or larger particles is approximately 10 %. As discussed earlier, differences in the results may be attributed to anatomical variances in the nasal cavities used. In summary, the good agreement between published experimental data and simulated results instill confidence that the present simulation model is sufficiently accurate to analyse laminar fluid flow as well as particle deposition in the three-dimensional nasal cavity.

You may have noticed from the previous section that micron particles deposit by inertial impaction caused by the particle's inertia. For submicron particles, there is an inherent difference in the deposition mechanism. The motion of a submicron particle is governed by Brownian diffusion, which then leads to diffusion deposition. If one is to think of the diffusion of a teabag in hot water, the motion of submicron particles dispersing randomly is similar. Thus the deposition patterns for a submicron particle and a micron particle are compared here to highlight their differences.

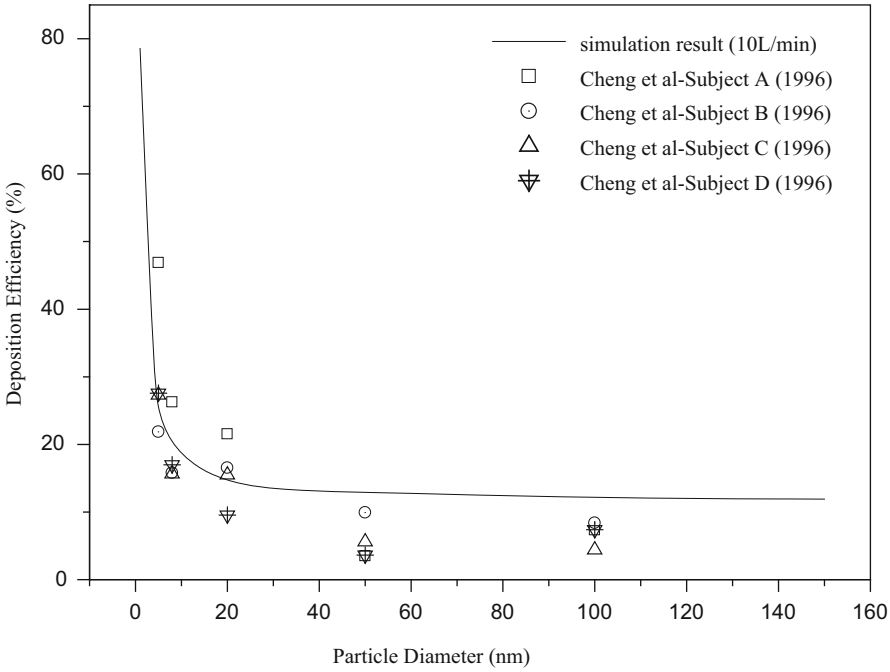


**Fig. 8.31** Deposition efficiency of 1–150 nm particles in a human nasal cavity at a steady inhalation rate of 10 L/min

The deposition efficiency for a 22 µm and a 1 nm particle are both approximately 80 %; however their different deposition mechanisms will inherently lead to different deposition patterns as shown in Fig. 8.32. The deposition pattern for a 1 nm particle shows an even distribution, not only throughout the entire nasal cavity, but also within each region. This even distribution is a result of the Brownian motion, which disperses the particles in random directions. In contrast, the deposition pattern for the 22 µm particle shows localised regions of deposition, which are caused by changes in direction of the flow field. As discussed earlier, the change of flow direction for inertial particles is the primary characteristic that defines particle deposition by inertial impaction. Thus the flow field is extremely important for the deposition of micron particles that experience inertial impaction.

Figure 8.33 shows the effects of airflow rates on the deposition efficiency of submicron and micron particles. Micron particles smaller than 10 µm exhibit low deposition efficiencies (<15 %);, however, the deposition efficiency increases rapidly when the diameter is larger than 10 µm. The deposition efficiency increases with an increase in the particle size as well as with an increase in the flow rate. Both the particle size and flow rate contribute to the inertial parameter. For submicron particles, the deposition efficiency increases with a decrease in the particle size. However for the flow rate, the three deposition curves in Fig. 8.33a converge when the particle size approaches 15 nm. The deposition efficiency decreases as the particles increase

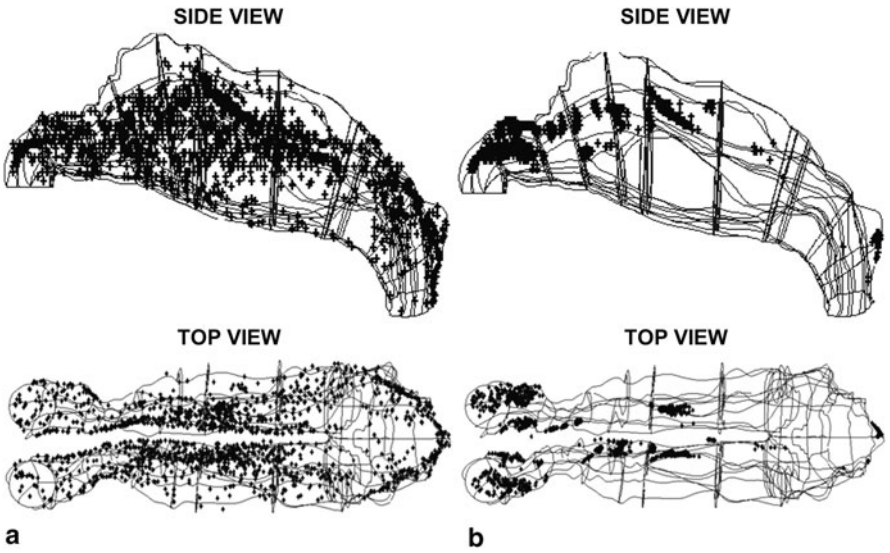


**Fig. 8.32** Deposition patterns of particles released uniformly from the nostrils for a flow rate of 10 L/min. **a** Nanoparticle having a density 1,000 kg/m$^3$ and a diameter of 1 nm. **b** Micron particle having a density 1,000 kg/m$^3$ and a diameter of 22 µm. Both particles exhibit the same deposition efficiency of 80 %

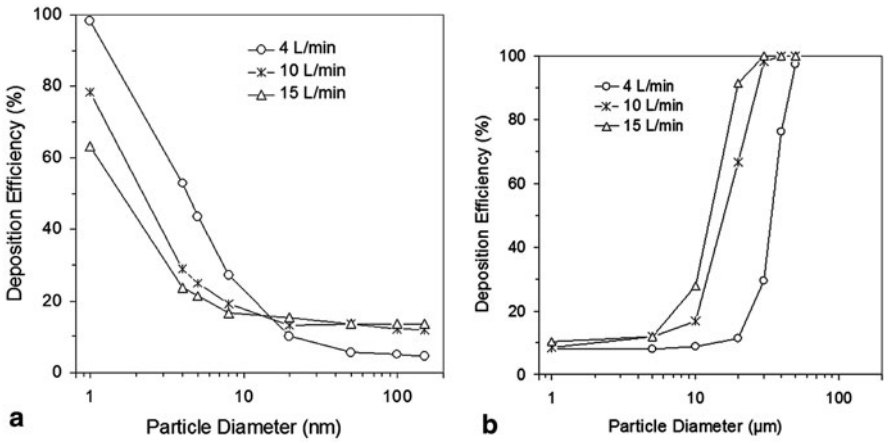


**Fig. 8.33** Deposition efficiency for submicron particles and micron particles under different flow rates

in size from 1 to 15 nm. For particles larger than 15 nm and up to 100 nm, only a slight decrease is observed in the deposition efficiency. This result may suggest that the 15 nm particle size is a critical value for distinguishing the type of deposition that is involved, i.e. where the effects of diffusion become less prominent and inertial

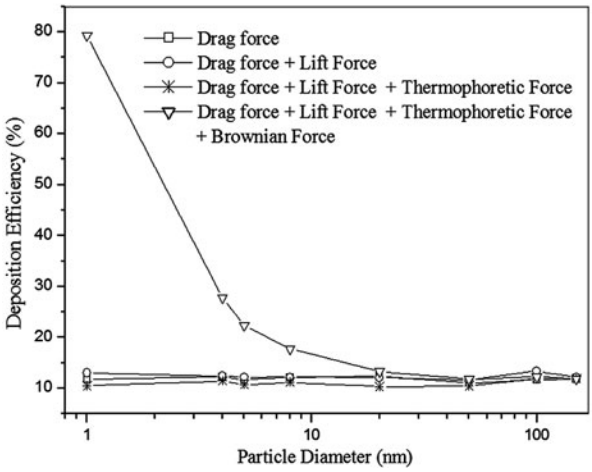


**Fig. 8.34** Comparison of different forces on nanoparticle deposition at the flow rate of 10 L/min

effects begin to contribute. In the nanoparticle range (<10 nm) the effects of the flow rate show that deposition efficiency increases with a decrease in the flow rate, which is quite different in comparison with micron particles. The lower flow rate for nanoparticles allows more time for the diffusion to take place, leading to greater particle dispersion and enhancing deposition. In contrast, a lower flow rate for micron particles reduces the particle inertia (particle relaxation time) and this allows the particle more *time* to follow any changes in the air flow field.

The effect of each force applied to a submicron particle on the deposition efficiency is shown in Fig. 8.34. The influence of the Brownian force becomes more significant as the particle size approaches 1 nm. For example, the total deposition efficiency of particles with the diameter of 1 nm increases by 66 % when the Brownian force is applied. Without the Brownian force the total deposition efficiency varies around 13 %. The drag force by itself produces a deposition of 11 %. The addition of the Saffman's lift force only increases the deposition slightly. Interestingly, the addition of the thermophoretic force decreases the deposition.

In general the deposition pattern for nanoparticles is spread out through the nasal cavity well. This has interesting applications for drug delivery where traditional nasal sprays are producing micron-sized droplets that are prone to inertial deposition. This deposition mechanism leads to high inertial impaction (up to 100 % for a mean atomized particle droplet of 50 μm) in the anterior region of the nasal cavity (Inthavong et al. 2006a, 2008a). However for high drug efficacy, the delivery of the droplets needs to be deposited in the middle regions of the nasal cavity, where the highly vascularised walls exist. Smaller particles such as 1 μm were found to be less affected by inertial properties, which allowed them to bypass the anterior region of the nasal cavity. However, because of the particles' ability to follow the streamlines more readily, the particles were less likely to deposit in any region of the nasal cavity and instead bypassed it completely, leading to the undesired effects of lung deposition. Delivery of nanoparticles, especially 1–5 nm particles, can therefore

provide improved deposition in the middle regions whilst minimising deep lung deposition.

#### 8.3.3.5 Deposition of Nanoparticles in a Nasal-sinus Cavity

Deposition studies in the human nasal cavity regions often omit the paranasal sinus regions. Because of the highly diffusive nature of nanoparticles, it is conjectured that deposition by diffusion may occur in the paranasal sinuses which may affect the residual deposition fraction that leaves the nasal cavity. A nasal cavity inclusive of the paranasal sinuses is reconstructed from CT-scans and cross-section slices in the coronary axis are shown in Fig. 8.35. The length from the anterior most region to the posterior nasopharynx region is approximately 9 cm, while the height from the main nasal passage floor to the superior tip of the frontal sinus is approximately 7 cm.

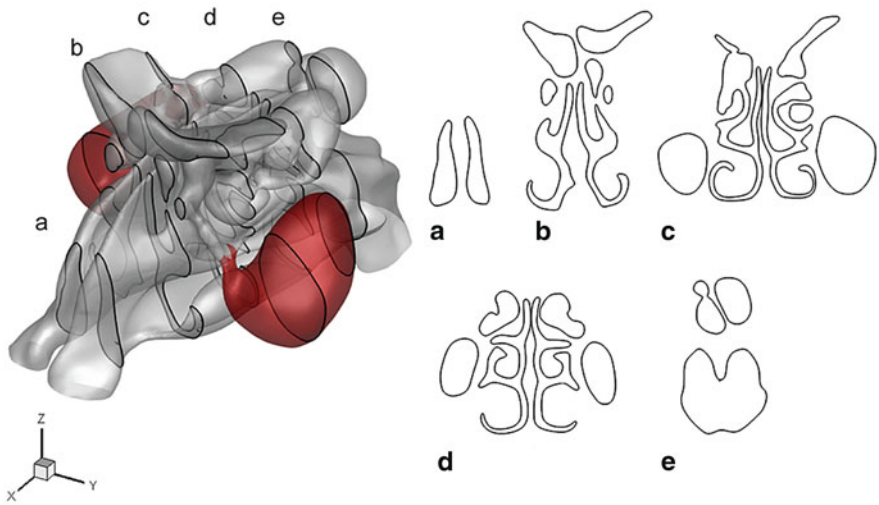


**Fig. 8.35** Computational model of a human nasal cavity inclusive of the paranasal sinus. The image is highlighted in *red* by the maxillary sinus

A laminar flow model of 10 L/min is applied to the outlet, and thus this is the total inhalation rate received from both nostril inlets. A low flow (i.e. 10 L/min) allows the simulation to focus on the diffusion process of the nanoparticles. The resulting streamlines for this inhalation rate is shown in Fig. 8.36. The streamlines initially accelerate near the nostril opening before passing mainly through the main nasal passage at mid-height. Some streamlines travel along the floor of the nasal cavity, while some reach the olfactory regions, and up towards the sphenoid and ethomoid sinuses, but these exhibit low velocity $\approx 0.1$ m/s.

Under an inhalation flow rate of 10 L/min, 70,000 nanoparticles for each particle size of 1, 5, 10, 40, and 100 nm were tracked within the two nasal cavity models. The total deposition efficiency for the region spanning from the anterior

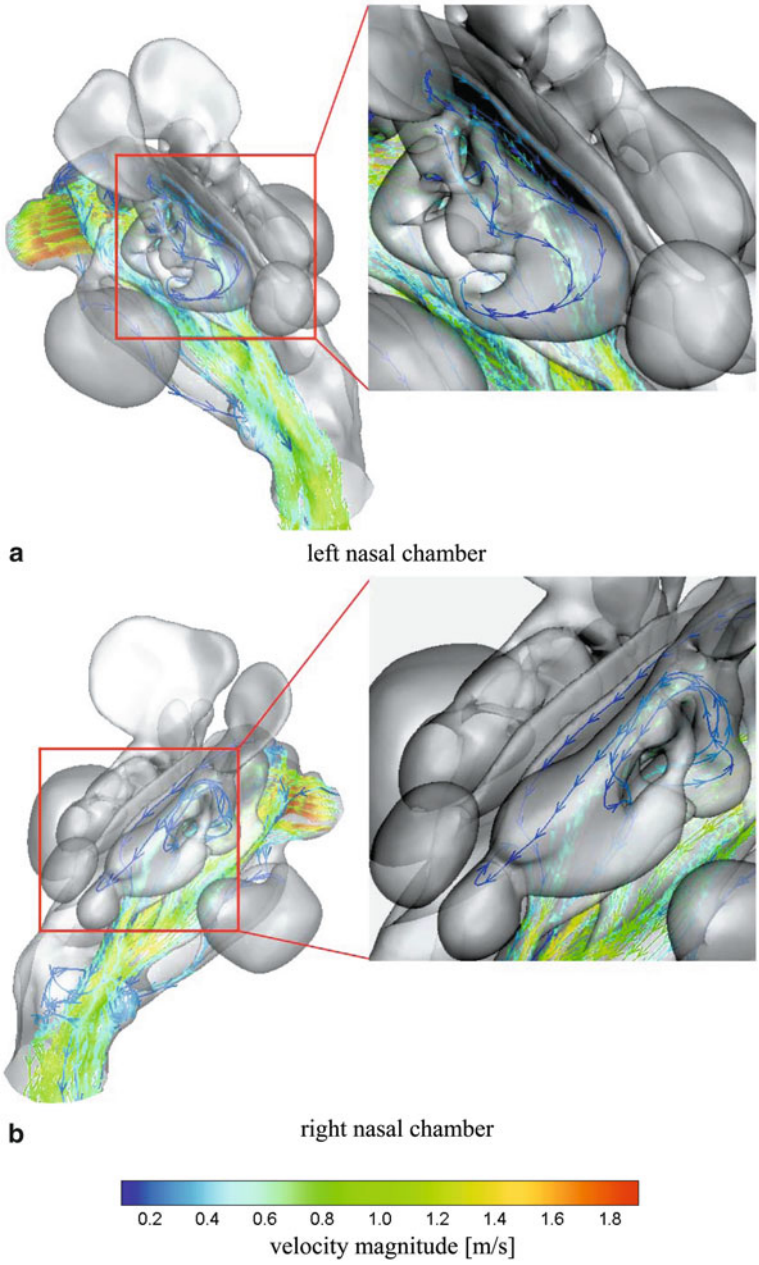


**Fig. 8.36** Streamlines passing through the nasal cavity that originates from the **a** *left* and **b** *right* nostrils at 10 L/min. *Magnified inset* highlights the flow streamlines that reach the sphenoid and ethmoid sinus regions

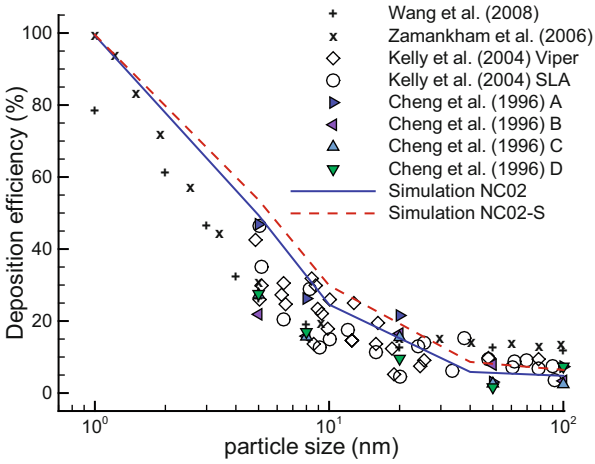


**Fig. 8.37** Comparison simulation data for nasal without sinus deposition efficiency for 10 L/min breathing rates

nostril opening conducting airway to the oropharynx was determined and compared with existing data (Fig. 8.37). The deposition efficiency profile exhibits the ubiquitous decreasing trend for the diffusion deposition of ultrafine particles, as the particle size increases. For 1 nm particles, there was 99.9 % deposition within the nasal cavity. For 10 nm particles the deposition decreases to 30 %. At 40 nm the deposition decreases to 9 % and remains at that level as the particle size increases to 100 nm. The decreasing deposition efficiency trend is due to the decreased Brownian excitation of the nanoparticle. A smaller Brownian excitation produces a smaller dispersion, and hence reduces the potential for the particles to diffuse into the ostia and sinus regions.

To confirm that the 1 nm excitation due to diffusion is much stronger at a lower flow rate, we track each individual particle and record its spatial coordinates after impaction onto the surrounding surfaces. The coordinates are plotted and coloured by residence time as shown in Fig. 8.38. The distribution of 1 nm shows that earlier deposition occurs where a large proportion of the particles persist for less than 0.022 s in the nasal-sinus cavity. The strength or influence of the Brownian diffusion increases as the flow rate decreases, and at a flow rate of 4 L/min, deposition is found within the anterior half of the nasal-sinus cavity while at a flow rate 10 L/min deposition is a little more disperse with deposition sites found in the posterior half.

The deposition pattern for 10 nm particles shows a more random and even distribution pattern. The residence time is 10x as great as that for 1 nm which suggests that the particles are transported with the inhaled flow field for longer and hence has the ability to travel deeper into the nasal cavity and perhaps down towards the lung region. The particle residence time is important for nanoparticle deposition studies as it gives an indication of the likelihood of deposition in different regions of the nasal cavity. For example the shorter residence time of 1 nm means that deposition occurs nearly immediately and the deposition zone is restricted to the nasal cavity and further deposition downstream is unlikely. This protects the sensitive lung airways from those nanoparticles that exhibit dangerous properties for respiratory

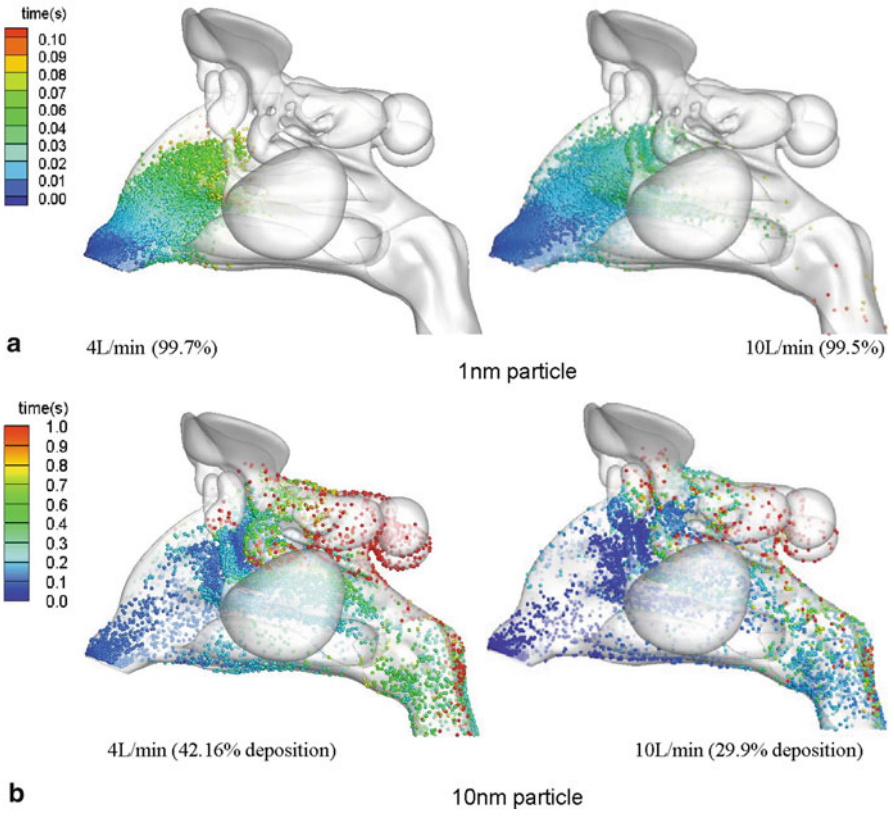


**Fig. 8.38** Nanoparticle deposition pattern in the nasal-sinus cavity for **a** 1 nm—resulting in 98 % deposition and **b** 10 nm—resulting in 29.8 % deposition. Particles are coloured by trajectory time within the nasal cavity before impacting onto the surfaces at 10 L/min

health. Conversely the ability to deposit particles in the middle regions of the nasal cavity or even deeper into the lung airways with high deposition, can be important for therapeutic drug delivery.

Deposition in the maxillary sinus is very low and our hypothesis that the diffusion process may be dominant enough for particles to pass into the paranasal sinuses appears to only be supported if there is some convection involved (e.g. deposition sites in the sphenoid and ethmoid sinuses). In the maxillary sinuses the ostium protrudes at nearly right angles to the main flow field. To further investigate this we examine the maxillary ostium and locate the deposition of individual 1, 10 and 40 nm particles within the region as shown in Fig. 8.38. In the right maxilliary sinus, inclusive of the ostium, a small percentage of particles <0.04 % are deposited. At a flow rate of 4 L/min there are no 1 nm particles depositing due to its early deposition in the main nasal passage. For both models, 10 and 40 nm particles are

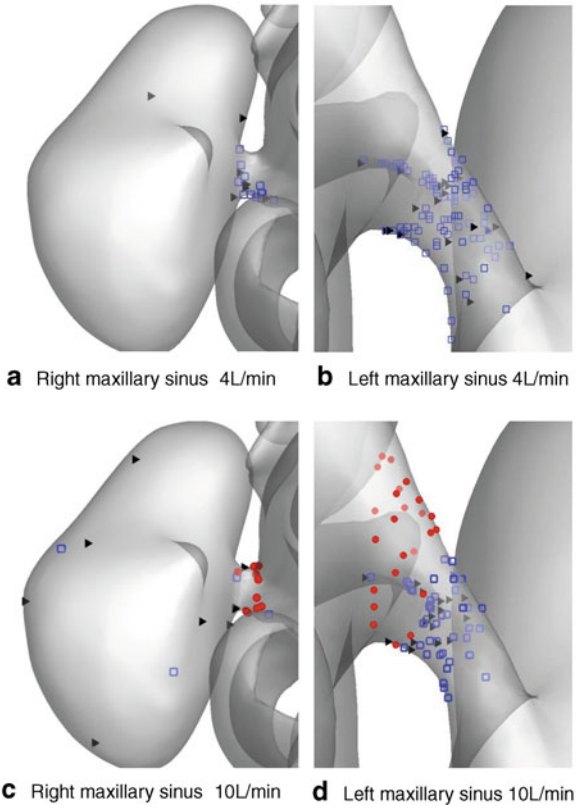


**Fig. 8.39** Frontal view showing the nanoparticle deposition in maxialliary ostium and sinus for the **a** *right* nasal cavity, and **b** the *left* nasal cavity at 10 L/min. Different sized particles are coloured as follows: 1 nm *red* circle; 10 nm *blue* square; 40 nm *black* triangle

found concentrated within the ostium. Thus it appears that despite a lower flow rate, there is a lack of particle deposition within the maxillary sinus.

For a flow rate of 10 L/min it can be seen that 1 nm particles are captured within the narrow ostium and in fact don't make it through to the maxilliary sinus. For the left maxilliary sinus, no particles were able to pass through the ostium, but a larger percentage of particles $<0.5$ % deposited within the ostium alone. This is mainly due to the curved geometry and longer ostium length providing a narrow tube passageway for the particles to diffuse onto. These results support the report by Hood et al. (2009), that ostium sinus ventilation is limited (unless the ostium is very large) and that the gas exchange of nitric oxide (NO) between the air in the maxillary sinus and the nasal air does not contributor greatly to the overall NO concentration (Fig. 8.39).

### 8.3.4 Closure

The introduction of particles into the airway presents additional modelling requirements. In this case study, the Lagrangian modelling approach is used where an equation representing the force balance on individual particles is applied in order to determine the particle velocity. The particles then become a secondary dilute phase (usually solid or liquid) present in the primary phase (usually gas or liquid).

Strategies for modelling different particle morphology such as spherical, non-spherical, submicron, and fibrous particles were shown. These different particles are representative of everyday particles that are inhalable through the respiratory system. For example, the modelling of spherical particles was applied to low-density drug particles; non-spherical particles for ragweed pollen; submicron particles for fumes, vapour, and drug particles; and fibres for asbestos and MMVFs. In some instances the modelling requirements were available within the commercial CFD software. Where there were insufficient models, additional custom models need to be written by the user.

The results showed that the effects of particle morphology on deposition patterns and deposition efficiencies were found to be significant for the nasal airway. The dominant mechanism of deposition is by inertial impaction, especially for particles greater than 5 μm at low flow rates. Under these conditions, the inertial parameter is a useful tool that allows comparisons between particles that exist in this inertial framework. Thus aerodynamic factors related to the particle morphology, such as the shape factor, must be accounted for through the drag coefficient. The application of spherical particle deposition was used to simulate wood dust inhalation, which is a common problem among wood crafting and processing. The simulations were able to show local deposition patterns where pine dust had much higher deposition efficiency than the heavy and light oak dusts within the anterior nasal segment, as pine dust comprised of much larger particles. The oak dusts consisted of smaller diameter particles, which lead to its lower deposition. Compared with heavy oak dust, the light oak dust had lower deposition efficiency, despite it having the same particle distribution as heavy oak dust. This was due to a lower material density that light oak dust exhibited and consequently a lower inertial parameter.

Allergenic ragweed pollen and toxic asbestos fibres were also considered. It was found that about 20 % of 16 μm pollen particles deposited in the main airway while for 30 μm pollen particles, 66.2 % deposited. These values are smaller when compared with a sphere having the same aerodynamic diameter which indicates that the drag coefficient for pollen is greater than for a spherical particle. For asbestos fibres, where the density and cross-sectional diameter are small, the fibre length becomes insignificant for the deposition efficiency. The deposition increased from 8.7 to 9.6 % for an increase in fibre length of 10–300 μm. Conversely, MMVFs with higher density and larger cross-sectional diameter exhibit greater mass per unit length, thus deposition increased from 14 to 50 % over the same fibre length range. It is imagined that these results may assist in the design of new particles and guide practical clinical tests for toxicity.

This case study builds on the knowledge of the airflow field in a nasal cavity from the previous case study, showing that there is a link between the nasal cavity geometry and its function to filter out airborne particles. In addition to the geometry is the physiology of the nose which includes the mucociliary (nasal hair) movement which traps and removes inhaled particles. Such configuration of the nasal passage may be a product of evolutionary development. While harmful particles are best kept out of the nasal cavity, drug particles delivered into the airway need to deposit in the highly vascularised mucus walls to allow the absorption of the drug composition into the blood stream. Therefore the delivery of the drug particles must overcome the evolutionary developments of the nasal cavity. While this case study touched briefly on the delivery of low-density as well as nanoparticles as an alternative for drug delivery, the following case study will investigate further the atomization of a drug formulation from a nasal spray device and how certain parameters associated with the atomization can affect the particle deposition.

Finally the deposition patterns of nanoparticles within a nasal-sinus cavity model are presented. A nasal cavity model including the sinuses was created in order to determine if any nanoparticles would deposit within the paranasal sinuses given that these particles are transported through the nasal cavity mainly by diffusion. Under a flow rate of 10 L/min it was shown that 1 nm particles deposited early and in the anterior half of nasal cavity with a deposition efficiency of 99 %. As the particle increased in size to 10 nm the diffusive nature of the nanoparticle decreased and the deposition efficiency reduced to 30 %. However a more evenly distributed deposition pattern was found for 10 nm particles.

## 8.4 Optimisation of Nasal Drug Delivery

Nasal drug delivery provides an alternative approach to traditional delivery methods such as oral drug routes that can fail in the systemic delivery of certain compounds since drugs taken orally are susceptible to unwanted breakdown within the digestive system. The nasal airway is dominated by the nasal turbinates that are lined with highly vascularised mucosa that contain openings to the paranasal sinuses. Because of these characteristics, it is hypothesised that drug delivery to combat health problems, such as lung diseases, cancers, diabetes, sinus infections etc., may be viable if the drug formulation can be deposited in the turbinate region (Kimbell et al. 2004). However this requirement tends to be poorly implemented where a large proportion of the drug particles are known to deposit in the anterior regions of the nasal vestibule, attributed to the sprayed particles existing in a high inertial regime (Inthavong et al. 2006a; Kelly et al. 2004; Zwartz and Guilmette 2001). Therefore studies into local particle deposition becomes of great significance in the delivery of drugs via the nasal airway. Knowledge of the atomized drug particles' initial conditions as they are introduced into nasal cavity is required in order to simulate and optimise delivery devices (nasal sprays) and correct drug formulations. In this case study, experimental

**Table 8.9** Variables related to the actuation of a nasal spray

| Consumer variables | Parameter affected |
|---|---|
| Increased/Decreased inhalation | Air flow rate |
| Nostrils opened (one or two) | Air flow pattern |
| Head tilt back/forward | Insertion angle inwards |
| Spraying away from septum walls | Insertion angle sideways |
| Strength of actuation | Particle size and velocity |
| Speed of actuation | Particle size and velocity |
| Insertion location | Surrounding geometry |

results are presented and the implementation of such data into a CFD simulation is shown.

Nasal particle deposition delivered by a spray device has been performed by Cheng et al. (2001) using a multi-sectional nasal airway replica model, and they found deposition patterns from four different nasal spray pumps. The results showed that particles deposited mainly in the anterior and turbinate regions and that deposition in the anterior region increased with an increase in spray cone angles and larger particles. Suman et al. (2002) investigated deposition patterns in relation to *in-vitro* measurements of two different nasal spray pumps having different performance characteristics. It was found that spray characteristics, such as spray angle and plume geometry, did not affect the distribution of droplets in the nose. The discrepancy between the two correlations may be attributed to the numerous variations that exist in nasal spray applications that are hard to quantify experimentally (Table 8.9).

### *8.4.1 Nasal Spray Atomization Experimental Images*

CFPD simulations of nasal drug delivery often neglect the initial spray particle conditions (e.g. particle velocity) and instead introduce particles entrained with the inhaled airflow into the nasal cavity. This section presents some experimental images which provides qualitative insight and improved understanding into the physical behaviour of nasal spray delivery. Firstly a steady stream of water is passed through a nasal spray that is placed in a perspex test chamber. A schematic of the setup is given in Fig. 8.40 which shows both the pressurised water supply and the visualisation system. An upstream pressure of 500 kPa was used to force water through the nasal spray. The transparent perspex test chamber encloses a nasal spray nozzle that is pointed downwards. Using high speed shadow lighting photography techniques with lasers, high resolution images in the near nozzle spray region can be captured to allow a better understanding of the physical behaviour of the spray. Initial measurements are made with the spray pointing downwards to avoid any interference from gravitational settling of droplets which is unavoidable if the nasal spray were to be directed upwards.

The nasal spray device was sliced open at the nozzle and a scan electron microscope (SEM) was used to determine the type of atomizer used. Figure 8.41 shows the 80X image SEM magnification of the internal atomizer which is a pressure swirl

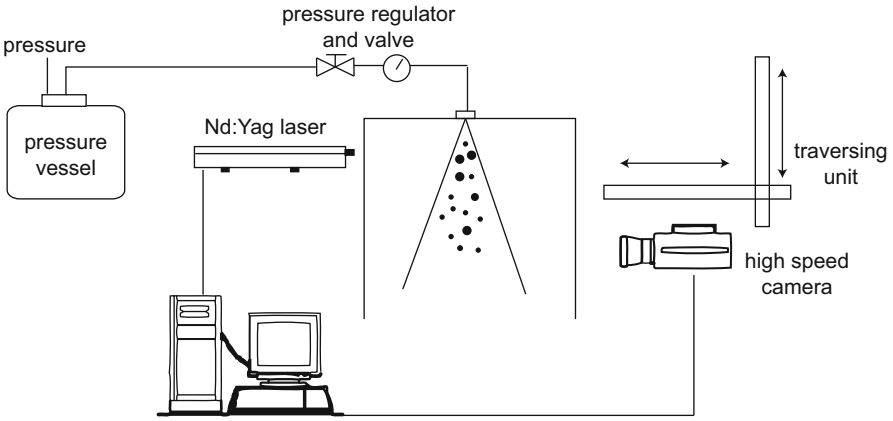


**Fig. 8.40** Schematic of the experimental setup to capture the spray atomization and particle size distribution

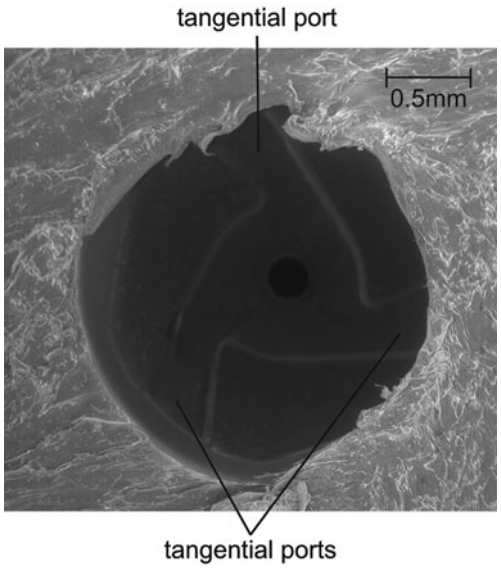


**Fig. 8.41** 80X scan electron microscope image of a cutaway of the nasal spray device showing the nozzle orifice and its tangential ports. Orifice diameter is 0.28 mm

type. In this case there are three tangential ports that force the drug formulation to swirl through the orifice which is 0.28 mm in diameter. Lefebvre (1989) notes that these atomizers produce much wider cone angles over plain orifice atomizers because of the swirling motion imparted to the liquid, spreading it out in the form of a conical sheet as soon as it leaves the orifice.

Figure 8.42 shows three images of a spray being formed in the near-nozzle region as well as a schematic that illustrates the physical behaviour of the ejected liquid and atomizes, to develop into a spray. Each region has a field of view of 3.85 mm-wide by 3.08 mm-high, and is spatially contiguous with other but taken at different times.

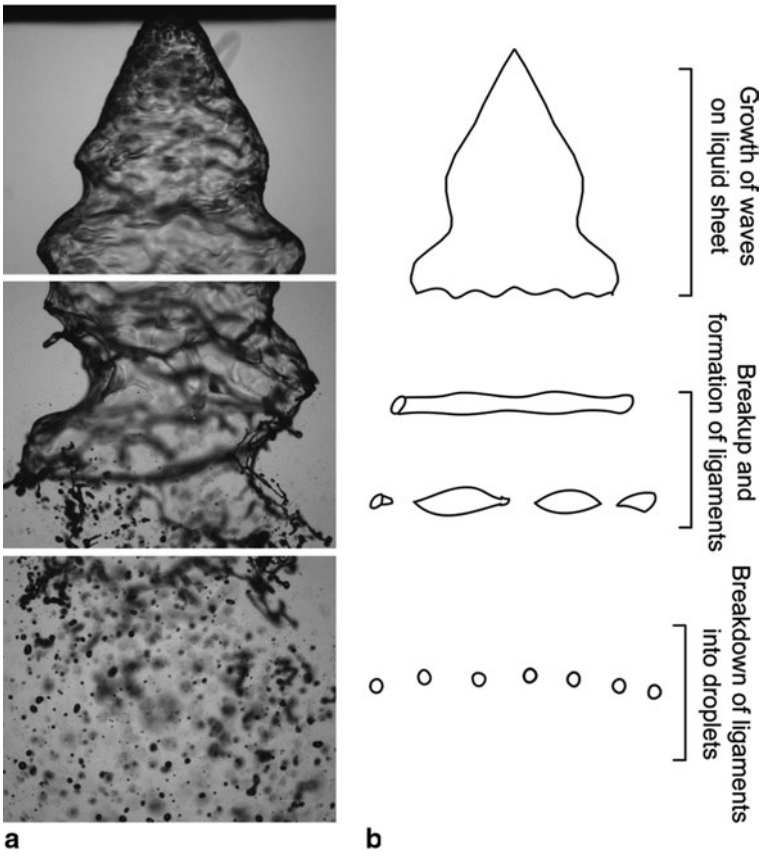


**Fig. 8.42** **a** Individual images of spray field in the near-nozzle region showing a swirling hollow sheet of liquid. **b** Schematic of primary spray breakup

It is observed that the pressure induced by the nasal spray actuation causes the liquid to emerge from the nozzle orifice under the action of both radial and axial forces. A swirling thinning sheet of liquid is formed which becomes unstable, breaking up into liquid ligaments before forming particles at a distance, called the break-up length, from the nozzle.

### *8.4.2 Nasal Spray Atomization*

A hollow spray cone is produced at the break-up length, with the majority of particles located at the periphery of the hollow cone (Fig. 8.43). This type of atomization is typical of pressure-swirl atomizers that are contained within the spray nozzle. Theories of pressure-swirl atomization has been studied extensively for the last century with the vast majority of literature focused on high pressure applications, such as fuel injectors found in the automotive industry; and the reader is referred to the

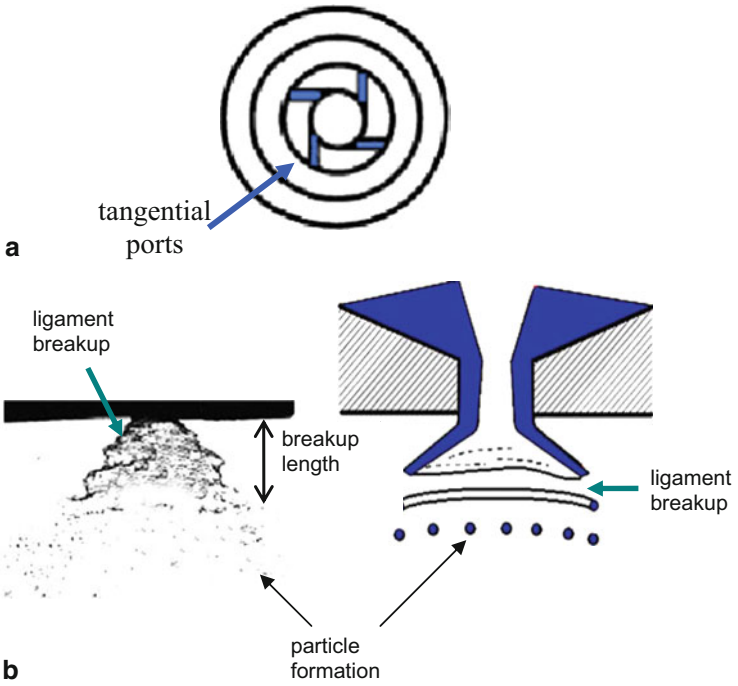


**Fig. 8.43** Pressure swirl atomizer characteristics. **a** internal swirl chamber showing the tangential ports within the atomizer and **b** atomization process

text by Lefebvre (1989) for further details. Although little has been researched on nasal sprays, it is evident that the parameters that may influence nasal drug deposition include *the spray cone angle, initial particle velocity, the insertion angle,* and *swirl effects* which will be evaluated for deposition efficiency under high and low inertial particles. In addition to these parameters, *the nozzle diameter, particle size distribution,* and *break-up length* may also have an influence.

The spray cone angle defines the degree of dispersion of the spray into the airway. Studies have shown that the spray angle is influenced by the nozzle dimensions, upstream pressure, liquid properties and the density of the medium into which the liquid is sprayed (Babu et al. 1982; Rizk and Lefebvre 1985). These design parameters can be altered to achieve the desired spray cone angle. Therefore in the simulation, the spray cone angle will be investigated to evaluate its performance. The diameter at the break-up length is important in terms of particle initialisation in the computational model as the particles need to be defined at the break-up length rather than at a point located at the spray nozzle.

This can be approximated by

$$d_{bul} = 2(d_n + L_{bu} \tan \phi) \tag{8.28}$$

where $d_{bul}$ is the diameter at the break-up length, $\phi$ is referred to as the half-cone angle which is the angle between the spray sheet and the spray centreline, $L_{bu}$ is the

**Table 8.10** Measured parameters from a spray device

| Measured Parameters | Value |
|---|---|
| Nozzle diameter | ≈0.5 mm |
| Diameter at break-up length | ≈4 mm |
| Spray cone angle | ≈30 ° |
| Initial particle velocity | ≈15 m/s |
| Break-up length | ≈3.5 mm |

break-up length and $d_n$ is the nozzle diameter. However this linear approximation doesn't take into account any momentum losses during the entire spray penetration and may give an over-prediction of the diameter as $L_{bu}$ gets further downstream.

Information such as the design sketches of nasal sprays are often sensitive due to corporate patents for the design, and detailed information such as the nozzle diameter, pressure-swirl chambers and cone angles can be difficult to obtain. One method to obtain the required information is to take an image of the spray device and measure the parameters needed through imaging analysis software. The measurements in Table 8.10 give approximate values, allowing a parametrical study to evaluate the performance of each parameter.

In addition to the measured data, a 2D velocity field produced by a Particle Image Velocimetry (PIV) system found that the exit velocity from the nozzle was approximately 15 m/s produced from a continuous spray under an upstream pressure of 600 kPa. Maximum velocity reached was 17 m/s approximately 0.1 m downstream (Fig. 8.44).

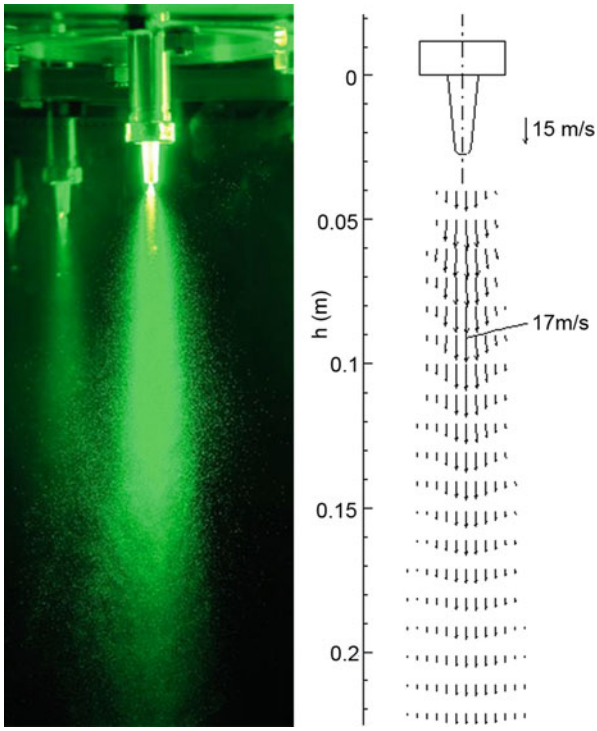


**Fig. 8.44** Single image snapshot of the spray under the PIV lasers, and the resulting PIV 2D vector plot which shows the averaged mean droplet velocity field of the spray nozzle

It should be noted that this value is a consequence of a continuous spray which induces continuous momentum to the bulk spray region from the upstream pressure. For nasal spray applications where the upstream pressure is applied within a short time, and is bounded by the nasal cavity, the continuous momentum does not exist. The *initial particle velocity* measured however is more applicable because the atomization near the nozzle is the same for a continuous spray as it is for a pulsed spray.

In addition to the measured values in Table 8.10, the *particle size distribution* is important for the CFD setup. The particle size distribution has been measured by Cheng et al. (2001) for a commercial spray device (Valois VP7/G 18/415) and is presented in Fig. 8.45.

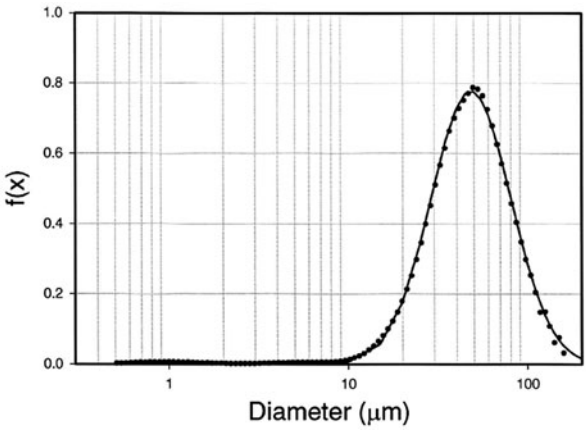


**Fig. 8.45** Typical particle size distribution results from the experimental work by Cheng et al. (2001)

### *8.4.3 Setup and Validation of the CFD Model*

Typically, when the properties of the particles that are being introduced into the airway can be inputted directly inputted into the CFD software.In the case where this is not possible, then each particle may have to be defined explicitly through a custom function or file. In this case study, the nasal cavity will be subjected to a constant air flow rate of 10 L/min to demonstrate the *effects of swirl* and 20 L/min to demonstrate the effects of *the spray cone angle, initial particle velocity,* and*the insertion angle*. The 20 L/min case is also used to demonstrate a turbulent flow regime and to show the modelling requirements applied. This adds further model equations, not only for the fluid flow but also for the particle turbulent dispersion (see Sect. 6.2.4), that need to be resolved through the CFD software. The turbulence model used in this case study is the *realizable k-ε* model, although variants of the model, such as the *k-ω* models and the *Reynolds Stress Model* (RSM), have been shown to produce good results. When a turbulence model is used, the near wall regions must have a very fine mesh to resolve the turbulent boundary layer, or a *wall function* is used which acts

as a black box to model the rapid gradients in the turbulent boundary layer. Here, an *enhanced wall function* is used to resolve the boundary layer (see Sect. 5.3.4).

The particles adopted the properties of spherical water droplets, as most drug formulations are diluted with water. The internal walls of the nasal cavity were set to a "trap" condition, meaning that particles touching a wall, deposit at that location. Monodispersed particles in the range of 1–30 µm were initially tested at an inhalation of 10, 20, 30 and 40 L/min. The turbulent dispersion of the particles is handled by the Eddy Interaction Model (EIM). Because of the problems with the near wall anisotropic behaviour as discussed in Sect. 6.2.4, the mean flow tracking (which infers no turbulent particle dispersion) was also applied. The EIM tracking, as expected, grossly overestimated particle deposition for an inertial parameter (IP) < 10,000. It also underestimated deposition for IP > 20,000, while the mean flow tracking overestimated particle deposition for IP < 8,000 and underestimated deposition for IP > 10,000.

Solutions to this problem require the application of custom functions to alter the turbulence fluctuation, and the reader is referred to Appendix C for these functions. A simpler method which combines the EIM model with the mean flow tracking may be used to capture the correct deposition efficiency. While this is not purely correct, it obviates the need for complex custom functions while providing correct deposition efficiencies for engineering problems. Thus a hybrid tracking method is used where the EIM tracking is used for larger particles where IP > 10,000 and a mean flow tracking is used for IP < 10,000 (Fig. 8.46), which is equivalent to $d_p \approx 5.5$ µm for a flow rate of 20 L/min. This ideal model is sufficient for the study of nasal spray particles that have mean particle sizes in the range of 50–70 µm (Cheng et al. 2001), which is much larger than the critical size for the applicable use of the EIM tracking method.

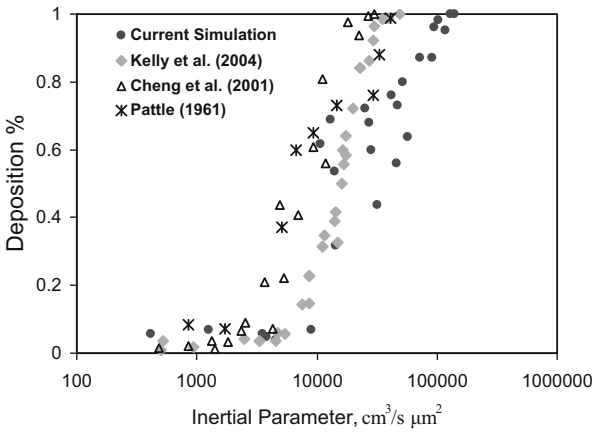


**Fig. 8.46** Deposition efficiency for monodisperse particles released into 20, 30 and 40 L/min airflow using a hybrid tracking technique

Differences in the comparison of particle deposition with the inertial parameter is discussed by Häußermann et al. (2001), such as the limitation of the inertial parameter not taking into account the changes in airway geometry. This constant air flow rate is a measure of the average impactability of the particle over the entire domain, as it doesn't factor in the changes in velocity which is significant when the geometry

under consideration is highly convoluted, narrow and complex. Furthermore, nasal cavity replicate casts with wider airways may cause less deposition due to secondary flows (Häußermann et al. 2001).

### *8.4.4 Swirl Fraction, λ*

The effects of swirl can be investigated by setting the swirl fraction. For this demonstration a flow rate of 10 L/min laminar flow is used. The swirl fraction sets the fraction of the velocity magnitude to go into the swirling component of the flow, and thus a higher fraction will produce a greater tangential velocity component. This increases the time taken to travel a given axial distance as the particle is swirling more and its residence time becomes longer. Additionally the induced drag from the cross-flow of air helps to reduce the initial high momentum of the particle, and the chances of particles travelling through the frontal regions of the nasal cavity increases. Figure 8.47 shows high deposition of particles occurring in the frontal regions (Regions 1–3).

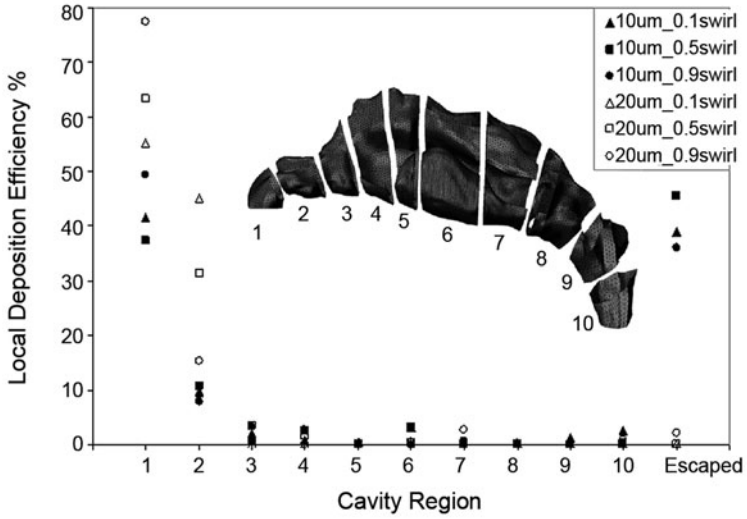


**Fig. 8.47** Particle deposition within different sections of the nasal cavity. Sections 1–3 are the frontal region, Sects 4–7 are the middle region and Sects 8–10 are the posterior region

The amount of swirl has a different effect for the two different particle sizes. For 10 μm particles with $\lambda = 0.9$, deposition in the frontal regions increases, while for $\lambda = 0.5$, a higher percentage of particles escape. Conversely, for 20 μm particles, an increase in the swirl fraction decreases the deposition in the frontal zones. Some deposition in the middle zones occurs, and 2.2 % of particles escape when the $\lambda = 0.9$. The reason for these local deposition patterns can be better understood

by observing the particle trajectories (Fig. 8.48). It is known that larger particles that possess high inertia (i.e. Stokes number characteristics) need to be aligned with the flow streamlines to avoid impaction. This implies that the particles need to be projected at a clear unobstructed path in the nasal airway rather than be projected at walls.

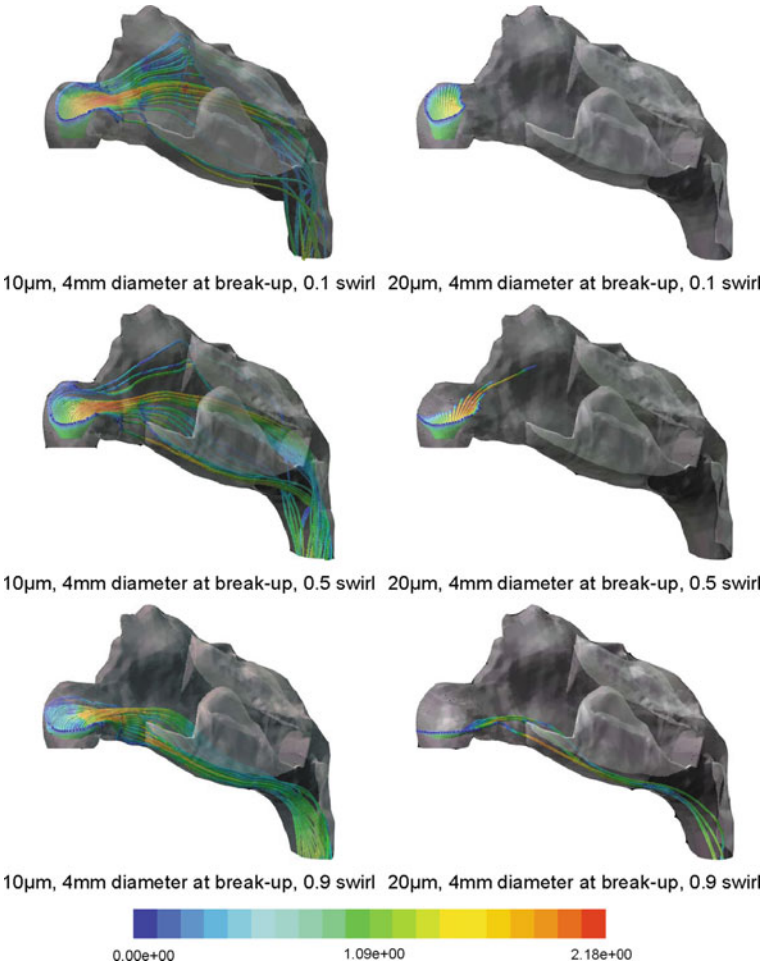


**Fig. 8.48** Particle trajectories for 10 and 20 μm particles at different swirl fractions

When $\lambda \rightarrow 0$, the velocity magnitude is entirely composed of axial velocity, which projects the particles vertically. High inertia particles are directed at the roof of the nasal vestibule and do not have enough time to slow down and adapt to the gas phase streamlines. However smaller inertia particles can adapt to the flow streamlines more readily. One idea to overcome this is to insert the nasal spray at an angle (insertion angle) that would provide such alignments with the flow streamlines (Inthavong et al.

2006a). However this technique is dependent on the user, the application of the nasal spray device and the precise location of the nozzle.

When $\lambda \rightarrow 1$, the velocity magnitude is entirely composed of a tangential velocity, and the particles are projected at a tangential direction to the nasal spray insertion angle. For 10 µm particles, deposition increases in the frontal zones as more particles are pushed towards the wall. For 20 µm particles this is also the case; however, instead of impaction into the upper roof when $\lambda = 0.1$, impaction is on the side walls. The horizontal projection of a small proportion of particles is then enhanced by the gas phase velocity which carries the particles along the floor of the nasal cavity.

Without any obstructions to the flow, the particles are transported through to the nasopharynx area. A small increase in deposition within the middle and anterior regions is observed. At the nasopharynx, the flow changes direction at 90° which acts as another filter to capture high inertia particles that impact at the back. Although a swirl fraction of 1 is extreme and indeed unrealistic to achieve practically within the atomizer design, its use in the present investigation provides a deeper understanding of the effects of the swirl fraction. The particle trajectories demonstrate that the swirling motion decreases the particles' initially high inertia due to the difference in the air and particle velocities.

### *8.4.5 Initial Particle Velocity*

In the previous section the effects of swirl fraction were demonstrated under a flow rate of 10 L/min. The following sections will now be run under a flow rate of 20 L/min which uses a turbulent flow. The initial particle velocity can be controlled in many ways, such as changing the nozzle diameter and the actuation mechanism. To avoid any variations in terms of the nozzle location and its orientation, monodisperse particles were released uniformly in a normal direction to the inlet surface of each nostril, and the average deposition within the left and right nasal cavity was recorded. Injected particle velocities were chosen to reflect a real nasal spray application. Velocities were calculated based on mass conservation, assumed nasal spray geometries and the experimental data from Fig. 8.44, which found velocities ranging between 10 to 17 m/s for pressure actuations up to 600 kpa. Quantitatively, the results obtained by using a uniform surface injection, normal to the nostril inlets, will differ from a real nasal spray application that produces an injection from a very small diameter. However, qualitatively, it provides a basis for the impactability of specific particles at different injection velocities.

The injected particles possess high initial momentum. However this energy is degenerated by the drag force acted on by the gas phase rapidly. The influence of the airflow on the particle is dependent on the particle Stokes number. The relationship for the particle-gas velocity ratio as a function of the Stokes number is given as

$$u^* = \frac{u_p}{u_g} \approx \frac{1}{1 + St} \tag{8.29}$$

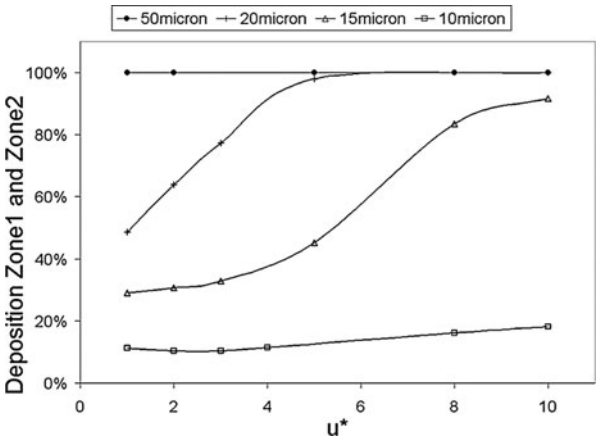


**Fig. 8.49** Total deposition in the first two regions of the nasal cavity at different particle injection velocities

where

$$St = \frac{\rho_p d_p^2}{18\,\mu_g}\frac{U}{D} = \tau\frac{U}{D} \tag{8.30}$$

This suggests that for small Stokes numbers (i.e. St $\rightarrow$ 0), the particle velocity approaches the airflow velocity quickly. For large Stokes numbers (i.e. St $\rightarrow \infty$), $u^*$ approaches zero meaning that the particle velocity is unaffected by the gas. Thus, it is expected that rapid changes in the particle velocity will occur within the anterior section of the nasal cavity. The anterior region of the nasal cavity is further divided into three regions, and particle flow paths and deposition patterns within this region are shown in Fig. 8.49 and 8.50a, 8.50b, and 8.50c.

Figure 8.49 shows the total particle deposition in the first two regions of the nasal cavity at different particle injection velocities. Regions are defined in Fig. 8.1. A small influence on the impactability of a 10 µm particle is observed when there is an increase in the initial particle velocity and is seen by the slight increase in deposition. The low Stokes number brings about a rapid decrease in velocity, and the particle assumes the airflow velocity before the change in direction of the flow. The influence of $u^*$ amplifies as the particle size increases, where a greater proportion of particles deposit in the two frontal zones. The geometry of the frontal section of the nasal cavity conforms to that of a 90° bend where the particle Stokes number is of importance. The larger particles exhibit much higher Stokes numbers which prevent the particles from following the curved streamlines. It is observed that 50 µm particles entrained in the flow ($u^*$=1) is an example of this. Therefore an injected 50 µm particle ($u^*$=10) exhibiting a greater amount of initial momentum will only exacerbate the linear projectile motion of the particle.

About 70 % of 15 µm particles are able to follow the curved streamlines when $u^*$=1 as particle impactablility is governed by the Stokes number only. However, significant deposition increases when $u^*$>4. The Stokes number, a ratio of the particle's relaxation time to the flow characteristic time, indicates how long it takes for

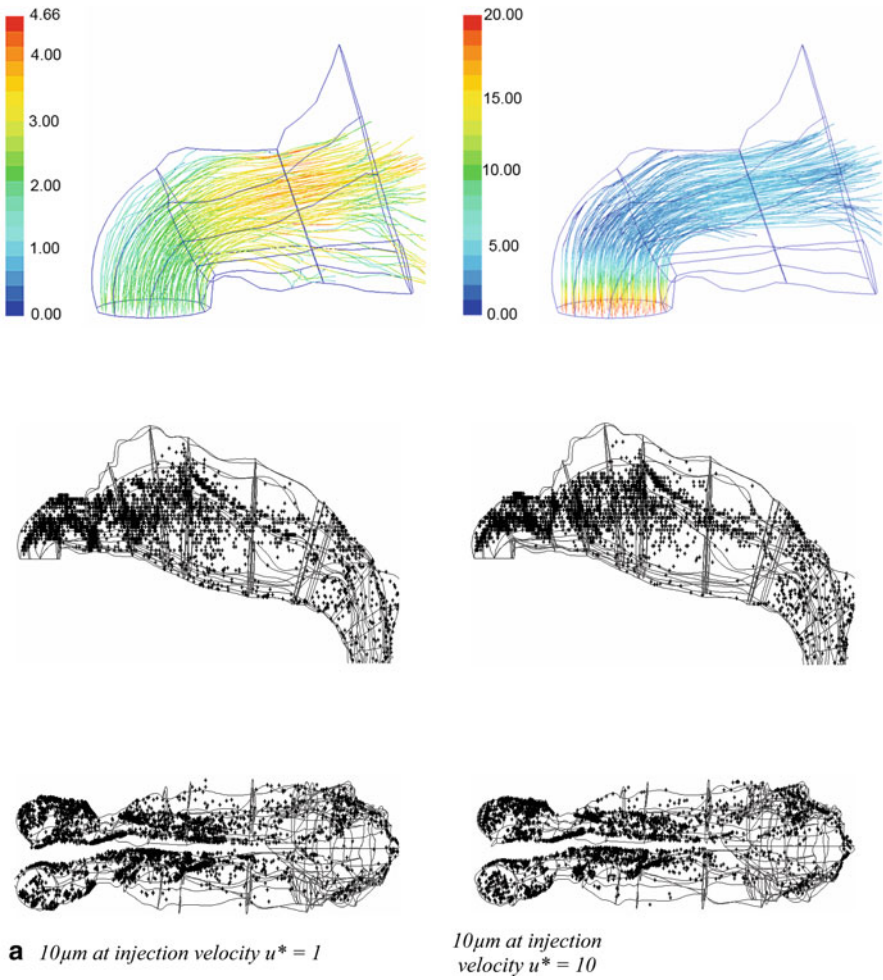


**Fig. 8.50** Deposition patterns for **a** 10 μm **b** 15 μm and **c** 50 μm particles released uniformly from the inlet surface normal to the nostril openings at $u^* = 1$ and $u^* = 10$

the particle to adjust to the airflow conditions. For a fixed distance (nostril opening to the top of the vestibule), an increase in $u^*$ will decrease the time taken to cover this distance. This leads to a shorter time and distance for the particle to adapt to the gas phase conditions and presents a higher impactability than that calculated by the Stokes number alone. The influence of the injected particle velocity is still felt as the airflow begins to curve. As particle size increases, so does the relaxation time that the particle needs to adapt to flow changes. As a result, significant deposition increases occur at lower $u^*$ values for larger Stokes numbers.

Figure 8.50 displays the deposition sites for the two extreme cases, $d_p = 10$ μm and $d_p = 50$ μm, and for a mid-range particle, $d_p = 15$ μm, subjected to $u^* = 1$

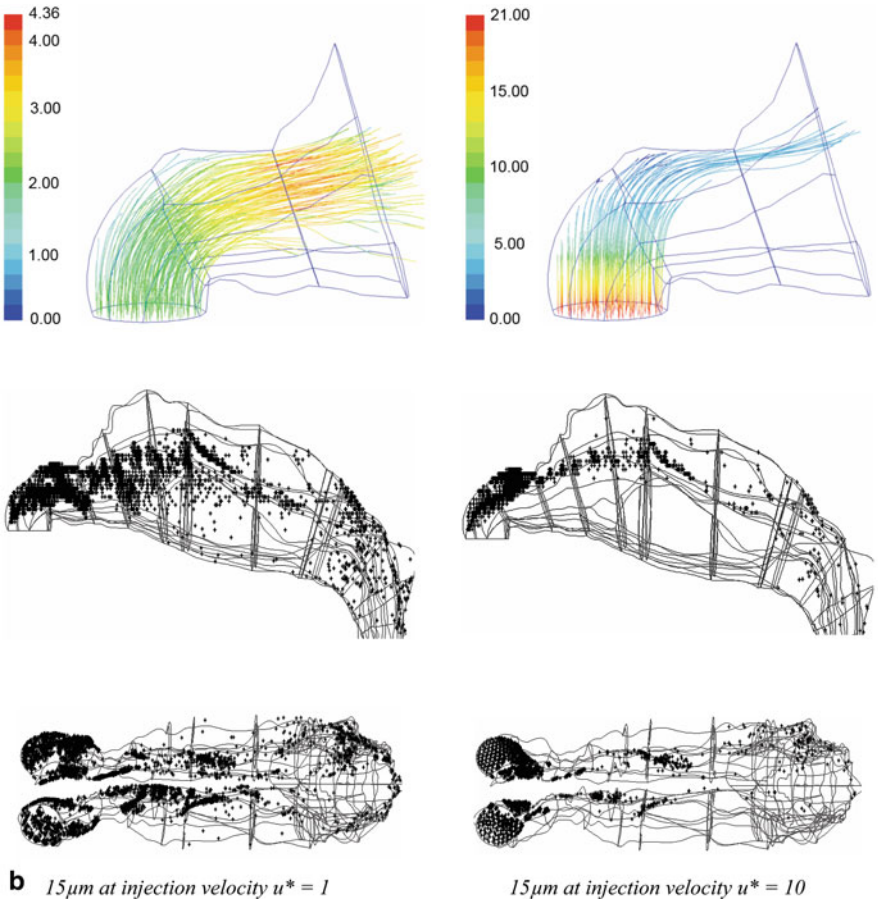


**Fig. 8.50** (continued)

and $u^* = 10$. The 50 μm particles impact at the top of the vestibule at $u^* = 10$; and at $u^* = 1$, only a small proportion begin to curve albeit for a short distance before impaction. In contrast, 10 μm particles are barely affected by the increase in injection velocity with local deposition sites being concentrated near the nasal valve region and septum walls, which is qualitatively similar to Zwartz and Guilmette (2001). The difference in deposition occurs at the entrance region where entrained particles released near the wall deposit readily through fluctuations in the flow whereas particles at higher velocities overcome this region. The particle flow for $u^* = 10$ enables the particles to travel further linearly which is evident in the particles' adapting to the flow changes at a later stage than particles at $u^* = 1$. This later adaption to the flow causes the particles to assume those streamlines closer to the ceiling of the nasal cavity compared with particles at $u^* = 1$. Beyond the first two zones of the nasal cavity, deposition sites are similar, locally.

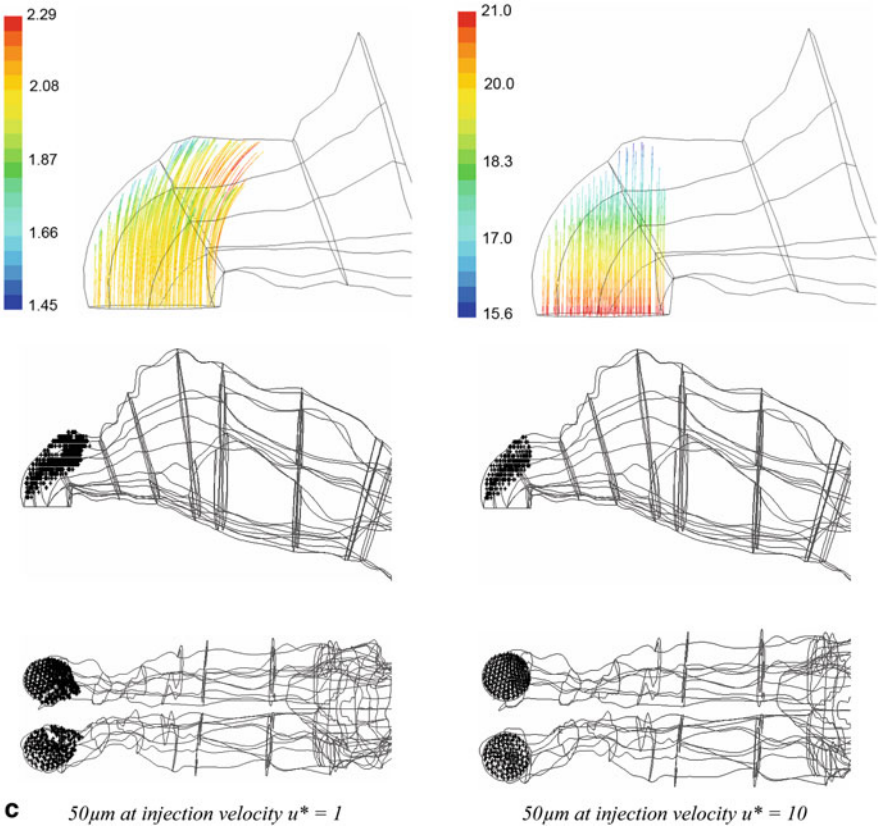


**Fig. 8.50** (continued)

Deposition of 15 μm particles at $u^* = 1$ are mainly concentrated within the vestibule, nasal valve regions and along the septum walls. Differences appear between the left-side and right-side of the cavity which is due to anatomical variations. The concentration of particles within the middle passage of the nasal cavity is lighter than that shown in 10 μm particles because the larger particles have a higher concentration within the anterior section of the nasal cavity. When $u^*$ is increased to 10 the particle is no longer just governed by its Stokes number, but also by the driving force of the initial injected velocity that adds initial momentum to the particle. This increase in momentum is dissipated by the difference in the velocities of the gas and particle phases. The particles travel further linearly in the normal direction to the nostril inlet with 88 % impacting at the top of the vestibule. Only 12 % of particles are able to adjust to the curvature in time, and these particles remain in the upper regions of the nasal cavity throughout the flow.

### 8.4.6 *Insertion Angle, α*

The insertion angle, $\alpha$, is the angle between the nasal spray device from the horizontal position (0° in the x-y plane), when looking into the side of a person's face (Fig. 8.51). Particle sizes of 10–20 µm were used at an initial velocity of 10 m/s. A uniform surface injection released from the inlet was used to eliminate variables such as location of the nozzle tip, nozzle diameter and spray cone angle.

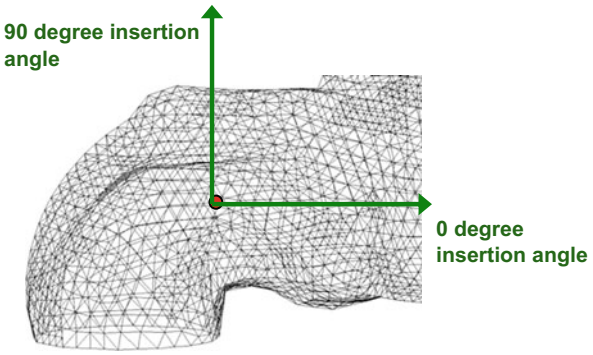


**Fig. 8.51** Side view of the nasal vestibule showing the insertion angle

Higher deposition occurred at 100° for most particles (Fig. 8.52) as the gas phase velocity cannot overcome the initial injected velocity of 10 m/s, which causes the particles to be discharged directly into the anterior walls of the nasal cavity. This concentration of particles can be seen in Fig. 8.53 for 15 µm particles. Minimum deposition for smaller sized particles, 10 and 15 µm, was found when $\alpha = 70°$. The 70° direction of particles enhances the ability of turning, as more particles assume the streamlines on the inside of the curvature. Further decreases in $\alpha$, where the direction of discharge approaches the horizontal, increases deposition of particles because a higher proportion of particles are now directed at the adjoining wall of the nostril, albeit at a small margin.

The 20 µm particles behave similarly but at lower $\alpha$. Minimum deposition in the two frontal zones was found at $\alpha = 45°$. Although more particles are directed into the adjoining wall, this is offset by more particles penetrating into the curvature instead of impacting straight into the roof of the vestibule as is the case when $\alpha = 90°$. These larger particles require a sharper angle of insertion to avoid impacting with the roof of the vestibule, thus aiding the alignment of the particles with the 90° bend and reducing the amount of deviation required in turning. The larger the particle (20 and 50 µm), the more effective the decrease of $\alpha$ becomes. Another insertion angle that can be considered is the orientation when looking into a person's face, front-on, in the *y*-*z* plane. This wasn't investigated because the same ideas regarding the particle size with its dependency on initial flow conditions exist.

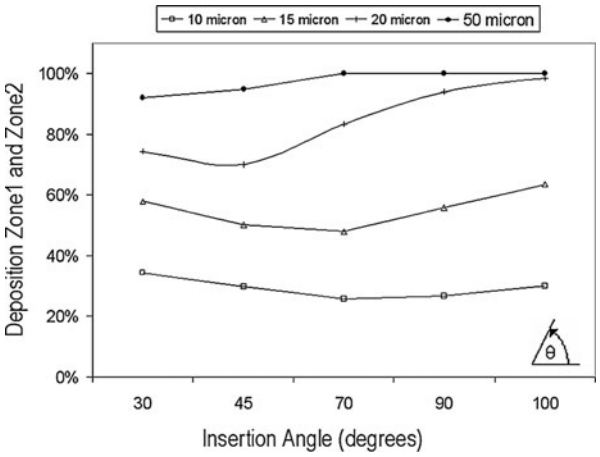


**Fig. 8.52** Deposition in Zone1 and Zone 2 for monodispersed particles released uniformly from the inlet surface at different insertion angles

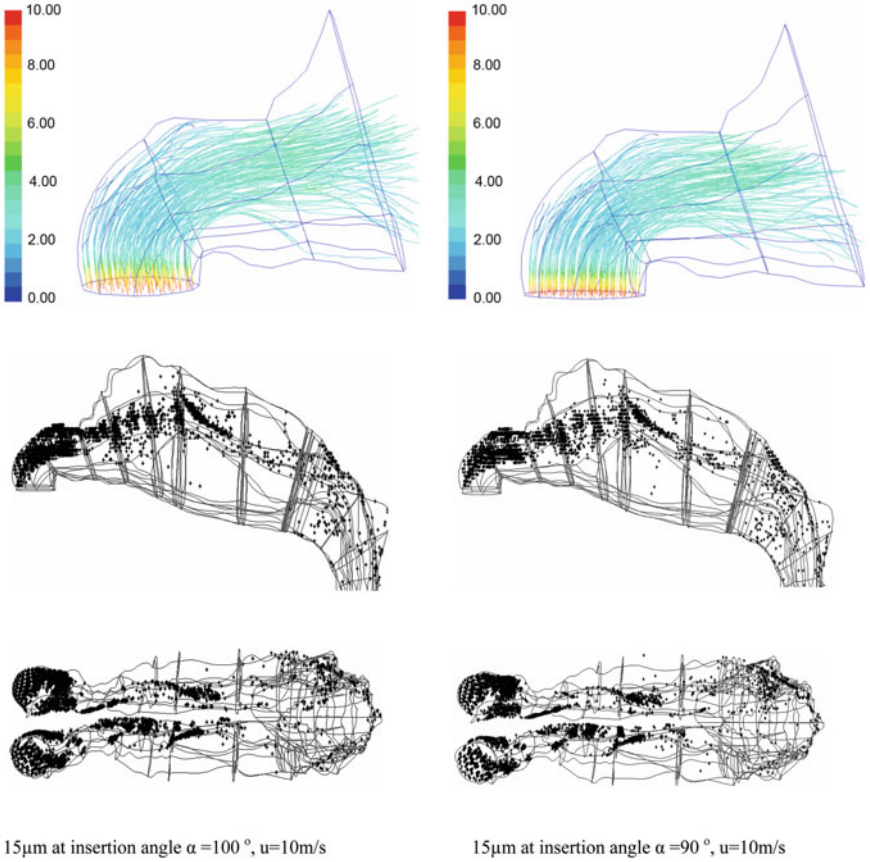


**a** 15μm at insertion angle α =100 °, u=10m/s

15μm at insertion angle α =90 °, u=10m/s

**Fig. 8.53** **a** Deposition patterns for 15 μm particles released uniformly from the inlet surface uniformly from the inlet surface at insertion angles 100 and 90°. **b** Deposition patterns for 15 μm particles released uniformly from the inlet surface at insertion angles 70 and 30°

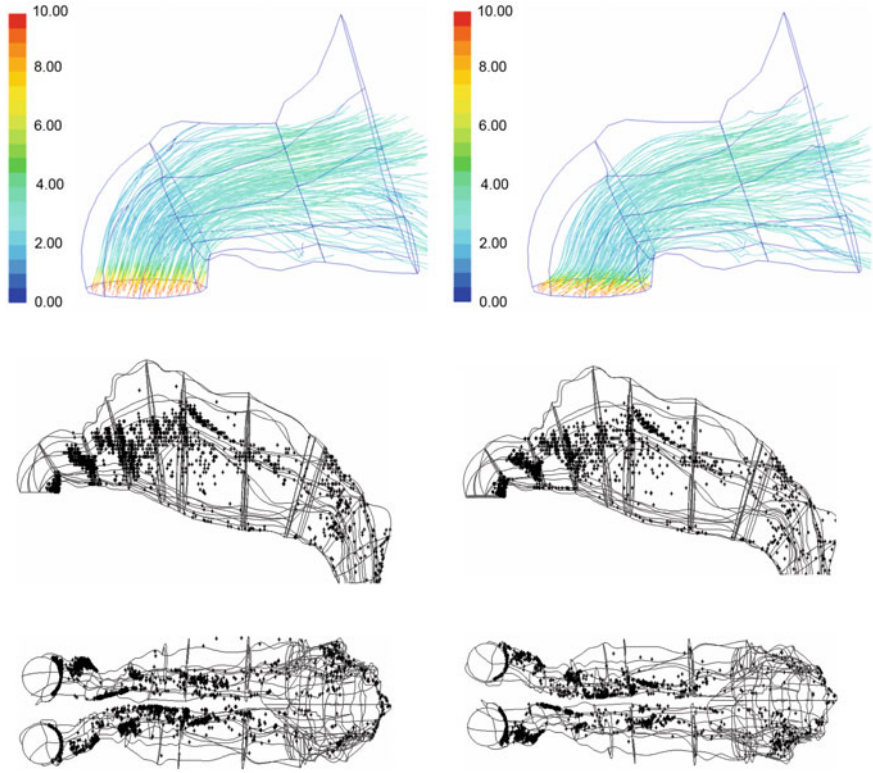


**b** 15μm at insertion angle α =70 °, u=10m/s

15μm at insertion angle α =30 °, u=10m/s

**Fig. 8.53** (continued)

### *8.4.7 Full Spray Cone Angle, β*

The full spray cone angle, $\beta$, is the dispersion of particles exiting from the nozzle tip. It is twice the angle of the half spray cone angle (Fig. 8.54). Particles were released from a small diameter compared with previous particle release methods, which used a uniform surface inlet at the nostril openings. This allows observation of the physical differences when changing $\beta$. Particles were released at 10 m/s from an internally fixed location with a diameter of 0.8 mm and a range of $\beta$ between 20 to 80°.

Deposition of 10 μm particles in the two frontal zones are unaffected by the change in $\beta$ (Fig. 8.55). Again the significance of $\beta$ is realised as particle size increases. The smaller ranged particles, that follow the gas phase velocity more readily, are optimised when released with a narrow $\beta$. A wider $\beta$ gives rise to a larger range of dispersion due to the nature of a 360° spray cone.

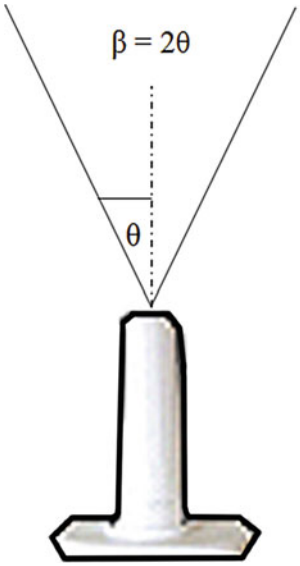


**Fig. 8.54** $\beta$—full spray cone angle in comparison with $\theta$—half-cone spray angle

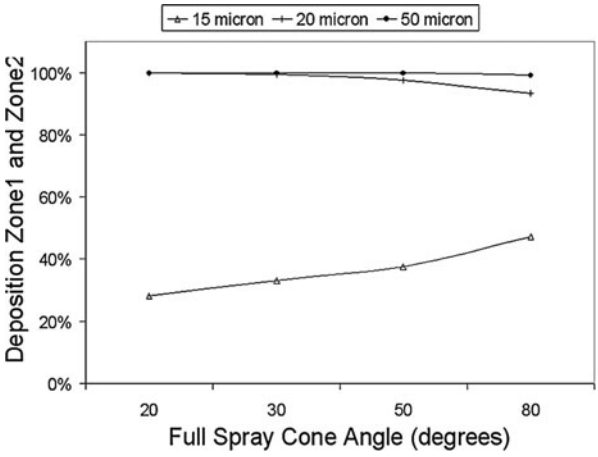


**Fig. 8.55** Deposition in zone1 and zone 2 for monodispersed particles released at 10 m/s from a small internal diameter at different spray cone angles

There is a low ratio of favourably dispersed particles (those pointing with the flow) to those being dispersed away from the curvature of the gas flow. Figure 8.56a shows the flow for 15 µm being centralised when $\beta = 20°$ and the increase in deviation from the centre when $\beta = 80°$. Deposition for $\beta = 20°$ remains along the roof of the nasal cavity and near the septum walls, with 33 % depositing in the first two zones. At $\beta = 80°$ a higher proportion of deposition is observed in the frontal zones.

The internal location of injection is closer to the roof of the vestibule than from the nostril inlet. This reduces the allowable distance for particles to relax their initial injected conditions to the gas phase conditions, thus enhancing impaction on the roof of the vestibule. This effect is more pronounced for larger, 20–50 µm particles.

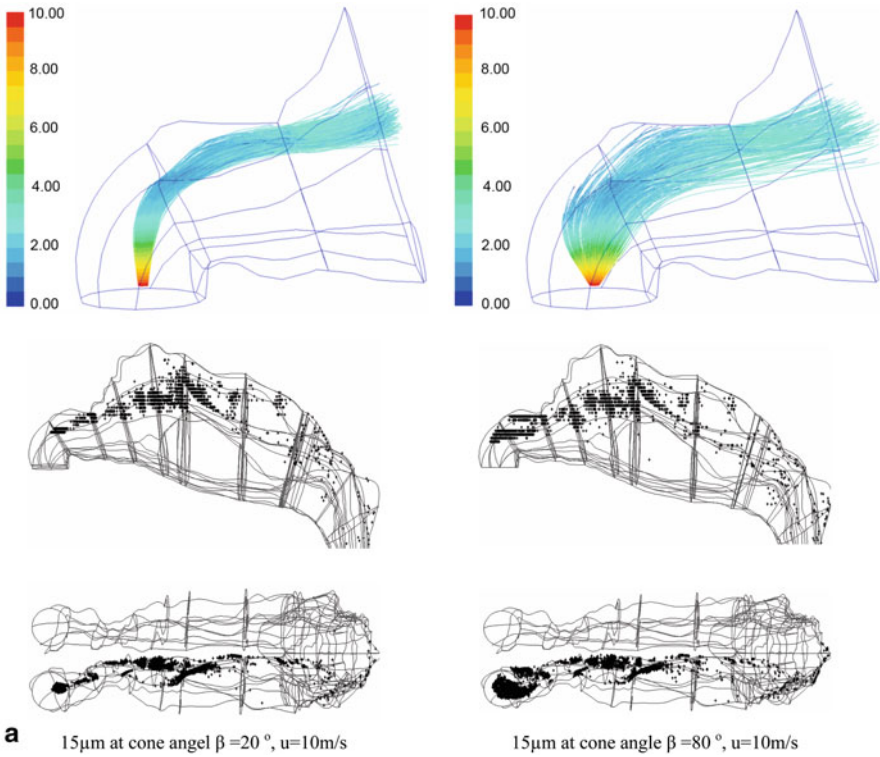


**Fig. 8.56** **a** Deposition patterns for 15 μm particles released at 10 m/s from a small internal diameter at the centre of the nostril inlet surface. The spray cone angles ranged from 20 and 80°. **b** Deposition patterns for 20 μm particles released at 10 m/s from a small internal diameter at the centre of the nostril inlet surface. The spray cone angles ranged from 20 and 80°

As seen earlier these particles have near 100 % deposition in the front two zones. Consequently, any deviation that is favourable will project the particles into the already curved streamlines, allowing particles, albeit a small proportion, to travel further. Figure 8.56b compares the two deposition patterns for 20 μm particles at $\beta = 20°$ and $\beta = 80°$. At $\beta = 20°$, impaction occurs directly above the injection release point in a concentrated area. When $\beta = 80°$, a wider area of deposition is observed in the frontal zones, while those particles projected favourably towards the nasal valve are able to travel beyond the 90° bend. However their deposition is imminent, and this occurs within the middle sections of the nasal cavities. Particles in the 15–20 μm range will exhibit an optimum $\beta$, which is based on the ratio of the change in favourably dispersed particles to the number of particles that are predestined to impact on the roof of the vestibule because of their particle size.

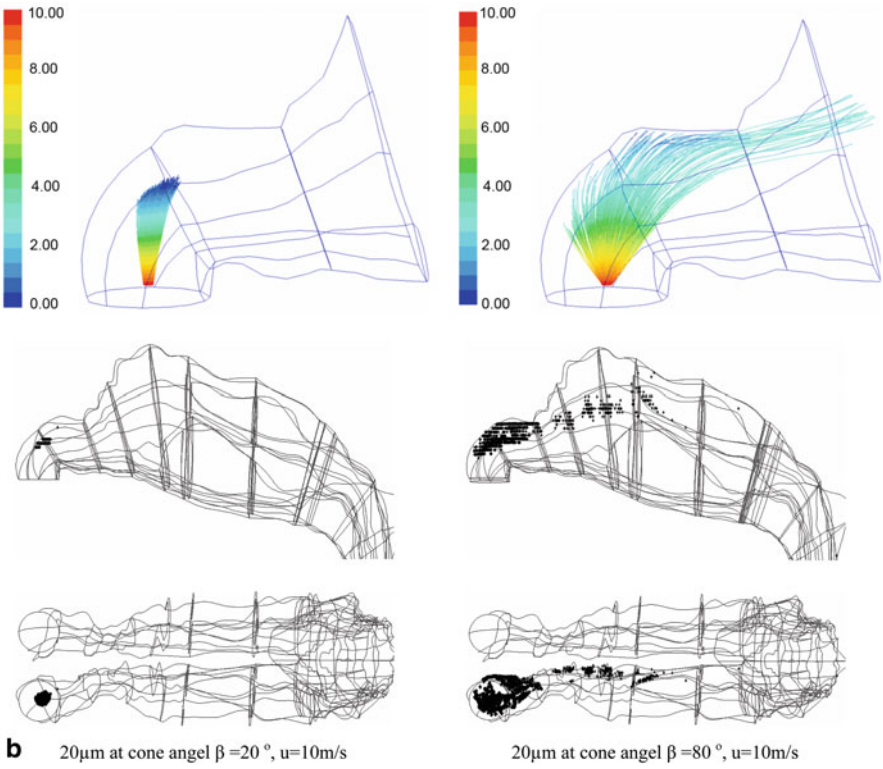


**Fig. 8.56** (continued)

### *8.4.8 Implications for Nasal Drug Delivery*

The absorption of nasal drug formulations into the bloodstream occurs most effectively in the main nasal passage (middle region) where curved turbinate structures exist (Davis and Illum 2003). The benefits of targeted drug delivery are evident in improving its efficacy while also reducing the bitter taste that users may experience from swallowing, mucociliary action, or forced movement by further sniffing. Current spray device designs administer drug formulations in a vertical position (Kublik and Vidgren 1998). This contradicts the directional path of the nasal cavity which is horizontal and often leads to high particle impaction at the top of the nostrils. This can improved by spray atomizer designs that produce finer droplet sizes to reduce the inertial propery of the particle, leading to less particles impacting early within the nostrils. Furthermore this may also enhance the absorption of drugs since aqueous drug solutions with small molecular size are more rapidly absorbed via the aqueous path of the mucous membrane.

The results from the case study were aimed at gaining a greater insight into what parameters are important in the design of nasal drug delivery devices. The results

revealed high deposition occurring in the frontal regions of the nasal cavity. It is well recognised that one of the functions of the nose is to filter out foreign particles during inhalation which was mainly thought to be attributed to cilia (nasal hairs) movement within the nose. However the filtering function also extends to the airway geometry at multiple locations in the nasal cavity. In the frontal sections, Regions 1 and 2, the flow experiences a curvature in the streamlines which acts similarly to inertial impactors that filter out high inertial, large particles. Another filter is the contraction of the nasal airway into the smallest cross-sectional area, the nasal valve region where particles are accelerated, increasing their inertial property. Finally, another 90° bend exists at the nasopharynx which acts as a final filter before particles enter the lower airways. This may be one explanation for the undesirable taste patients experience after taking drugs via the nasal cavity.

The filtering curvature in the frontal sections, along with the constricting nasal valve region, is most significant for therapeutic drug delivery because it prohibits larger particles from penetrating into the middle cavity region for deposition onto the highly vascularised mucosal walls. One possible solution is to instruct users to insert the spray deeper or to develop spray devices that will naturally be inserted deeper with particles being released beyond the frontal curvature.

The overall length of a nasal cavity from nostril inlet to the posterior end at the nasopharynx is approximately 97 mm and the height 47 mm, and exhibits very narrow passageway with a minimum cross-sectional area of $\approx$1.4 cm$^2$ located about 2.0 cm from the anterior tip of nose (Wen et al. 2008). The length and diameter of the spray plume is approximately 241 and 84 mm respectively (from Fig. 8.44), which means that the spray plume will not develop freely in the nasal cavity as it would during the experimental measurements made in this study. To determine how much of the spray plume is important for evaluation of nasal drug delivery, a simple illustrative CFD analysis can be performed to contextualise the nasal spray delivery and its formation under application. The nasal cavity model was created from CT-scans of a human subject (Fig. 8.54) and has been used in studies by the authors (Inthavong et al. 2006b; Inthavong et al. 2008a). Large particles (100 µm) with high inertia are delivered with an initial velocity of 15 m/s into the left nasal cavity with a negligible flow rate (0.01 L/min). The 100 µm particles were chosen for the high inertial property which retains its velocity and basically travels in a straight line unless it impacts onto the nasal surface wall. The initial conditions of the particles were described based on the shape of the measured spray plume. By tracking the particles, the wall deposition patterns and the spatial locations of the particles as they pass through cross-sectional slices labelled A to D can be shown. Three injection angles, 90, 45 and 30° are evaluated for which a user may perform, whereby more horizontal angles can be achieved by tilting the head backwards. The results in Fig. 8.54 show that the spray plume maximum length reached 47 mm for an injection angle of 30°.

At this length the measured spray would have a diameter of 22.6 mm which is much larger than the narrow cross-sections shown. The spatial locations of the particles that pass through each slice show that a narrow spray may enhance droplet deposition given the narrow cross-sections in comparison to the spray width. Furthermore there

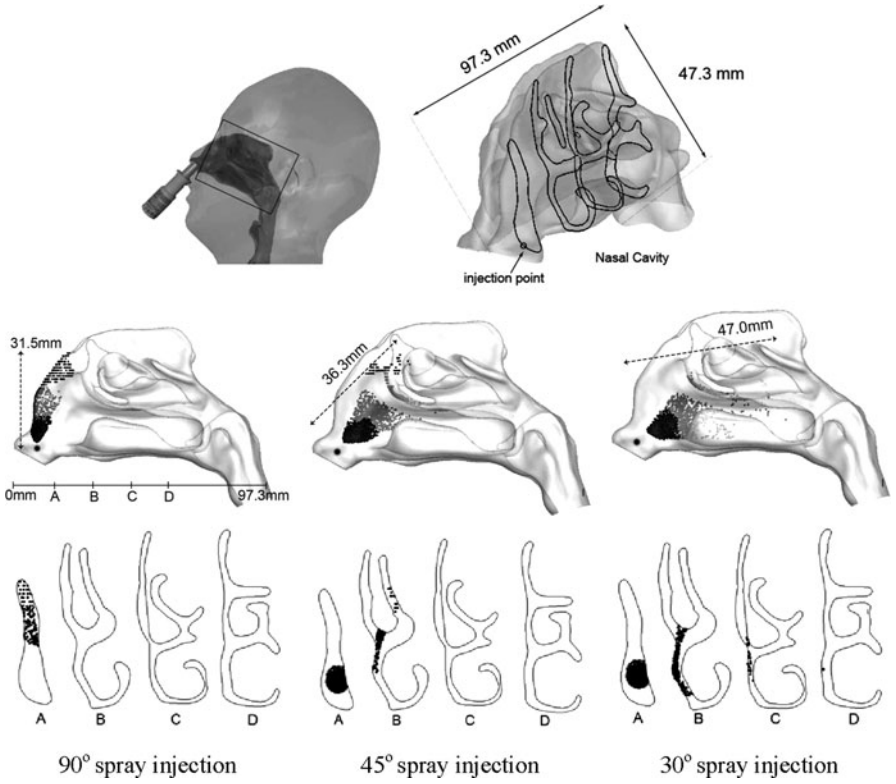


**Fig. 8.57** 3D visualisation of the unaffected experimental spray placed inside a human nasal cavity model. Four cross-sections are labelled A, B, C, D having widths of 8.1, 16.5, 17.1, 15.3 mm, and heights of 31.3, 42.0, 42.8, and 42.8 mm respectively. 100 μm particles are delivered into the nasal cavity at the location denoted by the *large black* dot just inside the nasal cavity. Subsequent particle deposition onto nasal cavity walls are marked with *small black* dots. Particles passing through the cross-sectional slices *A–D* are also denoted by *small black* dots

is potential for an increase in the spray penetration when the spray is more horizontally aligned. While the CFD visualisation is highly idealised it does put into context the spray geometry dimensions in relation to the nasal cavity. Evaluations of nasal spray performance should concentrate on the external and near field characteristics of the spray up to 50–60 mm from the spray nozzle, and certainly it would be unnecessary to measure the entire spray plume of up to 240 mm (Fig. 8.57).

### *8.4.9 Closure*

This case study extends beyond the last two case studies where turbulence was included into the flow and modelling strategies to resolve the turbulence airflow and

the particle flow were discussed. This case study also investigated further the application of nasal drug delivery. While the nasal cavity's natural function is to filter out toxic particles, there is an opportunity to exploit the highly vascularised walls for drug delivery. Nasal sprays deliver atomized particles into the nasal cavity at high velocities. The structure of the atomized spray from a nasal spray was presented in order to identify the parameters that would affect the setting up of the initial particle boundary conditions for the CFD simulations. Parameters that were important, among others, included *swirl effects, the spray cone angle, initial particle velocity* and *the insertion angle* which were evaluated for deposition efficiency under high and low inertial particles.

For a flow rate of 20 L/min 10–20 μm, particles were sensitive to initial injection velocity, insertion angle, and spray cone angle as their size increased. Larger particles exhibited very high Stokes numbers (inertial parameter) causing them to be insensitive to these parameters. Current commercially available nasal sprays produce mean size particles of 45–60 μm. This presents a problem because larger particles ($\geq$20 μm) are relatively insensitive towards initial injection conditions and are likely to deposit in the anterior portion of the nose decreasing the drug delivery's efficiency. Producing smaller particles ($\leq$20 μm) during atomization is an option for designers; however smaller particles are more inclined to follow the airflow and can lead to deposition beyond the nasal pharynx.

The ideas formulated can be used as a basis for improving the design of nasal spray devices to achieve better drug delivery, such as (i) redirecting the release point of the spray (i.e. the insertion angle) to align with flow streamlines, (ii) controlling the particle size distribution and (iii) controlling the particle's initial velocity. In the attempt to replicate actual nasal spray applications while isolating the investigating parameters, idealised injected conditions for the particles were used. Further studies have been performed (Kimbell et al. 2004, 2007) which also tested some of the spray characteristics. Interestingly, this field of research can be extended to compare results with other nasal cavities to include the permeability effects of nasal hairs and to establish more accurate initial particle conditions such as the instantaneous velocity at injection that can include swirl effects.

## 8.5 Effects of Asthma on the Fluid-Particle Dynamics in the Lung Airways

In this case study we move deeper into the respiratory system, to the tracheal-bronchial airway tree in the lungs. Models of the lung airways are presented along with some flow features and particle deposition. The case study will focus on a real application involving the affects of asthma. The physiological characteristics of asthma include variable airway obstruction and increased airway responsiveness to stimuli. This causes the passages to narrow, reducing the flow of air in and out of the lungs. A comparison between two models (one immediately after asthma and another thirty days later) is undertaken to determine the disparities in the inhalation efforts and the airway branch diameters caused by physiological changes in the airways.

The modelling of the lung airway is restricted to the CT-scans obtained, which often are end at the trachea. Therefore, the influence of the respiratory system upstream of the trachea is missing and the modelling requirements, assumptions, and expected errors are discussed.

### *8.5.1 Geometry and Computational Setup*

Two models were developed from CT scans by a helical 64-slice multidetector row CT scanner (General Electric) of a 66-year-old, non-smoking, asthmatic Asian male (height 171 cm and weight 58 kg) on the day after hospital admission with an acute exacerbation of asthma. At the time, his lung function by spirometry (Spirocard, QRS Diagnostic, Plymouth, Minnesota, USA) showed severe airflow obstruction with a forced expiratory volume in 1 s ($FEV_1$) of 1.02 L (41 % predicted). Data was acquired with 1 mm collimation, a 40 cm field of view (FOV), 120 kV peak and 200 mA. At baseline, 2 cm axial length of lung caudad to the inferior pulmonary ligament was scanned during a single full inhalation total lung capacity breath-hold (FEV1 was measured at 2.31 L), which yielded 146 contiguous images (slices in transverse direction, Z) of 1 mm thickness with voxel size 0.25 mm $\times$ 0.25 mm $\times$ 1 mm. An identical protocol was used to acquire images following recovery 30 days later, when his FEV1 was measured at 2.27 L (91 % predicted). The two computationally reconstructed models were then identified as the AA-model (acute asthma model) and the REC-model (recovered model).

For this study, a parabolic inlet profile from an extended trachea is used. In a recent study by Li et al. (2007), it was found that the type of velocity inlet condition and existence of cartilaginous rings influence the air flow field; however, their impact is less important in comparison with the variations in the upper airway geometry, e.g., branch curvature. A flow rate of 12 L/min was applied at the inlet, which corresponds to a Reynolds number of 863 at the inlet. The flow regime has been considered transitional for flow rates of 15–60 L/min (Zhang et al. 2008b) and for flow rates greater than 30 L/min (Re $\sim$ 2,500) (Jayarajua et al. 2008) based on the existence of the laryngeal jet producing transitional behaviour. Other researchers however, have applied a laminar flow regime for flow rates of 28–30 L/min (Re $\sim$ 2,000–2,500) (Nowak et al. 2003; van Ertbruggen et al. 2005) based on the argument that RANS turbulence models cannot predict the transitional behaviour reliably, that the flow within the lung branches rapidly becomes laminar after the initial bifurcations, and that the flow is mostly laminar because the Reynolds number is globally below the transitional value. In an investigation into the turbulence structures using Large Eddy Simulations (LES), (Kleinstreuer and Zhang 2003) showed that at a flow rate of 15 L/min inlet turbulence is damped out and that laminar flow prevails. Interestingly, deposition patterns were found to be unaffected by turbulent dispersion at 15 L/min, although particle deposition is enhanced by turbulence for flow rates of 30 and 60 L/min when $St \leq 0.06$.

Based on these findings and the limitation of this study (exclusion of the larynx) a steady laminar flow is used for a flow rate of 12 L/min. In addition, using a turbulence model that is not suitable for flow rates that exhibit some light transitional

flow does not necessarily imply greater accuracy (see Sect. 8.2.2). Furthermore in local regions of low flow rates, where laminar effects are dominant, turbulence models provide greater diffusion due to the turbulence production inherent in turbulence models. Sophisticated models such as LES and Direct Numerical Simulations, however, do resolve the transitional behaviour but are quite computationally expensive. The absence of the laryngeal jet is expected to produce an under-prediction of the deposition efficiency in the first bifurcation at the carina. However, deeper into the lung airways the effects of the laryngeal jet diminishes and eventually become negligible. A steady flow was applied based on a variety of criteria (Isabey and Chang 1981; Slutsky et al. 1981; Sullivan and Chang 1991) such as the Womersley parameter, $\alpha = D/2(\omega/\nu_g)^{0.5}$; a variant of the Womersley parameter, $\alpha^* = 1/2(\omega D/0.0075u_{ave})^{0.5} < 1$ (Pedley et al. 1977); and the Strouhal number, $S = \omega D/u_{ave}$ where $u_{ave}$ is the mean velocity, $\omega$ is the angular frequency of oscillation ($= 2\pi f$), D is the diameter of the tube; and $\nu_g$ is the viscosity.

The outlets were artificially extended downstream given by, $L_{extension} = 0.05\,\mathrm{Re}\,D$ to obtain fully developed profiles and hence avoid any reverse flow that may be caused due to an abrupt end to the flow field. Each model underwent mesh refinement by cell adaption techniques that included refining large volume cells, cells that displayed high velocity gradients, and near wall refinements. Velocity profiles were compared between each subsequent model until the profiles remained the same and hence became independent of the grid size. The final models had a mesh size between 1.1 to 1.5 million cells (Fig. 8.58).

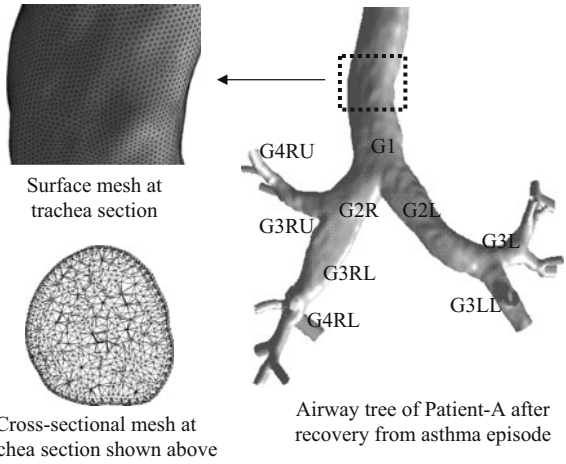


**Fig. 8.58** Computational model of the upper tracheobronchial airway tree with branch identification. The first two characters define the branch generation. The third character represents the *right* or *left* airway. The fourth character may be U, M or L representing *upper*, *middle* and *lower*, respectively

## *8.5.2 Airway Geometry Recovery*

The reconstructed model of the bronchial tree exhibits an asymmetric dichotomous branching pattern. The beginning of the bronchial tree begins with the trachea, which is a hollow cylinder in the shape of a horseshoe due to the C-shaped supporting

**Table 8.11** Average diameter of the tracheobronchial tree model (dimensions in millimetres)

| Diameter | G0 (Trachea) | G1 | G2R | G2L | G3R | G3L |
|---|---|---|---|---|---|---|
| Patient-A AA | 18.0 | 15.4 | 11.2 | 8.8 | A: 5.0<br>B: 8.2 | A: 6.2<br>B: 5.8 |
| Patient-A REC | 18.5 | 15.8 | 11.6 | 9.2 | A: 5.8<br>B: 8.7 | A: 6.1<br>B: 6.6 |
| Other[a] | 19 | 9–16 | 7–11 | | 5–7 | |

| *Branching Angles* | *G1-G2* | *G2-G3R* | *G2-G3L* | *G3L-Dorsal Angle* |
|---|---|---|---|---|
| Patient-A AA | 79° | 89° | 96° | 24° |
| Patient-A Rec | 81° | 90° | 91° | 31° |

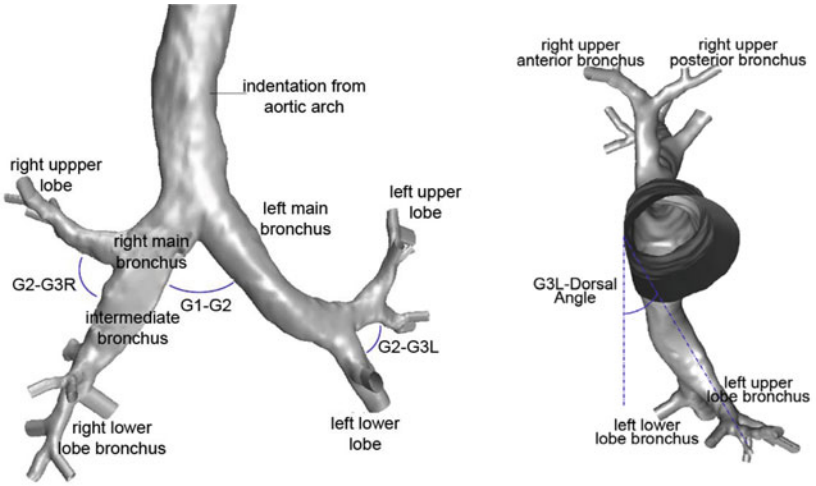


[a]Other measurements were extracted from Weibel (1963) for diameter and length and Sauret et al. (2002) for branching angle. Weibel (1963) measured a cadaver's airway and reported in a range value for each generation. Sauret el al. (2002) measured a healthy male volunteer's airway using CT images and reported the range value for all generations

cartilage found anteriorly and laterally. Completing the tracheal cylinder on the posterior side is a flat band of muscle and connective tissue called the posterior tracheal membrane. Along the airway downstream, the cartilage support becomes progressively smaller and less complete. An indentation can be found in the left lateral wall of the distal trachea caused by the aortic arch, which plays a significant role in particle deposition. The equivalent hydraulic diameter $D_h$, defined by $D_h = 4A_c/P$ where $A_c$ is the cross-sectional area and $P$ is the perimeter, was calculated for the entrance and bifurcating ends of each generation branch. The diameters given in Table 8.11 for each generation branch is taken as the average diameter from different slices through the branch and a comparison is made between the acute asthma model, the recovered model and results from other airway models (Sauret et al. 2002; Weibel 1963).

In general the right side of the airway is larger in diameter than is the left side. The recovery is measured as the percentage increase in the diameters from the AA-model to the REC-model and may be thought of as the dilation of the airway smooth muscle (ASM). A large increase was expected for the branches that were severely

affected by the asthma (G4LU and G4RU). Besides these affected branches, G3LL and G3RU also had a dilation greater than 10 % (Fig. 8.59). Overall the right airway exhibited greater dilation in comparison with the left airway especially from the fifth generation onwards. The effects of a greater dilation on particle deposition are uncertain, and this is discussed later in the results. Sections, G3LU, and G6R showed minor negative increases ($-0.2$ and $-0.4$ % respectively) which means that these sections were actually contracted. It is uncertain if this is within the margin of the modelling error or whether it reflects a real physiological feature, such as the after effects of airway narrowing by inflammation and edema of the lining airway mucosa, or even the accumulation of mucus and other fluids, which can plug the airways.

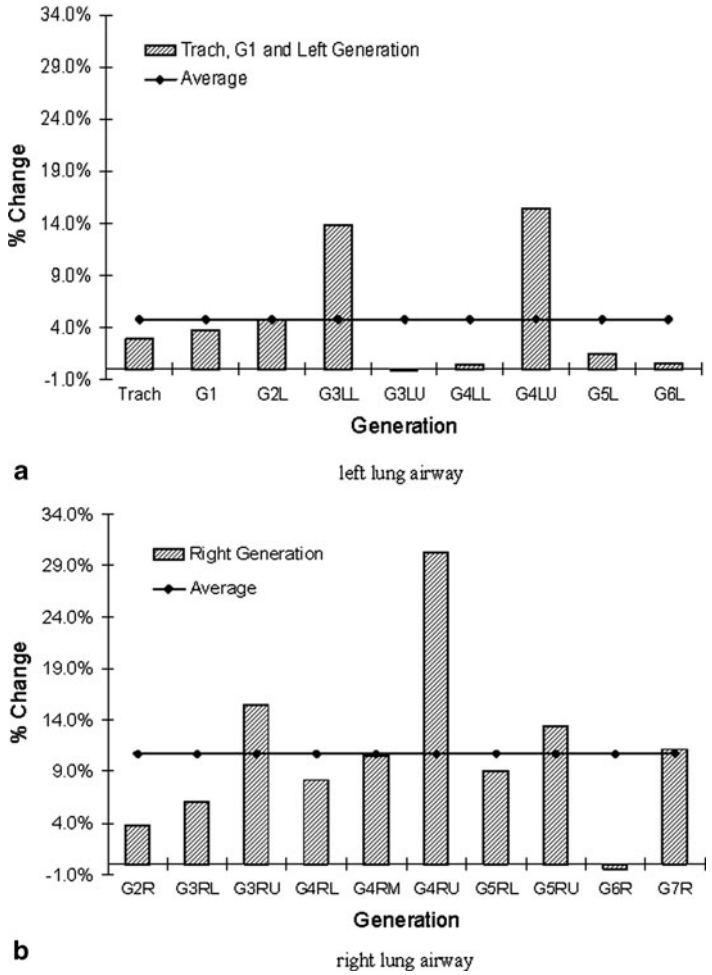


**Fig. 8.59** Percentage increase in the averaged diameter from the acute asthma model to the recovered model in the **a** *Left* lung airway **b** *Right* lung airway

### 8.5.3 Airflow Distribution and Pressure Coefficient

Contours of the pressure coefficient in reference to the inlet boundary conditions are shown in Fig. 8.60. The pressure coefficient is defined as

$$C_p = \frac{(p - p_{ref})}{\frac{1}{2}\rho_{ref} v_{ref}^2} \tag{8.31}$$

where $p$ is the static pressure, $p_{ref}$ is the reference pressure taken as 0 Pa, and $\frac{1}{2}\rho_{ref} v_{ref}^2$ is the reference dynamic pressure. The asthma affected model exhibits the greatest resistance: one and a half times greater than the recovered model and two times greater than Patient-B. Interestingly, Patient-A experiences higher resistance in the airway even after a thirty-day recovery when compared with Patient-B. The two patients are non-smoking, similar in height, weight and age, but of different sex. The patients' ages suggest that higher resistance in the recovered asthmatic airway may be caused by ASM tissue remodelling caused by the long-term persistence of asthma (Pascual and Peters 2005; Vignola et al. 2000). Along the main bronchus the pressure decreases steadily while there is a definite pressure drop from each main branch into the subsequent daughter branch. This is due to the bifurcation ridge where a local maximum occurs as a result of a buildup of pressure, similar to a stagnation point. Airflow distribution through individual branches shows a similar trend among the two patients. Greater mass flow rate passes through the right main bronchus (53–59 %) and continues down the right intermediate bronchus (40–42 %). In the left airway, the main continuation is also downwards along the left lower lobe bronchus.

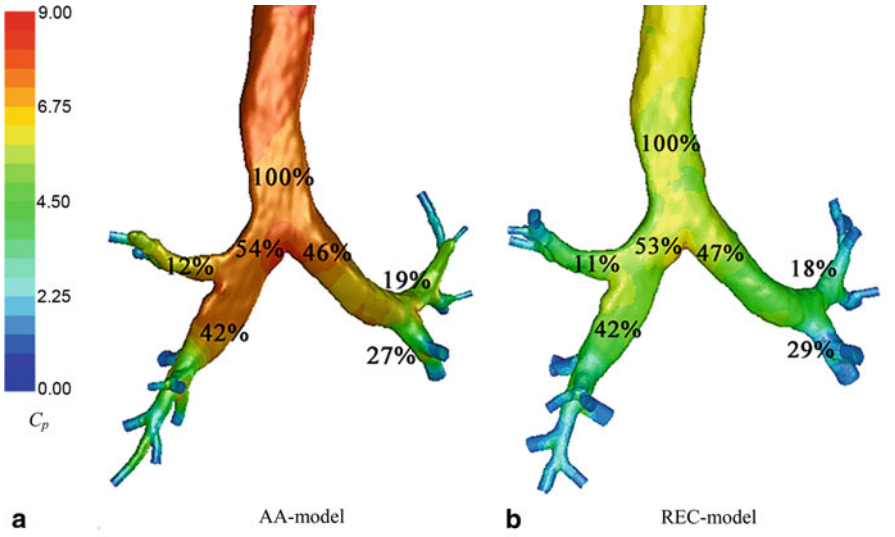


**Fig. 8.60** Pressure coefficient, $C_p$, values referenced against inlet boundary conditions and branch outlets set at 0 pa. **a** AA-model. **b** REC-model

There is only a small proportion entering the upper lobes of both sides of the airway, which is due to the lateral curve. It is therefore apparent that the branching angle has a significant influence on the airflow distribution. This influence transcends to particle deposition where low inertial particles will be greatly influenced.

### *8.5.4 Particle Deposition Patterns*

Deposition patterns for the computational models allow visualisation and deeper insight into the connections between the airway geometry and deposition sites. Figure 8.61 shows the concentration of particles generally impacting at each bifurcation as the airflow begins to separate. The percentage values displayed next to the outlets represent the percentage of particles that escape through those outlets. This shows that a large proportion of particles are travelling through the right main bronchus which leads to greater exposure to the particles. In addition, approximately 40 % of inhaled 5 µm particles penetrate past the sixth bifurcation via the right

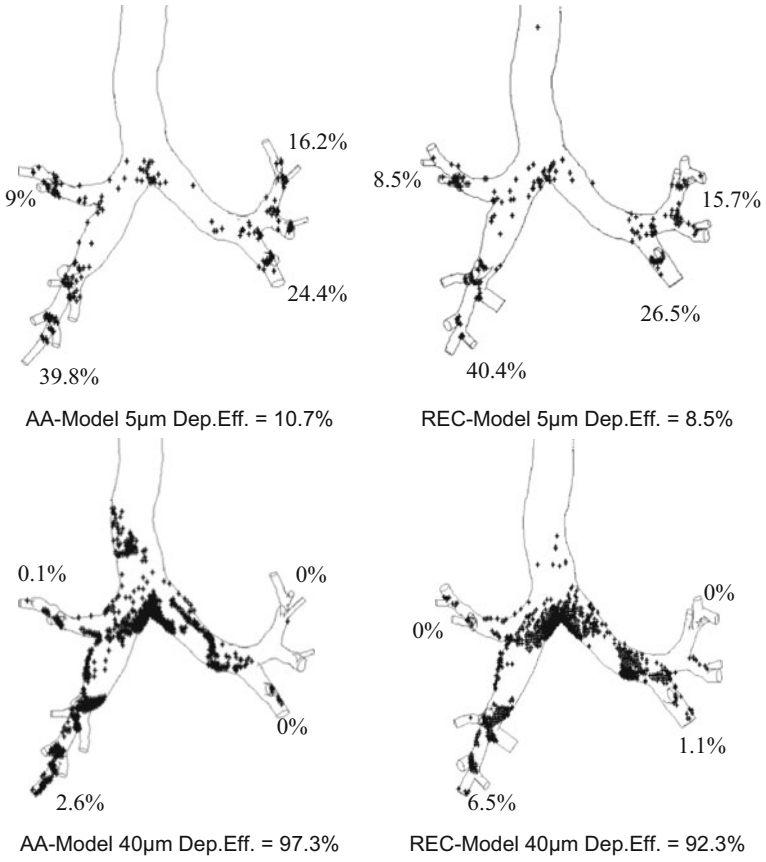


**Fig. 8.61** Particle deposition patterns for 5 and 40 µm particles for the three computational models

main bronchus. The lowest numbers of escaped particles are found in the upper right bronchus and the upper left bronchus, which is caused by the larger bifurcation angles as well as the G3 L-dorsal angles (Table 8.11). Comparisons between the AA-model and the REC-model show a difference of 2 and 5 % deposition for 5 and 40 μm particles, respectively. High deposition is found for 40 μm particles (92–98 %) as expected, but more interesting is the location of deposition. In the AA-model, deposition is found in the lower trachea region which is not found in the REC-model.

### *8.5.5 Considerations for Modelling Pulmonary Drug Delivery*

Ventilation in the respiratory airway is accomplished by the transport of inspired air down pressure gradients within the airways. This process involves the alternating contraction and relaxation of the respiratory muscles which overcome the pressure drop caused by viscous losses such as shearing forces within the fluid, the friction between the air and walls of the airways, and the resistance presented by the irregularities of the airways. Under steady laminar flow conditions of 15 L/min, the required effort by the respiratory muscle to overcome the pressure difference for the AA-model is nearly twice as high as that required for the REC-model. The primary cause of greater resistance in the AA-model is the narrowed airways and the occlusion of two of the branches. This suggests that during the period of an acute asthma episode, the work of breathing for the patient in order to achieve the same tidal volumes is doubled compared to the recovered state, which can lead to respiratory muscle fatigue. The walls created within the model are assumed rigid and smooth whereas in reality the walls may exhibit some roughness and elasticity. The inclusion of these attributes may alter the predicted magnitudes of the pressure drop, but it is unlikely to alter the comparative ratio between the two pressure drops from the computational models. Furthermore, to be included, such data need to be accurately obtained, since approximations may actually cause further errors if the elasticity and roughness of the airway walls are not well known.

Treatment of asthma is most commonly employed during the onset of the asthma episode. Particles are atomized into smaller particles through ventilators or other drug delivery devices and inhaled through the mouth. In this study the particle deposition patterns showed that the airway geometry had a significant affect. Although the indentations from the aortic arches of the AA-model and REC-model do not change significantly, the additional effect of the narrowed airways enhances the impactability of the particles. Drug particles are delivered with the target being the region of airway occlusion; however the deposition patterns show that particles travel through regions where the geometry does not deviate greatly and eventually deposit at the bifurcations. The results showed that a significant number of particles pass through the right main bronchus, and therefore deposition of particles will be in the right lung airways. This is a consequence of the airway branching angle at the carina bifurcation which produces the left main bronchus at a more obtuse angle than that

of the right main bronchus. This feature also affects small Stokes number particles, where approximately 40 % of the particles introduced at the trachea inlet penetrate past the sixth generation in the right lung airways. Therefore the efficacy of drug delivery will be low if the occluded airway is deep in the left lung airways and will lead to acute overdose in the localised regions of the right lung airways.

### *8.5.6 Closure*

This case study moves beyond the nasal cavity to present the flow and particle deposition patterns in the lung airways. Two models with six generations of the airway tree from an acute asthma episode and following recovery of the same patient thirty days apart were reconstructed from computed tomography (CT) scans in order to investigate the effects of acute asthma on a realistic airway geometry, the airflow patterns, the pressure drop, and the implications they have on targeted drug delivery. The comparisons in the geometry found that in general the right side of the airway is larger in diameter than the left side. The recovery of the airway was most significant in the severely asthma-affected regions. Overall, the right airway exhibited greater dilation in comparison with the left airway, especially from the fifth generation onwards. The required pressure difference at the inlet for the AA-model was nearly twice the value for the recovered model. This suggests that during the period of an acute asthma episode, the work of breathing for the patient in order to achieve the same tidal volumes is double compared to that in the recovered state, which can lead to respiratory muscle fatigue. Particle deposition patterns showed that the changes in the airway had significant influence on flow patterns. A majority of the particles deposited passed through or deposited in the right lung airways, as a consequence of the biased carina bifurcation. It was also shown that the narrowing of the airway magnifies the effects of the airway curvatures. This means that studies of therapeutic drug delivery in the airway should consider the effects of airway narrowing and not a recovered or a healthy airway.

## 8.6 Summary

Case studies were presented in this chapter to demonstrate the modelling strategies to account for the inhalation of air and particles in the human respiratory system. In the first case study, modelling requirements such as the flow regime (laminar/turbulent, steady/unsteady) for steady inhalation and the heat transfer process were shown. The first case study aimed to set a good foundation for the inclusion of particles into the nasal cavity.

After establishing the airflow field, particles were introduced into the airway. The modelling requirements for different particle morphology such as spherical, non-spherical, submicron, and fibrous particles were shown. A link between the nasal cavity geometry, the airflow field, and particle deposition was also found.

One important function of the nasal cavity is its natural ability to filter out airborne particles. This natural evolution in the nasal cavity geometry was important for deposition patterns of inhaled particles, but it also becomes a stumbling block for nasal drug delivery. The third case study was dedicated to understanding the requirements needed to simulate nasal drug delivery. The atomization process was presented in order to highlight the parameters that are involved in sprayed particle modelling. Three of these parameters were evaluated for their performance on targeted deposition in the main nasal passage. The case study also introduced a turbulent flow model to the airflow field and modelling of the turbulent particle dispersion.

The final case study moved away from the nasal cavity and demonstrated the airflow and particle dynamics in the tracheal-bronchial airway tree under the influence of asthma. The airway geometry was compared, and some significant differences were found which led to the recommendation that pulmonary drug delivery modelling should be performed on affected airway models and not necessarily on a healthy airway.

The chapter demonstrated some applications of CFPD for the respiratory system, by introducing the airway geometry and its flow features, and for particle inhalation and its deposition. While the case studies cover a variety of research topics in respiratory modelling, there are many more topics. The next chapter discusses some of these more advanced topics that are at the forefront of respiratory modelling and research. For example, several methods are proposed for integrating individual components of the respiratory system, since current modelling trends are limited to the extent and fidelity of the CT or MRI scans; moving and deforming mesh and its application to sleep apnea studies; advanced numerical techniques related to Fluid Structure Interaction (FSI) and how they can be used for more realistic modelling of physiological airway wall movements; and immersed boundary methods and their application in non-spherical particles. The future of air and particle flow modelling in the respiratory system will continue to advance, and sophisticated models will include a more complete respiratory system and the inclusion of more physiology and anatomical features.

## 8.7 Review Questions

1. What are the main factors that contribute to the airflow patterns in the nasal cavity?
2. List the physiological functions within the nose and discuss its modelling requirements and whether it is feasible to model.
3. What modelling considerations should be made when simulating low breathing rates (1–10 L/min) and high breathing rates (30–50 L/min)?
4. What should you expect from the results when applying a turbulent flow model for

   a) laminar flow
   b) transitional flow?

5. What should you expect from the results when applying a laminar flow model for

   a) transitional flow
   b) turbulent flow

6. What does a quasi-steady flow mean, and when can you apply such an assumption?
7. Where is the highest wall shear stresses found in the nasal cavity? What are some of the causes for this phenomenon?
8. What flow patterns are found in the olfactory region? Why do you think these flow patterns exist?
9. Discuss the flow distribution in the main nasal passage (turbinate region). How does this affect heat transfer and particle deposition?
10. Where does most of the heat transfer take place within the nasal cavity? Explain why this occurs in terms of the heat flux, ($q$).
11. What are the advantages of applying a spherical shape assumption for modelling particles?
12. Discuss the modelling requirements when considering different particle morphologies (micron sphere, non-sphere, nano, fibres).
13. Discuss the deposition mechanisms for the different types of particle morphologies (micron sphere, non-sphere, nano, fibres).
14. How does the breakup length in a nasal spray affect modelling of the initial particle setup?
15. If the initial velocity of a particle with St $= 0.1$ is ten times that of the air flow velocity, i.e. $u^* = 10 = U_{particle}/U_{air\ flow}$. How far into the nasal cavity does it travel before it has similar velocities to the airflow field and why?
16. Two particle trajectory profiles are shown below for mono-sized particles released from the bottom inlet. The trajectories are coloured by the particle velocity magnitude, where red represents the highest value and blue the lowest value. The initial particle velocity is ten times that of the air flow velocity, i.e. $u^* = 10 = U_{particle}/U_{air\ flow}$. Explain why the particle trajectories of flow path $a$ are so straight and why in flow path $b$ they curve? (hint: compare the velocity profiles).

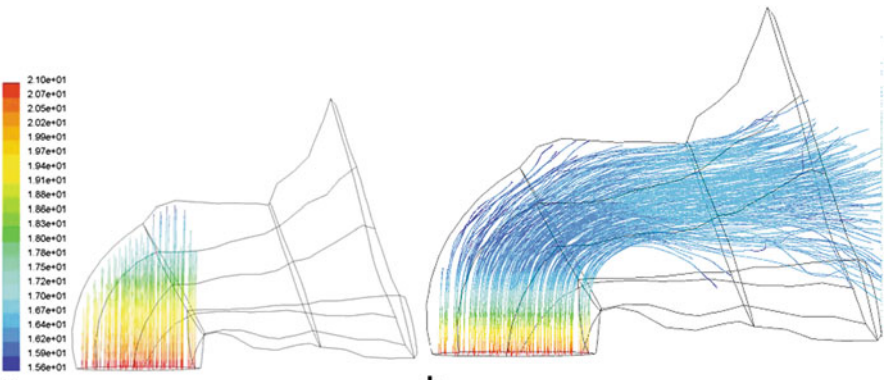

17. What are some of the difficulties that require simplifications or assumptions when dealing with the trachea-bronchial airway tree?
18. In the lower bifurcation branches, what flow regime (laminar or turbulent) would you expect the air flow to be? Discuss in terms of the Re number.
19. In what cases would you need to apply artificial extensions to the airway branches?
20. Towards which side of the lung is the airflow distribution biased and why? Investigate further and determine if this is consistent among the population.
21. Where do the majority of particles deposit in the airway tree?

# Chapter 9
# Advanced Topics and Future Trends

## 9.1 Introduction

Over the last three decades there has been considerable progress in computational modelling. However many issues still need to be resolved. Advances in computational resources and techniques will enable significant progress to be made in modelling realistic physiological scenarios of the respiratory system. The materials presented in this book thus far serve as an introduction to some of the current trends and modeling achievements, and in this chapter we present the latest developments and address some of the important issues and challenges that are currently faced by many researchers.

## 9.2 Advanced Modelling

### *9.2.1 Moving/Deforming mesh*

Moving meshes can provide dynamic modelling of physiological functions that are transient in nature. Take for example the changes in lung shape and volume that occur during inhalation and exhalation. When the muscles of the diaphragm move downwards during inhalation, the ribcage expands creating more room for the lungs to expand. The volume of the lung increases which decreases the pressure relative to the outside air. This pressure difference drives the movement of air for inhalation. We can model this physiological function by attaching a hollow space that depicts the lung volume to the primary bronchus (first generation) of the tracheobronchial airway tree. The lung mesh is allowed to move freely with time while the trachea and bronchi are fixed and not moving. The moving grid can be allowed to slide along the interface without deformation between the part of the grid that is attached to the static bronchi and the other parts of the lung that are changing in size. Other techniques include dynamic layering where automatic layers of cells may be added or removed as the mesh moves. Local refinements of the mesh can also be applied to regions where the cell size and quality degrade due to the boundary motion. The

J. Tu et al., *Computational Fluid and Particle Dynamics in the Human Respiratory System,* 321
Biological and Medical Physics, Biomedical Engineering,
DOI 10.1007/978-94-007-4488-2_9, © Springer Science+Business Media Dordrecht 2013

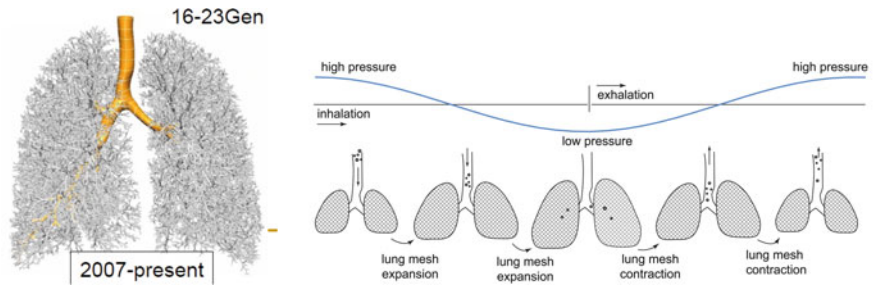


**Fig. 9.1** Schematic of the lung expansion and contraction to simulate the breathing process

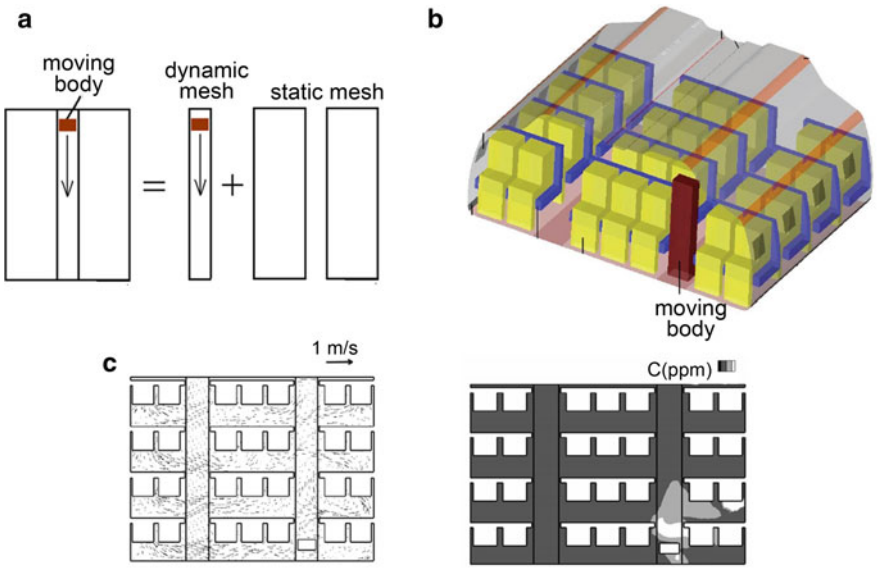


**Fig. 9.2** **a** CFD schematic of the computational domain for the cabin (Poussou et al. 2010), **b** 3D view of the cabin geometry, **c** velocity vector and contaminant transport due to movement of a person along the aisle (Mazumdar and Chen 2007)

grids do not have to match at the interface (which we call non-conformal meshing); this allows flexibility in employing different kinds of meshes and/or achieving the desired fineness in the respective domains. Except for difficulties in ensuring exact conservation, there are essentially no limitations on the applicability of this approach (Fig. 9.1).

As another example of a moving mesh, we present the work by Mazumdar and Chen (2007) which investigated the air and contaminant flows in an airline cabin induced by a moving body. The relevance to respiration is the potential inhalation and transmission of in-flight airborne infectious diseases leading to a global dissemination of the disease agents. The CFD model used is made up of a combined dynamic and static mesh scheme (Fig. 9.2a, b, c). The results show that the airflow patterns are disturbed by the moving body influencing the contaminants in the wake or rear of the moving body.

### 9.2.2 Fluid Structure Interaction

In all the examples presented thus far, the boundary walls have been treated as fixed rigid walls. However, respiratory functions are dynamic in nature with moving anatomical parts. As its name suggests, a fluid structure interaction (FSI) involves the influence of the moving fluid on a flexible structure which deforms and in turn influences the fluid flow. This differs from the deforming/moving mesh presented in Sect. 9.2.1 in that for FSI, the moving structures are determined through structural dynamics equations coupled with the fluid dynamics equations, whereas for a deforming mesh, the moving structure is predefined by an independent equation and is not influenced by the fluid dynamics. FSI involves multiphysics, and the different coupling methods to describe the transfer of the boundary conditions at the fluid-structure interface are a critically important feature of FSI. Generally there are two approaches to solve an FSI problem: monolithic and partition.

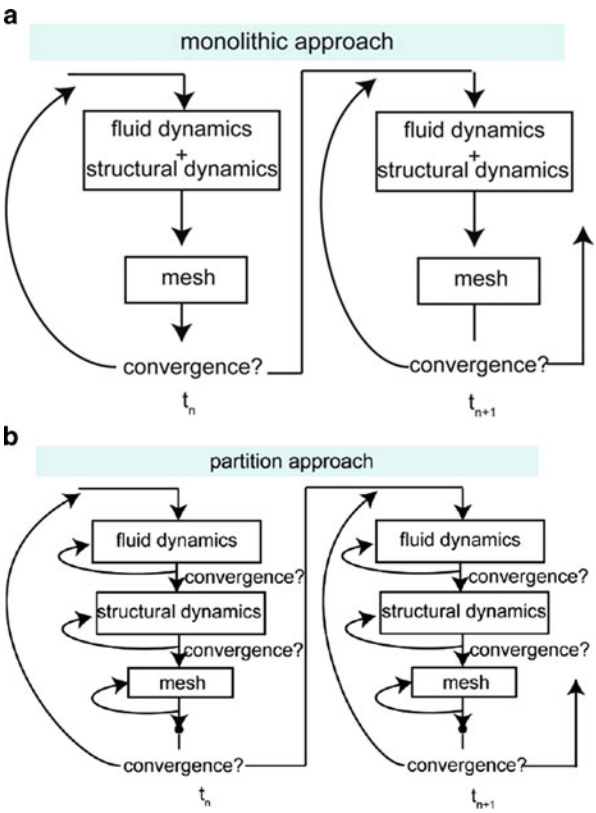


**Fig. 9.3** **a** Monolithic approach: the equations governing the flow and the displacement of the structure are solved simultaneously. **b** Partition approach: the equations governing the flow and the displacement of the structure are solved separately

In the *monolithic approach* (Fig. 9.3a), the governing equations are reformulated by combining the fluid and structural equations of motion that are solved and integrated in time simultaneously. This kind of method poses severe limitations because

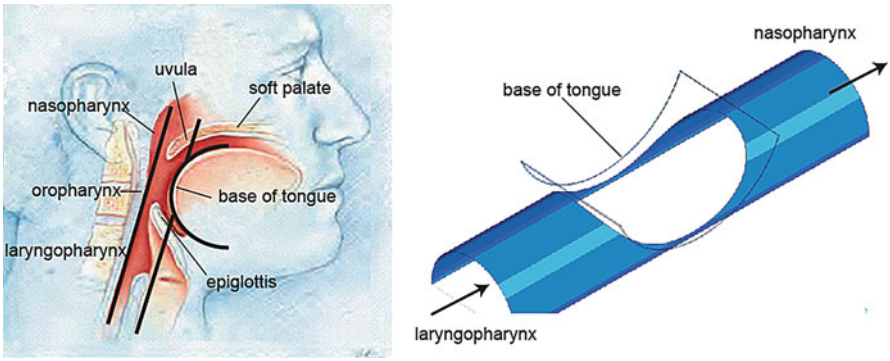


**Fig. 9.4** Pharyngeal airway model treated as a collapsible tube. The fixed structure is the respiratory walls, while the flexible structure is the base of the tongue

of the need to solve the equations in two different reference systems: fluid equations as Eulerian and structural equations as Lagrangian. The stiff set of equations for the structural system makes it virtually impossible to solve large scale problems by monolithic schemes which treat the interaction of the fluid and the structure at the mutual interface synchronously. For the *partitioned approach* (Fig. 9.3b) the structural and fluid equations are solved separately. This results in two different computational grids that may not be coincident at the interface or boundary. To establish a link between the respective regions, an interfacing technique is developed to exchange information back and forth between these modules.

Recently, there have been a number of FSI applications in the study of obstructive sleep apnea. Episodes of partial or full cessation of breathing during sleep are caused by the collapse of the soft tissues of the pharyngeal airway which obstructs airflow. The physiological mechanisms in the pharyngeal airway are very closely related to the flow in compliant tubes or channels. Here we present an example of FSI (Rasani et al. 2011) in a collapsible tube (Fig. 9.4).

The narrowed airway in the pharynx promotes increased transmural pressure via a venturi effect, resulting in partial collapse of the airway and a nonlinear flow rate retardation as the intraluminal pressure difference is increased—a typical observation in a collapsed channel called flow rate limitation. The governing fluid equations are based on a fixed Eulerian frame of reference in space. In order to account for boundary deformation and, thus, deformation of the fluid mesh, an Arbitrary Lagrangian-Eulerian (ALE) description is used. The fluid-structure interaction is achieved by satisfying either a velocity or displacement continuity and also the force equilibrium at the common interface between both fluid and solid domains. More information regarding FSI methodologies can be found in Chouly et al. (2008), and Liu et al. (2010b).

The fluid-structure-interaction model, its mesh and its flow patterns in the collapsible tube idealizing the pharyngeal airway are shown in Fig. 9.5. In general, when flow separates from the elastic wall, the bottom wall and the side walls, three-dimensional

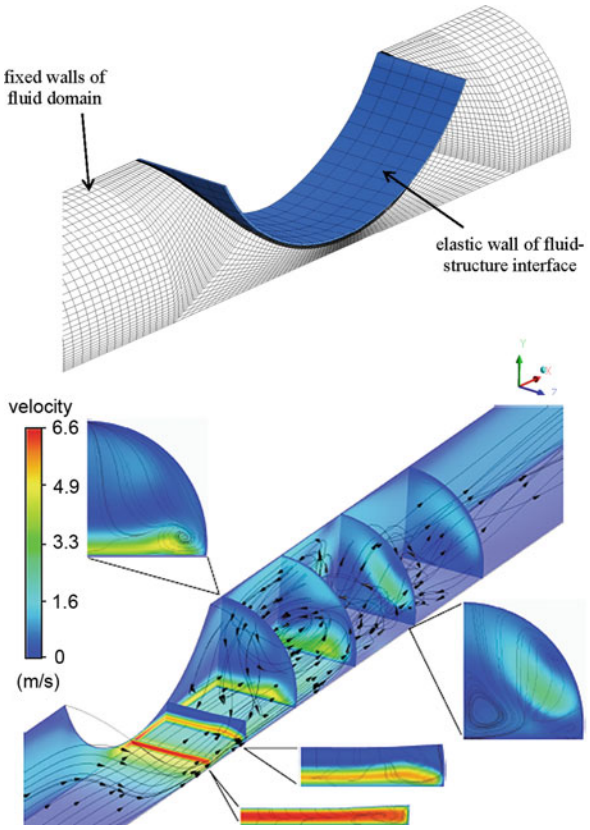


**Fig. 9.5** Streamline plot and contours of velocity along vertical symmetry plane, bottom wall and several axial cross-sections for $\Delta P = 20$ Pa taken from Rasani et al. (2011)

recirculation is observed immediately downstream of the elastic wall above the jet streams. Streamlines from the upper and bottom half of the inlet reveals the tendency for the stream to migrate towards the side walls, where the cross-sectional area is more open. Thus, the swirling strength of the inner recirculation core is increased as the outer streams follow the curvature of the walls.

As a further example of the research opportunities in using FSI for sleep apnea applications, stability analysis using a 3D realistic model for palatal snoring is presented here. A detailed schematic of the upper airway including the nasal and oral cavity separated by the soft palate in the pharyngeal area is shown in Fig. 9.6. Both nostrils and oral openings represent the inlet boundaries for the airway during inhalation, while the downstream end of the trachea represents the outlet boundary. The fluid domain is surrounded by rigid walls except at the soft palate which is the elastic fluid-structural interface region. A coupled fluid dynamics solver with structural dynamics solver is applied with a time-dependent constant inhalation rate can be applied to investigate the instability of the soft palate.

For the interested reader, additional examples of FSI in internal physiological flows is presented in Heil and Hazel (2011) which provides a review of self-excited

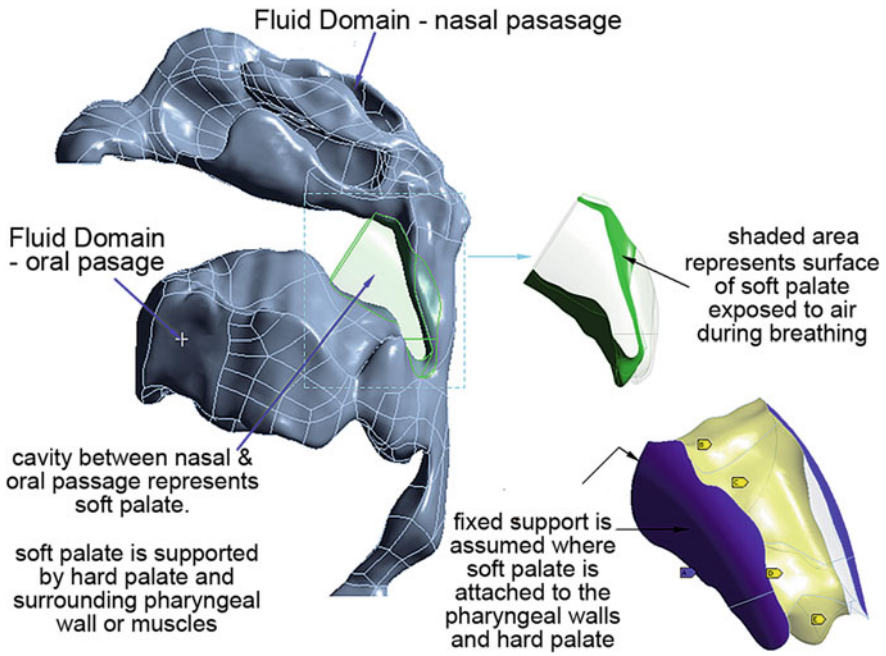


**Fig. 9.6** FSI geometry of an upper airway model with reconstructed soft palate

oscillations in collapsible tubes, focusing primarily on studies of an idealized model system, vocal-fold oscillations during phonation, closure and reopening of pulmonary airways, and also flows involving the airways' liquid lining. Other FSI applications include flow induced alveolar deformation (Dailey and Ghadiali 2007); the response of a stenotic trachea after a stent implantation (Malve et al. 2011).

## 9.3 Advanced Particle Modelling

### *9.3.1 Particle Breakup for Drug Delivery*

Nasal spray, metered dose inhaler, and dry powder inhaler devices produce atomized particles at high speeds from an orifice. The particles enter the respiratory airways via the nasal or oral route. Oral drug delivery has been used primarily for therapeutic treatment of the pulmonary organs, while the nasal route has been used for treating common airway congestion problems. However the nasal route also provides a great opportunity when considering new drug formulations, such as nicotine to assist in smoking cessation, calcium for osteoporosis, or insulin for diabetes. Therefore studies of local particle deposition are of great significance in the delivery of drugs via the nasal airway.

Particles that deform and breakup due to the shear they experience with the surrounding fluid are technically referred to as droplets. In this section, to avoid confusion we use the term particle in its place throughout. A particle subject to shear will deform which, if this deformation is large enough, will lead to particle breakup. The type of breakup can be characterised by the dimensionless Weber, *We*, and Ohnesorge, *Oh*, numbers. The Weber number is the ratio of the particle's inertia (contribution to deformation) compared to its surface tension (resistance to deformation):

$$We = \frac{\rho^g u^2 d_p}{\sigma} \tag{9.1}$$

where $\sigma$ is the surface tension and $u$ is the relative velocity between the particle and the surrounding gas. The ratio defined by the Weber number implies that increases in the diameter, gas density, and relative velocity will increase the particle deformation and above a certain value particle breakup occurs. It should be noted that the Weber number is also defined using the particle radius instead of its diameter.

The Ohnesorge number is the ratio of the viscous forces to inertial and surface tension forces:

$$Oh = \frac{\mu^p}{\sqrt{\rho^p \sigma d_p}} = \frac{\sqrt{We}}{\mathrm{Re}} \tag{9.2}$$

where $\mu$ is the particle viscosity. According to Pilch and Erdman (1987), there are five breakup regimes characterised by the initial Weber number which is based on observations of particle breakup in gas flow fields. These breakup regimes are depicted in Fig. 9.7.

Using the Lagrangian method, commonly used particle breakup models include the Wave breakup model (Reitz and Diwakar 1987), Schmel breakup (Schmehl et al. 2000) and the Taylor Analogy Breakup (TAB) breakup models (O'Rourke and Amsden 1987). A representative particle (a parcel in Sect. 6.2.1) will experience breakup when an instability criterion is sufficient (based on one of the breakup models). The particle breaks up into child droplets where the representative particle diameter is decreased to the child droplet diameter. The total mass of the particle remains constant, and therefore the reduction in diameter means that the representative child particle now represents a larger number of individual particles. Thus the new particles after breakup are tracked continuously rather than new particles being produced within the simulation.

As an example, a simulation of a spray breakup with the TAB breakup model is presented in Fig. 9.8a, b. The results show that more large droplets were located along the central axis and moved along the liquid sheet direction due to inertia, while small droplets were driven to the peripheral region by turbulent flow induced by the spray itself. Experimental imaging also provides a visual understanding of how the spray develops.

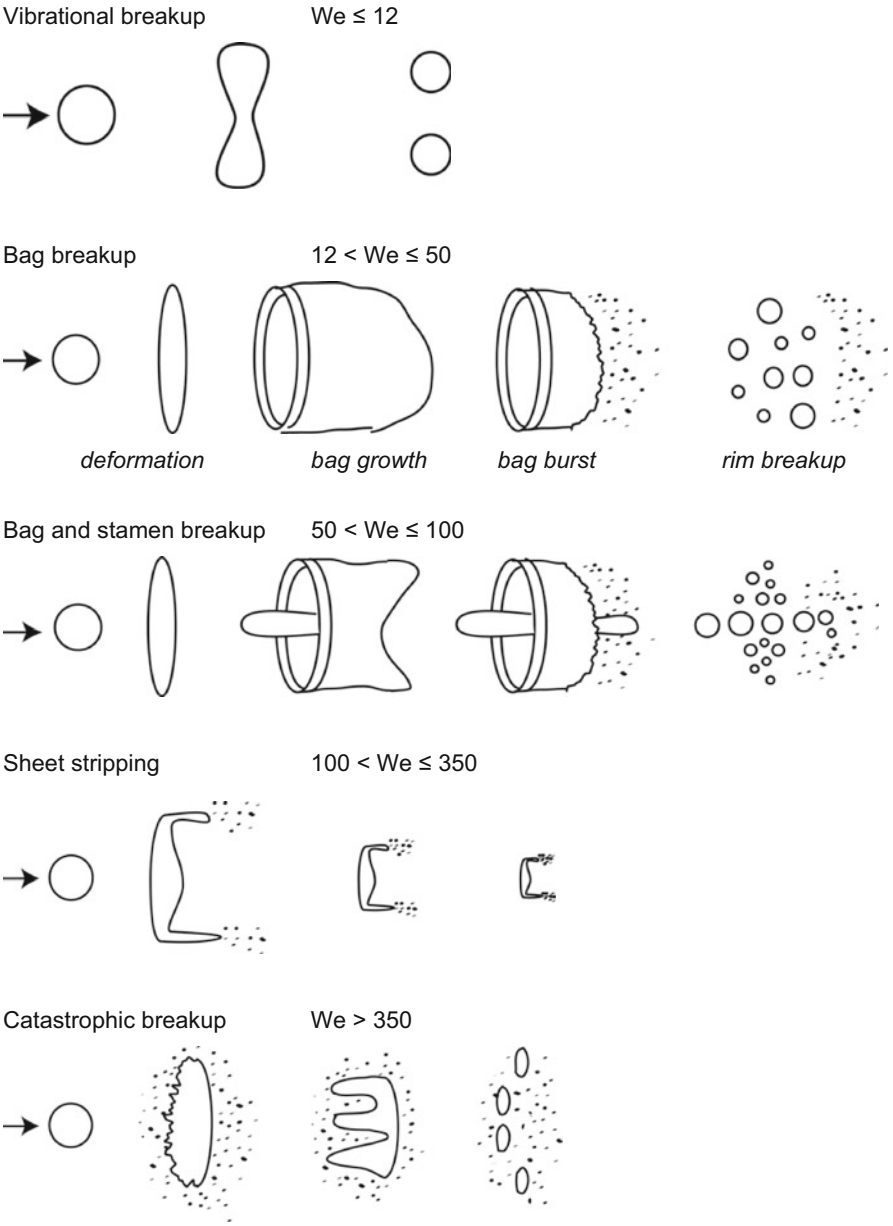


**Fig. 9.7** Schematic representation of particle breakup mechanisms reproduced from Pilch and Erdman (1987) where detailed descriptions of each breakup regime can be found

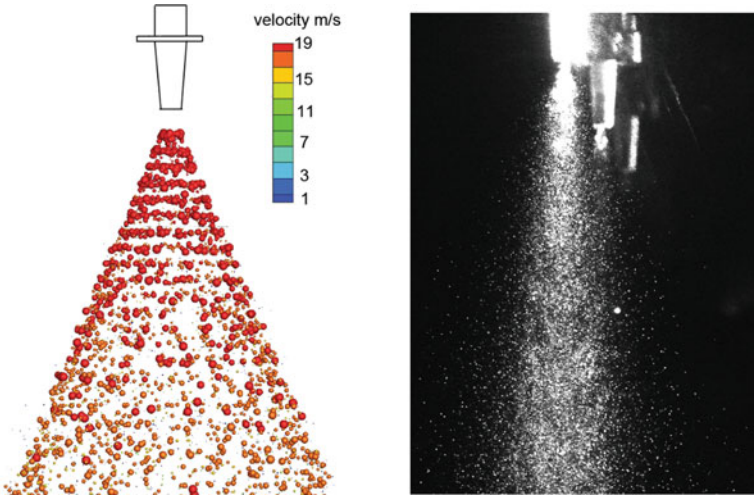


**Fig. 9.8** **a** CFPD simulation of particle breakup in a spray and **b** experimental visualisation using Particle Image Velocimetry

### *9.3.2 Particle-particle Collision and Turbulence Modulation*

In non-dilute gas-particle flows, the presence of particles in a turbulent flow can be affected by the presence of the dispersed phase, particularly if the particle concentration is high enough. The volume occupied by the particles displaces the fluid volume, which distorts the flow field streamlines and produces velocity gradients between the two phases. Additionally, the particles can produce a damping effect from the wake generated behind the particle. Crowe (2000) and Gore and Crowe (1989) found that small particles tend to attenuate turbulence and large particles tend to enhance turbulence. The data appeared to correlate with the ratio of the particle size $d_p$ to the turbulence length scale $l_t$ by the following:

$$\frac{d_p}{l_t} < 0.1 \quad \text{turbulence attenuation}$$

$$\frac{d_p}{l_t} > 0.1 \quad \text{turbulence augmentation}$$

From this definition, models for turbulence modulation can be defined and accounted for. Here we present the most accurate approach to represent turbulence by applying the direct numerical simulation to a gas-particle channel flow (Nasr et al. 2009). The inter-particle collisions, two-way coupling and particle aerodynamic interaction on dispersed and carrier phase fluctuations are included by using the direct numerical simulation of the Navier–Stokes equation via a pseudo-spectral method. The motion of each particle may be affected by the presence of other nearby particles in the flow.

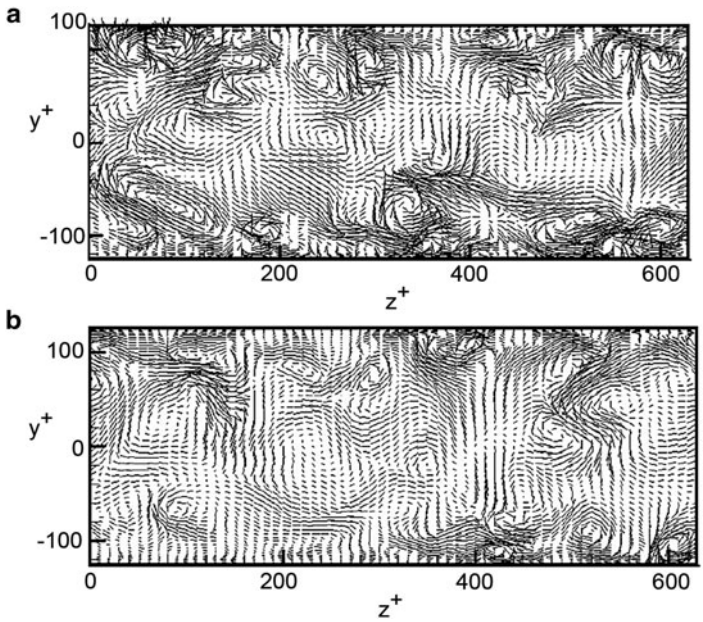


**Fig. 9.9** Velocity vector plot in the $y$–$z$ plane in the presence of $\tau^+ = 20$ with mass loading of 20 % in **a** one-way coupling and **b** four-way coupling

As a result, the particle aerodynamic interaction could influence the particle collision rate, as well as the particle and fluid phase fluctuations. The collisions were assumed to be binary since multiple collisions are extremely rare at the particle concentrations that were considered.

To perform a direct numerical simulation, the CFD code used a pseudo-spectral method for computing the fluid velocity field. That is, the fluid velocity is expanded in a three-dimensional Fourier-Chebyshev series. The fluid velocity field is expanded in Fourier series in the $x$- and $z$-directions, while a Chebyshev series is used in the y-direction. The code uses an Adams-Bashforth-Crank-Nickolson (ABCN) scheme to compute the nonlinear and viscous terms in the Navier–Stokes equation and performs three fractional time steps to advance the fluid velocity from time step ($n$) to time step ($n + 1$). The details of the numerical techniques were described by McLaughlin (1989).

Particles were uniformly distributed in the channel, and the initial velocity of each particle was set equal to the local fluid velocity evaluated at the centre of the particle. All results are averaged over the simulation time, and over the streamwise and spanwise directions. Figure 9.9a, b shows the results of one-way coupling compared with four-way coupling which indicates that the presence of solid particles damps the turbulence fluctuations and also decreases the number of eddies. Two-way coupling refers to particle–fluid interactions only while four-way coupling is also inclusive of particle-particle interactions. At sufficiently low particle volume fraction, two-way coupling is adequate; however, with higher particle loadings, the collisions will become dynamically significant and four-way coupling is required.

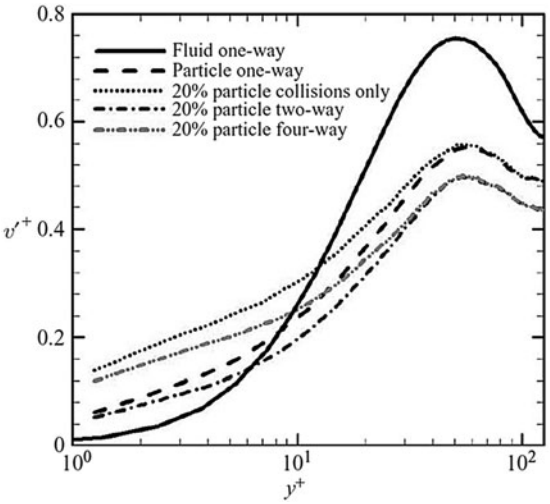


**Fig. 9.10** Normal fluctuating velocity vs. the distance from the wall for particles with $\tau^+ = 20$ at mass loading of 20 %

Figure 9.10 shows that the normal fluctuating velocity of particles in the case of the one-way coupling is less than the fluid in the $y^+ > 10$ region and is greater than the fluid in the wall region ($y^+ < 10$). The decrease in fluctuating velocity of the particles in the outer region is due to the fact that the inertial particles are not fully responsive to all turbulent eddies, and they fluctuate less than the flow. The increase of the normal fluctuating velocity of the particles in the wall region is perhaps due to the fact that, as a particle migrates towards the wall, it tends to retain the velocity it possessed when it was farther from the wall. Therefore, a wide range of particle velocities are found in the wall region, causing an increase in the normal particle fluctuating velocity.

For the case of the two-way coupling (in the absence of collision), the particle normal fluctuating velocity is lower in the entire channel in comparison to the one-way coupling case, and also decreases as particle mass loading increases. This trend can be explained in terms of turbulence attenuation effects due to the presence of the particle feedback force. In the case of the four-way coupling, the particle normal fluctuating velocity decreases in the outer region with $y^+ > 10$ and increases in the wall region with $y^+ < 10$ compared with the one-way coupling case. These results indicate that the two-way coupling effects decrease the particle normal fluctuating velocity, while inter-particle collisions enhance it.

### *9.3.3 Particle Dispersion and Deposition*

For particle deposition onto walls we simulate particle transport and deposition in a duct flow. Sample model predictions are reproduced in Fig. 9.11, which show the deposition velocity versus particle relaxation time in wall units.

Particle diameter is also shown in the figure for clarity. Figure 9.11 shows that the particle deposition velocity follows a v-shape curve. The deposition velocity

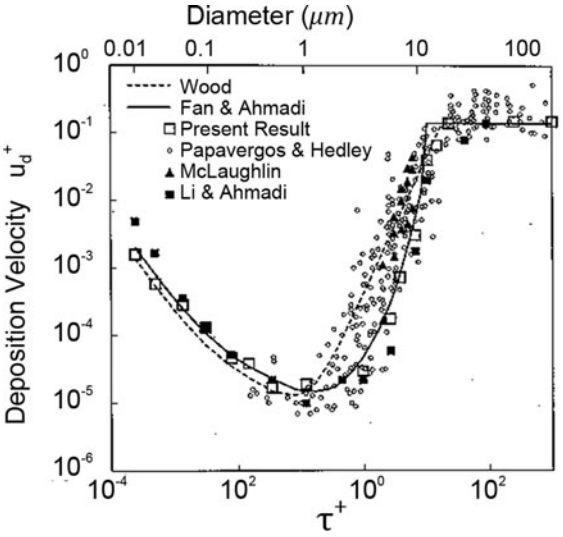


**Fig. 9.11** Comparison of computer simulations of He and Ahmadi (1998) for deposition of spherical particles in duct flows with experimental data collected by Papvergos and Hedley (1984), Papavergos and Hedley (1984), and earlier simulations of Li and Ahmadi (1993) and McLaughlin (1989), as well as model predictions of Fan and Ahmadi (1993) and Wood (1981)

is quite high for very small particles due to the increase in the particle diffusivity (Brownian motion). The deposition velocity then decreases as particle size increases since the particle diffusivity decreases with particle diameter. The minimum particle deposition occurs for non-dimensional relaxation time of the order of 0.1–1 (0.5 μm < d < 5 μm). The deposition velocity then increases for a larger relaxation time despite the decrease in the particle diffusivity. This is due to the interaction of these relatively large particles with turbulent eddies (Wood 1981). The inertia of these relatively large particles affects their transport in turbulent eddies, and their deposition rate increases. For particles with non-dimensional relaxation time larger than 15–20, deposition velocity approaches a saturation level of about 0.14. This is because of the very large inertia of the particles in this size range. Wood (1981) has suggested a simple empirical equation for the non-dimensional deposition velocity:

$$u_d^+ = 0.057\, {S_c}^{-2/3} + 4.5 \times 10^{-4} {\tau^+}^2 \tag{9.3}$$

where $S_c = \nu/D$ is the Schmidt number. Fan and Ahmadi (1993) developed an empirical equation for deposition of particles in vertical ducts that includes the effects of surface roughness and gravity along the flow direction and is given as

$$u_d^+ = \begin{cases} 0.084 {S_c}^{-2/3} + \dfrac{1}{2}\left[\dfrac{\left(0.64 k_r^+ + \frac{1}{2} d^+\right)^2 + \dfrac{{\tau^+}^2 g^+ {L_1}^+}{0.01085(1+{\tau^+}^2 {L_1}^+)}}{3.42 + ({\tau^+}^2 g^+ L_1^+)/(0.01085(1+{\tau^+}^2 {L_1}^+))}\right]^{1/(1+{\tau^+}^2 {L_1}^+)} \\ \times \left[1 + 8 e^{-(\tau^+ - 10)^2/32}\right] \dfrac{0.037}{1 - {\tau^+}^2 {L_1}^+ (1 + (g^+/0.037))} \quad \textit{if } u_d^+ < 0.14 \\ 0.14 \quad \textit{otherwise.} \end{cases}$$

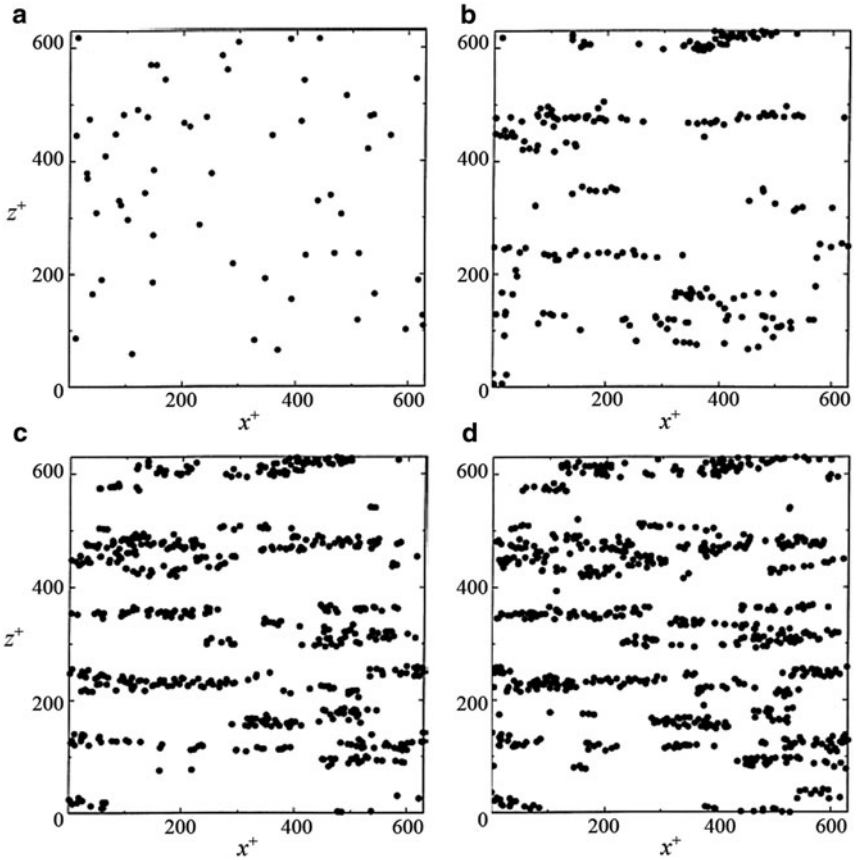


**Fig. 9.12** Distribution of the initial locations of deposited particles in the plane parallel to the wall **a** $d = 0.01$ μm, **b** 0.15 μm, **c** 25 μm, **d** 50 μm. (From Zhang and Ahmadi, 2000)

Here, $L_1^+ = 3.08/(Sd^+)$, $g^+ = (\nu/u^{*3})g$, and $k_r^+$ is the surface roughness (zero for smooth surfaces).

To shed light on the interaction of particles with near wall coherent eddies, Zhang and Ahmadi (2000) performed a series of simulations releasing the particles of different sizes near the wall and tracing their trajectory. For 0.01, 15, 25, and 50 μm particles that deposit on the wall, their locations are recorded and plotted in Fig. 9.12. Here the depositions within 100 wall units of time are considered. Figure 9.12a shows that the locations of deposited 0.01 μm particles are randomly distributed. This is because, for nanometre particles, the Brownian diffusion strongly affects the deposition process so that the effect of turbulence coherent eddies is smeared. Figure 9.12b shows that the locations of deposited 15 μm particles in the plane parallel to the wall are concentrated in certain bands, which are about 100 wall units apart. Similar

results for 25 µm and 50 µm particles that are deposited within 50–100 wall units are displayed in Fig. 9.12c and d. An examination of these figures shows that the locations of these deposited particles are also scattered around the same lines that are at a distance of about 100 wall units from each other. It is well known that the near wall turbulent structures form coherent eddies along the flow directions that are roughly about 100 wall units apart. These results presented in Fig. 9.12 clearly show that particles are captured by the near wall eddies and are moved toward the wall in the regions where these eddies form jets toward the wall. That is, the turbulent deposition of inertial particles is an impaction dominated process rather than one conducted by diffusion. This change in the deposition process is consistent with the trend seen in Fig. 9.11.

## 9.4 Multiphysics Respiratory Modelling

### *9.4.1 Mucous Surface Absorption Models*

The inherent dangers to the respiratory system caused by airborne particulate inhalation (e.g., exacerbating airway disease, increasing mortality incidence) are a challenging and critically important field of study. Similarly, the delivery of drugs through inhalation is important for new systemic drug development. Under both circumstances the deposition of particles tracked through the respiratory airways is determined through the CFPD methods described in this book. This is the limit for the gas-particle models since after the particles have deposited onto a surface wall, calculation is terminated.

Extending this work leads to the development of computational absorption submodels that determine local absorption of the chemical reaction occurring between the disperse phase and the mucous wall. These models are then integrated with existing CFPD simulations (Fig. 9.13).

We present a review of some methodologies and results that have been published in the literature. Cohen-Hubal et al. (1996) used mass-transfer resistance in the nasal lining (i.e. wall boundary in CFD model) incorporated into the CFD model for

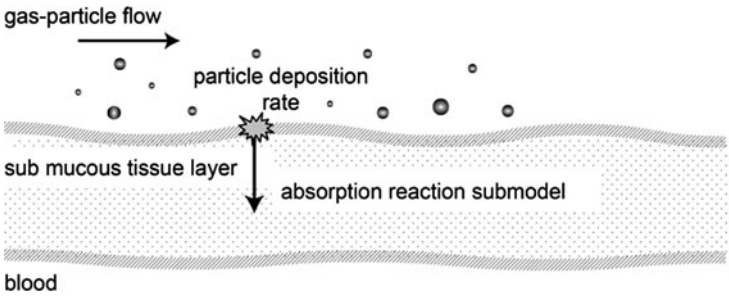


**Fig. 9.13** Schematic of submucous absorption-reaction model integrated with the gas-particle flow simulation from CFPD

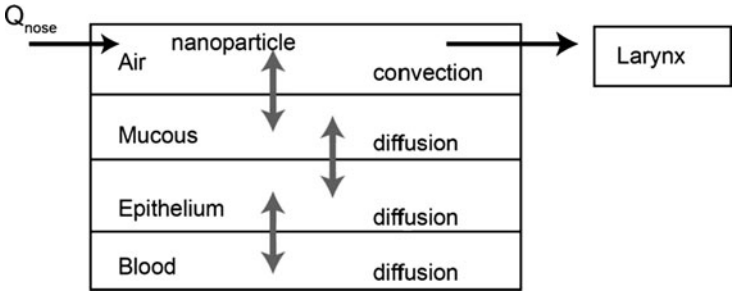


**Fig. 9.14** Schematic of a multi-compartment nasal cavity unit showing the subcompartments and its connection to the single larynx compartment

prediction of ozone dosimetry in the nasal passage of a rat. The nasal mucosa was treated as one layer to represent mucous-phase resistance only and blood- and tissue-phase resistance to mass transfer was neglected. They found that mucus resistance is important for describing the dosimetry of ozone and that mucus thickness may play a role in determining patterns of ozone-induced lesions in the rat's upper respiratory tract.

Keyhani et al. (1997) used a mass-transfer boundary condition at the nasal cavity wall that included the effects of solubility and diffusivity of odorants in the mucosal lining and the thickness of the mucus layer. The absorption of particles is assumed to occur by quasi-steady-state diffusion driven by diffusion flux and concentration. Tian and Longest (2010) improved these methods by developing a transient absorption model of vapours linked with CFD simulations of air-vapour transport in the respiratory airways. A detailed analytical approach describes the diffusion flux at the air-mucus interface as a function of the far-field air phase concentration. Their results showed that transient absorption differ significantly from the steady state predictions for highly and moderately soluble compounds.

An alternate but similar modelling technique for predicting the absorption dosimetry analysis is the physiologically based pharmacokinetic (PBPK) modelling. The development of a PBPK model is based on known analytical models of the chemical, anatomical and physiological responses to exposure to chemical substances. Typically the model consists of compartments that represent organs/tissues which are interconnected by the transporting fluid (air or blood flow). Each compartment is specified with physiological parameters, coefficients, and rates of change. These parameters form differential equations that represent the rate of flow and diffusion at each compartment, which are known *a priori.* Combining these equations together produces a system of differential equations (Fig. 9.14).

In a CFD-PBPK coupled solution, the dosimetry flux can be determined through the fluid dynamics of gas-particle flow and the particle deposition rate onto the boundary walls. The PBPK model uses this flux as the initial condition to produce a unique solution. Some applications include dosimetry of acrylic acid in the nasal model (Andersen et al. 2000), nasal tissue dosimetry of acetate (Andersen et al. 2002), and inter-individual variability in the pharmacokinetics of environmental chemicals (Bois et al. 2010).

### 9.4.2 *Lung Airway Multiscale Modelling*

A multiscale and multiphysics approach is needed to fully represent lung function. The development of the lung anatomy involves representation of the branching airways that exhibit large variation in size from the trachea and bronchi down to the microscopic terminal bronchioles. The physiological events that occur in achieving gas exchange at the air/blood interface include the transport of inhaled air through the complex branching system that is driven by changes in airway pressure. Here the multiphysics include the development of the fluid dynamics of airflow and diffusion of air molecules across the alveolar surface. We review the work being undertaken towards the development of a multiscale, multiphysics model of the lung airway.

In CFPD, simulations models of the lung conducting airways are now commonly three-dimensional to allow detailed visualisation of flow structures and particle flows. However there are limitations to the number of successive branch generations a three-dimensional model can resolve. This is due to the resolution of scanned images where progressively smaller branches become distorted and undetectable without the use of high resolution CT (HRCT). This problem is further compounded by the difficulty in meshing the rapid variations in dimensional scales.

An alternative method (although not technically a traditional CFD method) to develop the entire lung airway tree is to trace out the bifurcating airway paths by either using a standard lung model such as Weibel's model (Weibel 1963) or using in-vivo imaging from HRCT scans (Fig. 9.15). An algorithm to generate such a model is presented by Tawhai et al. (2000) and is based on Monte Carlo methods for growth of bifurcating systems. Each path is then associated with some diameter. Representative equations for convection and diffusion can be applied to the axial and radial path to simulate the physical phenomena required. An example is the work by Tawahai and Hunter (2004) which modelled the water vapour and heat transfer in the normal and the intubated airways.

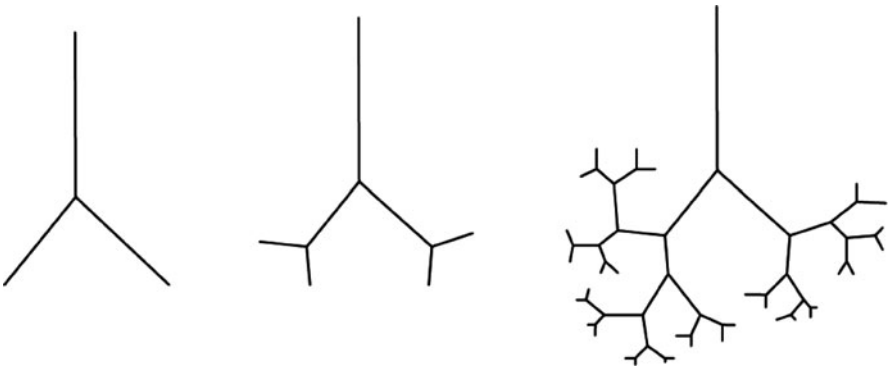

**Fig. 9.15** Example of tracing out the lung airway

Gas exchange takes place in the micro-scales of the alveoli, and its coupling to the lung model is a new and challenging field. An integrative model linking the

different spatial and temporal scales is presented by Chakraborty et al. (2007) and provides a quantitative analysis of pulmonary gas exchange. This model applies a convection-diffusion and reaction equation to quantify the transport and reaction rates of different processes during lung ventilation and perfusion.

## 9.5 Summary

New developments continue to be made in the field of computational fluid and particle dynamics for physiological functions. These developments open up new opportunities for simulating and representing the different respiratory functions. Moving meshes and fluid structure interactions allow for more realistic flow behaviour in regions of the respiratory airways that are non-rigid, such as the pharyngeal walls that are highly susceptible to collapse in apnoeic patients. Advanced particle/droplet dynamics, such as breakup, collisions and turbulence, are important for drug delivery that is administered through the respiratory airways. Aqueous drug solutions produce deformable particles that are prone to breakup while rigid solid particles are relevant for airborne pollutants. The dosimetry of inhaled particles can be evaluated by introducing an additional submodel that represents the behaviour of the particles occurring under the respiratory surface walls. This submodel then needs to be coupled with the CFPD simulations. Producing realistic whole-lung simulations is an advanced topic, given the large number of terminal bronchioles and alveoli that need to be considered. In addition, coupling of the air-blood gas exchange is required. These topics are just some of the major advancements and trends occurring in the computational modelling of the respiratory airways. This chapter aimed to provide an insight into each of the topics, rather than a critical review. Nevertheless, the topics presented should leave us with a sense of new opportunities and the multiple disciplines that are involved in the investigations of gas-particle flows in the respiratory system.

# Appendix A
# List of Computational Software

## A.1 DICOM Viewers

The listed DICOM viewers have similar functionality

| | |
|---|---|
| Acculite | *www.accuimage.com* |
| MicroDicom | *www.microdicom.com* |
| DICOM Works | *www.dicomworks.com* |
| Sante DICOM Viewer | *www.santesoft.com* |
| Mango | *ric.uthscsa.edu/mango* |
| OsiriX (MAC) | *www.osirix-viewer.com* |
| AMIDE | *amide.sourceforge.net* |
| Irfanview | *www.irfanview.com* |
| XNView | *www.xnview.com* |

## A.2 Open Source Medical Imaging and Segmentation

| | |
|---|---|
| CVIPTools | A UNIX/Win32-based package and contains a collection of C and C++ computer imaging tools that includes edge/line detection, segmentation, and many other functions (*www.ee.siue.edu/CVIPtools*) |
| Fiji/ImageJ | A Java-based image processing package that uses additional plugins for a variety of functionalities including segmentation algorithms (*pacific.mpi-cbg.de/wiki/index.php/Fiji*) |
| GemIdent | An interactive program that is designed for colour segmentation in images with few colours, and the objects of interest look alike with small variation (*www.gemident.com*) |
| ITK-SNAP | An interactive software application that allows users to navigate three-dimensional medical images, manually delineate anatomical regions of interest, and perform automatic image segmentation (*www.itksnap.org*) |

J. Tu et al., *Computational Fluid and Particle Dynamics in the Human Respiratory System,* 339
Biological and Medical Physics, Biomedical Engineering
DOI 10.1007/978-94-007-4488-2, © Springer Science+Business Media Dordrecht 2013

| | |
|---|---|
| Megawave 2 | Made up of C library modules, that contains original algorithms written by researchers and is run using Unix/Linux (*megawave.cmla.ens-cachan.fr*) |
| MITK and 3Dmed | Made up of C++ library for integrated medical image processing, segmentation, and registration algorithms (*www.mitk.net/download.htm*) |
| Slicer | Has a GUI that allows manual and automatic segmentation, registration, and three-dimensional visualization. It is a modular platform which means that it allows addition of new modules (*www.slicer.org*) |
| VXL | A collection of C++ libraries designed for computer vision research and implementation (*vxl.sourceforge.net*) |

## A.3 Commercial Medical Imaging and Segmentation

| | |
|---|---|
| 3D Doctor | An image processing and measurement software for MRI, CT, PET, microscopy, scientific, and industrial imaging applications (*www.ablesw.com/3d-doctor*) |
| Amira | Includes custom modules through C++ . There is also a research version called ZIBAmira (*http://amira.zib.de*) which provide licenses for joint research collaboration (*www.visageimaging.com/amira.html*) |
| Analyse | A software package for multi-dimensional display and segmentation (*www.analyzedirect.com*) |
| Mimics | An interactive tool for the visualization, 3D rendering, and segmentation of CT/MRI images. It also has a built in mesh program for CFD and structural analysis models (*www.materialise.com*) |
| SliceOmatic | Targeted at imaging of soft-tissue and for this, the use of MRI images is an advantage, however it can be used with CT (*www.tomovision.com*) |
| Vida Diagnostics | A lung analysis tool for Chronic Obstructive Pulmonary Disease, emphysema and asthma (*www.vidadiagnostics.com*) |

## A.4 Open Source Computer Aided Design Software

| | |
|---|---|
| FreeCAD | 3D computer assisted design program (*sourceforge.net/projects/free-cad*) |

| | |
|---|---|
| Open CASCADE | Allows for 3D surface and solid modeling, visualization, data exchange and rapid application development (*www.opencascade.org*) |
| BRL CAD | Has interactive editing for 3D solid modeling. Can also use for image processing and analysis (*brlcad.org*) |
| OpenSCAD | Used for creating solid 3D CAD objects (*www.openscad.org*) |

## A.5 Commercial Computer Aided Design Software

The listed CAD software have similar functionality in their ability to create 3D solid models ready for importing into a CFD meshing program.

| | |
|---|---|
| Geomagic | *www.geomagic.com* |
| CATIA | *www.3ds.com* |
| Autodesk | *www.autodesk.com* |
| Solidworks | *www.solidworks.com* |
| PRO/Engineer | *www.ptc.com* |
| IronCAD | *www.ironcad.com* |

## A.6 CFD Packages

| | |
|---|---|
| OpenFOAM | Open source CFD software package built using C++ and compiled under UNIX. The code is open and therefore allows full customisation and extensions to its standard capability (*www.openfoam.com*) |
| ANSYS | Includes ICEM meshing, CFX and Fluent CFD solvers, and CFD-Post for post processing. Also includes multi-physics for structural and FSI (*www.ansys.com*) |
| CD-Adapco | Includes STAR-CD and STAR-CCM for simulations involving flow of fluids and solids, heat transfer and stress analysis (*www.cd-adapco.co*) |
| CFDesign | Part of the Autodesk Simulation portfolio, it provides fluid flow simulation and thermal simulation (*www.cfdesign.com*) |
| Flow 3D | Modelling for liquids and gases in a wide range of industrial applications and physical processes (*www.flow3d.com*) |
| Numeca | Provides for fluid dynamics simulations for industrial applications (*www.numeca.be*) |

| | |
|---|---|
| Phoenics | Handles CFD simulations for fluid flow, heat or mass transfer, chemical reaction and combustion in engineering equipment and the environment (*www.cham.co.uk*) |

## A.7 Third Party Post Processing Software

| | |
|---|---|
| ParaView | An open-source, multi-platform data analysis and visualization application (*www.paraview.org*) |
| GNU Plot | An open source portable command-line graphing utility (*www.gnuplot.info*) |
| OpenDX | Uses IBM's visualisation data explorer interface for data input and output (*www.opendx.org*) |
| Ensight | Visualisation for most CFD data file formats (*www.ensight.com*) |
| Tecplot | Visualisation for most CFD data file formats (*www.tecplot.com*) |
| Plot3D | Interactive graphics program for visualizing CFD results (*www.openchannelfoundation.org*) |

# Appendix B
# Glossary

An aim of this book is to bring together the two streams of biomedicine with classical mechanical engineering. A student from one field is likely to encounter specialised terminology from the other. Therefore this glossary is collated in order to provide a quick reference to explain the terminology to allow the reader to understand the work they are reading.

## B.1 CFPD and Engineering Terminology

| | |
|---|---|
| Adverse pressure gradient | When the static pressure increases in the direction of the flow flow i.e. when the rate of change in pressure is positive (compare with *favourable pressure gradient*) |
| Aerodynamics | The study of flow of gases |
| Anisotropic turbulence | Where the turbulent fluctuations (u, v, w) are equal |
| Aspect Ratio | A type of descriptor for the quality and shape of a mesh cell describing its maximum dimension to its minimum dimension |
| Bernoulli's equation | Describes the behaviour of moving fluids along a streamline |
| Boundary conditions | Specification of the dynamic fluid state or properties at the computational domain boundaries |
| Boundary layer | A layer of fluid in the immediate vicinity of a surface |
| Buoyancy | Is the vertical force that a completely submerged body experiences which is equal to the weight of the displaced fluid |
| Capillary | A narrow tube or confined flow channel |
| Cavitation | Occurs when a liquid is subjected to rapid changes of pressure causing the formation of cavities in the lower pressure regions of the liquid |
| Cell Re | Local Reynolds number based on the cell velocity and cell length scale |

J. Tu et al., *Computational Fluid and Particle Dynamics in the Human Respiratory System,* 343
Biological and Medical Physics, Biomedical Engineering
DOI 10.1007/978-94-007-4488-2, © Springer Science+Business Media Dordrecht 2013

| | |
|---|---|
| CFL | Courant–Friedrichs–Lewy is a value or condition used to determine the convergence condition for solving hyperbolic partial differential equations. The CFL number should always be checked when dealing with transient simulations (i.e. explicit time marching schemes) |
| Coanda effect | Is the tendency for a stream of fluid to remain attached to a surface |
| Compressible flow | Fluid flow is considered compressible if there is variation in its density within the flow domain. This is important when setting up a CFPD problem so that the density changes are accounted for |
| Continuity | Is the name given to the mass conservation equation, (e.g. describes how mass in = mass out) |
| Convergence | *When the solution being iterated does not change with each successive iteration* |
| Density | The mass of fluid per unit volume ($kg/m^3$) |
| Diffussion | The process whereby random motion of molecules move from regions of higher concentration to regions of lower concentration |
| Domain | The entire region where the mesh encompasses |
| Drag coefficient | An opposing force in the flow direction exerted on an object by the fluid flowing around it, normalised by dynamic pressure and frontal area |
| Dynamic pressure | The pressure relative to a velocity reference |
| Eddy | See *vortex* |
| Euler equations | Simplified equations of fluid motion which describe the flow of a compressible inviscid fluid |
| Eulerian description | Describes fluid motion by following an individual fluid particle as it moves through space and time (compare with *Eulerian description*) |
| Favourable pressure gradient | When the static pressure decreases in the direction of the flow i.e. when the rate of change in pressure is negative (compare with favourable pressure gradient) |
| Finite difference (FD) | A numerical technique to solve differential and integral equations (see Sect. 7.21 of book) |
| Finite element | A numerical technique to solve differential and integral equations. An alternative to the finite difference and finite volume |
| Finite volume (FV) | A numerical technique to solve differential and integral equations (see Sect. 7.22) |
| Flow separation | The fluid boundary layer detaches from a surface when an adverse pressure gradient dominates the flow |
| Gauss divergence theorem | From vector calculus, which states that the outward flux through a closed surface (how much fluid flows out of a volume through its surface) is equal to the volume integral of the divergence of the vector field inside the volume (total sources inside the volume minus any sinks) |

| | |
|---|---|
| Hagen-Poiseuille flow | Flow is laminar viscous and incompressible and the flow is through a constant circular cross-section that is substantially longer than its diameter |
| Homogeneous fluid | Fluid having constant density |
| Homogenous multiphase flow | The assumption whereby each phase shares a common flow field as well as other relevant fields such as temperature and turbulence |
| Hydrostatic pressure | The forces from a fluid acting on the submerged surface of an object |
| Hydrostatics | The study of liquids at rest |
| Ideal gas | Is a concept that allows a simplified state for analysis. It is a theoretical gas composed of randomly moving non-interacting particles |
| Incompressible flow | Fluid flow is considered incompressible when its density remains constant within the flow domain. This is important when setting up a CFPD problem so that simpler models can be used for a constant density |
| Inhomogenous multiphase flow | A more complex representation of multiphase flows where each phase has its own flow (includeing temperature and turbulence) field |
| Invisicid flow | Flow without viscous effects, also known as potential flow. The viscous terms in the momentum equation are neglected |
| Irrotational flow | Flow where the streamlines ever loop back on itself, typically found in invisicid flows |
| Kinetic energy | Is the energy which the fluid possesses due to its motion, and is also usually defined as the dynamic pressure, determined by $1/2\ \rho u^2$ |
| Lagrangian description | Describes fluid motion by focussing on a fixed location in space through which the fluid flows as time passes (compare with Lagrangian *description*) |
| Laminar | An organized flow field where fluid particles flow in layers and do not readily mix. |
| Lift coefficient | A perpendicular force to the flow direction exerted on an object by the fluid flowing around it, normalised by dynamic pressure and frontal area |
| Mesh | Regions of the computational domain where the mathematical equations are applied to |
| Mesh independence | The method implemented to ensure that any further refinements to increase the number of mesh cells does not affect the results |
| Newtonian | Describes a fluid or flow that exhibits a constant viscosity and there is a linear stress versus strain rate curve |
| Nodes | Points in the mesh where data is stored |
| Non-Newtonian | Describes a fluid or flow where the viscosity is not constant and there is a non-linear relationship between the shear and strain rates |

| | |
|---|---|
| Normal stress | Also referred to as pressure, it is the component of stress that is perpendicular or normal to the material (compare with *shear stress*) |
| Potential flow | An idealised flow that is irrotational, and inviscid used for simplifying analysis of fluid flow |
| Residual | The measurement of the difference between the solutions during CFD—this value should decrease in a convergins solution |
| Shear stress | The component of stress that occurs in plane with the material (compare with *normal stress*) |
| Skewness | A type of descriptor for the quality and shape of a mesh cell |
| Slip velocity | The relative velocity between the particle and the surrounding fluid |
| Stability | Refers to the numerical stability of the chosen discretisation scheme whereby with each numerical iteration the solution converges rather than diverging |
| Static pressure | The pressure based on local atmospheric conditions and is independent of the flow conditions (compare with *dynamic pressure*) |
| Stokes flow | Also called creeping flow, where inertial forces are small compared with viscous forces. Typically the Reynolds number is less than 1, i.e. $Re << 1$ |
| Streamline | A path in a steady flow field along which a given fluid particle travels |
| Surface tension | Property of the surface of a liquid that allows it to resist an external force |
| Total pressure | The combination of static (local atmospheric conditions) and dynamic (any moving velocity conditions) pressure |
| Transition regime | The region where the flow changes from laminar to turbulent within the boundary layer |
| Transport equation | A generic equation that represents the various physical processes of a flow variable as it moves (i.e. transports) through a fluid (see Eq. 5.43 in Sect. 5.4) |
| Turbulent flow | Flow where the fluid inertia is dominant and particles move erratically, mixing greatly throughout the domain |
| Vapour pressure | Pressure at which the vapor of that substance is in equilibrium with its liquid or solid forms |
| Viscosity | A measure of the resistance of a fluid which is being deformed by shear stress |
| Vortex | The swirling of a fluid and its reverse current |
| Vorticity | The tendency for elements of the fluid to rotate or spin; defined as the circulation per unit area at a point in the flow field |
| Wake | The region of recirculating flow immediately behind a moving solid body, caused by the flow of surrounding fluid around the body |

| | |
|---|---|
| Wall function | Analytical equations or functions that connect the free stream flow to the near wall (see Sect. 5.3.5) |
| Isotropic turbulence | Where the turbulent fluctuations (u, v, w) are equal |
| CAD | Computer Aided Design |
| CAE | Computer Aided Engineering |
| DES | Detached Eddy Simulation—a type of turbulence model based on the LES model |
| DNS | Direct Numerical Simulation—the most sophisticated and complete method to handle turbulent flow |
| FEM | Finite Element Method—a computational approach to solve sets of mathematical equations |
| FSI | Fluid Structure Interaction—computational modelling approach that deals with both fluids and structural physics |
| FVM | Finite Volume Method—a computational approach to solve sets of mathematical equations |
| GUI | Graphical User Interface |
| IGES | Initial Graphics Exchange Specification—a type of image format file |
| LES | Large Eddy Simulation—an advanced type of turbulence model |
| PDF | Probability Density Function—a statistical method to represent large data sets |
| RANS | Reynolds Averaged Navier-Stokes |
| RNG | ReNormalization Group—a version of the k-epsilon turbulence model |
| RSM | Reynolds Stress Model |
| URANS | Unsteady Reynolds Navier-Stokes |
| VOF | Volume of Fluid—a simulation technique that allows visualisation of interfaces in multiphase flows |

## B.2 Biomedicine Terminology

| | |
|---|---|
| Adenoids | Pharyngeal tonsils |
| Aerobic | Requiring oxygen |
| Alveolar ventilation rate | The volume of gas per unit time that reaches the alveoli, calculated by (tidal volume—dead space) * breaths per min |
| Alveolus | Microscopic air scas of the luns |
| Anterior | Front side (Latin *ante*: before) |
| Anteroposterior | The axis or direction that runs from the head or front end to the opposite tail or back end of a body |
| Apnea | Suspension of breathing |
| Atmospheric pressure | The externalsurrounding force that exerts onto a surface |

| | |
|---|---|
| Atrophy | Is the partial or complete wasting away of a part of the body |
| Axial | Towards the central axis of the organism or an extremity |
| Basal lamina | A layer of extracellular matrix secreted by the epithelial cells, on which the epithelium sits |
| Basal surface | The surface near the base or the lower side or bottom of a structure |
| Benign | Not harmful, mild and nonprogressive disease |
| Boyle's Law | Describes the inverse relation between the absolute pressure of a gas with its volume |
| Bronchioles | The first airway branches inside the lung that no longer contain cartilage |
| Bronchus | One of the two main/primary branches that subtend from the trachea |
| Capillaries | Small blood vessels where exchnage between blood and tissue cells occur |
| Cartilage | White semi-opaqie connective tissue |
| Caudal | Of, at, or near the tail or the posterior end of the body. In the human case, towards the bottom of the feet (also the "tail" of the spinal cord, and body) |
| Chronic obstructive pulmonary disease (COPD) | Collective term for the disease of the lungs where the airways become narrowed |
| Cilia | Tiny hair like projections that ptrotude from cell surfaces and move in a rhytmic motion |
| Coagulation | The process where blood as a liquid joins together and forms a gel |
| Colloid | A mixture in which solute particles do not settle out readily and cannot pass through natural membranes |
| Contralateral | On the opposite from another structure, e.g. the left arm is contralateral to the right leg |
| COPD | See '*chronic obstructive pulmonary disease (COPD)*' |
| Craniocaudal | The direction or axis that runs from the head or front end to the opposite back end of a body |
| Cutaneous | Pertaining to the skin |
| Cytokines | Small protein molecules that are involved in cellular immunity |
| Dead space ventilation | Is the volume of gas per unit time that does not reach these respiratory portions, but instead remains in the airways (trachea, bronchi, etc.) |
| Dialysis | A process for removing waste and excess water from the blood |
| Diaphragm | The muscle that separates the thoracic cavity with the lower abdomen cavity, or any partition/wall that separates one region from another |
| Diastole | The period of time when the heart fills with blood after systole (contraction) |

| | |
|---|---|
| Dorsal | From the Latin word 'dorsum' meaning back |
| Dorsoventral | The axis or direction that runs from the spinal column (back) to the belly (front) |
| Dyspnea | Shortness of breath or air hunger, is the subjective symptom of breathlessness |
| Edema | abnormal build up of fluid in body pars or tissue that leads to swelling |
| Emphysema | A long-term, progressive disease of the lungs that primarily causes shortness of breath caused by the supporting tissues being destroyed |
| Enzyme | A protein that acts as a biological catalyst to speed up a chemical reaction |
| Epidermis | The surface layer of the skin, made up of keratinezed stratified squamous epithelium |
| Epiglottis | A flap of artilage behind the root of the tongue which is depressed during swallowing to cover the opening of the larynx |
| Epithelium | Thin tissue forming the outer layer of the body's surface, lining the cavities and surfaces of structures throughout the body |
| Erythrocytes | Red blood cells |
| Esophagus | A muscular tube through which food passes from the pharynx to the stomach |
| Eupnea | Normal respiratory rate and rhythm |
| Eustachian tube | *Auditory tube* |
| Excretion | Process where substances are spearated or expelled as waste |
| Fibrocartilage | A type of cartilage that is highly compressible |
| Fossa | A shallow depression or hollow |
| Gland | Body organ that secretes or excretes substnces for use by the body |
| Glottis | The part of the larynx that consists of the vocal cords and the slit-like opening between them |
| Goblet cells | Individual cells that produce mucous |
| Gustation | The action of tasting |
| Haemoglobin | See hemoglobin |
| Hemoglboin | A protein containing iron, responsible for transporting oxygen in the blood |
| Histology | The study of microscopic structure of tissues |
| Hyaline cartilage | The most abundant cartilage in the body that provides support |
| Hydrophilic | Dissoves, mixes, or is wetted easily with water |
| Hydrophobic | Unable to mix or repels with water |
| Hydrostatic pressure | Pressure of fluid in a system |
| Hypercapnia | High carbon dioxide levels in blood |
| Hypernea | Increased breathing when required to meet metabolic demand of body tissues, such as during or following exercise, or when the body lacks oxygen |

| | |
|---|---|
| Hypertension | High blood pressure |
| Hypertrophy | Enlargment of an organ ort issue caused by an increase in the size of its cells |
| Hyperventilation | Increased depth and rate of breathing |
| Hypocapnia | Low carbon dioxide levels in the blood |
| Hypodermis | Is the lowermost layer of the subcutaneous tissue (under the skin) |
| Hypotension | Low blood pressure |
| Hypoventilation | Decreased depth and rate of breathing |
| Hypoxia | When the body lacks oxygen |
| Hypoxia | Deficiency in the amount of oxygen reaching the tissues |
| In vitro | Process that takes place in a test tube or artificial environment |
| In vivo | Taking place in a living organism |
| Inferior vena cava | Vein that returns blood from body areas below the diaphragm |
| Inflammation | Localised region which becomes swollen, reddened, and painful as a defensive response to tissue injury |
| Innervation | The supply of nerves to parts of the body |
| Integumentary system | The outer protective skin layer and its parts |
| Internal respiration | The gas exchange process that occurs between blood and tissues |
| Interstitial fluid | Fluid between cells |
| Ipsilateral | On the same side as another structure e.g. the left arm is ipsilateral to the left leg |
| Lacrimal | Relating to the secretion of tears |
| Lamina | A thin layer or flat plate |
| Lateral | Towards or from one side to another |
| Leukocytes | White blood cell: a colourless cell which circulates in the blood and body and is involved in conteracting diseases and foreign substances |
| Ligament | A short band of flexible, fibrous tissue that connects bones |
| Lipid | Any class of fatty acids or their derivatives |
| Lumbar | Part of the back between the thorax and the pelvis |
| Lumen | Cavity inside a tube, blood vessel or any hollow structure |
| Lung compliance | Is a measure of the elastic properties of the lung and is a reflection of lung distensibility (movement) |
| Lung parenchyma | The bulk substances of the lung including the lung tissue, bronchioles, and bronchi |
| Lymph | Colourless fluid containing white blood cells |
| Macrophage | A large phagocytic cell commonly found in tissues that phagocytizes cells in response to infection |
| Malignant | Uncontrolled growth, tending to invade normal tissue |
| Mastication | Chewing |
| Meatus | An external opening or passageway that leads to the interior of a body |

| | |
|---|---|
| Mechanoreceptor | A sensory receptor organ that responds to mechanical stimuli such as touch or sound |
| Medial | Situated in the middle |
| Mediolateral | The axis or direction that runs from the centre (medial) of an object to one side or the other (lateral) |
| Medulla | The inner region of an organ or tissue |
| Mesothelium | The epithelium lining the ventral body cavity and covering its organs |
| Minute ventilation | The volume of gas ventilated in one minute, is expressed as (tidal volume $\times$ breaths/min) |
| Mucous membranes | A mucus-secreting membranes that line many of the body's cavities including the respiratory passageways |
| Mucus | A sticky, thick substance screted from the mucous membranes |
| Nares | Nostril openings |
| Occlusion | Blockage, obstruction, or closure |
| Oesophagus | See esophagus |
| Olfaction | The sense of smell |
| Osmosis | Diffusion process of molecules passing through a membrane from a dilute solution into a more concentrated solution |
| Oxidase | An enzyme that promotes the transfer of oxygen in oxidation-reduction reaction |
| Oxidation | Porcess of combining with oxygen or the removal or hydrogen |
| Palate | Roof of the mouth |
| Parasagittal planes | Any sagittal planes offset from the midline |
| Parenchyma | Is the functional parts of an organ in the body |
| Partial pressure | The pressure which the gas would have if it alone occupied the volume |
| Pathogen | A bacterium, virus or disease causing microorganism |
| Phagocytes | A cell that engulfs and absorbs bacteria and other foreign substances |
| Phagocytosis | Ingestion of bacteria or foreign substances by phagocytes |
| Pleura | A pair of serous membrances that lines the thorax and covers the lungs |
| Pleural cavity | A subdivision of the thoracic cavity; each housing a lung |
| Polyps | A small growth, usually benign, ptrotruding from a mucous membrane |
| Posterior | Back side (Latin *pos*t: after) |
| Pronation | Rotational movement of the hand, foot or limb, with the palm or sole turned downwards or posteriorly |
| Proximal | Situated nearer to the centre of the body or an area of attachment/interest |
| Proximodistal | The axis or direction that runs from an appendage (distal) to where it joins the body (proximal) |

| | |
|---|---|
| Pulmonary arteries | Vessesl that carry blood from the heart to the lungs to be oxygenated |
| Pulmonary edema | Leakage and accumulation of fluid into the air sacs and tissue of the lungs |
| Pulmonary veins | Vessels that carry oxygenated blood from the lungs to the heart |
| Pulmonary ventilation | Breathing consisting of both inhalation and exhalation |
| Respiration | The act of breathing; the process of delivering oxygen and removing carbon dioxide from the body |
| Rostrocaudal | The direction or axis that runs from the head or front end to the opposite back end of a body |
| Sagittal | A plane that can divide the body into a left and right side |
| Saliva | Liquid secreted into the mouth to assist in digestion |
| Sebaceous glands | The sebaceous glands are microscopic glands in the skin which secrete an oily/waxy matter, called sebum, to lubricate the skin and hair of mammals |
| Secretion | Process where substances are produced and discharged from a cell |
| Smooth muscle | Muscle tissue with unordered contractile fibres, unlike striated muscles which have aligned fibres |
| Solute | A substance that is dissolved in a solution |
| Stenosis | Abnormal narrowing or constriction of a passageway |
| Subcutaneous | Under the skin |
| Superficial | Near the outer surface of the organism, e.g. the skin is superficial to the muscle layer. The opposite is “deep”, or “visceral” |
| Superior vena cava | Veins that returns blood from body areas above the diaphragm |
| Supinate | Outward rotation of the hand, foot or limb, with the palm or sole turned upwards or anteriorly |
| Suture | An immovable joint between two parts |
| Symphysis | A place where two bones are joined with fibrocartilage and are immovable |
| Systemic | Systemic refers to something that is spread throughout, system-wide, affecting a group or system such as a body as a whole |
| Systemic | Relating to the whole body |
| Systemic circulation | Systemic circulation is the portion of the cardiovascular system which carries oxygenated blood away from the heart, to the body, and returns deoxygenated blood back to the heart. The term is contrasted with pulmonary circulation |
| Systemic disease | An illness that affects multiple organs, systems or tissues, or the entire body |
| Systemic venous system | Refers to veins that drain into the right atrium without passing through two vascular beds |
| Systole | The phase when the heart mucslces contract and pumps blood into the artery |

| | |
|---|---|
| Tachypnea | Rapid shallow breaths |
| Tendon | A flexible cord of dense fibrous tissue attaching a muscle to a bone |
| Thermogenesis | The production of body heat |
| Thorax | The part of the body from the neck to the abdomen which includes cavity enclosed by the ribs |
| Thrombus | A blood clot that develops and impedes blood flow |
| Tissue | A group of similar cells that perform a specific function |
| Tonsils | Small masses of lymphocyte tissue located around the entrance of the pharynx, on each side of the root of the tongue |
| Transverse | Horizontal; a plane that could cut the body into superior and inferior parts |
| Tumor | An abnormal growth of cells which can be benign or malignant |
| Vascular | Relating to blood vessels or is richly supplied with blood vessels |
| Vasoconstriction | The constriction of blood vessels, which increases blood pressure |
| Vasodilation | Widening of the blood vessues producing dilation |
| Venous blood | In the circulatory system, venous blood is blood returning to the heart (in veins) |
| Ventral | The abdomen or front side of a body, from (Latin venter; abdomen) |
| Venule | Small vein |
| Vesicle | A small fluid-filled sac or cyst within the body |
| Vestibule | In general, vestibule is a small space or cavity at the beginning of a canal |
| Vestibule | An enlarged area at the beginning of a passageway; from Latin *vesitbulum* meaning entrance court |
| Visceral | Associated with organs within the body's cavities |
| Visceral | Related to an internal organ of the body |
| Vital capacity | Is the maximum amount of air a person can expel from the lungs after a maximum inspiration |
| Vocal cords | Also called vocal folds, are two infoldings of mucous membrane stretched across the larynx for voice production (speech) |

# Appendix C
# Fluid Dynamics Dimensionless Numbers

| Name | Symbol | Equation | Description |
|---|---|---|---|
| Biot number | Bi | $\frac{hL_C}{k}$ | Defined as the ratio of the heat transfer resistances inside of and at the surface of an object |
| Biot number (mass transfer) | $\mathrm{Bi}_{\mathrm{mass}}$ | $\frac{h_m L_C}{D_{ab}}$ | Defined as the ratio between the the mass transfer rate to t the mass diffusion rate of an object |
| Dean number | De | $Re\left(\frac{L}{2R}\right)^{1/2}$ | Defined as the product of the Reynolds number (based on axial flow $V$ through a pipe of diameter L) and the square root of the curvature ratio |
| Froude number | Fr | $\frac{V}{(gL_C)^2}$ | Defined as the ratio of the inertia force on a body to the weight of the body—the inertial force divided by gravitational force |
| Grashof number | Gr | $\frac{g\beta\Delta TV}{\vartheta^2}$ | Defined as the ratio of the buoyancy force to viscous force acting on a fluid. Often used when natural convection is important |
| Knudsen number | Kn | $\frac{\lambda}{L}$ | Defined as the ratio of the molecular mean free path length to a representative physical length scale |
| Lewis number | Le | $\frac{\alpha}{D_{ab}}$ | Defined as the ratio of thermal diffusivity to mass diffusivity |
| Mach number | Ma | $\frac{V}{a}$ | A measure of velocity relative to the speed of sound, e.g. 1 Mach = 343 m/s in dry air at 20 ° C (68 °F) |
| Nusselt number | Nu | $\frac{hL_C}{k}$ | Defined as the ratio of convective to conductive heat transfer across (normal to) the boundary |
| Ohnesorge number | Oh | $\frac{\sqrt{We}}{\mathrm{Re}}$ | Defined as the ratio of the viscous forces to inertial and surface tension forces |
| Peclet number | Pe | $\frac{VL}{\widetilde{D}}$ | Defined as the ratio of advection (convection) to the rate of diffusion |

J. Tu et al., *Computational Fluid and Particle Dynamics in the Human Respiratory System,* Biological and Medical Physics, Biomedical Engineering
DOI 10.1007/978-94-007-4488-2, © Springer Science+Business Media Dordrecht 2013

| Name | Symbol | Equation | Description |
|---|---|---|---|
| Prandtl number | Pr | $\frac{\vartheta}{\alpha}$ | Defined as the ratio of momentum diffusivity (kinematic viscosity) to thermal diffusivity |
| Reynolds number | Re | $\frac{VL}{\vartheta}$ | Defined as the ratio of a characteristic velocity to a characteristic length. Used to determine the flow regime (laminar or turbulent) |
| Schmidt number | Sc | $\frac{\vartheta}{D_{ab}}$ | Defined as the ratio of momentum diffusivity and mass diffusivity |
| Stokes number | Stk | $\frac{\tau V}{L_C}$ | Defined as the ratio of the stopping distance of a particle to a characteristic dimension of the obstacle |
| Strouhal number | St | $\frac{\omega L}{V}$ | Defined as the ratio of the oscillations in a flow to the fluid inertia. Used to describe oscillating flow |
| Weber number | We | $\frac{\rho V^2 L}{\sigma}$ | Defined as the ratio of a fluid's inertia compared to its surface tension |
| Womersley number | $\alpha$ | $\frac{L}{2}\left(\frac{\omega}{\vartheta}\right)^{0.5}$ | Defined as the ratio of the pulsatile flow frequency to viscous effects |

## C.1 Nomenclature

$a$ speed of sound
$D_{ab}$ mass diffusivity
$\widetilde{D}$ diffusion coefficient
$g$ gravitational acceleration
$h$ heat transfer coefficient
$h_m$ mass transfer coefficient
$k$ thermal conductivity of the body
$L_C$ characteristic length, which is commonly defined as the volume of the body divided y the surface area of the body, $L_C = V_{body}/A_{surface}$
$L$ representative physical length scale
$V$ velocity
$\Delta T$ temperature difference
$\alpha$ thermal diffusivity, $\alpha = k/(\rho C_p)$ where $C_p$ is the specific heat capacity
$\beta$ volumetric thermal expansion coefficient equal to the inverse of the film temperature
$\lambda$ mean free path
$\rho$ fluid density
$\sigma$ surface tension
$\tau$ relaxation time of a particle defined as $\rho_p {d_p}^2/18\,\mu$, where subscripts $p$, denote particle, and $d_p$ is the particle diameter
$\vartheta$ kinematic viscosity
$\omega$ oscillation frequency, or breathing frequency

# References


AIAA. (1998). *Guide for the verification and validation of computational fluid dynamics, in AIAA—G-077–1998*. Reston: American Institute of Aeronautics and Astronautics.

Andersen, M., Sarangapani, R., Gentry, R., Clewell, H., Covington, T., & Frederick, C. B. (2000). Application of a hybrid CFD-PBPK nasal dosimetry model in an inhalation risk assessment: An example with acrylic acid. *Toxicological Sciences, 57,* 312–325.

Andersen, M. E., Green, T., Clay, F. B., & Bogdanffy, M. S. (2002). Physiologically based pharmacokinetic (PBPK) models for nasal tissue dosimetry of organic esters: Assessing the state-of-knowledge and risk assessment applications with methyl methacrylate and vinyl acetate. *Regulatory Toxicology and Pharmacology, 36,* 234–245.

Apodaca, G. (2002). Modulation of membrane traffic by mechanical stimuli. *American Journal of Physiology-Renal Physiology, 282,* F179–190.

Arcilla, A. S., Häuser, J., Eiseman, P. R., & Thompson, J. F. (1991). *Numerical grid generation in computational fluid dynamics and related fields*. North-Holland: Amsterdam.

Babu, K. R., Narasimhan, M. V., & Narayanaswamy, K. (1982). Correlations for prediction of discharge rate, cone angle and aircore diameter of swirl spray atomisers, in *Proceedings of the 2nd International Conference on Liquid Atomisation and Spray Systems*, Madison, Wisc., 91–97.

Badea, C. T., Fubara, B., Hedlund, L. W., & Johnson, G. A. (2005). 4-D Micro-CT of the Mouse Heart. *Molecular Imaging, 4,* 110–116.

Balashazy, I., & Hofmann, W. (1993). Particle deposition in airway bifurcations—I. Inspiratory flow. *Journal of Aerosol Science, 24,* 745–772.

Balásházy, I., & Hofmann, W. (1993). Particle deposition in airway bifurcations-II. Expiratory flow. *Journal of Aerosol Science, 24,* 773–786.

Balashazy, I., Hofmann, W., & Heistracher, T. (2003). Local particle deposition patterns may play a key role in the development of lung cancer. *Journal of Applied Physiology, 94,*1719–1725.

Bardina, J. E., Huang, P. G., & Coakley, T. J. (1997). Turbulence modeling validation testing and development. *NASA Technical Memorandum,* 110446. http://www.google.com.au/url?sa=t&rct=j&q=&esrc=s&source=web&cd=1&cad=rja&ved=0CEQQFjAA&url=http%3A%2F%2Fntrs.nasa.gov%2Farchive%2Fnasa%2Fcasi.ntrs.nasa.gov%2F19970017828_1997026179.pdf&ei=Cy02UMHuMYzkrAeU8YCgCA&usg=AFQjCNG_XkiAn7s57ILLX5c-ZqH4ISOlEw

Behin, F., Behin, B., Bigal, M. E., & Lipton, R. B. (2005). Surgical treatment of patients with refractory migraine headaches and intranasal contact points. *Cephalalgia, 25,* 439–443.

Bois, F. Y., Jamei, M., & Clewell, H. J. (2010). PBPK modelling of inter-individual variability in the pharmacokinetics of environmental chemicals. *Toxicology, 278,* 256–267.

Bousquet, J., Van Cauwenberge, P., Khaltaev, N., & W.H.O. (2001). Allergic rhinitis and its impact on asthma. *Journal of Allergy and Clinical Immunology, 108,* 147–334.

Brant, W. E., & Helms, C. A. (2007). *Fundamentals of diagnostic radiology*. Philadelphia: Lippincott Williams & Wilkins.




Biological and Medical Physics, Biomedical Engineering
DOI 10.1007/978-94-007-4488-2, © Springer Science+Business Media Dordrecht 2013

Breatnach, E., Abbott, G. C., & Fraser, R. G. (1984). Dimensions of the normal human trachea. *American Journal of Roentgenology, 142,* 903–906.

Brennen, C. E. (2005). *Fundamentals of multiphase flow*. Pasadena: Cambridge University Press.

Brenner, H. (1961). The slow motion of a sphere through a viscous fluid towards a plane surface. *Chemical Engineering Science, 16,* 242–251.

Canny, J. (1986). A computational approach to edge detection. *IEEE Transactions Pattern Analysis and Machine Intelligence, 8,* 679–698.

Carey, J. W., & Steegmann, A. T. J. (1981). Human nasal protrusion, latitude, and climate. *American Journal of Physical Anthropology, 56,* 313–319.

Caughey, R. J., Jameson, M. J., Gross, C. W., & Han, J. K. (2005). Anatomic risk factors for sinus disease: Fact or fiction? *American Journal of Rhinology, 19,* 334–339.

Chakraborty, S., Balakotaiah, V., & Bidani, A. (2007). Multiscale model for pulmonary oxygen uptake and its application to quantify hypoxemia in hepatopulmonary syndrome. *Journal of Theoretical Biology, 244,* 190–207.

Chang, H. K. (1989). Flow dynamics in the respiratory tract. In H. K. Chang & M. Paiva (Eds.), *Respiratory Physiology, an Analytical Approach* (pp. 54–138) New York: Dekker.

Cheng, K. H., Cheng, Y. S., Yeh, H. C., Guilmette, A., Simpson, S. Q., Yang, Y. H., & Swift, D. L. (1996). In-vivo measurements of nasal airway dimensions and ultrafine aerosol deposition in the human nasal and oral airways. *Journal of Aerosol Science, 27,* 785–801.

Cheng, K. H., Cheng, Y. S., Yeh, H. C., & Swift, D. L. (1997). Measurements of airway dimensions and calculation of mass transfer characteristics of the human oral passage. *Journal of Biomechanical Engineering, 119,* 476–482.

Cheng, Y. S., Holmes, T. D., Gao, J., Guilmette, R. A., Li, S., Surakitbanharn, Y., & Rowlings, C. (2001). Characterization of nasal spray pumps and deposition pattern in a replica of the human nasal airway. *Journal of Aerosol Medicine, 14,* 267–280.

Cherukat, P., & McLaughlin, J. B. (1990). Wall-induced lift on a sphere. *International Journal of Multiphase Flow, 16,* 899–907.

Cherukat, P., McLaughlin, J. B., & Graham, A. L. (1994). The inertial lift on a rigid sphere translating in a linear shear flow field. *International Journal of Multiphase Flow, 20,* 339–353.

Choi, L. T., Tu, J. Y., Li, H. F., & Thien, F. (2007). Flow and particle deposition patterns in a realistic human double bifurcation airway model. *Inhalation Toxicology, 19,* 117–131.

Chouly, F., Van Hirtum, A., Lagrée, P. Y., Pelorson, X., & Payan, Y. (2008). Numerical and experimental study of expiratory flow in the case of major upper airway obstructions with fluid-structure interaction. *Journal of Fluids and Structures, 24,* 250–269.

Chung, K. Y. K., Cuthber, R. J., Revell, G. S., Wassel, S. G., & Summer, N. (2000). A study on dust emission, particle size distribution and formaldehyde concentration during machining of medium density fibreboard. *Annals of Occ Hyg, 44,* 455–466.

Churchill, S., Shackelford, L. L., Georgi, N., & Black, M. (2004). Morphological variation and airflow dynamics in the human nose. *American Journal of Human Biology, 16,* 625–638.

Clift, R., Grace, J. R., & Weber, M. E. (1978a). *Bubbles, drops, and particles*. London: Academic Press Inc. London, Ltd.

Clift, R., Grace, J. R., & Weber, M. E. (1978b). *Drops and particles*. New York: Academic Press.

Coates, M. S., Fletcher, D. F., Chan, H.-K., & Raper, J. A. (2004). Effect of design on the performance of a dry powder inhaler using computational fluid dynamics. Part 1: Grid structure and mouthpiece length. *Journal of Pharmaceutical Sciences, 93,* 2863–2876.

Cohen Hubal, E. A., Kimbell, J. S., & Fedkiw, P. S. (1996). Incorporation of nasal-lining mass-transfer resistance into acfd model for prediction of ozone dosimetry in the upper respiratory tract. *Inhalation Toxicology, 8,* 831–857.

Crawford, J. H. (1949). Determination of the specific gravity of ragweed pollen (Ambrosia elatior) and conversion of gravity sample counts to volumetric incidence. *Public Health Reports, 64,* 1195–1200.

Croce, C., Fodil, R., Durand, M., Sbirlea-Apiou, G., Caillibotte, G., Papon, J. F., Blondeau, J. R., Coste, A., Isabey, D., & Louis, B. (2006). In vitro experiments and numerical simulations of airflow in realistic nasal airway geometry. *Annals of Biomedical Engineering, 34,* 997–1007.

Crowder, T. M., Rosati, J. A., Schroeter, J. D., Hickey, A. J., & Martonen, T. B. (2002). Fundamental effects of particle morphology on lung delivery: Predictions of Stokes law and the particular relevance to dry powder inhaler formulation and development. *Pharmaceutical Research, 9,* 239–245.

Crowe, C. T. (2000). On models for turbulence modulation in fluid-particle flows. *International Journal of Multiphase Flow, 26,* 719–727.

Crowe, C. T., Sommerfeld, M., & Tsuji, Y. (1998). *Multiphase flows with droplets and particles*. Boca Raton: CRC Press.

Crüts, B., van Etten, L., Törnqvist, H., Blomberg, A., Sandström, T., Mills, N. L., Borm, P. J. (2008). Exposure to diesel exhaust induces changes in EEG in human volunteers. *Part Fibre Toxicol, 11,* 4.

Cunningham, E. (1910). On the velocity of steady fall of spherical particles through fluid medium. *Proceedings of the Royal Society A, 83,* 357–365.

Dailey, H. L., & Ghadiali, S. N. (2007). Fluid-structure analysis of microparticle transport in deformable pulmonary alveoli. *Journal of Aerosol Science, 38,* 269–288.

Davis, S. S., & Illum, L. (2003). Absorption enhancers for nasal drug delivery. *Clinical Pharmacokinetics, 42,* 1107–1128.

de Berg, M., Ogtfried, C., van Kreveld, M., & Overmars, M. (2008). *Computational geometry: Algorithms and applications*. Heidelberg: Springer-Verlag.

de Rochefort, L., Vial, L., Fodil, R., Maitre, X., Louis, B., Isabey, D., Caillibotte, G., Thiriet, M., Bittoun, J., Durand, E., & Sbirlea-Apiou, G. (2007). In vitro validation of computational fluid dynamic simulation in human proximal airways with hyperpolarized 3He magnetic resonance phase-contrast velocimetry. *Journal of Applied Physiology, 102,* 2012–2023.

Demirkaya, O., Asyali, M. H., & Sahoo, P. K. (2009). *Image processing with matlab—application in medicine and biology*. Boca Raton: CRC Press.

Doorly, D. J., Taylor, D. J., Gambaruto, A. M., Schroter, R. C., & Tolley, N. (2008). Nasal architecture: Form and flow. *Philosophical Transactions of the Royal Society A: Mathematical, Physical and Engineering Sciences, 366,* 3225–3246.

Eccles, R. (1996). A role for the nasal cycle in respiratory defence. *European Respiratory Journal, 9,* 371–376.

Edwards, D. A., Ben-Jebria, A., & Langer, R. (1998). Recent advances in pulmonary drug delivery using large, porous inhaled particles. *Journal of Applied Physiology, 85,* 379–385.

Einstein, A. (1905). On the movement of small particles suspended in stationary liquids required by the molecular-kinetic theory of heat. 17:549–560.

Elad, D., Liebenthal, R., Wenig, B. L., & Einav, S. (1993). Analysis of air flow patterns in the human nose. *Medical & Biological Engineering & Computing, 31,* 585–592.

Elad, D., Naftali, S., Rosenfeld, M., & Wolf, M. (2006). Physical stresses at the air-wall interface of the human nasal cavity during breathing. *Journal of Applied Physiology, 100,* 1003–1010.

Elder, A., Gelein, R., Silva, V., Feikert, T., Opanashuk, L., Carter, J., Potter, R., Maynard, A., Ito, Y., Finkelstein, J., & Oberdörster, G. (2006). Translocation of inhaled ultrafine manganese oxide particles to the central nervous system. *Environment Health Perspective, 114,* 1172–1178.

Enarson, D. A., & Chan-Yeung, M. (1990). Characterization of health effects of wood dust exposures. *American Journal of Industrial Medicine, 17,* 33–38.

Eric, T. P., Jionghan, D., James, H. H., & Sean, B. F. (2011). Measurement of lung airways in three dimensions using hyperpolarized helium-3 MRI. *Physics in Medicine and Biology, 56,* 3107.

Escudier, M. (1988). Vortex breakdown: Observations and explanations. *Progress in Aerospace Sciences, 422,* 189–229.

Fan, F. G., & Ahmadi, G. (1993). A sublayer model for turbulent deposition of particles in vertical ducts with smooth and rough surfaces. *Journal of Aerosol Science, 24,* 45–64.

Faxen, H. (1923). Die Bewegung einer starren Kugel längs der Achse eines mit zäher Flüssigkeit gefüllten Rohres. *Arkiv Mat Astron Fys, 17*(27), 1–28.

Ferziger, J. H., & Perić, M. (1999). *Computational Methods for Fluid Dynamics*. Berlin: Springer-Verlag.

Flemmer, R. L. C., & Banks, C. L. (1986). On the drag coefficient of a sphere. *Powder Technology, 48,* 217–221.

Fletcher, C. A. J. (1991). *Computational Techniques for Fluid Dynamics*. Berlin: Springer-Verlag.

Franciscus, R. G., & Long, J. C. (1991a). Variation in human nasal height and breadth. *American Journal of Physical Anthropology, 85,* 419–427.

Franciscus, R. G., & Long, J. C. (1991b). Variation in human nasal height and breadth. *American Journal of Physical Anthropology, 85,* 419–427.

Fry, F. A., & Black, A. (1973). Regional deposition and clearance of particles in the human nose. *Aerosol Science, 4,* 113–124.

Fung, Y. C. (1988). A model of the lung structure and its validation. *Journal of Applied Physiology, 64,* 2132–2141.

Gabitto, J., & Tsouris, C. (2007). Drag coefficient and settling velocity for particles of cylindrical shape. *Powder Technology*: doi:10,1016/j.powtec.2007.1007.1031.

Ganser, G. H. (1993). A rational approach to drag prediction of spherical and non-spherical particles. *Powder Technology, 77,* 143–152.

Garcia, G. J. M., Bailie, N., Martins, D. A., & Kimbell, J. S. (2007a). Atrophic rhinitis: A CFD study of air conditioning in the nasal cavity. *Journal of Applied Physiology, 103,* 1082–1092.

Garcia, G. J. M., Bailie, N., Martins, D. A., & Kimbell, J. S. (2007b). Atrophic rhinitis: A CFD study of air conditioning in the nasal cavity. *Journal of Applied Physiology, 103,* 1082–1092.

Gelperina, S., Kisich, K., Iseman, M. D., & Heifets, L. (2005). The potential advantages of nanoparticle drug delivery systems in chemotherapy of tuberculosis. *American Journal of Respiratory and Critical Care Medicine, 172,* 1480–1490.

González, R., Woods, R. (2008). *Digital image processing*. Pearson/Prentice Hall. ISBN: 9780131687288.

Gore, R. A., & Crowe, C. T. (1989). Effect of particle size on modulating turbulent intensity. *International Journal of Multiphase Flow, 15,* 279–285.

Gupta, A. K., & Gupta, M. (2005). Synthesis and surface engineering of iron oxide nanoparticles for biomedical applications. *Biomaterials, 25,* 3995.

Haber, S., Butler, J. P., Brenner, H., Emanuel, I., Tsuda, A. (2000). Shear flow over a self-similar expanding pulmonary alveolus during rhythmical breathing. *Journal Fluid Mechanics, 405,* 243–268.

Hadfield, E. M. (1972). Damage to the human nasal mucosa by wood dust. In W. H. Walton (Ed.), *Inhaled Particles III*. Old Working: Unwin Bros.

Haefeli-Bleuer, B., & Weibel, E. R. (1988). Morphometry of the human pulmonary acinus. *The Anatomical Record, 220,* 401–414.

Hahn, I., Scherer, P. W., & Mozell, M. M. (1993). Velocity profiles measured for airflow through a large-scale model of the human nasal cavity. *Journal of Applied Physiology, 75,* 2273–2287.

Haider, A., & Levenspiel, O. (1989). Drag coefficient and terminal velocity of spherical and nonspherical particles. *Powder Technology, 58,* 3–70.

Harrington, J. B., & Metzger, K. (1963). Ragweed pollen density. *American Journal of Botany, 50,* 532–539.

Harris, R. S. (1959). Tracheal extension in respiration. *Thorax, 14,* 201–210.

Harris, R. S. (2005). Pressure-Volume curves of the respiratory system. *Respiratory Care, 50,* 78–99.

Häußermann, S., Bailey, A. G., Bailey, M. R., Etherington, G., & Youngman, M. J. (2001). The influence of breathing patterns on particle deposition in a nasal replicate cast. *Journal of Aerosol Science, 33,* 923–933.

He, C., & Ahmadi, G. (1998). Particle deposition with themophoresis in laminar and turbulent duct flows. *Aerosol Science and Technology, 29,* 525–546.

He, C., & Ahmadi, G. (1999). Particle deposition in a nearly developed turbulent duct flow with electrophoresis. *Journal of Aerosol Science, 30,* 739–758.

Heil, M., & Hazel, A. L. (2011). Fluid-structure interaction in internal physiological flows. *Annual Review of Fluid Mechanics, 43,* 141–162.

Henry, F. S., Butler, J. B., Tsuda, A. (2002). Kinematically irreversible acinar flow: A departure from classical dispersive aerosol transport theories. *Journal Applied Physiology, 92,* 835–845.

Hidy, G. M. (1984). *Aerosols, an Industrial and Environmental Science*. New York: Academic Press.

Hofmann, W., Golser, R., & Balashazy, I. (2003). Inspiratory deposition efficiency of ultrafine particles in a human airway bifurcation model. *Aerosol Science and Technology, 37,* 988–994.

Holden, W. E., Wilkins, J. P., Harris, M., Milczuk, H. A., & Giraud, G. D. (1999). Temperature conditioning of nasal air: Effects of vasoactive agents and involvement of nitric oxide. *Journal of Applied Physiology, 87,* 1260–1265.

Hood, C. M., Schroter, R. C., Doorly, D. J., Blenke, E. J. S. M., & Tolley, N. S. (2009). Computational modeling of flow and gas exchange in models of the human maxillary sinus. *Journal of Applied Physiology, 107,* 1195–1203.

Hörschler, I., Schröder, W., & Meinke, M. (2010). On the assumption of steadiness of nasal cavity flow. *Journal of Biomechanics, 43,* 1081–1085.

Horsfield, K., Gladys, D., Olson, D. E., Finlay, G. F., & Cumming, G. (1971). Models of the human bronchial tree. *Journal of Applied Physiology, 31,* 207–217.

Hubbard, B. J., & Chen, H. C. (1994). A chimera scheme for incompressible viscous flows with applications to submarine hydrodynamics. *AIAA* Paper 94–2210.

Huupponen, E., Saunamäki, T., Saastamoinen, A., Kulkas, A., Tenhunen, M., & Himanen, S. L. (2009). Improved computational fronto-central sleep depth parameters show differences between apnea patients and control subjects. *Medical and Biological Engineering and Computing, 47,* 3–10.

IARC/WHO (1995). I.A.R.C monographs on the evaluation of carcinogenic risks to humans. Vol. 62: Wood Dust and Formaldehyde. International Agency for Research on Cancer/World Health Organization

ICRP (1960). Report of Committee II on permissible dose for internal radiation. *Annals of the ICRP/ICRP Publication, 2,* 1–40.

ICRP (1994). *Human respiratory tract model for radiological protection*. Tarrytown: Elsevier Science.

Inthavong, K., Tian, Z. F., Li, H. F., Tu, J. Y., Yang, W., Xue, C. L., & Li, C. G. (2006a). A numerical study of spray particle deposition in a human nasal cavity. *Aerosol Science Technology,* 40.

Inthavong, K., Tian, Z. F., Li, H. F., Tu, J. Y., Yang, W., Xue, C. L., & Li, C. G. (2006b). A numerical study of spray particle deposition in a human nasal cavity. *Aerosol Science and Technology, 40,* 1034–1045.

Inthavong, K., Tian, Z. F., Tu, J. Y., Yang, W.,& Xue, C. (2008a). Optimising nasal spray parameters for efficient drug delivery using computational fluid dynamics. *Computers in Biology and Medicine, 38,* 713–726.

Inthavong, K., Wen, J., Tian, Z. F., & Tu, J. Y. (2008b). Numerical study of fibre deposition in a human nasal cavity. *Journal of Aerosol Science, 39,* 253–265.

Inthavong, K., Tian, Z. F., & Tu, J. Y. (2009a). Effect of ventilation design on removal of particles in woodturning workstations. *Building and Environment, 44,* 125–136.

Inthavong, K., Wen, J., Tu, J. Y., & Tian, Z. F. (2009b). From CT Scans to CFD Modelling—fluid and heat transfer in a realistic human nasal cavity. *Engineering Applications of Computational Fluid Mechanics, 3,* 321–335.

Inthavong, K., Tu, J., Ye, Y., Ding, S., Subic, A., & Thien, F. (2010). Effects of airway obstruction induced by asthma attack on particle deposition. *Journal of Aerosol Science, 41,* 587–601.

Inthavong, K., Ge, Q., Se, C. M. K., Yang, W., & Tu, J. Y. (2011). Simulation of sprayed particle deposition in a human nasal cavity including a nasal spray device. *Journal of Aerosol Science, 42,* 100–113.

Isabey, D., & Chang, H. K. (1981). Steady and unsteady pressure-flow relationships in central airways. *Journal of Applied Physiology, 51,* 1338–1348.

Jaber, S., Carlucci, A., Boussarsar, M., Fodil, R., Pigeot, J., Maggiore, S., Harf, A., Isabey, D., & Brochard, L. (2001). Helium-oxygen in the postextubation period decreases inspiratory effort. *American Journal of Respiratory and Critical Care Medicine, 164,* 633–637.

Jackson, C. L., & Huber, J. F. (1943). Correlated applied anatomy of the bronchial tree and lungs with a system of nomenclature. *Chest, 9,* 319–326.

Jayarajua, S. T., Brounsa, M., Lacora, C., Belkassemb, B., & Verbanckc, S. (2008). Large eddy and detached eddy simulations of fluid flow and particle deposition in a human mouth–throat. *Journal of Aerosol Science, 39,* 862–875.

Jeong, S.-J., Kim, W.-S., & Sung, S.-J. (2007). Numerical investigation on the flow characteristics and aerodynamic force of the upper airway of patient with obstructive sleep apnea using computational fluid dynamics. *Medical Engineering & Physics, 29,* 637–651.

Jonathan Richard, S. (2002). Delaunay refinement algorithms for triangular mesh generation. *Computational Geometry, 22,* 21–74.

Kawaguchi, T., Tanaka, T., & Tsuji, Y. (1998). Numerical simulation of two-dimensional fluidized beds using the discrete element method (comparison between the two- and three-dimensional models). *Powder Technology, 96*(2), 129–138.

Keay, D., Smith, I., White, A., & Hardcastle, P. F. (1987). The nasal cycle and clinical examination of the nose. *Clinical Otolaryngology & Allied Sciences, 12,* 345–348.

Keck, T., Leiacker, R., Heinrich, A., Kuhneman, S., & Rettinger, G. (2000a). Humidity and temperature profiles in the nasal cavity. *Rhinology, 38*(4), 167–171.

Keck, T., Leiacker, R., Riechelmann, H., & Rettinger, G. (2000b). Temperature profile in the nasal cavity. *Laryngoscope, 110,* 651–654.

Kelly, J. T., Prasad, A. K., & Wexler, A. S. (2000). Detailed flow patterns in the nasal cavity. *Journal of Applied Physiology, 89,* 323–337.

Kelly, J. T., Asgharian, B., Kimbell, J. S., & Wong, B. A. (2004). Particle deposition in human nasal airway replicas manufactured by different methods. Part 1: Inertial regime particles. *Aerosol Science and Technology, 38,* 1063–1071.

Keyhani, K., Scherer, P. W., & Mozell, M. M. (1995). Numerical simulation of airflow in the human nasal cavity. *Journal Biomechanical Engineering, 117,* 429–441.

Keyhani, K., Scherer, P. W., & Mozell, M. M. (1997). A numerical model of nasal odorant transport for the analysis of human olfaction. *JournalTheoretical Biology, 186,* 279–301.

Khan, K., Arino, J., Hu, W., Raposo, P., Sears, J., Calderon, F., Heidebrecht, C., Macdonald, M., Liauw, J., Chan, A., & Gardam, M. (2009). Spread of a novel influenza a (H1N1) virus via global airline transportation. *New England Journal of Medicine, 361,* 212–214.

Kiely, J., & McNicholas, W. (2000). Cardiovascular risk factors in patients with obstructive sleep apnoea syndrome. *European Respiratory Journal, 16,* 128–133.

Kim, K., McCracken, K., Lee, B., Shin, C., Jo, M., Lee, C., & Ko, K. (1997). Airway goblet cell mucin: Its structure and regulation of secretion. *European Respiratory Journal, 10,* 2644–2649.

Kimbell, J., Shroeter, J. D., Asgharian, B., Wong, B. A., Segal, R. A., Dickens, C. J., Southall, J. P., & Miller, F. J. (2004). Optimisation of nasal delivery devices using computational models. *Respiratory Drug Delivery, 9,* 1.

Kimbell, J. S., Segal, R. A., Asgharian, B., Wong, B. A., Schroeter, J. D., Southall, J. P., Dickens, C. J., Brace, G., & Miller, F. J. (2007). Characterization of deposition from nasal spray devices using a computational fluid dynamics model of the human nasal passages. *Journal of Aerosol Medicine, 20,* 59–74.

Kino, A., Takahashi, M., Ashiku, S. K., Decamp, M. M., Lenkinski, R. E., & Hatabu, H. (2007). Optimal breathing protocol for dynamic contrast-enhanced MRI of solitary pulmonary nodules at 3 T. *European Journal Radiology, 64,* 397–400.

Kirkpatrick, A., & Willson, B. (1998). Computation and experimentation on the web with application to internal combustion engines. *Journal of Engineering Education, 87,* 529–537.

Kleinstreuer, C., & Zhang, Z. (2003). Laminar-to-turbulent fluid-particle flows in a human airway model. *International Journal of Multiphase Flow, 29,* 271–289.

Kleinstreuer, C., & Zhang, Z. (2010). Airflow and particle transport in the human respiratory system. *Annual Review of Fluid Mechanics, 42,* 301–334.

Krieger, J. (1992). Long-term compliance with nasal continuous positive airway pressure (CPAP) in obstructive sleep apnea patients and nonapneic snorers. *Sleep, 15,* S42–46.

Kublik, H., & Vidgren, M. T. (1998). Nasal delivery systems and their effect on deposition and absorption. *Advanced Drug Delivery Reviews, 29,* 157–177.

Kuipers, J. A. M. (2000). Multilevel modelling of dispersed multiphase flows. *Oil & Gas Science and Technology—Rev. IFP, 55,* 427–435.

Kumar, H., Tawhai, M. H., Hoffman, E. A., & Lin, C.-L. (2009). The effects of geometry on airflow in the acinar region of the human lung. *Journal of Biomechanics, 42,* 1635–1642.

Lang, C., Grützenmacher, S., Mlynski, B., Plontke, S., & Mlynski, G. (2003). Investigating the nasal cycle using endoscopy, rhinoresistometry, and acoustic rhinometry. *The Laryngoscope, 113,* 284–289.

Lee, J.-H., Na, Y., Kim, S.-K., & Chung, S.-K. (2010). Unsteady flow characteristics through a human nasal airway. *Respiratory Physiology & Neurobiology, 172,* 136–146.

Lefebvre, A. H. (1989). *Atomization and Sprays*. New York: Hemisphere Publishing Corporation.

Leith, D. (1987). Drag on nonspherical objects. *Aerosol Science and Technology, 6,* 153–161.

Lerman, A. (1979). *Geochemical processes*. New York: Wiley.

Li, A., & Ahmadi, G. (1992). Dispersion and deposition of spherical particles from point sources in a turbulent channel flow. *Aerosol Science and Technology, 16,* 209–226.

Li, A., & Ahmadi, G. (1993). Deposition of aerosols on surfaces in a turbulent channel flow. *International Journal of Engineering Science, 31,* 435–451.

Li, Z., Kleinstreuer, C., & Zhang, Z. (2007). Simulation of airflow fields and microparticle deposition in realistic human lung airway models. Part I: Airflow patterns. *European Journal of Mechanics B/Fluids, 26,* 632–649.

Lienar, K., Leiacker, R., Lindemann, J., Rettinger, G., & Keck, T. (2003). Nasal mucosal temperature after exposure to cold, dry air and hot, humid air. *Acta Otolaryngol, 123,* 851–856.

Lin, C.-L., Tawhai, M. H., McLennan, G., & Hoffman, E. A. (2007). Characteristics of the turbulent laryngeal jet and its effect on airflow in the human intra-thoracic airways. *Respiratory Physiology & Neurobiology, 157,* 295–309.

Lindemann, J., Brambs, H.-J., Keck, T., Wiesmiller, K. M., Rettinger, G., & Pless, D. (2005). Numerical simulation of intranasal airflow after radical sinus surgery. *American Journal of Otolaryngology, 26,* 175–180.

Lippman, M. (1990). Effects of fibre charcteristics on lung deposition, retention and disease. *Environmental Health Perspectives, 88,* 311–317.

Liseikin, V. D. (1999). *Grid generation methods*. Berlin: Springer-Verlag.

Littman, H., Morgan, M. H., Jovanovic, S. D., Paccione, J. D., Grbavcic, Z. B., & Vukovic, D. V. (1995). Effect of particle diameter, particle density and loading ratio on the effective drag coefficient in steady turbulent gas-solids transport. *Powder Technology, 84,* 49–56.

Liu, Y., Matida, E. A., & Johnson, M. R. (2010a). Experimental measurements and computational modeling of aerosol deposition in the Carleton-Civic standardized human nasal cavity. *Journal of Aerosol Science, 41,* 569–586.

Liu, Y., So, R. M. C., & Zhang, C. H. (2003). Modeling the bifurcating flow in an asymmetric human lung airway. *Journal of Biomechanics, 36,* 951–959.

Liu, Z., Xu, X., Lim, F. F. J., Luo, X., Hirtum, A., & Hill, N. A. (2010b). Modeling and Simulation of Human Upper Airway. In C. T. Lim & J. C. H. Goh (Eds.), *6th World Congress of Biomechanics (WCB 2010)* 1–6 August 2010. (pp. 686–689). Singapore: Springer

Lo, S. H. (1985). A new mesh generation scheme for arbitrary planar domains. *International Journal Numerical Methods Engineering, 21,* 1403–1426.

Longest, P. W., & Xi, J. (2007). Computational investigation of particle inertia effects on submicron aerosol deposition in the respiratory tract. *Journal of Aerosol Science, 38,* 111–130.

Luo, H. Y., & Liu, Y. (2009). Particle deposition in a CT-scanned human lung airway. *Journal of Biomechanics, 42,* 1869–1876.

Malve, M., del Palomar, A. P., Chandra, S., Lopez-Villalobos, J. L., Finol, E. A., Ginel, A., & Doblare, M. (2011). FSI Analysis of a Human Trachea Before and After Prosthesis Implantation. *Journal of Biomechanical Engineering, 133,* 071003–071012.

Marcum, D. L., & Weatherill, N. P. (1995). Unstructured grid generation using iterative point insertion and local reconnection. *AIAA, 33,* 1619–1625.

Marr, D., & Hildreth, E. (1980). Theory of edge detection. *Proceedings of Royal Society of London, 207,* 187–217.

Martonen, T. B., Zhang, Z., & Lessmann, R. C. (1993). Fluid dynamics of the human larynx and upper tracheobronchial airways. *Aerosol science and technology, 19,* 23.

Mavriplis, D. J. (1997). Unstructured grid techniques. *Annual Review of Fluid Mechanics, 29,* 473–514.

Mazumdar, S., & Chen, Q. (2007). Impact of moving bodies on airflow and contaminant transport inside aircraft cabins., In *Proceedings of the 10th International Conference on Air Distribution in Rooms, Roomvent 2007*, Helsinki, Finland, 165.

McCarthy, J. R., Kelly, K. A., Sun, E. Y., & Weissleder, R. (2007). Targeted delivery of multifunctional magnetic nanoparticles. *Nanomedicine, 2,* 153–167.

McLaughlin, J. B. (1989). Aerosol Particle Deposition in Numerically Simulated Channel Flow. *Physics of Fluids, A7,* 1211–1224.

McLaughlin, J. B. (1991). Inertial migration of a small sphere in linear shear flows. *Journal Fluid Mechanics, 224,* 261–274.

McNitt-Gray, M. F. (2002). AAPM/RSNA physics tutorial for residents: topics in CT. *Radiographics, 22,* 1541–1553.

Mead, J., Takishima, T., & Leith, D. (1970). Stress distribution in lungs: A model of pulmonary elasticity. *Journal of Applied Physiology, 28,* 596–608.

Mei, R. (1992). An approximate expression for the shear lift force on a spherical particle at finite reynolds number. *International Journal of Multiphase Flow, 18,* 145–147.

Menter, F. R. (1994). Two-equation eddy-viscosity turbulence models for engineering applications. *American Institute of Aeronautics and Astronautics Journal, 32,* 1598–1605.

Menter, F. R., Langtry, R. B., Likki, S. R., Suzen, Y. B., Huang, P. G., & Volker, S. (2006). A correlation-based transition model using local variables—Part I: model formulation. *Journal of Turbomachinery, 128,* 413–422.

Mitsakou, C., Mitrakos, D., Neofytou, P., & Housiadas, C. (2007). A simple mechanistic model of deposition of water-soluble aerosol particles in the mouth and throat. *Journal of Aerosol Medicine, 20,* 519–529.

Moore, K. L., & Dalley, A. F. (2006). *Clinically oriented anatomy*. Baltimore: Lippincott Williams and Wilkins.

Morgan, W. K. C., Reger, R. B., & Tucker, D. M. (1997). Health effects of diesel emissions. *Annals of Occupational Hygiene, 41,* 643–658.

Morsi, S. A., & Alexander, A. J. (1972). An investigation of particle trajectories in two-phase flow systems. *Journal Fluid Mechanics, 55,* 193–208.

Moshfegh, A., Shams, M., Ahmadi, G., & Ebrahimi, R. (2009). A novel surface-slip correction for microparticles motion. *Colloids and Surfaces A: Physicochemical and Engineering Aspects, 345,* 112–120.

Naftali, S., Rosenfeld, M., Wolf, M., & Elad, D. (2005). The air-conditioning capacity of the human nose. *Annals of Biomedical Engineering, 33,* 545–553.

Nallasamy, M. (1987). Turbulence models and their applications to the prediction of internal flows: A review. *Computers & Fluids, 15,* 151–194.

Nasr, H., Ahmadi, G., & Mclaughlin, J. B. (2009). A DNS study of effects of particle-particle collisions and two-way coupling on particle deposition and phasic fluctuations. *Journal of Fluid Mechanics, 640,* 507–536.

Newman, S. P., Moren, F., & Clarke, S. W. (1998). Deposition pattern of nasal sprays in man. *Rhinology, 26*(2), 111–120.

Nowak, N., Kakade, P. P., & Annapragada, A. V. (2003). Computational fluid dynamics simulation of airflow and aerosol deposition in human lungs. *Annals of Biomedical Engineering, 31,* 374–390.

Nucci, G., Suki, B., & Lutchen, K. (2003). Modeling airflow-related shear stress during heterogeneous constriction and mechanical ventilation. *Journal of Applied Physiology, 95,* 348–356.

O'Rourke, P. J., & Amsden, A. A. (1987). *The tab method for numerical calculation of spray droplet breakup*.

Oberdörster, G., Sharp, Z., Atudorei, V., Elder, A., Gelein, R., Kreyling, W., & Cox, C. (2004). Translocation of inhaled ultrafine particles to the brain. *Inhalation Toxicology, 16,* 437–445.

Oberdörster, G., Oberdörster, E., & Oberdörster, J. (2005). Nanotoxicology: An emerging discipline evolving from studies of ultrafine particles environmental health perspectives. *Environmental Health Perspectives, 113,* 823–839.

Oseen, C. W. (1910). Uber die stokessche formel und uber die verwandte aufgabe in der hydrodynamik. *Arkiv Math Aston Fys, 6,* 237–262.

Otsu, N. (1979). A threshold selection method from grey-level histograms. *IEEE Transactions Systems, Man, and Cybernetics, 9,* 62–66.

Ounis, H., Ahmadi, G., & McLaughlin, J. B. (1991a). Brownian diffusion of submicrometer particles in the viscous sublayer. *Journal of Colloid and Interface Science, 143,* 266–277.

Ounis, H., Ahmadi, G., & McLaughlin, J. B. (1991b). Brownian diffusion of submicrometer particles in the viscous sublayer. *Journal Colloid and Interface Science, 143,* 266–277.

Ozlugedik, S., Nakiboglu, G., Sert, C., Elhan, A., Tonuk, E., Akyar, S., & Tekdemir, I. (2008). Numerical Study of the Aerodynamic Effects of Septoplasty and Partial Lateral Turbinectomy. *The Laryngoscope, 118,* 330–334.

Papavergos, P. G., & Hedley, A. B. (1984). Particle deposition behaviour from turbulent flows. *Chemical Engineering Research and Design, 62,* 275–295.

Pascual, R. M., & Peters, S. P. (2005). Airway remodeling contributes to the progressive loss of lung function in asthma: An overview. *Journal of Allergy and Clinical Immunology, 116,* 477–486.

Patankar, S. V. (1980). *Numerical heat transfer and fluid flow*. Taylor & Francis ISBN: 9780891165224.

Pattle, R. E. (1961). The retention of gases and particles in the human nose. In C. N. Davies (Ed.), *Inhaled particles and vapors* (302–309). Oxford: Pergamon Press.

Pedley, T. J., Schroter, R. C., & Sudlow, M. F. (1977). Gas flow and mixing in the airways. In J. West (Ed.), *Bioengineering Aspects of the Lung.* New York: Dekker.

Pilch, M., & Erdman, C. A. (1987). Use of breakup time data and velocity history data to predict the maximum size of stable fragments for acceleration-induced breakup of a liquid drop. *International Journal of Multiphase Flow, 13,* 741–757.

Pless, D., Keck, T., Wiesmiller, K., Rettinger, G., Aschoff, A. J., Fleiter, T. R., & Lindemann, J. (2004). Numerical simulation of air temperature and airflow patterns in the human nose during expiration. *Clinical Otolaryngology, 29,* 642–647.

Polo, O., Berthon-Jones, M., Douglas, N. J., & Sullivan, C. E. (1994). Management of obstructive sleep apnoea/hypopnoea syndrome. *The Lancet, 344,* 656–660.

Poussou, S. B., Mazumdar, S., Plesniak, M. W., Sojka, P. E., & Chen, Q. (2010). Flow and contaminant transport in an airliner cabin induced by a moving body: Model experiments and CFD prediction. *Atmospheric Environment, 44,* 2830–2839.

Proctor, D. F. (1982). The upper airway. In D. F. Proctor & I. Anderson (Eds.), *The Nose* (22–43). New York: Elsevier Biomedical Press.

Radjaï, F., & Dubois, F. (Eds.). (2011). *Discrete-element Modeling of Granular Materials*. France: Wiley, University of Montpellier.

Rasani, M. R., Inthavong, K., & Tu, J. Y. (2011). Simulation of pharyngeal airway interaction with air flow using low-re turbulence model. *Modelling and Simulation in Engineering, 2011,* 1–9.

Reeves-Hoche, M., Meck, R., & Zwillich, C. (1994). Nasal CPAP: An objective evaluation of patient compliance. *American Journal of Respiratory and Critical Care Medicine, 149,* 149–154.

Regan, M., & Sheppard, S. (1996). Interactive multimedia courseware and the hands-on learning experience: An assessment study. *Journal of Engineering Education, 85,* 123–131.

Reitz, R. D., & Diwakar, R. (1987). Structure of high-pressure fuel sprays. *SAE Technical Paper,* 870598.

Richmond, C. (2004). Sir godfrey hounsfield. *British Medical Journal, 329,* 687.

Ridler, T. W., & Calvard, S. (1978). Picture thresholding using an iterative selection method. *IEEE Transactions Systems, Man and Cybernetics, 8,* 630–632.

Rizk, N. K., & Lefebvre, A. H. (1985). Internal flow characteristics of simplex swirl atomisers. *AIAA Journal of Propulsion and Power, 1,* 193–199.

Robert, G. H. (2001). Forced inspiratory nasal flow–volume curves: A simple test of nasal airflow. *Mayo Clinic Proceedings, 76,* 990–994.

Rogers, D. F. (1994). Airway goblet cells: Responsive and adaptable front-line defenders. *European Respiratory Journal, 7,* 1690–1708.

Roy, C. (2003). Grid convergence error analysis for mixed-order numerical schemes. *AIAA, 41*(4), 595–604.

Saffman, P. G. (1965). The lift on a small sphere in a slow shear flow. *Journal of Fluid Mechanics, 22,* 385–400.

Saffman, P. G. (1968). Corrigendum to the lift on a small sphere in a slow shear flow. *Journal of Fluid Mechanics, 31*(3), 624.

Sandeau, J., Katz, I., Fodil, R., Louis, B., Apiou-Sbirlea, G., Caillibotte, G., & Isabey, D. (2010). CFD simulation of particle deposition in a reconstructed human oral extrathoracic airway for air and helium-oxygen mixtures. *Journal of Aerosol Science, 41,* 281–294.

Sauret, V., Halson, P. M., Brown, I. W., Fleming, J. S., & Bailey, A. G. (2002). Study of the three-dimensional geometry of the central conducting airways in man using computed tomographic (CT) images. *Journal of Anatomy, 200,* 123–134.

Schlesinger, R. B., & Lippmann, M. (1978). Selective particle deposition and bronchogenic carcinoma. *Environmental Research, 15,* 424–431.

Schmehl, R., Maier, G., & Wittig, S. (2000). CFD analysis of fuel atomization, secondary droplet breakup and spray dispersion in the premix duct of a LPP combustor. In *Proceedings of 8th International Conference on Liquid Atomization and Spray Systems,* Pasadena, CA, USA.

Schroeter, J. D., Kimbell, J. S., & Asgharian, B. (2006). Analysis of particle deposition in the turbinate and olfactory regions using a human nasal computational fluid dynamics model. *Journal of Aerosol Medicine, 19,* 301–313.

Seren, E., & Seren, S. (2009). Morphological adaptation of the nasal valve area to climate. *Medical Hypotheses, 72,* 471–472.

Shanley, K. T., Zamankhan, P., Ahmadi, G., Hopke, P. K., & Cheng, Y.-S. (2008). Numerical simulations investigating the regional and overall deposition efficiency of the human nasal cavity. *Inhalation Toxicology, 20,* 1093–1100.

Shephard, M. S., & Georges, M. K. (1991). Automatic three-dimensional mesh generation by the finite octree technique. *International Journal for Numerical Methods in Engineering, 32,* 709–749.

Shi, H. W., Kleinstreuer, C., & Zhang, Z. (2007). Modeling of inertial particle transport and deposition in human nasal cavities with wall roughness. *Journal of Aerosol Science, 38,* 398–419.

Shi, H., Kleinstreuer, C., & Zhang, Z. (2008). Dilute suspension flow with nanoparticle deposition in a representative nasal airway model. *Physics of Fluids, 20,* 1–23.

Slutsky, A. S., Berdine, G. G., & Drazen, J. M. (1981). Oscillatory flow and quasi-steady behavior in a model of human central airways. *Journal of Applied Physiology, 50,* 1293–1299.

Spalart, P. R. (2000). Strategies for turbulence modelling and simulations. *International Journal of Heat and Fluid Flow, 21,* 25–263.

Stabl, W. H. (1992). Experimental investigation of the vortex flow on delta wings at high incidence. *AIAA Journal, 30,* 1027–1032.

Stöber, W. (1972). Dynamic shape factors of nonspherical aerosol particles. In T. Mercer et. al (Eds.), *Assessment of airborne particles* (pp. 249–289). Springfield: Charles C. Thomas.

Su, W. C., & Cheng, Y. S. (2005). Deposition of fiber in the human nasal airway. *Aerosol Science andTechnology, 39,* 888–901.

Sullivan, K. J., & Chang, H. K. (1991). Steady and oscillatory trans-nasal pressure-flow relationships in healthy adults. *Journal of Applied Physiology, 71,* 983–992.

Suman, J. D., Laube, B. L., Lin, T. C., Brouet, G., & Dalby, R. (2002). Validity of in vitro tests on aqueous spray pumps as surrogates for nasal deposition. *Pharma Res, 19,* 1–6.

Sung, J., Padilla, D., Garcia-Contreras, L., VerBerkmoes, J., Durbin, D., Peloquin, C., Elbert, K., Hickey, A., & Edwards, D. (2009). Formulation and pharmacokinetics of self-assembled rifampicin nanoparticle systems for pulmonary delivery. *Pharmaceutical Research, 26,* 1847–1855.

Suri, J., Wilson, D., Laxminarayan, S. (2005). *Handbook of Biomedical Image Analysis: Volume II: Segmentation Models*. Springer.

Sussman, R. G., Cohen, B. S., & Lippmann, M. (1991). Asbestos fiber deposition in human tracheobronchial cast. I.- Experimental. *Inhalation Toxicology, 3,* 145–160.

Swift, D. L., & Kesavanathan, J. (1996). The anterior human nasal passage as a fibrous filter for particles. *Chemical Engineering Communications, 151,* 65–78.

Sznitman, J. (2008). Respiratory flows in the pulmonary acinus and insights on the control of alveolar flows. In *Institute of Fluid Dynamics*, Swiss Federal Institute of Technology, Zurich, 240.

Tannehill, J. C., Anderson, D. A., & Pletcher, R. H. (1997). *Computational fluid mechanics and heat transfer*. Hemisphere Publications, ISBN: 156032046X.

Tawahai, M. H., & Hunter, P. J. (2004). Modeling water vapor and heat transfer in the normal and the intubated airways. *Annals of Biomedical Engineering, 32,* 609–622.

Tawhai, M. H., Pullan, A. J., & Hunter, P. J. (2000). Generation of an anatomically based three-dimensional model of the conducting airways. *Annals Biomedical Engineering, 28,* 793–802.

Taylor, D. J., Doorly, D. J., Schroter, R. C. (2010). Inflow boundary profile prescription for numerical simulation of nasal airflow. *Journal of The Royal Society Interface, 7,* 515–527.

Thompson, J. F., Warsi, Z. U. A., & Mastin, C. W. (1985). *Numerical Grid Generation—Foundations and Applications*. New York: Elsevier.

Thomson, D. J. (1987). Criteria for the selection of stochastic models of particle trajectories in turbulent flows. *Journal of Fluid Mechanics, 180,* 529–556.

Tian, G., & Longest, P. W. (2010). Development of a CFD boundary condition to model transient vapor absorption in the respiratory airways. *Journal of Biomechanical Engineering, 132,* 051003–051013.

Tian, L., & Ahmadi, G. (2007). Particle deposition in turbulent duct flow- Comparison of different model predictions. *Journal of Aerosol Science, 38,* 377–397.

Tian, Z. F., Inthavong, K., & Tu, J. Y. (2007). Deposition of inhaled wood dust in the nasal cavity. *Inhalation Toxicology, 19,* 1155–1165.

Timbrell, V. (1982). Deposition and retention of fibres in the human lung. *Annals of Occupational Hygiene, 26,* 347–369.

Tran-Cong, S., Gay, M., & Michaelides, E. E. (2004). Drag coefficients of irregularly shaped particles. *Powder Technology, 139,* 21–32.

Tsuda, A., Henry, F. S., Butler, J. P. (1995). Chaotic mixing of alveolated duct flow in rhythmically expanding pulmonary acinus. *Journal of Applied Physiology, 79,* 1055–1063.

Tsuda, A., Filipovic, N., Haberthur, D., Dickie, R., Matsui, Y., Stampanoni, M., Schittny, J. C. (2008). Finite element 3D reconstruction of the pulmonary acinus imaged by synchrotron X-ray tomography. *Journal of Applied Physiology, 105,* 964–976.

Tu, J., Yeoh, G. H., & Liu, C. (2008). *Computational fluid dynamics: A practical approach*. Butterworth-Heinemann. ISBN: 0750685638.

Tu, J. Y., & Fuchs, L. (1992). Overlapping grids and multigrid methods for three-dimensional unsteady flow calculations in IC engines. *International Journal Numerical Methods Fluids, 15,* 693–714.

Umbaugh, S. (2005). *Computer imaging: Digital image analysis and processing*. Taylor & Francis.

van Ertbruggen, C., Corieri, P., Theunissen, R., Riethmuller, M. L., & Darquenne, C. (2008). Validation of CFD predictions of flow in a 3D alveolated bend with experimental data. *Journal of Biomechanics, 41,* 399–405.

van Ertbruggen, C., Hirsch, C., & Paiva, M. (2005). Anatomically based three-dimensional model of airways to simulate flow and particle transport using computational fluid dynamics. *Journal of Applied Physiology, 98,* 970–980.

Vanpeperstraete, F. (1974). The cartilaginous skeleton of the bronchial tree. *Advances in Anatomical Embryology Cell Biology, 48,* 1–15.

Vargaftik, N. B. (1975). *Tables on Thermophysical Properties of Liquids and Gases*. Washington, DC: Hemisphere.

Versteeg, H. K., & Malalasekera, W. (2007). *An introduction to computational fluid dynamics: The finite volume method*. Pearson Education Ltd.

Vignola, A. M., Kips, J., & Bousquet, J. (2000). Tissue remodeling as a feature of persistent asthma. *Journal of Allergy and Clinical Immunology, 105,* 1041–1053.

Wadell, H. (1933). Sphericity and roundness of rock particles. *Journal of Geology, 41,* 310–331.

Wang, C., Altes, T. A., Mugler, J. P., Miller, G. W., Ruppert, K., Mata, J. F., Cates, G. D., Borish, L., & de Lange, E. E. (2008). Assessment of the lung microstructure in patients with asthma using hyperpolarized 3He diffusion MRI at two time scales: Comparison with healthy subjects and patients with COPD. *Journal of Magnetic Resonance Imaging, 28,* 80–88.

Wang, S. M., Inthavong, K., Wen, J., Tu, J. Y., & Xue, C. L. (2009). Comparison of micron- and nanoparticle deposition patterns in a realistic human nasal cavity. *Respiratory Physiology & Neurobiology, 166,* 142–151.

Wankat, P. C. (2002). Integrating the Use of Commercial Simulators into Lecture Courses. *Journal of Engineering Education, 91,* 19–23.

Weibel, E. R. (1963). *Morphometry of the human lung*. New York: Academic Press.

Weibel, E. R. (1997). Design of airways and blood vessels considered as branching trees. In R. G. Crystal, J. B. West, E. R. Weibel & P. J. Barnes, (eds.) *The Lung: Scientific Foundations* (pp. 1061–1071). Philadelphia: Lippincott-Raven Publishers.

Weinhold, I., & Mlynski, G. (2004). Numerical simulation of airflow in the human nose. *European Archive Otorhinolaryngology, 261,* 452–455.

Wen, J., Inthavong, K., Tu, J. Y., & Wang, S. (2008). Numerical simulations for detailed airflow dynamics in a human nasal cavity. *Respiratory Physiology & Neurobiology, 161,* 125–135.

Wendt, J. F., & Anderson, J. D. (2009). *Computational fluid dynamics: An introduction*. Springer.

West, J. B. (2008). *Respiratory physiology: The essentials*. Wolters Kluwer Health/Lippincott Williams & Wilkins.

Wilcox, D. (1993). *Turbulence Modeling for CFD*. DCW Industries, Inc., 5354 Palm Drive, La Canada, California 91011.

Womersley, J. R. (1955). Method for the calculation of velocity, rate of flow and viscous drag in arteries when the pressure gradient is known. *Journal Physiol,* 127.

Wood, N. B. (1981). A simple method for the calculation of turbulent deposition to smooth and rough surfaces. *Journal of Aerosol Science, 12,* 275–290.

Xi, J., Longest, P. W., & Martonen, T. B. (2008). Effects of the laryngeal jet on nano- and microparticle transport and deposition in an approximate model of the upper tracheobronchial airways. *Journal of Applied Physiology, 104,* 1761–1777.

Xi, J., Si, X., Kim, J. W., & Berlinski, A. (2011). Simulation of airflow and aerosol deposition in the nasal cavity of a 5-year-old child. *Journal of Aerosol Science, 42,*156–173.

Xiong, G., Zhan, J., Zuo, K., Li, J., Rong, L., & Xu, G. (2008). Numerical flow simulation in the post-endoscopic sinus surgery nasal cavity. *Medical and Biological Engineering and Computing, 46,* 1161–1167.

Yeh, H.-C., & Schum, G. M. (1980). Models of human lung airways and their application to inhaled particle deposition. *Bulletin of Mathematical Biology, 42,* 461–480.

Yeoh, G. H., & Tu, J. (2009). *Computational Techniques for Multiphase Flows*. Oxford: Elsevier Science & Technology

Yerry, M., & Shephard, M. (1984). A modified-quadtree approach to finite element mesh generation. *IEEE Computer Graphics Applications, 3,* 39–46.

Yushkevich, P. A., Piven, J., Hazlett, H. C., Smith, R. G., Ho, S., Gee, J. C., Gerig, G. (2006). User-guided 3D active contour segmentation of anatomical structures: Significantly improved efficiency and reliability. *NeuroImage, 31,* 1116–1128.

Zaichik, L., Alipchenkov, V. M., & Sinaiski, E. G. (2008). *Particles in turbulent flows*. Wiley-VCH.

Zamankhan, P., Ahmadi, G., Wang, Z., Hopke, P. H., Cheng, Y. S., Su, W. C., & Leonard, D. (2006). Airflow and deposition of nanoparticles in a human nasal cavity. *Aerosol Science and Technology, 40,* 463–476.

Zhang, H., & Ahmadi, G. (2000). Aerosol particle transport and deposition in vertical and horizontal turbulent duct flows. *Journal of Fluid Mechanics, 406,* 55–80.

Zhang, Y., Finlay, W. H., & Matida, E. A. (2004). Particle deposition measurements and numerical simulation in a highly idealized mouth-throat. *Journal of Aerosol Science, 35,* 789–803.

Zhang, Z., Kleinstreuer, C., & Kim, C. S. (2002). Cyclic micron-size particle inhalation and deposition in a triple bifurcation lung airway model. *Journal of Aerosol Science, 33,* 257–281.

Zhang, Z., & Kleinstreuer, C. (2003). Modeling of low Reynolds number turbulent flows in locally constricted conduits: A comparison study. *AIAA Journal, 41,* 831–840.

Zhang, Z., Kleinstreuer, C., Donohue, J. F., & Kim, C. S. (2005a). Comparison of micro- and nano-size particle depositions in a human upper airway model. *Journal of Aerosol Science, 36,* 211–233.

Zhang, Z., Kleinstreuer, C., Donohue, J. F., & Kim, C. S. (2005b). Comparison of micro- and nano-size particle depositions in a human upper airway model. *Journal of Aerosol Science, 36,* 211–233.

Zhang, Z., Kleinstreuer, C., & Kim, C. S. (2008a). Airflow and nanoparticle deposition in a 16-generation tracheobronchial airway model. *Annals of Biomedical Engineering, 36,* 2095–2110.

Zhang, Z., Kleinstreuer, C., & Kim, C. S. (2008b). Comparison of analytical and CFD models with regard to micron particle deposition in a human16-generation tracheobronchial airway model. *Journal of Aerosol Science*. doi: 10.1016/j.jaerosci.2008.08.003.

Zhang, Z., Chen, X., Mazumdar, S., Zhang, T., & Chen, Q. (2009). Experimental and numerical investigation of airflow and contaminant transport in an airliner cabin mockup. *Building and Environment, 44,* 85–94.

Zhao, K., Scherer, P. W., Hajiloo, S. A., & Dalton, P. (2004). Effect of Anatomy on human nasal air flow and odorant transport patterns: Implications for olfaction. *Chemical Senses, 29,* 365–379.

Zhao, K., Dalton, P., Yang, G. C., & Scherer, P. W. (2006). Numerical modeling of turbulent and laminar airflow and odorant transport during sniffing in the human and rat nose. *Chemical Senses, 31,* 107–118.

Zhu, H. P., Zhou, Z. Y., Yang, R. Y., & Yu, A. B. (2007). Discrete particle simulation of particulate systems: Theoretical developments. *Chemical Engineering Science, 62,* 3378–3396.

Zhu, J. H., Lee, H. P., Lim, K. M., Lee, S. J., & Wang, D. Y. (2011). Evaluation and comparison of nasal airway flow patterns among three subjects from Caucasian, Chinese and Indian ethnic groups using computational fluid dynamics simulation. *Respiratory Physiology & Neurobiology, 175,* 62–69.

Zwartz, G. J., & Guilmette, R. A. (2001). Effect of flow rate on particle deposition in a replica of a human nasal airway. *Inhalation Toxicology, 13,* 109–127.

# Index




J. Tu et al., *Computational Fluid and Particle Dynamics in the Human Respiratory System,* Biological and Medical Physics, Biomedical Engineering
DOI 10.1007/978-94-007-4488-2, © Springer Science+Business Media Dordrecht 2013